Determining Velocity, Temperature and Occupancy Comfort within a 3D Room

by

Adel Sulaiman Hamad Al-Hamed

A Thesis Presented to the

FACULTY OF THE COLLEGE OF GRADUATE STUDIES

KING FAHD UNIVERSITY OF PETROLEUM & MINERALS

DHAHRAN, SAUDI ARABIA

In Partial Fulfillment of the
Requirements for the Degree of

MASTER OF SCIENCE

In

MECHANICAL ENGINEERING

January, 1990

INFORMATION TO USERS

DETERMINING VELOCITY, TEMPERATURE AND OCCUPANCY COMFORT WITHIN A 3-D. ROOM.

BY

ADEL SULAIMAN HAMAD AL-HAMED

A Thesis Presented to the

FACULTY OF THE COLLEGE OF GRADUATE STUDIES

KING FAHD UNIVERSITY OF PETROLEUM & MINERALS

DHAHRAN, SAUDI ARABIA

In Partial Fulfillment of the
Requirements for the Degree of

MASTER OF SCIENCE

In

MECHANICAL ENGINEERING

JANUARY   1990

UMI Number: 1379309

UMI
300 North Zeeb Road
Ann Arbor, MI 48103

KING FAHD UNIVERSITY OF PETROLEUM AND MINERALS

DHAHRAN 31261, SAUDI ARABIA

COLLEGE OF GRADUATE STUDIES

This thesis, written by *ADEL SULAIMAN HAMAD AL-HAMED* under the direction of his Thesis Advisor and approved by his Thesis Committee, has been presented to and accepted by the Dean of the College of Graduate Studies, in partial fulfillment of the requirements for the degree of *MASTER OF SCIENCE IN MECHANICAL ENGINEERING.*

Spec
A
1
.H3533

C.2

10/2633/10/3226

Thesis Committee

Thesis Advisor(Dr. A.F.M. Abdul Ali)

Member(Dr. M.A.Z. Hasan)

Member(Dr. S.A.M. Said)

Department Chairmen
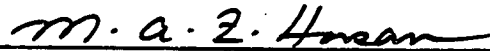
Dean, College of Graduate Studies

18-9-90

Date

DEDICATION

This Thesis is dedicated to my dear Mother and Father, my Brothers Nabil and Omar, my Sister, my Wife and my beloved Children Mohammed and May.

ACKNOWLEDGEMENT

TABLE OF CONTENTS

CHAPTER 7
RESULTS AND DISCUSION   171

LIST OF TABLES

LIST OF FIGURES

xxiii

ABSTRACT

A computer program for simulating 3-D room ventilation problems is described and employed to predict the mean air temperatures and velocities for a number of realistic supply air inlet and outlet locations. The program, TEACH-3D, solves the steady state conservation equations of mass, momentum and thermal energy using a finite difference scheme, based on the control volume approach. Due to the nature of turbulence, encountered in this research, the k- ε turbulence model was selected to transform the open form of the governing conservation equations to closed form. The SIMPLE scheme was employed in the numerical code to handle the velocity-pressure link. The flow field predicted by the numerical code are supported by experimental measurements done by others.

To decide on the effect the geometrical locations of the inlet and outlet has on comfort, the computed results are translated into PMV indices over the entire occupied zone of the room. The PPD is also employed to render judgement on the human thermal comfort response, such that if the PPD is less than 20%, then comfort is claimed to be attained. In addition to varying the inlet and outlet locations, the supply air temperature and velocity has also been varied for a particular arrangement in an attempt to achieve thermal comfort.

Out of the four different arrangements of supply and exhaust ports investigated here, the one having the inlet on the floor near the West side wall and the outlet on the ceiling near the East side wall satisfied occupancy thermal comfort. While the arrangement least achieving thermal comfort of the occupants is the one having the inlet on the ceiling near the West wall and the outlet on the East wall adjacent to the floor.

الخلاصة

برنامج كمبيوتر لتمثيل التهوية في غرف ثلاثية الأبعاد يتم وصفه واستخدامه للتنبؤ عن متوسط درجات الحرارة والسرعة الاتجاهية للهواء في عدد من الأنظمة الواقعية لمواقع منفذ ومخرج الهواء في الغرف . البرنامج TEACH - 3 D يحل معادلات محافظة الكتلة وكمية التحرك والطاقة الحرارية في حالة الاستقرار باستعمال نظام الاختلاف المحدود مبنية على طريقة الحجم المحكم . ونظراً لطبيعة اضطراب الهواء في هذا البحث فقد تم اختيار نموذج الاضطراب ع – k لتحويل الهيئة المفتوحة للمعادلات الحاكمة إلى مغلقة . وكذلك فإن منهج SIMPLE استخدم في برنامج الكمبيوتر لمعالجة الرابطة بين السرعة الاتجاهية والضغط . ومجال انسياب الهواء المتنبأ بواسطة برنامج الكمبيوتر تم دعمه بواسطة قياسات مختبرية قام به آخرون . ولتحديد تأثير المواقع الجيومترية لمنفذ ومخرج الهواء على الراحة الحرارية فقد تم تحويل النتائج المحسوبة إلى إشارات PMV في جميع أرجاء النطاق المأهول من الغرفة . وكذلك تم استخدام الـ PPD للحكم في رد الفعل للبشر من ناحية الراحة الحرارية بحيث إذا كانت الـ PPD أقل من ٢٠ ٪ فيقتضي ذلك إدراك الراحة الحرارية . وكذلك فقد تم تغيير درجة الحرارة والسرعة الإتجاهية للهواء العابر من خلال المنفذ في محاولة الوصول إلى الراحة الحرارية . من مجموعة الأشكال الأربعة من منفذ الهواء ومخرجه المدروسة هنا فإن كون المنفذ على أرض الغرفة قريب من الجدار الغربي والمخرج على السقف قريب من الجدار الشرقي حقق الراحة الحرارية للساكنين . والشكل الذي حقق أقل راحة حرارية للساكنين كان بوجود منفذ الهواء على السقف قريب من الجدار الغربي والمخرج على الجدار الشرقي قريب من الأرضية .

CHAPTER I

INTRODUCTION

To state that a particular arrangement of an air conditioning system within a room to be satisfactory, with regard to the occupants thermal sensation response, necessitates previous knowledge of the distribution of temperature and velocity fields within the occupied space. In a practical air conditioning set up, the resulting fluid flow is, for the most part, turbulent, non-isothermal, recirculating and three dimensional. Thus, the task of estimating the velocity and temperature fields for such conditions by experimental measurements represent quite a difficult, if not a completely impossible undertaking. This statement may be substantiated by the fact that to produce a moderate estimate of velocity and temperature for a particular room design, will require the erection of a prototype for that room and experimental studies need to be carried out on the prototype to determine as much as may physically be possible about the flow field and then make an educated estimate or guess on the remaining part of the flow field. Apart from the fact that this estimate does not represent the actual occurrence within the designed room, any modifications or changes done to the design requires a compatible physical modification done to the prototype which is costly and time consuming. In addition to this, physical models are not always possible to construct at full scale. That is to say, air distribution studies for large enclosures (e.g. theaters, indoor stadiums,

1

auditoriums, etc.) can only be feasibly conducted with reduced scale models, such that the experimental investigations carried out on the scaled model should be made with dynamic and thermal similarity in mind if a proper comparison is to be made with the full scale room. This normally calls for the equality of the Reynolds number, Re, and the Archimedes number, Ar which is physically not possible to achieve for a particular model at the same time. Furthermore, since most of the air distribution methods developed through physical modelling are unique for a particular set up, experimentalests are quite often forced to use a rule of thumb approach for a somewhat different airconditioning arrangement. This, however, is not a desirable design practice, as it almost always over-estimates the need of the occupants by either supplying a cooler environment during summer or a warmer environment during winter. The result of this coarse approach is obviously inefficient systems, with regard to energy consumption. Moreover, occupants will, most likely, not attain the thermal sensation of comfort or close to it, which is actually the main and foremost objective of an effective air conditioning system.

In view of all what has been said above, numerical solutions may prove to be quite suitable for air distribution system design as results can be obtained readily and modifications can be implemented to the code, as required, within a relatively short space of time. Furthermore, the same numerical code may be employed as design optimization tools. However, due to the complexity of the air flow and heat transfer processes in a room, the numerical solutions to these flow problems use iterative procedures that require large computing time and memory.

Turbulent, recirculating (elliptic), non-isothermal air flow in a three dimensional enclosure is not determined by direct application of the full form of the equations describing the air flow, where these equations are as follows [1,2,3],

Conservation of Mass (Continuity) Equation

$$\frac{\partial \rho}{\partial t} + \frac{\partial}{\partial x_i} \left(\rho U_i \right) = 0 \tag{1.1}$$

Conservation of Momentum (Navier-Stokes) Equation:

$$\frac{\partial}{\partial t}\left(\rho \, U_i \right) + \frac{\partial}{\partial x_j} \left(\rho U_i U_j \right) = -\frac{\partial p}{\partial x_i} + \mu \frac{\partial^2 U_i}{\partial x_j \partial x_j} - \rho \cdot g_i + S_i \tag{1.2}$$

Thermal Energy Equation

$$\frac{\partial}{\partial t} (\rho \, T) + \frac{\partial}{\partial x_j} (\rho U_j T) = \lambda \frac{\partial^2 T}{\partial x_i \partial x_i} + \frac{1}{C_p}\left(\frac{\partial p}{\partial t}\right) + S_T \tag{1.3}$$

where U_i, g_i and S_i are the instantaneous velocity component, gravitational acceleration and momentum source term, in the x_i direction, respectively. p and T are the instantaneous static pressure and instantaneous temperature, respectively. ρ, ρ_r, μ, λ and C_p are the density, reference density, dynamic viscosity, thermal diffusivity and specific heat, respectively. To the knowledge of the author there has not been any serious breakthroughs in resolving the aforesaid equations, in their present form, for practical flow situations.

An attempt to use equations (1.1), (1.2) and (1.3) for real flow problems proves to be successful if supplemented by additional complementary relations. The relations implemented in this research are the turbulent kinetic energy (k) and the turbulent kinetic energy dissipation (ε) equations, the so-called k - ε turbulence model [3,4,5,6,15]. The transport equations of k and ε for a steady, buoyant and high Reynolds number flow are

Turbulence Kinetic Energy Equation

$$\frac{\partial}{\partial x_i}(\rho\, U_i k) = \frac{\partial}{\partial x_i}\left(\Gamma_k \frac{\partial k}{\partial x_i}\right) + \rho\,(S_k + S_B) - C_D\,\rho\,\varepsilon \tag{1.4}$$

Turbulence Kinetic Energy Dissipation Equation:

$$\frac{\partial}{\partial x_i}(\rho U_i \varepsilon) = \frac{\partial}{\partial x_i}\left(\Gamma_\varepsilon \frac{\partial \varepsilon}{\partial x_i}\right) + C_1\,\rho\,\frac{\varepsilon}{k}(S_k + S_B) - C_2\,\rho\frac{\varepsilon^2}{k} \tag{1.5}$$

By solving the conservation equations (i.e. continuity, momentum and energy), after introducing some simplifications to be described later, in conjunction with the turbulent kinetic energy equation and the corresponding dissipation equation, through an iterative approach, it is possible to evaluate the temperature and velocity fields within the enclosure.

It should be noted here that there are two major restrictions on using the k - ε turbulence model and these are :

1) Introducing the Boussinesq approximation [1,29,40,45] which assumes that the fluid is incompressible except in the buoyancy term.

2)   The constants used in the k - ε turbulence model need to be evaluated by experimental means which limits the general usage of the model.

The numerical code chosen to compute the relevant flow field variables is a modified three-dimensional version of the TEACH code developed at the Imperial College of London [31,32] where the idiom TEACH stands for T eaching E lliptic A xisymmetric C haracteristics H eruistically. This code uses the finite volume approach [43], which contains some of the characteristics of both the finite difference and the finite elements schemes, to discretize the relevant conservation equations and then solve for the corresponding discretization coefficients from which the variables describing the flow field may be estimated . In this research four different configurations of the inlet supply and outlet exhaust locations are investigated, such that the geometrical locations of these openings on the walls of the room are varied from one configuration to the other, and the resulting effect this will have on the flow field is investigated. The heat fluxes and temperatures of the walls of the room will be varied for two of the four configurations studied corresponding to different times of the day(i.e.: morning, noon and afternoon) resulting in three distinct wall boundary conditions , whereas the remaining configurations is only considered at one time, resulting in only one wall boundary condition.

By using these pertinent variables as input to the comfort equation [7,10] the thermal sensation response of the occupants may be estimated.

The thermal sensation response of the inhabitants are determined by using simple mathematical models that simulate human physiological regulatory response to the surrounding environment.

An earnest attempt has been conducted to make use of the Pierce and the KSU two-node models [9,10] but with limited success being achieved. In particular the KSU model proved to be insensitive to variations in clothing and activity of the occupants. As a result of this the author turned to Fanger's classical one-node thermo-regulatory model [7,8,10] . This mathematical model predicts the thermal comfort response of occupants in an enclosure by evaluating indices referred to as the P redicted M ean V ote (PMV) indices and handles a relatively wide range of situations and constraints. Moreover, the basic idea behind it is quite simple and straightforward, where it treats the human body as a whole, exchanging energy to the surrounding environment. By solving the energy balance equation over the human body the sensation indices are estimated. Fanger , by extensive investigations in human preception to the environment, was able to produce a thermal comfort scale given in table 1.1, below.

TABLE 1.1 Fanger's Thermal comfort scale.

PMV INDEX	HUMAN PHYSIOLOGICAL RESPONSE
-3	COLD
-2	COOL
-1	SLIGHTLY COOL
0	NEUTRAL
1	SLIGHTLY WARM
2	WARM
3	HOT

CHAPTER II

LITERATURE SURVEY

2.1 PREVIOUS WORK ON NUMERICAL SOLUTIONS

Interest grew quite rapidly in developing general fluid flow and heat transfer programs to simulate the flow of air in enclosures. One of the reasons that helped to fuel this sudden interest is mainly due to the advancements attained in the hardware and software of computer technology in the late Sixties and early Seventies. Forecasting the flow field of air in a room was even more of a concern in the mid-Seventies due to the attention given to energy and energy efficient systems, as a result of the oil embargo.

One of the most earliest studies done to implement numerical codes in the simulation of air movement and heat transfer within rooms was carried out by Neilson [12], through his Ph.D. thesis work, where he adopted a two-dimensional analysis approach such that the flow can be fully represented by a plane surface having the velocity components and gradients of fluid properties normal to the plane to be zero.

It was quite a common practice at Neilson's time, and still occuring at the present time, to assume roughly that a fluid flow is two dimensional even though in most cases it is not so. The motivation behind such an assumption being that once two dimensionality is assumed, stream function and vorticity may be used in preference to the primitive variables (i.e.: the

8

two velocity components and pressure) thus the whole problem is reduced by one less variable to solve for, which generally is an improvement and advantage to have but, on the condition that the assumption of two dimensionality is true. In reality, air flow in rooms are mostly three dimensional, where even if a slot diffuser is employed and placed at the symmetry plane of the room the wall end effects are felt almost through the room breadth.

Neilson also assumed the flow within the room as isothermal, the reasons being that during the time of his research work, which spanned from 1970 to 1973, most of the codes available were generally limited to the aforementioned restrictions as his investigation coincided with the infancy of numerical fluid flow simulations.

Holmberg et al. [13] in 1975, nearly repeated the work done by Neilson [12], mentioned earlier, where Holmberg's conclusions and shortcomings are quite identical.

Hjertager et al. [16] in 1977 applied numerical models to the study of turbulent air movement and heat transfer in rooms, which maybe considered as a one step improvement over the work done previously by Neilson and Holmberg, mentioned earlier. Hjertager employed a different formulation of the conservation equations in numerical form and solved them for the whole flow field in three dimensions using the primitive variable form (i.e. the three velocity components and pressure). An advantage of using primitive variables, in two dimensions, is that they can readily be extended to compute three dimensional flow configurations. The same may not be said of the stream function and vorticity method, since the

stream function cannot be defined in a three dimensional flow simulation. Comparisons with experiments for the isothermal situation was quite satisfactory, while the non- isothermal case compared poorly to the experiments conducted. The reason for such indiscrepancy may be attributed to the fact that he did not include a buoyancy generation term in the turbulent kinetic energy equation and the corresponding dissipation equation. Thus, Hjertager's work contained some of the weaknesses of previous works.

The investigation done by Larsson et al [18] may be considered as a special case of Hjertager's analysis, mentioned above, in a sense that the study was limited to two dimensional flow, which may be achieved by having the inlet and outlet ports span over the breadth of the room and neglecting the wall end effects. The study also considered non-isothermal situation. The numerical predictions of the temperature and velocity was claimed to compare moderately well with the experimental data. The contribution made by this work over its predecessors was the introduction of the buoyancy source term into the turbulent kinetic energy equation and the corresponding dissipation equation.

Neilson et al [17] used a formulation similar to that of Hjertager. He used the primitive variable approach instead of the stream function and vorticity method. Here, the authors limited the area of the computed flow domain in such a way to exclude the initial jet development zone, where the characteristics of a spreading wall jet, established through experimental work, were imposed as a boundary condition to the remaining part of the flow domain. This boundary was placed at a distance from the jet

source. The inclination for doing this was to reduce the number of grid lines and consequently the number of nodes necessary for the numerical prediction. The computed results compared quite well with the measurements made. The $k - \varepsilon$ turbulence model was also studied. Some of the weak points of this approach is that it may only be applied, with confidence, to the isothermal flow situation, where no accommodation to include buoyancy generation in both the turbulent kinetic energy equation and the corresponding dissipation equation has been attempted. Furthermore, to insist the exclusion of the initial jet development zone makes the problem specific and almost empirical, in the sense that for a different arrangement corresponding measurements must be made at the initial jet development zone, which deteriorates one of the intents of numerical predictions.

Restivo [6] in his Ph.D. thesis made a detailed study on turbulent flow in ventilated rooms, where it seems his experimental work was of a more concern than his numerical approach. His numerical analysis is similar, to an extent, to that of Hjertager [16] and Larsson [17], since Restivo implemented the non-isothermal flow for two dimensional investigations, while for three dimensional studies the flow was limited to isothermal situations. He also included the buoyancy source term in the turbulent kinetic energy and dissipation equations as did Larsson et al. [18]. Hence, no genuine evident advantage concerning the numerical investigation has been produced.

Neilson et al. [19], basing his work on the aforementioned thesis by Restivo [6], studied the influence of buoyancy in ventilated rooms. Some reasonably good comparisons with experimental data was achieved. But this was limited to buoyant, two dimensional flow, since the numerical work by Restivo was for such situation.

Gosman et al. [20], uses an approach similar to what has been reported by Restivo [6]. Here, an isothermal three dimensional flow is assumed. One of the fascinating observations made in this study was that although differential conservation equations were solved for, the variations that occurred in the prediction of the turbulent kinetic energy and the corresponding dissipation are fairly regular, and an algebraic formulation is possible for these two variables. But, later on, he withdrew this claim due to the vast range of geometric arrangements associated with ventilation problems. Therefore, it seems more appropriate to sacrifice efficiency in computer time in lieu of greater generality associated with the implementation of the transport equations for turbulent kinetic energy and the corresponding dissipation rate.

Sakamoto et al. [21] employed the Marker-and-Cell (MAC) method developed at the Los Alamos Scientific Laboratory by Harlow et al. [22] in which the three velocity components and pressure were taken as dependent. The problem considered here was an isothermal flow in a rectangular room with a square ceiling-mounted supply air diffuser and a low side-wall extract. Two different turbulence closure models were utilized: the standard turbulent kinetic energy and corresponding dissipation model [15]

and a more advanced model: the 'Large eddy simulation' approach [23], referred to as the Deardorff model [24]. Computed results of the mean flow field compared fairly well with the experimental data, although some of the turbulence properties evaluated through the numerical analysis did not compare well. Regarding the two turbulence closure models implemented in this research (i.e. the $k-\varepsilon$ and the Deardorff turbulence models), the difference between the predicted distributions of mean velocity for both approaches was not large. Therefore, it was concluded to use the $k-\varepsilon$ turbulence model in preference over the Deardorff model owing to the fact that the former can produce the solutions for the whole flow field in considerably less computer time than the latter. Consequently, this work has not expanded on previous accomplishments other than to back up the two equation turbulence model.

Markatos [26], conducted a three dimensional air flow and heat transfer analysis of a large complex building enclosure, representing a television studio. The numerical solver used to simulate the velocity and temperature contours was the PHOENICS Code [27], which is an idiom for Parabolic, Hyperbolic or Elliptic Numerical Code Series. Markatos described the formulation of the governing differential equations and identified the numerical technique used in attaining a solution. Two different geometrical configurations were considered. No comparisons have been made with experimental measurements, although the predicted results seem to be quite physically plausible. Owing to the fact that Markatos has used such an advanced multi-purpose code, it appears not necessary to resort to

such a refined scheme for ventilation problems as the CPU time consumed for forecasting air movement and heat transfer within enclosures might be excessively more than what is really necessary.

Kato et al. [28] performed numerical simulation of velocity profiles and the distribution of contaminants in a downward flow, three dimensional clean room, for different numbers of supply openings. Their main concern was not the comfort of the occupants, but instead to achieve a 'clean' environment for the production of highly sensitive electronic IC circuits. The flow was assumed to be isothermal. Thus, in spite of the fact that the spread of contaminates was predicted, the buoyancy effects were not incorporated into the conservation equations and the energy equation was not solved for. Comparisons were made with experimental measurements, and claimed to be satisfactory.

Whittle [29] made a moderately detailed review of the numerical computation of air movement and convective heat transfer within buildings. Albeit only two dimensional formulation was presented. No comparisons has been made with experimental data. Two practical numerical examples of summer cooling and winter heating were presented using the TEACH-T code [31,32].

Alamdari et al. [30] developed a computational procedure based upon that produced by Gosman et al. [31,32]. The turbulent kinetic energy and corresponding dissipation equations were used as the turbulence closure model. The heat transfer coefficients for the internal surfaces of a room heated by a three dimensional warm air jet were sought for

through the numerical code. The objective of this investigation was to introduce the computed distribution of heat transfer coefficients over the room surfaces into thermal simulation programs. it was claimed that the average heat transfer coefficients for the walls, ceiling and floor were in general agreement with the CIBSE Guide [33].

Quingyan et al. [34] utilized two and three dimensional numerical codes, which are the CHAMPION [35] and PHOENICS [27] codes respectively. A grid dependency demonstration was performed using the aforementioned three dimensional numerical solver. A reduction factor of 1/5 in CPU time was achieved by using a coarser grid in return for sacrificing a maximum variance of 1°C for the temperature and 4.0 cm/sec. for the velocity. It was concluded that computations made by PHOENICS was in agreement with measurements, for both the temperature and velocity fields, while the CHAMPION code did not perform well. Thus, the three dimensional code was recommended for ventilation and heat transfer problems. Furthermore, the inlet size and location were claimed to be a very important factor affecting temperature and velocity distributions. Additionally, the authors asserted that the calculated heat transfer coefficients were always less than that estimated through measurements.

An international conference which deals in various aspects of air distribution in ventilated spaces [45] has been held a short time ago. This convention was made up of five separate sessions, where out of those, the third session titled "Prediction Models" might be of some concern to this current research. Although most of the papers and reports of this segment

does not seem to expand significantly on the above review.

Kurabuchi et al. [36] started an investigation which may be considered as nothing more than a repetition of what Kato et al. [28] did, but with a different arrangement of the supply inlet and exhaust outlet. Therefore, the conclusions and shortcomings mentioned in [28] may be extended to this work.

Recently, Davidson [5] made an extensive study through his Ph.D. thesis research where his work may be regarded as a collection of papers and internal reports which deal with the simulation of ventilation problems. In the second paper of his work Davidson et al. also reported [37] a simplified version of the turbulent kinetic energy and dissipation equations, referred to as the KL1 turbulence model, where it has been asserted that this new turbulence model in parabolic flows gives as good agreement with experimental data as the $k - \varepsilon$ turbulence model and even better for a wall jet, with the advantage of reduced CPU time. But the standard $k - \varepsilon$ turbulence model in elliptic flow situations surpassed the performance by the KL1 turbulence model. In the sixth paper of this treatise [5] ,Davidson implements the CELS solver of Galpin et al. [38] after extending it to handle large density variations. He then developed a variant form of the standard $k - \varepsilon$ model [15] to be applied specifically for low Reynolds flow situations (e.g., non-mechanically ventilated enclosures or near wall flow). Comparisons with experimental measurements, for near wall flow, were made and found to be in general agreement. It was also claimed that the modified CELS solver was up to three times as fast as the SIMPLEC sol-

ver of Van Doormaal et al. [39]. In another study mentioned in this dissertation, also appearing in [41], an attempt to investigate local age and purging rates in ventilated rooms has been reported. This work considers two and three dimensional flow fields, where the former is isothermal and the latter is buoyant. Regarding the three dimensional situation, a simplified endeavour to vary the inlet supply port from the top to the bottom of a particular side wall, while keeping the outlet exhaust port at the same place on this side wall, was introduced. It was claimed that the predicted results compared moderately with experimental measurements for temperature, while it compared poorly with velocity distributions.

Awbi [40] described a computational fluid dynamics solver produced by Gosman et al. [31,32]. This numerical code has been applied to predict the air flow in a two dimensional enclosure and a three dimensional version of this scheme has been used to simulate the flow of a wall jet over surface-mounted obstacles. Experimental measurements were performed for a two dimensional test room cooled by a ceiling jet. Furthermore, comparisons were done and claimed to be within reason. No experimental verification was done for the three dimensional situation. He concludes with the need for a validation of the existing numerical schemes and specifically singles out the necessity for a turbulence closure model more accurate than the standard turbulent kinetic energy and corresponding dissipation equations turbulence model [15].

From the examination of the above, it is quite obvious that the numerical simulation of air flow and heat transfer within enclosures has

received a considerable amount of attention. <u>But none of the above, to the extent of the author's knowledge, have made an extensive numerical study, using a particular solver, that takes into account the effect of seriously varying the inlet and/or outlet geometrical locations in a room, on the resulting temperature and velocity profiles, not to mention the direct consequences this has on occupancy comfort</u> . Although it must be noted that Davidson et al. [41] made a simplified attempt to vary the inlet location, where it was kept on the same side wall and only shifted along the vertical axis. This may not be considered as a drastic change in inlet geometrical displacement due to the fact that the throw of the jet and the bulk of the inertia are nevertheless in the same general direction (i.e. along the X-direction). Also, the inlet location relative to the outlet does not seem to represent a practical set up. Moreover, the consequence of changing the outlet exhaust port location has not been examined by Davidson.

Thus, it seems worthwhile, to investigate the implementation of a numerical solver to predict the air movement of a three dimensional , turbulent, buoyant, elliptic flow field while varying the geometrical location of the inlet supply and outlet exhaust ports.

Then to use these computed results to interpret the thermal comfort sensation indexes by an appropriate model of human physiological regulatory response, and the model chosen in this research is Fanges's model [7], mentioned earlier.

CHAPTER III

PROPOSED INVESTIGATION

By recalling the discussion given in Chapter II of this investigation, it is quite obvious that there is virtually an overwhelming need to consider the effect of transporting the inlet supply and outlet exhaust ports on various walls within a room, and to observe the aftermath that this displacement might have on the resulting velocity and temperature flow fields, through a suitable numerical solver. Furthermore by employing an appropriate model of human physiological regulatory response, the consequences of transporting the inlet and outlet locations may be translated into human thermal sensation indexes which in turn might give an insight on human comfort.

3.1 GEOMETRICAL SHAPE

The room to be examined is shown in Fig. 3.1, where all the pertinent wall dimensions and orientations are displayed on the figure.

At the commencement of this study eight different inlet supply and outlet exhaust configurations were studied, but later on some were discarded on account of the fact that only summer cooling is considered and also due to the time limit assigned to this research. The four main cases considered are depicted in Figs. 3.2a to 3.2d, where the abrevations WE, NN, SN and NE are such that the first letter refers to the wall on which

19
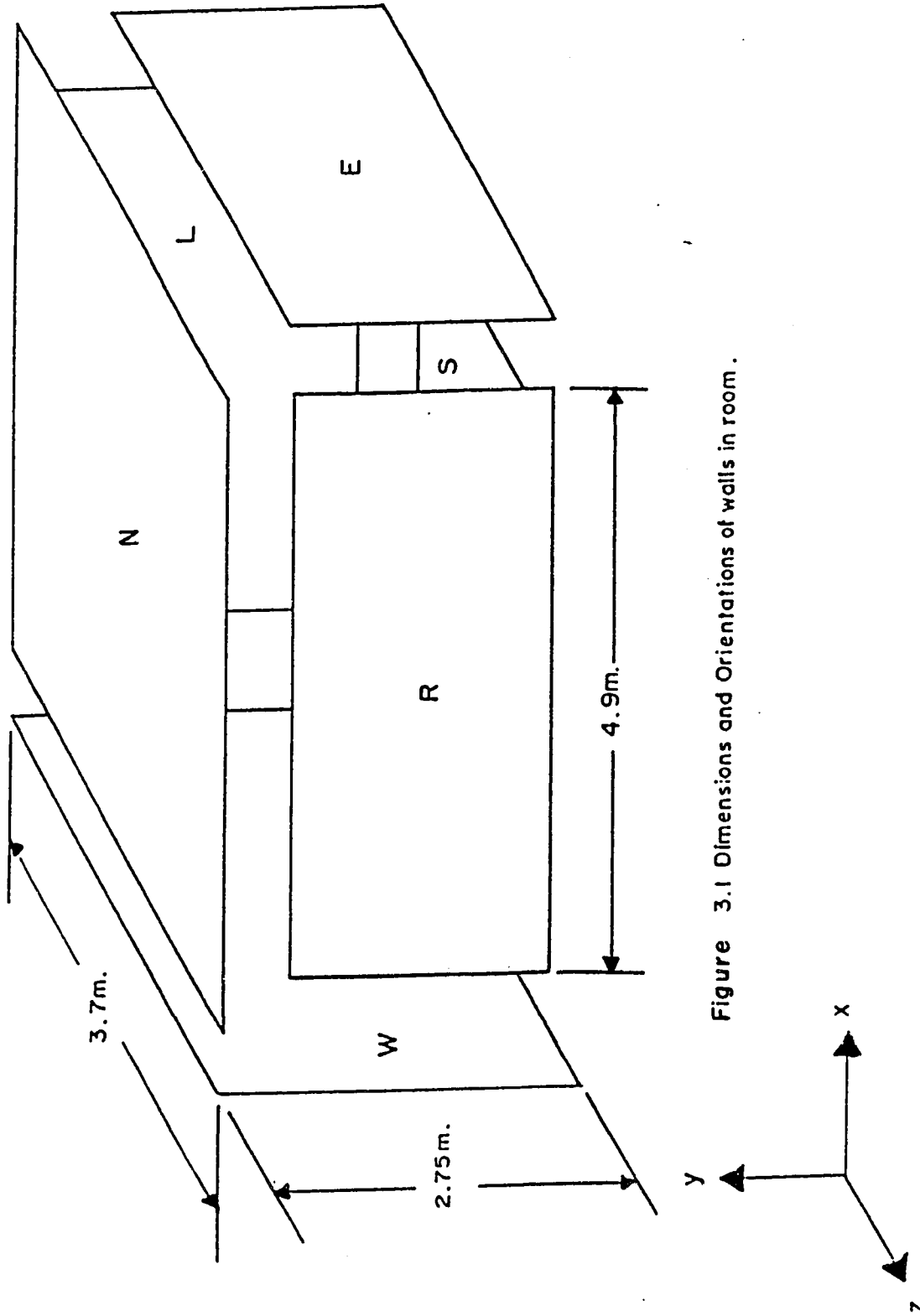
Figure 3.1 Dimensions and Orientations of walls in room.
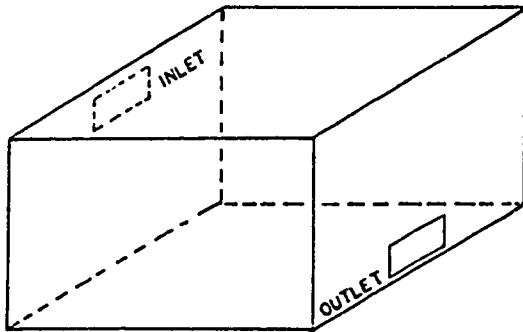
a) Inlet on West wall and outlet on East wall (WE).
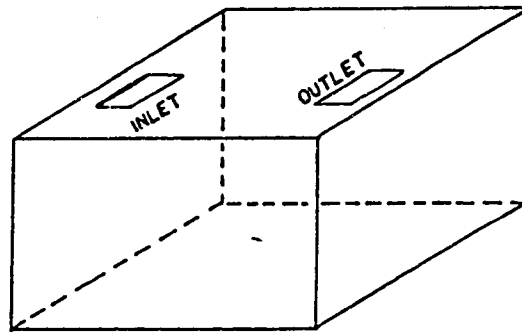
b) Inlet and outlet on North wall (NN).
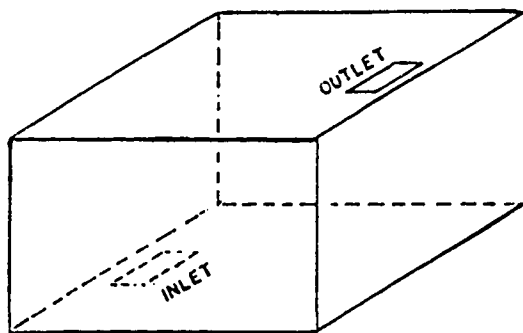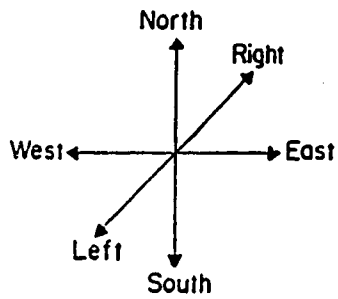
c) Inlet on South wall and outlet on North wall (SN).
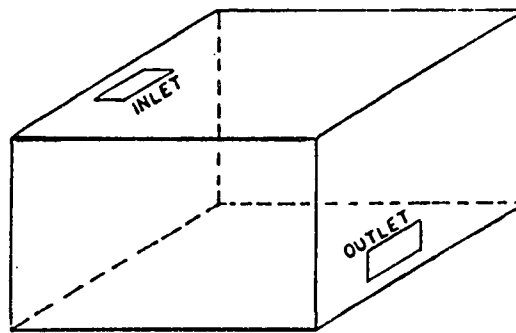
d) Inlet on North wall and outlet on East wall (NE).

Figure 3.2 The differant configurations studied in this research

the inlet port is located while the last letter indicates where the outlet port is.

The numerical solver implemented here has the ability to vary the heat fluxes and temperatures at any of the six walls, thus allowing to study their effect on the desired computation.

3.2 NUMERICAL CODE

The numerical scheme to be implemented in this investigation is a variant of the code by Gosman et al. [31,32], modified for three dimensional , air movement and heat transfer studies in rooms, referred to as TEACH-3D [5,40,52] .

The code uses the finite volume approach [43] which may be considered as a refinement to the finite difference concept, but with some aspects of finite elements introduced.

Here the SIMPLE algorithm of Patankar et al. [43] will be used. The logo SIMPLE is an idiom for for S emi- I mplicit M ethod for P ressure L inked E quations.

A wholehearted effort will also be made to replace the SIMPLE algorithm by SIMPLER [44] , standing for SIMPLE R revised, where it has been claimed [46] that a savings of up to 30-50% in computer time is possible.

To represent the transport equations in numerical form, a hybrid formulation [46,47] will be employed to express the convection of diffusion fluxes across the boundaries of each control volume (see Fig. 5.3). Endeavours will also be made to implement the power law scheme favored by Patankar [43] over the hybrid approach. Comparisons between the two different schemes will be done.

The rectangular finite difference grid covering the flow domain is of a specified size. An effort shall be undertaken to, perhaps, show grid dependency, keeping in mind not to sacrifice accuracy on the one hand, and CPU time on the other.

3.3 HUMAN COMFORT MODEL

Strives shall be pursued in trying to translate the calculated results into human thermal comfort sensation indexes, through which the achievement of thermal comfort (or not) may be decided upon in a relatively straightforward manner. The comfort model to be examined in this study is Fanger's PMV, one node thermo-regulatory model [7,9,10].

In normal practices, [10,50] thermal sensation indexes are evaluated by taking the arithmetic mean of all the relevant variables within the room and thus to produce a so called 'mean' perception of thermal comfort within the occupied zone. This attitude completely diminishes the scrutinizing accuracy sought for through the afore described numerical code.

To overcome this, a novel approach will be undertaken which will consist of using the pertinent computed variables from the numerical code

directly into the designated human physiological model. Thus avoiding the process of averaging the raw primitive variables in the flow field. The thermal sensation indexes are then evaluated throughout the occupied zone [51] defined as that region from the floor to a height of 1.8 meters, and more than 0.6 meter from side walls (see Fig. 3.1). These indexes will be estimated for both the sitting and standing postures. Afterwards, if required, the preception indexes are averaged over the gravitational direction (i.e.: y-direction) at an x-z mesh in the inhabited region, for both posture planes separately. Once the thermal indexes at every grid node within the occupied zone and their average values are calculated, they will be converted into contour plots, parallel to the horizontal plane. By observing the plots and noting if the majority of the contours lie between -0.8 to +0.8 of the thermal sensation scale (Table 1.1), which defines the 'acceptable thermal environment' [51] , a definite conclusion on the general satisfaction of occupancy thermal comfort, or not, is reached.

CHAPTER IV

METHODOLOGY

Air movement and heat transfer in simple rectangular rooms are, in general, fully turbulent, elliptic and non-isothermal. Thus, an advanced solver is necessary to simulate this type of flow.

The numerical scheme employed to simulate room air flow in this research is a three dimensional , modified version of the TEACH code by Gosman et al. [31,32]. The idiom TEACH stands for T eaching E lliptic A xisymmetric C haracteristics H eruistically. There are numerous reasons for adopting this code over others, some of which are : the accessibility to the source code, the simplicity by which it is written, ease of expanding and modifying the program, and the highly acclaimed success by many investigators [18,29,40,42,52] .

Due to the nature of the problem, the flow field is solved in an iterative manner, where convergence is enhanced by the proper selection of under-relaxation (damping) factors [43].

The finite volume method [43,46], will be used to discretize integral versions of the transport differential conservation equations, which describe the motion of air and heat transfer for contiguous control volumes enclosing each nodal point.

Owing to the elliptic type of flow encountered in normal air conditioning studies, it is essential to overcome the velocity-pressure link. The method utilized here is the SIMPLE algorithm [43,44,46], mentioned earlier. This approach does not employ additional equations for pressure, but instead the pressure in each computational cell, see Fig. 5.3 in chapter 5 of this thesis, is linked to the velocities of the neighboring control volumes in such a manner that compliance with the mass conservation equation is always assured. This results in a pressure-correction equation used to evaluate the variation in pressure required to achieve the corresponding change in velocity, whereby continuity of flow is fulfilled. A 'staggered' grid [43] should be used here (see Fig. 5.6). This mesh has the distinctive feature of defining the scaler quantities (i.e. p, T, k, ε and ρ) at the central grid node of a control volume cell, while the vector components (i.e. U, V and W) are acting at the faces of this cell. The grid is devised in such a way that room boundaries coincide with the control volume walls. For grid points within the vicinity of a solid boundary, a wall function or log-law is to be employed [14,15,47]. Depending on the local Reynolds number (y^{+}) of a control volume close to a solid wall, the wall function can either be that for laminar or turbulent boundary layers.

The finite difference scheme employed in this solver is the hybrid scheme [29,43]. This scheme is favored over some others due to its lucidity and enhancement of computational stability.

The discretized equations (i.e.: equations in algebraic form relating the variables of a grid point to the surrounding variables) will be solved for

by resorting to the T̲ ri- D̲ iagonal M̲ atrix A̲ lgorithm (TDMA) or Thomas algorithm [43,52], where the flow field is swept plane-by-plane until every node within the room has been visited. This sweeping process is normally repeated for the same iteration more than once. The reason for this is to enhance stability and increase accuracy, thus possibly reduce overall computational time to convergence.

On account of the conservation equations containing some unknown correlations, as previously mentioned, it is imperative to introduce additional equations. These equations are the turbulent kinetic energy and the corresponding dissipation equations.

The selected code TEACH-3D has the ability to accept various temperatures and heat fluxes at the surrounding solid walls. Therefore, many runs shall be made for a particular geometric configuration (see Fig. 3.2.a to 3.2.d), varying only the temperature and/or heat flux at the wall to imitate as much as possible real set-ups.

Some of the main items to be investigated in this research are:

i.   Debug and become familiarized with the source code.

ii.   Modify source code as necessary for various situations considered.

iii. Obtain 'optimized' group of under-relaxation factors for every situation considered such that the numerical code does not diverge.

iv. Validate the numerical code by comparing the computed results with available experimental results.

v. Construct a routine to interpret the computed flow field variables into thermo-regulatory sensation responses.

vi. Employ a different scheme (i.e.: SIMPLER) into the source code and compare with original source code.

vii. Introduce the power-law scheme into the source code and compare results with the original source code.

viii. Vary the grid size employed in the source code and compare with the original source code.

CHAPTER V
MATHEMATICAL MODELLING

5.1 INTRODUCTION

In this chapter an endeavour is made to describe, in some detail, all pertinent transport equations and complimentary relations. The conservation equations used are the continuity, momentum and energy equations. Owing to the nature of turbulence these group of equations do not form a closed set. Complimentary relations are therefore needed to make the collection of equations into a closed form. The relations chosen to take care of the aforesaid problem are the turbulent kinetic energy and the corresponding dissipation turbulence model or better known as the $k - \varepsilon$ turbulence model [3,5,6,15,16,20,43,52].

Due to the existence of a pressure gradient term in the momentum equation, to be described later, it is necessary to use a direct method to determine the pressure field. The method applied here is the SIMPLE algorithm [43,46]. To represent the momentum and energy equations in numerical form the hybrid scheme [43] is utilized. This method is used to express the convection and diffusion fluxes across the boundaries of each control volume, and is detailed below.

The numerical scheme employs the control-volume or Finite-Volume approach [5,43] to discretize all relevant equations. This method has the benefit of being comparablly straightforward and permits more freedom of choice

in selecting different profile assumptions for integrating various terms in the differential equation.

The discretized equations are solved by the $\underline{L}$ ine- $\underline{B}$ y - $\underline{L}$ ine (LBL) method [43,52] which has been extended to three dimensions and thus making it $\underline{P}$ lane - $\underline{B}$ y - $\underline{P}$ lane (PBP) method. This method is a combination of the Thomas algorithm or the $\underline{T}$ ri - $\underline{D}$ iagonal $\underline{M}$ atrix $\underline{A}$ lgorithim (TDMA) and the Gauss-Seidel method. One of the main benefits of this approach is it's relative economy in CPU time over other available approaches [52].

Out of the numerous thermo-regulatory sensation models available, the $\underline{P}$ redicted $\underline{M}$ ean $\underline{V}$ ote (PMV) [7] model has been adopted, details of which is given below.

5.2 EQUATIONS AND ASSUMPTIONS

The equations which govern fluid flow and convective heat transfer of any nature are the conservation equations of momentum, energy and mass. These are the fundamental laws which form the basis of any detailed, rigorous method for predicting air velocity and temperature distribution within a room. To make these relations complete they must be supplemented with thermodynamic equations, a turbulence model and prescribed boundary conditions.

5.2.1 The Conservation Equations

The general transport equations describing flow fields similar to that investigated in this research in tensor notation are,

Conservation of Mass (continuity) equation

$$\frac{\partial \rho}{\partial t} + \frac{\partial (\rho U_i)}{\partial x_i} = 0 \qquad (5.1)$$

Conservation of Momentum (Navier-Stokes) equation

$$\frac{\partial}{\partial t}(\rho U_i) + \frac{\partial}{\partial x_j}(\rho U_i U_j) = -\frac{\partial p}{\partial x_i} + \mu \frac{\partial^2 U_i}{\partial x_j \partial x_j} - g_i \rho + S_i \qquad (5.2)$$

Conservation of Energy (Temperature) Equation

$$\frac{\partial}{\partial t}(\rho T) + \frac{\partial}{\partial x_i}(\rho U_j T) = \mu \frac{\partial^2 T}{\partial x_i \partial x_i} + \frac{1}{C_p}(\frac{\partial p}{\partial t}) + S_T \qquad (5.3)$$

where U_i, g_i and S_i are the instantaneous velocity component, gravitational acceleration and momentum source term, respectively. p and T are the instantaneous static pressure and temperature, respectively, ρ, ρ_r, μ, λ and C_p are the density, reference density, dynamic viscosity, thermal diffusivity and specific heat of air, respectively.

The preceding set of equations together with an equation of state, relating the local density ρ to the local value of T, form a closed set. But due to the character of turbulence it is not possible, with the computer resources available, to utilize these equations for flow situations of practical relevance.

5.2.2 Assumptions and Simplifications:

As stated above the conservation laws (5.1), (5.2) and (5.3) can not at present be solved for general flow situations. Therefore, some suggestions and approximations are proposed as follows:

a. A statistical approach, postulated by Osborne Reynolds and reported in [3,6] has been adopted, in which the instantaneous values of velocity, pressure and temperature are decomposed into time mean and fluctuating quantities. Thus we may write

$$U_i = \overline{U}_i + u_i \ , \quad p = \overline{p} + p' \ , \quad T = \overline{T} + T' \tag{5.4}$$

where the mean quantities are defined as:

$$\overline{U}_i = \frac{1}{t_2 - t_1} \int_{t_1}^{t_2} U_i \, dt \ , \quad \overline{p} = \frac{1}{t_2 - t_1} \int_{t_1}^{t_2} p \, dt \ ,$$

$$\overline{T} = \frac{1}{t_2 - t_1} \int_{t_1}^{t_2} T \, dt \tag{5.5}$$

and the averaging time $(t_2 - t_1)$ is long compared to the time scale of turbulent motion. For brevity, overbars indicating mean values will be omitted in all variables henceforth.

b. In the flows to be considered in this study the variations of velocity are small compared to the speed of sound and the changes in density due thermal expansion represents only a small fraction of the average density. Hence, as suggested by [3,5,6] and others the Boussinesq

approximation is adopted, so that the influence of variable density appears only in the buoyancy term, which is the third term on the right hand side of equation (5.2). To implement this method the static pressure term in (5.2) is separated into a hydrostatic part as follows [53]

$$\frac{\partial p}{\partial x_i} = -\rho_r g_i \qquad (5.6)$$

the remaining part represents the static pressure minus the hydrostatic pressure at reference density ρ_r. This will replace the pressure term appearing in the momentum equation while retaining the symbol p to represent it.

c. It may be implied from the Boussinesq approximation above that the flow is basically incompressible, except in the buoyancy term where variations are permitted.

d. In this investigation only the steady-state condition shall be addressed. Thus in the conservation equations any term containing $\frac{\partial}{\partial t}$ is omitted.

e. The source terms S_i in the momentum equation portrays extra viscous terms whose affect is small except where changes in fluid properties are substantial. Therefore, it may be omitted where warranted.

f. Similarly to (e) above, the source term S_T, representing heat generation due to viscous dissipation, is small and can be droped out where justified.

g.   Turbulent character prevailing over the flow domain, away from the solid boundaries, and its corresponding insensitivity to changes in the Reynolds number, for Re over 6000, in room air flows, resembling those investigated here, is postulated. This has been confirmed through preliminary experimental measurements by Restivo [6], in models having geometries similar to those in this research, where frequency spectra of the longitudinal velocity fluctuations were estimated in several regions of the flow. Spectra studies indicate a regular distribution of energy over a wide range of frequencies and no preferred frequencies were detected. The Reynolds number was varied between 3000 and 8000 by varying the inlet velocity accordingly, and the mean and root mean square velocities were registered at distinct points distributed over the entire flow. The outcome of the measurements shows that both the mean and the root mean square velocities tend to become constant at higher Reynolds numbers, and the differences between them for values recorded at Re = 5000 and Re = 8000 are negligible. This substantiates our earlier assumption of the turbulent character of the flow and its weak dependence on the Reynolds number for Re ≥ 5000.

The Reynolds number evaluated in the study of room enclosures, and adopted in this research is as follows [5,6,40,45]

$$Re = \frac{U_o \cdot \rho_o \cdot A_o^{1/2}}{\mu_o} \tag{5.7}$$

where U_o is the longitudinal velocity acting at and normal to the inlet plane

and ρ_o, A_o and μ_o are the density, surface area and dynamic viscosity at the room inlet, respectively. The value of the Reynolds number in this investigation is in the upper 30,000 range.

5.2.3 The Simplified Form of the Conservation Equation

After implementing the foregoing assumptions and approximations the conservation equations transforms to

Conservation of mass (continuity) equation

$$\frac{\partial U_i}{\partial x_i} = 0 \tag{5.8}$$

Conservation of momentum (Navier-Stokes) equation

$$U_i \frac{\partial U_i}{\partial x_j} = -\frac{1}{\rho_r} \frac{\partial p}{\partial x_i} + \frac{\partial}{\partial x_j} \left(v \frac{\partial U_i}{\partial x_j} - \overline{u_i u_j} \right) - g_i \frac{(\rho - \rho_r)}{\rho_r} \tag{5.9}$$

Conservation of energy (Temperature) equation

$$U_i \frac{\partial T}{\partial x_i} = \frac{\partial}{\partial x_i} \left(\lambda \frac{\partial T}{\partial x_i} - \overline{u_i T'} \right) \tag{5.10}$$

In addition to the assumptions made earlier further approximations will be exercised, without sacrificing accuracy of the outcome for most engineering problems, as given below [2,3]

h.   The apparent or turbulent stress ($-\overline{u_i u_j}$) , away from the region of the

wall, is much larger than the viscous or laminar stress ($\nu \dfrac{\partial U_i}{\partial x_j}$), and thus

the latter may be neglected in comparison to the former.

i.   The turbulent heat flux ($-\overline{u_i T'}$), is also much larger than the viscous heat

flux ($\lambda \dfrac{\partial T}{\partial x_i}$). Therefore, the laminar part is dropped-out in favour of the

turbulent portion.

Introducing approximations (h) and (i) above, into equations (5.9)
and (5.10), respectively will result in

Conservation of Momentum (Navier-Stokes) equation

$$U_j \frac{\partial U_i}{\partial x_j} = -\frac{1}{\rho_r}\frac{\partial p}{\partial x_j} + \frac{\partial}{\partial x_j}(-\overline{u_i u_j}) - g_i\frac{(\rho - \rho_r)}{\rho_r} \tag{5.11}$$

Conservation of Energy (Temperature) equation

$$U_i \frac{\partial T}{\partial x_i} = \frac{\partial}{\partial x_i}(-\overline{u_i T'}) \tag{5.12}$$

The averaging process applied to the basic transport equations of (5.1),
(5.2) and (5.3) has introduced *unknown correlations* between fluctuating
velocities, $\overline{u_i u_j}$, and between fluctuating velocity and fluctuating temperature
$\overline{u_i T'}$. The relationship between the fluctuating components are detailed in [54]

and are given below:

$$U_k \frac{\partial \overline{u_i u_j}}{\partial x_k} = -\frac{\partial}{\partial x_k} \left[\overline{u_i u_j u_k} + \overline{\frac{p}{\rho}(\delta_{jk} u_i + \delta_{ik} u_j)} - v \frac{\partial \overline{u_i u_j}}{\partial x_i} \right]$$

$$- \left[\overline{u_i u_k} \frac{\partial U_j}{\partial x_k} + \overline{u_j u_k} \frac{\partial U_i}{\partial x_k} \right] - \beta \left[g_i \overline{u_j T'} + g_j \overline{u_i T'} \right]$$

$$- 2v \left[\overline{\frac{\partial u_i}{\partial x_k} \frac{\partial u_j}{\partial x_k}} \right] + \overline{\frac{p}{\rho} \left[\frac{\partial u_i}{\partial x_j} + \frac{\partial u_j}{\partial x_i} \right]} \tag{5.13}$$

where, the left hand side of the equation represents convection of Reynolds stresses, and on the right hand side the 1st term is the diffusive transport, 2nd term is the production by shear, 3rd term is the production by buoyant forces, 4th is the viscous dissipation and the last term is the is pressure strain.

Equation for $\overline{u_i T'}$ (turbulent transport of heat):

$$U_k \frac{\partial \overline{u_i T'}}{\partial x_k} = -\frac{\partial}{\partial x_j} \left[\overline{u_i u_j T'} + \frac{1}{\rho} \delta_{ij} \overline{pT'} - \lambda \frac{\overline{u_i \partial T'}}{\partial x_j} - v \frac{\overline{T' \partial u_i}}{\partial x_j} \right]$$

$$- \left[\overline{u_i u_j} \frac{\partial T}{\partial x_j} + \overline{u_j T'} \frac{\partial U_i}{\partial x_j} \right] - \beta \left[g_i \overline{T'^2} \right] - (\lambda + v) \left[\overline{\frac{\partial u_i}{\partial x_j} \frac{\partial T'}{\partial x_j}} \right]$$

$$+ \frac{1}{\rho} \left[\overline{\frac{p \partial T'}{\partial x_i}} \right] \tag{5.14}$$

where, left hand side of (5.14) represents the convection of the turbulent transport of heat flux and on the right hand side of the equal sign the first

term is the diffusive transport, 2nd term is the mean field production, 3rd term is the buoyant production, 4th term is the dissipation, and the last term is the pressure scrambling.

By referring to equations (5.13) and (5.14) above it is quite obvious that new unknown correlations have been produced. If we were to follow the same reasoning regarding these new correlations and develop corresponding new transport relations, this will only result in additional unknown correlations. Furthermore, the number of unknown correlations grow faster than the number of transport equations. Thus the system of equations, describing fluid flow and heat transfer within an enclosure (i.e: equations (5.8), (5.11), and (5.12)), cannot be closed by resorting to equations of higher and higher order.

From the preceding argument it is evident that a different approach to this enigma must be adopted. The methodology chosen to accomplish this is the so called 'turbulence model', described in the following sections.

5.3 THE TURBULENCE MODEL

Not withstanding all the recent progress made in computer technology, turbulent flow equations cannot at present be solved without resorting to some simplifying assumptions [1,2,3,53,54]. The precise formula describing the turbulent motion [1,2] (the Navier-Stokes equations), and their corresponding numerical schemes are readily available [44]. However, the storage

capacity and speed of present day computers are still not sufficient to permit a solution for any viable turbulent flow situation. The reason behind this is that the turbulent motion incorporates elements which are considerably smaller than the extent of the flow domain, typically of the order of 10^{-3} times smaller. To determine the movement of these elements in a numerical scheme the mesh size of the numerical grid would have to be even smaller, hence, at least 10^9 grid points would be necessary to cover the flow domain in three dimensions. Also appreciating the fact that the number of variables per grid point may vary from about four to more than ten, depending on the type of problem under study, and to store these pertinent flow variables at so many grid points remains far beyond the ability of the fast-access memory of contemporary computers. In addition to this the number of arithmetic operations required will be so large that the computing time would also be quite prohibitive. Thus the turbulent kinetic energy and corresponding dissipation equations are one of many methods to overcome this difficulty, and is described below.

5.3.1 Basic Form of the Turbulent Kinetic Energy Equation

The time-averaged general transport equation for turbulent kinetic energy at high Reynolds number is [3,55]

$$\frac{\partial k}{\partial t} + U_i \frac{\partial k}{\partial x_i} = -\frac{\partial}{\partial x_i}\left[\overline{u_i(\frac{u_i u_i}{2} + \frac{p}{\rho})}\right] - \overline{u_i u_j} \frac{\partial U_i}{\partial x_j}$$

$$- \beta g_i \overline{u_i T'} - \nu \overline{\frac{\partial u_i}{\partial x_j} \frac{\partial u_i}{\partial x_j}} \qquad (5.15)$$

where

$$k = \frac{1}{2} \overline{u_i u_i} \qquad (5.16)$$

the first term on the left hand side of (5.15) represents the rate of change of turbulent kinetic energy, and the 2nd term is the convective transport of turbulent kinetic energy, and the 1st term on the right hand side of the equation is the diffusive transport of turbulent kinetic energy, the 2nd term is production by shear, the 3rd term is buoyant production/ destruction and the last term is viscous dissipation.

By simple inspection of equation (5.15), it is obvious that the full form of the turbulent kinetic energy equation does not help in clearing up the predicament mentioned earlier. On the contrary it produces new unknown correlations. Thus approximations and assumptions must be made to render this equation useful.

5.3.2 Assumptions Implemented to the Turbulent Kinetic Energy Equation

The following are the assumptions implemented in this investigation:

a. Since only steady-state situations are considered here, the first term on the left hand side of equation (5.15) drops out.

b. The diffusion flux of the turbulent kinetic energy, embodied in the first term on the right hand side of (5.15), is often assumed proportional to the gradient of the turbulent kinetic energy [3] as

$$-\overline{u_i\left(\frac{u_iu_j}{2} + \frac{p}{\rho}\right)} = \frac{\nu_t}{\sigma_k}\frac{\partial k}{\partial x_i}\tag{5.17}$$

where σ_k is an empirical constant.

c.   By dimensional arguments the viscous dissipation term (i.e: the last term on the right hand side of (5.15)) is usually modelled by an expression [54,55] given by

$$\varepsilon = C_D\frac{k^{3/2}}{L}\tag{5.18}$$

where ε is the dissipation of turbulent kinetic energy, C_D is an empirical constant and L is a length scale of turbulence. Equation (5.18) above may be justified by the fact that as ε , is governed by large-scale motions, even though the dissipation takes place at the smallest eddies, and as this large scale motion is characterized by k and L, equation (5.18) follows from dimensional analysis.

d.   Eddy-viscosity concept, which assumes that the turbulent stresses are proportional to the mean-velocity gradients [15,40,54,55] is

$$-\rho\,\overline{u_iu_j} = \mu_t\left(\frac{\partial U_i}{\partial x_j} + \frac{\partial U_j}{\partial x_i} - \frac{2}{3}\rho\,k\delta_{ij}\right)\tag{5.19}$$

where δ_{ij} is the Kronecker delta and defined as :

$$\delta_{ij} = \left\{ \begin{matrix} 1 & 0 & 0 \\ 0 & 1 & 0 \\ 0 & 0 & 1 \end{matrix} \right\}$$

and μ_t is the turbulent or eddy viscosity, which is not a fluid property but depends strongly on the state of turbulence, and may vary substantially from one point in the flow to another and also from flow to flow. Substituting equation (5.19) into (5.11) and after some rearrangement yields the final form of the *momentum equation* to be used in this investigation :

$$\frac{\partial}{\partial x_j}\left(\rho U_i U_j\right) = -\frac{\partial p}{\partial x_i} + \frac{\partial}{\partial x_j}\left[\mu_t\left(\frac{\partial U_i}{\partial x_j} + \frac{\partial U_j}{\partial x_i}\right) - \frac{2}{3}\rho k \delta_{ij}\right] - g_i\left(\rho - \rho_r\right) \quad (5.20)$$

By simple inspection of (5.20) it is obvious that the input from the turbulence model is necessary only in the second term on the right hand side of the equal sign. The focus is now shifted to finding out the distribution of μ_t.

e. Eddy-diffusivity concept, the turbulent heat transport is often assumed to be proportional to the gradient of the mean temperature [3,15,54] as

$$-\rho \overline{u_i T'} = \Gamma_t \frac{\partial T}{\partial x_i} \quad (5.21)$$

where Γ_t is the turbulent diffusivity coefficient of heat and defined as:

$$\Gamma_t = \frac{\mu_t}{\sigma_t} \quad (5.22)$$

An expression used to relate the eddy viscosity, μ_t , to the local values of ρ , k and ε is :

$$\mu_t = C_\mu \frac{\rho k^2}{\varepsilon} \tag{5.23}$$

where C_μ is an empirical value which is constant for high Reynolds number.

Substituting equation (5.21) into (5.12) results in the transport *equation for energy* to be adopted in this investigation as :

$$\frac{\partial}{\partial x_j}(\rho U_j T) = \frac{\partial}{\partial x_i} (\Gamma_t \frac{\partial T}{\partial x_i}) \tag{5.24}$$

Contribution from the turbulence model is required on the right hand side of this expression.

f.   The assumption of high Reynolds number flow, stated in sub- section 5.2.2, is reaffirmed here to prevail.

Implementing the above approximations into equation (5.15) yields:

$$U_i \frac{\partial k}{\partial x_i} = \frac{\partial}{\partial x_i} \left(\frac{v_t}{\sigma_k} \frac{\partial k}{\partial x_i} \right) + v_t \left(\frac{\partial U_i}{\partial x_j} + \frac{\partial U_j}{\partial x_i} \right) \frac{\partial U_i}{\partial x_j}$$

$$+ \beta g_i \frac{v_t}{\sigma_t} \frac{\partial T}{\partial x_i} - C_D \frac{k^{3/2}}{L} \tag{5.25}$$

5.3.3 The Turbulent Kinetic Energy Dissipation Equation

The turbulent length scale L in Eqn. (5.25) characterizing the size of the large, energy-containing eddies is subject to transport processes. Also dissipation affects the length scale, which causes the destruction of small eddies and consequently increases the effective eddy size. Moreover, the vortex stretching related to the energy cascade reduces the eddy size. The balance of all the aforesaid operations can be outlined in a model transport equation for L which can then be used to calculate the distribution of L.

Out of numerous turbulent length scale models available [3, 14, 15, 22, 41, 54, 55] the turbulent kinetic energy dissipation equation (5.18) requires only a single empirical constant to be implemented at near or far wall flows and it also does not necessitate the introduction of a secondary term in the transport equation. In view of this, the $k - \varepsilon$ **turbulence model** has become one of the most popular and successful turbulent models, of the past two decades. This ε transport equation shall not be stated here but will be reported in a full form in the next sub-section together with the k-equation so that a representation of the complete model may be made.

5.3.4 The k - ε Turbulence Model

The k- ε Turbulence model as given in [15] is detailed below:

Turbulent kinetic energy (k) transport equation (5.25) re-arranged

$$\frac{\partial}{\partial x_i} (\rho U_i k) = \frac{\partial}{\partial x_i} (\Gamma_k \frac{\partial k}{\partial x_i}) + \rho (S_k + S_B) - C_D \rho \varepsilon \qquad (5.26)$$

Turbulent kinetic energy dissipation (ε) transport equations

$$\frac{\partial}{\partial x_i} (\rho U_i \, \varepsilon) = \frac{\partial}{\partial x_i} (\Gamma_\varepsilon \frac{\partial \varepsilon}{\partial x_i}) + C_1 \, \rho \, \frac{\varepsilon}{k} \, (S_k + S_B) - C_2 \, \rho \frac{\varepsilon^2}{k} \qquad (5.27)$$

where, the left hand side of (5.27) represents the convection of the dissipation of turbulent kinetic energy, and on the right hand side the 1st term is the diffusion of the dissipation of turbulent kinetic energy, the 2nd term is the generation-destruction of the dissipation of tur- bulent kinetic energy.

Definition of other terms in equation (5.26) and (5.27) above are:

The source term for turbulent kinetic energy:

$$S_k = \frac{\mu_t}{\rho} \frac{\partial U_i}{\partial x_j} \left(\frac{\partial U_i}{\partial x_j} + \frac{\partial U_j}{\partial x_i} \right) \qquad (5.28)$$

The source term for buoyancy:

$$S_B = -\beta \, g_j \, \frac{\mu_t}{\rho \sigma_t} \frac{\partial T}{\partial x_j} \qquad (5.29)$$

The diffusion coefficient for turbulent kinetic energy:

$$\Gamma_k = \frac{\mu_t}{\sigma_k} \qquad (5.30)$$

The diffusion coefficient for the dissipation of turbulent kinetic energy:

$$\Gamma_\varepsilon = \frac{\mu_t}{\sigma_\varepsilon} \qquad (5.31)$$

Some of the equations above include empirical constants C_D, C_1, C_2, C_μ, σ_k, σ_ϵ and σ_t and are discussed below.

5.3.5 Empirical Constants Used in the k - ε Model

Although no one set of empirical constants can be applied to every type of flow situation, there does exist an accord that a particular group of these empirical constants may be applied to a relatively wide range of problems without the need of varying any of the parameters in this group [15,54,55]. Thus a sacrifice of some accuracy is tolerated in view of a sense of generality in the empirical constants. The contrariwise approach to this would be to modify the collection of empirical constants for every different situation through empirical analysis and thus resulting with nothing more than an elaborate empirical approach. The turbulent kinetic energy and corresponding dissipation equation turbulence model are assigned experimental constants [3,15,54,55] as listed in Table 5.1.

5.4 BOUNDARY CONDITIONS

The turbulent transport equations reviewed above (i.e. equations (5.8), (5.20), (5.24), (5.26), and (5.27)) are used collectively to predict the air velocity and temperature distribution in mechanically air conditioned rooms. To make a particular solution distinctive specification of a unique set of boundary conditions is required. Thus an accurate representation of these condit-

TABLE 5.1. Empirical constants used in the k - ε turbulence model

C_μ	C_D	C_1	C_2	σ_k	σ_ε	σ_t
0.09	1.0	1.44	1.92	1.0	1.22	0.75

ions are essential to produce a reliable solution of the entire flow domain. For ventilated rooms it is necessary to identify the boundary conditions prevailing at the inlet, outlet and on the internal surfaces of the room, this is dealt with below.

5.4.1 Inlet Conditions

For the investigations conducted here the character of turbulence prevails over the inlet supply vent, thus the velocity profile is assumed to be uniform over the inlet opening and equal to U_o [5,28]. Also the temperature, T_o, kinetic energy of turbulence, k_o, and the corresponding energy dissipation rate, ε_o, are also proposed to be constant over the inlet vent [5,6,20,26,29,40], and wherever available, experimental results for these parameters are utilized. However, when warranted approximate data proposed by other researchers [3,5,6] are introduced, which are common to the investigations conducted in this study. Density of air at the inlet, ρ_o, is obtained from the air tables at the specified temperature, T_o. The dynamic viscosity, μ_o, is obtained by using Sutherland's theory of viscosity [2]:

$$\mu_o = \left(\frac{T_o^{3/2}}{T_o + S_1}\right) \cdot \left[\frac{\mu_r \cdot (T_r + S_1)}{T_r^{3/2}}\right] \qquad (5.32)$$

where T_o, μ_o and T_r, μ_r are the temperatures in °K and dynamic viscosities at the inlet and a reference temperature , respectively and S_1 is a constant

which, for air, assumes the value

$$S_1 = 110 \ ^\circ K \qquad (5.33)$$

The other two velocity components, in the plane of the inlet opening, V_o and W_o along the y-axis and z-axis, respectively are assigned the value of zero. Furthermore, the pressure is also assumed to be zero at the inlet which serves as the reference pressure for all other points in the flow domain.

The kinetic energy of turbulence at the inlet is obtained by using [5,40]:

$$k_o = \frac{3}{2} I_u^2 \ U_o^2 \qquad (5.34)$$

where I_u^2 is the turbulence intensity of the velocity component acting at and vertical to the inlet plane. In the absence of measured values [5]

$$I_u = 0.14 \qquad (5.35)$$

The turbulent kinetic energy dissipation rate is evaluated by [6]:

$$\varepsilon_o = \frac{k_o^{3/2}}{\lambda_\varepsilon \cdot H_\varepsilon} \qquad (5.36)$$

where λ_ε is a turbulence constant and assigned the value:

$$\lambda_\varepsilon = 0.005 \qquad (5.37)$$

and H_ε is the height of the room or the square root of the cross sectional area of the room.

Experience shows [5,40] that calculations with different values of k_o and ε_o resulted in minor effect on the end results.

5.4.2 Outlet Conditions

The longitudinal velocity component, U_e, is taken to be uniform over the entire exit plane [5,6,16,45]. It is estimated by applying the mass balance equation over the whole room, and then solving for U_e, as follows

$$U_e = U_o \frac{A_o}{A_e} \frac{\rho_o}{\rho_e} \qquad (5.38)$$

where A_o, ρ_o and A_e, ρ_e are the areas and densities of air at the inlet supply and outlet exhaust vents, respectively.

The exit temperature T_e is obtained by employing the energy equation for the entire flow field and taking into account the heat transfer across all boundaries. T_e is considered to be uniform on the exit plane. Boundary condition values for k and ε at the outlet are not required because an up-wind computational scheme, described later, is used. However, the gradients of k and ε at the exit plane are specified to be zero, as follows

$$\frac{\partial k}{\partial x_e} = 0 \quad \text{and} \quad \frac{\partial \varepsilon}{\partial x_e} = 0 \qquad (5.39)$$

where x_e is the axis vertical to the outlet plane.

5.4.3 Wall Boundary

The wall region is described by defining a local Reynolds number, y^+, [2,5,6,15],

$$y^+ = \frac{U_\tau \cdot \rho \cdot x_n}{\mu} \tag{5.40}$$

where ρ and μ are the local density and laminar viscosity, respectively and x_n is the vertical distance from the solid wall to the following grid node in the flow field and U_τ is the friction velocity, which is evaluated from [2,5,16]

$$U_\tau = \sqrt{\tau_\omega / \rho} \tag{5.41}$$

where τ_ω is the wall shear stress, and may be determined by [5,57]:

$$\tau_\omega = \frac{\rho \left(C_D^{1/2} \cdot k \right)^{1/2} 1/2 \cdot \vec{V} \cdot \kappa}{\ln \left(E \cdot y^+ \right)} \tag{5.42}$$

where $\vec{V}$ is the resultant velocity parallel to the wall, κ is the Von Karman constant taken equal to 0.4187 and E is an integration constant which depends on the magnitude of the variation of shear stress across this region and on the roughness of the wall. In this study the value of E is taken to be 9.793, which corresponds to smooth walls with constant shear stress [5,6,40].

The wall region is assumed to have constant shear stress and heat flux. It is made up of three distinct zones [2,5,52,56]. The viscous sublayer $(0 < y^+ < 5)$ where viscous effects dominate, the transitional or buffer layer

$(5 < y^+ < 30)$ of highly active turbulence dynamics where the flow is neither completely governed by viscous forces nor entirely turbulent and the inertial sublayer $(30 < y^+)$ where flow is assumed to be completely turbulent.

In the neighborhood of a wall region laminar viscosity becomes more significant than turbulent viscosity and as a result of this the k - ε turbulent model, equations (5.26) and (5.27) are not employed within this region. Furthermore when boundary conditions are supplied at a solid surface, the corresponding transport equations describing the flow should be solved from the wall surface across the viscous sublayer up to the inertial sublayer. Near the wall, effective transport coefficients change by more than an order of magnitude as vigorous turbulent mixing gives way to purely molecular transport at the wall, resulting in steep gradients of properties within this region. To resolve this transitional layer, properly with an appropriate numerical scheme necessitates a very fine mesh around those edges of the region contained by a wall. In adopting such an approach the calculations will prove to be prohibitively expensive. In addition to this the high Reynolds number assumption adopted earlier is not true here. Therefore, to avoid the aforesaid difficulties current practice [2,5,6,15,29,40,52] is to employ empirical relations, called *wall-functions* or *log-law of the wall*, which relates the boundary conditions at the wall with the flow properties in the turbulent inertial sublayer. These expressions, detailed later, have been derived from one-dimensional analysis of Couette flow in the proximity of the wall [2,15]. This wall-function approach disposes of the buffer layer, described earlier, by defining a point at

$y^+ = 11.63$, where the linear velocity profile of the viscous sublayer meets the logarithmic velocity profile in the inertial sublayer. Below this defined point the flow is assumed to be purely viscous and above which it is assumed to be completely turbulent. In accordance with this approach the wall region is now divided into two domains as follows [5,15,40]

a. The laminar layer, where

$$y^+ \leq 11.63 \ ,$$

$$\mu_t / \mu << 1. \ ,$$

$$\Gamma_t / \Gamma << 1. \ ,$$

$$\tau_\omega \text{ and the wall heat fluxes are constant} \tag{5.43}$$

Thus,

$$U^+ = y^+ \tag{5.44}$$

where U^+ is a non-dimensional velocity which represents momentum and is equal to

$$U^+ = \vec{V} / U_\tau \tag{5.45}$$

and

$$T^+ = \sigma y^+ \tag{5.46}$$

for which T^+ is a non-dimensional heat flux temperature and σ is a viscous

laminar number, defined as

$$\sigma = C_p \, \mu \, / \, \lambda \tag{5.47}$$

where C_p, μ and and λ are the specific heat, dynamic viscosity and thermal diffusivity of air, respectively.

b. The turbulent sublayer, where :

$$y^+ > 11.63 \ ,$$

$$\mu_t \, / \, \mu >> 1 . \, ,$$

$$\Gamma_t \, / \, \Gamma >> 1 . \, ,$$

$$\tau_\omega \text{ and the wall heat fluxes remain constant} \tag{5.48}$$

Thus :

$$U^+ = \frac{1}{\kappa} \ln \, (\, E.y^+ \,) \tag{5.49}$$

and

$$T^+ = \frac{\rho \, U_\tau \, C_p \, (T_w - T)}{q_w} = \sigma_t \left[U^+ + f(\sigma / \sigma_t) \right] \tag{5.50}$$

where T_w and q_w are the temperature and heat flux at the wall, respectively. σ_t is the turbulent Prandtl number. $f(\sigma/\sigma_t)$ is a function of the ratio σ/σ_t given as [40,52]:

$$f(\sigma/\sigma_t) = 9.24 \left[\left(\frac{\sigma}{\sigma_t} \right)^{0.75} - 1 \right] \cdot \left\{ 1 + 0.28 \exp \left[-0.007 \left(\frac{\sigma}{\sigma_t} \right) \right] \right\} \tag{5.51}$$

This function is valid only for impermeable, smooth walls. q_w can be treated as an additional source term in the energy equation.

5.5 THE NUMERICAL PROCEDURE

Until now all of the previous sections of this Chapter have dealt with the basic conservation equations and the approximations applied to them. No details have been given to the calculation of the flow field. This will be the core topic of the sub-sections to follow.

5.5.1 The General Form of the Differential Equation

By referring to the transport equations (5.8), (5.20), (5.24), (5.26), and (5.27) it may be observed that all these expressions can be set into one *common form* [5,29,40,52]

$$\frac{\partial}{\partial x_i} (\rho U_i \Phi) = \frac{\partial}{\partial x_i} (\Gamma_\Phi \frac{\partial \Phi}{\partial x_i}) + S_\Phi \tag{5.52}$$

where Φ may represent any of the dependent variables under investigation. The term on the left hand side of equation (5.52) is the convection of Φ, while the 1st term on the righthand side of the equation is the diffusion of Φ and the last term represents the source term of Φ which may be either generation or destruction of Φ.

It is to be noted that whenever any transport equation does not exactly match the general format of eqn. (5.52), the extraneous terms will be included

in the source term S_Φ, keeping the convection and diffusion terms unaltered. Γ_Φ thus collectively represents all the coefficients appearing in the diffusion term of the original transport equations.

As a direct consequence of applying eqn. (5.52) to the original transport equations Table 5.2 was derived, and is shown below.

The advantage of having the conservation equations reduced into the standard differential equation and treating these conservation relations as a particular case of the general form is an important time-saving step, requiring us to be concerned with the numerical solution of only equation (5.52). Furthermore, when constructing the computer program a general sequence of operations for solving this standard differential equation can be repeatedly employed for different dependent variables supplemented by suitable expressions for Γ_Φ and S_Φ, with appropriate initial and boundary conditions.

5.5.2 Control Volume Technique

In the preceding sub-section we have arrived to a general form of the differential equation for various dependent parameters describing the flow field. Now the task is to develop a numerical solution of this differential equation from which the distribution of the particular dependent variable under consideration may be determined. In doing so a sacrifice of some accuracy must be accepted in favour of reasonable calculation costs and also to the limited

TABLE 5.2 : Diffusion Coefficients and Source Terms used in eq.(5.52).

Equation	Dependent Variable (Φ)	Diffusion Coefficent (Γ_t)	Source Term (S_Φ)
Continuty	1	0	0
Momentum	U	μ_t	$-\dfrac{\partial p}{\partial x} + \dfrac{\partial}{\partial x}(\mu_t \dfrac{\partial U}{\partial x} - \dfrac{2}{3}\rho k) + \dfrac{\partial}{\partial y}(\mu_t \dfrac{\partial V}{\partial x})$ $+ \dfrac{\partial}{\partial z}(\mu_t \dfrac{\partial W}{\partial x})$
Momentum	V	μ_t	$-\dfrac{\partial p}{\partial y} + \dfrac{\partial}{\partial x}(\mu_t \dfrac{\partial U}{\partial y}) + \dfrac{\partial}{\partial y}(\mu_t \dfrac{\partial V}{\partial y} - \dfrac{2}{3}\rho \cdot k)$ $+ \dfrac{\partial}{\partial z}(\mu_t \dfrac{\partial W}{\partial y}) + g(\rho - \rho_r)$
Momentum	W	μ_t	$-\dfrac{\partial p}{\partial z} + \dfrac{\partial}{\partial x}(\mu_t \dfrac{\partial U}{\partial z}) + \dfrac{\partial}{\partial y}(\mu_t \dfrac{\partial V}{\partial z})$ $+ \dfrac{\partial}{\partial z}(\mu_t \dfrac{\partial W}{\partial z} - \dfrac{2}{3}\rho k)$
Temperature	T	$\dfrac{\mu_t}{\sigma_t}$	0
Turbulent kinetic Energy	k	$\dfrac{\mu_t}{\sigma_k}$	$\rho(S_k + S_B) - \rho \cdot \varepsilon \cdot C_D$
Dissipation of Turbulent kinetic energy	ε	$\dfrac{\mu_t}{\sigma_\varepsilon}$	$C_1 \rho \dfrac{\varepsilon}{k}(S_k + S_B) - C_2 \rho \dfrac{\varepsilon^2}{k}$

computer resources available. Therefore, a numerical technique utilizes the dependent variable at a finite number of locations, referred to from now on as *grid points* or *grid nodes* , as the primary unknowns in the calculation domain. This necessitates the description of a solution mesh or grid that covers the entire flow field. The control volume method is introduced here, where the calculation domain is divided into a finite number of nonoverlapping control volumes so that there is one control volume surrounding each grid node, (see Fig. 5.1 below). The differential equation is then integrated over each control volume. The variation of the dependent variables between the grid points uses piecewise profiles instead of a continuous profile . The reason for using piecewise profiles is due to the nature of turbulence which causes sudden changes in the dependent variables, and to use one profile over the whole flow field to describe these changes will make the problem highly complicated. The control volume approach is some-what comparable to the finite difference scheme, but the distribution of the main grid points are not identical. Also no distinct control volume is obvious in the finite difference mesh (see Figures 5.1 and 5.2).

5.5.3 The Discretization Equation

Once an 'acceptable' distribution of the dependent variables, within the calculation domain, has been chosen we turn our attention to the process of discretizing the differential equations.
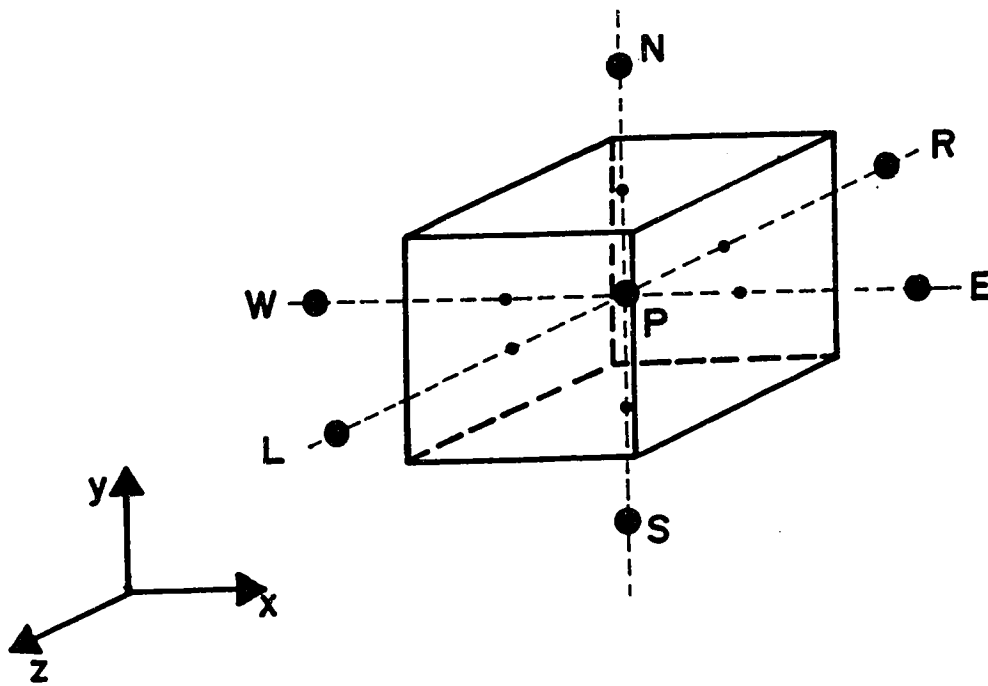
Figure. 5·1 A typical 3 – D. control volume.

i,j+1   i,j   i-1,j

i+1,j

Surface i+(1/2),j

Surface i-(1/2),j

•i,j+1   •i,j   •i-1,j

•

•i+1,j

•

i,3   i,2   i,1

i-1,2

i-1,1

i+1,2

i+1,1

i+2,1

•i,3   •i,2   •i,1

•

•i+1,2

•i+1,1

•i-1,2

•i-1,1

Y(j)

X(i)

Figure 5·2(a) Control volume mesh.

Figure 5·2(b) Finite difference mesh.

A discretization equation is nothing more than an algebraic relation joining the values of a dependent variable among a group of grid points. Such an equation follows from the differential expression describing the dependent variable over the flow domain, and thus should contain the same physical information as the differential equation. The reason that only a few grid points show up in a particular discretization equation is a result of the discontinuous, piecewise profiles, mentioned earlier. As a direct consequence of this the value of the dependent variable at a grid point affects the distribution of the same variable in the immediate surrounding nodes. Ideally as the number of grid nodes becomes larger and larger the solution of the discretization equation should approach the exact solution of the corresponding differential equation.

5.5.3.1 Derivation of the discretization equation

Details on how the final form of the algebraic discretization equation has been deduced is presented now.

Going back to equation (5.52) above and writing it in Cartesian tensor notation for three dimensional flow, it may be given as [5,6]

$$\frac{\partial J_x}{\partial x} + \frac{\partial J_y}{\partial y} + \frac{\partial J_z}{\partial z} = S_\Phi \tag{5.53}$$

where J_x, J_y, and J_z are the total fluxes acting on a specific control volume surface and are defined as,

$$J_x = \rho U_\Phi - \Gamma_\Phi \frac{\partial \Phi}{\partial x} \qquad (5.54a)$$

$$J_y = \rho V_\Phi - \Gamma_\Phi \frac{\partial \Phi}{\partial y} \qquad (5.54b)$$

$$J_z = \rho W_\Phi - \Gamma_\Phi \frac{\partial \Phi}{\partial z} \qquad (5.54c)$$

Integrating equation (5.53) over the control volume, depicted in Fig. (5.3), would result in

$$(J_e - J_w) + (J_n - J_s) + (J_r - J_l) = S_\Phi \cdot \Delta x \cdot \Delta y \cdot \Delta z \qquad (5.55)$$

In most practical problems the source term, S_Φ, is quite often a function of the dependent variable, Φ. Furthermore, as we are striving to produce a linear algebraic discretization relation, the source term should also be 'linearized'. The common practice typically adopted by many researchers [5,6,26,29,40,42,57] is as follows:

$$S_\Phi = S_{\Phi,c} + S_{\Phi,p} \Phi_p \qquad (5.56)$$

where $S_{\Phi,c}$ represents the constant part of S_Φ, while $S_{\Phi,p}$ is the coefficient of Φ_p. Inserting equation (5.56) into (5.55) gives

$$J_e - J_w + J_n - J_s + J_r - J_l = (S_{\Phi,c} + S_{\Phi,p} \cdot \Phi_p) \Delta x \cdot \Delta y \cdot \Delta z \qquad (5.57)$$

Here Φ_p is assumed to prevail over the entire control volume. In addition J_e, J_w, J_n, J_s, J_r and J_l describes the integrated total fluxes on the control
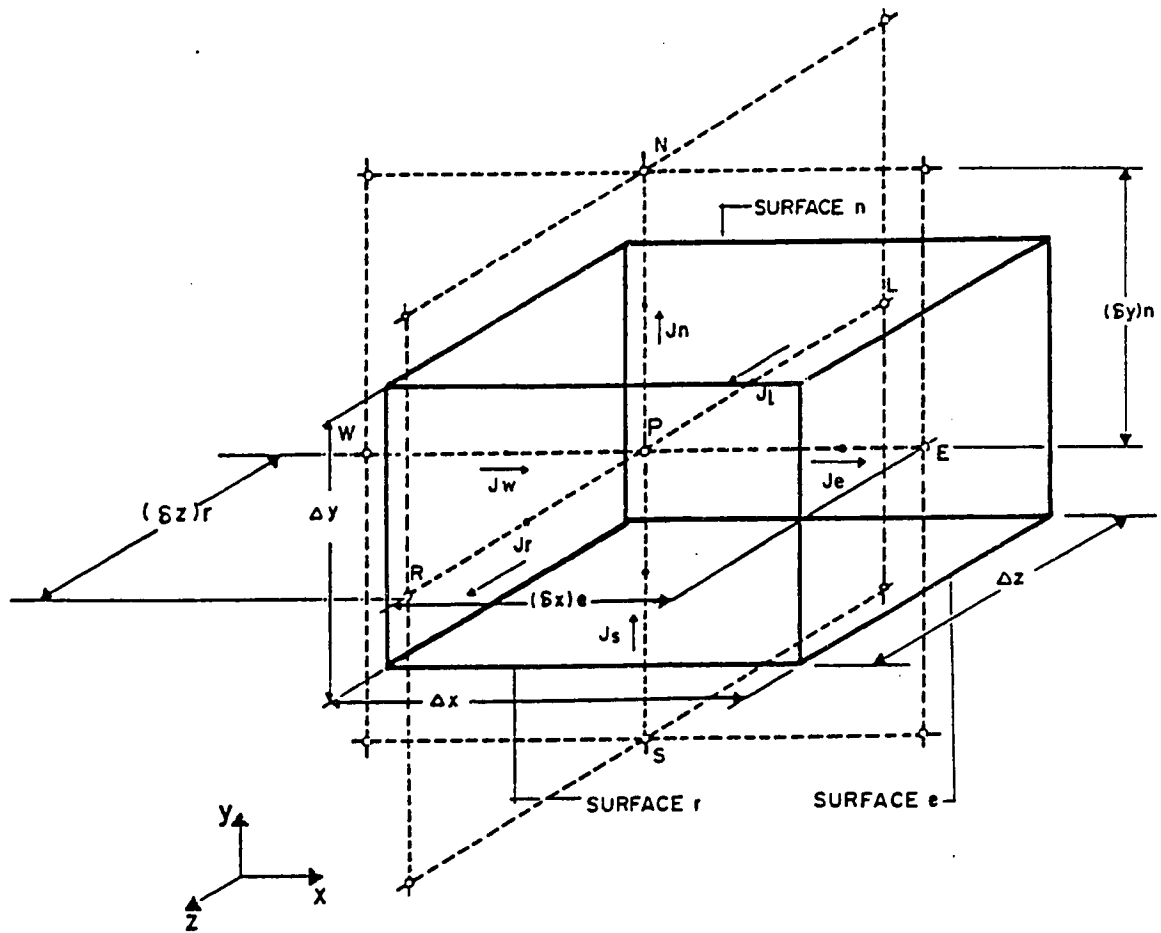
Figure 5.3. Control volume in three dimensions, showing the total flux acting at the faces.

volume surfaces, as shown in Fig. 5.3. To ensure that the continuity is satisfied, equation (5.8) is integrated over the same control volume and by doing so we get,

$$F_e - F_w + F_n - F_s + F_r - F_l = 0 \qquad (5.58)$$

such that F_e, F_w, F_n, F_s, F_r and F_l are the mass flow rates through the faces of the control volume. They may be expressed as follows

$$F_e = (\rho U)_e \, \Delta y \, \Delta z \qquad (5.59a)$$

$$F_w = (\rho U)_w \, \Delta y \, \Delta z \qquad (5.59b)$$

$$F_n = (\rho V)_n \, \Delta x \, \Delta z \qquad (5.59c)$$

$$F_s = (\rho V)_s \, \Delta x \, \Delta z \qquad (5.59d)$$

$$F_r = (\rho W)_r \, \Delta x \, \Delta y \qquad (5.59e)$$

$$F_l = (\rho W)_l \, \Delta x \, \Delta y \qquad (5.59f)$$

If we multiply equation (5.58) by Φ_p and then subtract it from equation (5.57), we would result in

$$(J_e - F_e \Phi_p) - (J_w - F_w \Phi_p) + (J_n - F_n \Phi_p) - (J_s - F_s \Phi_p) + (J_r - F_r \Phi_p)$$
$$- (J_l - F_l \Phi_p) = (S_{\Phi,c} + S_{\Phi,p} \, \Phi_p) \Delta x \, . \, \Delta y \, . \, \Delta z \qquad (5.60)$$

This relation is a discretization equation, but it is not in the final form. To

arrive to the final form requires the implementation of a discretization scheme, which will be handled in the following sub-section.

5.5.3.2 The discretization scheme.

Out of the numerous schemes available [43,58,59], the *hybrid scheme* will be utilized in this investigation. Reasons for such a selection is detailed later, but for now the scheme is described below.

The hybrid scheme, as the name suggests, is a crossbreed of two other finite difference schemes which are the central-difference scheme and the upwind scheme. The hybrid scheme resembles the central-difference scheme for low absolute values of the Peclet number, Pe, while for larger values it is identical to the upwind scheme. That is to say

Hybrid scheme ≡ Central - Difference scheme, for - 2 ≤ Pe ≤2

Hybrid Scheme ≡ Upwind scheme, for Pe < −2 and Pe > 2.

where the Peclet number may be physically interpreted as the ratio of convection to diffusion, as follows,

$$Pe = \frac{\rho \bar{V} L}{\Gamma} \tag{5.61}$$

such that $\bar{V}$ is the velocity in the direction of flow, L is a length scale and Γ is the diffusion coefficient.

Some of the benefits gained by using the hybrid scheme may be listed as :

1. No negative discretization coefficients, to be mentioned later on, would appear. Thus guarantying a physically realestic solution [43].

2. Does not overestimate the diffusion at large absolute values of the Peclet number.

3. Is simple to implement into a numerical code and proves to be economical in calculation costs in comparison to similar performance schemes.

5.5.3.3 The final form of the discretization equation:

A common practice [5,6,29,40,43] typically is to explicitly display the dependent variables of the control volume together with its immediate neighbours, (see Figure 5.3). The hybrid discretization scheme when applied to equation (5.60) yields the discretization expression to be employed henceforth,

$$J_e - F_e \Phi_P = a_E (\Phi_P - \Phi_E) \tag{5.62a}$$

$$J_w - F_w \Phi_P = a_W (\Phi_W - \Phi_P) \tag{5.62b}$$

$$J_n - F_n \Phi_P = a_N (\Phi_P - \Phi_N) \tag{5.62c}$$

$$J_s - F_s \Phi_P = a_S (\Phi_S - \Phi_P) \tag{5.62d}$$

$$J_r - F_r\Phi_P = a_R (\Phi_P - \Phi_R) \tag{5.62e}$$

$$J_l - F_l\Phi_P = a_L (\Phi_L - \Phi_P) \tag{5.62f}$$

where Φ_P is the dependent variable of the control volume and Φ_E, Φ_W, Φ_N, Φ_S, Φ_R and Φ_L are the dependent variables at the surrounding grid points (outside the control volume) S, N, E, W, R and L, respectively while a_E, a_W, a_N, a_S, a_R and a_L are the discretization coefficients at the respective locations, (see Fig. 5.3). These discretization coefficients are defined as follows [5,43]

$$a_E = D_e . A(|Pe_e|) + AMAX1(-F_e, 0) \tag{5.63a}$$

$$a_W = D_w . A(|Pe_w|) + AMAX1(F_w, 0) \tag{5.63b}$$

$$a_N = D_n . A(|Pe_n|) + AMAX1(-F_n, 0) \tag{5.63c}$$

$$a_S = D_s . A(|Pe_s|) + AMAX1(F_s, 0) \tag{5.63d}$$

$$a_R = D_r . A(|Pe_r|) + AMAX1(-F_r, 0) \tag{5.63e}$$

$$a_L = D_l . A(|Pe_l|) + AMAX1(F_l, 0) \tag{5.63f}$$

where D_e, D_w, D_n, D_s, D_r and D_l are the diffusion conductances across the faces of the control volume. They are defined by

$$D_e = \frac{\Gamma_e \, \Delta y \, \Delta z}{(\delta x)_e} \qquad (5.64a)$$

$$D_w = \frac{\Gamma_w \, \Delta y \, \Delta z}{(\delta x)_w} \qquad (5.64b)$$

$$D_n = \frac{\Gamma_n \, \Delta z \, \Delta x}{(\delta y)_n} \qquad (5.64c)$$

$$D_s = \frac{\Gamma_s \, \Delta z \, \Delta x}{(\delta y)_s} \qquad (5.64d)$$

$$D_r = \frac{\Gamma_r \, \Delta x \, \Delta y}{(\delta z)_r} \qquad (5.64e)$$

$$D_l = \frac{\Gamma_l \, \Delta x \, \Delta y}{(\delta z)_l} \qquad (5.64f)$$

The functions $A(|Pe_e|)$, $A(|Pe_w|)$, $A(|Pe_n|)$, $A(|Pe_s|)$, $A(|Pe_r|)$ and $A(|Pe_l|)$ appearing in equations (5.63) represent a compact form of the discretization scheme adopted, indicating that it is a function of the absolute value of the local Peclet number. For the hybrid scheme they are as follows [5,40,43] ,

$$A\,(|Pe_e|) = AMAX1\,(0, 1 - 0.5 \cdot |Pe_e|) \qquad (5.65a)$$

$$A\,(|Pe_w|) = AMAX1\,(0, 1 - 0.5 \cdot |Pe_w|) \qquad (5.65b)$$

$$A\,(|Pe_n|) = AMAX1\,(0, 1 - 0.5 \cdot |Pe_n|) \qquad (5.65c)$$

$$A\ (|Pe_s|)\ =\ AMAX1\ (0, 1 - 0.5 \cdot |Pe_s|) \tag{5.65d}$$

$$A\ (|Pe_r|)\ =\ AMAX1\ (0, 1 - 0.5 \cdot |Pe_r|) \tag{5.65e}$$

$$A\ (|Pe_l|)\ =\ AMAX1\ (0, 1 - 0.5 \cdot |Pe_l|) \tag{5.65f}$$

In equations (5.63) and (5.65) above, a new function AMAX1 has been introduced which is identical to the function in the FORTRAN computer language, and stands for the maximum value of the parameters within the bracket.

Applying the hybrid scheme given by equations (5.62), into equation (5.60) and after some rearrangement would result in [5,6,29,40,43],

$$a_P \Phi_P\ =\ a_E \Phi_E + a_W \Phi_W + a_N \Phi_N + a_S \Phi_S + a_R \Phi_R + a_L \Phi_L + b \tag{5.66}$$

where

$$a_P\ =\ a_E + a_W + a_N + a_S + a_R + a_L - S_{\Phi,p} \cdot \Delta x \cdot \Delta y \cdot \Delta z \tag{5.67a}$$

$$b\ =\ S_{\Phi,c} \cdot \Delta x \cdot \Delta y \cdot \Delta z \tag{5.67b}$$

Equation (5.66) is the final form of the discretization equation sought for. Equations (5.59), (5.63), (5.64), (5.65) and (5.67) are the corresponding supplemental equations. Equation (5.66) is sometimes written in a short form by using the summation indices [40,43],

$$\left(\Sigma\ a_i - S_{\Phi,p} \cdot \Delta x \cdot \Delta y \cdot \Delta z \right) \Phi_P\ =\ \Sigma\ (a_i\ \Phi_i) + S_{\Phi,c} \cdot \Delta x \cdot \Delta y \cdot \Delta z \tag{5.68}$$

where the summation index i varies as : N, S, E, W, R and L.

5.6 THE STAGGERED GRID

Calculation of some of the transport equations given in Table 5.2 requires the prior knowledge of the pressure field which is evaluated indirectly by the continuity equation such that by introducing the correct pressure field into the momentum equations, produces a velocity field that would, inturn, satisfy the continuity equation. However, this approach proves to be highly inappropriate due to the iterative nature of this investigation.

Another common approach used in two-dimensional flow is the stream function-vorticity technique which does not involve the evaluation of the pressure. However, in this method there appears some serious drawbacks some of which are :

a.   The difficulty of specifying the vorticity at a solid wall.

b.   If the pressure field is desired then it must be obtained from the vorticity, which increases the calculation requirements.

c.   It can not be easily expressed in three dimensions, where the streamfunction does not exist.

In view of the above limitations the stream function-vorticity approach is not considered in this study and instead the solution for the primitive variables is preferred and investigated later.

Referring to Table 5.2, it is observed that the pressure appears as a gradient in the source term of the momentum equations. Considering this gradient and integrating it over the control volume (Fig. 5.3), will result in

$$\int\limits_{w}^{e}\int\limits_{s}^{n}\int\limits_{l}^{r} -\frac{\partial p}{\partial x} dx\, dy\, dz = \left(p_w - p_e\right) \cdot \Delta y \cdot \Delta z \tag{5.69a}$$

$$\int\limits_{w}^{e}\int\limits_{s}^{n}\int\limits_{l}^{r} -\frac{\partial p}{\partial y} dx\, dy\, dz = \left(p_s - p_n\right) \cdot \Delta x \cdot \Delta z \tag{5.69b}$$

$$\int\limits_{w}^{e}\int\limits_{s}^{n}\int\limits_{l}^{r} -\frac{\partial p}{\partial z} dx\, dy\, dz = \left(p_l - p_r\right) \cdot \Delta x \cdot \Delta y \tag{5.69c}$$

where p_w, p_e, p_s, p_n, p_l, and p_r are the pressures acting at the faces of the control volume. Equations (5.69) above represent the potential or pressure drop from the upstream faces of the control volume to the downstream faces. These pressure losses are felt by the control volume as forces exerted on the surface areas. To express the surface pressures in terms of grid point pressures, a piecewise linear profile has been assumed and the control volume faces are set equidistant between the grid points. Under these conditions equations (5.69) may be expressed by

$$p_w - p_e = \frac{p_W + p_P}{2} - \frac{p_P + p_E}{2} = \frac{p_W - p_E}{2} \tag{5.70a}$$

$$p_s - p_n = \frac{p_S + p_P}{2} - \frac{p_P + p_N}{2} = \frac{p_S - p_N}{2} \tag{5.70b}$$

$$p_l - p_r = \frac{p_L + p_P}{2} - \frac{p_P + p_R}{2} = \frac{p_L - p_R}{2} \qquad (5.70c)$$

where p_P, p_W, p_E, p_N, p_S, p_R, and p_L are the pressure values at the corresponding grid nodes.

It is obvious that, when equations (5.70) is applied to the source term in the integrated form of the momentum equations it will incorporate the pressure difference between two alternate grid points, not between two neighbouring ones. Some of the grave consequences resulting from this is listed as follows:

1. As the pressure difference is taken from a grid point to an alternate grid point, the resulting effective mesh describing this net pressure is actually coarser than the one adopted to describe the flow field. This will naturally demote the accuracy of the calculation.

2. Another enigma from this approach is that if a checkerboard pattern is used to describe the pressure field, where the value at the grid nodes of every alternate pressure are equal while neighbouring pressures are different, the resulting pressure gradient in the source term of the momentum equations would completely disappear. Hence, an actually non-homogeneous pressure field would be accepted as a uniform field. Furthermore, any pressure field having a checkerboard distribution would not produce any changes to the momentum equations, and thus no unique solution would result.

In attempting to discretize the differential form of the continuity equation a dilemma similar to the above discussed pressure gradient term in the momentum equations reappears. The profiles describing the velocities between the grid points are assumed to be piecewise and linear. The faces of the control volumes are chosen to lie midway between adjacent grid points. After discretizing the continuity equation, the velocity at a grid node becomes equal to the velocity at alternate grid points, for all three Cartesian space coordinate directions. Thus if the velocity field was represented by a fictitious checkerboard pattern it would satisfy the continuity equation, but would result with an absurd distribution of the velocity.

The aforementioned difficulties are simply taken care of by specifying a displaced or staggered grid. This will be the topic of the sub-section to follow.

5.6.1 Description of the Staggered Grid

The staggered grid has first been reported in [22], later on it has been adopted by many [4,5,6,20,26,29,31,32,35,37,40,43,44,46,52]. In this approach the vector variables (i.e.: U, V and W) are specified normal to the center of the control volume faces, while the scalar quantities (i.e: T, k, p, ε, ρ) are situated at the grid point P of the control volume, from now on known as the main grid point, see Fig. 5.4 . Considering the location of the vector quantities relative to the main grid node it may be observed that for a particular direction, such as the x-direction (see Fig. 5.5.a), the corresponding velocity
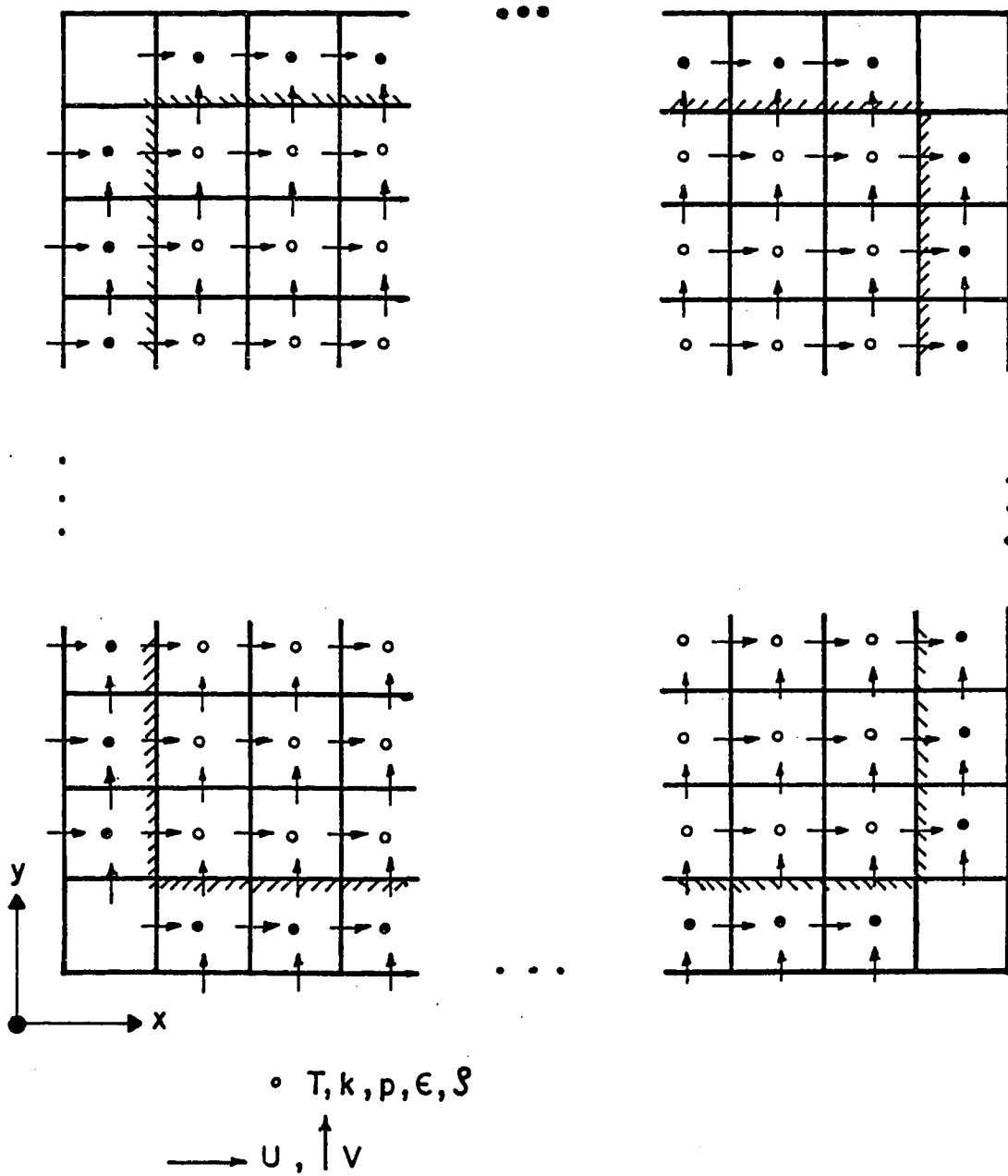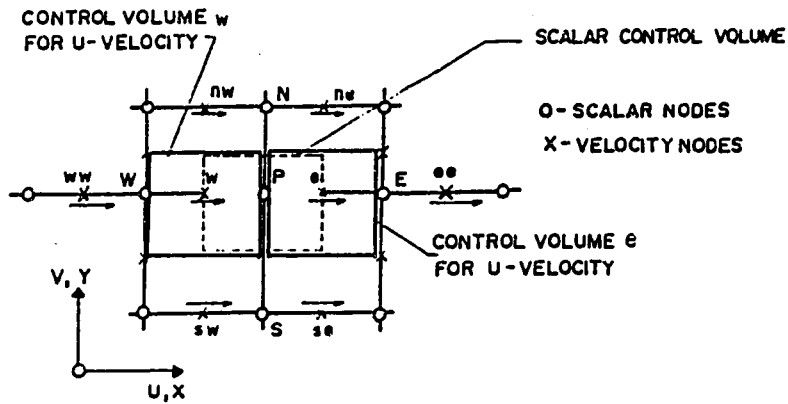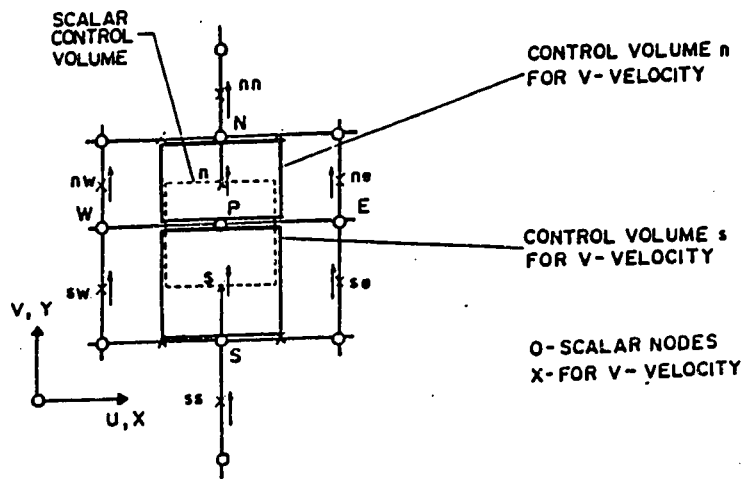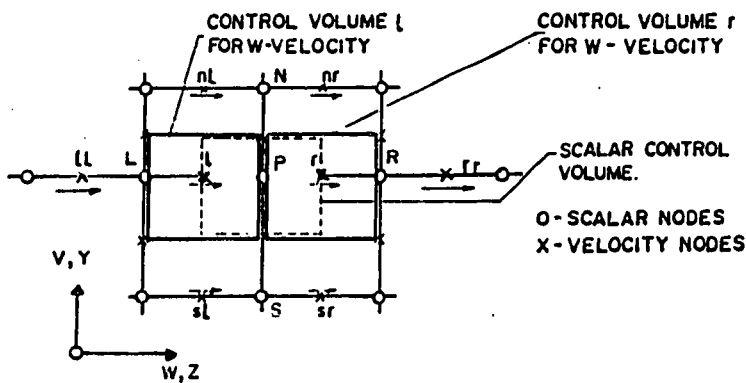
Figure 5.4. Staggered grid shown over the entire flow field.

a.) Control volumes for U- Velocity.

b) Control volumes for V - Velocity.

c.) Control volumes for W-velocity.

Figure 5.5 Velocity control volumes

(i.e: the U-velocity) will be displaced up-stream, midway the distance between the main node and the one just before it. This location is referred to as the *minor* grid node w. The control volume enclosing this minor grid point is known as the vector or velocity control volume. A reasoning parallel to the above may be carried out for the other Cartesian directions, producing minor grid nodes and vector control volumes for the V and W velocities (see Figs. 5.5.b, 5.5.c).

Some of the advantages perceived from adopting the displaced grid approach may be listed as follows :

a. The mass flow rates of equations (5.59) above, which act at the minor grid nodes, can now be evaluated straightforwardly, not requiring the interpolation of the relevant velocities, because the staggered velocity locations coincide with the mass flow rates, which even though was not sought for, but turned out as a positive development.

b. The algebraic discretized form of the continuity equation will consist of the differences of neighbouring velocity components instead of alternating ones. Thus the possibility of accepting highly fictitious velocity fields as a probable solution has been completely eliminated.

c. The pressure difference between two adjacent main grid points, now becomes the inherent driving force for the velocity component situated in between these grid nodes. Hence, absurd pressure fields, such as the checkerboard pattern, would not be accepted as uniform pressure fields.

The above staggered grid approach is not without faults. A program using this method must define the geometric locations of the minor grid nodes and conduct tedious interpolations. But many researchers, [5,6,16,18,19,20,25,29, 30,37,40,43,45,46,52] acquainted with this technique, admit that its benefits far outweighs its shortcomings.

5.7 The VELOCITY-PRESSURE COUPLING

In employing the staggered grid to the flow field under study, it is obvious that only the discretized form of the transport momentum equations for U, V and W shall alter somewhat, because the locations where these variables act has been displaced, as discussed earlier. While the other discretization equations describing the remaining variables are not changed, on account that they still act at the main grid node. The discretized form of the momentum equation acting on the six faces of the control volume (see Fig. 5.3), may be written as follows [5,43,46,52] :

$$a_e U_e = \Sigma a_{nb,e} U_{nb,e} + b_e + (p_P - p_E) \cdot A_e \qquad (5.71a)$$

$$a_w U_w = \Sigma a_{nb,w} U_{nb,w} + b_w + (p_W - p_P) \cdot A_w \qquad (5.71b)$$

$$a_n V_n = \Sigma a_{nb,n} V_{nb,n} + b_n + (p_P - p_N) \cdot A_n \qquad (5.71c)$$

$$a_s V_s = \Sigma a_{nb,s} V_{nb,s} + b_s + (p_S - p_P) \cdot A_s \qquad (5.71d)$$

$$a_r W_r = \Sigma\, a_{nb,r}\, W_{nb,r} + b_r + (p_P - p_R) \cdot A_r \qquad (5.71e)$$

$$a_l W_l = \Sigma\, a_{nb,l}\, W_{nb,l} + b_l + (p_L - p_P) \cdot A_l \qquad (5.71f)$$

In equation (5.71) the lower case subscript refer to the surface faces of the control volume, or more accurately the minor grid point locations. While the upper case subscripts refers to the main grid nodes. a_e, a_w, a_n, a_s, a_r and a_l are the discretization coefficients for the e, w, n, s, r and l velocity control volumes, respectively (see Fig. 5.5). These coefficients may be stated as follows :

$$a_e = \Sigma\, a_{nb,e} - S_{p,e} \cdot (\delta x)_e \cdot \Delta y \cdot \Delta z \qquad (5.72a)$$

$$a_w = \Sigma\, a_{nb,w} - S_{p,w} \cdot (\delta x)_w \cdot \Delta y \cdot \Delta z \qquad (5.72b)$$

$$a_n = \Sigma\, a_{nb,n} - S_{p,n} \cdot \Delta x \cdot (\delta y)_n \cdot \Delta z \qquad (5.72c)$$

$$a_s = \Sigma a_{nb,s} - S_{p,s} \cdot \Delta x \cdot (\delta y)_s \cdot \Delta z \qquad (5.72d)$$

$$a_r = \Sigma a_{nb,r} - S_{p,r} \cdot \Delta x \cdot \Delta y \cdot (\delta z)_r \qquad (5.72e)$$

$$a_l = \Sigma a_{nb,l} - S_{p,l} \cdot \Delta x \cdot \Delta y \cdot (\delta z)_l \qquad (5.72f)$$

where the summation terms on the right hand side of equation (5.71) stands for :

$$\Sigma \, a_{nb,e} \cdot U_{nb,e} \; = \; a_{ee} \cdot U_{ee} + a_w \cdot U_w + a_{ne} \cdot U_{ne}$$

$$+ \; a_{se} \cdot U_{se} + a_{re} \cdot U_{re} + a_{le} \cdot U_{le} \qquad (5.73a)$$

$$\Sigma \, a_{nb,w} \cdot U_{nb,w} \; = \; a_e \cdot U_e + a_{ww} \cdot U_{ww} + a_{nw} \cdot U_{nw}$$

$$+ \; a_{sw} \cdot U_{sw} + a_{rw} \cdot U_{rw} + a_{lw} \cdot U_{lw} \qquad (5.73b)$$

$$\Sigma \, a_{nb,n} \cdot V_{nb,n} \; = \; a_{nn} \cdot V_{nn} + a_s \cdot V_s + a_{ne} \cdot V_{ne}$$

$$+ \; a_{nw} \cdot V_{nw} + a_{nr} \cdot V_{nr} + a_{nl} \cdot V_{nl} \qquad (5.73c)$$

$$\Sigma \, a_{nb,s} \cdot V_{nb,s} \; = \; a_n \cdot V_n + a_{ss} \cdot V_{ss} + a_{se} \cdot V_{se}$$

$$+ \; a_{sw} \cdot V_{sw} + a_{sr} \cdot V_{sr} + a_{sl} \cdot V_{sl} \qquad (5.73d)$$

$$\Sigma \, a_{nb,r} \cdot W_{nb,r} \; = \; a_{rr} \cdot W_{rr} + a_l \, W_l + a_{nr} \cdot W_{nr}$$

$$+ \; a_{sr} \cdot W_{sr} + a_{re} \cdot W_{re} + a_{rw} \cdot W_{rw} \qquad (5.73e)$$

$$\Sigma \, a_{nb,l} \cdot W_{nb,l} \; = \; a_r \cdot W_r + a_{ll} \cdot W_l + a_{nl} \cdot W_{nl}$$

$$+ \; a_{sl} \cdot W_{sl} + a_{le} \cdot W_{le} + a_{lw} \cdot W_{lw} \qquad (5.73f)$$

The first term on the right hand side of equation (5.72) may be represented by expressions similar to that of (5.73), but without the velocities, U, V and W appearing, while the second term describes the variable part of the 'linearized' source term.

The second term on the R.H.S. of equation (5.71) is the 'constant' part of the linearized source term, integrated over the specific control volume under consideration, as follows

$$b_e = S_{c,e} \cdot (\delta x)_e \cdot \Delta y \cdot \Delta z \qquad (5.74a)$$

$$b_w = S_{c,w} \cdot (\delta x)_w \cdot \Delta y \cdot \Delta z \qquad (5.74b)$$

$$b_n = S_{c,n} \cdot \Delta x \cdot (\delta y)_n \cdot \Delta z \qquad (5.74c)$$

$$b_s = S_{c,s} \cdot \Delta x \cdot (\delta y)_s \cdot \Delta z \qquad (5.74d)$$

$$b_r = S_{c,r} \cdot \Delta x \cdot \Delta y \cdot (\delta z)_r \qquad (5.74e)$$

$$b_l = S_{c,l} \cdot \Delta x \cdot \Delta y \cdot (\delta z)_l \qquad (5.74f)$$

A_e, A_w, A_n, A_s, A_r and A_l appearing in (5.71) are the surface areas of the control volume (see Fig. 5.3) which may be expressed as :

$$A_e = (\Delta y \cdot \Delta z)_e \qquad (5.75a)$$

$$A_w = (\Delta y \cdot \Delta z)_w \qquad (5.75b)$$

$$A_n = (\Delta x \cdot \Delta z)_n \qquad\qquad (5.75c)$$

$$A_s = (\Delta x \cdot \Delta z)_s \qquad\qquad (5.75d)$$

$$A_r = (\Delta x \cdot \Delta y)_r \qquad\qquad (5.75e)$$

$$A_l = (\Delta x \cdot \Delta y)_l \qquad\qquad (5.75f)$$

The striking distinction between the discretization equation for scalar variables, i.e., equation (5.66) and for vector variables, i.e., equation (5.71), is the appearance of an additional term on the right hand side of equation (5.71). This term was present in equation (5.66) but was not apparent, because it was embodied into the constant part of the source term and may be interpreted as the net force acting on a particular face of the control volume due to the pressure difference between the two nodes encompassing this face.

By simple inspection of equation (5.71) it is obvious that to solve for the velocity field, a prior knowledge of the pressure distribution within this field is necessary. Furthermore, there is no straightforward relation available to solve for the pressure. Thus, this will be handled in the subsection to follow.

5.7.1 The Decomposition of Velocity and Pressure

In reference to the discretization equation (5.71), it will be reaffirmed here that to solve for the velocity field a pressure distribution must be avail-

able. The only condition binding the selection of the pressure distribution is that the resulting velocity field is required to satisfy the continuity equation. Therefore, it is quite evident that we must resort to an iterative approach to the problem. In this approach we first assume a pressure field designated by p^* and substituting this proposed pressure field into the discretization equations (5.71) would result in an approximate velocity distribution, i.e. U^*, V^* and W^* which will most probably not satisfy the continuity equation. This is achieved as follows

$$a_e \cdot U^*_e = \Sigma \, a_{nb,e} \cdot U^*_{nb,e} + b_e + \left(p^*_P - p^*_E \right) \cdot A_e \qquad (5.76a)$$

$$a_w \cdot U^*_w = \Sigma \, a_{nb,w} \cdot U^*_{nb,w} + b_w + \left(p^*_W - p^*_P \right) \cdot A_w \qquad (5.76b)$$

$$a_n \cdot V^*_n = \Sigma \, a_{nb,n} \cdot V^*_{nb,n} + b_n + \left(p^*_P - p^*_N \right) \cdot A_n \qquad (5.76c)$$

$$a_s \cdot V^*_s = \Sigma \, a_{nb,s} \cdot V^*_{nb,s} + b_s + \left(p^*_S - p^*_P \right) \cdot A_s \qquad (5.76d)$$

$$a_r \cdot W^*_r = \Sigma \, a_{nb,r} \cdot W^*_{nb,r} + b_r + \left(p^*_P - p^*_R \right) \cdot A_r \qquad (5.76e)$$

$$a_l \cdot W^*_l = \Sigma \, a_{nb,l} \cdot W^*_{nb,l} + b_l + \left(p^*_L - p^*_P \right) \cdot A_l \qquad (5.76f)$$

To refine the assumed pressure field p^* we now require a technique such that the calculated velocity distribution U^*, V^* and W^*, from equation (5.76) will

eventually fulfill the continuity equation. To do this, first of all we will express the rectified pressure as

$$p = p^* + p' \tag{5.77}$$

where p' is known as the pressure correction. This shall be employed over the entire flow field. Analogous to this, the velocity components shall be divided into two distinctive parts as follows

$$U = U^* + U' \tag{5.78a}$$

$$V = V^* + V' \tag{5.78b}$$

$$W = W^* + W' \tag{5.78c}$$

where U', V' and W' are the velocity corrections acting in the three Cartesian directions of x, y and z, respectively.

If we now subtract equations (5.76) from equations (5.71) in the respective order given and make use of equations (5.77) and (5.78) the outcome would be

$$a_e \cdot U'_e = \Sigma a_{nb, e} \cdot U'_{nb,e} + \left(p'_P - p'_E\right) \cdot A_e \tag{5.79a}$$

$$a_w \cdot U'_w = \Sigma a_{nb, w} \cdot U'_{nb, w} + \left(p'_W - p'_P\right) \cdot A_w \tag{5.79b}$$

$$a_n \cdot V'_n = \Sigma a_{nb, n} \cdot V'_{nb, n} + \left(p'_P - p'_N\right) \cdot A_n \tag{5.79c}$$

$$a_s \cdot V'_s = \Sigma\, a_{nb,s} \cdot V'_{nb,s} + \left(p'_S - p'_P\right) \cdot A_s \qquad (5.79d)$$

$$a_r \cdot W'_r = \Sigma\, a_{nb,r} \cdot W'_{nb,r} + \left(p'_P - p'_R\right) \cdot A_r \qquad (5.79e)$$

$$a_l \cdot W'_l = \Sigma\, a_{nb,l} \cdot W'_{nb,l} + \left(p'_L - p'_P\right) \cdot A_l \qquad (5.79f)$$

The first term on the R.H.S. of equation (5.79) is neglected. A detailed justification for this has been reported in [43,46], some of which is given later. As a result of this approximation equations (5.79) read as

$$a_e \cdot U'_e = \left(p'_P - p'_E\right) \cdot A_e \qquad (5.80a)$$

$$a_w \cdot U'_w = \left(p'_W - p'_P\right) \cdot A_w \qquad (5.80b)$$

$$a_n \cdot V'_n = \left(p'_P - p'_N\right) \cdot A_n \qquad (5.80c)$$

$$a_s \cdot V'_s = \left(p'_S - p'_P\right) \cdot A_s \qquad (5.80d)$$

$$a_r \cdot W'_r = \left(p'_P - p'_R\right) \cdot A_r \qquad (5.80e)$$

$$a_l \cdot W'_l = \left(p'_L - p'_P\right) \cdot A_l \qquad (5.80f)$$

Rearranging equations (5.80) results in,

$$U'_e = d_e \cdot \left(p'_P - p'_E\right) \qquad (5.81a)$$

$$U'_w = d_w \cdot \left(p'_W - p'_P\right) \tag{5.81b}$$

$$V'_n = d_n \cdot \left(p'_P - p'_N\right) \tag{5.81c}$$

$$V'_s = d_s \cdot \left(p'_S - p'_P\right) \tag{5.81d}$$

$$W'_r = d_r \cdot \left(p'_P - p'_R\right) \tag{5.81e}$$

$$W'_l = d_l \cdot \left(p'_L - p'_P\right) \tag{5.81f}$$

Equations (5.81) above are known as the *velocity-correction* formula [5,40,43,46,52], where the coefficient of the pressure difference in equations (5.81) are,

$$d_e = A_e / a_e \tag{5.82a}$$

$$d_w = A_w / a_w \tag{5.82b}$$

$$d_n = A_n / a_n \tag{5.82c}$$

$$d_s = A_s / a_s \tag{5.82d}$$

$$d_r = A_r / a_r \tag{5.82e}$$

$$d_l = A_l / a_l \tag{5.82f}$$

Now by substituting equations (5.81) into equations (5.78) the following equations are obtained,

$$U_e = U_e^* + d_e(p'_P - p'_E) \tag{5.83a}$$

$$U_w = U_w^* + d_w(p'_W - p'_P) \tag{5.83b}$$

$$V_n = V_n^* + d_n(p'_P - p'_N) \tag{5.83c}$$

$$V_s = V_s^* + d_s(p'_S - p'_P) \tag{5.83d}$$

$$W_r = W_r^* + d_r(p'_P - p'_R) \tag{5.83e}$$

$$W_l = W_l^* + d_l(p'_L - p'_P) \tag{5.83f}$$

A simple inspection of equations (5.83) reveals how the pressure correction, p', directly affects the assumed velocity fields (i.e.: $U_e^*, U_w^*, V_n^*, V_s^*, W_r^*$ and W_l^*) to yield an 'improved' velocity distribution, making it obvious our previous concern about the determination of the pressure corrections rather than the velocity corrections which does not appear at all in equations (5.83) above. We thus require a scheme to determine the pressure corrections. This will be presented in a separate sub-section to follow.

5.7.2 The Pressure Correction Formula

In the preceding subsection we came to the conclusion that to determine the velocity field we require previous knowledge of the distribution of the

pressure correction field. To accomplish this we need an equation to describe the pressure correction, p' , which is the intent of this subsection.

To develop the pressure correction equation, we shall turn to the differential form of the continuity equation mentioned earlier and integrate it over the control volume, see Fig. 5.3. Before arriving to the discretized form of the continuity equation, some of the assumptions used are listed as follows :

1. For the specific investigations undertaken in this study, the flow may be considered incompressible as the velocity is well below the sonic velocity and consequently the density has a weak dependence on pressure. Thus it will be postulated that the density does not directly depend on pressure.

2. The value of the density at the main grid node, will be taken constant over the entire control volume.

3. Velocity components at the surface of a control volume are uniform and are taken equal to the velocity acting at the the centre of the face.

With the above assumptions the discritized form of the continuity equation becomes [5,29,35,40,43,52] ,

$$\left[(\rho U)_e - (\rho U)_w\right] \cdot \Delta y \cdot \Delta z + \left[(\rho V)_n - (\rho V)_s\right] \cdot \Delta z \cdot \Delta x +$$
$$\left[(\rho W)_r - (\rho W)_l\right] \cdot \Delta x \cdot \Delta y = 0 \qquad (5.84)$$

Now substituting equations (5.83) into equation (5.84) and arranging it in a way comparable to equation (5.66), we acquire the discretized form of the *pressure correction formula* [5,43,52]

$$a_P \cdot p'_P = a_E \cdot p'_E + a_W \cdot p'_W + a_N \cdot p'_N + a_S \cdot p'_S + a_R \cdot p'_R + a_L \cdot p'_L + b \qquad (5.85)$$

where $a_P, a_E, a_W, a_N, a_S, a_R$ and a_L are the discretization coefficients for equation (5.85) and is expressed by

$$a_E = \rho_e d_e \, \Delta y \, \Delta z \qquad (5.86a)$$

$$a_W = \rho_w d_w \, \Delta y \, \Delta z \qquad (5.86b)$$

$$a_N = \rho_n d_n \, \Delta x \, \Delta z \qquad (5.86c)$$

$$a_S = \rho_s d_s \, \Delta x \, \Delta z \qquad (5.86d)$$

$$a_R = \rho_r d_r \, \Delta x \, \Delta y \qquad (5.86e)$$

$$a_L = \rho_l d_l \, \Delta x \, \Delta y \qquad (5.86f)$$

The last term on the right hand side of equation (5.85) is a 'constant' term and represents all the terms not containing the p' variable and is given by [43] as ,

$$b = \left[(\rho U^*)_w - (\rho U^*)_e \right] \Delta y \, \Delta z + \left[(\rho V^*)_s - (\rho V^*)_n \right] \Delta x \, \Delta z +$$
$$\left[(\rho W^*)_l - (\rho W^*)_r \right] \Delta x \, \Delta y \qquad (5.87)$$

The coefficients ρ_e, ρ_w, ρ_n, ρ_s, ρ_r and ρ_l appearing in the equations above, are a representative value of the density at the corresponding interfaces of the control volume.

By comparing equations (5.84), i.e.: the discretized continuity equation, and (5.87), we see that the latter is nothing more than the negative of the former. Thus ideally when the exact solution is achieved the left hand side of (5.87) should reduce to zero. When that occurs equation (5.87) becomes identical to the continuity equation. Bearing this in mind we may interpret the parameter b to portray a kind of 'mass source' which the pressure corrections in association with the velocity corrections, must try to eliminate.

5.7.3 The SIMPLE Scheme

There has been many attempts to handle the velocity-pressure link stated above, [39, 60, 61 , 62] with varying degrees of success. But the algorithm to receive most attention, in the author's view, is the SIMPLE technique which stands for $\underline{S}$ emi - $\underline{I}$ mplicit $\underline{M}$ ethod for $\underline{P}$ ressure - $\underline{L}$ inked $\underline{E}$ quations, reported originally in [44]. This method has been adopted by many researchers [5,6,12,13,16,18,19,20,25,29,30,37,40,42, 52] on account of its reasonable ease of implementation, relatively high success rate and acceptable CPU time.

To solve for the flow field in a clear and concise manner a sequence of distinct steps should be taken as follows [5,6,29,40,42,52] (See Fig. 5.6):

```
                    ┌─────────┐
                    │  START  │
                    └────┬────┘
                         │
                         ▼
        ┌────────────────────────────────────────┐
        │ Initialize all veriables in the entire  │
        │ flow field.                             │
        │ Set: U , V , W , k , T , S , E , p      │
        └────────────────────────────────────────┘
                         │
   ┌─────────────────────┼
   │                     ▼
   │    ┌────────────────────────────────────────┐
   │    │ Solve for: U*, V* and W* from equation  │
   │    │ (5.76)                                  │
   │    └────────────────┬───────────────────────┘
   │                     ▼
   │    ┌────────────────────────────────────────┐
   │    │ Solve for : p from equation (5.85)      │
   │    └────────────────┬───────────────────────┘
   │                     ▼
   │    ┌────────────────────────────────────────┐
   │    │ Solve for: p from equation (5.77)       │
   │    └────────────────┬───────────────────────┘
   │                     ▼
   │    ┌────────────────────────────────────────┐
   │    │ Solve for: U,V, and W from equation     │
   │    │ (5.83)                                  │
   │    └────────────────┬───────────────────────┘
   │                     ▼
   │    ┌────────────────────────────────────────┐
   │    │ Solve for: T, K, and E from equation    │
   │    │ (5.66)                                  │
   │    └────────────────┬───────────────────────┘
   │                     ▼
   │    ┌────────────────────────────────────────┐
   │    │ Solve for: S from the ideal equation of │
   │    │ state                                   │
   │    └────────────────┬───────────────────────┘
   │                     ▼
   │    ┌────────────────────────────────────────┐
   │    │ Solve for: b from equation (5.87)       │
   │    └────────────────┬───────────────────────┘
   │           NO        ▼
   └─────────────(  IF b ≤ Δtol  )
                        │ YES
                        ▼
                    ┌─────────┐
                    │   END   │
                    └─────────┘
```
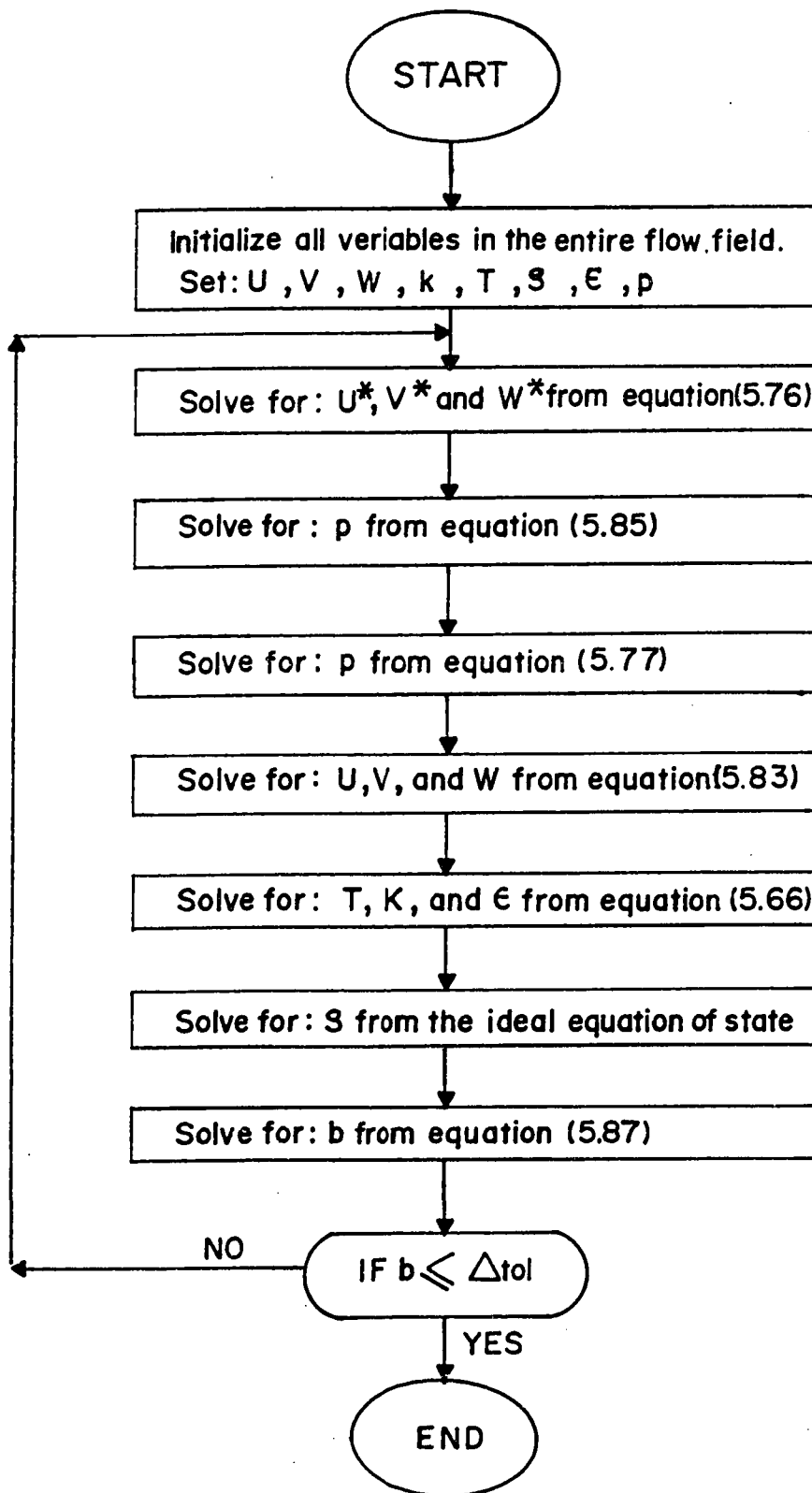
Figure 5.6 Flow chart describing the SIMPLE algorithim.

I.   Initialize all the relevant parameters in the entire flow field. [It is worthwhile to note here that as the initial choice of the variables are physically more realistic it will have a positive effect on assuring convergence and reducing the overall CPU time] .

II. Insert the guessed variables into the discretized momentum equations (5.76) to produce a first estimate of the velocity components U^*, V^* and W^* by the LBL method, to be given later.

III. This will provide all the necessary components to solve for the pressure correction p' of equation (5.85) given by the LBL method.

IV. Substitute p' into equation (5.77) to solve for the pressure p .

V.   Insert the respective values of p' into equations (5.83) to compute the velocity components U, V and W. [Note that, U, V and W are the improved values of the earlier U^*, V^* and W^* , respectively] .

VI. Evaluate the remaining scalar variables (i.e: T, k and ε) by employing their corresponding discretization equations. Also solve for the density by using the equation of state (under the assumption of having ideal fluid flow).

VII. Go back to step II above, treating all the variables evaluated up to now as a guess to replace the original one. This shall be repeated untill the criteria for convergence has been attained.

5.7.4   Some Consequences of Neglecting the Summation Term in Equations (5.79)

Going back to equations (5.79) we recall that the first term on the right hand side of this equation was omitted. Some of the reasons behind this are now analyzed [5,6,43,46,52] :

i.   The summation term is in reality a sum of all the immediate neighbouring nodes surrounding the grid point under investigation. Consequently every element in this sum will also consist of a summation term relating it to the surrounding neighbours, and so on. Thus if equations (5.79) were not simplified as suggested above they will contain the terms of all the flow field. This will prove to be a tedious task to undertake even by the computer. Thus it has been dropped out.

ii.   The first two words of SIMPLE (i.e: $\underline{S}$ emi - $\underline{I}$ mplicit) is indicative to the absence of the summation variable, where this term represents an indirect or implicit effect on the velocity due to the pressure correction.

iii. The final converged solution arrived by the SIMPLE method does not contain any inaccurate results. This may be confirmed by the fact that the last calculated velocity field will satisfy the continuity equation and hence no effect of dropping out the summation term is realized.

iv. The pressure correction equation is not actually made use of in the final iteration. The control of convergence is achieved by having the mass source, b, attain a relatively small value. This value may be taken, for all practical purposes, as zero and inserting this into the pressure correction equation (5.85) will result with a plausible solution for p′ over the entire flow field. In doing so the pressure correction equation will have no control over the final converged solution. Thus any approximations made to arrive at equation (5.79) would not be felt in the end result.

All necessary elements to take care of the distinctive velocity pressure coupling have been developed thus far. We now turn our attention to describe the specific techniques, such as the LBL method, to solve the relevant discretized transport equations for the pertinent variables describing the entire flow field. This is the topic of the subsection to follow.

5.8 SOLUTION of the ALGEBRAIC RELATIONS

There are an abundance of techniques available to solve algebraic discretized equations in an iterative fashion, some of which may be found in [63,64]. One of the most prominent of these techniques is the Gauss-Seidel method [64]. This method has proven to be relatively superior to others due to due the simplicity and straightforwardness embodied in it. The basic idea behind this procedure is to evaluate the specific variable under consideration

by 'visiting' each individual grid node in a particular sequence. At every iteration only one group of variables are kept in computer memory. The main drawback of the Gauss-Seidel method is that it is relatively expensive to run for problems similar to that of the present investigation. The reason being is that it solves for the variables of the flow field in a point-by-point approach thus the boundary condition data will be conveyed at a rate of one grid spacing per iteration. Consequently the number of iterations necessary is comparable to the number of grid nodes and variables in the flow field. This will require a prohibitively high CPU time. It is thus concluded that a different method for solving the discretized algebraic equations ought to be employed. The method chosen to undertake this task will be addressed in the subsections to follow.

5.9 THE LINE-BY-LINE METHOD

The scheme employed in this investigation ia a convenient combination of the Gauss-Seidel method, with some restrictions to be mentioned later on, and the T ri - D iagonal M atrix A lgorithm (TDMA) cited in [5,6,40,43,52,64]. Before presenting this scheme, it will be necessary to rewrite the discretized transport equation into a useful form, given below.

5.9.1 Re-Casting the Discretized Equation

In view of what was stated earlier regarding the possibility of expressing the discretized algebraic transport equations, for all of the pertinent variables, in terms of a general form as given in equation (5.66), we will, therefore, consolidate our efforts to handle only the geneal form of the equation. Equation (5.66), rearranged, reads as

$$a_P \Phi_P = a_N \Phi_N + a_S \Phi_S + c' \qquad (5.88)$$

where

$$c' = a_E \Phi_E + a_W \Phi_W + a_R \Phi_R + a_L \Phi_L + b \qquad (5.89)$$

The term b in equation (5.89) will vary according to the specific variable sought for. If we desire to solve for T, k or ε we should resort to (5.67b) to evaluate b. If U, V or W are required then b will be calculated from equations (5.74), which are comparable to (5.67b) less the pressure term. Finally, if we need to solve for p', then b is obtained from equation (5.87).

5.9.2 Constructing the Tri-Diagonal Matrix

To start the above mentioned computation a grid line of the entire mesh is chosen at which the particular variable to be computed is currently unknown, while the neighbouring grid lines are assumed to contain temporarily known values of the same variable from their most recent values, acquired through initialization or previous iterations, (see Fig. 5.7). Consequently, for

BOUNDARY VALUES

TEMPORARLY KNOWN

UN KNOWN

TRAVERSE
DIRECTION

SWEEP
DIRECTION

y, j

x, i

LINE PRESENTLY SOLVED FOR
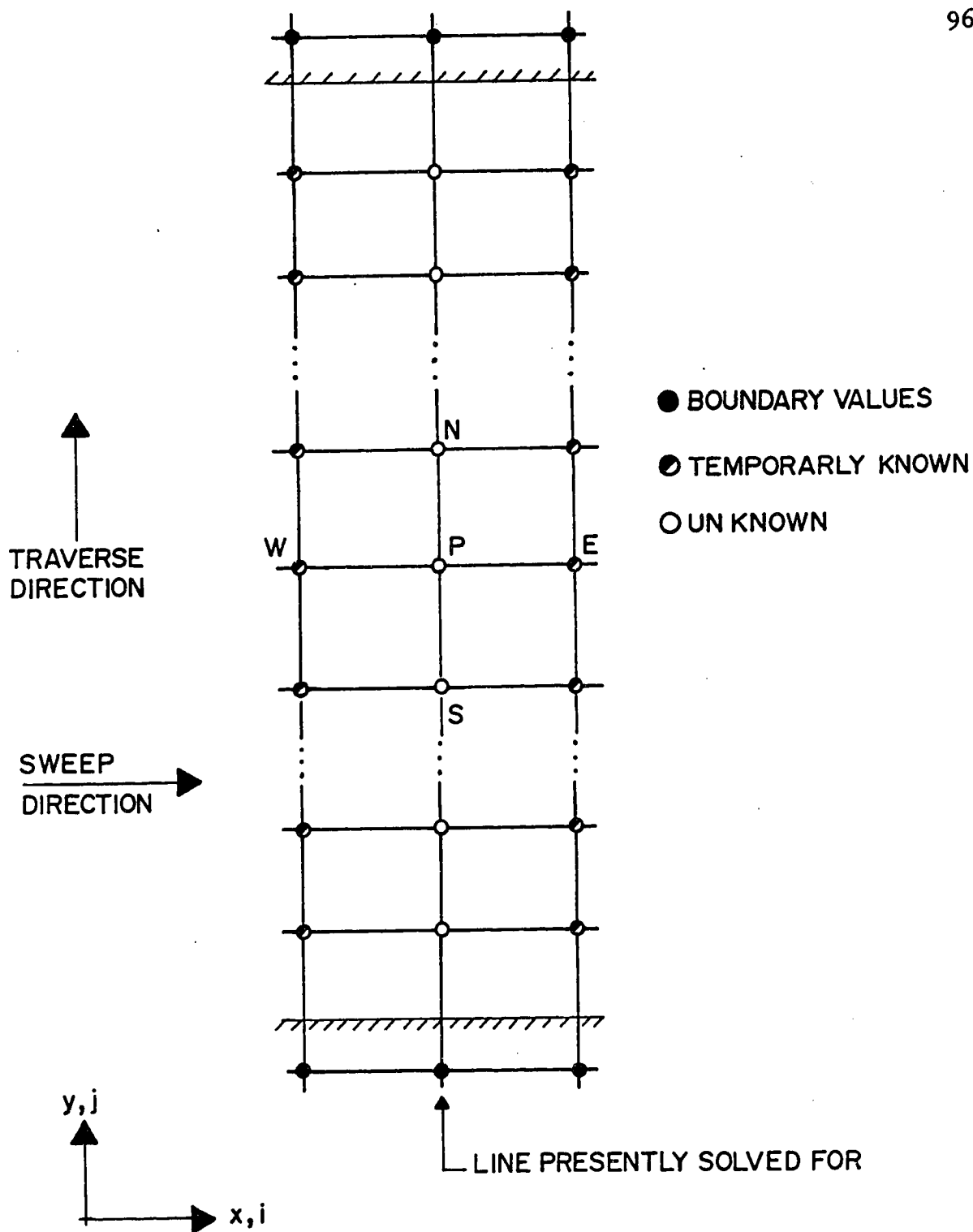
Figure 5.7. Segment of the flow mesh describing the traverse and
sweep of the Line-By- Line (LBL) method.

every grid point on the grid line being solved for, the algebraic discretization equation reduces to where only three values, i.e., Φ_P, Φ_N and Φ_S are unknown. Arranging this into a convenient matrix form, will result in,

$$
\left[
\begin{array}{c}
-\beta_2\Phi_1 + D_2\Phi_2 - \alpha_2\Phi_3 \\
\quad -\beta_3\Phi_1 + D_3\Phi_3 - \alpha_3\Phi_4 \\
\ddots \\
\quad\quad -\beta_j\Phi_{j-1} + D_j\Phi_j - \alpha_j\Phi_{j+1} \\
\ddots \\
\quad\quad\quad -\beta_n\Phi_{n-1} + D_n\Phi_n - \alpha_n\Phi_{n+1}
\end{array}
\right]
=
\left(
\begin{array}{c}
c'_2 \\
c_3' \\
\vdots \\
c_j' \\
\vdots \\
c_n'
\end{array}
\right)
\tag{5.90}
$$

where:

$$
D = a_P, \quad \alpha = a_N \text{ and } \beta = a_S \tag{5.91}
$$

also, Φ_1 and Φ_n are the values of the variables at the upper and lower boundaries and are thus, temporarily, known. The matrix described above represents the collection of discretization equations for grid points traversing from South to North (i.e.: in the y-direction). The distinctive feature about the matrix on the left hand side of the equal sign in (5.90) is that the main diagonal, super diagonal and subdiagonals are non-zero while the remaining diagonals consist of zero elements. This type of matrix is known as a tri-diagonal matrix. There exists a method specifically designed to handle these kind of matrices. This method is the TDMA scheme cited earlier. This proves to be

a very powerful and suitable algorithm for one- dimensional, direct methods. But when attempting to solve a three-dimensional, non-linear problem (requiring iterations), this method requires an excessive amount of computer storage and CPU time. Therefore, this approach for solving the matrix (5.90) in a direct method shall be modified to an iterative method. Details of this is described in the subsection to follow.

5.9.3 Discussion of the Solution Method by TDMA

Recalling the discussion above regarding the inappropriate handling of the TDMA method for problems resembling those in this specific investigation, a technique must be developed to overcome this, and this is accomplished by simply considering only one particular grid line in the entire three-dimensional mesh, containing discretization equations for the grid points along this grid line, such that, for the time being, this grid line will embody unknown quantities along its grid nodes. While all other remaining grid lines, in the flow field is assumed to consist of temporarily known quantities at their mesh nodes (see Fig. 5.7). Having done this we produce a nominally one-dimensional problem from an originally multi-dimensional one. Therefore, for such a situation the TDMA method may be implemented, without any drawbacks such as high CPU time and memory requirements. The selection of the grid line to be solved is done according to preference, where the orientation of the chosen grid line might be in any of the three Cartesian directions, traversing along a designated grid line (e.g.: the x-direction) from

West to East or vice versa. Also the sweep direction from one grid line to another could be done (e.g.: in the x-direction) from North to South and from Right to Left or the opposite. The control over the traverse and sweep directions are basically due to the type of boundary conditions specified. What has been discussed above forms the basis for the L ine - B y - L ine (LBL) method [5,6,12,29,40,43,46,52].

Some of the advantages of using the (LBL) method are :

a. The convergence of the LBL method is relatively fast. The reason being is that the boundary condition data from the ends of a grid line is conveyed at once to the interior flow field, regardless of how many grid points lie along the line. The data from the grid nodes in the surrounding grid lines are communicated in a speed comparable to the point by point method (i.e.: the Gauss-Siedel method).

b. The amount of active storage memory necessary is only proportional to the number of grid nodes along a Cartesian direction.

c. The convenience of being able to alter the traverse and sweep direction help in ensuring convergence and its speed.

5.9.4 Deriving the Recurrence Formula for the LBL Method

Going back to the matrix depicted in equation (5.90) we will construct from it a recurrence relation capable of handling the three-dimensional, elliptic, non-linear equations encountered in this research.

Firstly the jth equation appearing in the aforesaid matrix shall be re-arranged as

$$\Phi_j = Q_j \cdot \Phi_{j+1} + R_j \cdot \Phi_{j-1} + Z_j \qquad (5.92)$$

where

$$Q_j = \frac{\alpha_j}{D_j} \qquad (5.93a)$$

$$R_j = \frac{\beta_j}{D_j} \qquad (5.93b)$$

$$Z_j = \frac{c'_j}{D_j} \qquad (5.93c)$$

Repeating what has been done in equation (5.92) to the remaining equations in (5.90) we would obtain

$$\Phi_2 = Q_2 \cdot \Phi_3 + R_2 \cdot \Phi_1 + Z_2 \qquad (5.94a)$$

$$\Phi_3 = Q_3 \cdot \Phi_4 + R_3 \cdot \Phi_2 + Z_3 \qquad (5.94b)$$

$$\Phi_4 = Q_4 \cdot \Phi_5 + R_4 \cdot \Phi_3 + Z_4 \qquad (5.94c)$$

$$\Phi_{n-1} = Q_{n-1} \cdot \Phi_n + R_{n-1} \cdot \Phi_{n-2} + Z_{n-1} \qquad (5.94d)$$

Since Φ_1 in equation (5.94a) represents the value of the particular variable Φ at the boundary and is a known value, we may thus express equations (5.94) as follows

$$\Phi_2 = A_2 \cdot \Phi_3 + c''_2 \tag{5.95a}$$

where

$$A_2 = Q_2 \tag{5.95b}$$

and

$$c''_2 = R_2 \cdot \Phi_1 + Z_2 \tag{5.95c}$$

Substituting (5.95a) into (5.94b) we would obtain

$$\Phi_3 = Q_3 \cdot \Phi_4 + R_3 \cdot (A_2\Phi_3 + c''_2) + Z_3 \tag{5.96}$$

Rearranging equation (5.96) gives

$$\Phi_3 = A_3 \cdot \Phi_4 + c''_3 \tag{5.97a}$$

where

$$A_3 = \frac{Q_3}{(1 - A_2 R_3)} \tag{5.97b}$$

and

$$c''_3 = \frac{R_3 c''_2 + Z_3}{(1 - A_2 R_3)} \tag{5.97c}$$

Also using (5.97a) to eliminate Φ_3 from (5.94c) would produce

$$\Phi_4 = Q_4 \cdot \Phi_5 + R_4 \cdot (A_3 \cdot \Phi_4 + c''_3) + Z_4 \tag{5.98}$$

Re-expressing equation (5.98) into the following form

$$\Phi_4 = A_4 \cdot \Phi_5 + c''_4 \tag{5.99a}$$

where

$$A_4 = \frac{Q_4}{(1 - A_3 R \cdot _4)} \tag{5.99b}$$

$$c''_4 = \frac{R_4 \cdot c''_3 + Z_4}{(1 - A_3 \cdot R_4)} \tag{5.99c}$$

By simple inspection of equations (5.95), (5.97) and (5.99) we may deduce that they are comparable. Thus a recuerance relation may be conceived by induction, which reads as [5, 43, 52]

$$\Phi_j = A_j \cdot \Phi_{j+1} + c''_j \tag{5.100}$$

where

$$A_j = \frac{\alpha_j}{(D_j - \beta_j \cdot A_{j-1})} \tag{5.101a}$$

$$c''_j = \frac{\beta_j \cdot c''_{j-1} + c'_j}{(D_j - \beta_j \cdot A_{j-1})} \tag{5.101b}$$

Noting that

$$A_1 = 0 \quad \text{and} \quad c''_1 = \Phi_1 \qquad \qquad (5.101c)$$

In equations (5.100) and (5.101) the subscript j refers to the particular grid point under investigation, and it ranges from $j = 2$ up to $j = n-1$, which encompasses the flow regime from one side of the boundary to the opposite side along the grid line being considered. To account for the entire flow field the recurrence formula should be implemented for all remaining grid lines.

To make use of the LBL iterative scheme in an effective fashion requires a systematic approach to the problem, this is discussed below.

5.9.5 The General Solution Procedure of the LBL Scheme

In applying the recurrence relation described above, we are compelled to use a methodical approach to the problem. The strategy adopted to manage this task is listed as follows :

I.   Having available the discretization coefficients for the specific variable being solved for, we evaluate the A and c'' from equations (5.101) for a particular chosen grid line. The value of these parameters are stored from $j = 2$ up to $j = n-1$.

II. Now we solve for the variable Φ_j using the recurrence equation

(5.100), noting that Φ_1 and Φ_n are known from the boundary conditions. The sequence in which these variables are solved is from Φ_{n-1} up to Φ_2, resembling the backward substitution of the Gaussian method. The motive behind this reverse approach may be clearly understood by examining equation (5.100) above, such that to solve for Φ_2 we would require Φ_3 and to solve for Φ_3 we would require Φ_4 and etc. But if the problem were executed in a converse manner then the first variable to be computed would be Φ_{n-1}, needing only Φ_n which is already available from the boundary condition. Next we proceed to evaluate Φ_{n-2} where we would require to know Φ_{n-1}, which has previously been calculated and so on, traversing[1] from one side of this grid line to the other untill all the variables at the mesh points along this grid line have finally been accounted for.

III. We repeat steps I and II above for neighbouring grid lines in the same direction using the most recently calculated Φ traversing from North to South. We scan through the whole flow field until all grid points in the flow regime have been visited.

IV. Steps I, II and III are repeated for grid lines traversing from East to West.

----

1. Traverse : is the movement along a specific grid line.

V.   Steps I, II and III are also repeated for grid lines traversing from Right to Left.

VI.   The entire flow mesh may be swept[2] more than once for the same iteration, depending on the particular variable sought for and the problem under consideration. In doing so we will attempt to better the value of the variables using the same discretization coefficients.

To clarify the steps above we will apply them to our specific situation (see Fig. 5.7). The process is started from a North-South grid line at $i = 2$ and $k = 2$ traversing the length of this line. Next, it is repeated along successive neighbouring North-South lines (i.e: $i = 3$, $i = 4$, ... $i = n_i - 1$). When this has been accomplished we may say that the entire grid has been swept through. After this, the whole approach is repeated along East-West lines beginning at $j = 2$ and $k = 2$ traversing along this grid line. This technique is then carried on for all the neighbouring East-West grid lines, untill the entire flow field is completely swept. Finally this same process is applied to the Right-Left grid lines commencing at $i = 2$ and $j = 2$ and continuing as before till the whole regime has been swept. All the sweeps mentioned here represents just one iteration.

----

2. Sweep : Is the movement from one grid line to another.

5.10 NUMERICAL STABILITY and ACCURACY

All what has been developed up to now will prove to be futile unless by some means a strategy was developed to enhance the accuracy and stability of the outcome. This is dealt with in the subsections to follow.

5.10.1 Convergence and Numerical Stability

The investigations to be carried out in this research involves turbulent, non-isothermal, elliptical and three-dimensional flow, which will make it a worthy problem to overcome. In view of the nature of this work the ability to achieve a converged solution is not ensured. But there do exist some basic guidelines, if followed, may limit the probability of divergence. A list of some of these rules and regulations shall follow [5,6,29,40,43,46,52]

I.   Achieving *compatibility of fluxes* at a shared control volume face. In other words the magnitude of flux passing through a control volume surface and received by a neighbouring control volume on the other side of this surface must be equivalent, else equilibrium of this flux over the entire flow field will not be attained.

II.   Assurance of *always positive* discretization coefficients for all discretization equations is a prerequisite to plausible solutions. This may be apprehended more easily by picturing a control volume surrounded by neighbouring control volumes (see Fig. 5.1). If a positive growth

of a specific variable occured in this element a corresponding positive growth must also be realized in the surrounding elements. But if the coefficients were of opposite signs then no certainty may be said about the effect on adjacent control volumes.

III. Maintaining negative $S_{\phi,p}$, in equation (5.56), is one of the most serious conditions that must be adhered to. Not satisfying this recommendation will most certainly cause the computations to fail. If $S_{\phi,p}$ was positive, this entails that as Φ increases the source term will also increase and in the case of having no sink term, Φ will enlarge even more and this continues indefinitely. The result will be a highly unrealistic solution.

IV. The sum of the neighbouring control volume discretization coefficients must be balanced by the corresponding coefficient of the control volume. In doing this we guarantee that if a growth or depreciation of the variables in surrounding control volumes happen than a likewise occurance will be appreciated by the central control volume. This condition has actually been fulfilled through equation (5.67a) given earlier.

V. In strongly non-linear fluid flow problems, as is the case in this study, it is often common practice to reduce the speed of alterations in the dependent variable, from iteration to iteration. This may be accomplished by using what is known as *damping* or *under-relaxation*. The technique through which under-relaxation has been utilized in this

research will be to rearrange the general discretization equation (5.68) to read as [5,6,43,52] :

$$\Phi_p = \frac{\Sigma(a_i \, \Phi_i) + S_{\Phi,c} \cdot \Delta x \cdot \Delta y \cdot \Delta z}{\Sigma a_i - S_{\Phi,p} \cdot \Delta x \cdot \Delta y \cdot \Delta z} \qquad (5.102)$$

If we we define Φ_p^* to be the value of the dependent variable at the preceding iteration, and introducing Φ_p^* into equation (5.102) as given below,

$$\Phi_p = \Phi_p^* + \left\{ \frac{\Sigma(a_i \, \Phi_i) + S_{\Phi,c} \, \Delta x \cdot \Delta y \cdot \Delta z}{\Sigma a_i - S_{\Phi,p} \Delta x \, \Delta y \, \Delta z} - \Phi_p^* \right\} \qquad (5.103)$$

the term within the brackets may be physically interpreted to stand for the variation in the dependent variable as a consequence of the current iteration. The amount of this variation can be curtailed somewhat by inserting a coefficient into this equation, which is known as an U nder R elaxation F actor (URF). This may be performed as follows

$$\Phi_p = \Phi_p^* + URF \cdot \left\{ \frac{\Sigma(a_i \, \Phi_i) + S_{\Phi,c} + S_{\Phi,c} \cdot \Delta x \cdot \Delta y \cdot \Delta z}{\Sigma a_i - S_{\Phi,p} \cdot \Delta x \cdot \Delta y \cdot \Delta z} - \Phi_p^* \right\} \qquad (5.104)$$

the URF described above will be a number lying between 0 and 1, such that if URF is set to zero than maximum underrelaxtion occurs and no alteration whatsoever occurs from one iteration to the other. Whereas having the URF equal to one would result in no underrelaxtion at all. The introduction of the URF coefficient into the general discretization equation will have no effect on the converged value of the dependent variable sought for, but will only reduce the speed by which the final solution is attained.

Underrelaxation should be applied to all dependent variables in the flow field, where warranted. The amount of underrelaxation required will vary according to the boundary conditions, type of flow, the particular parameter to be relaxed the number of grid points, grid spacing and many other factors. Through first hand research, experienced by the author, underrelaxation has been highly substantiated and the need for it can not be stressed enough. Where the success or failure of the numerical scheme relied enormously on the correct selection of the URF group. There is no systematic methodology, to the knowledge of the researcher, in obtaining the appropriate URFs. The approach normally taken to evaluate an acceptable set of URFs is simply by trial and error. This process is expensive to attain. But once achieved a set of URFs may be used for different flow situations with only moderate effort expended in optimizing the URFs.

5.10.2 Accuracy and Economy

The ultimate standing of any numerical code is how much tolerance may be achieved and what CPU time will the scheme require to accomplish such an accuracy ? Thus a complete segment of this subsection has been devoted to this goal. The fulfillment of this, demands meeting numerous requirements, some of which shall be listed below [5,6,29,40,43,46,52] as follows:

I.   Accuracy of the outcome in this study is influenced by the extent to which the solution satisfies the finite discretization equations. The degree of this accuracy is reflected by the residual sources. This is unlike the common practice in which the largest difference between successive iterations at the grid points of all the dependent variables

is compared with a pre-specified tolerance, and if this change were to fall below this tolerance the iterations will cease and the solution attained at this final iteration shall be taken as the *correct* answer. This approach is not suitable for our type of studies, where strong underrelaxation may prevail, which will result in having the alterations between consecutive iterations deliberately reduced, and create an illusion of convergence, although the calculated results may not have converged. Therefore, the residual source, stated earlier, shall be adopted as a technique to certify convergence. The procedure to execute this method may be done by altering the general discrezation equation (5.68) for every grid point as follows:

$$R = \Sigma(a_i\Phi_i) + S_{\Phi,c}\Delta x\, \Delta y\, \Delta z - (\Sigma a_i - S_{\Phi,p}\,\Delta x\, \Delta y\, \Delta z)\Phi_p \qquad (5.105)$$

Where R should be, theoretically, equal to zero when the discretization equation is satisfied, which will occur for an infinitely large number of grid points. But for practical situations we will accept the solution as converged if, $|R|$ is less than a specified tolerance. Now when strong underrelaxation occurs, this will not have any effect on the residual R so that no misconception regarding convergence may be claimed.

II. Refining the grid by as much as possible. This should be exercised at locations of steep gradient changes of the variables (e.g.: close to a solid wall or inlet). While at the other locations the use of a coarser mesh may suffice. Thus a balance between accuracy and economy may be attained.

III.   As a turbulent model is used in connection with other transport equations, the accuracy of the calculated results will depend, to an extent, on the experimentally evaluated turbulent constants. The only true way to assess this effect is to compare with experiments.

IV.   'Good' specification of the initial field will enhance accuracy and reduce the computational time considerably. One of the techniques that may be employed to realize this is to use flow fields from similar previous calculations.

V.   Improving the URFs by means of trial and error which should help in achieving faster convergence.

VI.   A realistic value for the convergence criterion should be specified, where if a very small number is specified than convergence may take a prohibitively long time to occur.

5.11   SIMULATION of HUMAN THERMAL SENSATION via A PHYSIOLOGICAL REGULATORY RESPONSE MODEL

All the relevant information describing the entire flow field should have been computed by now. Having obtained this we will turn our attention to the procedure by which these calculated raw variables may be translated into a distinct group of data from which a conclusion may be rendered regarding the response of of human thermal comfort sensation to the flow field. First of all we will direct our attention to the development of a heat balance over the human body.

5.11.1 Derivation of the General Comfort Equation

In the ASHRAE standard [51] thermal comfort of man is defined as "That condition of mind which expresses satisfaction with the thermal environment". Thus to acquire this satisfaction an equilibrium between the human body and it's surroundings must be attained, such that the net heat gain and internal heat production by the body cancel out resulting in no build-up or storage of heat in the individual. This occurance may be represented by [7,10,66]:

$$M - E_d - E_{sw} - E_{re} - L = Q_r + Q_c \qquad (5.106)$$

for better comprehension a pictorial representation of equation (5.106) has been given in Fig. 5.8. Where M is the metabolic rate of energy production in the human body, and may be denoted by:

$$M = H + W \qquad (5.107)$$

where H is the heat production and W is the external mechanical work of the body. It is common practice to relate W to M by an external mechanical efficiency as follows:

$$\eta = \frac{W}{M} \qquad (5.108)$$
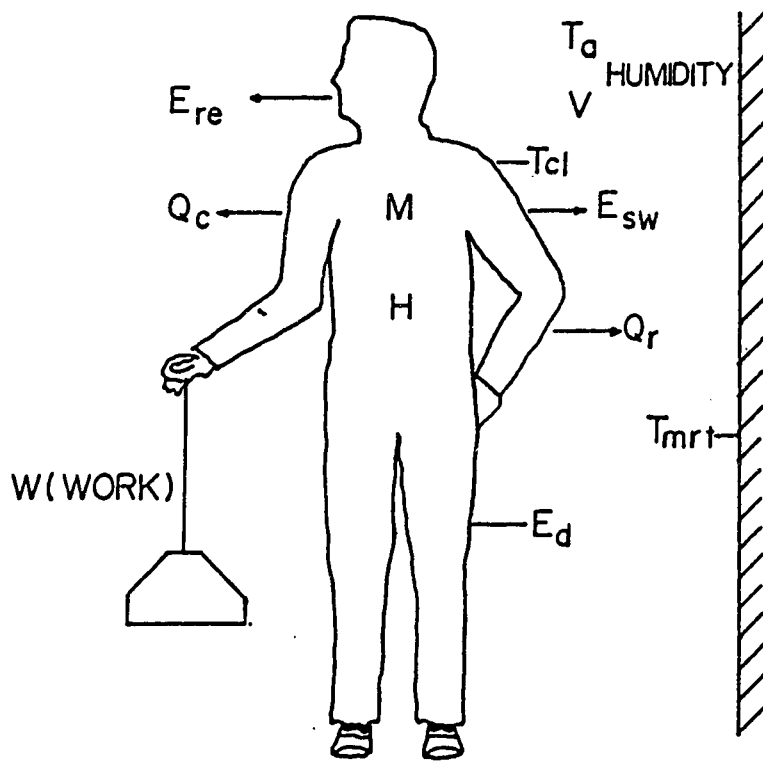
Figure 5.8. Exchange of energy between man and the surroundings.

For the investigations conducted in this research only sedentary situations is considered. Thus η will be zero and the metabolic rate will only comprise of heat production, equivalent to one met or 50 kcal / (h.m^2)[1].

The second term on the left hand side of (5.106) is the amount of heat loss by vapor diffusion through the skin, E_d, which is estimated by [7,66]:

$$E_d = \lambda_d m \, A_{Du}(p_s - p_a) \tag{5.109}$$

where λ_d is the heat of vaporization of water (575 kcal / Kg at 35°C), m is the permeance coefficient of the skin (6.1x10^{-4}Kg/hrm^{2}mmHg). The term A_{Du} is the DuBois surface area which is the surface area of the nude body and is computed from [66]:

$$A_{Du} = 0.202 \cdot w^{0.425} \cdot h^{0.725} \tag{5.110}$$

where w is the body mass and h is the body height. p_s and p_a, appearing in (5.109), are the saturated vapor pressure at skin temperature and vapor pressure in the ambient air, respectively and Since mean skin temperature T_s, is easier to grasp than p_s a linear expression relating these two parameters may be given [7] as,

$$p_s = 1.92T_s - 25.3 \tag{5.111}$$

equation (5.111) above may be applied for 27°C $< T_s <$ 37°C with a loss of

----

1 : For reasons of consistency an effort shall be made to adopt the same units appearing in the original documents [7,10]. Furthermore, the end results are not effected by the intermediate units chosen.

accuracy of less than 3%. Substituting the recommended values for λ_d , m and equation (5.111) into equation (5.109) gives:

$$E_d = 0.35A_{Du}(1.92T_s - 25.3 - p_a) \tag{5.112}$$

The third term on the left hand side of equation (5.106), E_{sw} , represents heat loss from the surface of the skin due to the evaporation of sweat. For a specific activity level (i.e.: number of mets) the only physiological parameters influencing the balance of heat are the skin temperature T_s , and sweat secretion E_{sw} which are estimated by employing a regression analysis, performed by Fanger [7,66] for persons in thermal comfort, as follows:

$$T_s = 35.7 - 0.032M \tag{5.113}$$

$$E_{sw} = 0.42(M - 50) \tag{5.114}$$

The fourth term on the left hand side of equation (5.106) symbolizes the amount of latent heat loss due to respiration. This is evaluated from the following relation [7,10,65,66]:

$$E_{re} = 0.0023M(44 - p_a) \tag{5.115}$$

The last term on the left hand side of (5.106) is the dry respired heat loss from the body due to the temperature difference between expired and inspired air, it may be represented by [7] :

$$L = 0.0014M(34 - T_a) \tag{5.116}$$

The first term on the right hand side of (5.106) is the net heat loss by

radiation from the outer surface of the clothed body to the surroundings, and can be expressed by Stefan - Boltzman's law [7,66] as :

$$Q_r = A_{eff} \cdot e \cdot \sigma \left[(T_{cl} + 273)^4 - (T_{mrt} + 273)^4 \right] \qquad (5.117)$$

Where A_{eff} is the effective radiation area of the clothed body, and is estimated form:

$$A_{eff} = f_{eff} \cdot f_{cl} \cdot A_{Du} \qquad (5.118)$$

here f_{eff} is the effective radiation area factor which represents the ratio of the effective radiation area of the human body to the total surface area of the body. f_{eff} varies according to the posture of the irradiated person, but a value of 0.71 is claimed reasonable [7]. f_{cl} is the ratio of the surface area of the clothed body to the surface area of the nude body, e is the emitance of the outer surface of the clothed body. Where for the human skin the emitance is close to 1.0, while for most type of clothings it is about 0.95, therefore, a value of 0.97 is used here. σ is the Stefan - Boltzman's constant $(4.96 \cdot 10^{-8} \text{kcal/m}^2 \cdot \text{hr} \cdot \text{K}^4)$. T_{cl} is the mean temperature of the outer surface of the clothed body. T_{mrt} is the mean radiant temperature, the evaluation of which will be dealt with later on. Substituting e, σ and equation (5.118) into (5.117) gives:

$$Q_r = 3.14 \cdot 10^{-8} A_{Du} f_{cl} \left[(T_{cl} + 273)^4 - (T_{mrt} + 273)^4 \right] \qquad (5.119)$$

The last term on the right hand side of equation (5.106) represents the heat loss by convection from the outer surface of the clothed body. The value

of which is calculated from [7,10,66]:

$$Q_c = A_{Du} \cdot f_{cl} \cdot h_c \cdot (T_{cl} - T_a) \qquad (5.120)$$

Where h_c is the convective heat transfer coefficient. The magnitude of h_c depends upon the type of convection process, such that for a still air situation free convection takes place and h_c becomes a function of the temperature difference $(T_{cl} - T_a)$. While for higher velocities, forced convection exists and h_c is then a function of velocity. A convenient method for application in the digital computer is to combine expressions for both free and forced convection as follows [7,8,66],

$$h_c = AMAX1 \left[2.05(T_{cl} - T_a)^{0.25} , 10.4 \cdot \vec{V}^{0.5} \right] \qquad (5.121)$$

where $\vec{V}$ is the resultant velocity. This formula may be used for barometric pressures at sea level [7].

Now using relations (5.112), (5.113), (5.114), (5.115), (5.119), (5.120), and (5.121) in (5.106) and dividing by A_{Du} will yield [7,8,10]:

$$\frac{M}{A_{Du}} - 0.35 \left[43 - 0.061 \frac{M}{A_{Du}} - p_a \right] - 0.42 \left[\frac{M}{A_{Du}} - 50 \right]$$

$$- 0.0023 \frac{M}{A_{Du}} (44 - p_a) - 0.0014 \frac{M}{A_{Du}} (34 - T_a) =$$

$$3.4 \ 10^{-8} f_{cl} \left[(T_{cl} + 273)^4 - (T_{mrt} + 273)^4 \right] + f_{cl} h_c (T_{cl} - T_a) \qquad (5.122)$$

this relation represents the general thermal comfort equation through which the achievement of optimal thermal comfort, or not, could be found out.

Inspecting equation (5.122) we arrive to to the conclusion that no definite expression has been developed, yet to estimate T_{cl}. This is discussed below.

For reasons of energy balance the amount of heat loss by radiation and convection from the outer surface of the clothed body must be equivalent to the amount of heat loss by conduction from the outer surface of the skin shell to the outer surface of the clothed body K (see Fig. 5.8). This amount of conducted energy is calculated from [7]:

$$K = A_{Du} \cdot \frac{T_s - T_{cl}}{0.18 I_{cl}} \tag{5.123}$$

Where I_{cl} is the intrinsic insulation and represents the total resistance from the skin to the outer surface of the clothed body expressed in clo units. Now if we replace the right hand side of (5.122) by the expression for K given by equation (5.123), after dividing this relation by A_{Du} and using equation (5.113) to represent T_s, and finally if we solve for T_{cl} we get:

$$T_{cl} = 35.7 - 0.032\frac{M}{A_{Du}} - 0.18 I_{cl}\left[\frac{M}{A_{Du}} - 0.35(43 - 0.061 \cdot \frac{M}{A_{Du}} - p_a)\right.$$

$$- 0.42(\frac{M}{A_{Du}} - 50) - 0.0023 \cdot \frac{M}{A_{Du}}(44 - p_a) -$$

$$0.0014 \cdot \frac{M}{A_{Du}} \cdot (34 - T_a)\bigg] \tag{5.124}$$

Hence, equation (5.122) together with equations (5.121), (5.124) and expressions for f_{cl} and T_{mrt} will form a closed set through which the solution of the comfort equation is achieved. However, this will only provide us information as to how the various parameters should be combined to produce a situation

of *optimal* thermal comfort. Therefore, it is not directly suitable for determining the thermal sensation of individuals in an environment where the existing variables are expected to be far away from meeting the condition of optimal thermal comfort. Consequently we will turn our attention to modifying the original comfort equation so as to be useful in predicting the thermal preception of man to the surrounding environment. This will be given in the sub-section to follow

5.11.2 Predicted Mean Vote

There are many models available to simulate the effect of the environment on man, some of which may be found in [7,8,9,10,66]. Out of these numerous models the $\underline{P}$ redicted $\underline{M}$ ean $\underline{V}$ ote (PMV) of Fanger [7] has been utilized to forecast the thermal response of occupants to the computed flow field conditions in an enclosure. The general comfort equation (5.122) given above is manipulated in such a way to produce a thermal sensation model.

An index scale of thermal sensation response, for any given combination of activity level, clothing, and thermal environmental parameters attainable is given in Table 1.1 [7].

To be able to predict thermal sensation at situations other than optimal thermal comfort a new parameter shall be introduced by assuming that the thermal preception for a particular activity level is a function of the bodies thermal load L_o. This thermal load describes the net difference between internal heat production and heat loss to the surroundings for a man

hypothetically kept at the comfort values of the mean skin temperature and sweat secretion at the true activity level. Based on this definition, L_o is expressed by resorting to the general comfort equation (5.122) and after rearranging, the thermal load can be evaluated from [7]:

$$L_o = \frac{M}{A_{Du}} - 0.35\left[43 - 0.061\frac{M}{A_{Du}} - p_a\right] - 0.42\left[\frac{M}{A_{Du}} - 50\right]$$

$$- 0.0023\frac{M}{A_{Du}}(44 - p_a) - 0.0014\frac{M}{A_{Du}}(34 - T_a)$$

$$- 3.4 \cdot 10^{-8}f_{cl}\left[(T_{cl} + 273)^4 - (T_{mrt} + 273)^4\right] + f_{cl}\,h_c(T_{cl} - T_a) \tag{5.125}$$

where T_{cl} is found by iteratively solving the following equation

$$T_{cl} = 35.7 - 0.032\frac{M}{A_{Du}} - 0.18I_{cl} \cdot \left[3.4 \cdot 10^{-8}f_{cl} \cdot \left\{(T_{cl} + 273)^4\right.\right.$$

$$\left.\left. - (T_{mrt} + 273)^4\right\} + f_{cl}h_c(T_{cl} - T_a)\right] \tag{5.126}$$

and h_c is estimated from equation (5.121), given previously.

Exhaustive experimental investigations were conducted by Fanger [7] from which an equation was developed relating the PMV to the L_o as follows :

$$PMV = \left(0.352EXP^{-0.042 \cdot (M/A_{Du})} + 0.032\right) \cdot L_o \tag{5.127}$$

Inserting the thermal load equation (5.125) into (5.127) we arrive at [7,10]:

$$PMV = \left(0.352 EXP^{-0.042 \cdot (M/A_{Du})} + 0.032\right) \cdot \left[\frac{M}{A_{Du}} - 0.35(43 - 0.061 \cdot \frac{M}{A_{Du}}\right.$$

$$- p_a) - 0.42(\frac{M}{A_{Du}} - 50) - 0.0023 \frac{M}{A_{Du}}(44 - p_a) - 0.0014 \frac{M}{A_{Du}}(34 - T_a)$$

$$\left. - 3.4 \cdot 10^{-8} f_{cl}\left\{(T_{cl} + 273)^4 - (T_{mrt} + 273)^4\right\} - f_{cl} h_c (T_{cl} - T_a)\right] \qquad (5.128)$$

Where equation (5.128) together with equations (5.121) and (5.126) are employed to assess the PMV for a sizeable collection of people as a function of activity M (kcal/hr · m²) , effective insulation of clothing I_{cl} (clo), air temperature $T_a(°C)$, mean radiant temperature $T_{mrt}(°C)$, resultant air velocity $\vec{V}$ (m/s) and air humidity (mm Hg). In view of the involved nature of euqation (5.128) as well as the complementary relations (5.121) and (5.126) it is recommended that the PMV indexes be sought for through the use of a digital computer. To do this a systematic methodology is adopted as follows:

I.   Given M, h, w, I_{cl} of clothing ensemble, T_a, T_{mrt}, relative humidity and air velocity.

II.   Compute T_{cl}^*, which is a first estimate of T_{cl} from equation (5.124), and use this to evaluate h_c^* from equation (5.121).

III. Estimate an improved value of T_{cl}, by introducing the previous T_{cl} and h_c^* into the right hand side of equation (5.126).

IV. Compare the absolute difference between the current value of T_{cl} and the one from the previous iteration against a tolerance δ_{tol}.

V. If this difference is less than δ_{tol} then evaluate the PMV index from equation (5.128), otherwise go back to (III) treating the current T_{cl} as T_{cl}^*.

A flow-chart portraying the steps above is given in Fig. 5.9.

5.11.3 Estimation of the Mean Radiant Temperature

The mean radiant temperature T_{mrt}, for an individual at a specific body posture and ensemble of clothing situated at a definite location within the room, is defined as that uniform temperature of black surroundings which will produce radiant heat loss from the individual identical to that in the room under investigation. The mean radiant temperature has a significant effect on a persons exchange of heat and consequently the resulting sensation of thermal comfort.

The mean radiant temperature T_{mrt} is evaluated for an individual situated within an enclosure comprising of N distinctive isothermal surfaces, having the temperatures T_1, T_2, ...,$T_N(°K)$. The angle factors between the person and the surrounding surfaces are F_{P-1}, F_{P-2}, ... ,F_{P-N}. Most building materials have a high emitance, on account of this the calculations may be simplified by applying a common acceptable approximation which is to ignore the

START

Given: M, h, w, I_{cl}, T_a, T_{mrt}, RH, V, δtol

Compute T_{cl} as a rough estimate from eq.(5.124) Assign it as T_{cl}^*

Use T_{cl}^* in eq.(5.121) to estimate h_c^*

Replace T_{cl}^* by T_{cl}

Solve for T_{cl} from eq.(5.126)

IF $\left| T_{cl}^* - T_{cl} \right| \leq \delta$tol

NO

YES

Calculate PMV from eq.(5.128)

END
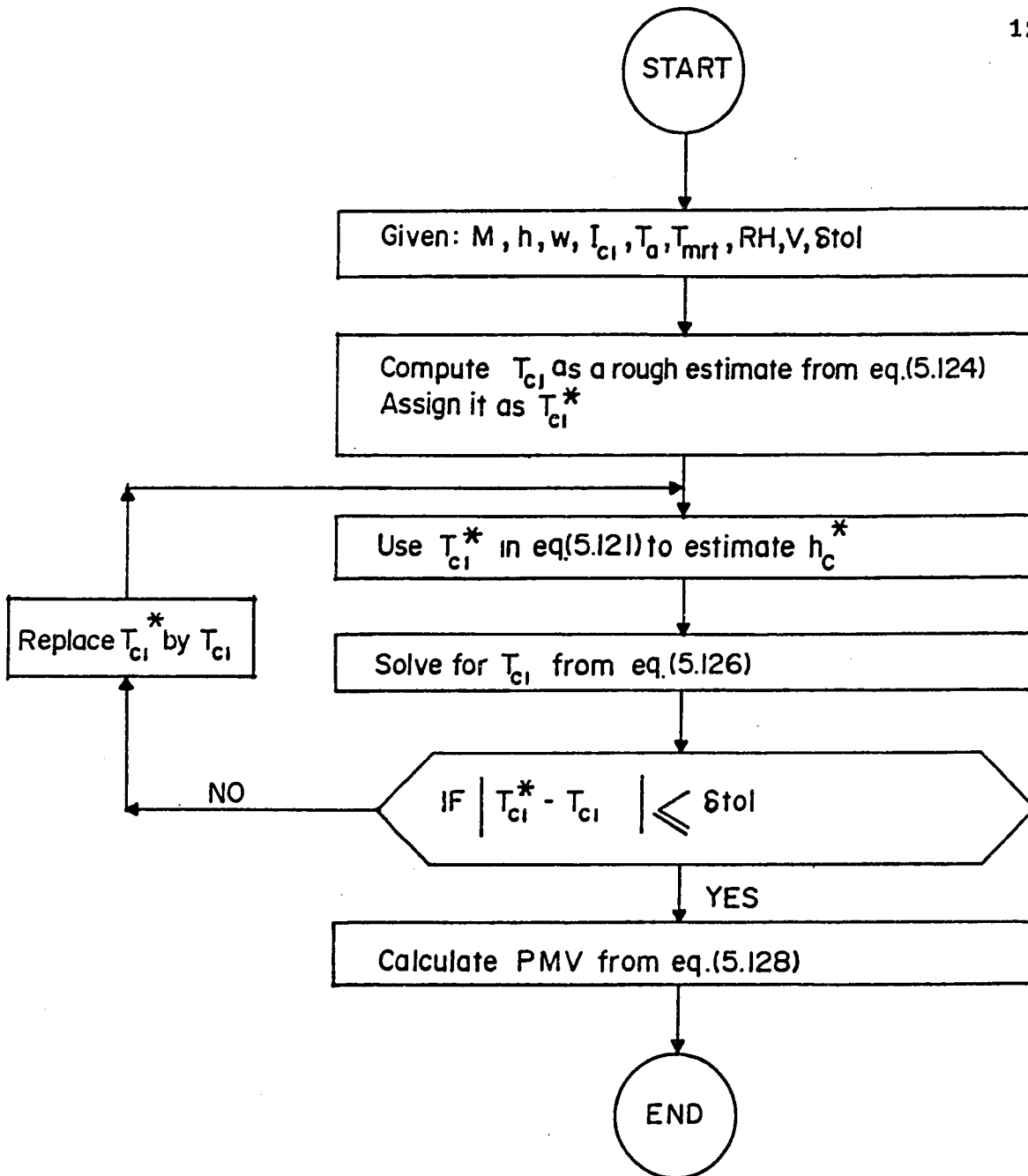
Figure 5.9. Flow chart describing the iterative solution of the PMV index.

reflections and assume all surfaces in the room to be black [7]. In doing so the mean radiative temperature is evaluated from [51]:

$$T_{mrt} = \left(\sum_{i-1}^{N} T_i^4 \cdot F_{P-i} \right)^{1/4} \tag{5.129}$$

Since the sum of all the angle factors within the enclosure is unity, then the mean radiative temperature of equation (5.129) may be comprehended to be equal to the mean value of the surrounding surface temperatures, weighted according to the size of the respective angle factors.

We will direct our attention to the evaluation of these factors. This is the topic of the subsection to follow.

5.11.4 The Angle Factors

The angle factors are needed to estimate the T_{mrt} to be employed in the radiative heat loss from the human body.

The walls in a normal room are most often rectangular in shape, as is the case in this particular study. Based on this we will be concerned with the determination of the angle factors between the person in the enclosure and the surrounding vertical and horizontal rectangular walls.

Before attempting to solve for the shape factors in the entire room we will consider the situation shown in Fig. 5.10, where the person is positioned in the orthogonal coordinate system at point P facing the rectangle with the centre of this individual passing through the origin (0, 0, 0).
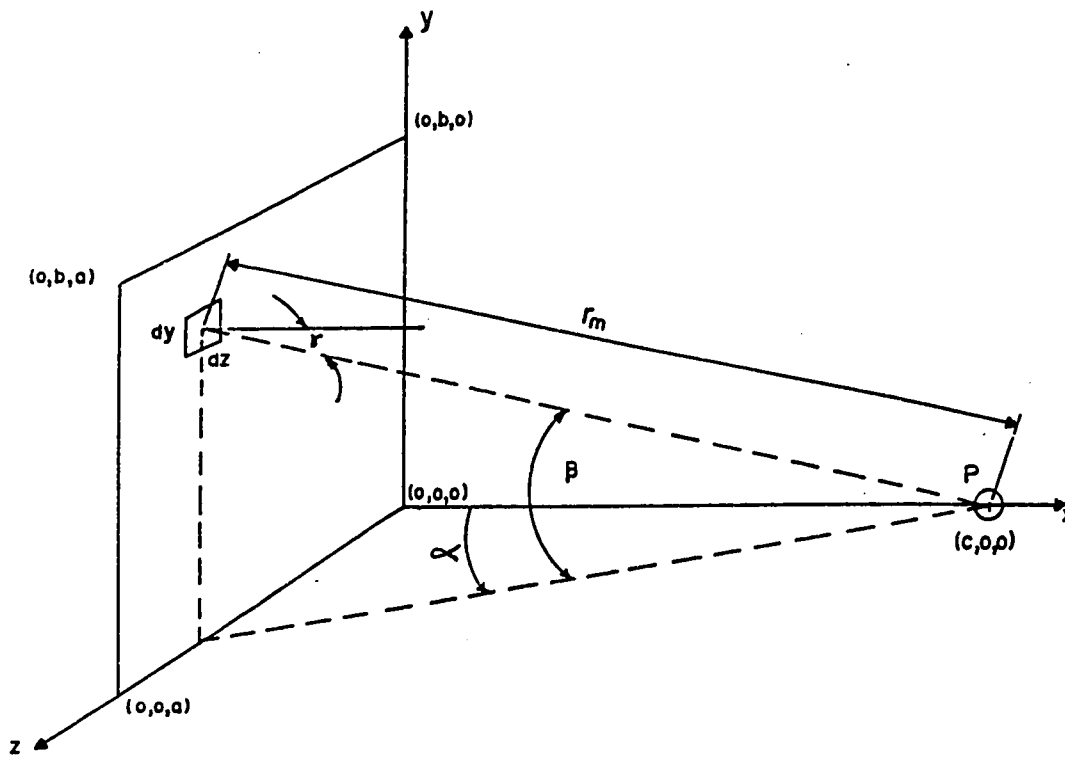
Figure 5.10. Showing a person at point P facing the center of the rectangle (a x b) in the Y-Z plane.

First of all we examine a differential area element $dA = dy\, dz$, located on the y-z plane having the coordinates $(0, y, z)$. By using the reciprocating principle [7,67,68] we may obtain:

$$A_{eff} \cdot d\, F_{P-dA} = dA\, F_{dA-P} \qquad (5.130)$$

where A_{eff} is the effective radiation area of the human body and $d\, F_{P-dA}$ is the differential shape factor between the person, P and the differential area dA, while F_{dA-P} is the angle factor between dA and P .

Since the view factor from dA to P may be expressed as [7,68]:

$$F_{dA-P} = \frac{1}{\pi}\frac{A_p}{r_m^2} \cdot \cos\gamma \qquad (5.131)$$

where A_p is the projected area of the human body which varies according to the posture and are determined experimentally. A_p may be related to A_{eff} through the projected area factor f_p as follows:

$$f_p = \frac{A_p}{A_{eff}} \qquad (5.132)$$

r_m and γ are shown in Fig. 5.9.

From trigonometry

$$r_m^2 = x^2 + y^2 + z^2 \qquad (5.133a)$$

and

$$\cos \gamma = \frac{x}{\sqrt{x^2+y^2+z^2}} \tag{5.133b}$$

Substituting equations (5.133) into (5.131) we get:

$$F_{dA-P} = \frac{1}{\pi} \cdot A_p \cdot \frac{x}{(x^2+y^2+z^2)^{3/2}} \tag{5.134}$$

Inserting equation (5.134) into equation (5.130) and replacing dA by (dx · dz) we may solve for dF_{P-dA} to obtain:

$$d F_{P-dA} = \frac{1}{\pi} \cdot \frac{A_p}{A_{eff}} \cdot \frac{x}{(x^2+a^2+z^2)^{3/2}} \tag{5.135}$$

To determine the angle factor F_{P-A} between the person and the entire rectangular wall (a x b), we integrate equation (5.135), after introducing equation (5.132), over the whole wall:

$$F_{P-A} = \frac{1}{\pi} \int_{z-0}^{z-a} \int_{y-0}^{y-b} \frac{f_p \cdot x}{(x^2+y^2+z^2)^{3/2}} dy \, dz \tag{5.136a}$$

to eliminate x from the numerator of equation (5.136a) we note that the distance from the point P along the x-axis is equal to c, thus

$$F_{P-A} = \frac{1}{\pi} \int_{\frac{z}{x}-0}^{\frac{z}{x}-\frac{a}{c}} \int_{\frac{y}{x}-0}^{\frac{y}{x}-\frac{b}{c}} \frac{f_p}{\left[1 + (\frac{y}{x})^2 + (\frac{z}{x})^2\right]^{3/2}} \cdot d(\frac{y}{x}) \cdot d(\frac{z}{x}) \tag{5.136b}$$

For the investigations done in this research we know the location of the individual in the room (i.e.: the orthogonal coordinates of his centre), but his ori-

entation (i.e.: the azimuth angle α) is not known. Thus we will have to modify equation (5.136b) to enable it to calculate a mean value for $0 < \alpha < 2\pi$, which reads as [7] :

$$\overline{F}_{P-A} = \frac{1}{2\pi^2} \int_{\frac{z}{x}-0}^{\frac{z}{x}-\frac{a}{c}} \int_{\frac{y}{x}-0}^{\frac{y}{x}-\frac{b}{c}} \int_{\alpha-0}^{\alpha-2\pi} \frac{f_p}{\left[1 + (\frac{y}{x})^2 + (\frac{z}{x})^2\right]^{3/2}} \cdot d(\frac{y}{x}) \cdot d(\frac{z}{x}) \, d\alpha \quad (5.137)$$

where $\overline{F}_{P-A}$ expresses the average of the shape factor between a person and a rectangular surface, such that the person rotates around a vertical axis passing through his center. In equation (5.137) f_p can only be determined through empirical means. Therefore, a deviation to what has been described here shall be adopted to compute the angle factors. This will be handled below.

5.11.5 Computation of the Angle Factors

In what was stated above we confirmed the need to use empirically estimated data for projected area factors f_p to produce angle factors. But before we can generate these angle factors we must first of all solve equation (5.137), with the empirical f_p by means of numerical integration. To obtain view factors by this approach requires that we undertake two distinctive steps, which are the interpolation of experimentally determined f_p and then numerical solution of equation (5.137). Due to this we have decided to embark on a different route to evaluate these angle factors, by utilizing data available in [7,51] , and then employ numerical interpolation to this data to arrive at the appropriate angle factors for various situations.

Refering to [7] we note that there are figures that are used to estimate angle factors for seated and standing postures over a wide range of geometrical situations. To make use of these figures we translate them into raw data points that are easily inserted into the computer. Having done this we then resort to a numerical interpolation scheme that helps us to determine the angle factors for various conditions. The algorithm chosen to accomplish this task is the *cubic spline approximation function* [64]. This function is made up of cubic polynomial segments on subintervals, joined together with some specific smoothness conditions.

The cubic spline function to be solved is as follows [64]:

$$S_i(x) = \frac{d_{i+1}}{6h_i}(x-t_i)^3 + \frac{d_i}{6h_i}(t_{i+1}-x)^3 + (\frac{y_{i+1}}{h_i} - \frac{d_{i+1}h_i}{6}) \cdot (x-t_i)$$

$$+ (\frac{y_i}{h_i} - \frac{d_i h_i}{6}) \cdot (t_{i+1}-x) \tag{5.138}$$

Where $S_i(x)$ is the cubic spline polynomial that approximates the data points between t_i and t_{i+1}, while t_i is a ratio of the persons geometrical position relative to the room walls. y_i is the corresponding angle factor for t_i. h_i is the difference between t_{i+1} and t_i on the condition that $t_i < t_{i+1}$. d_i is equivalent to the second derivative of the function of equation (5.138) at t_i. The subscript i here refers to a particular x and y being investigated, where i progressively varies from 1 to the number of data points n. For further clarifications refer to Fig. 5.11. An essential condition to be imposed here is the continuity of the first derivative of the function in equation (5.138) so that for
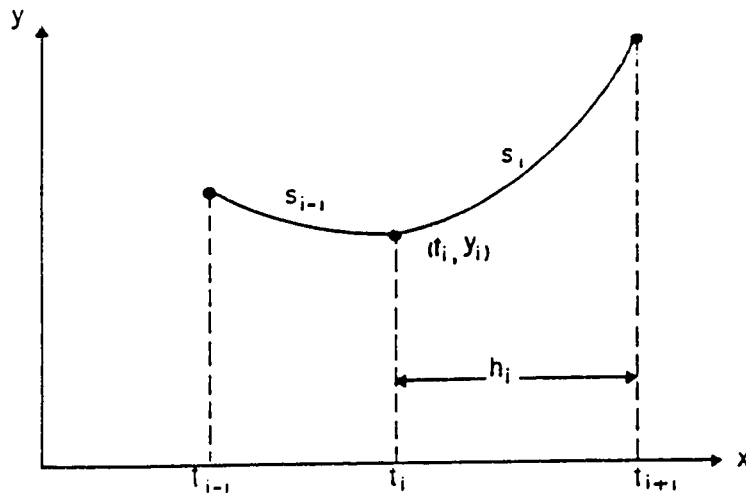
Figure 5.11. Parameters used in the cubic spline polynomial.

t_i $(2 \le i \le n-1)$ we will have:

$$\frac{d}{dx}S_{i-1}(t_i) = \frac{d}{dx}S_i(t_i) \qquad (5.139)$$

Evaluating the derivatives of equation (5.139) and substituting them back into (5.138) and after some rearrangement we get [64]

$$h_{i-1} \cdot d_{i-1} + 2(h_{i-1}+h_i)d_i + h_i d_{i+1} = \frac{6}{h_i}(y_{i+1}-y_i) - \frac{6}{h_{i-1}}(y_i-y_{i-1}) \qquad (5.140)$$

This equation is true for $2 \le i \le n-1$. Thus, we will produce $n-2$ relations from equation (5.140) which are linear, symmetric and tri-diagonal, where everything is known except $d_2, d_3, \dots, d_{n-1}$. The values of d_1 and d_n have been assigned a value of zero. A routine to handle this has been developed by the author. A brief description of how to resolve the system of equations in (5.140) is

I.   Evaluate $h_i = t_{i+1} - t_i$ for $i = 1, 2, \dots, n-1$.

II.   Evaluate a temporary term $b_i = \dfrac{6(y_{i+1}-y_i)}{h_i}$, for $i = 1, 2, \dots, n-1$.

III.   Set $u_2 = 2(h_1 + h_2)$ and then compute, progressively

$$u_i = 2(h_{i-1}+h_i) - \frac{h_{i-1}^2}{u_{i-1}} \quad , \text{for } i = 3, 4, \dots, n-1.$$

IV.   Set $v_2 = b_2 - b_1$ and then evaluate, progressively

$$v_i = b_i - b_{i-1} - h_{i-1} \cdot \frac{v_{i-1}}{u_{i-1}} \text{ , for } i = 3, 4 \ldots , n - 1.$$

V.   Solve for the d's in a reverse manner by setting $d_n = 0$ and then evalu-

ate progressively $d_i = \dfrac{(v_i - h_i \cdot d_{i+1})}{u_i}$, for $i = n - 1, n - 2 \ldots , 3, 2.$

Once the d_i's have been estimated we may use them in equation (5.138) to determine the angle factors for any position of the individual within the room. Having obtained these shape factors we insert them into equation (5.129) to compute the resulting mean radiative temperatures, which inturn is introduced into equation (5.128) to estimate the PMV indices.

The PMV index gives an indication of the general degree of discomfort, but for practical situations it is difficult to translate what the value of the computed PMV implys. Therefore, to have a better comprehension of the thermal sensation of the occupants the PMV is employed to obtain the **P**ercentage of **P**eople **D**issatisfied (PPD) [7,10] through a curve similar to that given in Fig. 5.12 where the PPD in percent is plotted against the absolute value of the PMV. Having obtained the PPD a conclusion may be reached on whether (or not) occupancy comfort is obtained such that if at least 80% of the people are satisfied (i.e., PPD at most 20%) then occupancy comfort will be claimed to be reached [51] and this value of PPD coincides to an absolute PMV of about 0.8.
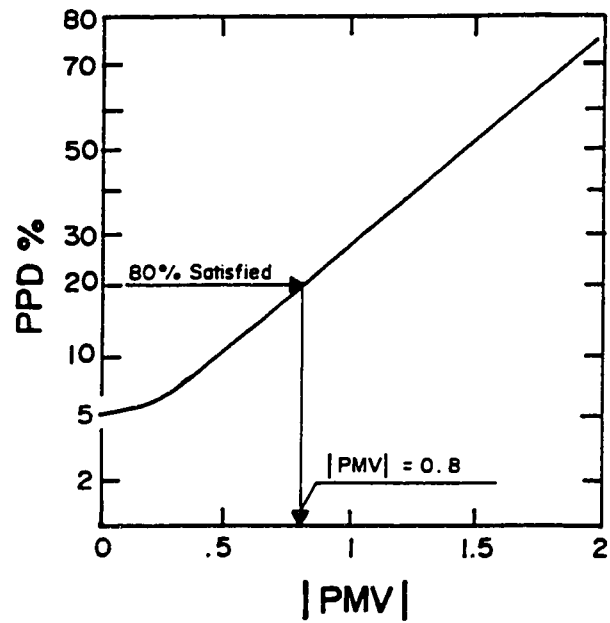
Figure5.12. Predicted Percentage Dissatisfied (PPD) Versus the absolute value of the Predicted Mean Vote (PMV).

CHAPTER VI
THE NUMERICAL CODE

The computer program utilized in this investigation is a variation to the TEACH (T aching E lliptic A xisymmetric C haracteristics H euristically) solvers developed at the Imperial College of London [32, 37]. One of the main distinctive modifications done to the original solver [5, 29, 37, 40, 52, 70] is to extend it so that it may handle three dimensional situations and is thus referred to as TEACH-3D.

In the sections and sub-sections to follow a brief account of the problem at hand is presented together with a break-down of the primary routines to fluid flow problems such as those investigated here.

6.1 DESCRIPTION of CASE STUDY

The air in rooms ventilated by mechanical means in this study is fully turbulent [6, 45], elliptic (i.e.: recirculating and two-way coordinate affects) and three-dimensional [4, 5, 16, 20, 21, 29, 40, 52]. Furthermore if the incoming air and wall temperatures are at different temperatures from the air within the enclosure then non-isothermal buoyant flow situations must also be considered. Furthermore, steady-state condition is assumed. A detailed description of the problem at hand has been dealt with previously in Chapter five.

To simulate the type of flows investigated here will prove to be a formidable task, thus a versatile numerical solver is required that has economy, ease of manipulation and accuracy in mind. The function and details of such a code is the theme of the next few sections.

6.2 STRUCTURE of the NUMERICAL CODE

On account of the type of problems encountered in this research it is quite plausible to anticipate that the computer program will be somewhat involved. Accordingly vital features and aspects of routines which make up the code is given below. A pertinent flow chart is also given in Figs. 6.1 and 6.2. It should be noted here that there are resemblances among some of the sub-sections to follow, in particular between sub-sections 6.2.4 to 6.2.10. The reason for this being that we have developed a general representative form of the transport equation (5.52) and consequently it should follow that these subroutines will have a similar layout.

6.2.1 Structure and Functions of MAIN

This segment lies at the top of the numerical code so that to make it easy for a potential user to manipulate and accommodate it according to his specific needs. Also here, as well as in all the other parts, it is divided into distinctive chapters to facilitate comprehension of the entire program and how one subroutine interacts with another. The various chapters of MAIN and their functions are given in ascending order as follows :

START

MAIN

- Read input data and fluid properties for air.
- Set indexes for grid size, inlet edges and outlet edges.
- Specify arrangement and distribution of grid lines.
- Specify wall heat fluxes and temperatures.
- Establish a 'suitable' URF group, MAXIT and SORMAX.
- Call subroutine INIT.
- Set temperatures of boundary nodes = Corresponding wall temperature.
- Initialize local Reynolds numbers for all walls.
- Call subroutine PROPS.
- START Main Iteration Loop
  — Call subroutine CALCU.[a]
  — Call subroutine CALCV.[a]
  — Call subroutine CALCW.[a]
  — Call subroutine CALCP.[b]
  — Call subroutine CALCTE.[a]
  — Call subroutine CALCED.[a]
  — Call subroutine CALCT.[a]
  — Call subroutine PROPS
  — Normalize absolute residual sorce sum for all variables and set maximum = SORCE

INIT

- Calculate geometrical dimensions of scalar and vector control volumes.
- Initialize all variables in flow field to zero, except T, TE, ED, DEN, VIS, VISCT and GAMH.
- RETURN.

PROPS

- Calculate DEN, VIS, VISCT and GAMH.
- RETURN.

YES

IF NITER > 50 AND SORCE >> SORMAX

NO

Divergence Occured.
- Modify URF group and/or adjust grid line arrangement.
- RUN program again.

YES

IF NITER = MAXIT

NO

Termination Tests.

Converged solution not reached, but allowable number of iterations used up.
- Increase MAXIT and/or modify URF group and/or grid line distribution.
- RUN program again.

YES

IF SORCE > SORMAX

NO

- Converged solution reached.
- Call PRINT to produce pertinent output.

END

FIGURE 6·1 Flowchart showing basic operations in the source code.

a.   Refer to Fig. 6·2·b
b.   Refer to Fig. 6·2·a

ENTER from MAIN

- Calculate discretization coefficients over entire flow field.
- Modify sources and boundary conditions by calling PROMOD.*
- Assemble discretization coefficients and evaluate Absolute Residual Sorce Sums.
- Call LISOLV to solve equations

RETURN to MAIN

LISOLV

- Apply the LBL iteration algorithim for N—S lines, then E—W lines, then R—L lines.
- RETURN

Figure 6.2.b.Flowchart showing general structure for CALCU, CALCV,CALCW,CALCT,CALCTE and CALCED.

★ A detailed description of PROMOD is given later.

ENTER from MAIN

- Calculate discretization coefficients and Absolute Residual Source Sum over entire flow field.
- Assemble discretization coefficients.
- Call LISOLV to solve for PP.
- Apply corrections PP to velocity components and pressure.
- Set PP to zero.

RETURN to MAIN

Figure 6.2.a.Flowchart showing general structure for CALCP.

i. **Chapter 0 : Preliminaries :**

Here all the COMMON blocks containing variable names to be resorted to throughout the program are given, as well as the magnitude of variable quantities, that seldom necessitate modification are listed.

ii. **Chapter 1 :**

This chapter specifies the room size (in meters), grid size, integers defining the edges of the inlet and outlet ports and their respective locations. Furthermore, the distribution of the grid lines within the flow field in the three Cartesian directions have been supplied, where a non- uniform rectangular grid arrangement has been adopted to ensure a fine spacing between the mesh lines at or close to solid boundaries and the openings of the inlet and outlet. While away from these boundaries the spacing grows coarser as we get closer to the room's geometrical center. To achieve this we resort to the following expression, given here for the x-direction, (see Fig. 3.1) :

$$X(I) = L \cdot \left[\frac{(I-1)}{(NI-1)} - EXPX \cdot \frac{Sin\left\{ \frac{2\pi (I-1)}{(NI-1)} \right\}}{2\pi} \right] \tag{6.1}$$

where X (I) describes a mesh plane parallel to the y-z plane and at a distance of X(I) from it, L is the length of the room in the x-direction, NI is the number of grid nodes, EXPX is the grid expansion constant in the x-direction varying as $0 \le EXPX \le 1$, so that if EXPX $= 0$ then

a uniform grid spacing is produced. While, on the other hand, if EXPX = 1 then an inhomogeneous distribution of grid lines occur where the density of these lines is high close to room surfaces and low close to or at the middle of the room. The index I ranges from 2 to I = (NI - 1), enclosing the entire room volume less the solid boundaries. An approach similar to this is done for the y and z directions. Some of the grid lines in the vicinity of the inlet and outlet have been overwritten to specify there exact size. The occupied zone which is defined by, [65] as: *" The region within a space normally occupied by people, generally considered to be between the floor and 180 cm above the floor and more than 60 cm from walls or fixed airconditioning equipment "* , has been identified in this chapter. For reasons of satisfying overall mass balance, the inlet and outlet surface areas together with the incoming mass flow rate are also evaluated in this chapter. Choosing a specific dependent variable to be solved is done here by setting the corresponding logical constant (i.e. : INCALU, INCALV, INCALW, INCALP, INCALK, INCALD, INCALT) to TRUE otherwise we specify it as FALSE. To update the fluid properties (i.e. : air density, DEN, and dynamic viscosity, VIS) from iteration to iteration INPRO is selected as TRUE else it is given as FALSE. The property of air at the inlet opening, wall heat fluxes and temperatures together with the turbulent constants used in the $k - \varepsilon$ turbulence model are defined here. As pressure in this investigation is treated as a relative variable, not an absolute one [43] a reference pressure location is designated in this chapter. This chap-

ter is also used to identify the under-relaxation factors (URFU, URFV, URFW, URFP, URFE, URFK and URFT), maximum number of iterations, MAXIT, and the tolerance of the dependent variables absolute residue, SORMAX. A monitoring station within the flow field has been selected here as a representative node giving an insight on the rate of convergence or divergence of the dependent variables.

iii.   **Chapter 2 :**

In this segment of MAIN all the geometrical locations of the scalar and vector grid nodes together with the spacings between them are evaluated and an initial rough estimate of the dependent variables in the entire flow field is done via a *call* to the routine INIT. The values of the parameters at the solid boundaries and the inlet nozzle plane are supplied here. The properties of air in the flow domain are computed in this chapter as a first estimate by calling subroutine PROPS, also normalization factors for the absolute residual sources of the dependent variables at the monitoring station is calculated here.

iv.   **Chapter 3 - *The main iteration loop* :**

This chapter is the most significant part of MAIN in which all the dependent variables are evaluated and improved through iteration. The parameters calculated here are U, V, W, p, k, ε , and T by calling the routines CALCU, CALCV, CALW, CALCP, CALCTE,

CALCED and CALCT respectively. Once all of these have been computed the fluid properties of air are updated by calling subroutine PROPS. There are three distinctive conditions in this chapter whereby fulfilling anyone of them will cause the *termination* of the iteration loop. These criterions may be listed as follows :

a. If the maximum of the absolute residual source sums, SORCE, is very much larger than the given tolerance SORMAX and the number of iterations completed as of now are greater than fifty, selected from past experience.

b. If the number of iterations achieved has reached the pre-stated maximum count, MAXIT.

c. If the largest value of the Absolute Residual Source Sum(ARSS) is SORCE, and less than or equivalent to the allowable tolerance SORMAX.

Part (a), in the termination tests above, indicates a severe divergence and failure of the iteration, while part (b) does not suggest divergence but also does not signify definite convergence and part (c) symbolizes convergence of the iteration. As confirmation, the field variables of the flow domain may be printed if desired. Also here the Reynolds number is calculated.

v.   ***Chapter 4 - Output :***

This chapter produces the dependent variables and their corresponding absolute source sums for the selected monitoring station. In

addition, the field variables for the entire flow regime is printed here in such a fashion so that it may be utilized in other output devices and numerical codes straightforward.

MAIN is totally problem dependent in a sense that for any alterations regarding the type of problem to be studied, a similar alteration must follow in MAIN.

6.2.2 Structure and Functions of Subroutine INIT

This routine lies just after MAIN. It consists of three chapters and its general function is to initialize the flow field. The chapters contained here are as follows :

i. *Chapter 0 - Preliminaries* :

It consists of common blocks describing the parameters required in INIT.

ii. *Chapter 1 - Calculate geometrical quantities* :

Here the locations and sizes of the scalar and vector control volume cells are computed such that the faces of a cell will lie mid-way between neighbouring main grid nodes, although the mesh distribution may not be uniform.

iii. *Chapter 2 - Initialization of variables* :

Where all pertinent variables and parameters in the entire flow field are set to zero, except temperature, T, turbulent kinetic energy,

TE, and its dissipation, ED, density, DEN, laminar, VISCOS, and turbulent viscosity, VISCT, and finally the diffusion coefficient for temperature, GAMH. The variables in the flow field that were not set to zero are initiated according to :

a.   an average area weighted value of the temperatures of all the surrounding walls for temperature of air in the enclosure.

b.   the turbulent kinetic energy and the corresponding dissipation at the inlet port are taken over the whole flow regime.

c.   the air flow properties at the inlet are assumed to be the same for the entire domain.

This routine will, in general, not necessitate any modifications for a wide range of flow situations.

6.2.3 Structure and Functions of Subroutine PROPS

The transfer to this subroutine is made from MAIN, where it may be called to update the fluid properties for air after every iteration, on account of the fact that these properties will vary with varying air temperature. This routine consists of the following :

i.   Chapter 0 - Preliminaries :

Where all relevant variables necessary for PROPS are supplied.

ii.   ***Chapter 1*** :

This chapter is concerned with updating the fluid properties by evaluating the density DEN, diffusion coefficient GAMH, turbulent viscosity VISCT and effective or total viscosity of air VIS for the whole flow field. To slow down the rate by which the viscosities are modified from iteration to iteration they are under-relaxed which might result in a higher CPU time but at the benefit of stabilizing the outcome and diminishing the possibility of divergence. It is recommended to resort to PROPS after a complete iteration is achieved, although there is no objection to visiting it more or less frequently by modifying the logical constants described earlier in MAIN.

This routine will, generally not require any alteration for different flow situations. The exit of props is made back to MAIN.

6.2.4 Structure and Function of CALCU

The entry to this subroutine is made from MAIN. One of the primary intents of CALCU is to evaluate the U velocity component, details of this will be found in the following :

i.   ***Chapter 0 - Preliminaries*** :

Contains the common blocks of variables and constants pertinent to CALCU.

ii.   *Chapter 1 - Assembly of Coefficients* :

The coefficients and source terms of the discretization equation for the U-momentum relation are computed here. This is accomplished by evaluating the flow rate and diffusion coefficients for every U-cell control volume separately, and by using the hybrid scheme, described in detail earlier, the preliminary main discretization coefficients at the U-grid nodes are assembled. Also the viscosities acting at the faces of the U-cell are estimated by an appropriate interpolation technique. It should be noted that the domain of solution here is the rectangular region bounded by I = 3 to NI - 1, and I = 2 to NJ - 1, and K = 2 to NK - 1. The reason for this is because the upstream face of the main control volumes at I = 2 are made to coincide with the solid boundary.

iii.   *Chapter 2 - Problem modifications* :

Here a transfer to the routine PROMOD (details of this subroutine will be supplied later) is made where the sources and boundary conditions are modified by means of the wall functions to suit the particular problem under investigation.

iv.   *Chapter 3 - Final coefficient assembly* :

Here the discretization coefficient of the U-cell is solved for by applying a relation comparable to equation (5.67a). Having evaluated this, the ARSS for all the U-control volumes in the domain of interest is computed. The discretization coefficient for every U-cell is

then under-relaxed which in effect causes the U velocity component to be under-relaxed.

v.   *Chapter 4 - Solution of the discretized equations* :

Now we have all the necessary ingredients to solve for the U velocity in the entire flow field of interest. This is done by resorting to the subroutine LISOLV, to be discussed in detail later on. LISOLV may be called more than once to achieve a better estimate of the U velocity while using the same discretization coefficients and source terms. The number of times LISOLV is called from CALCU is given by NSWPU.

In general CALCU will not require any modifications for a wide variety of flow situations.

Finally, the exit of this routine is made back to MAIN.

6.2.5 Structure and Function of CALCV

Access to this routine is performed at MAIN. The principal purpose of CALCV is to evaluate the V velocity component, a description of this and other related issues follows:

i.   *Chapter 0 - Preliminaries* :

Contains the common blocks of variables and constants pertinent tor CALCV.

ii. ***Chapter 1 - Assembly of coefficients :*** -

The coefficients and source terms of the discretization equation for the V-momentum relation are evaluated here. To do this we first of all need to know the diffusions and flow rates at the faces of every V-cell control volume. These coefficients are then manipulated by the hybrid scheme to produce preliminary discretization coefficients at the V-cell grid nodes. Afterwards the viscosities are estimated at the V-cell surfaces by means of a suitable interpolation method. The domain of interest here is the parallelpiped region enclosed by the mesh lines $I = 2$ to $I = NI-1$, and $J = 3$ to $J = NJ-1$, and $K = 2$ to $k = NK-1$. The reason for this is to match the V-cell grid nodes at $J = 2$ with the solid boundary. Some additional features are also performed here. The first is the computation of the buoyancy force at every V-cell grid node, the reason being that we have set the y-direction in the Cartesian space to conform to the negative direction of the pull of gravity. Thus all buoyancy forces appear here and is later included in the source term.

For cases of non-isothermal flow, instability occurs in the estimation of the vertical velocity component V which results in non-converged solutions. A method to overcome this has been suggested by Ideriah [71] and has been reported elsewhere [5,40,52]. This technique is referred to as the inertia relaxation method and may be utilized by re-arranging the discretization equation (5.68) for V as [40] :

$$V_P = \frac{\Sigma(a_i V_i) + S_{\Phi,c} \cdot \Delta x \cdot \Delta y \cdot \Delta z + I \cdot V_P^*}{\Sigma a_i - S_{\Phi,P} \cdot \Delta x \cdot \Delta y \cdot \Delta z} \qquad (6.2)$$

where V_P^* is the vertical component of velocity at grid node P estimated from a previous iteration, and I is the Inertia relaxation factor and may be defined as

$$I = \frac{\alpha \rho g \beta (T_P - T_r)}{\sqrt{g \beta T_r L}} \qquad (6.3)$$

A value of 0.2 is assigned to α, L is the room dimension perpendicular to the inlet surface area. T_P and T_r are the temperatures at the grid node P and a reference point r, respectively. Note that T_r is in degrees Kelvin. β is the volumetric expansion coefficient and for room air flow situations it may be taken as:

$$\beta = \frac{1}{T_r} \qquad (6.4)$$

Substituting equation (6.4) into (6.3) will result in :

$$I = \frac{\alpha \rho g \frac{(T_P - T_r)}{T_r}}{\sqrt{gL}} \qquad (6.5)$$

By employing relations (6.2) in conjunction with (6.5) it was possible to enhance the stability and a converged solution was achieved for a wider selection of flow cases.

iii. **Chapter 2 - Problem modifications :**

At this stage we require to modify the source terms and boundary conditions for the specific problem being investigated. This is accomplished by calling routine PROMOD where the wall functions are introduced, details of which will be given later on.

iv. **Chapter 3 - Final coefficients assembly :**

For every individual V-cell the final form of the discretization coefficient is formed by implementing equation (5.67a). After this the absolute residual source sums for all the control volumes in the flow field is computed and used as an indication to the degree of convergence attained in the V velocity components. Finally, here V is indirectly under-relaxed by under-relaxing the discretization coefficients of the V-cell grid nodes.

v. **Chapter 4 - Solution of the discretized equations :**

By now we have acquired all the detail necessary to solve for the V velocity from their corresponding discretized equations. The solution is achieved by calling the routine LISOLV. It may prove wise to resort to LISOLV *more than once for the same iteration* , in the hope that the resulting V velocities will be improved upon keeping the source terms and discretization coefficients unaltered. The number of times CALCV may resort to LISOLV in the same iteration is specified by NSWPV.

In general CALCV will not require any modifications for a wide spectrum of flow situations. The exit of this routine is made back to MAIN.

6.2.6 Structure and Function of CALCW

The general lay-out of this subdivision will follow that of subsection 6.2.4. Entry to this routine is made from MAIN. One of the chief purposes of CALCW is to estimate the W velocity components in the entire flow field. Details of this process is given now :

i.   *Chapter 0 - Preliminaries* :

This chapter comprises common blocks of the constants and variables pertinent to the proper operation of CALCW.

ii.   *Chapter 1 - Assembly of coefficients* :

The coefficients of the discretized differential equation of the W-momentum equation and the corresponding source terms are evaluated here. This task is executed by first computing the flow rates and diffusion coefficients at the faces of every W-cell control volume. Next, by introducing these terms together with the geometrical information about the W-cell into the hybrid scheme a first estimate of the discretization coefficients are assembled. Owing to the fact that the W-grid nodes are displaced relative to the main grid nodes, it necessitates the utilization of an appropriate interpolation technique to evaluate the viscosities at the faces of the W-cell. The domain of the solution is defined by a rectangular zone bounded by I = 2 to NI-1,

and J = 2 to NJ-1, and K = 3 to NK-1. The reason behind this is because the main grid nodes at K = 1 are embeded into the surrounding solid walls, which results in having the upstream faces of these main control volumes super- imposed on the wall and thus all W component velocities are disregarded here.

iii.   *Chapter 2 - Problem modifications* :

The source terms and corresponding boundary conditions are modified by implementing the wall-functions at all walls perpendicular to the z direction. This task is achieved by resorting to PROMOD, to be described later.

iv.   *Chapter 3 - Final coefficient assembly* :

The discretization coefficients of the W-cell are obtained here by employing an expression parallel to equation (5.67a). Once these have been calculated the absolute residual source sums for all the W-control volumes in the solution domain are evaluated. This residue is used as an indicator to the convergence of the W velocity component. Also, here, the discretization coefficient for every W-cell is under-relaxed which in effect causes the W velocity component to be under-relaxed.

v.   *Chapter 4 - Solution of the discretized equations* :

At this point in subroutine CALCW we should have all the relevant terms and parameters necessary to resolve the discretized form

of the W momentum differential equation at hand. By inserting these components into subroutine LISOLV the W velocity component may be solved for. To efficiently make use of the coefficients evaluated in CALCW for the same iteration and to improve the W velocities attained from LISOLV it is recommended to visit the latter subroutine a number of times for a specific iteration accomplished in the former. These number of calls to LISOLV is given in NSWPW.

For most flow situations no alterations to CALCW is warranted. After completing all the above operations CALCW exits back to MAIN.

6.2.7 Structure and Function of CALCP

The transfer to this subroutine is done in MAIN. Here the evaluation of the pressure corrections and relative pressures at the main grid nodes represent the primary purpose of this routine. CALCP is divided into distinctive chapters as follows :

i.   *Chapter 0 - Preliminaries* :

In this segment the common blocks describing all the relevant constants and variables to be utilized by CALCP are given.

ii.   *Chapter 1 - Assembly of coefficients* :

In this chapter the densities at the surfaces of the main control volume are evaluated by a suitable interpolation method. The finite

difference coefficients of the pressure correction equation is calculated next via expressions similar to equation (5.86). The source terms afterwards are computed by combining the mass sources acting at the faces of this particular cell and by accumulating the absolute value of this for all the control volumes in the entire flow field the residual mass source, RESORM, is attained. This residual acts as an indication to the stability and rate of convergence of the solution. No residual sources for the pressure correction is sought for because they provide no useful information. The solution domain here may be represented by the parallelpiped enclosed by the planes: $I = 2$ to NI-1, $J = 2$ to NJ-1 and $K = 2$ to NK-1.

iii. *Chapter 2 - Final coefficient assembly* :

The coefficients of the pressure correction equation, in discretized form, is calculated here for all main grid nodes in the flow field of interest.

iv. *Chapter 3 - Solution of the discretization equations* :

Once all the essential coefficients and parameters are evaluated we now turn to resolving the finite difference pressure correction equations over the whole domain under study. This is achieved by calling LISOLV to compute the pressure correction. LISOLV is resorted to more than once for the same iteration of CALCP which should help in attaining a better estimate of the pressure correction. The number of times LISOLV is visited is equivalent to NSWPP.

v.   *Chapter 4 - Correcting velocities and pressures:*

The velocity correction relations are used to rectify the velocities in all three Cartesian directions. This is done for the domains of U, V and W described earlier. The relative values of the pressures are under-relaxed, in the entire domain, so as to to enhance stability and convergence. Finally the pressure corrections, PP, are all set to zero.

No modifications to this subroutine is required for a diversity of flow situtions. As soon as all the operations listed above have been realized CALCP will depart back to MAIN.

6.2.8 Structure and function of CALCT

The transfer to this subroutine from MAIN is made only after concluding transfers to all the routines listed above.

The main intent of CALCT is to assess the temperature field at all main grid nodes in the flow domain. Details of this may be found in the following chapters :

i.   *Chapter 0 - Preliminaries* :

All the constants and variables necessary for CALCT to operate properly are supplied here.

ii.   *Chapter 1 - Assembly of coefficients* :

Here the flow rate and diffusion coefficients for all the main grid cells are evaluated by means of an appropriate interpolation

technique. Subsequently the preliminary form of the coefficients for the discretized energy equation is calculated by employing the hybrid scheme over the entire flow field. Having done this the source terms are then computed. It should be noted here that the calculation domain is confined to that region defined by the planes: $I = 2$ to $NI-1$, $J = 2$ to $NJ-1$ and $K = 2$ to $NK-1$.

iii.   *Chapter 2 - Problem Modifications* :

The source terms and boundary conditions at this point in CALCT must be modified according to the particular problem considered. This is achieved by resorting to PROMOD where the *log-law of the wall* is employed.

iv.   *Chapter 3 - Final coefficient assembly* :

The discretization coefficient at every control volume cell is estimated by utilizing the temperature in the form of equation (5.67a). After this the absolute residual source sums of all cells within the calculation domain is computed and utilized as an indication to the degree of stability and convergence in the outcome. Finally the temperatures for all control volumes are under-relaxed to enhance convergence.

v.   *Chapter 4 - Solution of the discretization equations* :

At present all the ingredients necessary to solve for the temperature field has been evaluated and we thus turn to solving the finite

difference form of the energy equation. This task is taken care of by calling LISOLV, where the more number of times LISOLV is called, per iteration, improves the computed temperature field. The number of times LISOLV is called equals NSWPT.

In general no alterations to CALCT is required for a large group of flow situations. Once all the operations in this routine are fulfilled, CALCT exits back to MAIN.

6.2.9 Structure and Function of CALCTE

Access to CALCTE is made via MAIN. This subroutine is mainly concerned with the determination of the turbulent kinetic energy k. To solve for k we are required to go through a sequence of segments given below :

i. *Chapter 0 - Preliminaries* :

Here a list of all variables and constants pertinent to the operation of CALCTE are given in the form of common blocks.

ii. *Chapter 1 - Assembly of coefficients* :

The diffusion and flow rate coefficients at the faces of the main control volumes are estimated via a suitable interpolating method. An additional feature here is the computation of velocity differentials at the faces of the control volume. These terms are then used to evaluate the generation of turbulence by shear from the mean flow. Having accomplished this the source terms and preliminary coefficients of

the discretized turbulent kinetic energy equation are determined. Buoyancy forces are calculated and incremented to the proper source terms. The calculation domain here is enclosed by the planes: I = 2 to NI-1, J = 2 to NJ - 1 and K = 2 to NK-1.

iii.   *Chapter 2 - Problem Modifications* :

At this point in CALCTE we need to modify the source terms and boundary conditions for the specific case under investigation. This task is achieved by calling routine PROMOD where the log-law of the wall and its relevant relations are implemented.

iv.   *Chapter 3 - Final coefficient assembly* :

Having obtained all the necessary components, the discretization coefficients are computed next by utilizing a relation comparable to equation (5.67a), in terms of the turbulent kinetic energy. Once this is done the absolute residual source sums of k for the entire domain of interest is estimated. Finally in this chapter the turbulent kinetic energy are under-elaxed to improve stability and convergence of the results.

v.   *Chapter 4 - Solution of the discretization equations* :

The discretized form of the turbulent kinetic energy equation is now solved by introducing the relevant parameters evaluated above into LISOLV, resulting with an estimate for k, which may be improved by resorting to LISOLV more than once for the same itera-

tion of CALCTE. The number of times LISOLV is visited is given by NSWPK.

No modification to CALCTE is warranted for the investigations conducted in this research.

Finally after all operations in this routine are complete, exit is made back to MAIN.

6.2.10 Structure and Function of CALCED

The transfer to this segment is made from MAIN. The principal purpose of CALCED is to estimate the dissipation of turbulent kinetic energy, ε. Brief description of this may be found in the discussion to follow :

i.   Chapter 0 - Preliminaries :

Incorporates the common blocks of variables and constants necessary for CALCED to function.

ii.   Chapter 1 - Assembly of Coefficients :

Here the factors and source terms for the algebraic discretized form of the turbulent kinetic energy dissipation transport equation are determined. This is performed by first calculating the convection and diffusion coefficients for every individual scalar control volume. These coefficients are then compiled by the hybrid scheme to produce tentative estimates of the coefficients at the main scalar

node. The buoyancy forces acting at the scalar mesh points and affecting the dissipation parameters are next incremented to the appropriate source terms. The domain of interest here may be represented by a parallelpiped region enclosed by the grid lines I = 2 to NI-1, and J = 2 to NJ-1, and k = 2 to Nk-1.

iii.   ***Chapter 2 - Problem Modifications* :**

Until now the boundaries have been intentionally excluded from all calculations, the reason being that it must be handled in a distinctive manner. This is taken care of in this chapter by a transfer to PROMOD, which will be detailed later.

*iv. **Chapter 3 - Final Coefficient Assembly* :***

The discretization factor for every scalar grid node in the entire flow field are calculated here by utilizing an expression similar to equation (5.67a). Subsequently the absolute residual source sums for ε at all mesh points is computed. For reasons discussed earlier, the dissipation parameter is dampened indirectly by under-relaxing the corresponding discretization coefficients. The amount of under-relaxation applied is equivalent to URFE.

v.   ***Chapter 4 - Solution of the discretized equations* :**

Finally we have constructed all the necessary components to compute the dissipation term, ε , in the concerned flow regime. The set of discretization equations are solved by resorting to the subroutine

LISOLV. It is recommended to visit LISOLV more than once for the same CALCED run to attain a better estimate of ε. The number of times LISOLV is called is equivalent to NSWPD.

In general CALCED will not require any alterations for a relatively large group of flow situations. The exit of this routine is made back to MAIN.

6.2.11 Structure and Function of LISOLV

The transfer to and from this segment is done via all the CALC type routines (i.e. : CALCU, CALCV, CALCW, CALCT, CALCTe and CALCED). The main purpose of this subroutine is to solve for the various variables of the conservation equations describing the flow field by means of the Line-By-Line technique (LBL), details of which may be found in chapter five. A brief account of LISOLV and other related issues will follow:

i. *Chapter 0 - Preliminaries :*

LISOLV is the only active subroutine for which a transfer of earlier estimated parameters is necessary. Some of the important transfer parameters are ISTART, JSTART and KSTART which indicate the starting indices of traverse and sweep. Also PHI which represents an array containing the variable of the previous iteration to be computed when entering LISOLV, and is replaced by the solution when leaving this routine. A common block is supplied here for those terms which do not require a transfer. Finally some convenient expressions are evaluated.

ii. **Chapter 1 - Main Operations :**

In this section the South-North traverse is commenced for a particular West-East and Right-Left sweep (for further insight into this refer to sub-section 5.10). For every individual grid node (scalar or vector) the coefficients of the tri-diagonal matrix are compiled. Having attained these coefficients the corresponding parameters of the recurrence formula (5.101) are evaluated. These are then introduced into the recurrence expression (5.100) to produce an estimate of the particular variable under investigation. In one call to LISOLV the LBL procedure is implemented three times, each for a specific Cartesian direction. The number of times the entire routine is visited is equal to the number of sweeps specified in the transfer.

This routine will, in general, not require any modifications for a large variety of flow situations. The return of LISOLV is made to the routine from which the call was initiated.

6.3 Structure and Function of PROMOD

The name PROMOD is the short form of PRO blem MOD ification, meaning that for every different problem the corresponding modifications are introduced into the source code through PROMOD.

It is divided into distinctive chapters, each chapter pertaining to a particular variable. There are separate entry and return points for each chapter. The access to a particular chapter of PROMOD is made via an integer

IROUTE, specified at the subroutine MAIN. A modest description of the components of PROMOD is given below.

6.3.1 Chapter 0 - Preliminaries

Consists of all the variables and constants, in the form of common blocks, for PROMOD to operate properly. Various call routines corresponding to the appropriate chapter is also done here.

6.3.2 Chapter 2 - U-Momentum

The indirect transfer to this chapter is made from CALCU where IROUTE has been set equal to two. The solution domain here is identical to that given in the discussion on CALCU. Each of the active chapters are subdivided into six segments corresponding to the six boundary walls enclosing the room. These are :

I. Top (NORTH) wall :

This wall is parallel to the xz plane and at y = HEIGHT of the room. Before commencing the calculations a simple check is made for every node in this plane by confirming that the turbulent kinetic energy [43] has not become negative, and if so then the previous values at the boundary are used instead. Additional parameters are evaluated and utilized in the computation of the local Reynolds number, YPLUSA, at all mesh points in this plane. Once YPLUSA is known then a conclusion may be reached to the predominance of

turbulence or viscosity at the point under investigation. This will affect the manner in which the wall shear stress, parallel to this plane, together with the source term are computed. In view of the arrangement of the mesh (i.e., to have the first and last scalar nodes embeded into the solid surfaces) the corresponding discretization coefficient relating the grid point in the flow field immediately adjacent to the wall to the grid point implanted inside the wall is set equal to zero, as recommended by some investigators [5, 26, 29, 40, 43, 52]. This is done to ensure that the U velocity acting at the mesh point in the wall is zero and no contribution from it is felt at the node in the flow field.

II. Floor (SOUTH) wall:

A treatment similar to that discussed in the segment above for the top wall is repeated, with some minor differences, all of which is a result of having the mesh points on a xz plane at y = 0. At first a test is done to confirm that the turbulent kinetic energy, k, is positive. Then YPLUSA is calculated, from which the appropriate equations to evaluate the wall shear stresses and source terms are chosen. Finally the discretization coefficient for the node in the floor is set to zero.

III. NORTH (RIGHT) wall:

The solution domain in this portion is parallel to the xy-plane and at a distance equivalent to the room width along the z-axis. A verification is done here to substantiate that k does not take on negative values, and if this is true the local Reynolds number, ZPLUSA, is computed and used to select the

suitable equations to calculate the wall shear stress and source term at all nodes within the regime of concern. Afterwards the discretization coefficients for the grid nodes embeded in this wall are appropriately set to zero.

IV. SOUTH (Left) wall :

The discussion given here will follow that presented for the NORTH wall, the exception here is that the solution plane will pass through the origin of the Cartesian coordinates, parallel to the XY-plane. A validity test for the positiveness of k is done and if satisfied ZPLUSA is evaluated, from which the appropriate equations to compute the wall shear stresses and source terms are selected. Finally, the discretization coefficient for the mesh point implanted in this wall is set to zero.

V. WEST and EAST walls :

As the selection of the coordinate axis are such that the West and East walls are perpendicular to the x-axis, thus no source terms or wall shear stresses in the x-direction will appear and only the discretization coefficients for the nodes in the West and East walls, less the inlet and outlet port openings, are given a value of zero. Also in this chapter of PROMOD the mass flow rate at the inlet supply port is computed and is used to solve for the velocity at the outlet port on the East wall, such that the V and W components of velocity are set to zero, while the U component is distributed evenly over the outlet.

Once all computations are finished the exit of this routine is made back to CALCU.

6.3.3 Chapter 3 - V-Momentum

In view of the fact that the general lay out of the V-momentum routine resembles that of the U-momentum, only a brief description is given here, particularly mentioning the distinctions between this subsection and 6.3.2.

The indirect transfer to this chapter is made from CALCV where IROUTE has been given the value of three. The calculation field is similar to that given in CALCV. In the following a discussion of the major variations between this chapter and chapter 6.3.2 will be listed

I. FLOOR and TOP wall :

Here the floor and top wall planes are perpendicular to the y-axis, thus no wall shear stress or source terms are estimated.

II. NORTH and SOUTH walls :

The same treatment for these walls in 6.3.2 will follow here except the calculation domain will follow that from CALCV.

III. EAST and WEST walls :

For these walls there exists some difference from the East and West walls described in 6.3.2, in that the wall shear stresses and source terms in the y-direction are evaluated. The solution domain is also identical to that of CALCV.

Once all computations are finished the exit of this routine is made back to CALCV.

6.3.4 Chapter 4 - W - Momentum

The access to this chapter is possible by setting IROUTE equal to nine. The domain of interest here resembles that of CALCW. Also here, as in 6.3.3, only a discussion of the discrepancies between this chapter and 6.3.2 will be presented.

I. FLOOR and TOP wall :

A practice analogous to that of the floor and top wall of 6.3.2 is applied here, except that the solution domain will follow from CALCW.

II. EAST and WEST walls :

The approach by which these walls are handled are similar to that for the same walls of 6.3.3, with the computational field resembling that of CALCW.

III. NORTH and SOUTH walls:

Here the solution domains are perpendicular to the z-axis and, accordingly, there will not be any wall shear stresses or source terms.

Finally, the exit from here is made back to CALCW.

6.3.5 Chapter 6 - Thermal Energy

The indirect transfer to this chapter is made from CALCT where IROUTE has been set equal to seven. The region of interest is the same as that of CALCT. Six definite sections of this chapter are provided for each of the six surrounding walls. There exists a strong similarity among these various sections. Thus only one out of these six is described. The one selected is the Top wall.

TOP wall :

The plane containing the grid nodes here is parallel to the xz plane and passes through the scalar mesh points in the flow field immediate to the Top wall. A check is done for every node in the calculation field for the turbulent kinetic energy, k, to confirm that no unrealistic negative value for k is accepted. Afterwards YPLUSN, estimated earlier, is used as an indicator to the predominance of turbulence or viscous affects which will directly affect the choice of the equation to be used to compute the heat flux from this wall. The source terms for the energy equation is then estimated. Finally, the total heat flux leaving this wall due to the temperature gradient between the wall

and air, in addition to the pre-specified heat flux from this surface, are evaluated.

In view of the necessity to satisfy heat equilibrium over the entire room, a heat balance is performed at the end of this chapter, whereby the temperatures at the nodes in the flow field immediately bordering the outlet port opening are estimated.

After executing all operations in this chapter the transfer is made back to CALCT.

6.3.6 Chapter 7 - Turbulent Kinetic Energy

The indirect access to this chapter is made from CALCTE where IROUTE has been set equal to five. The solution field here is identical to that of CALCTE. There are six separate subdivisions in this chapter corresponding to the six surrounding solid surfaces. It will be noticed here, as in the precedeing chapters, that a resemblance among these subdivisions exist. Consequently only one out of these six is detailed below. The subdivision chosen to be described here is the Top Wall.

TOP wall :

The calculation field here is parallel to the xz plane and passes through the scalar grid node in the flow field just under this wall. A test of acceptable positive turbulent kinetic energy, k, at all nodes are made, while if negative k

were to appear they are replaced by the k from previous runs. Some parameters necessary for the estimation of the generation of k in the U and W directions due to wall shear are evaluated next. The local Reynolds number, YPLUSN, and gradients of U and W in the y-direction are evaluated and used to calculate the remaining part of the generation of k, GENRES. By combining this generation with those for wall shear, produces the total generation of k. Two distinctive relations are available to estimate the source terms for k, the appropriate relation is decided upon via YPLUSN. To suppress the non-existent k in the plane embeded into this wall, the discretization coefficients are set to zero.

Once all operations in this chapter are complete the departure is made back to CALCTE.

6.3.7 Chapter 8 - Dissipation of Turbulent Kinetic Energy

The indirect access to this chapter is made from CALCED, where IROUTE was given a value of six. The calculation field is equivalent to that of CALCED. This chapter consists of six definite segments each representing one of the six surrounding walls. As with the other preceding chapters, because of the strong resemblance between these segments only one of them is discussed in detail and is representative of the others. The section selected is the top wall.

TOP wall :

The solution domain here may be represented by a plane of grid nodes parallel to the xz plane and passing thorough the mesh point in the flow field immediately adjacent to this wall. A check at every grid node is done to confirm that the turbulent kinetic energy is physically realistic (i.e. : positive quantities). Having achieved this the source terms for the discretized form of the dissipation of the turbulent kinetic energy transport equation are computed.

After performing all operations in this chapter a return call is made back to CALCED.

In view of the precedeing discussions it is quite obvious that the significance of PROMOD in the source code as a whole may not be stressed enough. This subroutine is strongly problem dependent and thorough care needs to be exercised when attempting to modify it.

CHAPTER VII

RESULTS AND DISCUSSION

Some of the pertinent variables describing the flow field, computed by the source code presented in Chapter VI, are displayed here in the form of plots, profiles, contours and tables, and the various room configurations and boundary conditions attempted are detailed. The resulting thermo-regulatory responses of occupants within the occupied zone of the room is presented in the form of horizontal planes of PMV index contours for the sitting and standing postures. Different grid sizes, for a particular configuration and boundary condition, have been studied the results of which will also appear below. An endeavour to replace the finite difference scheme used in the source code by another has been done and comparison is made between the two. To substantiate the results of the computer program employed here, an experimental investigation done by other researchers is compared with the data simulated by this numerical code. This is the first topic to be discussed below.

7.1 VALIDATION of the NUMERICAL CODE

The extent by which the results of any numerical investigation agrees to that occurring in reality may only be known by conducting exper-

imental measurements and comparing the results obtained here with those predicted by the numerical solver. Ideally, it would be best to have an experimental verification for every numerical prediction, but this being impractical, computational approach is sought which allows as many variations as needed for system optimization. In view of this, experimental measurements done on a physical model is compared to predictions by the numerical solver for a given situation and the degree by which the simulated results match those given by empirical methods is used to substantiate the numerical code.

A number of experimental investigations are available concerning room ventilation problems, but not all of these closely match the configuration adopted in this study. One empirical measurement done by Restivo [6] on three-dimensional room models were similar to the present investigation and could be duplicated in the numerical code with no serious difficulties encountered. A description of a room model configuration together with some measurements by Restivo are given in the subsection to follow.

7.1.1 Configuration and Boundary Conditions

The room model configuration is such that the inlet opening is located on a side wall adjacent to the ceiling while the outlet exhaust opening is situated opposite to the inlet adjacent to the floor and extending over the breadth of the model. (See Fig. 7.1). The velocity at the inlet was given as 1.368 m/sec., while the density, Prandtl number and viscosity of the air were 1.189 kg/m^3, 0.7086 and 1.816 x 10^{-5} N.s/m^2, respectively.
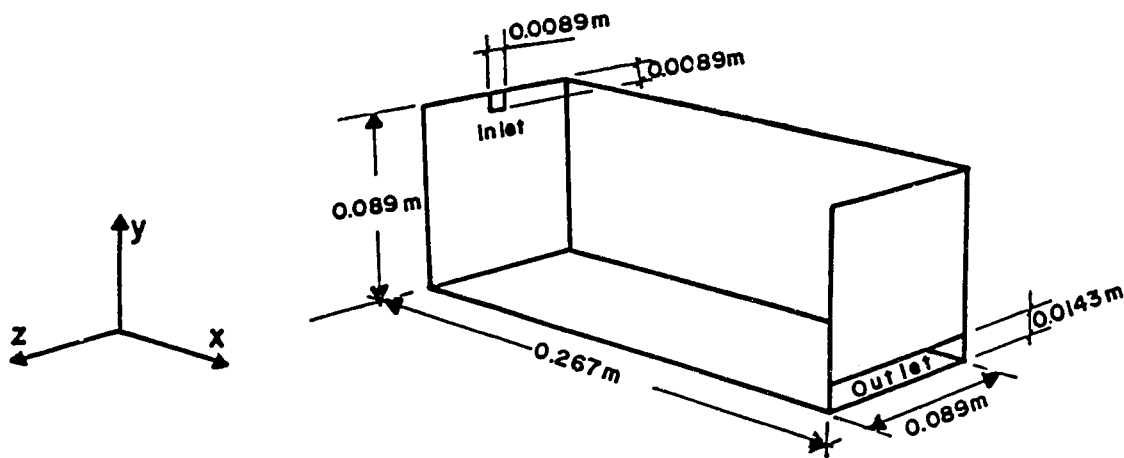
Figure 7·1 Configuration and dimensions of room model by Restivo [6].

The temperature of the air and the surrounding walls were at 21°C, as Restivo only performed isothermal investigations on his three-dimensional room model.

7.1.2 Results and Discussion

Restivo presented his results in the form of velocity profiles for the U velocity component along the x-axis normalized with the velocity at the inlet opening. These profiles were measured over the room height and at different cross-sections, the geometrical locations being normalized by the height of the room (See Figs. 7.2 and 7.3). In this investigation, the form of the results produced by the numerical code is managed in such a way so that it may be compared with the experimental measurements.

The grid size employed in this comparison was 20x18x18 and the maximum absolute residual source sum was set at 0.01. No visible fluctuations occurred during the run and the converged solution was attained at a total CPU time of 14.54 minutes while 732 iterations were required.

The results shown in Fig. 7.2 are dimensionless U velocity profiles at a plane normal to the z-axis and passing through the center of the inlet which is also the center of the room (i.e. : $z/H = 0.5$), where H is the room height. By simple inspection of Fig. 7.2, we note that the experimental and the computed results are comparable and is accepted to be accurate enough for general engineering purposes.

For a further insight into the validity of the numerical code employed in this research, a second set of predicted results are compared
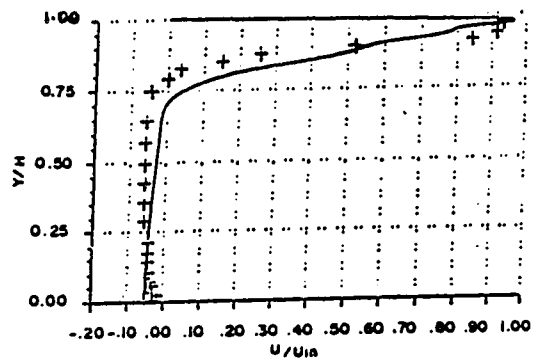
a) X/H = 0.5 and Z/H = 0.5
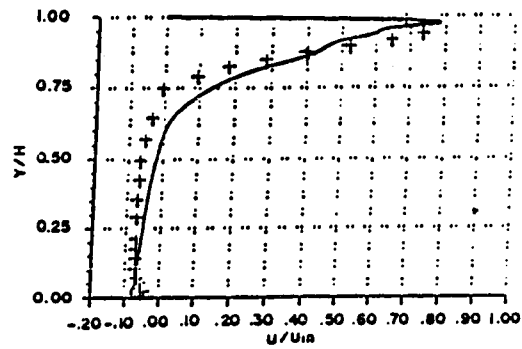
b) X/H = 1.0 and Z/H = 0.5
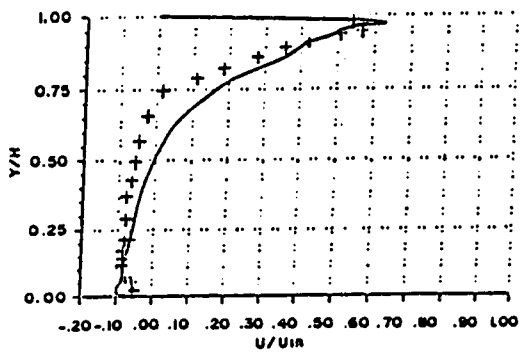
c) X/H = 1.5 and Z/H = 0.5
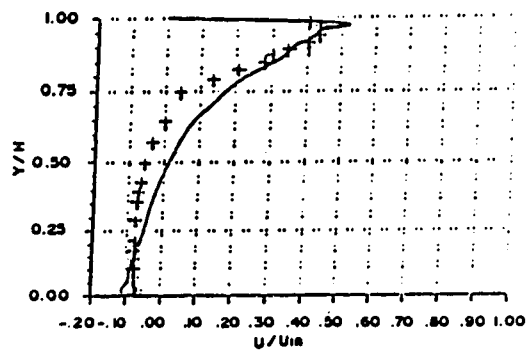
d) X/H = 5.0 and Z/H = 0.5
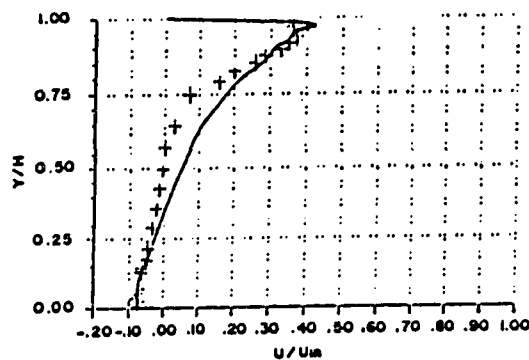
e) X/H = 2.5 and Z/H = 0.5

Figure 7.2. Dimensionless U - velocity profiles at mid
section of room. Solid lines computed by
numerical code + Experiments by Restivo [6].
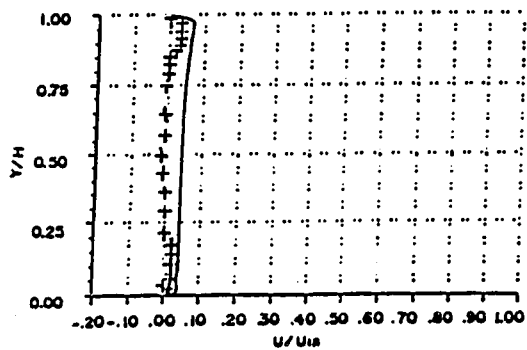
a) X/H = 0.5 and Z/H = 0.9
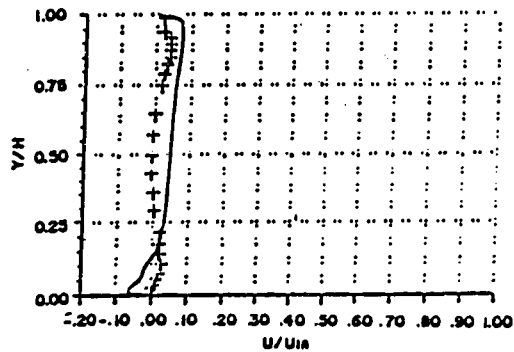
b) X/H = 1.0 and Z/H = 0.9
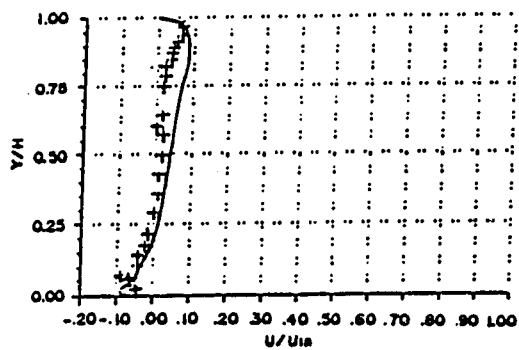
c) X/H = 1.5 and Z/H = 0.9
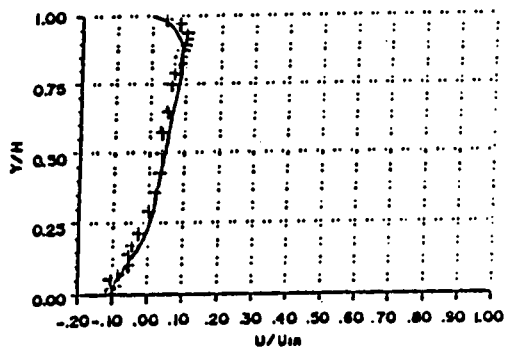
d) X/H = 5.0 and Z/H = 0.9
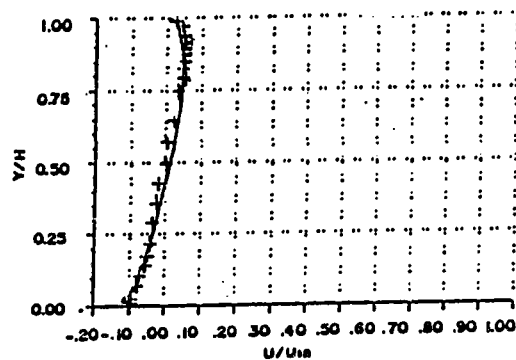
e) X/H = 2.5 and Z/H = 0.9

Figure 7.3. Dimensionless U - velocity profiles close to
the side wall of room. Solid lines computed by
numerical code. + Experiments by Restivo [6].

with experimental measurements. These are given in Fig. 7.3, for which dimensionless U velocity profiles (U / U_{in}) are plotted against dimensionless y locations (y/H) at a number of x dimensionless cross-sections (x/H) for a z plane close to the side wall (i.e. : at z = 0.9 · H). Comparing the experimental measurements and computed results, we observe similar patterns as that of Fig. 7.2. Even though the two do not form a perfect match but the overall appearance of the computed dimensionless U velocity profiles, seems to compare reasonably with the experimental profiles. In Figs. 7.2 and 7.3, a 'better' approximation of the computed results would have possibly been obtained by either selecting a smaller grid size or setting the absolute residual source sum to a smaller tolerance or both. It is noted here that the experimental measurements by Restivo [6] might also contain some inherent inaccuracy, as do most empirical estimates. Thus a perfect match would prove to be inappropriate.

7.2 CONFIGURATIONS and BOUNDARY CONDITIONS

As mentioned earlier, four distinctive geometrical arrangements are considered in this investigation where the location of inlet and/or outlet is varied while keeping the inlet and outlet openings and room size identical for all configurations studied. The dimensions of the room are 4.9 m (in x-direction), 2.75 m (in y-direction) and 3.7 m (in z-direction), whereas, the inlet and outlet openings are identical in size and equal to 0.3 m X 0.3 m.

The different arrangements of inlet and outlet considered are as follows :

(a)   WE: which is the short form for the inlet on the West wall close to the ceiling and the outlet on the East wall close to the floor.

(b)   NN: which refers to having the inlet on the top wall close to the West wall and the outlet also on the top wall but close to the East wall.

(c)   SN: where it is identical to NN except that the inlet is on the floor close to the West wall, while the outlet is at the same location given in NN.

(d)   NE: this configuration represents a combination of the inlet location for NN and the outlet location for WE.

For the research conducted here, the wall temperatures and heat fluxes are required and these were computed for a room enclosure situated in Dhahran at the design month of August 21st [65] having a common construction of 6 inches of light weight concrete and 2 inches of insulation with no suspended ceiling for the roof and 6 inches of heavy weight concrete for the surrounding walls, while the floor was considered to be adiabatic and isothermal at 24°C. The wall temperatures and heat fluxes, as computed through the ASHRAE Fundamentals [65], for the specific times employed in this research are shown in Table 7.1.

Owing to the fact that numerically acceptable 'converged' values should be attained for a particular run and noting the time limit granted, a

TABLE 7.1 : __Wall temperatures and heat fluxes for different times__

Time of Day	Temperatures (°C) of the inside Surfaces						Heat Flux W/m² of					
	Ceiling	Floor	East	West	North	South	Ceiling	Floor	East	West	North	South
9.00 A.M	24.9	24.0	25.4	25.2	24.8	24.9	5.9	0.0	34.6	31.2	19.2	20.80
12.00 Noon	29.4	24.0	27.2	26.4	25.9	26.0	33.6	0.0	80.0	60.0	47.70	49.4
3.00 P.M	33.1	24.0	28.2	27.1	26.7	27.1	57.0	0.0	104.8	76.9	68.2	76.6

thorough investigation has been made for all the wall temperatures and heat fluxes data of Table 7.1 for the geometrical configurations WE and NN, while the boundary conditions at Noon have been used for the SN and NE arrangements. The inlet velocity and temperature have been varied according to the corresponding configuration and boundary conditions so that thermal comfort of the occupants or close to it may be achieved.

In a typical run of the source code, a sizeable amount of data is produced after convergence is reached. However, it is quite impractical to report all data generated due to the need for conciseness. We, thus, will resort to plots and contours of the pertinent variables which may give a better picture of the entire flow field and its response to a change in any of the boundary conditions. Results and discussions for the various configurations and boundary conditions is given in the subsections to follow.

7.2.1 The WE Configuration

In this configuration , three distinct boundary conditions are applied to the surrounding walls of the room, which correspond to the time of 9:00 A.M., 12:00 Noon and 3:00 P.M. .In view of the changing boundary conditions with time, the thermal sensation response of the occupants within the room similarly changed, and to still be able to satisfy the comfort requirements of the occupants [51] , efforts have been made in varying the temperatures and/or velocities at the inlet opening.

In general, all the runs were initiated with initial inlet temperature and velocity of 15°C and 1.9 m/s. Other data were generated by using dif-

ferent temperature or velocity as given in Table 7.2, so as to arrive at a comfortable environment. It should be noted that to arrive at this inlet temperature and velocity, at which comfort was attained, required numerous runs. But, for reasons of brevity, only the results of the initial and final numerical runs are reported.

7.2.1.1 Velocity vector plots

To portray the resulting velocity flow fields within an enclosure vector plots were employed. These plots are given for vertical x-y planes at 0.6 m (coinciding with right edge of the occupied zone) 1.85 m (passing through the center of the room, the inlet and the outlet) and 3.1 m (left edge of occupied zone) along the z-axis (see Fig. 3.2), and horizontal x-z planes at 0.14 m (passing through the center of the outlet), 0.76 m, 1.76 m and 2.51 m (passing through the center of the inlet), along the y-axis. These plots show the overall flow of air, recirculation, vortices, points of stagnation and points of relatively high velocity. A brief discussion and comparisons of the data for the times of 9:00 A.M., 12:00 Noon and 3:00 P.M. shall now follow.

(i) Velocity Vector Plots at 9:00 A.M.

Figs. 7.4 and 7.6 are x-y velocity vector plots, at the same locations and boundary conditions, except that Fig. 7.4 is for an inlet temperature, T_{in}, of 15.0°C while Fig. 7.6 is at 18.0°C and U_{in}, in both figures is equal to 1.9 m/sec.. Comparing Figs. 7.4 and 7.6 we note that the velocity vector pattern in both of them are quite similar, to the extent that no obvious dif-

TABLE 7.2 : Inlet Velocities and Temperatures Employed in the WE Configuration

Time of Day	T_{in} (°C)	U_{in} (m/sec.)
9 A.M.	15.0	1.9
9 A.M.	18.0	1.9
12 Noon	15.0	1.9
12 Noon	12.0	3.0
3 P.M.	15.0	1.9
3 P.M.	10.0	4.0

1.90 M/SEC.

a) X-Y Section at Z = 0.600 m

b) X-Y Section at Z = 1.850 m

c) X-Y Section at Z = 3.100 m
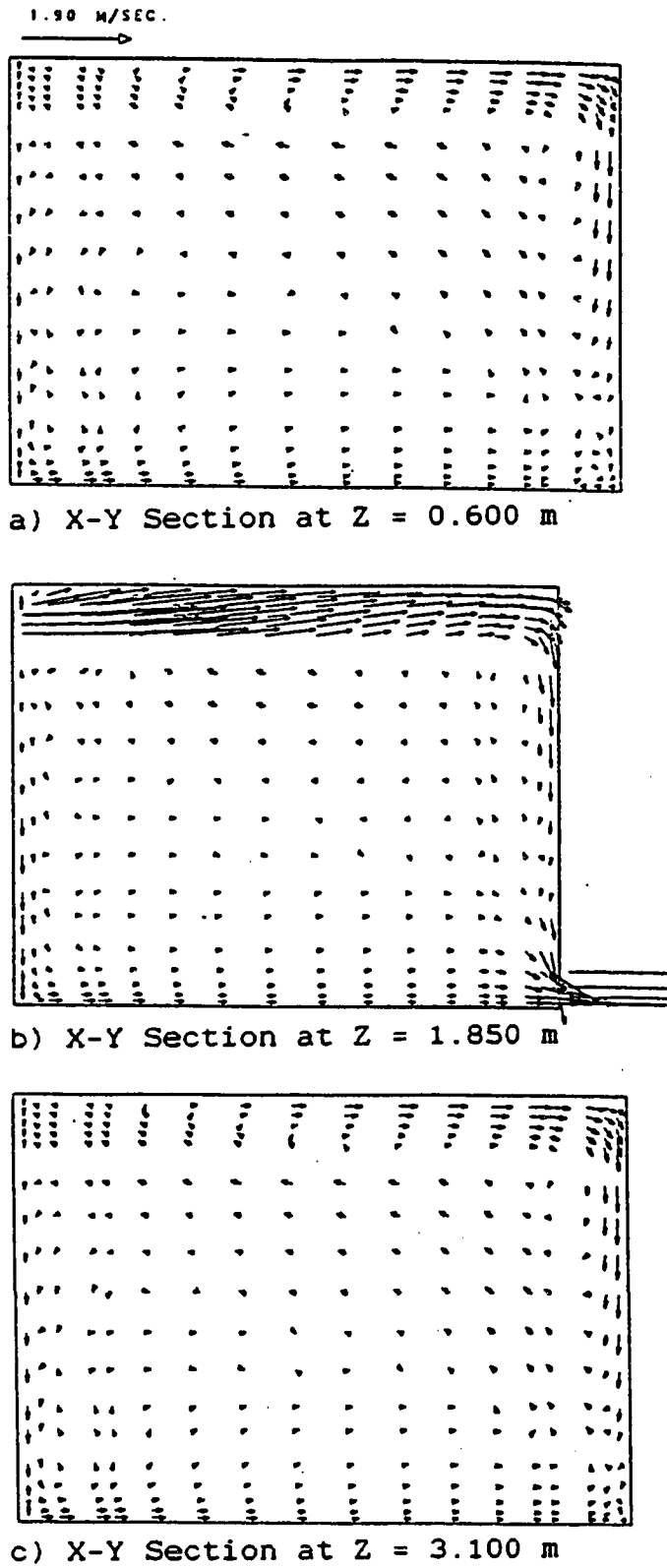
Figure 7.4. Velocity vector plots in the X-Y plane at 9 am, Tin = 15 °C and Uin = 1.9 m/sec for the WE configuration.

184

1.90 M/SEC.

a) X-Z Section at Y = 0.141 m

b) X-Z Section at Y = 0.756 m

c) X-Z Section at Y = 1.759 m

d) X-Z Section at Y = 2.510 m
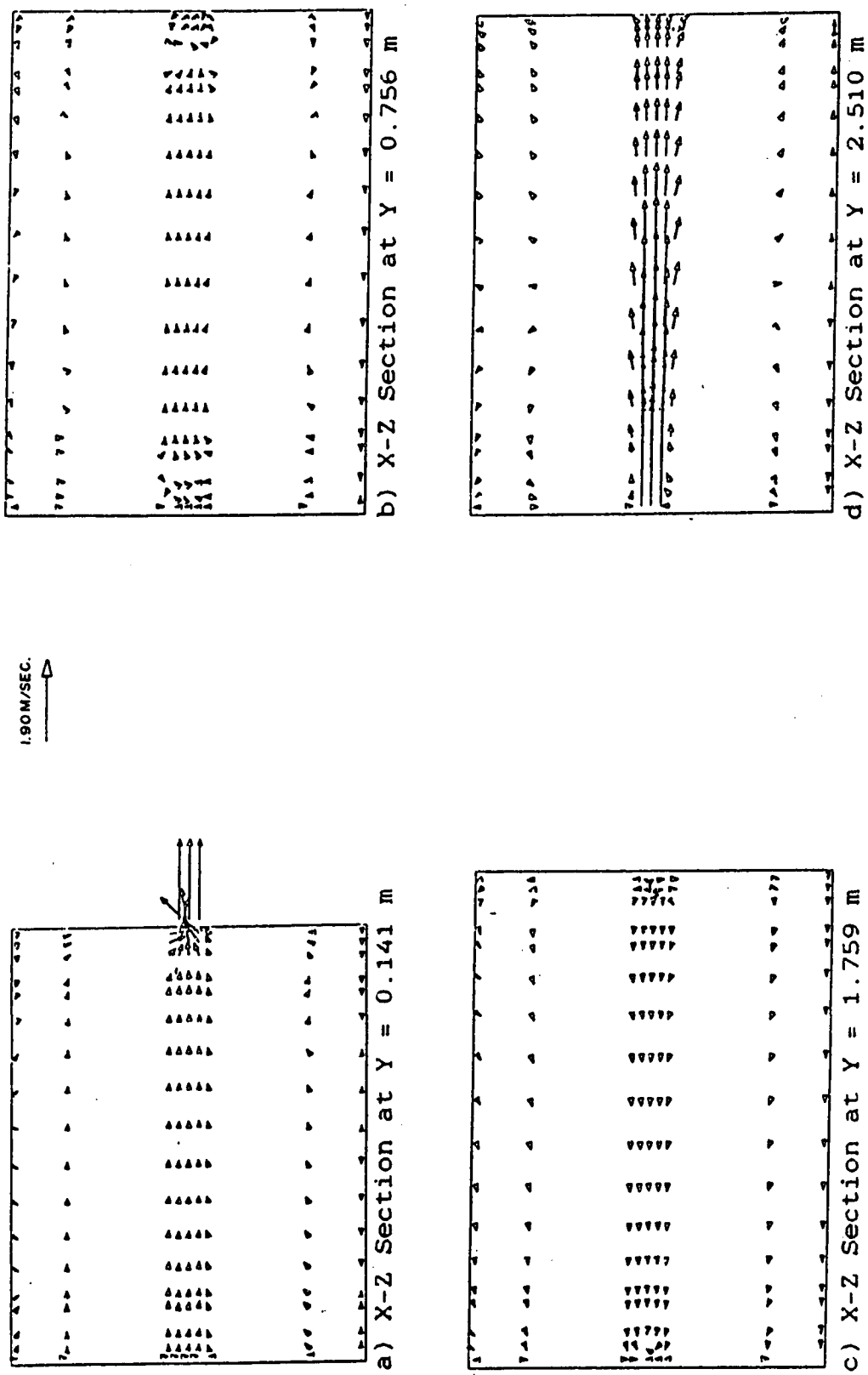
Figure 7.5. Velocity vector plots in the X-Z plane at 9 am, Tin = 15 °C and Uin = 1.9 m/sec for the WE configuration.

1.90 M/SEC.
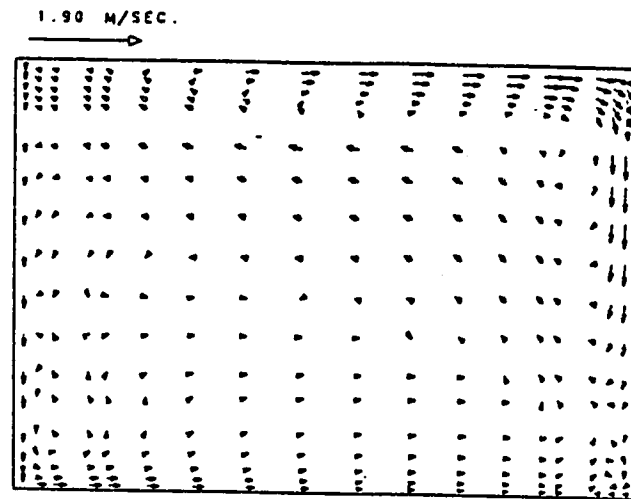
a) X-Y Section at Z = 0.600 m
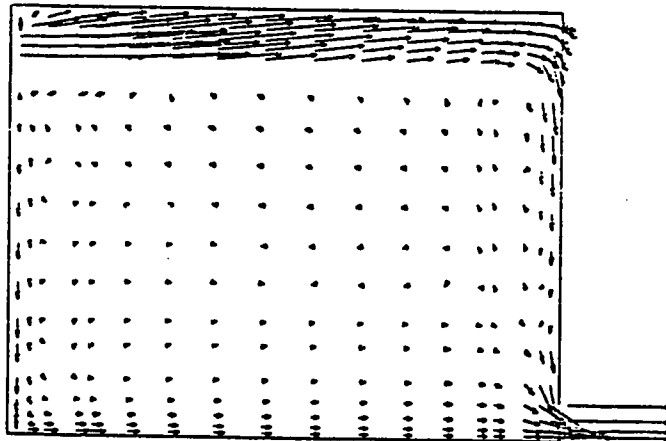
b) X-Y Section at Z = 1.850 m
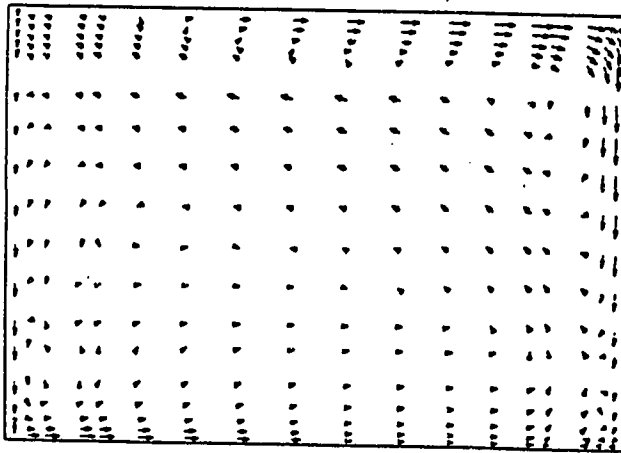
c) X-Y Section at Z = 3.100 m

Figure 7.6. Velocity vector plots in the X-Y plane at 9 am, Tin = 18 °C and Uin = 1.9 m/sec for the WE configuration.

186

a) X-Z Section at Y = 0.141 m

b) X-Z Section at Y = 0.756 m

c) X-Z Section at Y = 1.759 m

d) X-Z Section at Y = 2.510 m

1.90 M/SEC.
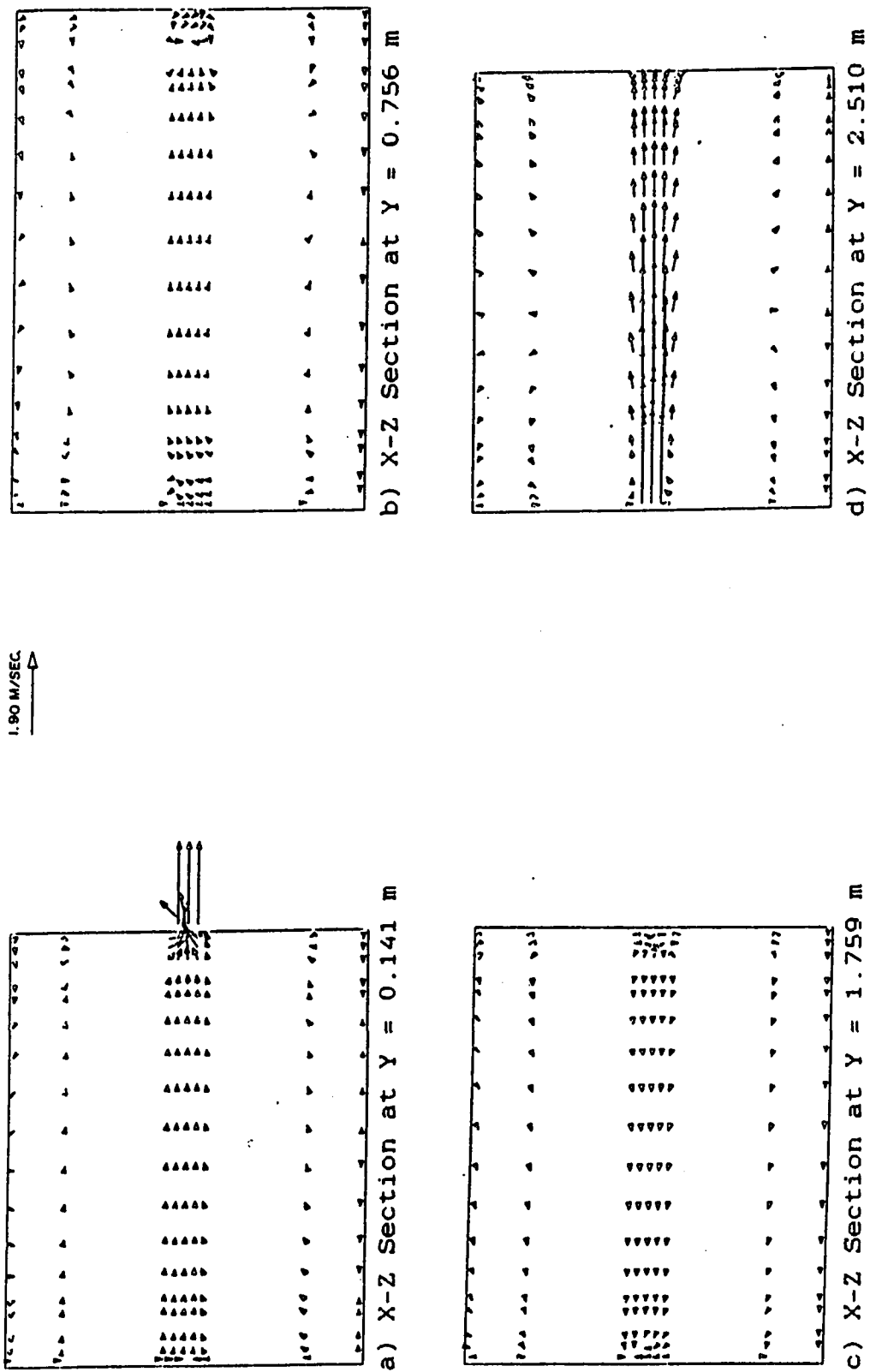
Figure 7.7. Velocity vector plots in the X-Z plane at 9 am, Tin = 18 °C and Uin = 1.9 m/sec for the WE configuration.

ferences among the two were observed. The reason for this is due to the fact that the inlet velocity, U_{in}, was identical and the temperature difference between the two was relatively low so that the effect of buoyancy did not appear in most of the flow field.

Figs. 7.5 and 7.7 are x-z velocity vector plots, and what has been said regarding Figs.7.4 and 7.6, applies here.

(ii) Velocity Vector Plots at 12:00 Noon

The change in the inlet temperature and velocity are now substantial enough to cause an observable variation among the plots, such that in Figs. 7.8 and 7.9, T_{in} and U_{in} are 15°C and 1.9m/sec., respectively while those for Figs. 7.10 and 7.11 are equal to 12°C and 3.0m/sec., respectively. Comparing Figs. 7.8.a and 7.10.a close to the ceiling at the midsection of the room the relative magnitudes of the velocity are higher in Fig.7.8.a causing the velocity to spread along the ceiling for a relatively longer distance than that of Fig.7.10.a, while the relative magnitudes of the velocity close to the bottom part of the East wall region is higher in Fig. 7.10.a, the reason is due to the relatively higher negative buoyancy forces in Fig. 7.10. It may be observed that the relative magnitude of the velocity in the vicinity of the ceiling close to the East wall depreciates faster in Fig. 7.8.b relative to Fig. 7.10.b; this is due to a lower U_{in} in Fig. 7.8.b, and thus the velocity dies out sooner. This observation is more obvious when comparing Figs. 7.9.d and 7.11.d.

The overall general features for both situations in a relative viewpoint are comparable.
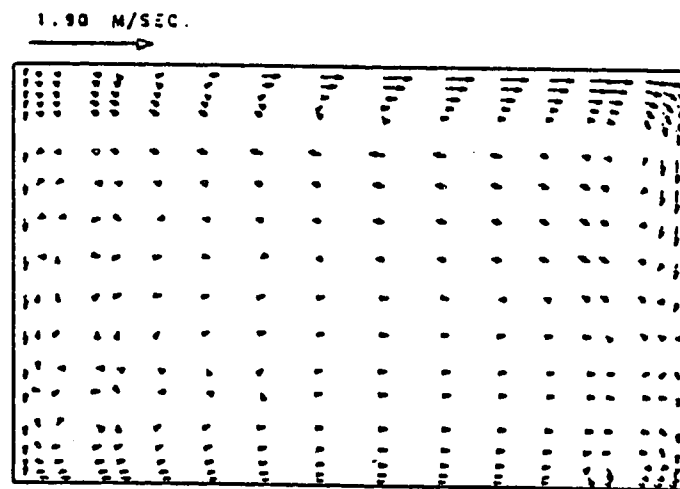
1.90 M/SEC.

a) X-Y Section at Z = 0.600 m
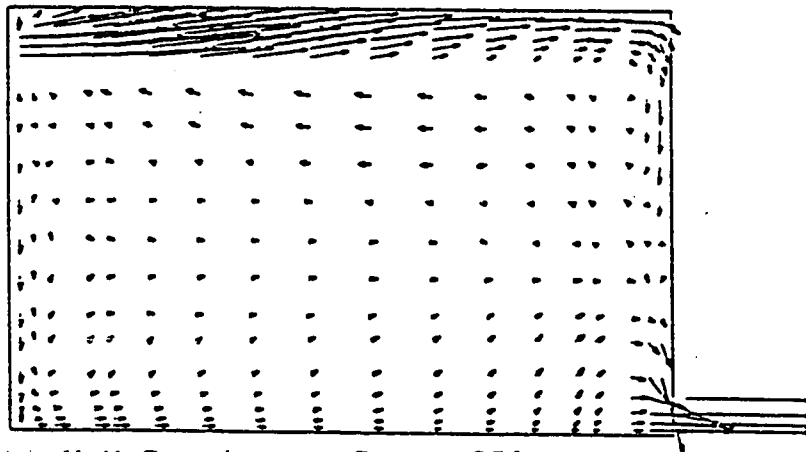
b) X-Y Section at Z = 1.850 m
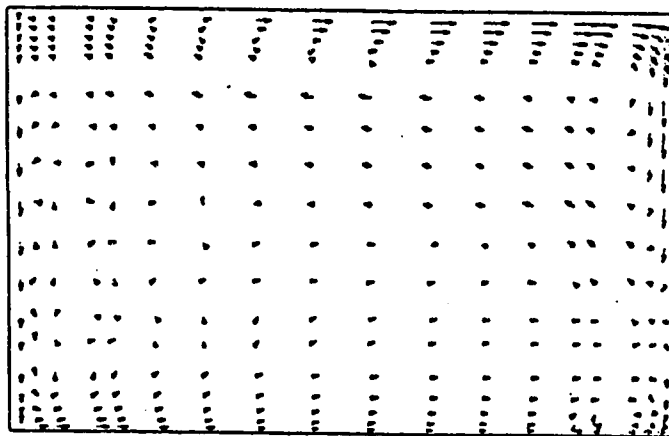
c) X-Y Section at Z = 3.100 m

Figure 7.8. Velocity vector plots in the X-Y plane at noon, Tin = 15 °C and Uin = 1.9 m/sec for the WE configuration.

1.90 M/SEC
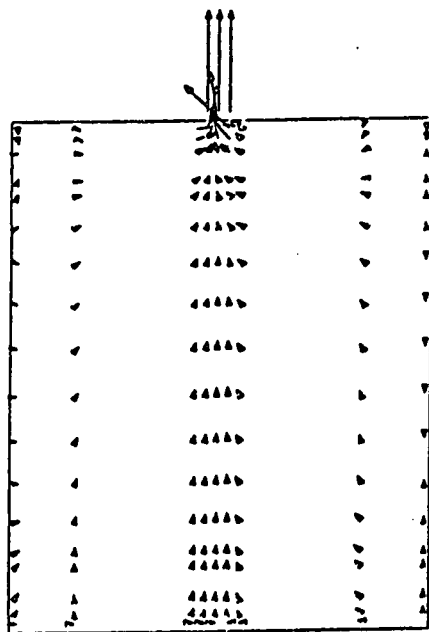
a) X-Z Section at Y = 0.141 m
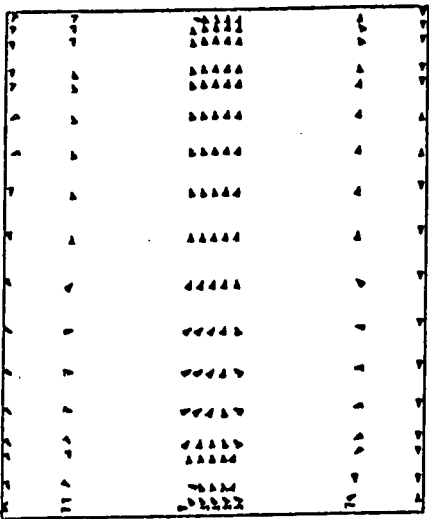
b) X-Z Section at Y = 0.756 m
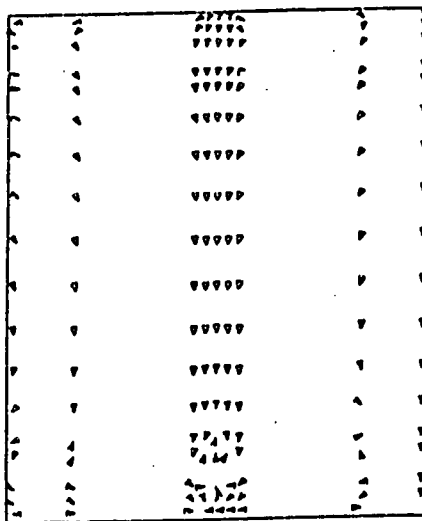
c) X-Z Section at Y = 1.759 m
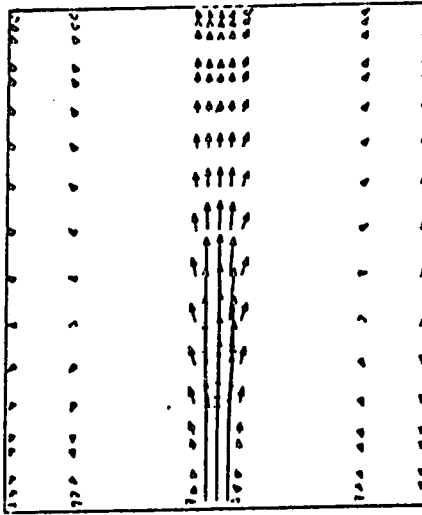
d) X-Z Section at Y = 2.510 m

Figure 7.9. Velocity vector plots in the X-Z plane at noon, Tin = 15 °C and Uin = 1.9 m/sec for the WE configuration.

3.00 M/SEC.
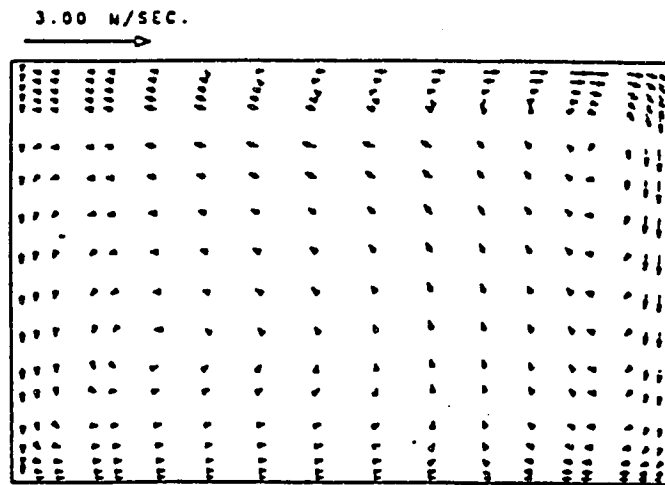
a) X-Y Section at Z = 0.600 m
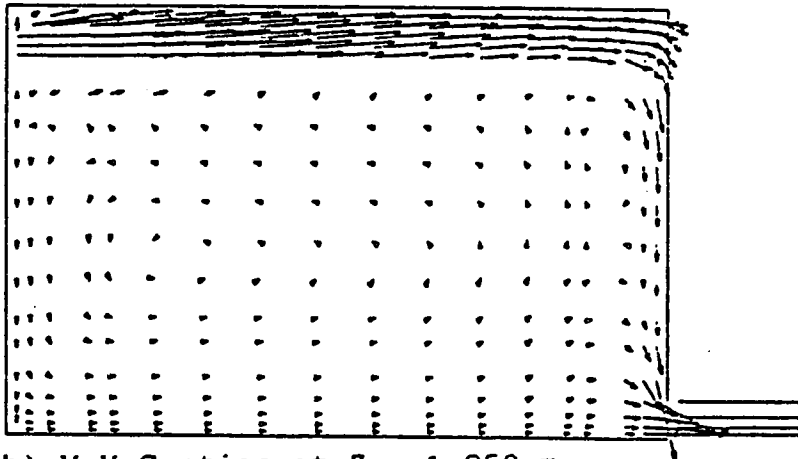
b) X-Y Section at Z = 1.850 m
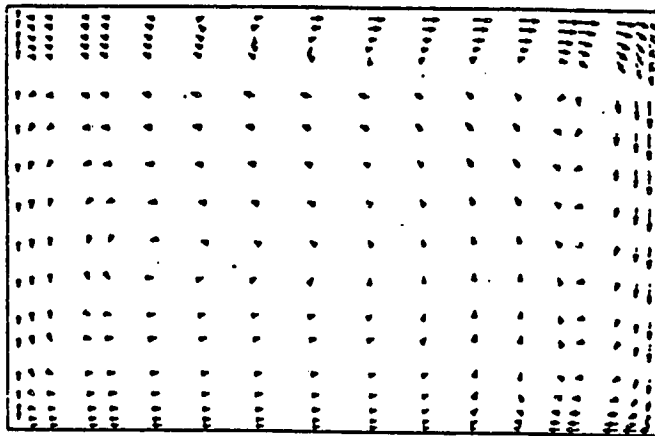
c) X-Y Section at Z = 3.100 m

Figure 7.10. Velocity vector plots in the X-Y plane at noon,
Tin = 12 °C and Uin = 3.0 m/sec for the WE
configuration.

191
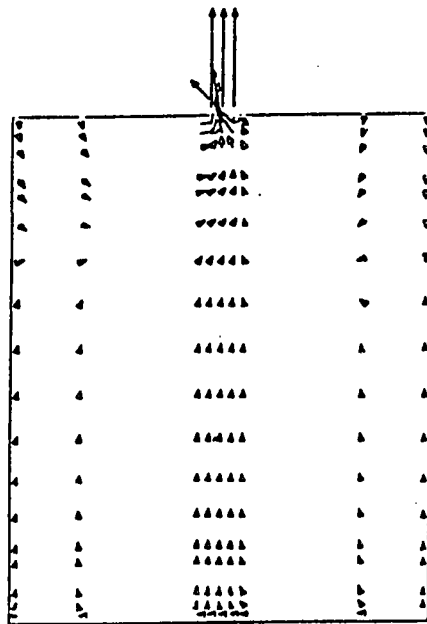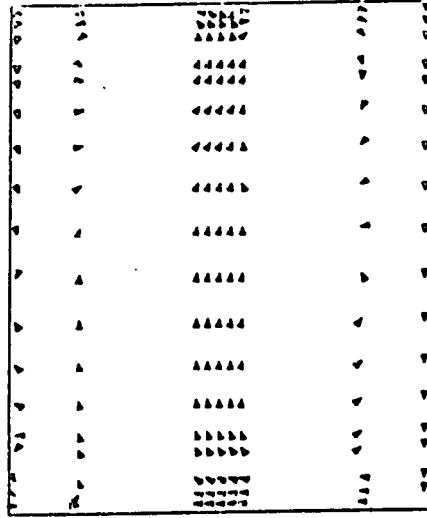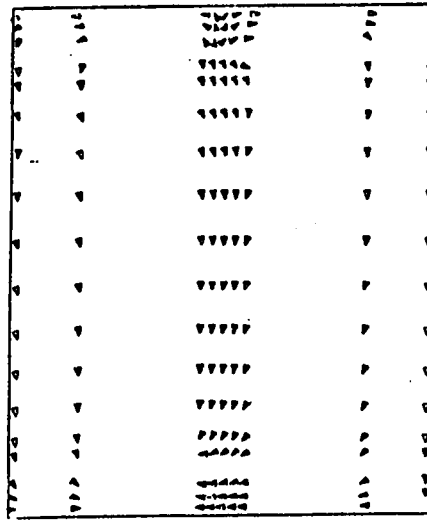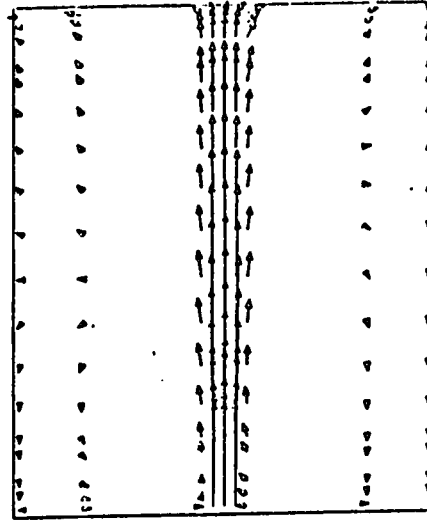
Figure 7.11. Velocity vector plots in the X-Z plane at noon, Tin = 12 °C and Uin = 3.0 m/sec for the WE configuration.

(iii) Velocity Vector Plots at 3:00 P.M.

Observations similar to those discussed for the velocity vector plots at 12:00 Noon are noticed here, such that the relative magnitude of the velocity at the room center close to the ceiling is higher in Fig. 7.12.a than that of Fig. 7.14.a, while the relative velocity close to the East wall is higher in Fig. 7.14.a which is due to a, relatively higher U_{in} and a lower T_{in} (see Table 7.2), causing a correspondingly higher negative buoyancy force pulling the air down. The depreciation of the relative magnitude of the velocity at the top part of the room, close to the East wall is higher in Fig. 7.12.b than in Fig. 7.14.b which is due to the higher U_{in} in Fig. 7.14.b. This depreciation in the magnitude of the velocity is more obvious when comparing the relative velocity vectors passing through the mid-section of the room, shown in Fig. 7.13.d with that of Fig. 7.15.d. An interesting observation to note in Fig. 7.14 is the appearance of a clockwise vortex in the Eastern part of the room and a counter-clockwise vortex in the Western part of the room. No such observation is noticed in Fig. 7.12.

7.2.1.2 Velocity profiles

To have a better understanding of the effect of varying U_{in} and T_{in} on the resulting velocity profile along the x-direction the U velocity vectors have been undimensionalized by U_{in} and are taken at z planes passing through the center of the room and another close to the left wall.

1.90 M/SEC.
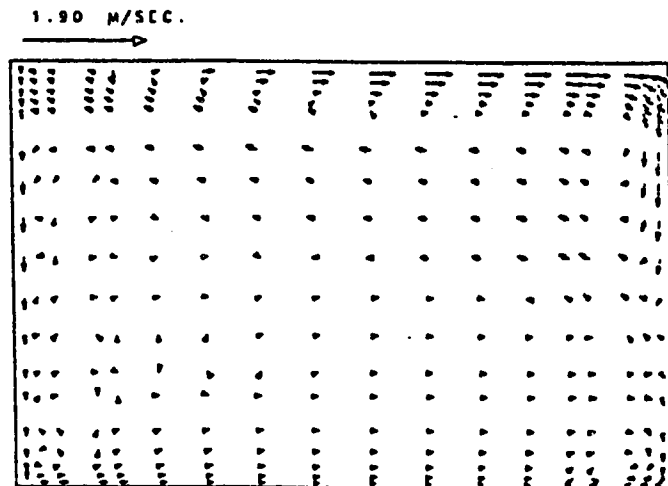
a) X-Y Section at Z = 0.600 m
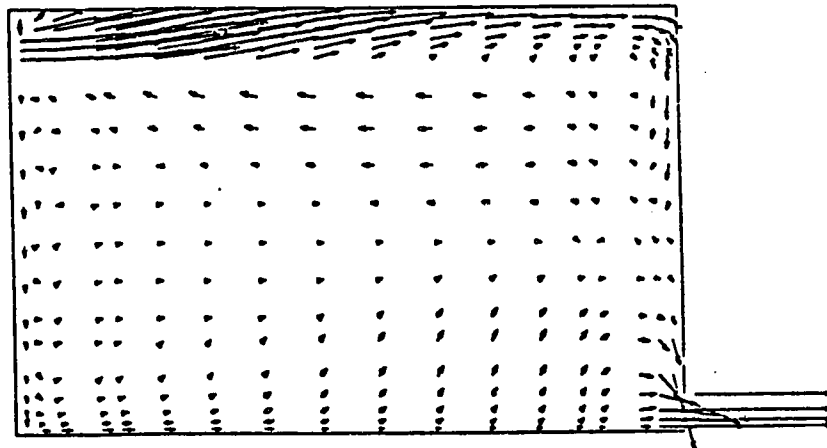
b) X-Y Section at Z = 1.850 m
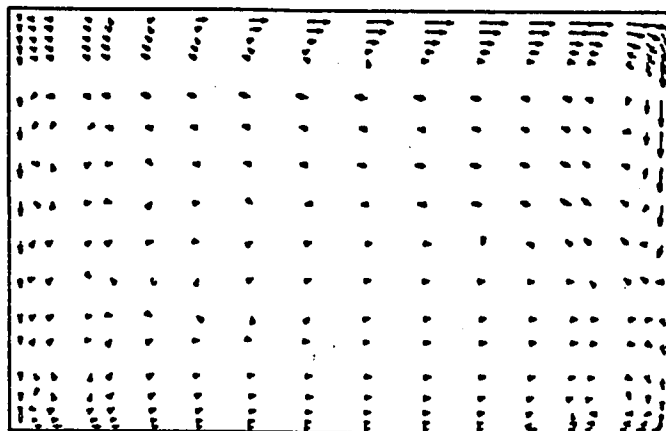
c) X-Y Section at Z = 3.100 m

Figure 7.12. Velocity vector plots in the X-Y plane at 3 pm,
Tin = 15 °C and Uin = 1.9 m/sec for the WE
configuration.

194

b) X-Z Section at Y = 0.756 m

d) X-Z Section at Y = 2.510 m

a) X-Z Section at Y = 0.141 m

c) X-Z Section at Y = 1.759 m

1.90M/SEC.
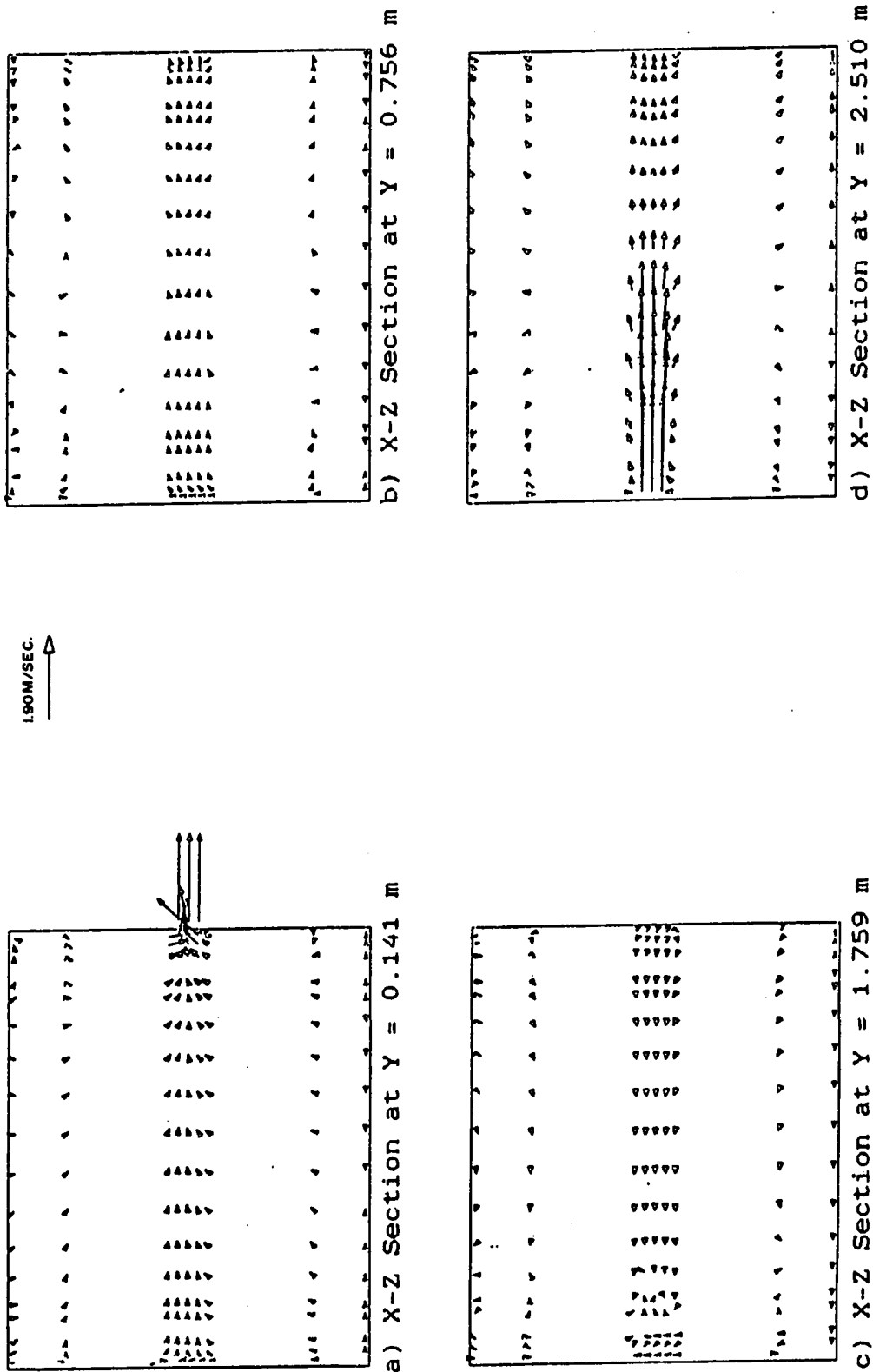
Figure 7.13. Velocity vector plots in the X-Z plane at 3 pm, Tin = 15 °C and Uin = 1.9 m/sec for the WE configuration.
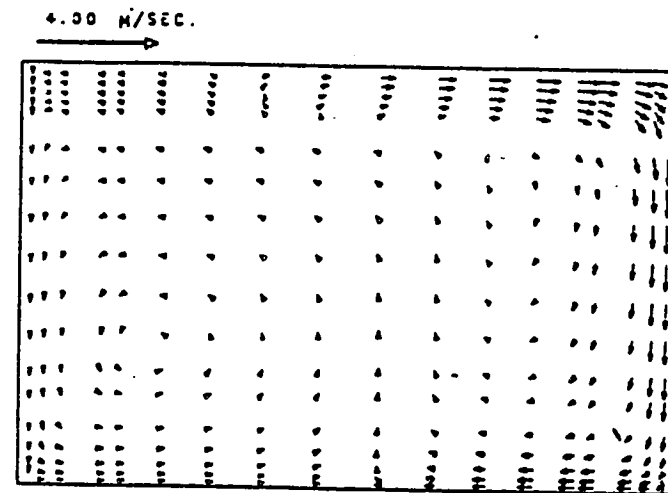
a) X-Y Section at Z = 0.600 m
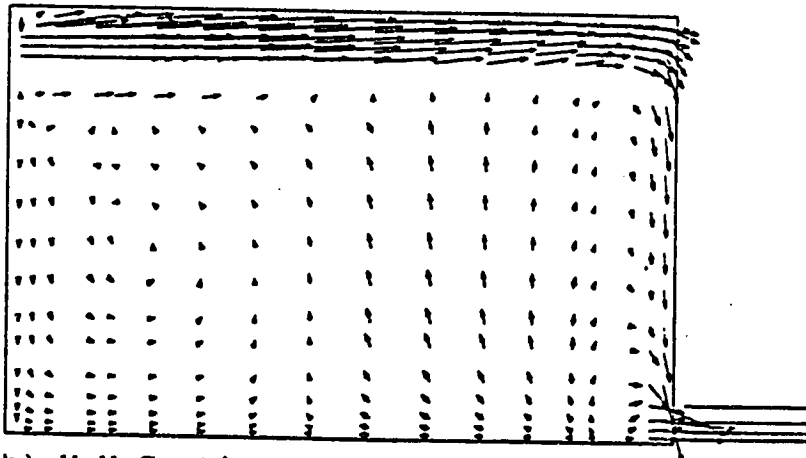
b) X-Y Section at Z = 1.850 m
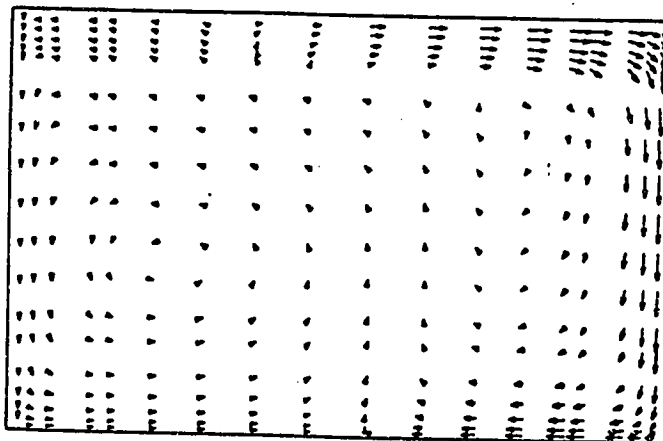
c) X-Y Section at Z = 3.100 m

Figure 7.14. Velocity vector plots in the X-Y plane at 3 pm, Tin = 10 °C and Uin = 4.0 m/sec for the WE configuration.

a) X-Z Section at Y = 0.141 m

b) X-Z Section at Y = 0.756 m

c) X-Z Section at Y = 1.759 m

d) X-Z Section at Y = 2.510 m
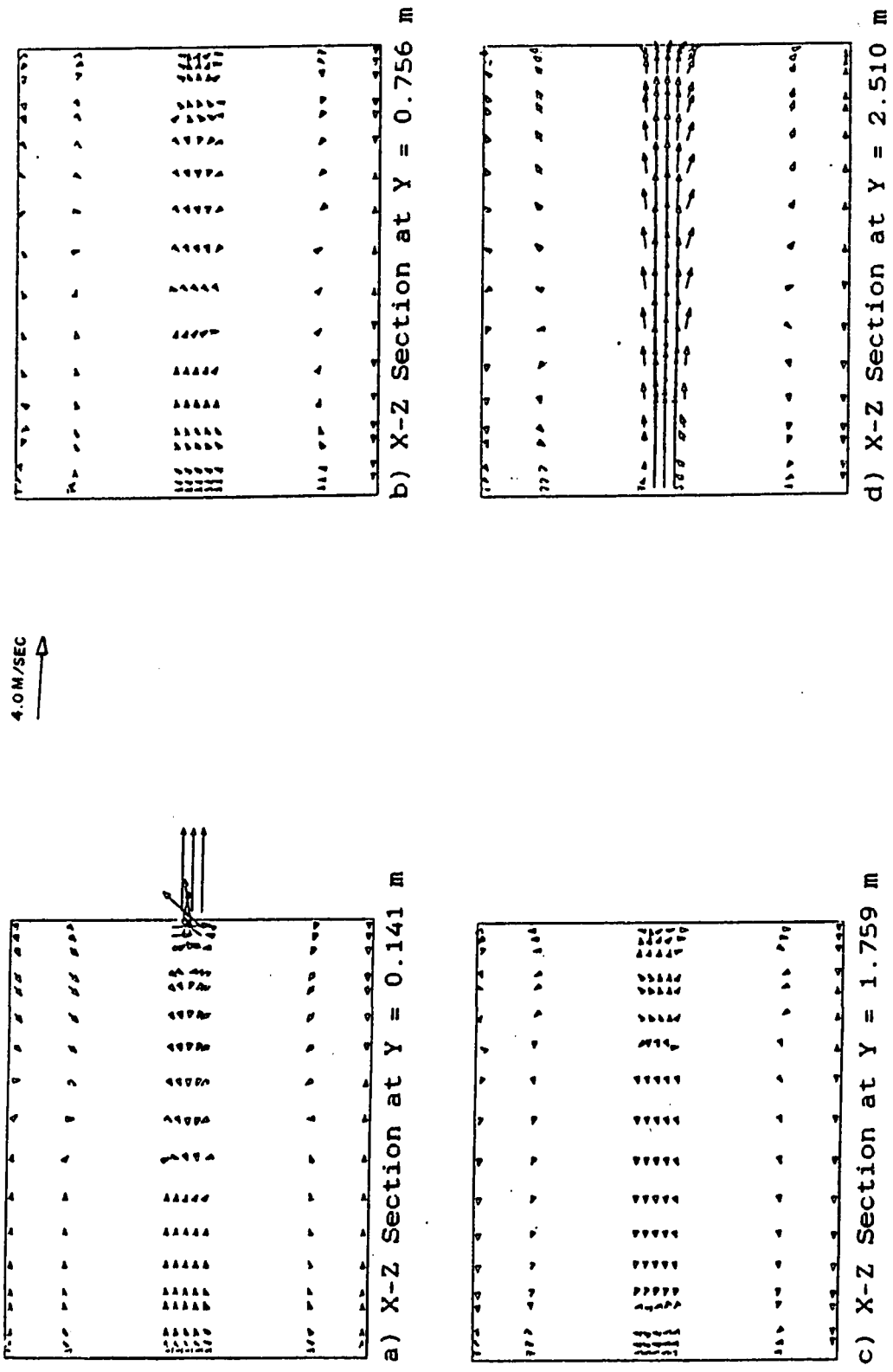
4.0M/SEC

Figure 7.15. Velocity vector plots in the X-Z plane at 3 pm, Tin = 10 °C and Uin = 4.0 m/sec for the WE configuration.

(i) Velocity Profiles at 9:00 A.M.

As U_{in} in Fig. 7.16 and Fig. 7.18 were the same, no strong distinctions between these plots are noticed, other than a larger peak at $y = 2.5$ m in Fig. 7.16.a. Thus only a discussion on Fig. 7.16 is given. Referring to Fig. 7.16.a we notice that the bulk of the velocity is contained within the jet of air, while under the jet negative velocity appears which is due to the void caused by the air jet. Close to the floor the velocity profile is positive and is due to the suction at the outlet on the East wall adjacent to the floor. Progressing along the x-axis, shown in Figs. 7.16.b to Fig. 7.16.d, the velocity at the inlet has depreciated considerably while that at the room center is almost uniform, and the velocity in the bottom part of the floor remains, but grows deeper into the room.

Velocity profiles away from the plane of symmetry of the room and close to the left wall have been plotted in Fig. 7.17 and Fig. 7.19 which for the most part are comparable. In Fig. 7.17.a negative flow occurs in the upper part of the room while positive flow is mainly in the lower part. Progressing along the x-axis in Fig. 7.17.b the velocity profile in the top part of the room turns positive caused by the spreading of the air jet. The negative velocity or back-flow profile still occupies the portion under the inlet but it is more pronounced, now. The peak of the velocity profile at the bottom part of the room is reduced slightly, but its extent is farther up the room. In Fig.7.17.c the peak of the velocity profile, close to the ceiling, grows larger indicating the engulfment of the surrounding air by the air jet and a transfer of energy also follows, while for the portion under the inlet
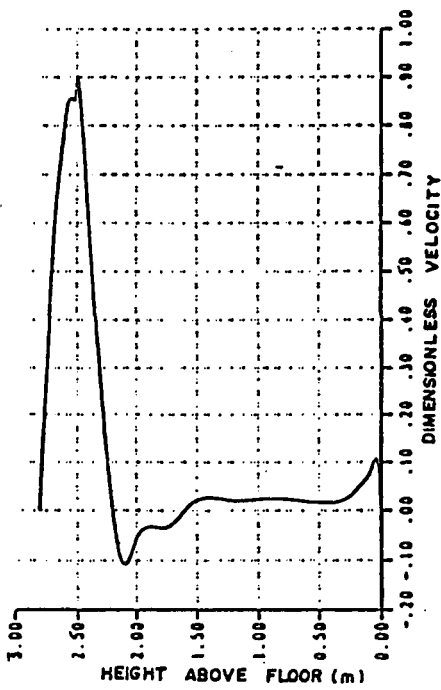
a) X/H = 0.4 and Z/W = 0.5
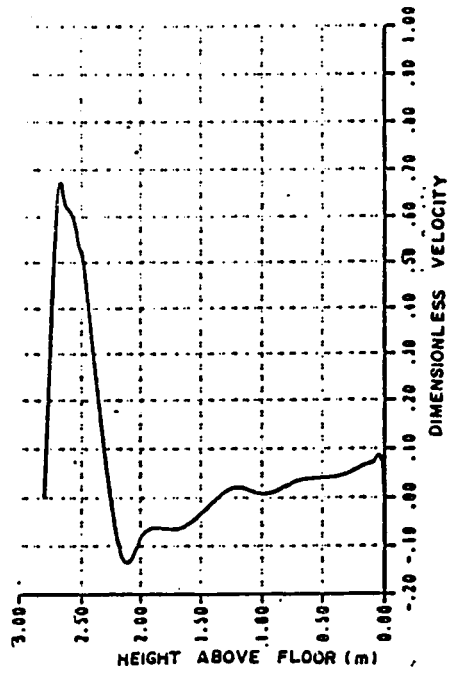
b) X/H = 0.8 and Z/W = 0.5
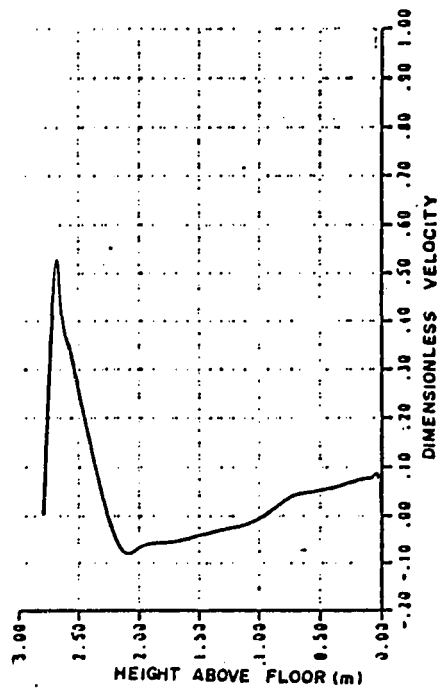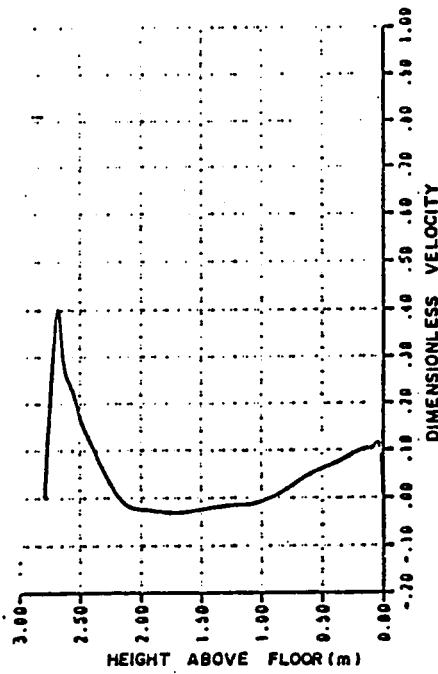
c) X/H = 1.2 and Z/W = 0.5

d) X/H = 1.6 and Z/W = 0.5

Figure 7.16. Dimensionless velocity profiles over height of room at mid section at 9 am, Tin = 15 °C and Uin = 1.9 m/sec for the WE configuration.
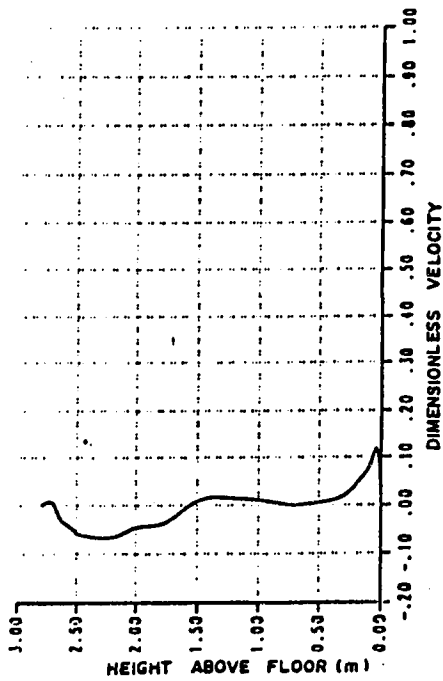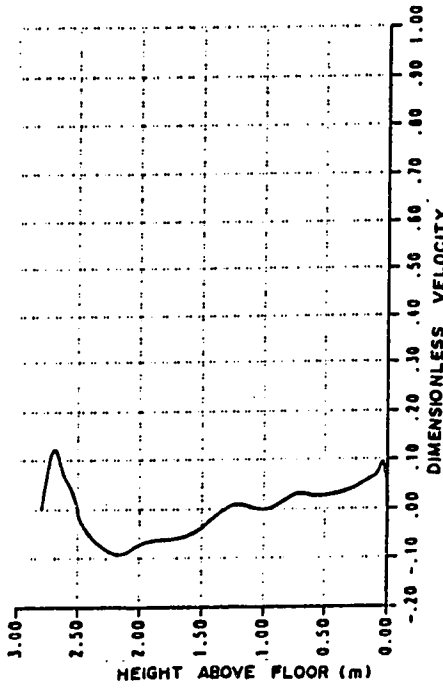
b) X/H = 0.8 and Z/W = 0.84

d) X/H = 1.6 and Z/W = 0.84

a) X/H = 0.4 and Z/W = 0.84

c) X/H = 1.2 and Z/W = 0.84

Figure 7.17. Dimensionless velocity profiles over height of room near right wall at 9 am, Tin = 15 °C and Uin = 1.9 m/sec for the WE configuration.
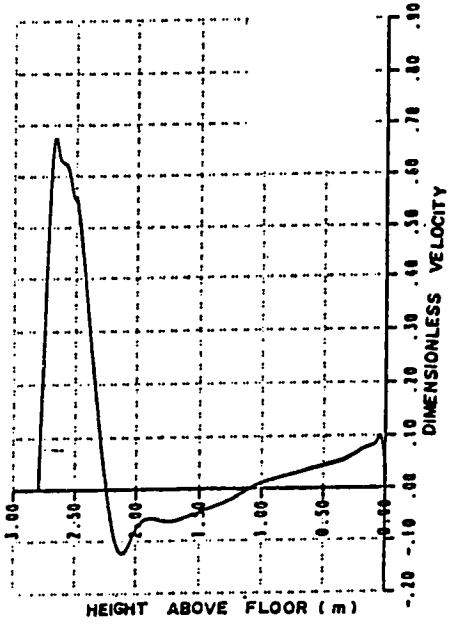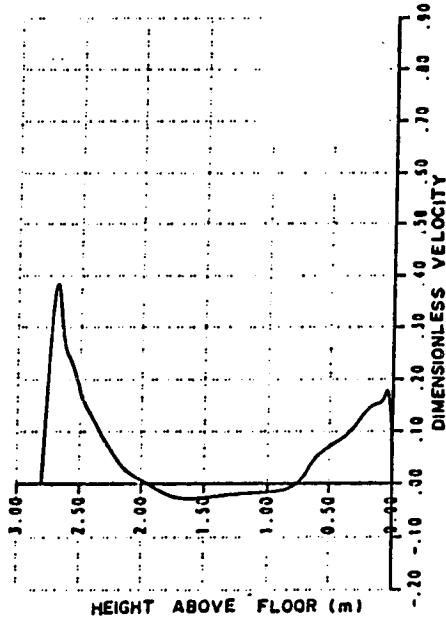
b) X/H = 0.8 and Z/W = 0.5
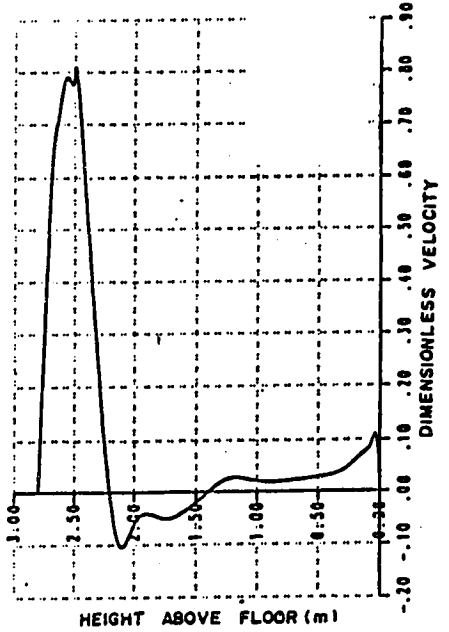
d) X/H = 1.6 and Z/W = 0.5
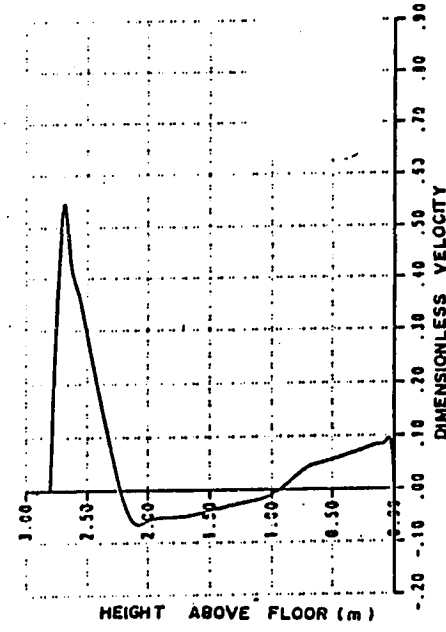
a) X/H = 0.4 and Z/W = 0.5

c) X/H = 1.2 and Z/W = 0.5

Figure 7.18. Dimensionless velocity profiles over height of room at mid section at 9 am, Tin = 18 °C and Uin = 1.9 m/sec for the WE configuration.
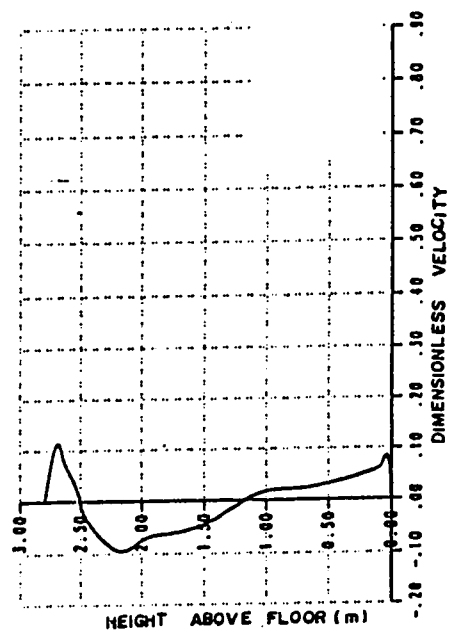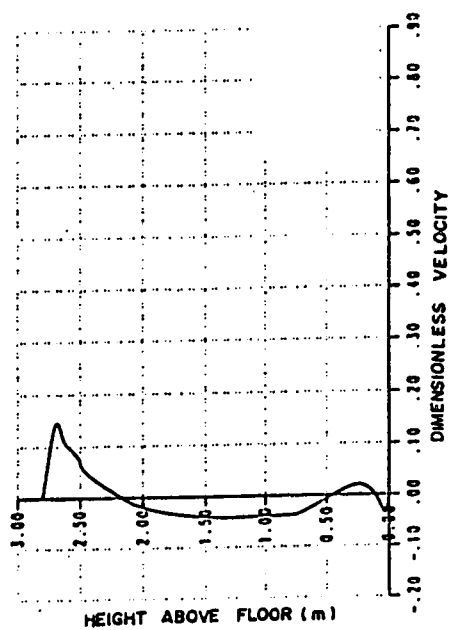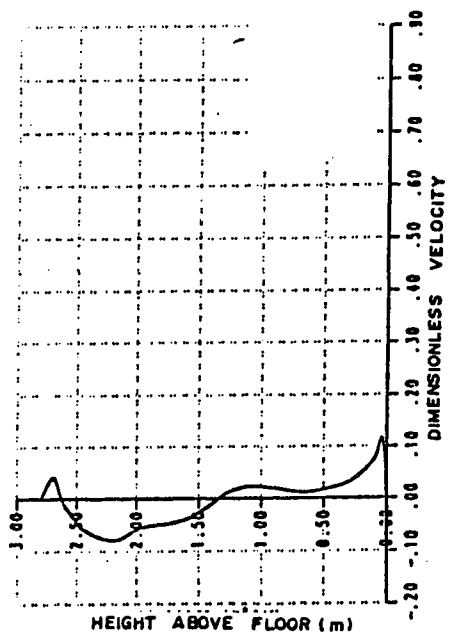
Figure 7.19. Dimensionless velocity profiles over height of room near right wall at 9 am, Tin = 18 °C and Uin = 1.9 m/sec for the WE configuration.

vent the velocity profile is negative and is relatively linear in comparison to that of Fig.7.17.b and finally the bottom part of the velocity profile close to the floor is, relatively, more uniform with a distinctive peak. In Fig. 7.17.d the peak of the positive velocity profile in the upper part of the room is almost identical to that of Fig. 7.17.c, where it was expected to be higher. The reason for this is due to the proximity to the East wall. The velocity profile below the inlet opening is still negative, but is more uniform and the peak is not as high as in Fig. 7.17.c. The point of inflection from the negative to the positive velocity profile, at the bottom part of the room, is lower than that of Fig. 7.17.c and the magnitude is smaller. The reason for this might also be attributed to the proximity to the East wall causing the bulk of the air jet energy to be transferred to the y and z directions.

(ii) Velocity Profiles at 12:00 Noon

In Figs. 7.20 and 7.21, dimensionless U velocity profiles are plotted over the height of the room at a z plane passing through the center of the inlet and a z plane close to the left wall. Velocity profiles at a different U_{in} and T_{in} are also plotted in Figs. 7.22 and 7.23. The velocity profile below the inlet opening in Fig. 7.20 is highly irregular while that of Fig. 7.22 is more or less uniform, except close to the East wall where back-flow affects the uniformity. The shape of the upper part of the profiles for both figures are approximately identical, except that the peaks of Fig. 7.22 are always larger. The velocity profile below the inlet opening in Fig. 7.21 is highly irregular while that of Fig. 7.23 is somewhat linear and more uniform. In the portion of the room from the inlet opening to the ceiling there is no
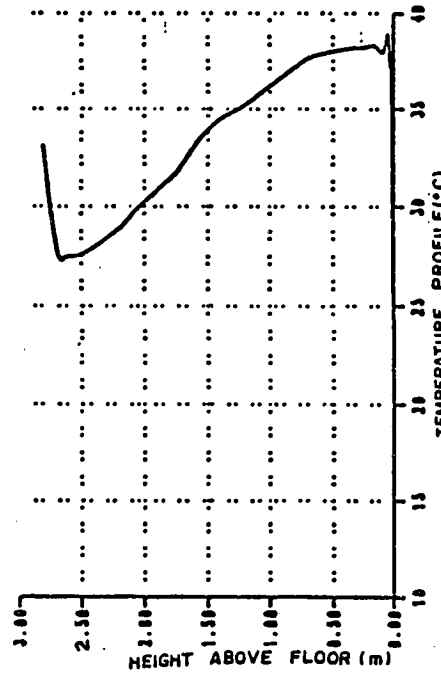
203
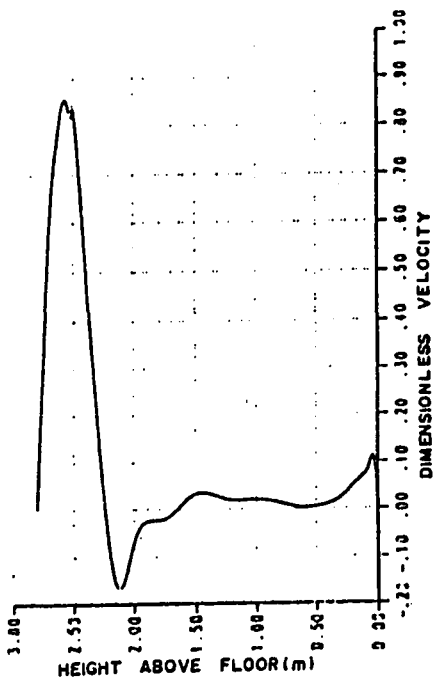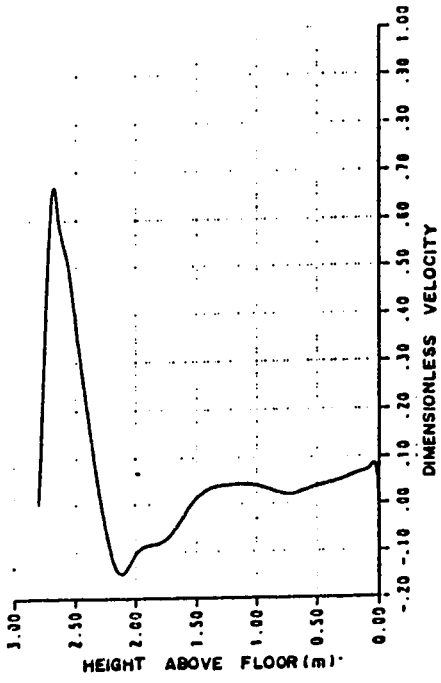
b) X/H = 0.8 and Z/W = 0.5
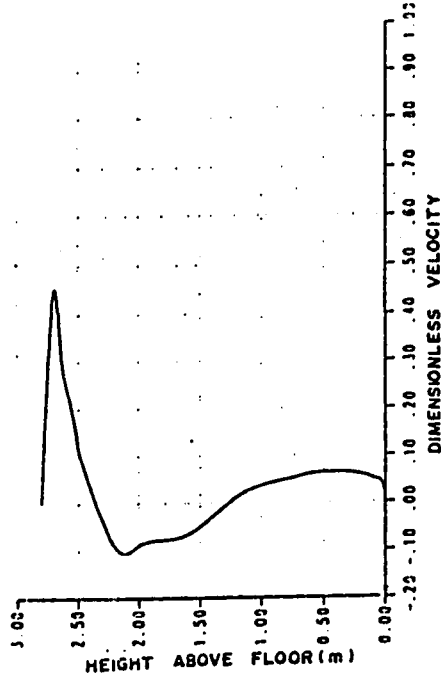
d) X/H = 1.6 and Z/W = 0.5
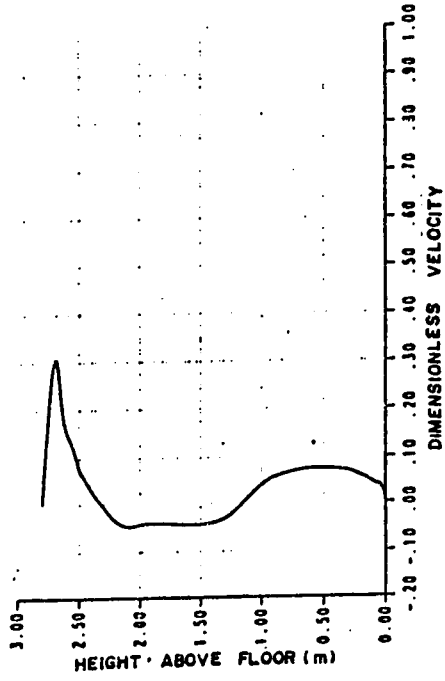
a) X/H = 0.4 and Z/W = 0.5

c) X/H = 1.2 and Z/W = 0.5

Figure 7.20. Dimensionless velocity profiles over height of room at mid section at noon, Tin = 15 °C and Uin = 1.9 m/sec for the WE configuration.
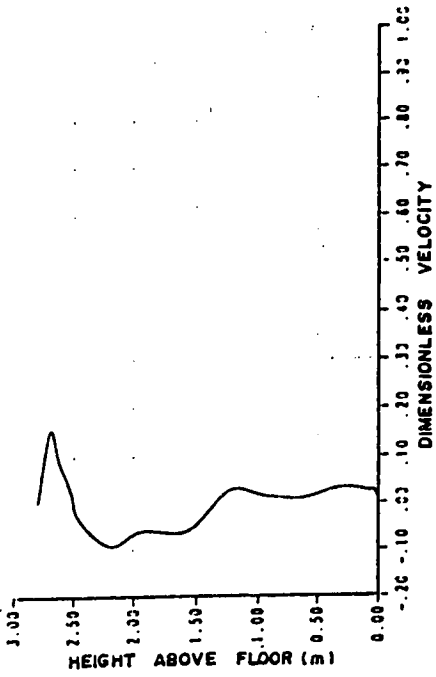
a) X/H = 0.4 and Z/W = 0.8
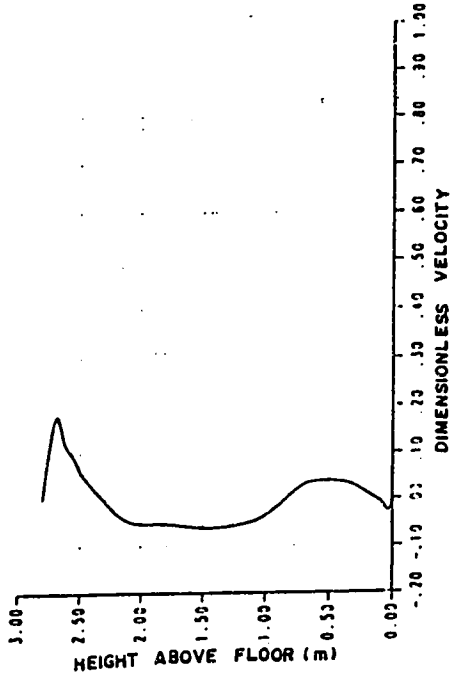
b) X/H = 0.8 and Z/W = 0.8
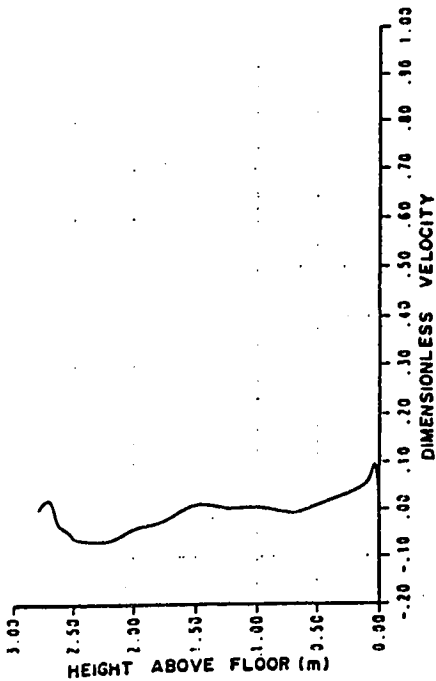
c) X/H = 1.2 and Z/W = 0.8
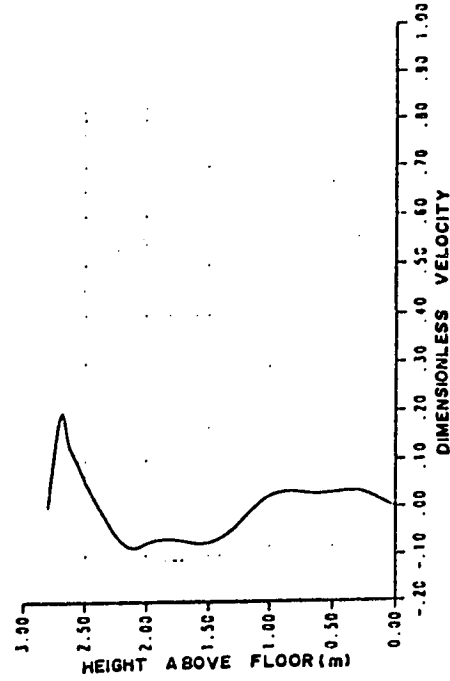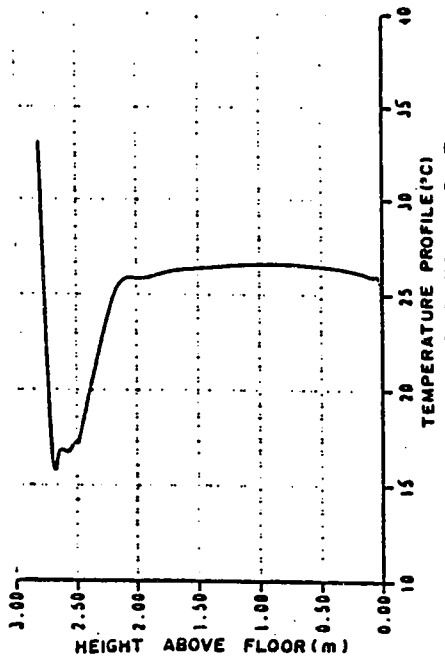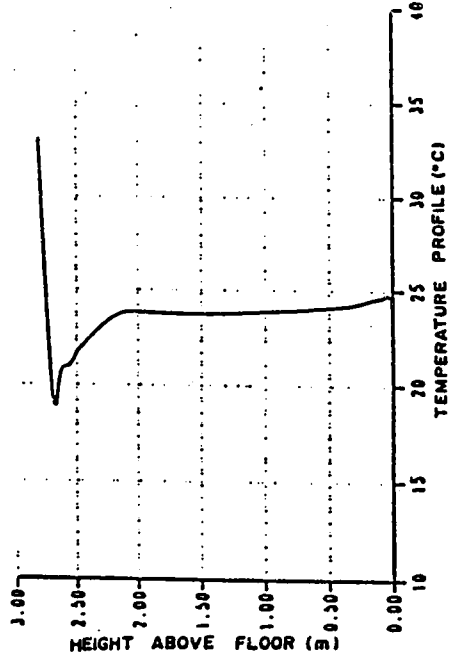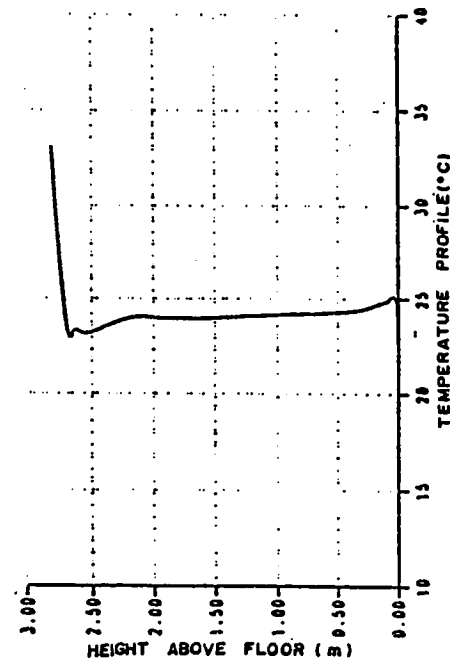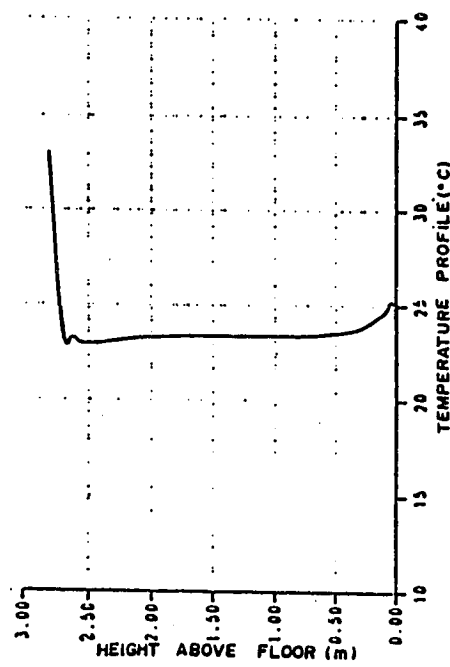
d) X/H = 1.6 and Z/W = 0.8

Figure 7.21. Dimensionless velocity profiles over height of room near right wall at noon, Tin = 15 °C and Uin = 1.9 m/sec for the WE configuration.
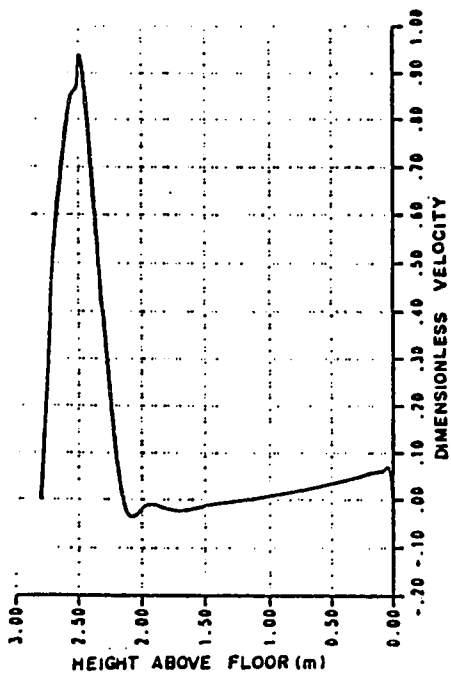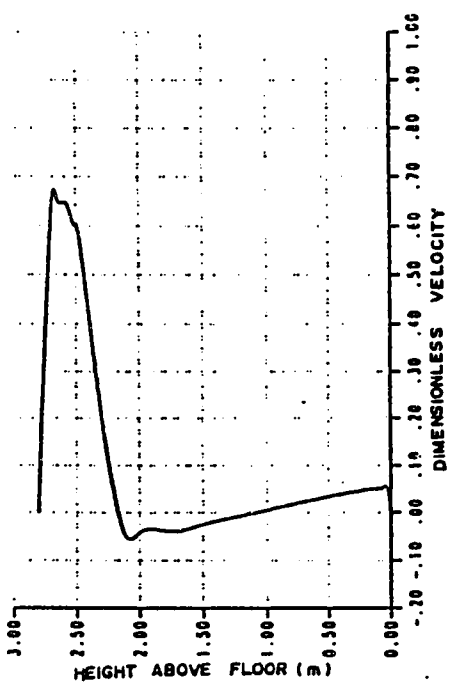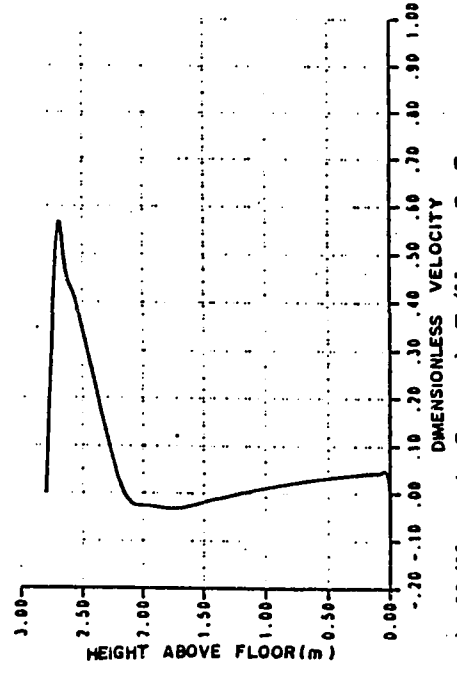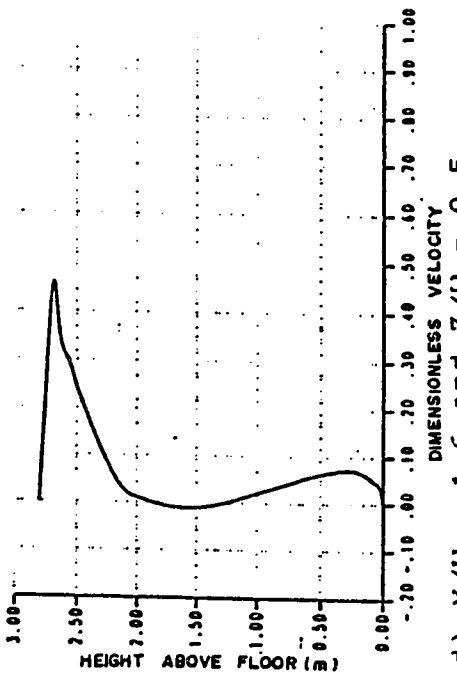
Figure 7.22. Dimensionless velocity profiles over height of room at mid section at noon, Tin = 12 °C and Uin = 3.0 m/sec for the WE configuration.

b) X/H = 0.8 and Z/W = 0.8

d) X/H = 1.6 and Z/W = 0.8

a) X/H = 0.4 and Z/W = 0.8

c) X/H = 1.2 and Z/W = 0.8
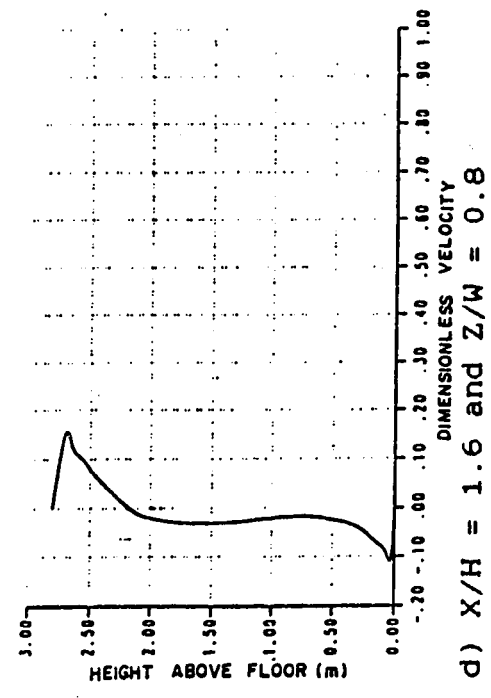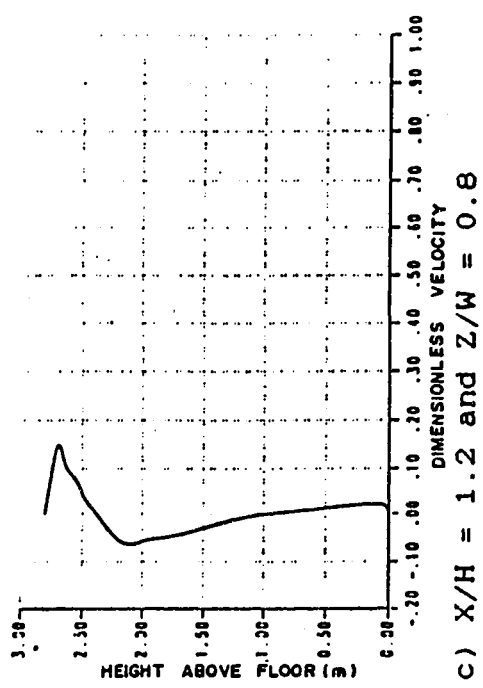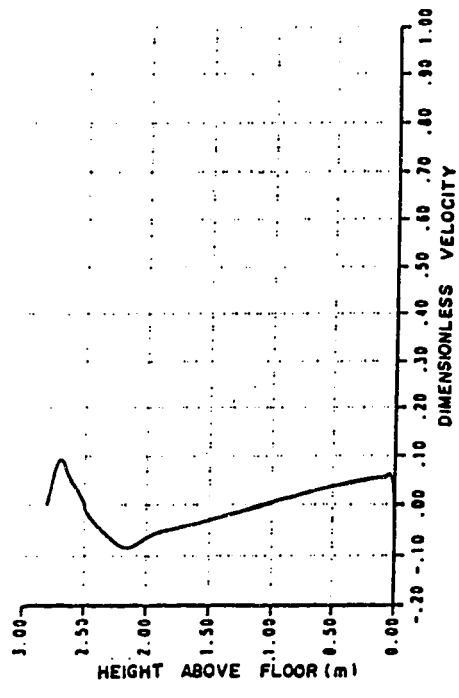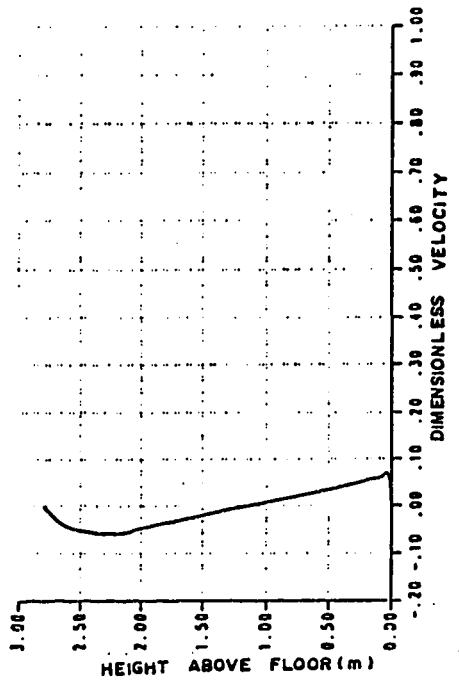
Figure 7.23. Dimensionless velocity profiles over height of room near right wall at noon, Tin = 12 °C and Uin = 3.0 m/sec for the WE configuration.

positive velocity registered in Fig. 7.23.a, while in Fig. 7.21.a, a small positive velocity appears. In Fig. 7.21.b to Fig. 7.21.d, the form of the upper part of the velocity profile is comparable to that of Fig. 7.23.b to 7.23.d, except that the relative peak in the latter figures are less pronounced.

(iii) Velocity Profiles at 3:00 P.M.

The velocity profile below the inlet opening in Fig. 7.26 are nearly uniform while that of Fig. 7.24 are highly irregular. Also the extent of the negative velocity profile in the former is not as pronounced as in the latter. The shape of the velocity profiles from the bottom edge of the inlet opening to the ceiling are similar in both plots although the magnitude of the peak in the Fig.7.26 is larger than that of Fig.7.24, also in the region below the inlet opening the velocity profiles are irregular in Fig. 7.24 while that of Fig.7.26 are more uniform, and the same is obvious for the velocity profiles below the inlet openings of Figs. 7.25 and 7.27, respectively. In the upper part of the room, positive velocity is evident in Fig. 7.25.a while in Fig. 7.27.a this does not appear. In Fig.7.25.b to Fig. 7.25.d the peak of the positive velocity is larger than that of Fig. 7.27.b to Fig.7.27.d, although the general forms are identical.

7.2.1.3 Temperature Contours

Temperature contours parallel to the x-z plane have been plotted at different heights above the floor, i.e.: at $y = 0.76$m (passing midway the center of the body and back of neck for a sitting person), $y = 1.76$m (passing close to the back of the neck for a standing person) and $y = 2.51$m

b) X/H = 0.8 and Z/W = 0.5

d) X/H = 1.6 and Z/W = 0.5

a) X/H = 0.4 and Z/W = 0.5

c) X/H = 1.2 and Z/W = 0.5

Figure 7.24. Dimensionless velocity profiles over height of room at mid section at 3 pm, Tin = 15 °C and Uin = 1.9 m/sec for the WE configuration.
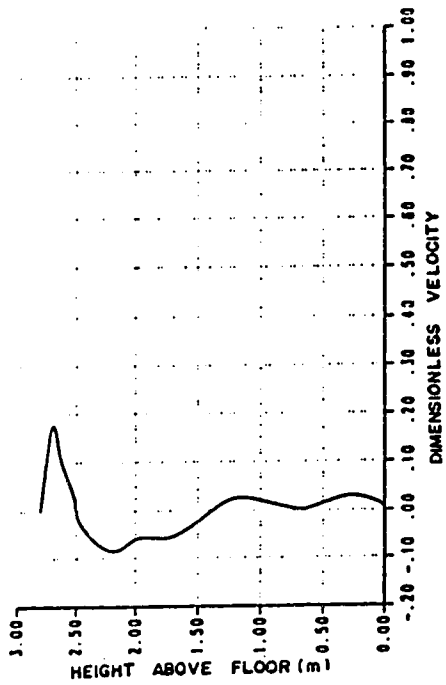
b) X/H = 0.8 and Z/W = 0.8

d) X/H = 1.6 and Z/W = 0.8

a) X/H = 0.4 and Z/W = 0.8

c) X/H = 1.2 and Z/W = 0.8

Figure 7.25. Dimensionless velocity profiles over height of room near right wall at 3 pm, Tin = 15 °C and Uin = 1.9 m/sec for the WE configuration.

b) X/H = 0.8 and Z/W = 0.5

d) X/H = 1.6 and Z/W = 0.5

a) X/H = 0.4 and Z/W = 0.5

c) X/H = 1.2 and Z/W = 0.5

Figure 7.26. Dimensionless velocity profiles over height of room at mid section at 3 pm, Tin = 10 °C and Uin = 4.0 m/sec for the WE configuration.

b) X/H = 0.8 and Z/W = 0.8

d) X/H = 1.6 and Z/W = 0.8

a) X/H = 0.4 and Z/W = 0.8
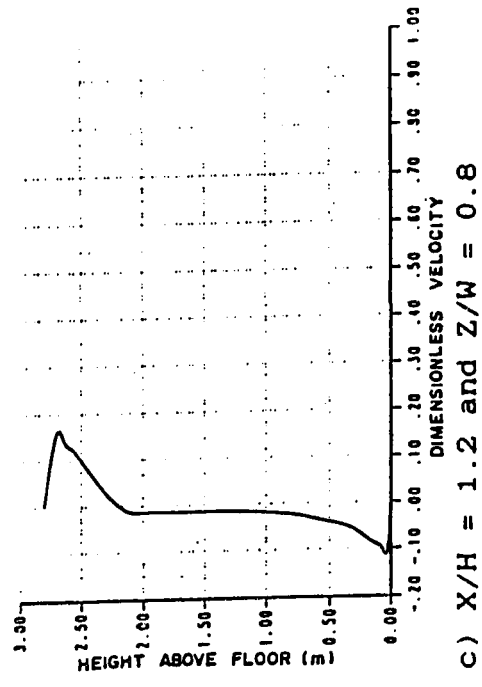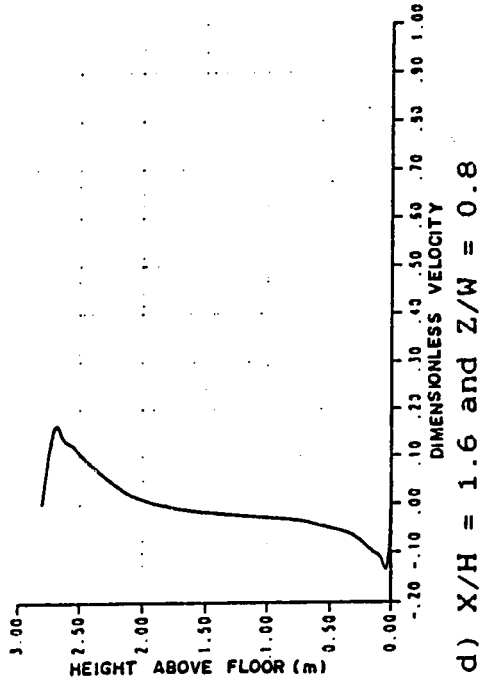
c) X/H = 1.2 and Z/W = 0.8

Figure 7.27. Dimensionless velocity profiles over height of room near right wall at 3 pm, Tin = 10 °C and Uin = 4.0 m/sec for the WE configuration.

(passing through the center of the inlet opening). Furthermore, these contours are plotted only within the boundaries of the occupied zone (i.e. : 0.6 m away from all side walls). The contours and an accompanying discussion now follows.

(i) Temperature Contours at 9:00 A.M.

The temperature contours for the two cases reported here are given in Figs. 7.28 and 7.29 for a T_{in} and U_{in} as given in Table 7.2. As expected, the magnitude of the temperature contours in Fig. 7.29 are higher than that in Fig.7.28, but the general appearance of the two are somewhat comparable. In Fig. 7.28.a and Fig. 7.29.a, the relatively coolest region is close to the center of the East side of the occupied zone which is on account of the inlet opening being opposite to the East wall and, at this time of day, the heat flux from the roof is relatively low. Thus, the air jet flowing along the roof will probably still be at a relatively low temperature as it reaches the East wall and the negative buoyancy force together with the abrupt collision with the solid East wall will cause it to flow down, thus help in removing much of the heat inflow from this wall, resulting in a relatively cooler region. The part of the occupied zone away from the East wall is almost at a uniform temperature in Fig. 7.28.a, while that in Fig.7.29.a is not as uniform. A reasoning similar to that given above follows for the Figs.7.28.b and 7.29.b which reveals that as we go more from the East side to the West side of the occupied zone, the temperature level gradually increases. Figs. 7.28.c and 7.29.c are quite similar in shape, although the level of temperature is obviously lower in the former plot.
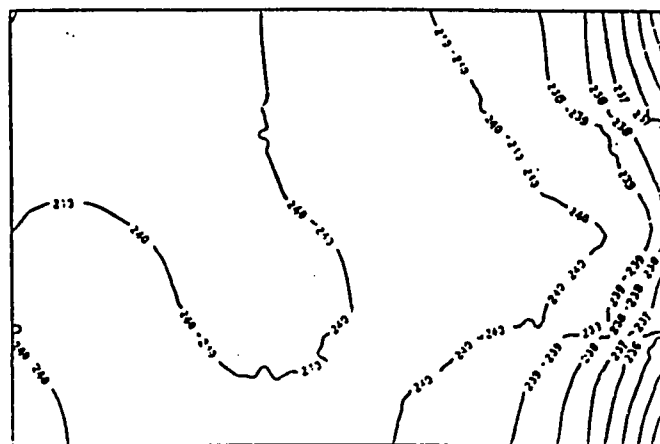
a) Y = 0.76 m,   * Fac = 10.0
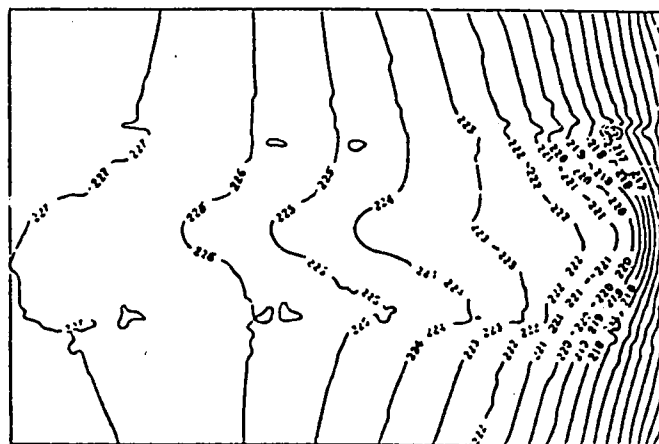
b) Y = 1.76 m,   Fac = 10.0
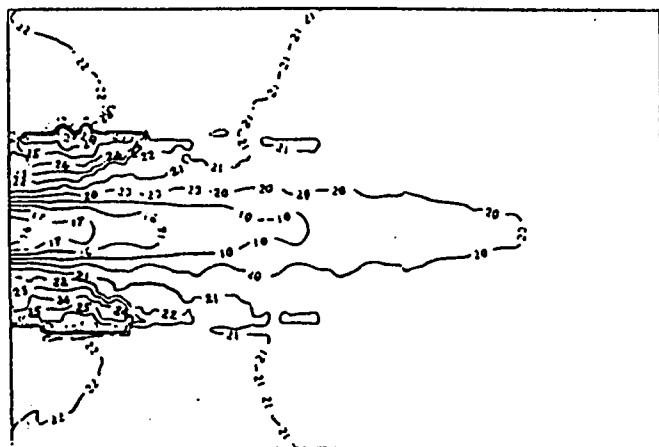
c) Y = 2.51 m,   Fac = 1.0

Figure 7.28. Temperature contours in the X-Z plane at 9 am,
              Tin = 15 °C and Uin = 1.9 m/sec for the WE
              configuration.

NOTE: * Only contours of whole numbers can be plotted, thus
        a multiplication factor (Fac) is used to reveal more
        detail.
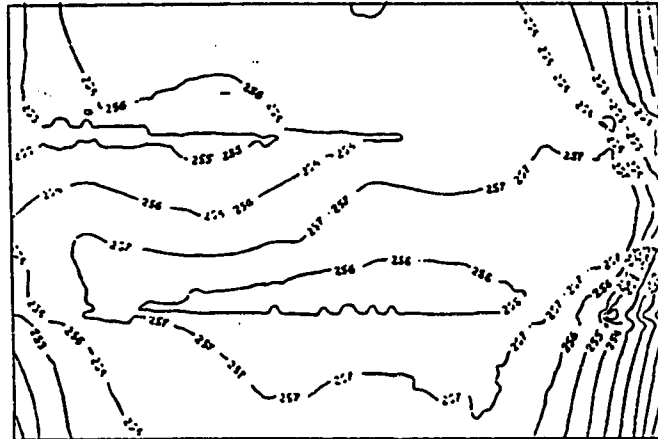
a) Y = 0.76 m, Fac = 10.0
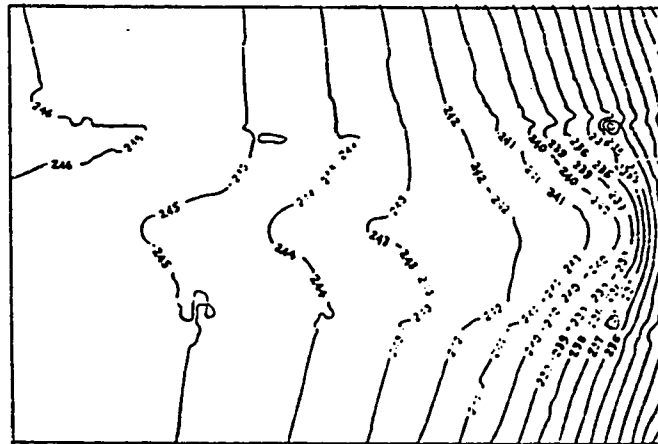
b) Y = 1.76 m, Fac = 10.0
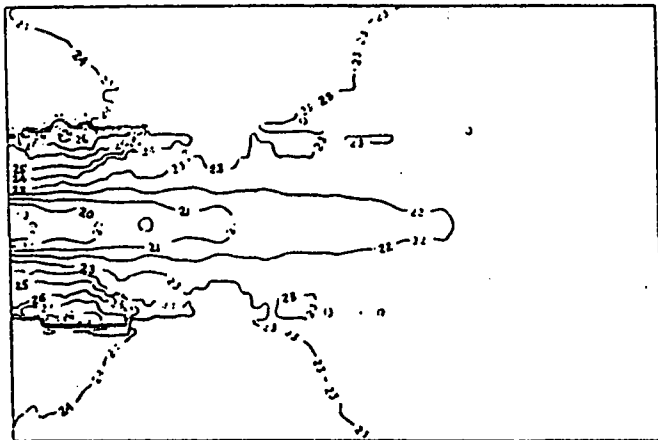
c) Y = 2.51 m, Fac = 1.0

Figure 7.29. Temperature contours in the X-Z plane at 9 am, Tin = 18 °C and Uin = 1.9 m/sec for the WE configuration.

The extent to which the effect of the air jet reaches, as displayed in Fig. 7.28.c, is almost 3/4 of the upper part of the room while the areas on both sides of the inlet opening are not as much influenced by the air jet, indicating low mixing and possible stagnation. The remaining part of this area is nearly uniform.

(ii) Temperature Contours at 12:00 Noon

The temperature contours for the time of 12:00 Noon are given in Figs. 7.30 and 7.31 where the T_{in} and U_{in} employed here are listed in Table 7.2. The rate at which the level of temperature varies in Fig.7.31.a is higher than that of Fig.7.30.a which is due to the fact that as T_{in} is lower and U_{in} is higher in the former relative to the latter plots, the degree of mixing and heat exchange with the jet of air is greater in Fig.7.31.a. The general features of Figs.7.30.b and 7.31.b are similar, although the level of temperature is higher in the former figure compared to the latter. Also, the relatively cooler region is the East side of the occupied zone while the West side is the warmest. This occurrence resembles that observed in Figs. 7.28.b and 7.29.b and, therefore, the discussion given for 9:00 A.M. concerning this similarity also applies here. The temperature contours of Figs. 7.30.c and 7.31.c are at a horizontal plane passing through the center of the inlet opening such that the former plot is similar to Figs. 7.28.c and 7.29.c, while the latter is somewhat different. On account of this, a discussion relevant for Fig. 7.31.c will only be given. As U_{in} is relatively high, the depth of penetration of the air jet, in the form of temperature contours is seen to reach the East side, above the occupied zone, while at the areas
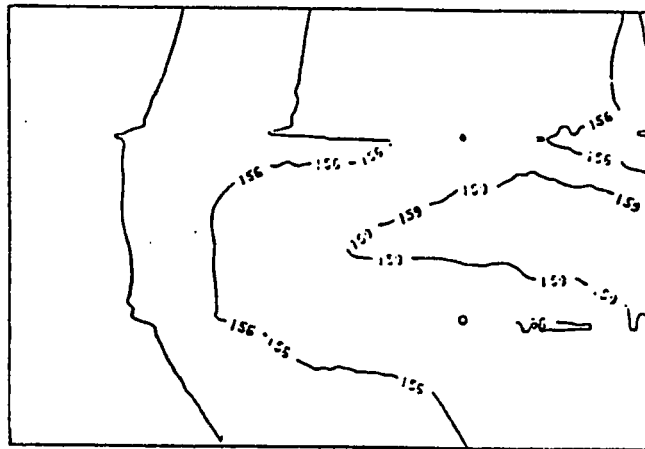
a) Y = 0.76 m,   Fac = 5.0
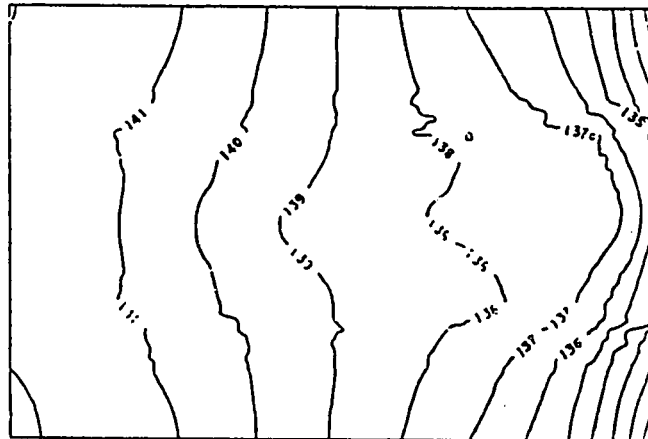
b) Y = 1.76 m,   Fac = 5.0
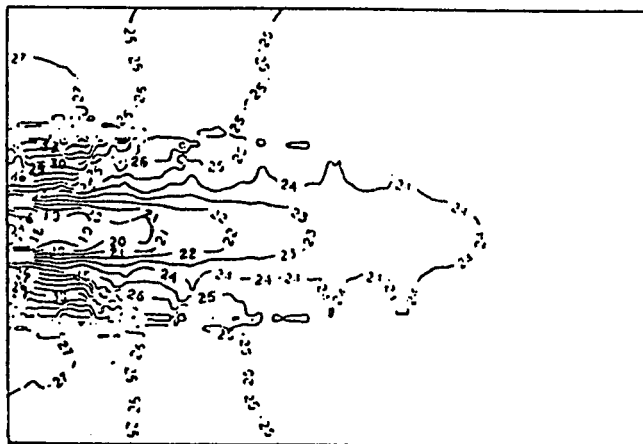
c) Y = 2.51 m,   Fac = 1.0

Figure 7.30. Temperature contours in the X-Z plane at noon,
Tin = 15 °C and Uin = 1.9 m/sec for the WE
configuration.
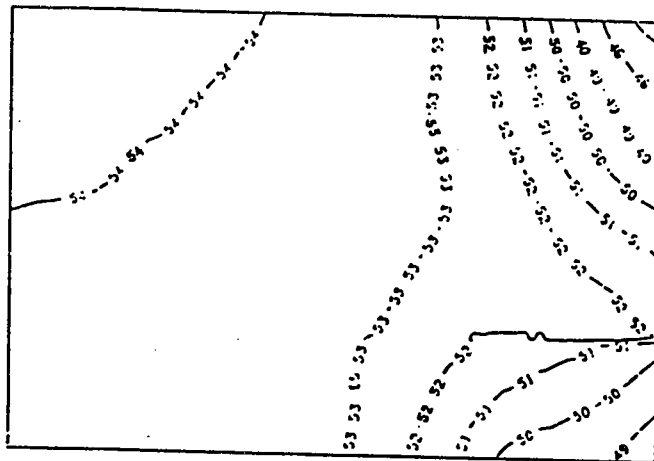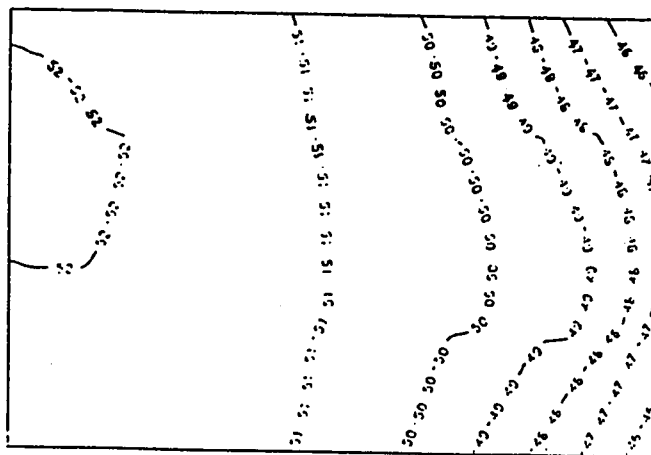
a) Y = 0.76 m,   Fac = 2.0

b) Y = 1.76 m,   Fac = 2.0
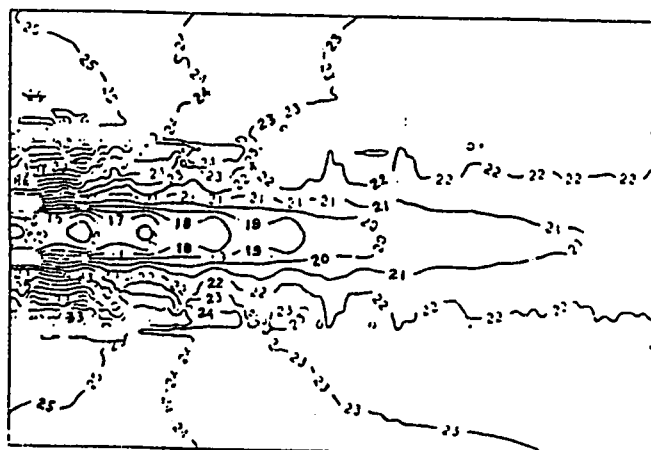
c) Y = 2.51 m,   Fac = 1.0

Figure 7.31. Temperature contours in the X-Z plane at noon, Tin = 12 °C and Uin = 3.0 m/sec for the WE configuration.

on both sides of the inlet opening, the density of contours are relatively high indicating a steep gradient of the temperature which is due to, relatively low mixing of the air jet in these regions, and as we progress away from the inlet towards the East wall we notice that the change in the temperature is relatively low.

(iii) Temperature Contours at 3:00 P.M.

The temperature contours at 3:00 P.M. are plotted in Figs. 7.32 and 7.33 which have a T_{in} and U_{in} as listed in Table 7.2. It is observed that unlike the previous investigations Fig.7.32.a is not as orderly and the relatively warmest is the central area of the occupied zone while the remaining regions are at a lower level of temperature . The reason for this may possibly be the extreme conditions existing at this time, where the heat fluxes and temperatures are at their maximum (see Table 7.1) and the East wall has the highest heat flux into the room and furthermore, as the recirculating air jet flowing along this wall would have absorbed a considerable amount of heat, so that by the time it reaches to the level of Fig. 7.32.a the ability of the air to remove heat has been diminished considerably. An overview of the numerical values of the contours in Fig.7.32.a shows no large distinction among them, relative to that of Fig. 7.33.a, where the contours of the former are nearly homogeneous. A resemblance between Fig. 7.33.a and those at the same plane for the different cases stated above, is apparent. The reason for this is on account of the relatively low T_{in} and high U_{in} causing the East side of the occupied zone to be cooler than other localities such that while moving away from the East side of the occupied
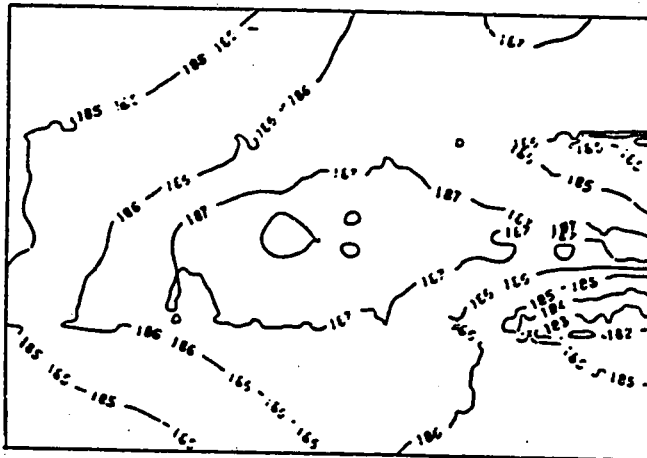
a) Y = 0.76 m,   Fac = 5.0
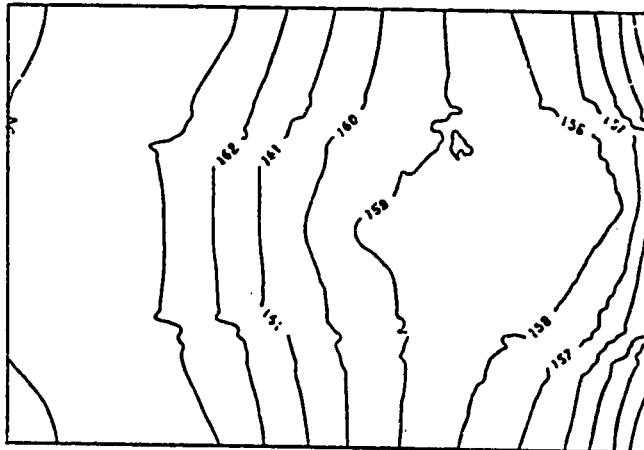
b) Y = 1.76 m,   Fac = 5.0
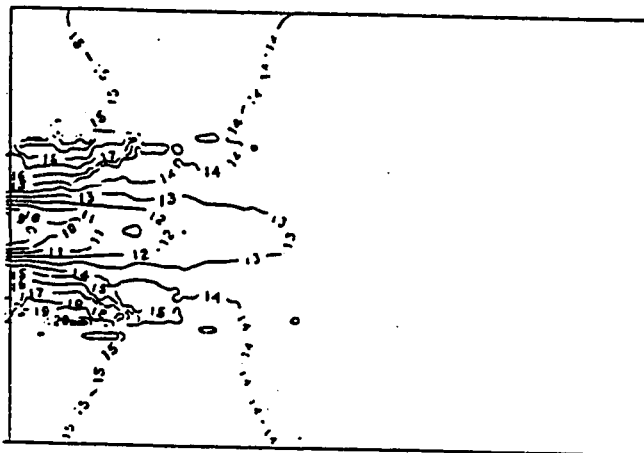
c) Y = 2.51 m,   Fac = 1/2

Figure 7.32. Temperature contours in the X-Z plane at 3 pm,
Tin = 15 °C and Uin = 1.9 m/sec for the WE
configuration.
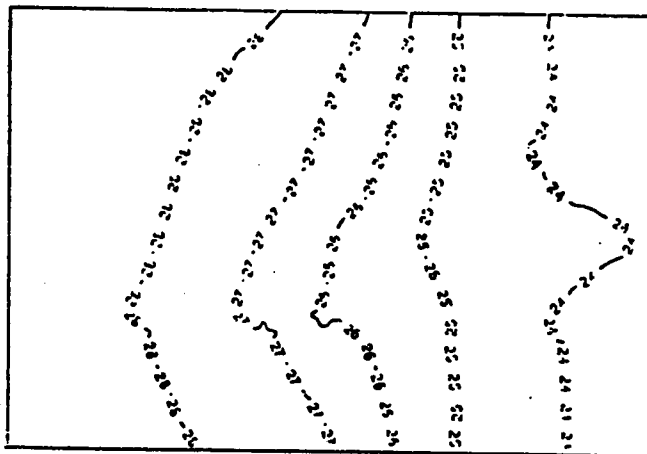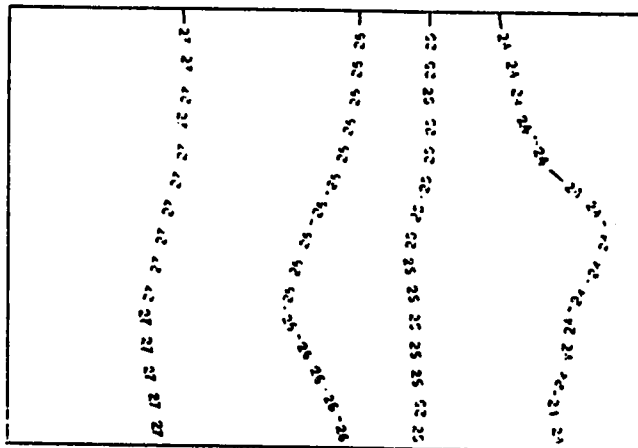
a) Y = 0.76 m,   Fac = 1.0

b) Y = 1.76 m,   Fac = 1.0
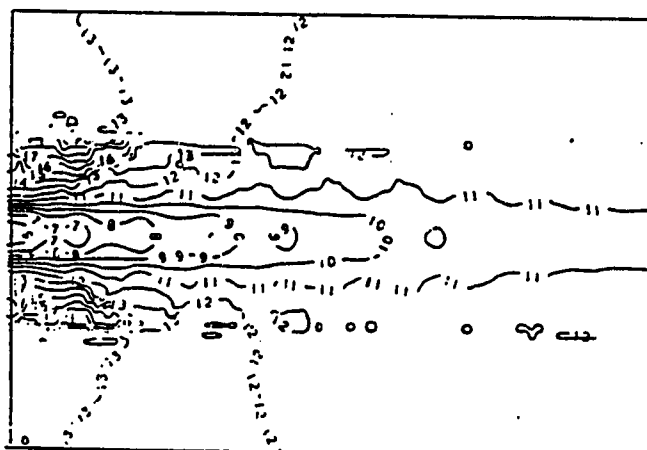
c) Y = 2.51 m,   Fac = 1/2

Figure 7.33. Temperature contours in the X-Z plane at 3 pm,
Tin = 10 °C and Uin = 4.0 m/sec for the WE
configuration.

zone to the West side, the level of temperature progressively increases. In Figs. 7.32.b and 7.33.b, a similarity exists, such that the temperature is lowest on the East side of the occupied zone and highest on the West side, although the level of temperature in both are not identical. This occurrence resembles that for contours at the same plane reported earlier for the other times considered in this configuration and the discussions given there apply here. Horizontal planes passing through the center of the inlet opening showing the corresponding temperature contours for the two cases reported are given in Figs. 7.32.c and 7.33.c and a resemblance between the former and latter plots appear in Figs. 7.30.c and 7.31.c, respectively. Discussions regarding the earlier plots will also be valid here.

7.2.1.4 Temperature Profiles

For the various U_{in}, T_{in} and boundary conditions reported earlier, temperature profiles have been plotted so that the stratification of the temperature , which directly influences the comfort of inhabitants over the occupied zone may be observed. The profiles are taken at the center of the room (passing through the inlet and outlet openings) and another at the edge of the occupied zone over the entire room cross-section. These will now be presented below together with an accompanying discussion.

(i) Temperature Profiles at 9:00 A.M.

The temperature profiles for $T_{in} = 15°C$ and $U_{in} = 1.9$ m/sec. are plotted in Figs. 7.34 and 7.35, while that for $T_{in} = 18°C$ and $U_{in} = 1.9$ m/sec. are plotted in Figs. 7.36 and 7.37. Comparing Figs. 7.34 and 7.36, a general resemblance is apparent, except that the upper part ot the profiles in the former plots are at a relatively lower temperature than those of

a) X/H = 0.4 and Z/W = 0.5

b) X/H = 0.8 and Z/W = 0.5

c) X/H = 1.2 and Z/W = 0.5

d) X/H = 1.6 and Z/W = 0.5

Figure 7.34. Temperature profiles over height of room at mid section at 9 am, Tin = 15 °C and Uin = 1.9 m/sec for the WE configuration.

b) X/H = 0.8 and Z/W = 0.8

d) X/H = 1.6 and Z/W = 0.8

a) X/H = 0.4 and Z/W = 0.8
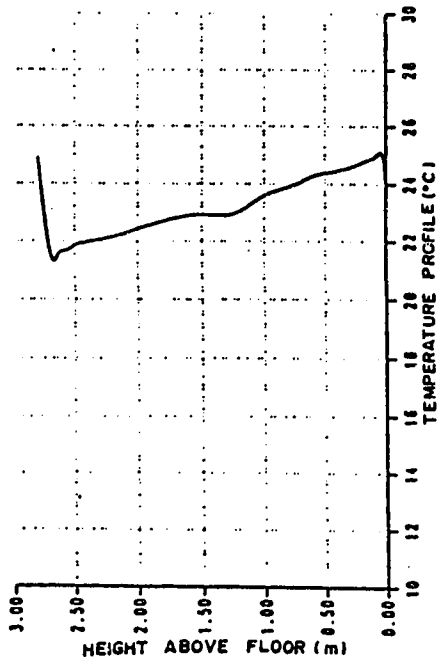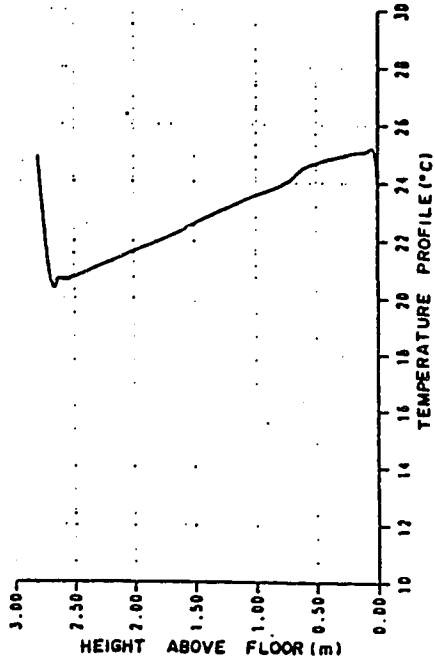
c) X/H = 1.2 and Z/W = 0.8

Figure 7.35. Temperature profiles over height of room near right wall at 9 am, Tin = 15 °C and Uin = 1.9 m/sec for the WE configuration.

b) X/H = 0.8 and Z/W = 0.5

d) X/H = 1.6 and Z/W = 0.5

a) X/H = 0.4 and Z/W = 0.5
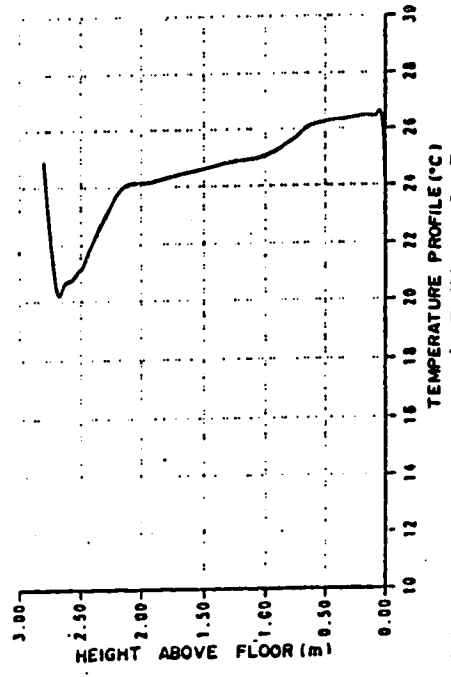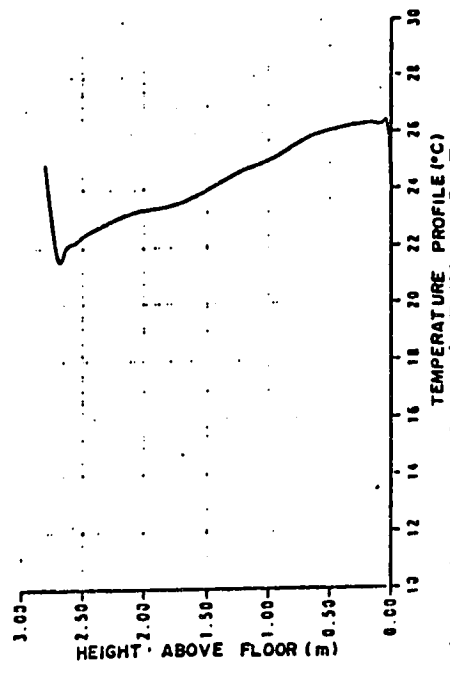
c) X/H = 1.2 and Z/W = 0.5

Figure 7.36. Temperature profiles over height of room at mid section at 9 am, Tin = 18 °C and Uin = 1.9 m/sec for the WE configuration.

b) X/H = 0.8 and Z/W = 0.84

d) X/H = 1.6 and Z/W = 0.84

a) X/H = 0.4 and Z/W = 0.84

c) X/H = 1.2 and Z/W = 0.84

Figure 7.37. Temperature profiles over height of room near right wall at 9 am, Tin = 18 °C and Uin = 1.9 m/sec for the WE configuration.

the latter plots, due to lower T_{in}. Thus, a discussion of Fig. 7.34 will only be given. In Fig. 7.34.a, the coolest region is from the bottom edge of the inlet opening to the ceiling, while below this region, the temperature profile grows gradually until it reaches the floor which has the highest temperature in the occupied zone. In Fig. 7.34.b the temperature profile in the upper part of the room, from the inlet opening to the ceiling has reduced, while the part below this is nearly the same as that in Fig. 7.34.a, except that the absolute value of the slope of the temperature profile close to the floor is relatively larger. In Fig.7.34.c, the peak of the upper part of the temperature profile has decreased even further while the remaining part below the inlet opening is almost identical. Finally, at the farthest point away from the inlet for which temperature profiles are plotted is shown in Fig. 7.34.d where the lowest temperature remains in the area opposite to the inlet opening but not as pronounced as before and the slope of the temperature profile below the inlet is nearly uniform with the highest temperature close to the floor. The temperature profiles close to the right wall are given in Figs. 7.35 and 7.37, the plots in both are similar, except that the slope in the latter is more vertical.

(ii) Temperature Profiles at 12:00 Noon

Temperature profiles for 12:00 Noon at different x-locations and passing through the center of the room are plotted for $T_{in} = 15.0°C$ and $U_{in} = 1.9$ m/sec. given in Fig. 7.38, while Fig. 7.40 is identical to that of Fig. 7.38 except that $T_{in} = 12.0°C$ and $U_{in} = 3.0$ m/sec. By comparing the plots of Figs.7.38.a and 7.40.a, which are closest to the inlet opening, we may observe that the general form of the two are somewhat comparable, although the former figure seems to be shifted more to the right indicating

227
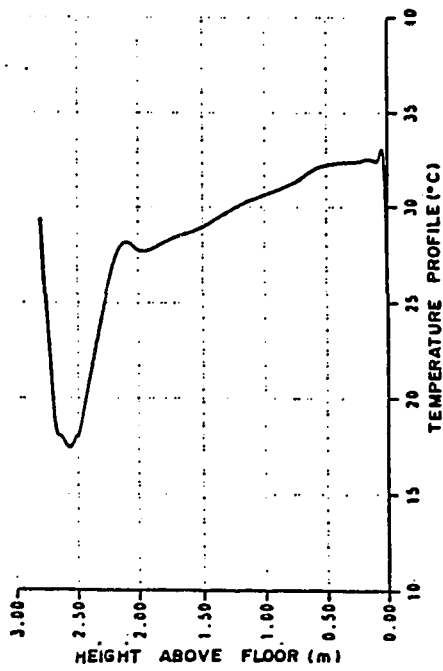
b) X/H = 0.8 and Z/W = 0.5

d) X/H = 1.6 and Z/W = 0.5

a) X/H = 0.4 and Z/W = 0.5
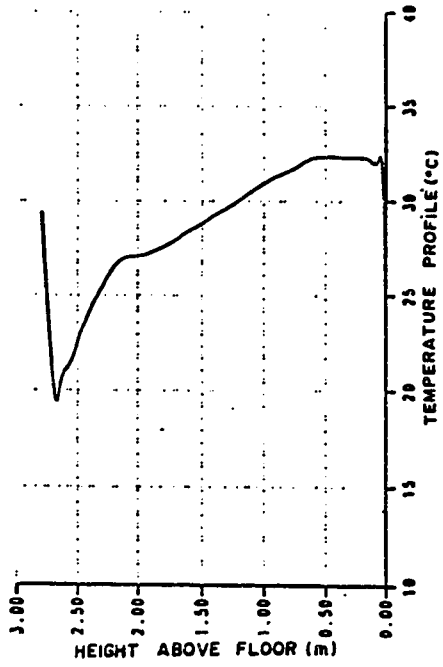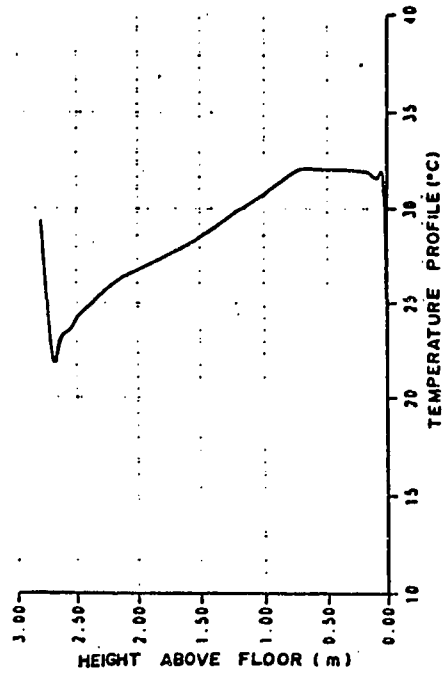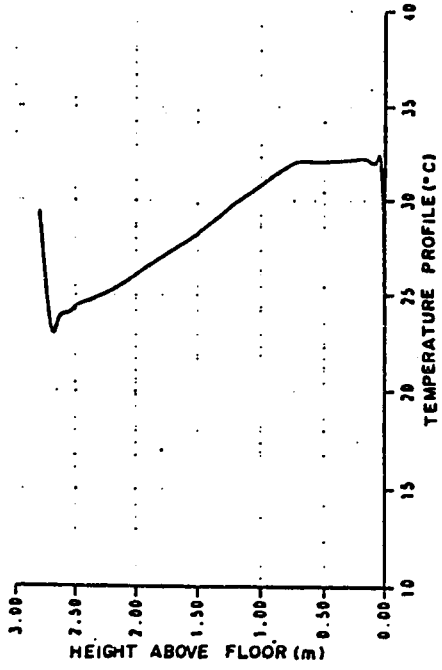
c) X/H = 1.2 and Z/W = 0.5

Figure 7.38. Temperature profiles over height of room at mid section at noon,
Tin = 15 °C and Uin = 1.9 m/sec for the WE configuration.

b) X/H = 0.8 and Z/W = 0.8

a) X/H = 0.4 and Z/W = 0.8

d) X/H = 1.6 and Z/W = 0.8

c) X/H = 1.2 and Z/W = 0.8

Figure 7.39. Temperature profiles over height of room near right wall at noon, Tin = 15 °C and Uin = 1.9 m/sec for the WE configuration.
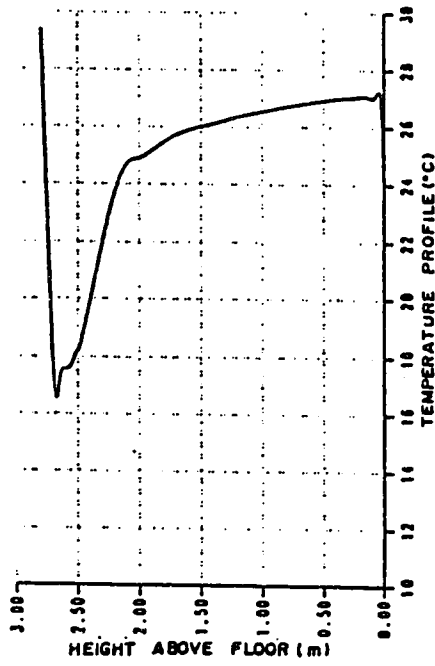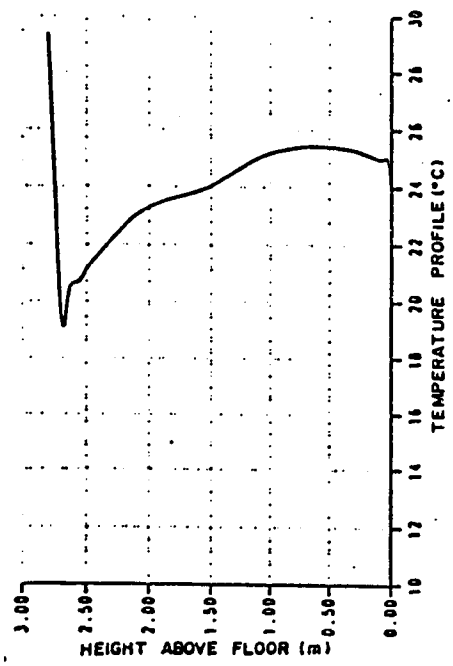
b) X/H = 0.8 and Z/W = 0.5
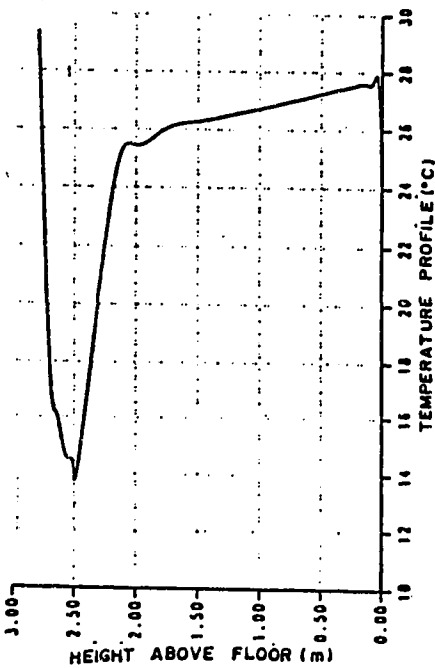
d) X/H = 1.6 and Z/W = 0.5
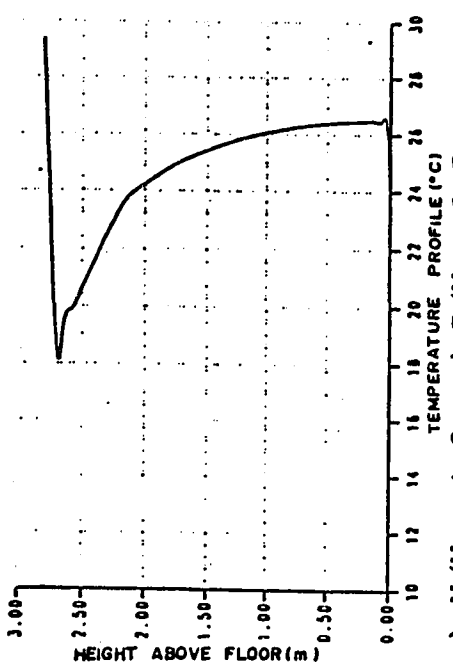
a) X/H = 0.4 and Z/W = 0.5

c) X/H = 1.2 and Z/W = 0.5

Figure 7.40. Temperature profiles over height of room at mid section at noon, Tin = 12 °C and Uin = 3.0 m/sec for the WE configuration.
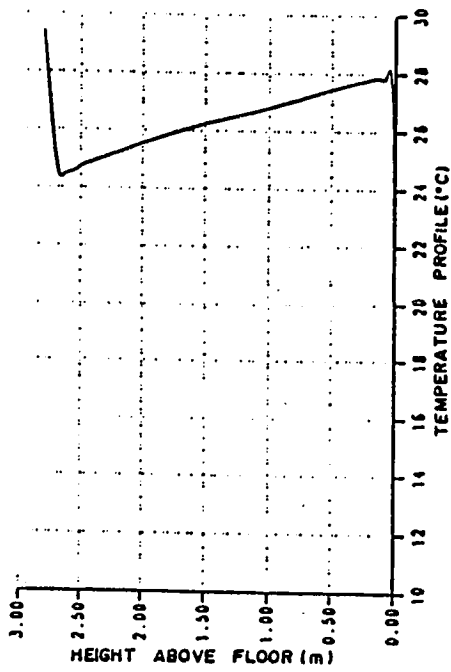
b) X/H = 0.8 and Z/W = 0.8

d) X/H = 1.6 and Z/W = 0.8

a) X/H = 0.4 and Z/W = 0.8
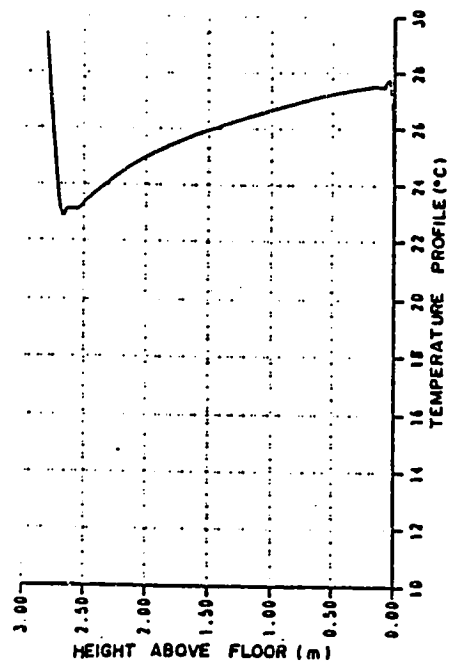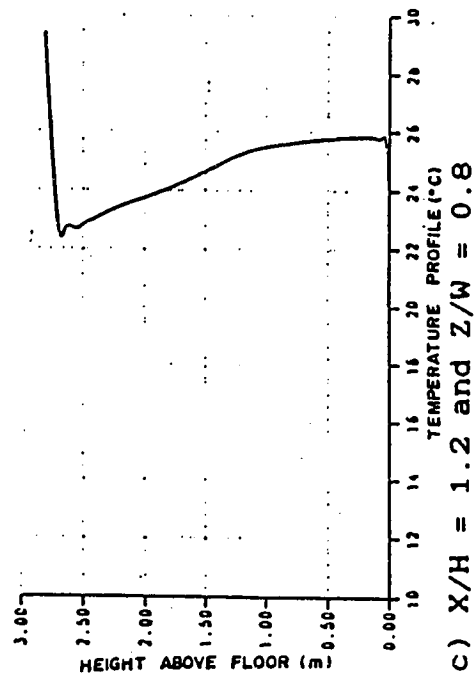
c) X/H = 1.2 and Z/W = 0.8

Figure 7.41. Temperature profiles over height of room near right wall at noon, Tin = 12 °C and Uin = 3.0 m/sec for the WE configuration.

a higher level of temperature, such that the relatively coolest portion is in the upper part of the room, while in the region below the inlet opening, temperature gradually increases in an almost linear fashion reaching the peak close to the floor. An interesting observation is that the absolute slope of the temperature profile below the inlet vent in Fig.7.40.a is larger than that in Fig. 7.38.a such that an increase of only about 2.5°C occurs in the former while an increase of about 5.5°C occurs in the latter and this will have a direct impact on the level of comfort, as will be described later on. Progressing farther from the inlet at 0.8 the height of the room we observe that the peak in both Figs. 7.38.b and 7.40.b has decreased to a higher temperature , but the temperature profile under the inlet vent is shifted to a relatively cooler temperature level in the latter figure, while only the bottom and upper parts of the temperature profile below the inlet opening of the former figure has decreased whereas the middle portion is nearly the same as that in Fig. 7.38.a. An occurrence similar to that from Fig.7.38.a to Fig. 7.38.b repeats itself from the latter Figure to Fig.7.38.c and the same is said when progressing from Fig.7.40.b to Fig.7.40.c. At this point, we notice how much the slope of the temperature profile, in Fig. 7.38.c, below the inlet and above about 0.75 m from the floor is tilted and the change of temperature over the occupied zone is relatively high while in Fig. 7.40.c the temperature profile over the height of the occupied zone is much more uniform and the variation of the temperature over this region is relatively less. In Figs. 7.38.d and 7.40.d, the peaks in the upper part of the room both decreases to a higher temperature but the temperature profile below the inlet opening in the former figure is nearly the same as that in Fig. 7.38.c while that of Fig.7.40.d is considerably less than that of Fig.7.40.c. Temperature profiles for both cases reported above are

repeated in Figs. 7.39 and 7.41, which are plotted away from the mid-plane of the room, passing the right side of the occupied zone, having a $T_{in} = 15°C$ and $U_{in} = 1.9$ m/sec., in the former and a $T_{in} = 12°C$ and $U_{in} = 3.0$ m/sec. in the latter. A resemblance in the general features of both sets of plots exists such that the relatively coolest temperature is in the upper part of the room while the warmest is close to the floor. In Figs. 7.39.a and 7.41.a, the temperature profiles at a distance of 0.4 the height of the room from the west wall are plotted and the variation of temperature over the height of the room in the former figure is relatively greater than that in the latter and not as uniform. Temperature profiles at the same z-plane but at a distance of 0.8 the height of the room along the x-axis are plotted in Figs.7.39.b and 7.41.b in which the peaks of the upper parts of the temperature profiles have increased to a lower temperature while that in the bottom half part of the room of the former figure is almost the same as in Fig. 7.39.a, but the level of temperature is correspondingly lower than that appearing in Fig.7.41.a indicating a reduction in the level of temperature as we move farther from the West wall. Progressing along the x-axis and away from the West wall at a distance of 1.2 the height of the room, the temperature profile in Fig. 7.39.c has changed very little while that of Fig.7.41.c reduced considerably such that the overall slope of the temperature profile is less tilted and the air jet mixed more thoroughly with the surrounding air in the room. In Fig.7.39.d, the temperature profile at a distance of 1.6 the height of the room along the x-axis is plotted where it may be observed that the peak in the upper part of the room has not changed while the peak in the region close to the floor has increased and the slope of the temperature in between these two limits is relatively larger than that of Fig.7.39.c. The temperature profile for

Fig.7.41.d is now nearly uniform with a slight peak temperature remaining close to the floor and it should be noted here that this type of uniform profile within the range of temperature given in the Figure is highly desirable and produces a relatively acceptable level of comfort, which will be discussed below.

(iii) Temperature Profiles at 3:00 P.M.

The temperature profiles for T_{in} = 15°C and U_{in} = 1.9 m/sec., are given in Figs. 7.42 and 7.43 while that for T_{in} = 10°C and U_{in} = 4.0 m/sec., are given in Fig.7.44 and Fig.7.55. Comparing Fig.7.42.a and Fig.7.44.a, which are the temperature profiles plotted at the center of the room and at a distance of 0.4 the height of the room along the x-axis, we notice that the plots are generally similar except that the peak in the upper part of the room for the latter figure is at a considerably lower temperature owing to the relatively lower T_{in} and high U_{in} here, while the temperature profile below the inlet in the former figure is not as steep as that of the latter which has a nearly uniform level of temperature over the height of the occupied zone. Moving along the same z-plane to Fig. 7.42.b and Fig.7.44.b, we see that the low temperature peak at the upper part of the room in both have reduced to a correspondingly higher temperature and the bottom part of the temperature profile close to the floor has also reduced to a lower temperature while the slope of the temperature profile in the middle portion of the room for the former figure has not changed much whereas in Fig. 7.44.b the temperature profile below the opening of the inlet is more steeper and the corresponding variation of temperature

234

a) X/H = 0.4 and Z/W = 0.5

b) X/H = 0.8 and Z/W = 0.5

c) X/H = 1.2 and Z/W = 0.5
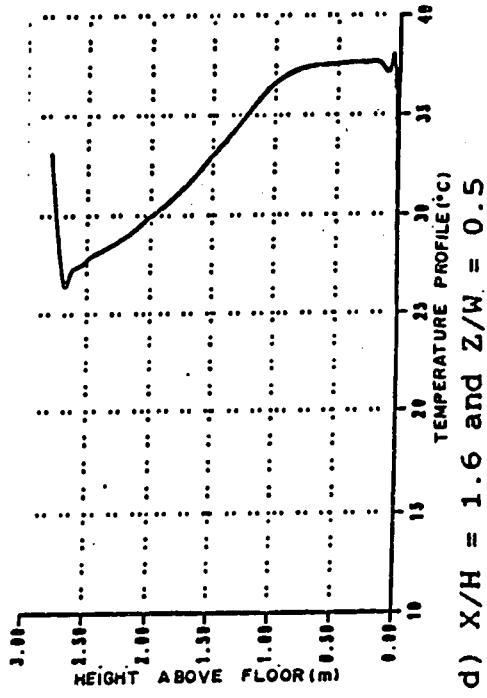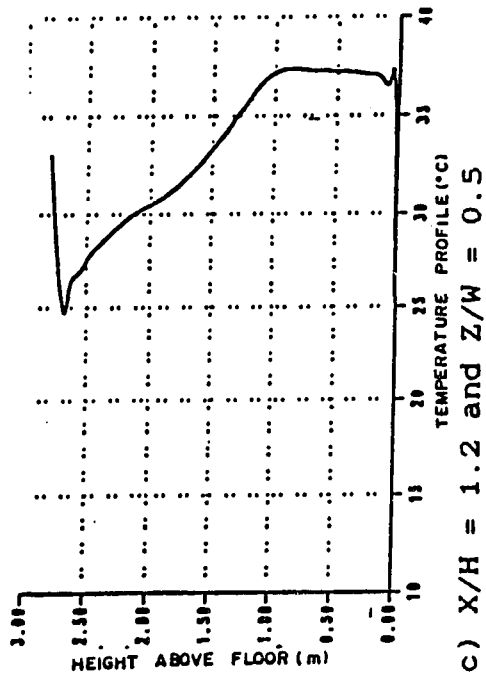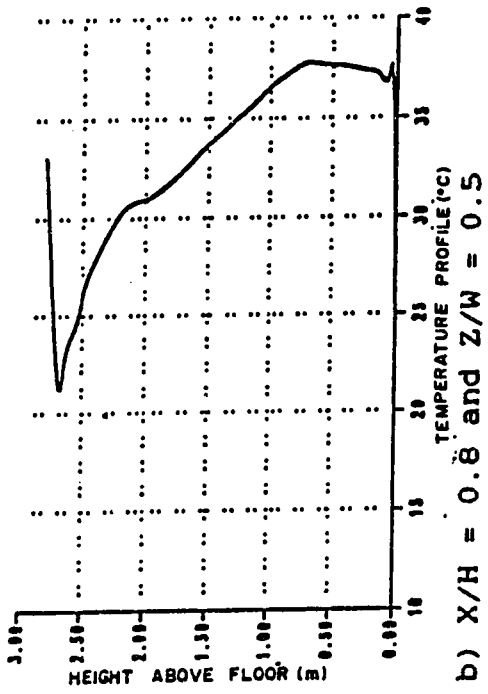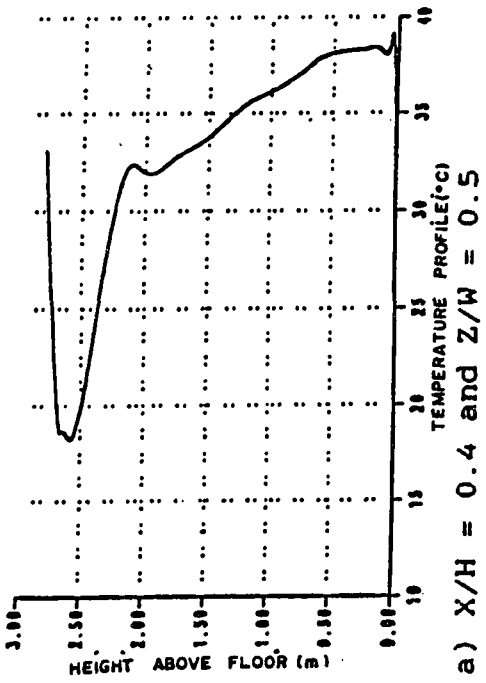
d) X/H = 1.6 and Z/W = 0.5

Figure 7.42. Temperature profiles over height of room at mid section at 3 pm, Tin = 15 °C and Uin = 1.9 m/sec for the WE configuration.
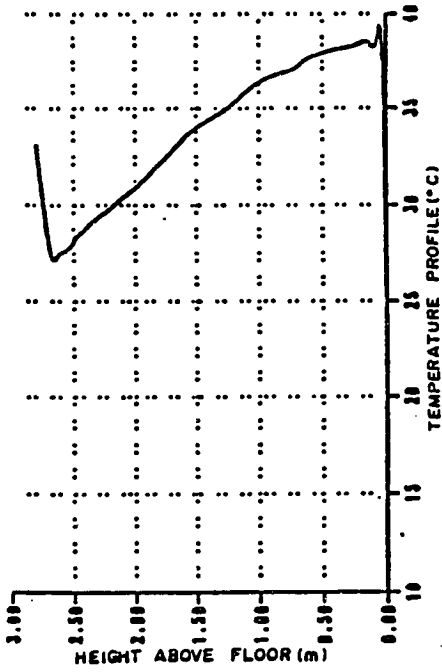
b) X/H = 0.8 and Z/W = 0.8

d) X/H = 1.6 and Z/W = 0.8

a) X/H = 0.4 and Z/W = 0.8

c) X/H = 1.2 and Z/W = 0.8

Figure 7.43. Temperature profiles over height of room near right wall at 3 pm, Tin = 15 °C and Uin = 1.9 m/sec for the WE configuration.
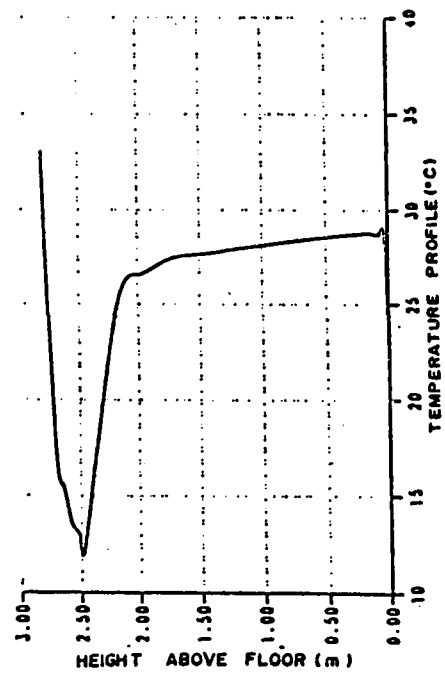
b) X/H = 0.8 and Z/W = 0.5
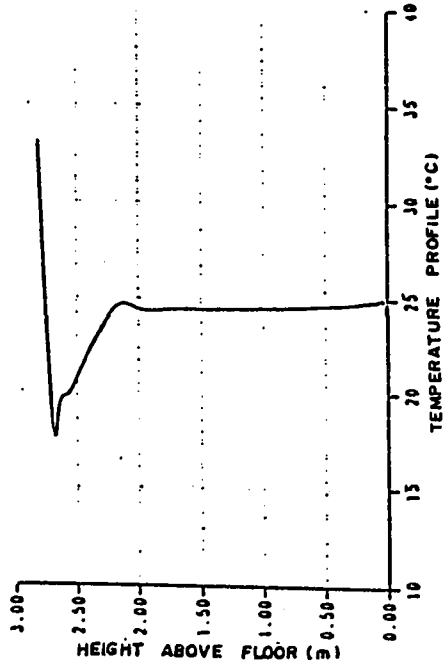
d) X/H = 1.6 and Z/W = 0.5

a) X/H = 0.4 and Z/W = 0.5

c) X/H = 1.2 and Z/W = 0.5

Figure 7.44. Temperature profiles over height of room at mid section at 3 pm, Tin = 10 °C and Uin = 4.0 m/sec for the WE configuration.
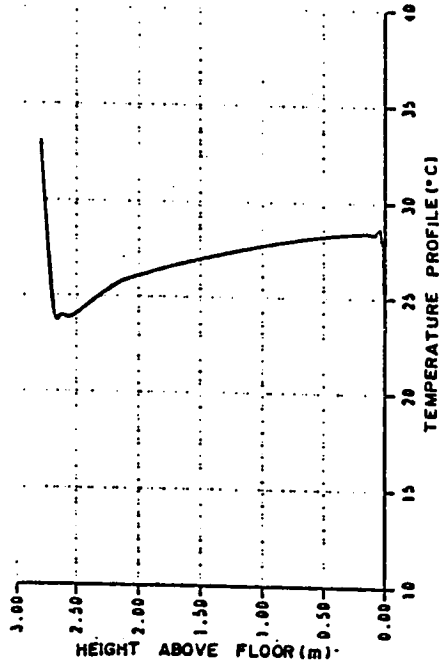
b) X/H = 0.8 and Z/W = 0.8

d) X/H = 1.6 and Z/W = 0.8

a) X/H = 0.4 and Z/W = 0.8
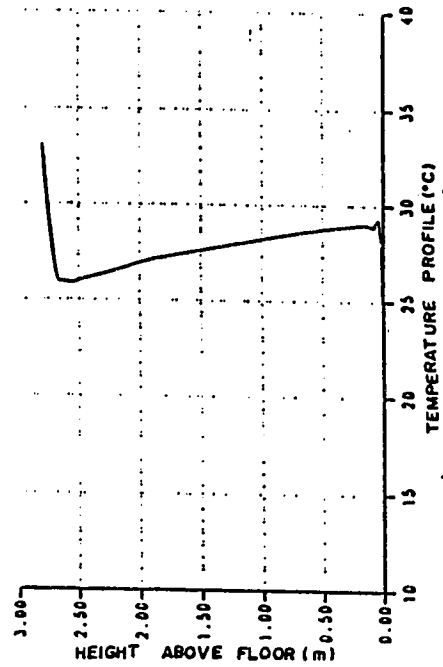
c) X/H = 1.2 and Z/W = 0.8

Figure 7.45. Temperature profiles over height of room near right wall at 3 pm, Tin = 10 °C and Uin = 4.0 m/sec for the WE configuration.

over the occupied zone has almost completely disappeared resulting in a suitable level of comfort for the occupants. At a distance of 1.2 the height of the room along the x-axis the temperature profiles are given in Figs. 7.42.c and 7.44.c where the low peak temperature in the upper part of both figures have reduced and other than that the remaining temperature profile of the former figure is almost identical to that in Fig.7.42.b while in the latter figure, the temperature profile , below the inlet opening, has shifted to a relatively lower level of temperature and the slope has become nearly vertical, which is a desirable occurrence to satisfy comfort for the level of temperature given. The temperature profiles of Figs. 7.42.d and 7.44.d resemble those of Figs. 7.42.c and 7.44.c, respectively and consequently no more will be said about these figures. In Figs. 7.43 and 7.45, the temperature profiles at the right edge of the occupied zone are plotted. At a distance of 0.4 the height of the room along the x-axis the temperature profiles are given in Figs. 7.43.a and 7.45.a where the peak of the lower temperature in both is at the upper part of the room, while the highest temperature is .close to the floor, and the temperature at both these extremes in the former figure is relatively higher than that in the latter, respectively. A more serious observation to be made here is that the slope of Fig. 7.45.a is larger than that of Fig. 7.43.a implying a relatively less variation of temperature over the height of the occupied zone and producing a relatively more comfortable environment for the occupants. Farther away from the West wall at a distance of 0.8 the height of the room along the x-axis, temperature profiles are given in Figs. 7.43.b and 7.45.b where the low temperature peak at the upper part of the room has increased to a

lower temperature for both figures while most of the remaining part of the temperature profile in Fig. 7.43.b is almost identical to that of Fig.7.43.a whereas the temperature profile in Fig. 7.45.b has shifted completely to a lower temperature . Moving along the x-axis to a distance of 1.2 the height of the room from the West wall, the temperature profiles have been plotted in Figs. 7.43.c and 7.45.c where the former figure is nearly identical to Fig.7.43.b while the latter figure has changed considerably such that the peak of the low temperature in the upper part of the room has almost completely disappeared and the temperature profile is nearly vertical indicating low variation of temperature over the height of the occupied zone. Finally, at a distance of 1.6 the height of the room along the x-axis, the temperature profile in Fig. 7.43.d is tilted considerably indicating a high variation of temperature over the occupied zone while that of Fig. 7.45.d is for all practical purposes vertical, implying a uniform temperature over the height of the occupied zone.

7.2.1.5 PMV Contours

To display the occupancy thermal response the Predicted Mean Votes (PMV) have been plotted in the form of horizontal x-z planes at pre-determined elevations above the floor for both the sitting and standing postures. To have an overall view of comfort for a particular arrangement, average PMV contours for both postures, over the height of the occupied zone have been estimated by two distinctive means which are :

(a)   Inserting the pertinent computed variables describing the flow field at all grid nodes within the occupied zone directly into the PMV

equation, (5.128), and then the resulting PMV indexes are averaged over the height of the occupied zone, resulting with only one horizontal x-z plane of Calculated Mean PMV contours (CMPMV).

(b)   Averaging the flow variables over the height of the occupied zone so that we would result with only one horizontal x-z plane of averaged flow variables and then these variables are inserted into (5.128) producing a horizontal z plane of Simple Average PMV contours (SAPMV).

The PMV contours are estimated at the time of 9:00 A.M., 12:00 Noon and 3:00 P.M. Discussions on these will follow.

(i) PMV Contours at 9:00 A.M.

The PMV contours at 9:00 A.M. for the sitting posture are given in Figs. 7.46 and 7.47. In both these figures, U_{in} is identical (1.9 m/sec), but T_{in} is equal to 15°C in the former figure and 18°C in the latter. Figs. 7.48 and 7.49 are plotted with the T_{in} and U_{in} as given in Figs. 7.46 and 7.47, respectively, but for the standing posture. In Figs.7.46.a and 7.47.a, the PMV contours at a height of 0.24 m (corresponding to the ankle level) are given in the former figure all the PMV indexes* are negative, indicating a cool sensation, while the PMV index in the latter are a mixture of positive and negative values. The overall appearance of both figures are compara-

----

*   Note a factor is used for the PMV indices to give an insight on its variation.
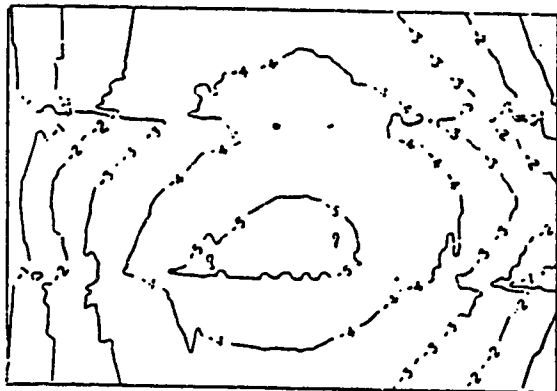
a) Y = 0.24 m, Fac = 10.0
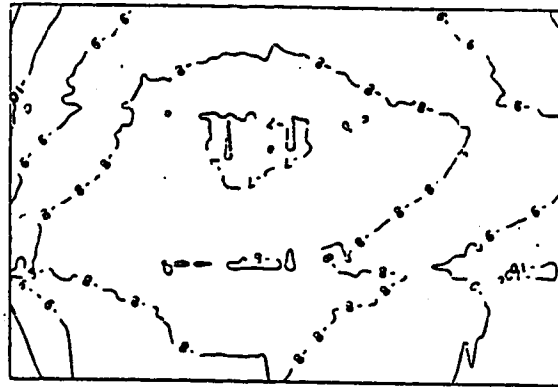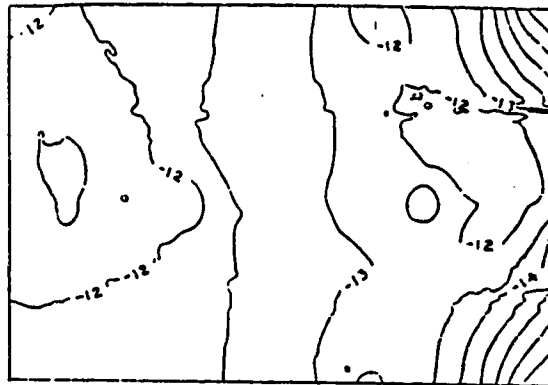
b) Y = 0.60 m, Fac = 25.0
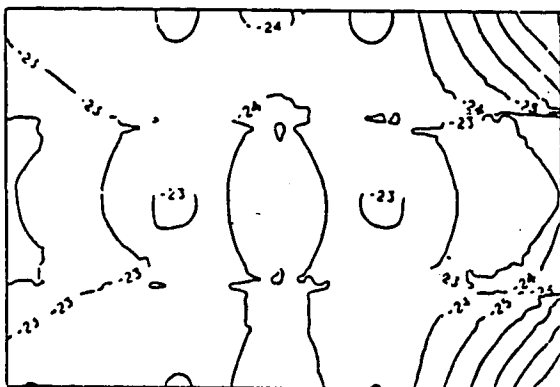
c) Y = 1.00 m, Fac = 25.0
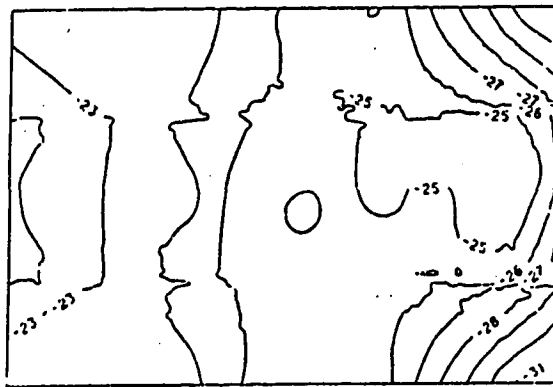
d) CMPMV   Fac = 50.0

e) SAPMV   Fac = 50.0

Figure 7.46. PMV contours for the sitting posture in
the X-Z plane at 9 am, Tin = 15 °C and
Uin = 1.9 m/sec. for the WE configuration.
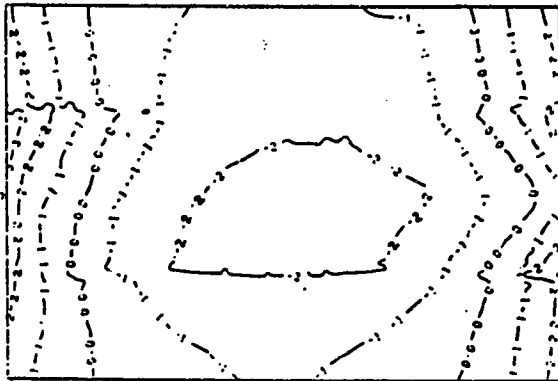
a) Y = 0.24 m, Fac = 10.0
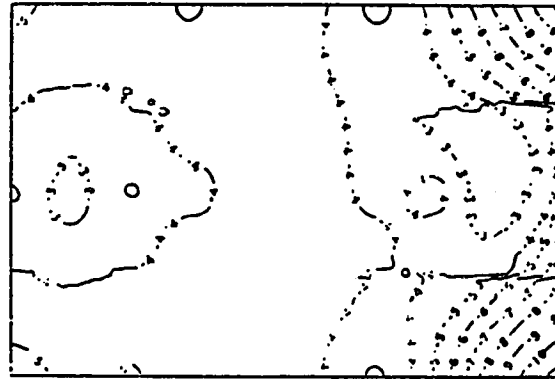
b) Y = 0.60 m, Fac = 25.0
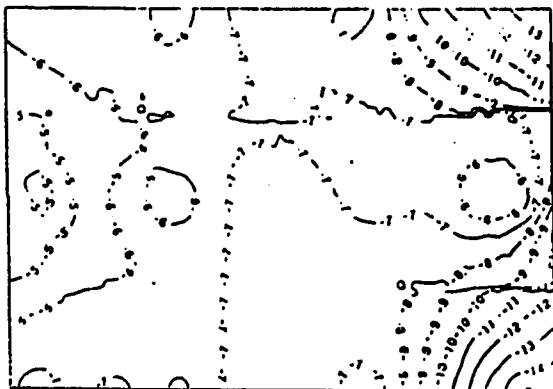
c) Y = 1.00 m, Fac = 25.0
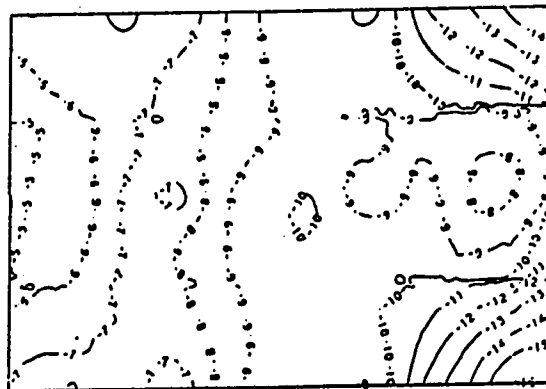
d) CMPMV   Fac = 50.0

e) SAPMV   Fac = 50.0

Figure 7.47. PMV contours for the sitting posture in
           the X-Z plane at 9 am, Tin = 18 °C and
           Uin = 1.9 m/sec. for the WE configuration.

a) Y = 0.24 m, Fac = 10.0
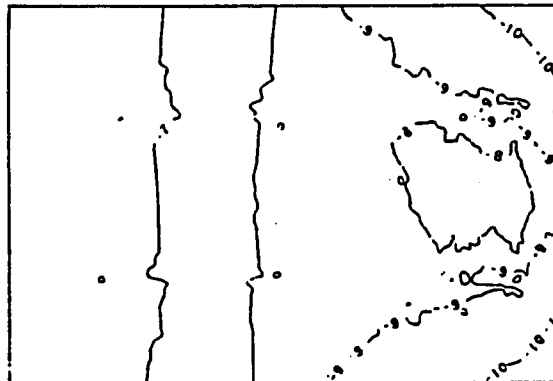
b) Y = 0.60 m, Fac = 25.0

c) Y = 1.00 m, Fac = 10.0
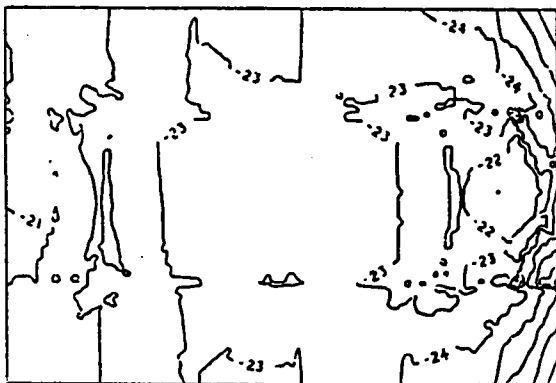
d)   CMPMV   Fac = 50.0
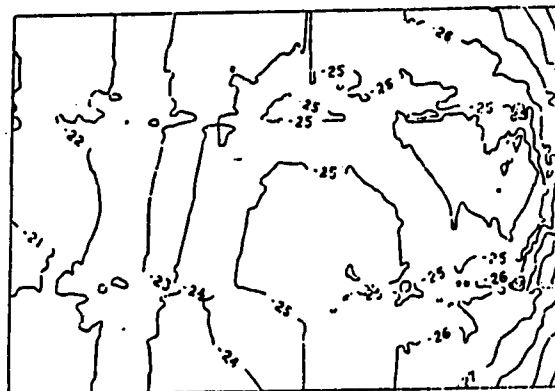
e)   SAPMV   Fac = 50.0

Figure 7.48. PMV contours for the standing posture in
the X-Z plane at 9 am, Tin = 15 °C and
Uin = 1.9 m/sec. for the WE configuration.
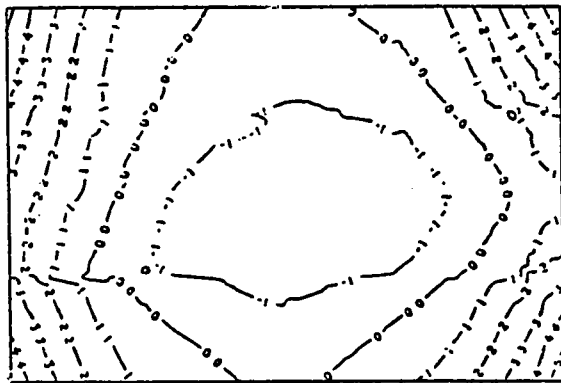
a) Y = 0.24 m, Fac = 10.0
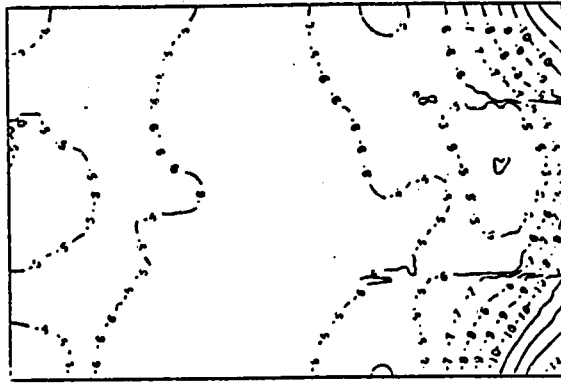
b) Y = 0.60 m, Fac = 35.0
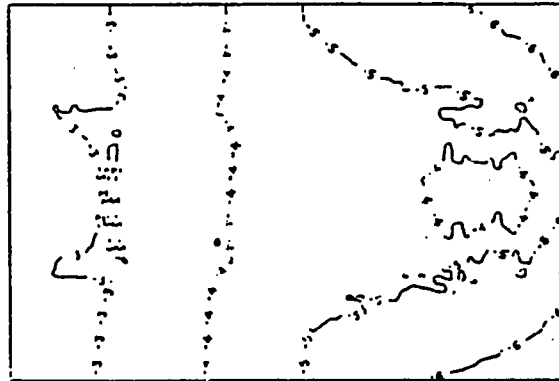
c) Y = 1.00 m, Fac = 10.0
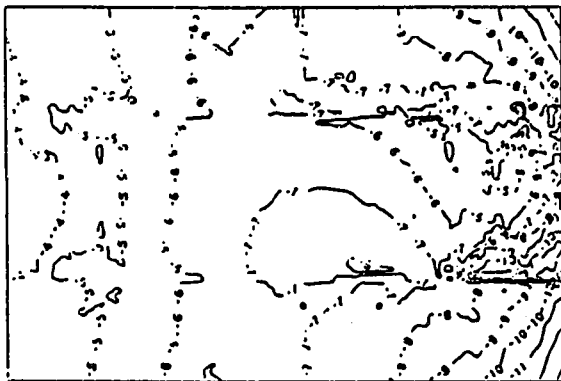
d)　CMPMV　　　　Fac = 50.0
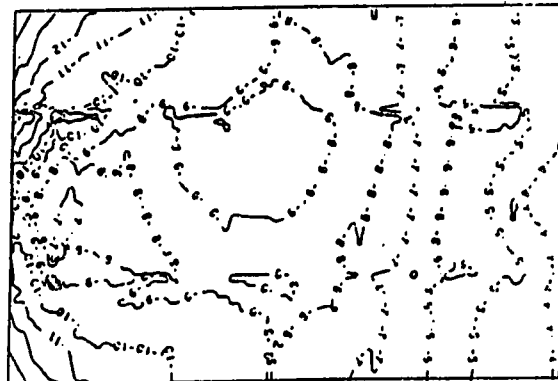
e)　SAPMV　　　　Fac = 50.0

Figure 7.49. PMV contours for the standing posture in
the X-Z plane at 9 am, Tin = 18 °C and
Uin = 1.9 m/sec. for the WE configuration.

ble, such that the lowest PMV is in the central area of the occupied zone and gradually increases as we move towards the East or West sides of the room. Progressing along the height of the occupied zone to y = 0.6 m (corresponding to the center of the body of a sitting person), the PMV contours given in Figs. 7.46.b and 7.47.b show that the relative PMV indices are considerably lower in the former figure relative to the latter which is generally at or close to thermal neutrality (i.e. PMV equal to zero). At a height of y = 1.0 m (corresponding to the height of the back of the neck for a sitting person), PMV contours are plotted in Figs.7.46.c and 7.47.c where it is noticed that all absolute PMV indexes in the former figure is greater than that in the latter figure, indicating that the level of comfort sensation in Fig. 7.47.c is higher than that of Fig. 7.46.c. To compare the two cases investigated here the CMPMV contours are plotted in Figs.7.46.d and 7.47.d where it is obvious that the majority of the CMPMV contours in the latter figure are well within the acceptable comfort limit [7 , 51] , described earlier, while that of the former figure is at a lower level of comfort, see Table 7.3. An observation similar to this is made by comparing Figs.7.46.e and 7.47.e. The PMV contours for the standing posture in Figs.7.48 and 7.49 resembles that given in Figs. 7.46 and 7.47, respectively, thus no discussion regarding these PMV contours are necessary.

(ii) PMV Contours at 12:00 Noon

The PMV contours at Noon for the sitting posture are given in Figs. 7.50 and 7.51 where T_{in} and U_{in} in the first plot are 15°C and 1.9 m/sec.,

TABLE 7.3: Fanger's Thermal Comfort Scale.

PMV Index	Thermal Response
-3	COLD
-2	COOL
-1	SLIGHTLY COOL
0	THERMALLY NEUTRAL
1	SLIGHTLY WARM
2	WARM
3	HOT
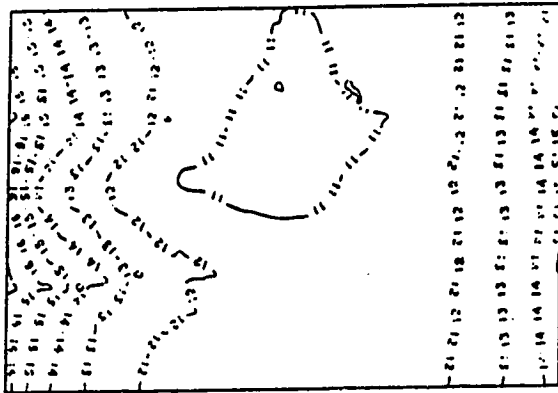
a) Y = 0.24 m, Fac = 10.0
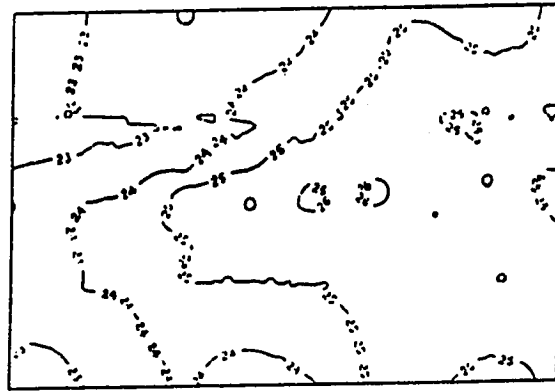
b) Y = 0.60 m, Fac = 20.0
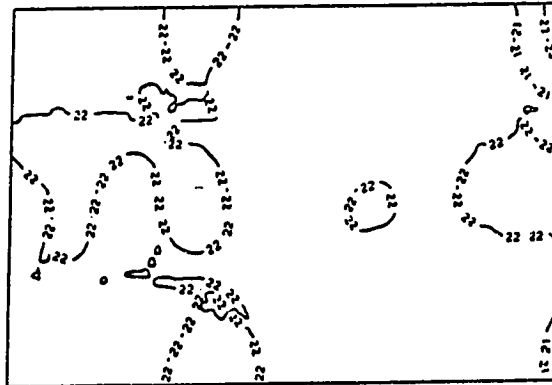
c) Y = 1.00 m, Fac = 20.0
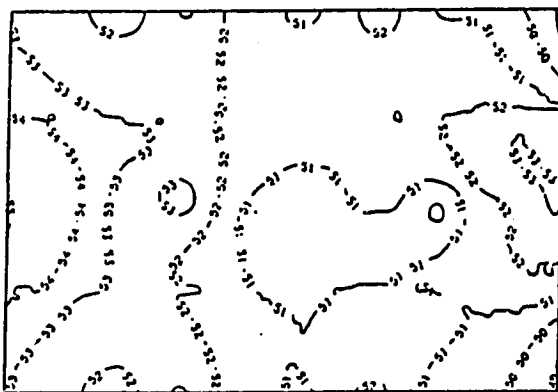
d) CMPMV   Fac = 50.0
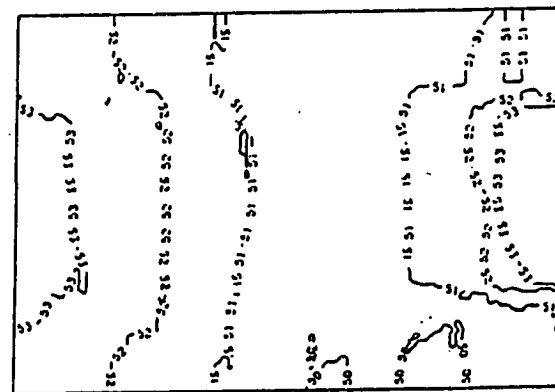
e) SAPMV   Fac = 50.0

Figure 7.50. PMV contours for the sitting posture in
the X-Z plane at noon, Tin = 15 °C and
Uin = 1.9 m/sec. for the WE configuration.
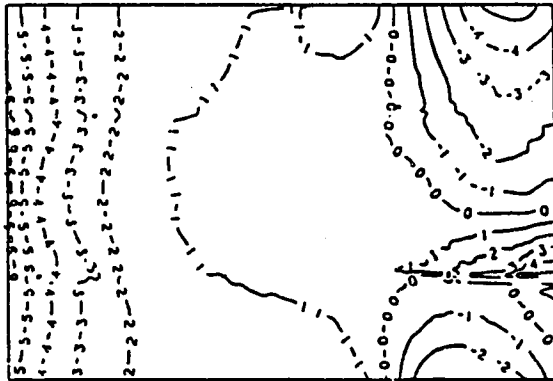
a) Y = 0.24 m, Fac = 10.0
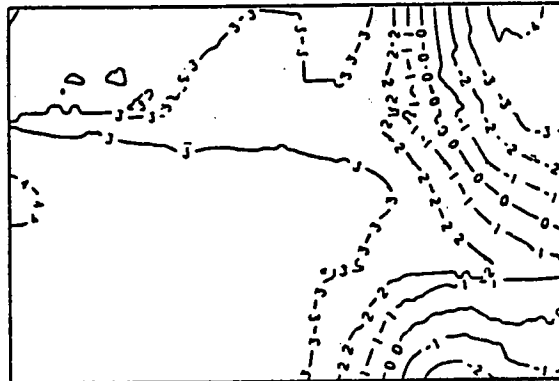
b) Y = 0.60 m, Fac = 10.0
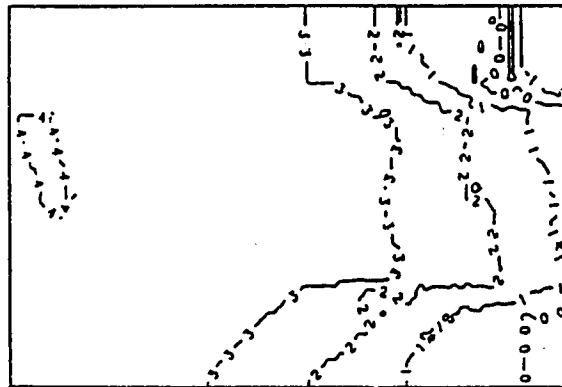
c) Y = 1.00 m, Fac = 10.0
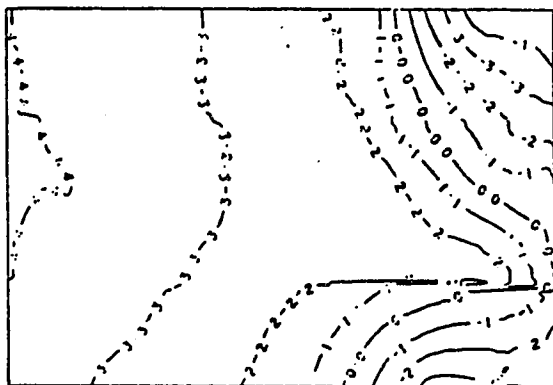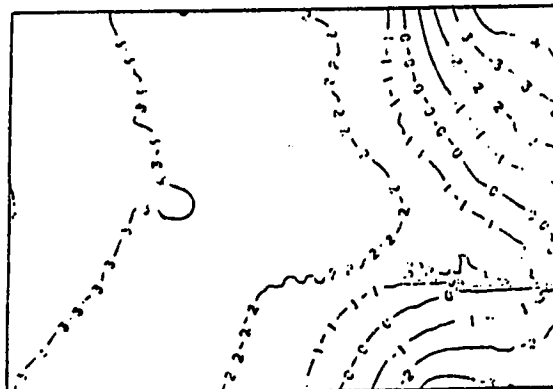
d) CMPMV   Fac = 10.0

e) SAPMV   Fac = 10.0

Figure 7.51. PMV contours for the sitting posture in
the X-Z plane at noon, Tin = 12 °C and
Uin = 3.0 m/sec. for the WE configuration.

respectively and in the second plot they are 12°C and 3.0 m/sec., respectively. Figs. 7.52 and 7.53 are plotted for a T_{in} and U_{in} equal to that of Figs. 7.50 and 7.51, respectively, but for the standing posture. Comparing the PMV contours for the sitting posture at a height of 0.24 m above the floor, given in Figs. 7.50.a and 7.51.a, we notice that the lowest PMV contour is at the center of the occupied zone in the former figure while that in the latter figure appears to be close to the Eastern side of the occupied zone. This is due to the fact that since the East wall is opposite to the inlet opening, the air jet collides with it and removes a relatively considerable amount of heat influx. The majority of the contours in Fig.7.50.a are between the slightly warm and warm sensation (Table 7.3), which is not acceptable as being comfortable. Whereas the PMV contours of Fig.7.51.a extends on both sides of the thermally neutral sensation scale (i.e.: PMV = 0) and none of which reach the slightly cool or slightly warm limits. The PMV contours shown in Fig.7.50.b and 7.51.b are plotted at a height of 0.6 m above the floor where the variation of the PMV contours in the former figure is less than that of the latter, but the magnitude of all the PMV contours in Fig.7.50.b are greater than the slightly warm limit of Table 7.3 while that of Fig.7.51.b is close to thermal neutrality and extends even less on both sides of PMV = 0 than Fig.7.51.a. Moving upwards to a height of 1.0 m above the floor the corresponding PMV contours are given in Fig. 7.50.c and 7.51.c where the PMV contours in the former figure are at nearly one level while those in the latter are not. The PMV contours of Fig.7.50.c are still above the slightly warm sensation scale, whereas that of Fig.7.51.c remains close to thermal neutrality, but more

a) Y = 0.24 m, Fac = 10.0
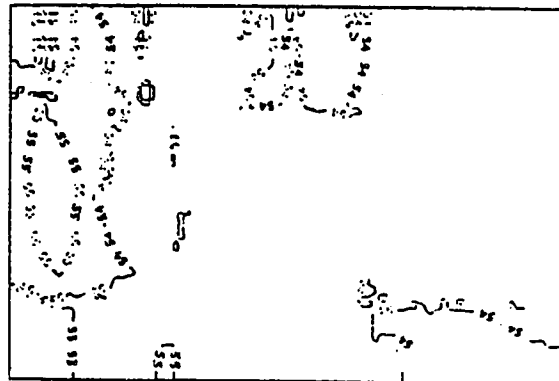
b) Y = 0.60 m, Fac = 50.0
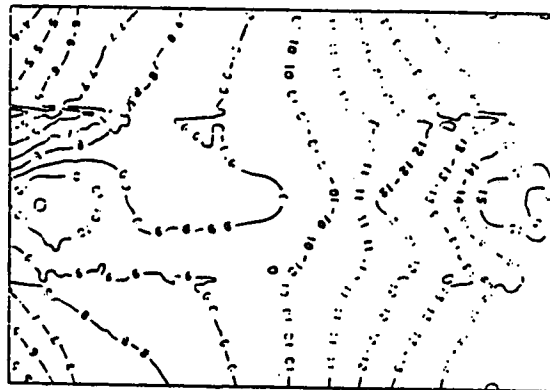
c) Y = 1.00 m, Fac = 20.0

d)   CMPMV   Fac = 50.0
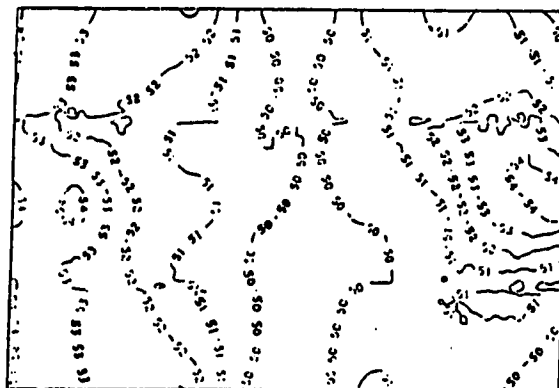
e) SAPMV   Fac = 50.0

Figure 7.52. PMV contours for the standing posture in
             the X-Z plane at noon, Tin = 15 °C and
             Uin = 1.9 m/sec. for the WE configuration.

a) Y = 0.24 m, Fac = 10.0
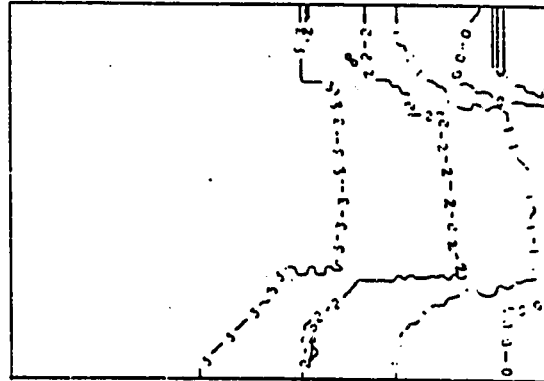
b) Y = 0.60 m, Fac = 10.0
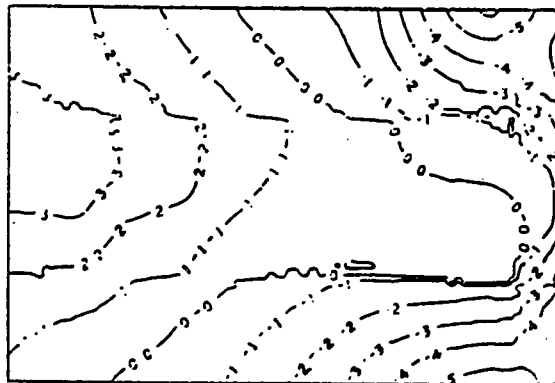
c) Y = 1.00 m, Fac = 10.0
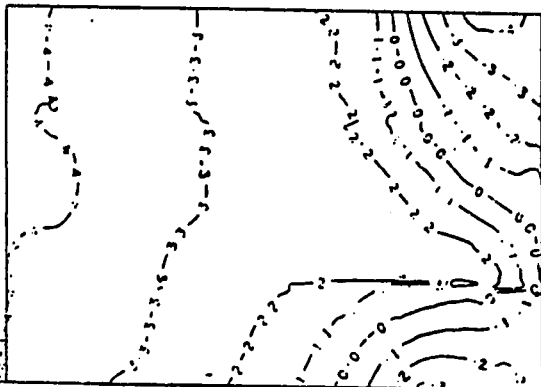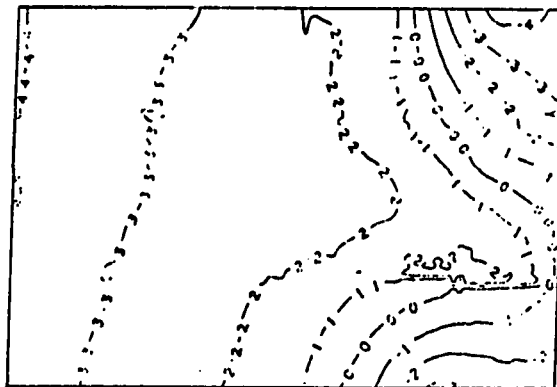
d)   CMPMV   Fac = 10.0

e) SAPMV   Fac = 10.0

Figure 7.53. PMV contours for the standing posture in
the X-Z plane at noon, Tin = 12 °C and
Uin = 3.0 m/sec. for the WE configuration.

positive PMVs are apparent than negative ones. The CMPMV contours are plotted in Figs.7.50.d and 7.51.d where the majority of the CMPMV contours of the former are above the slightly warm and below the warm thermal sensation scales, while that of the latter figure is close to thermal neutrality such that the Eastern side of the occupied zone consists of mainly negative CMPMVs and as we progress towards the West side of the occupied zone the CMPMVs gradually increase to positive values while the variation in CMPMVs reduces. An observation similar to this is concluded when comparing the SAPMVs of Figs.7.50.e and 7.51.e.

The PMV contours for the standing postures in Figs. 7.52 and 7.53 resembles that given in Figs. 7.50 and 7.51, respectively, thus no discussion regarding the PMV contours of the standing posture is presented.

(iii) PMV Contours at 3:00 P.M.

The PMV contours at 3:00 P.M. for the sitting posture are given in Figs. 7.54 and 7.55 such that T_{in} and U_{in} in the former plots are 15°C and 1.9 m/sec., respectively while that in the latter are 10°C and 4.0 m/sec. . Figs. 7.56 and 7.57 are PMV contour plots for the standing posture with a T_{in} and U_{in} equal to that of Figs.7.54 and 7.55, respectively. At a height of 0.24 m above the floor, the PMV contours are plotted in Figs. 7.54.a and 7.55.a where it may be observed that the former figure shows PMV values above the slightly warm sensation, while in the latter figure the PMVs extend on both sides of the thermal neutrality level but much lower than the slightly cool or slightly warm levels. Moving upwards to a height of
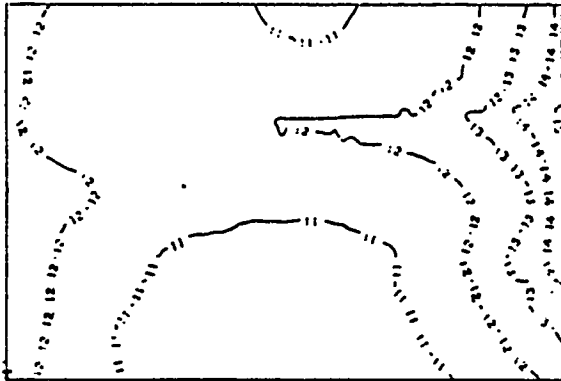
a) Y = 0.24 m, Fac = 5.0
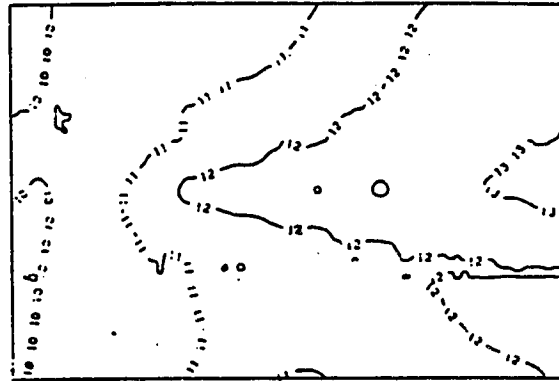
b) Y = 0.60 m, Fac = 5.0
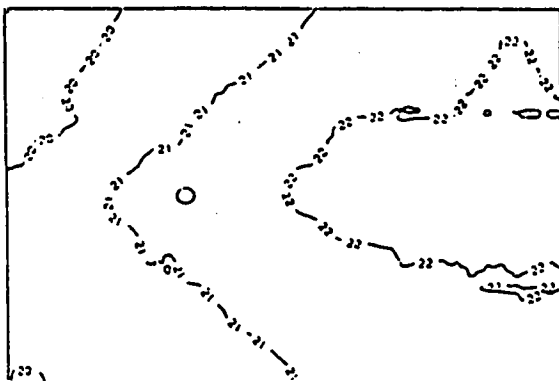
c) Y = 1.00 m, Fac = 5.0

d) CMPMV   Fac = 10.0
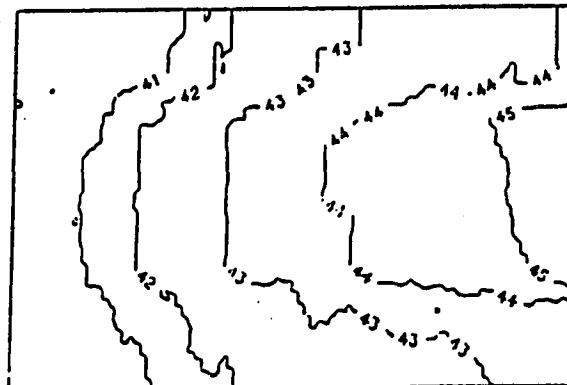
e) SAPMV   Fac = 20.0

Figure 7.54. PMV contours for the sitting posture in
the X-Z plane at 3 pm, Tin = 15 °C and
Uin = 1.9 m/sec. for the WE configuration.
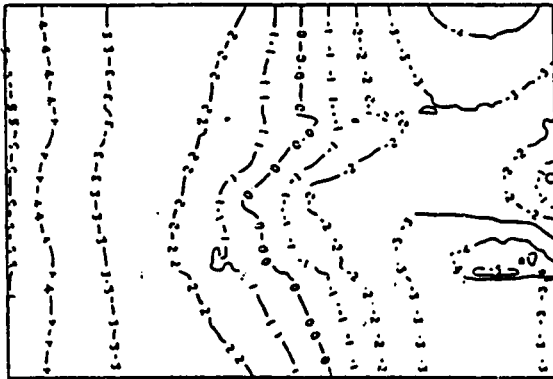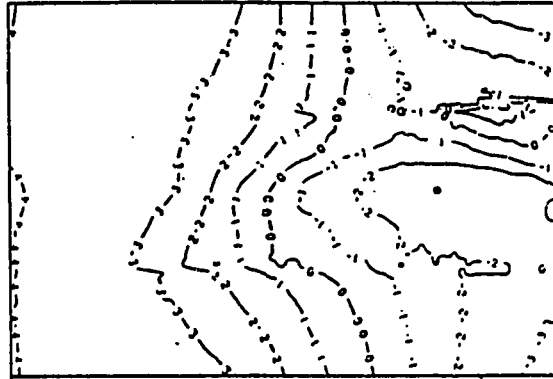
a) Y = 0.24 m, Fac = 5.0
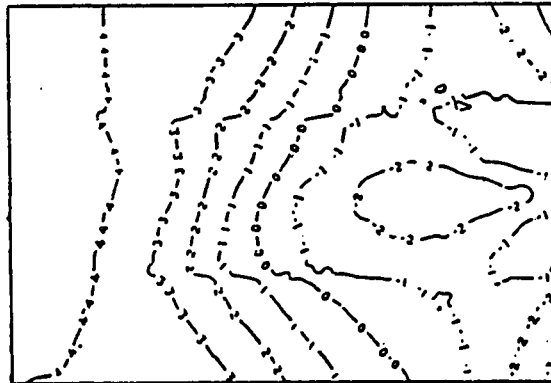
b) Y = 0.60 m, Fac = 5.0
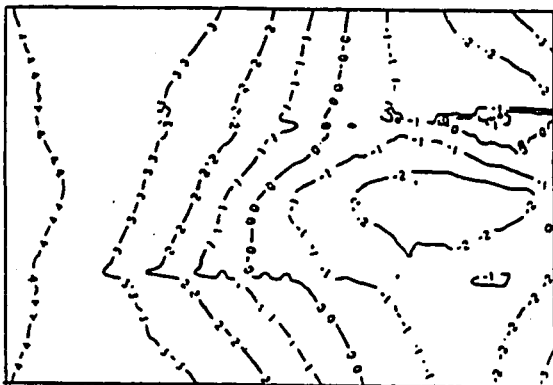
c) Y = 1.00 m, Fac = 5.0
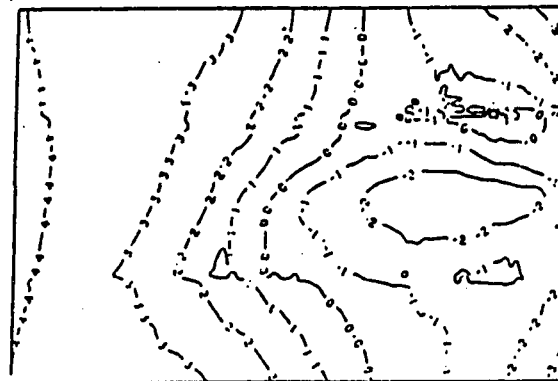
d)   CMPMV   Fac = 5.0

e) SAPMV   Fac = 5.0

Figure 7.55. PMV contours for the sitting posture in
the X-Z plane at 3 pm, Tin = 10 °C and
Uin = 4.0 m/sec. for the WE configuration.
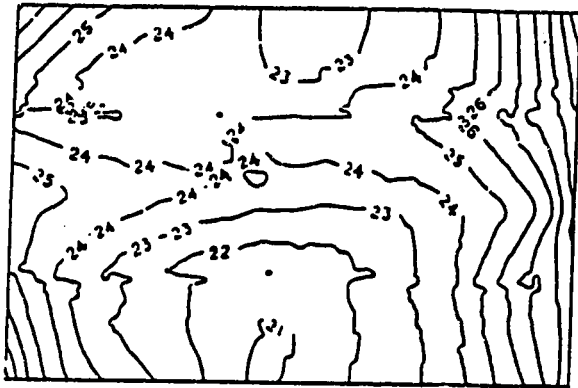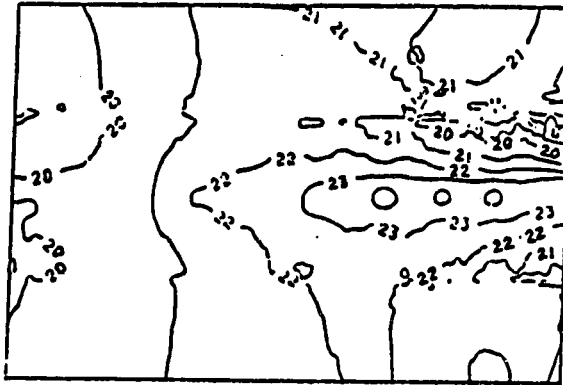
a) Y = 0.24 m, Fac = 10.0
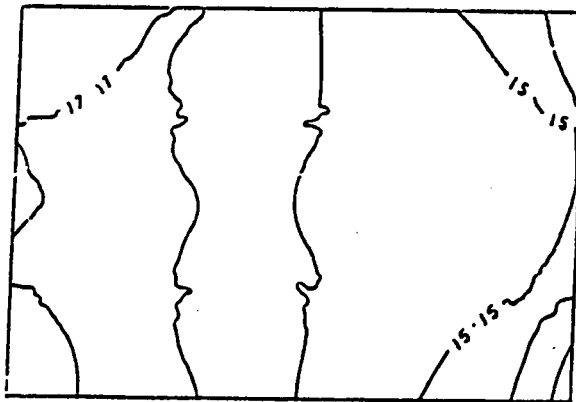
b) Y = 0.60 m, Fac = 10.0
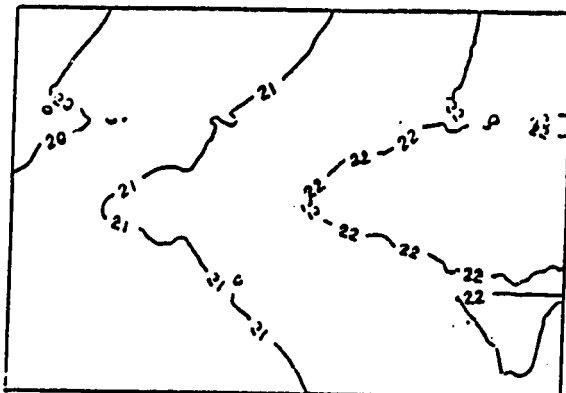
c) Y = 1.00 m, Fac = 10.0
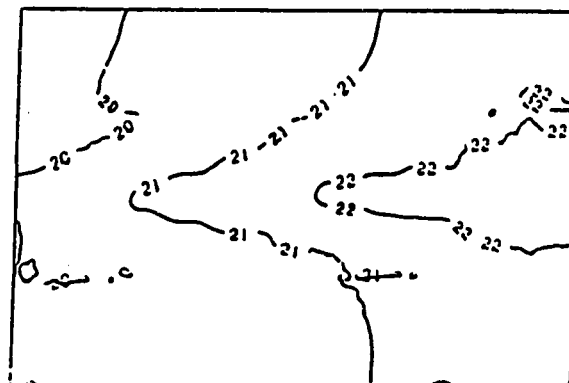
d)   CMPMV   Fac = 10.0

e) SAPMV   Fac = 10.0

Figure 7.56. PMV contours for the standing posture in
the X-Z plane at 3 pm, Tin = 15 °C and
Uin = 1.9 m/sec. for the WE configuration.
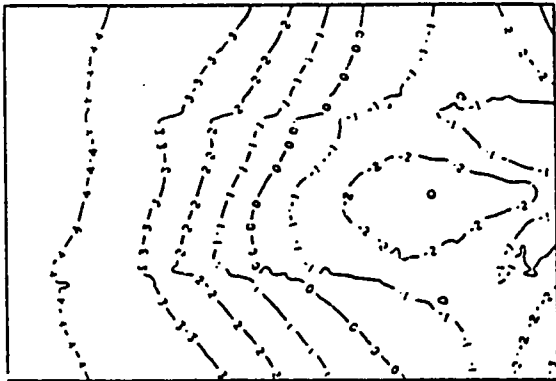
a) Y = 0.24 m, Fac = 5.0
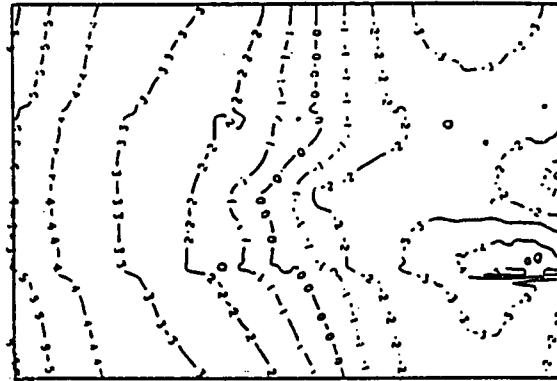
b) Y = 0.60 m, Fac = 5.0
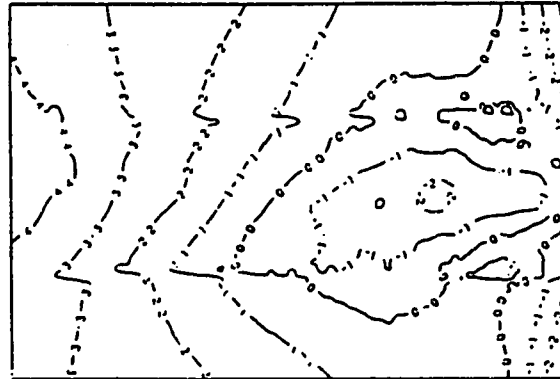
c) Y = 1.00 m, Fac = 5.0
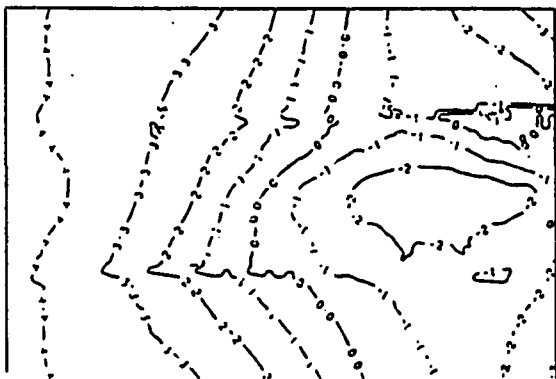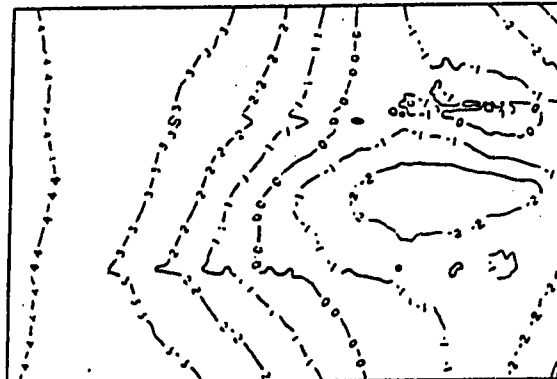
d)   CMPMV   Fac = 5.0

e)   SAPMV   Fac = 5.0

Figure 7.57. PMV contours for the standing posture in
          the X-Z plane at 3 pm, Tin = 10 °C and
          Uin = 4.0 m/sec. for the WE configuration.

0.6 m above the floor (Figs. 7.54.b and 7.55.b) the PMV contours are generally comparable and the variation of the PMV over the occupied zone is lower than the corresponding PMV contours at a height of 0.24 m above the floor. Similar observations are made about the PMV contours for a height of 1.0 m above the floor (Figs. 7.54.c and 7.55.c.) The CMPMVs given in Figs.7.54.d and 7.55.d shows that the the majority of the contours in the former figure is higher than the warm thermal sensation while that of the latter figure are mostly close to thermal neutrality for which the thermal sensation of comfort would be attained. An analysis similar to that for Figs. 7.54.d and 7.55.d follows for the SAPMV contours in Figs. 7.54.e and 7.55.e, respectively. The PMV contours for the standing posture in Figs. 7.56 and 7.57 resembles that given in Figs. 7.54 and 7.55, respectively, thus no further discussion is necessary.

7.2.2 The NN Configuration

As in the WE configuration , there are three types of boundary conditions applied in the NN configuration at the times of 9:00 A.M., 12:00 Noon and 3:00 P.M.. Variations in T_{in} and/or U_{in} were necessary to achieve an acceptable level of comfort [7 , 51] .

The original guess for T_{in} and U_{in} together with those producing the 'best' possible level of comfort are given in Table 7.4 for the different boundary conditions investigated.

TABLE 7.4 : Inlet Velocities and Temperatures employed in the NN configuration

Time of Day	T_{in} (°C)	U_{in} (m/sec.)
9:00 A.M.	15.0	1.9
9:00 A.M.	22.0	1.9
12:00 Noon	15.0	1.9
12:00 Noon	10.0	2.2
3:00 P.M.	15.0	1.9
3:00 P.M.	15.0	3.5

7.2.2.1 Velocity vector plots

The computed velocity flow field within the room are depicted in the form of vector plots, which for reasons of consistency, have been plotted at geometrical locations similar to that in the WE configuration .

(i) *Velocity Vector Plots at 9:00 A.M.*

The plots of Figs. 7.58 and 7.60 are the x-y velocity vector plots at T_{in} = 15.0°C and 22.0°C , respectively while the U_{in} in both is the same and equal to 1.9 m/sec. Comparing Figs. 7.58.a and 7.60.a, we note that there is one definite clockwise vortex in the former figure whereas there are two vortices in the latter, one in the East side of the room moving in a clockwise direction and the other is counter-clockwise in the West side of the room. Figs. 7.58.b and 7.60.b pass through the center of the inlet and outlet openings where, in the former figure the velocity at the midsection of the room close to the ceiling is relatively larger than that in the latter figure the reason for this is on account of the fact that the air jet in Fig. 7.58.b is relatively much cooler than that of Fig. 7.60.b and thus does not mix with the air in the room as does that of the latter figure. In Figs. 7.58.c and 7.60.c the general features and observations are comparable to that observed in Figs. 7.58.a and 7.60.a, respectively. The velocity vector plots of Figs. 7.59 and 7.61 have T_{in} and U_{in} identical to those of Figs. 7.58 and 7.60, respectively, but now horizontal x-z cross sections are considered. In Figs. 7.59.a and 7.61.a, the velocities close to the West wall are relatively
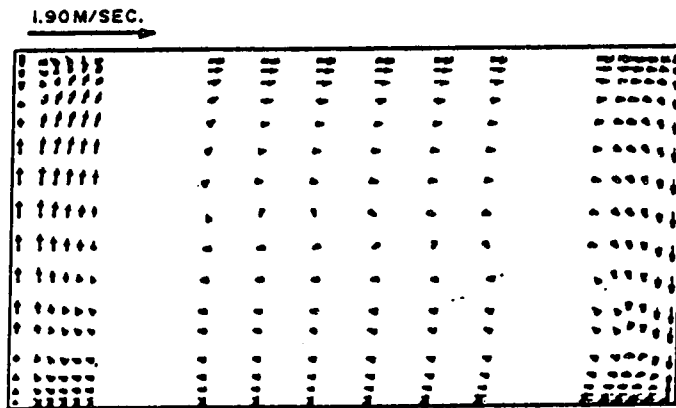
a) X-Y Section at Z = 0.600 m
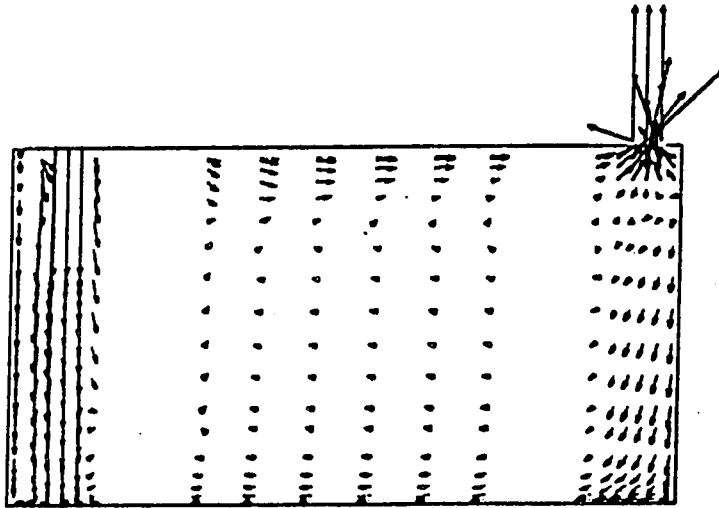
b) X-Y Section at Z = 1.850 m
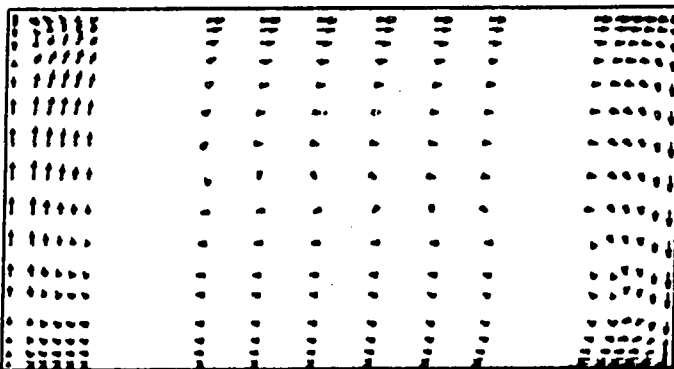
c) X-Y Section at Z = 3.100 m

Figure 7.58. Velocity vector plots in the X-Y plane at 9 am, Tin = 15 °C and Uin = 1.9 m/sec for the NN configuration.

261

190 M/SEC.
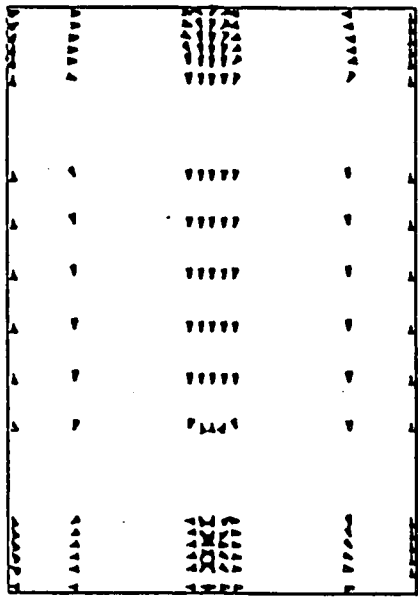
b) X-Z Section at Y = 0.756 m
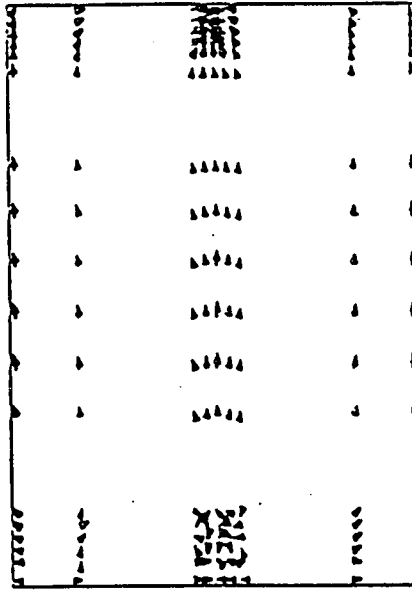
d) X-Z Section at Y = 2.510 m
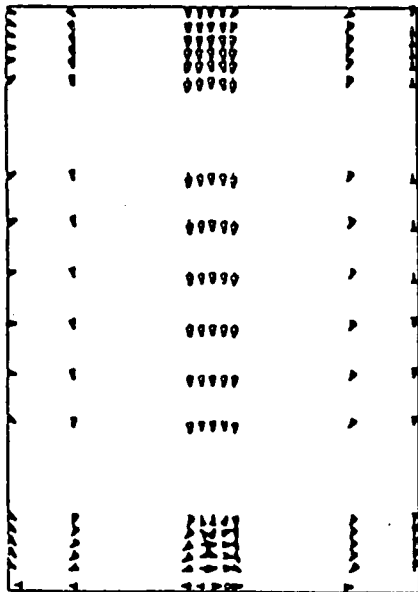
a) X-Z Section at Y = 0.141 m
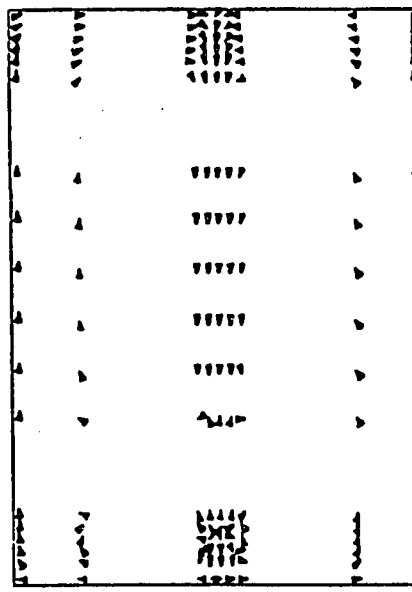
c) X-Z Section at Y = 1.759 m

Figure 7.59. Velocity vector plots in the X-Z plane at 9 am, Tin = 15 °C and
Uin = 1.9 m/sec for the NN configuration.
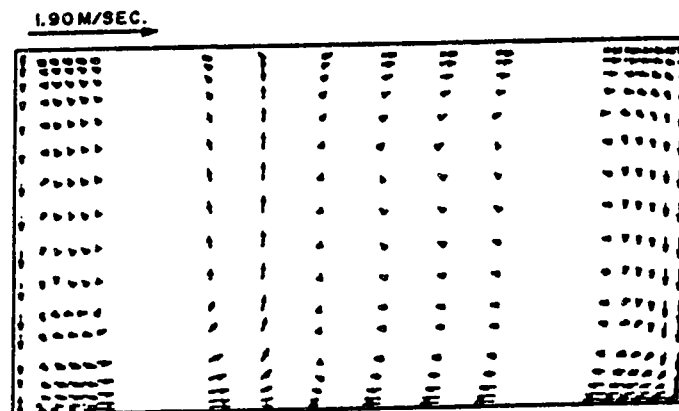
a) X-Y Section at Z = 0.600 m
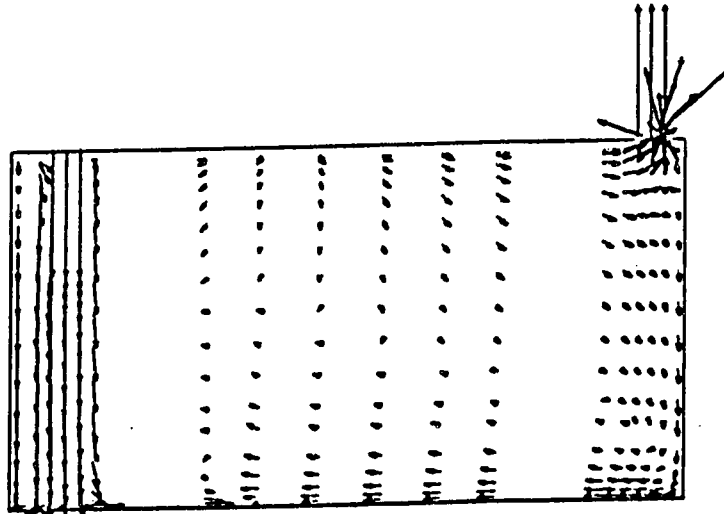
b) X-Y Section at Z = 1.850 m
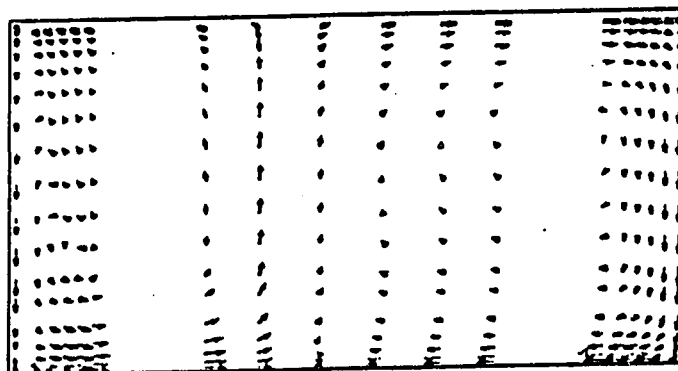
c) X-Y Section at Z = 3.100 m

Figure 7.60. Velocity vector plots in the X-Y plane at 9 am, Tin = 22 °C and Uin = 1.9 m/sec for the NN configuration.
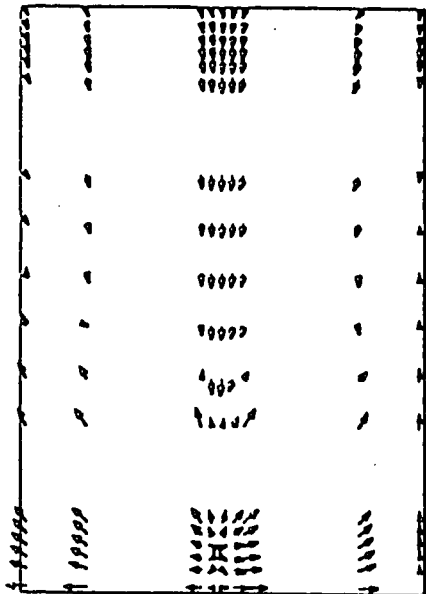
b) X-Z Section at Y = 0.756 m

d) X-Z Section at Y = 2.510 m

a) X-Z Section at Y = 0.141 m

c) X-Z Section at Y = 1.759 m

1.90 M/SEC.
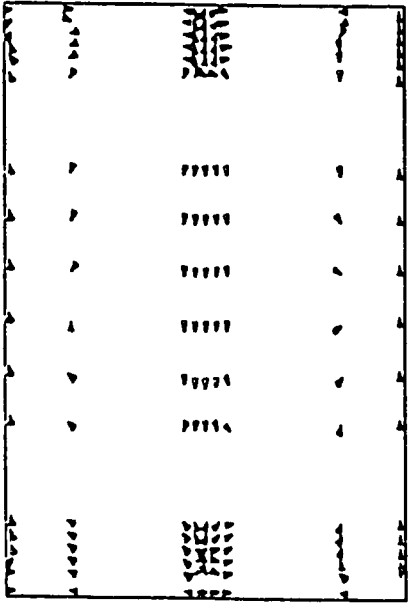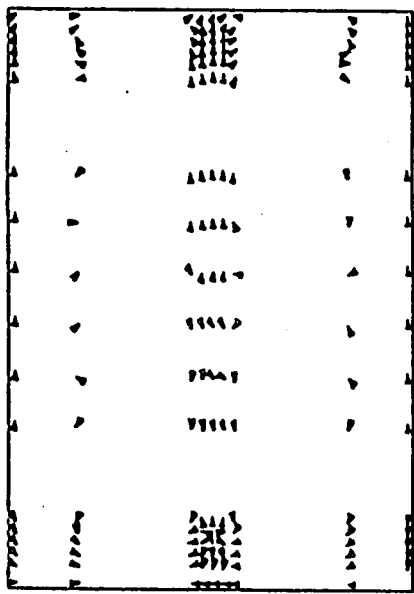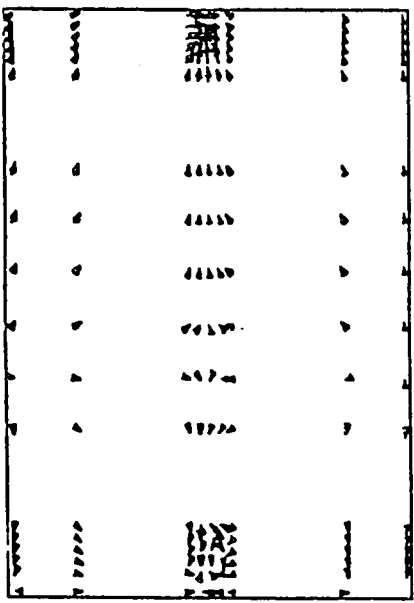
Figure 7.61. Velocity vector plots in the X-Z plane at 9 am, Tin = 22 °C and Uin = 1.9 m/sec for the NN configuration.

lower in the former figure than in the latter, and the general direction of the velocity vectors in Fig. 7.59.a is from the East wall to the West, in Fig. 7.61.a, the same occurs up-to about half the width of the room, but afterwards the velocities tend to move from West to East. Figs. 7.59.b and 7.59.c are comparable to Fig. 7.59.a, also Figs.7.61.b and 7.61.c are comparable to Fig. 7.61.a and not much may be deducted from these plots. In Fig. 7.59.d, the general direction of the vectors is from the West to the East and their relative values are higher than that of Fig.7.61.d in which no definite direction of flow is noticed.

(ii) Velocity Vector Plots at 12:00 Noon

In Figs. 7.62 and 7.64, the velocity vector plots in the vertical xy-plane is given, such that T_{in} and U_{in} in the former is 15.0°C and 1.9 m/sec, while that of the latter are 10.0°C and 2.2 m/sec., respectively. The general features for both these sets of figures are comparable, thus a discussion of only one shall be given, which is Fig. 7.62. In Fig. 7.62.a a vortex appears at the center of the room moving in a clockwise direction, with the upper and East sides of the vortex relatively faster than the other sides. In Fig. 7.62.b, the vortex remains but with relatively higher velocities at the upper part of the room and the bottom part. It should be noted that the extent of the air jet from the inlet in Fig. 7.62.b does not penetrate as deep as that in Fig. 7.64.b, due to the relatively higher U_{in} and lower T_{in} in the latter figure. The observations made in Fig. 7.62.a are extended to Fig. 7.62.c where the two have similar general features.

a) X-Y Section at Z = 0.600 m

b) X-Y Section at Z = 1.850 m

c) X-Y Section at Z = 3.100 m
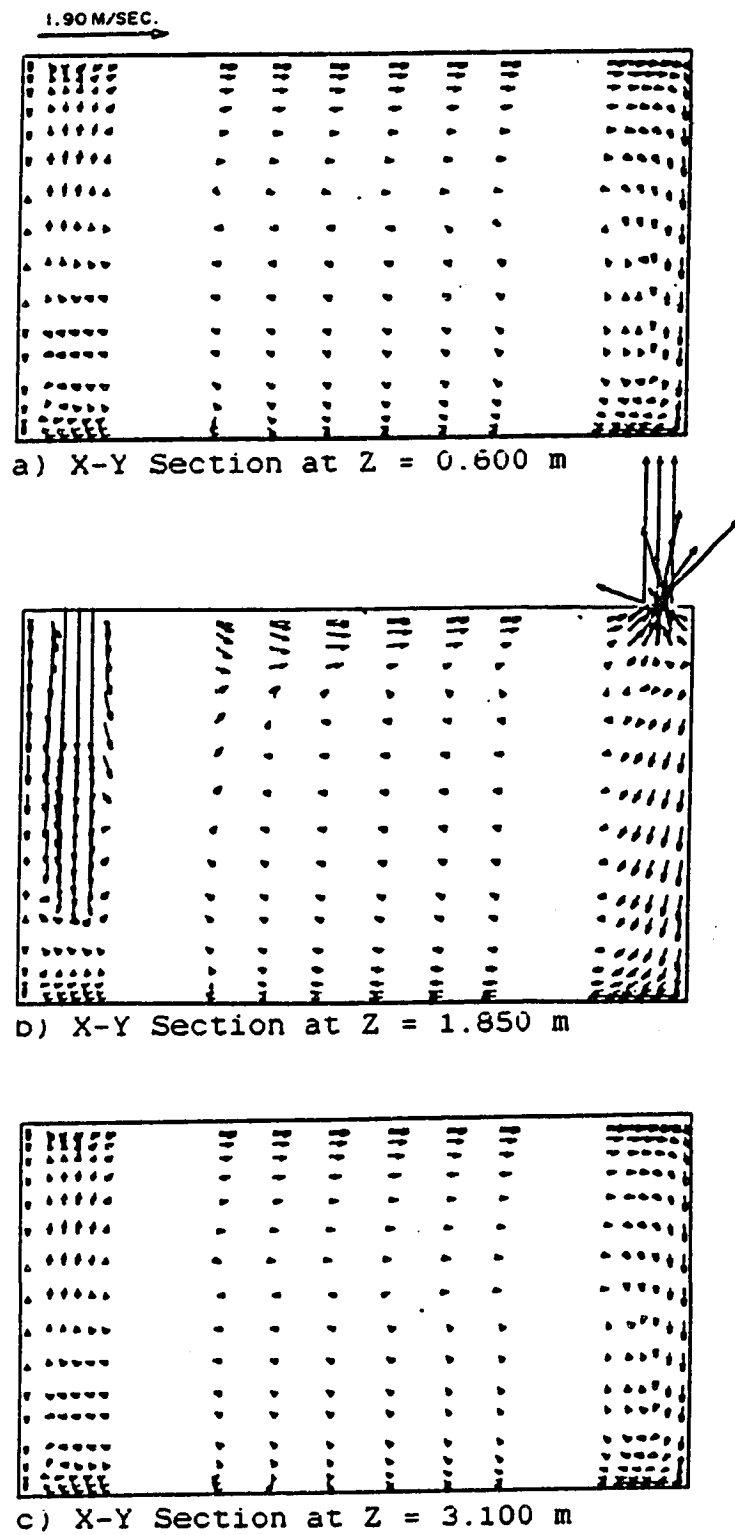
Figure 7.62. Velocity vector plots in the X-Y plane at noon, Tin = 15 °C and Uin = 1.9 m/sec for the NN configuration.

266

a) X-Z Section at Y = 0.141 m

b) X-Z Section at Y = 0.756 m

c) X-Z Section at Y = 1.759 m

d) X-Z Section at Y = 2.510 m

1.90M/SEC.
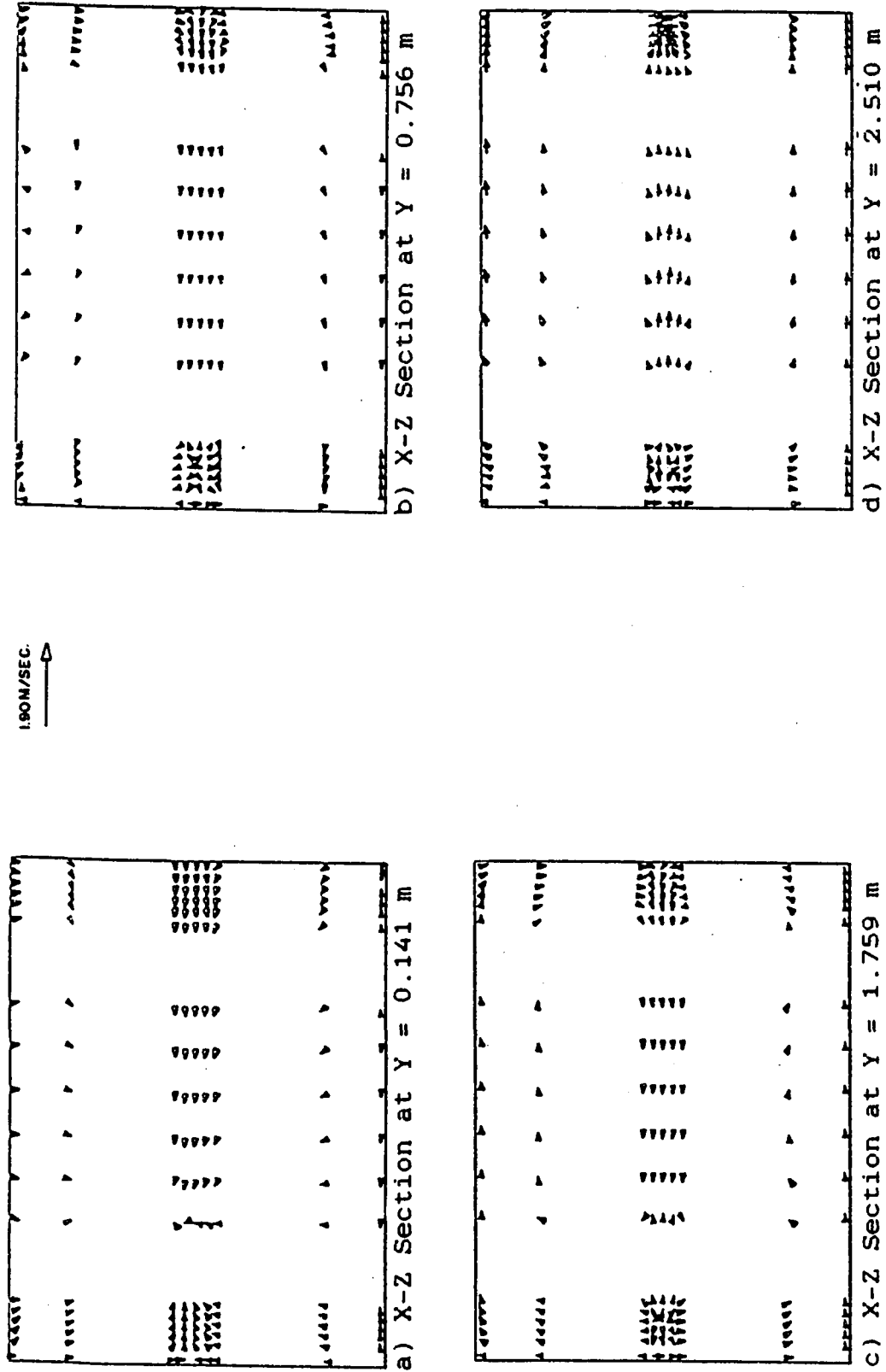
Figure 7.63. Velocity vector plots in the X-Z plane at noon, Tin = 15 °C and Uin = 1.9 m/sec for the NN configuration.
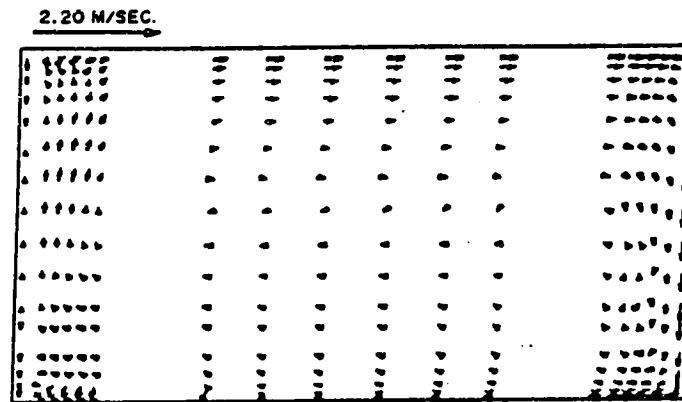
a) X-Y Section at Z = 0.600 m
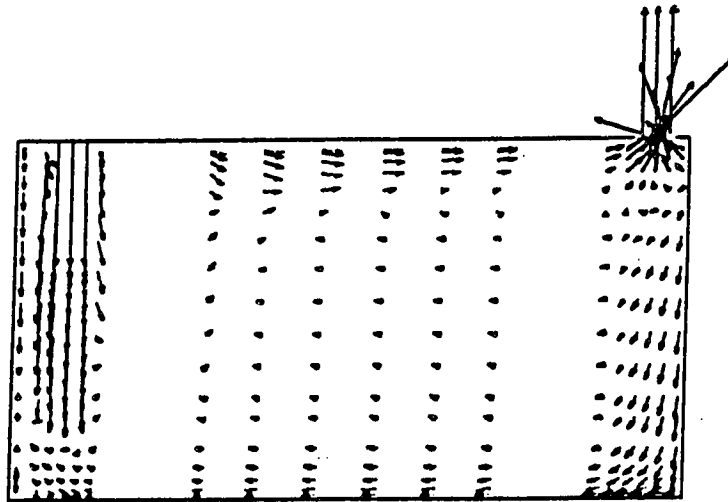
b) X-Y Section at Z = 1.850 m
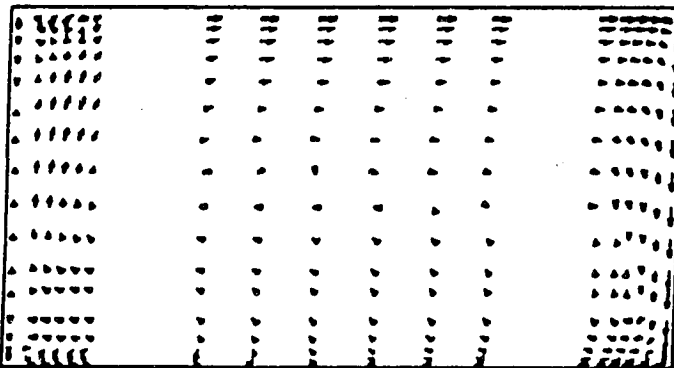
c) X-Y Section at Z = 3.100 m

Figure 7.64. Velocity vector plots in the X-Y plane at noon, Tin = 10 °C and Uin = 2.2 m/sec for the NN configuration.

2.20M/SEC.

b) X-Z Section at Y = 0.756 m

d) X-Z Section at Y = 2.510 m

a) X-Z Section at Y = 0.141 m

c) X-Z Section at Y = 1.759 m
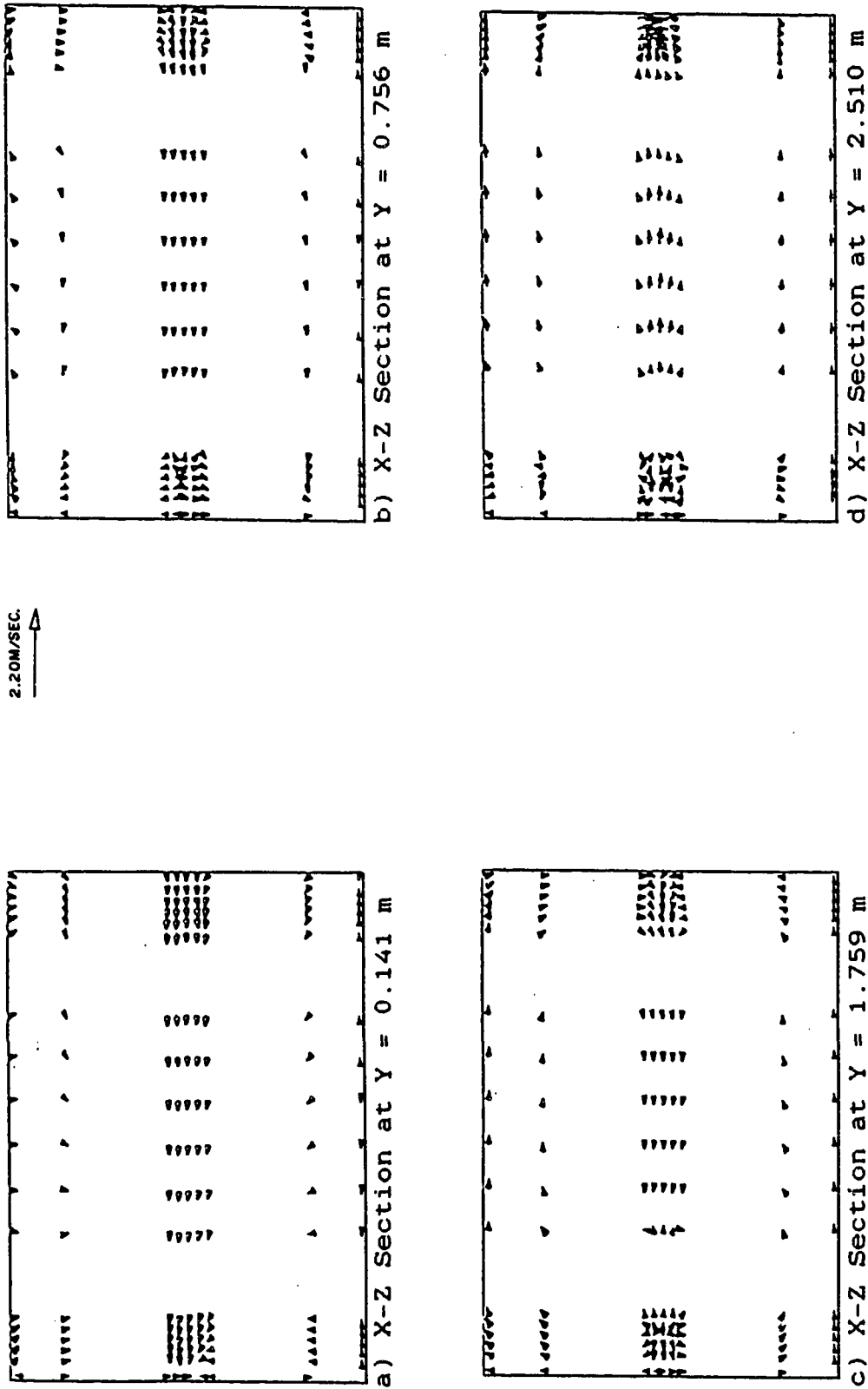
Figure 7.65. Velocity vector plots in the X-Z plane at noon, Tin = 10 °C and Uin = 2.2 m/sec for the NN configuration.

Figs. 7.63 and 7.65 have the same T_{in} and U_{in} of Figs.7.62 and 7.64, respectively, but plotted in the horizontal xz-plane. The general feature of these plots are quite comparable thus a discussion of only one set, i.e., Fig. 7.63 is given. In Fig. 7.63.a the velocity vectors tend to move in a general direction, from the East to the West, except in the vicinity of the West wall, this is observed more clearly in Fig. 7.63.b, where the majority of the velocities move from East to West. In Fig. 7.63.c, the velocities at the region of the symmetry plane of the room are generally still moving from East to West, while on both sides of this region the air moves in a generally opposite direction. In Fig. 7.63.d the velocity vectors are moving from West to East which is due to the suction by the outlet exhaust on the ceiling close to the East wall, and also possibly due to the spreading of the air jet as it leaves the inlet opening.

(iii) *Velocity Vector Plots at 3:00 P.M.*

The plots given in Figs. 7.66 and 7.68 are vertical xy-cross sectional plots having a T_{in} and U_{in} of 15°C and 1.9 m/sec. for the former figure and 15°C and 3.5 m/sec. for the latter. Figs. 7.67 and 7.69 have identical values of T_{in} and U_{in} as that in Figs. 7.66 and 7.68, respectively except that they are plotted in the horizontal xz-plane. In Fig. 7.66.a, a single vortex is observed at the center of the room with the velocities at the upper and Eastern sides relatively larger than those at the lower and Western sides of the room, whereas in Fig. 7.68.a, two vortices are observed such that there is a clockwise vortex in the Eastern half of the room and a counter-clockwise vortex in the Western half of the room having the relative velocities close to the floor and along the East wall higher than that close to the cei-

a) X-Y Section at Z = 0.600 m
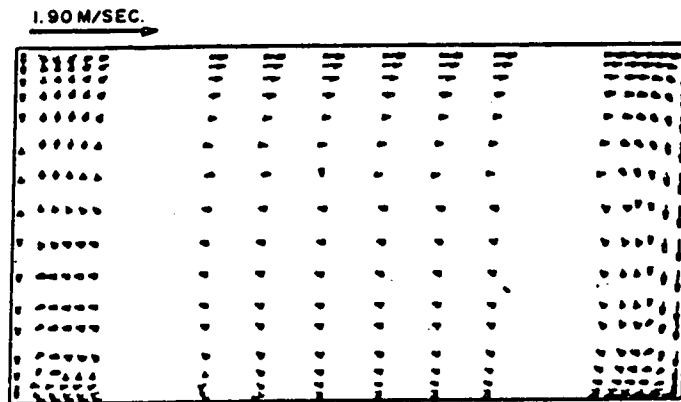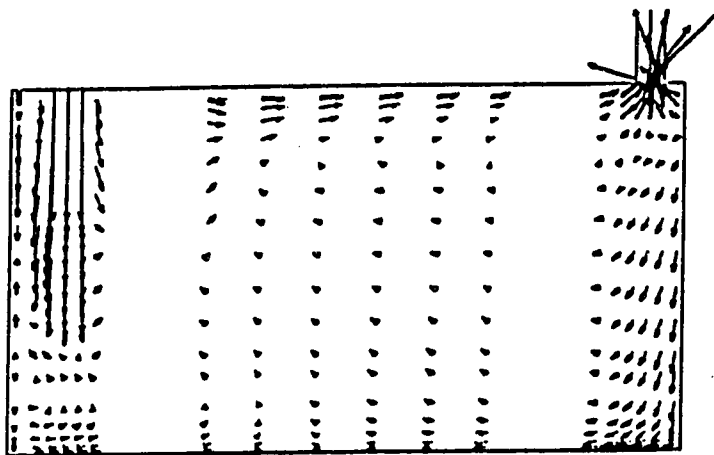
b) X-Y Section at Z = 1.850 m
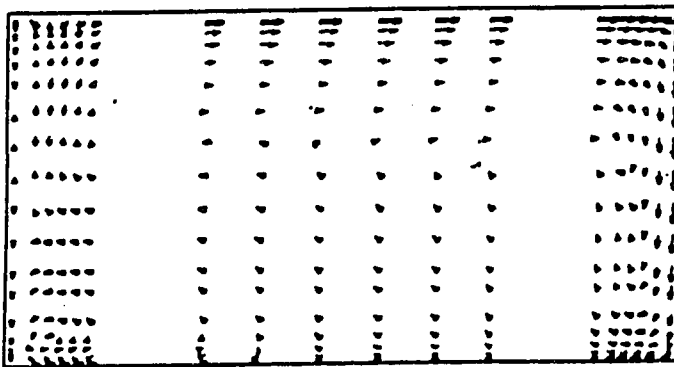
c) X-Y Section at Z = 3.100 m

Figure 7.66. Velocity vector plots in the X-Y plane at 3 pm, Tin = 15 °C and Uin = 1.9 m/sec for the NN configuration.

b) X-Z Section at Y = 0.756 m

d) X-Z Section at Y = 2.510 m

a) X-Z Section at Y = 0.141 m

c) X-Z Section at Y = 1.759 m

1.90 M/SEC.
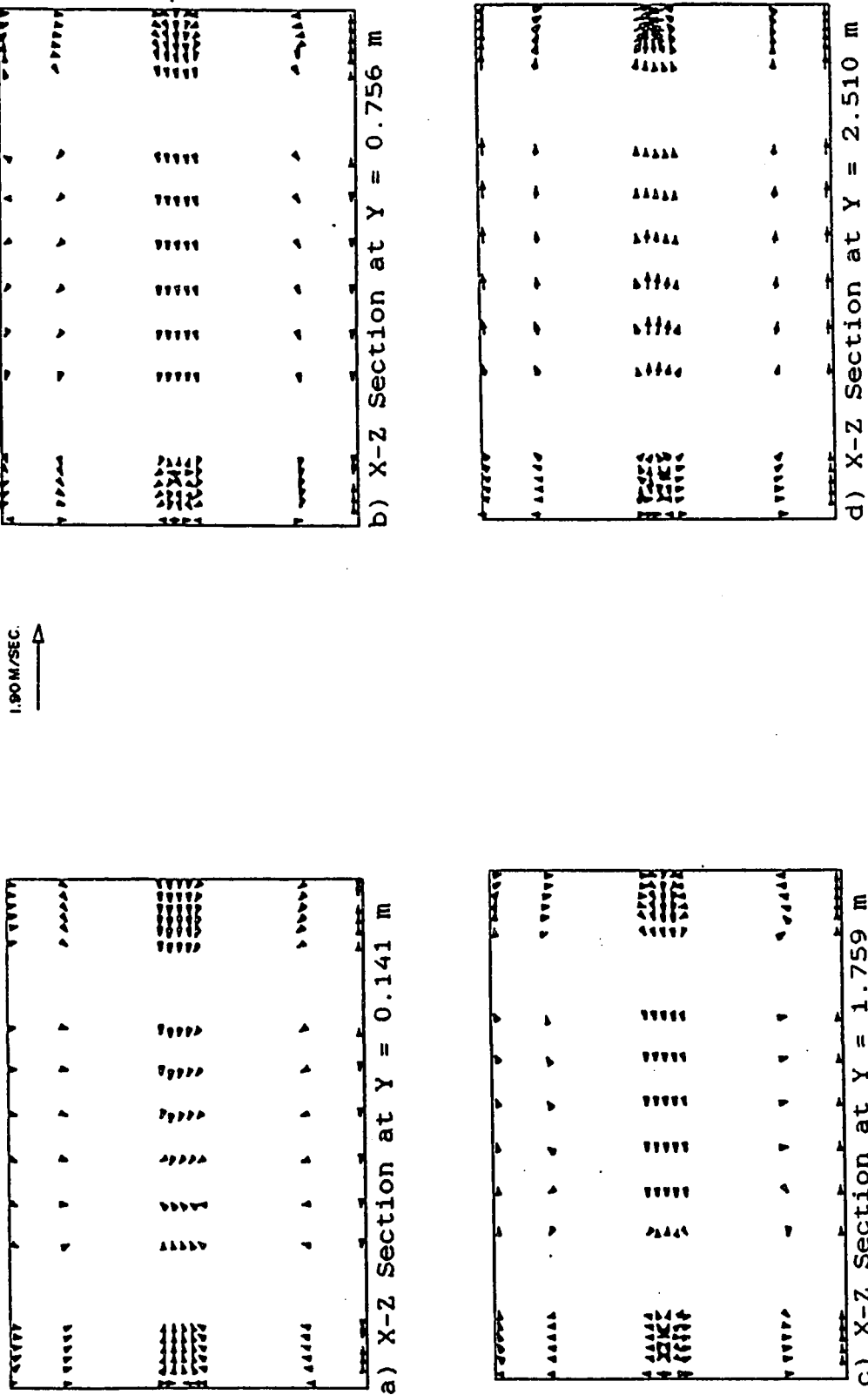
Figure 7.67. Velocity vector plots in the X-Z plane at 3 pm, Tin = 15 °C and Uin = 1.9 m/sec for the NN configuration.

3.50 M/SEC.
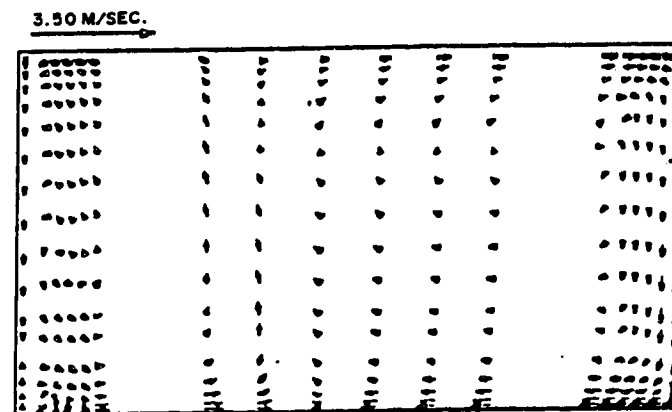
a) X-Y Section at Z = 0.600 m
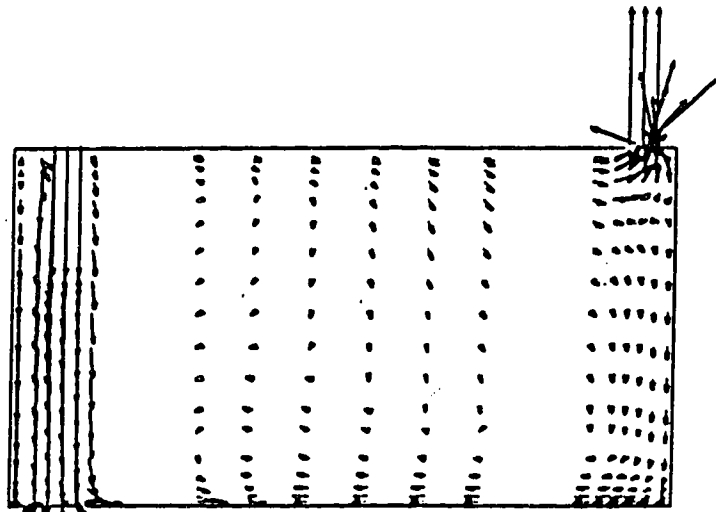
b) X-Y Section at Z = 1.850 m
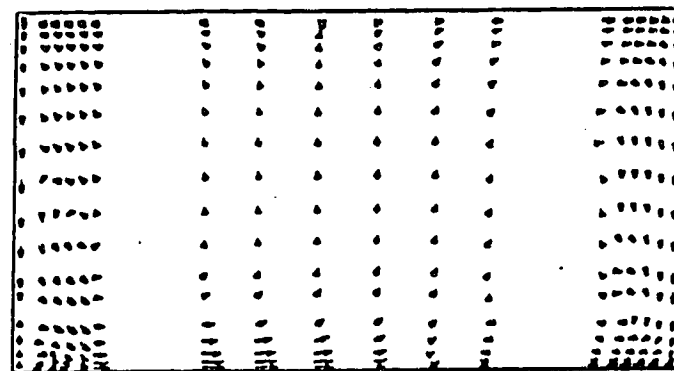
c) X-Y Section at Z = 3.100 m

Figure 7.68. Velocity vector plots in the X-Y plane at 3 pm, Tin = 15 °C and Uin = 3.5 m/sec for the NN configuration.

273

3.50M/SEC.

b) X-Z Section at Y = 0.756 m

d) X-Z Section at Y = 2.510 m

a) X-Z Section at Y = 0.141 m

c) X-Z Section at Y = 1.759 m
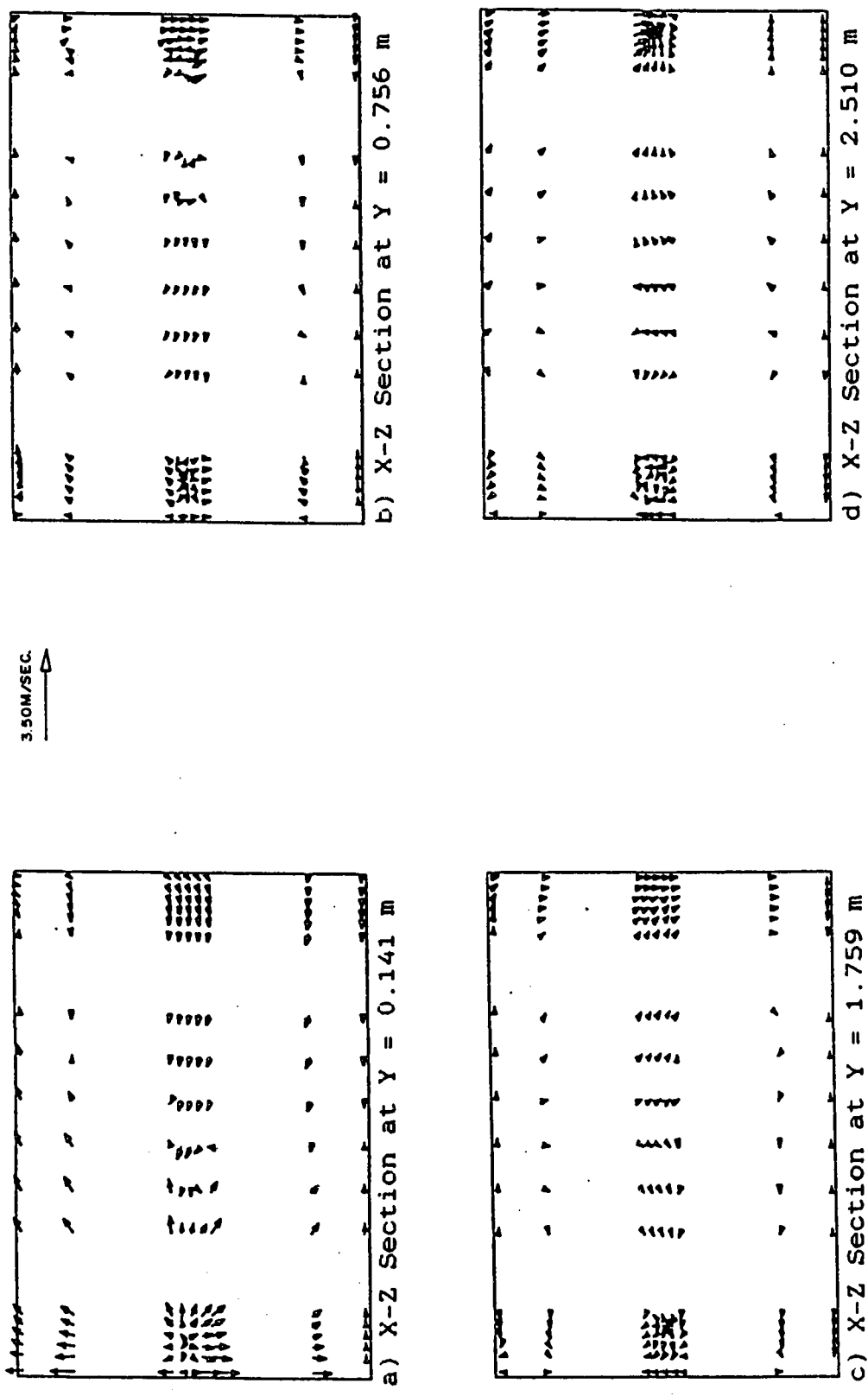
Figure 7.69. Velocity vector plots in the X-Z plane at 3 pm, Tin = 15 °C and Uin = 3.5 m/sec for the NN configuration.

ling and along the West wall. Figs. 7.66.b and 7.68.b have vortices comparable to those observed in Figs. 7.66.a and 7.68.a except that the Western side has relatively larger velocities due to the air jet. The penetration depth of the air jet in Fig.7.66.b reaches only to about 2/3rds of the room height before dyeing out, while in Fig. 7.68.b the air jet reaches the floor on account of the relatively higher U_{in} in the latter figure. The vector plots of Figs. 7.66.c and 7.68.c are comparable to those of Figs. 7.66.a and 7.68.a, respectively. In Fig. 7.67.a, there is a general tendency for the velocity to move from the East side to the West side of the room, except in the region of the West wall where the flow is opposite, while in Fig. 7.69.a a similar observation is noticed in the Eastern half of the room at the region of the symmetry plane, while on both sides of this plane, the flow is relatively higher and moving in a generally opposite direction also in the region adjacent to the West wall, air spreads in all directions due to the impingement of the air jet on the floor. The general features of Figs. 7.67.b and 7.67.c are comparable where the overall tendency of the flow is from the East to the West side of the room. Also Figs. 7.69.b and 7.69.c are comparable such that the flow in the center of the room is from East to West, while in the region close to the East wall, the flow direction is from the left side wall to the right side wall and in the region close to the West wall, the air flow is random, possibly due to the impingement of the air jet on the floor. Figs. 7.67.d and 7.69.d are comparable, except that the velocities in the former are relatively larger than that in the latter which is due to the spreading of the airjet and engulfment of the stagnant surroundings much sooner in Fig. 7.67.d.

7.2.2.2 Velocity Profiles

As in the WE configuration, velocity profiles have been plotted, but as U_{in} is in the direction of the y-axis, the velocity profiles have been taken normal to U_{in} and at various heights above the floor both at the mid-plane of the room and close to a side wall. These are given now.

(i) Velocity Profiles at 9:00 A.M.

The plots of Figs. 7.70 and 7.72 are taken at the mid-plane of the room and the value of T_{in} used, is equal to 15°C and 22°C , respectively, while U_{in} in both are the same and equal to 1.9 m/sec. . Figs. 7.71 and 7.73 are velocity profiles plotted close to the right side wall of the room and have values of T_{in} and U_{in} identical to those of Figs. 7.70 and 7.71, respectively. Comparing Figs. 7.70.a and 7.72.a, it is obvious that the general features are similar except that the extent of the velocity due to the air jet from the inlet, is relatively much deeper in the latter figure. Furthermore, the absolute slope of the dimensionless velocity profile is greater than zero beyond the air jet up to about 1/3 of the room length, and opposite the outlet opening there is a negative velocity occurring in both figures which is on account of the proximity to the East wall region which is relatively warmer causing the cooler adjacent air to move down due to buoyancy. What has been observed in Figs. 7.70.a and 7.72.a, is comparable to that appearing in Figs. 7.70.b and 7.72.b, respectively except that the relative magnitudes in the latter group of figures are more pronounced. The same reasoning follows for Figs. 7.70.c and 7.72.c, except that we not-

a) Y/H = 0.051 and Z/W = 0.5
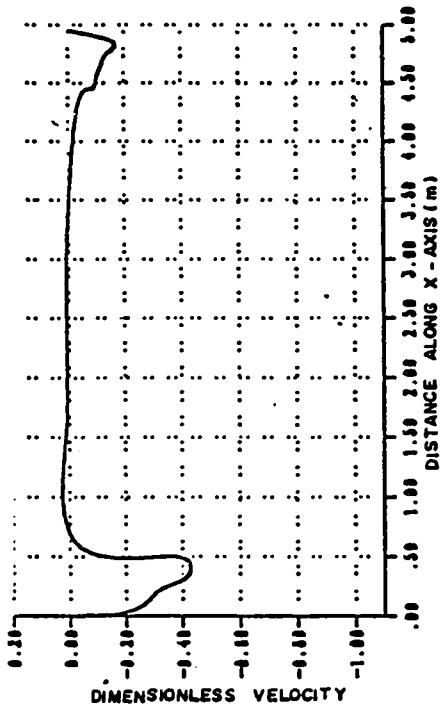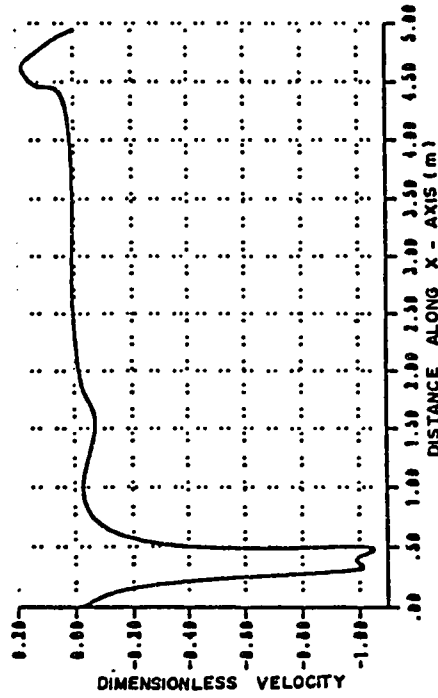
b) Y/H = 0.28 and Z/W = 0.5
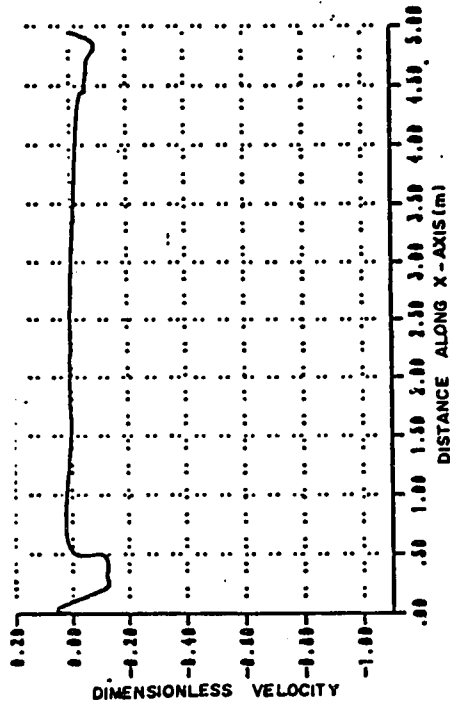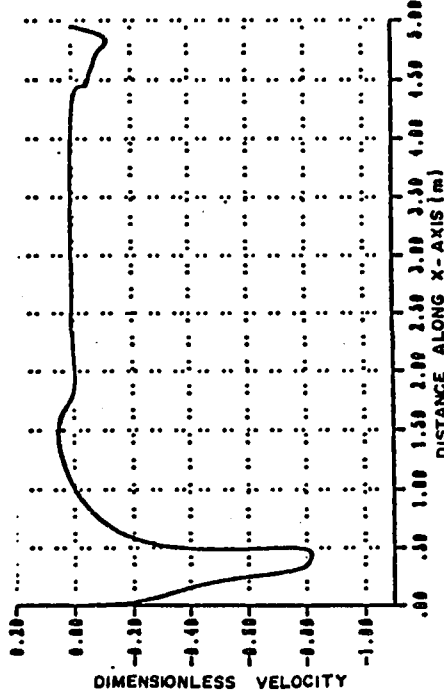
c) Y/H = 0.64 and Z/W = 0.5

d) Y/H = 0.91 and Z/W = 0.5

Figure 7.70. Dimensionless velocity profiles over length of room at mid section at 9 am, Tin = 15 °C and Uin = 1.9 m/sec for the NN configuration.
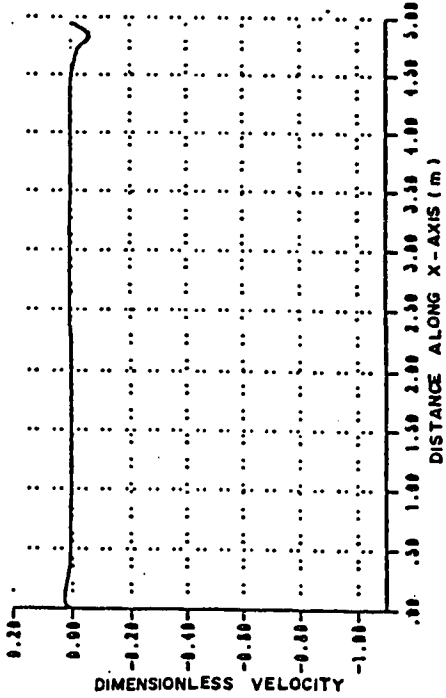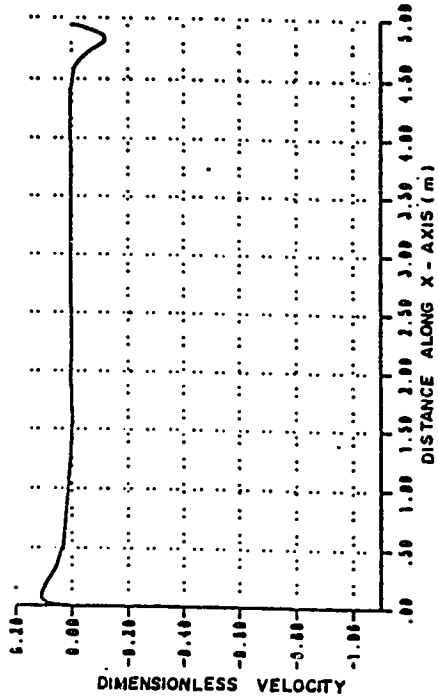
b) Y/H = 0.28 and Z/W = 0.84
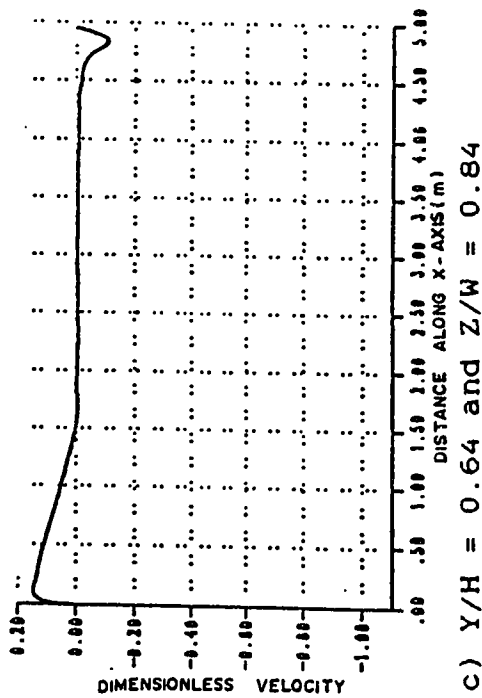
a) Y/H = 0.051 and Z/W = 0.84
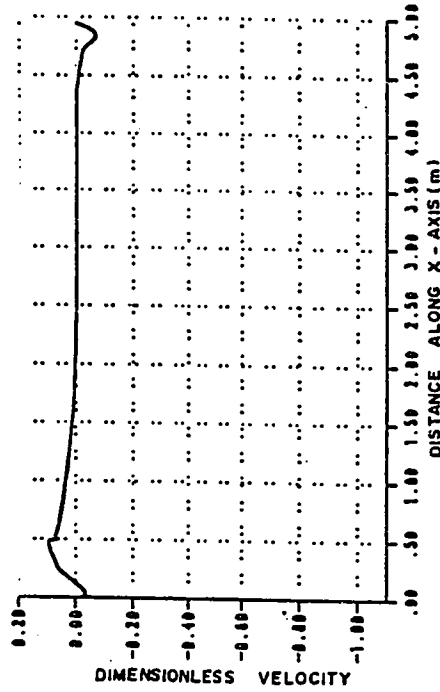
d) Y/H = 0.91 and Z/W = 0.84

c) Y/H = 0.64 and Z/W = 0.84

Figure 7.71. Dimensionless velocity profiles over length of room near right wall at 9 am, Tin = 15 °C and Uin = 1.9 m/sec for the NN configuration.
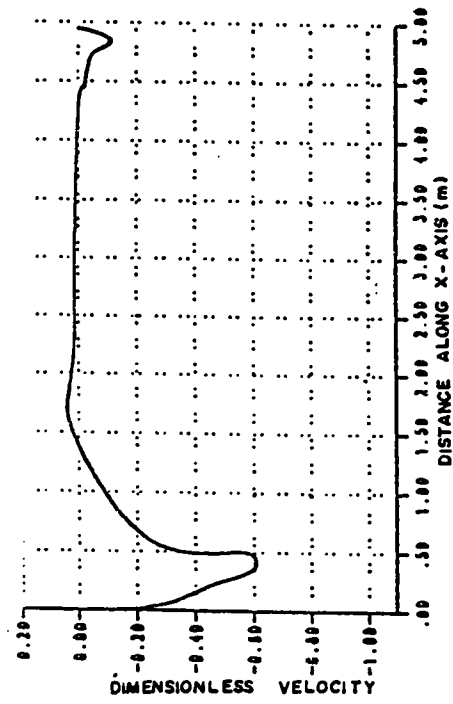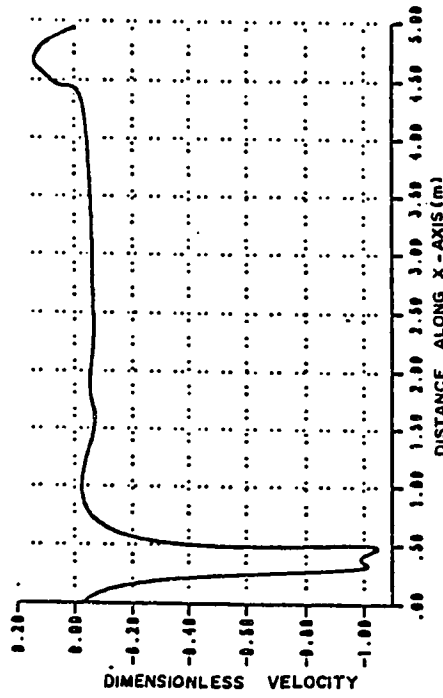
a) Y/H = 0.051 and Z/W = 0.5
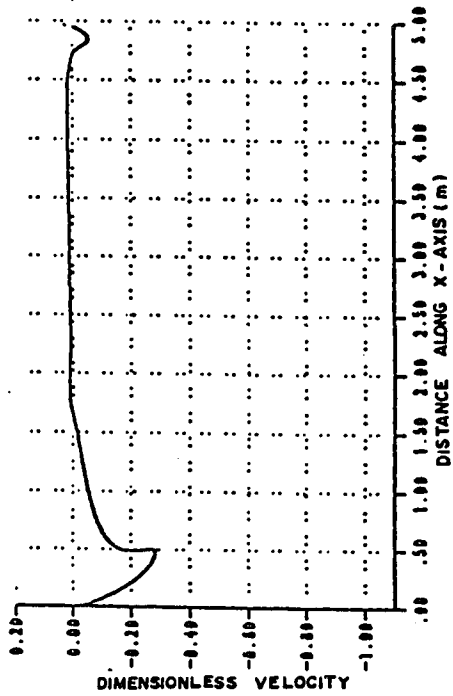
b) Y/H = 0.28 and Z/W = 0.5
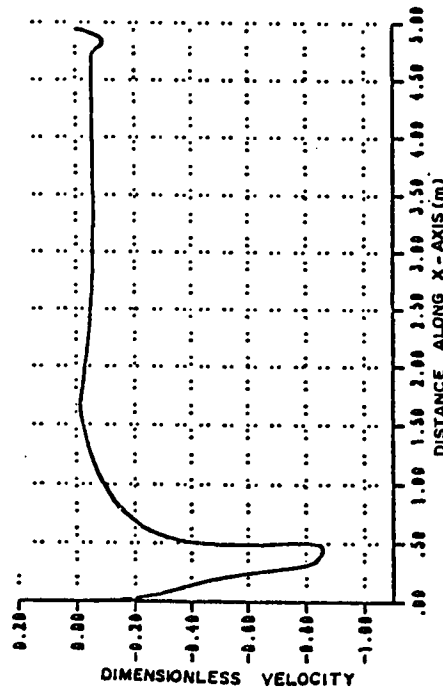
c) Y/H = 0.64 and Z/W = 0.5

d) Y/H = 0.91 and Z/W = 0.5

Figure 7.72. Dimensionless velocity profiles over length of room at mid section at 9 am, Tin = 22 °C and Uin = 1.9 m/sec for the NN configuration.
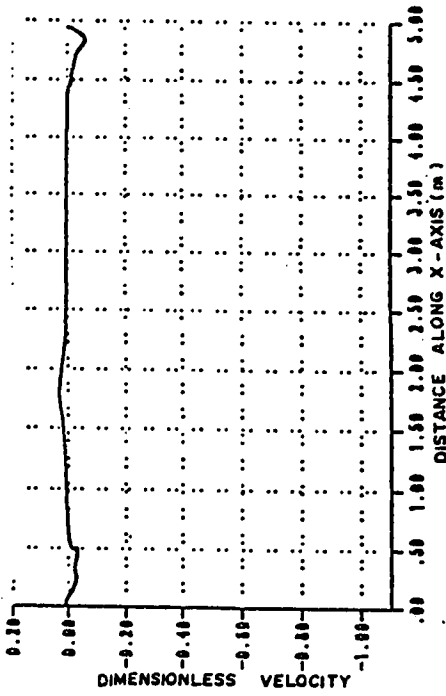
b) Y/H = 0.28 and Z/W = 0.84

d) Y/H = 0.91 and Z/W = 0.84

a) Y/H = 0.051 and Z/W = 0.84
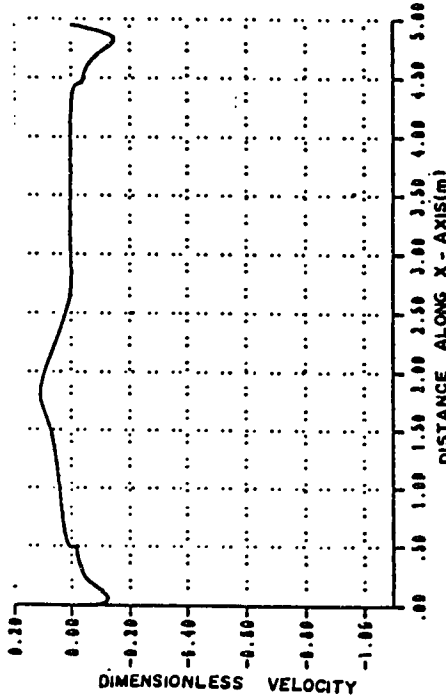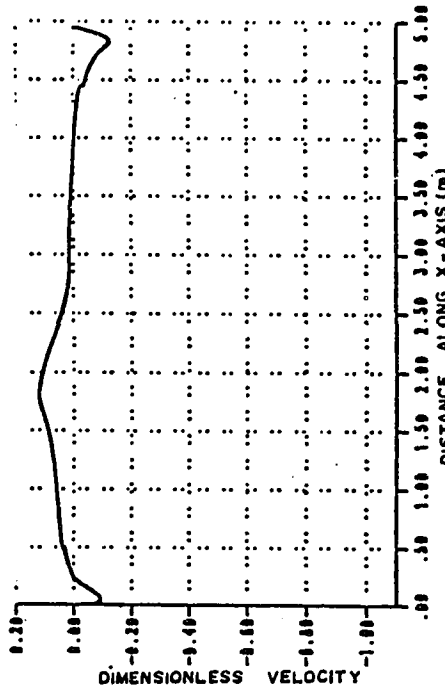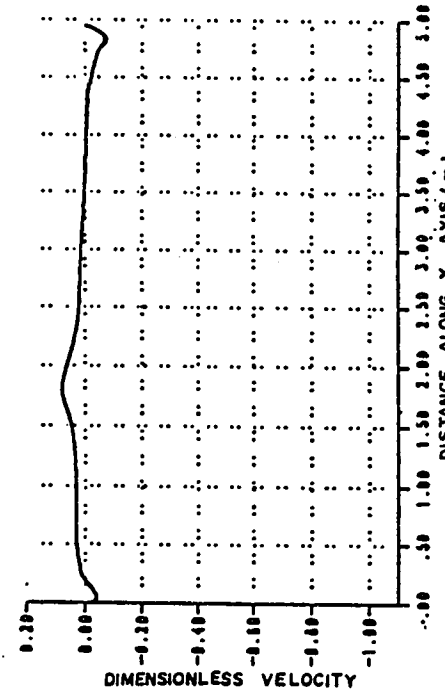
c) Y/H = 0.64 and Z/W = 0.84

Figure 7.73. Dimensionless velocity profiles over length of room near right wall at 9 am, Tin = 22 °C and Uin = 1.9 m/sec for the NN configuration.

ice the negative velocity peak close to the East wall is reduced in both fig-
ures which is due to the fact that we are relatively closer to the outlet
opening at which suction occurs. Furthermore, a positive velocity appears
just after the inlet opening and then it drops to zero, up to the outlet edge
in the former figure while in the latter, this is not observed. In Figs. 7.70.d
and 7.72.d, the velocity profile opposite the inlet is mostly intact with the
peak extending beyond -1.0, probably due to the buoyancy force, while the
velocity profile opposite the outlet opening is positive and the peak of this
profile in the former figure is relatively smaller than that in the latter and
the velocity profile in the central part of the room is negative in Fig.
7.72.d, while that in Fig. 7.70.d is mostly zero. The profiles in Figs. 7.71.a
and 7.73.a are very close to zero, except close to the East wall, where in
both cases there is a small negative peak of the velocity profile, while close
to the West wall, a positive profile appears in the former figure, while a
negative profile appears in the latter. Figs. 7.71.b to 7.71.d are generally
comparable such that a positive peak of the velocity profile appears close
to the West wall while a negative peak appears close to the East wall and
the remaining part of the velocity profile except close to the West Wall, is
nearly zero. As above, Figs. 7.73.b to 7.73.d are comparable such that
negative peaks of the velocity profile appear on the East and West sides of
the room, while at the center of the room in the Western half positive
velocities appear, and on the opposite side of this the velocities are nearly
zero up to the edge of the outlet.

(ii) Velocity Profiles at 12:00 Noon

The velocity profiles of Figs.7.74 and 7.75 are taken at the mid-plane of the room and close to the right wall of the room, respectively having a T_{in} = 15°C and U_{in} = 1.9 m/sec., whereas Figs. 7.76 and 7.77 are plotted in the same locations of Figs. 7.74 and 7.75, respectively and have T_{in} = 10°C and U_{in} = 2.2 m/sec.. The dimensionless velocity profiles in Figs. 7.74 and 7.76 are comparable, and for brevity, a discussion of the former is given. In Fig. 7.74.a the majority of the velocities in the y-direction are nearly zero except close to the East wall, where a negative peak profile appears, it should be noted that a slightly negative peak occurs in the vicinity of the West wall while a slightly positive peak appears close to the same location of Fig. 7.76.a. In Fig.7.74.b, the negative peaks of the velocity profile appear more pronounced on both the East and West walls with the positive velocities appearing on both sides of the air jet, emerging from the inlet. In Fig.7.74.c, the velocity profile of the air jet close to the West wall is relatively much larger and the positive velocity profile East of the inlet opening remains, but that adjacent to the West wall disappeared, and the negative peak of the velocity profile close to the East wall is relatively smaller, while the remaining part of the room has a zero velocity profile. In Fig. 7.74.d, there appears to be no positive velocity except opposite the outlet opening, while the peak of the velocity profile opposite the inlet opening has extended to about -1.0 due to the proximity to the ceiling, and the positive profile on the East side of the inlet opening has now become completely negative, whereas the remaining part of the veloc-

282
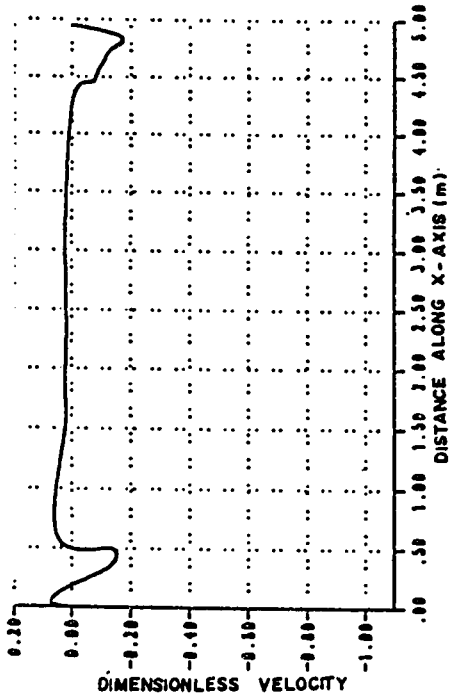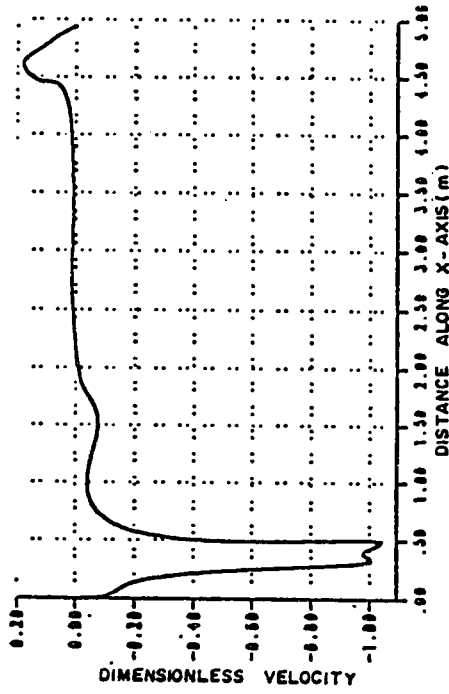
b) Y/H = 0.28 and Z/W = 0.5
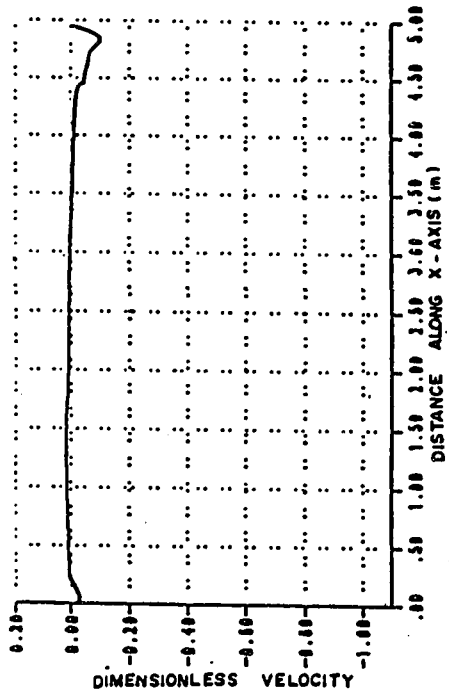
d) Y/H = 0.91 and Z/W = 0.5
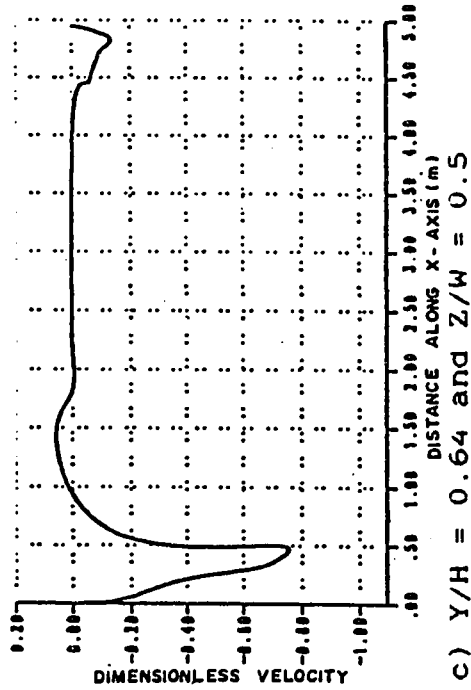
a) Y/H = 0.051 and Z/W = 0.5

c) Y/H = 0.64 and Z/W = 0.5

Figure 7.74. Dimensionless velocity profiles over length of room at mid section at noon, Tin = 15 °C and Uin = 1.9 m/sec for the NN configuration.
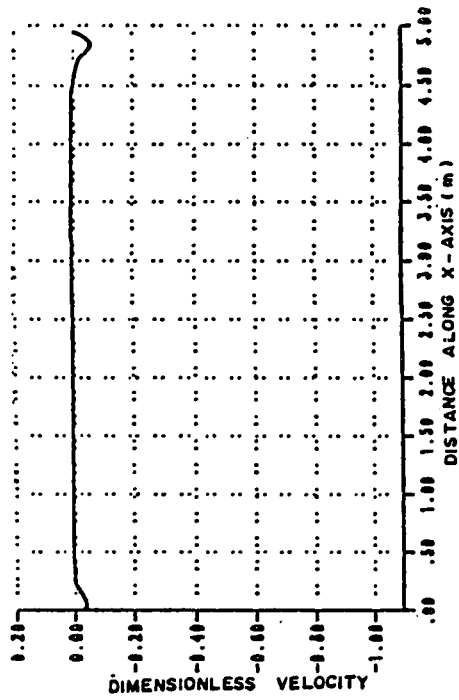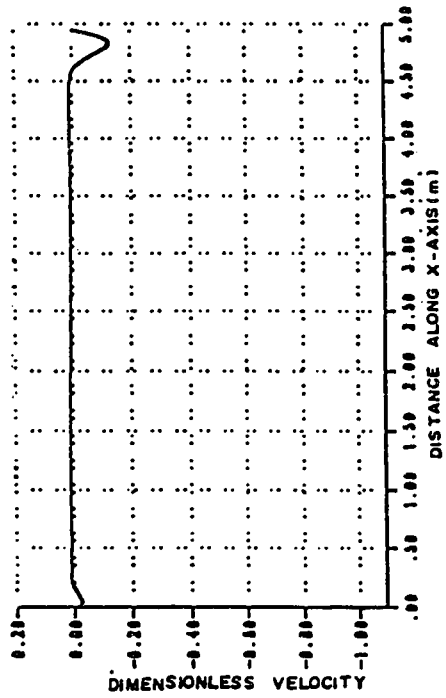
b) Y/H = 0.28 and Z/W = 0.84
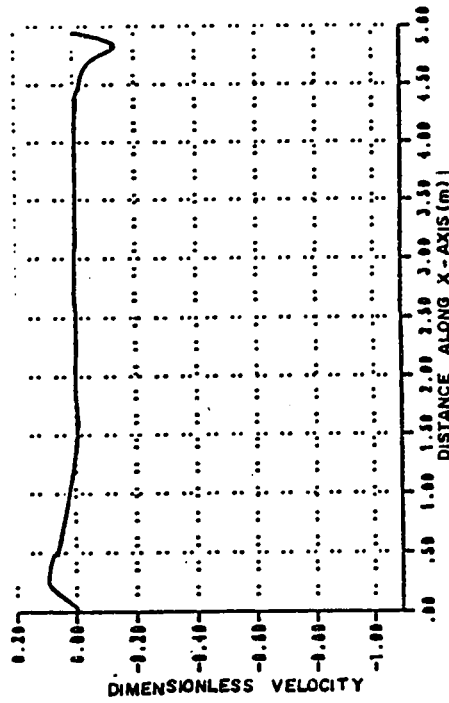
d) Y/H = 0.91 and Z/W = 0.84
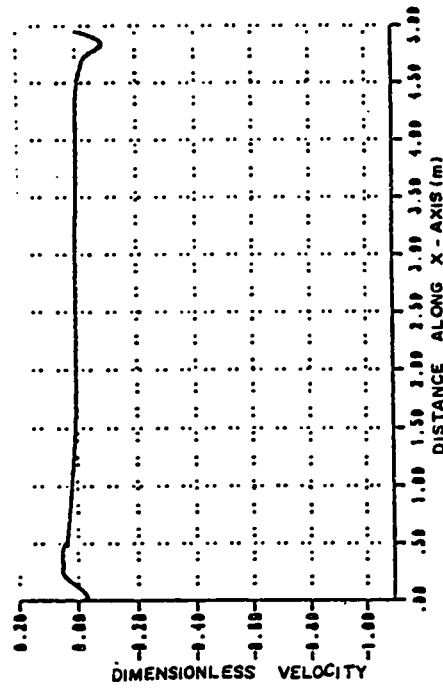
a) Y/H = 0.051 and Z/W = 0.84

c) Y/H = 0.64 and Z/W = 0.84

Figure 7.75. Dimensionless velocity profiles over length of room near right wall at noon, Tin = 15 °C and Uin = 1.9 m/sec for the NN configuration.
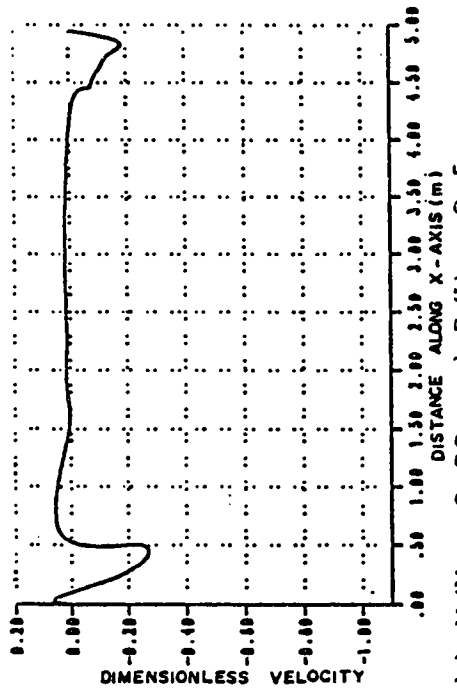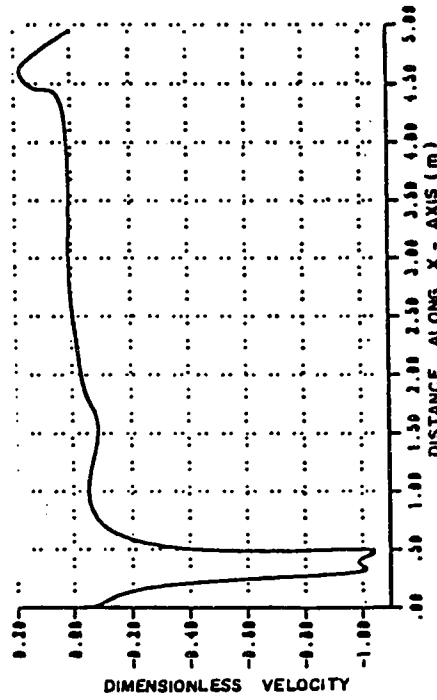
b) Y/H = 0.28 and Z/W = 0.5
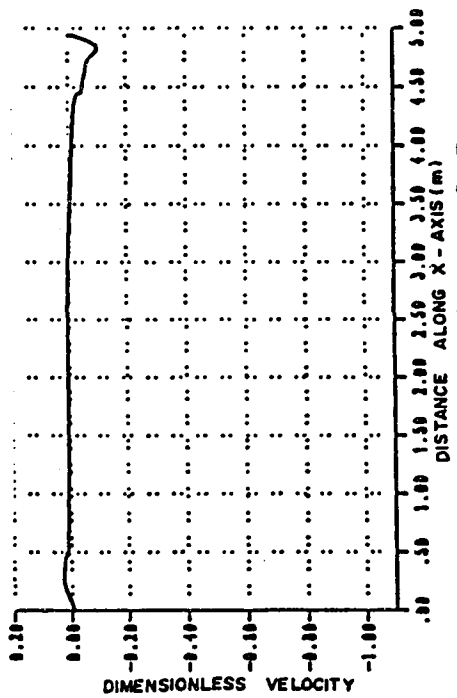
d) Y/H = 0.91 and Z/W = 0.5
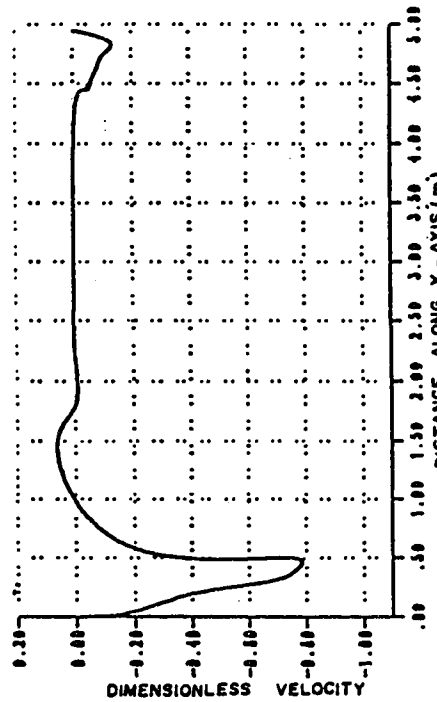
a) Y/H = 0.051 and Z/W = 0.5

c) Y/H = 0.64 and Z/W = 0.5

Figure 7.76. Dimensionless velocity profiles over length of room at mid section at noon, Tin = 10 °C and Uin = 2.2 m/sec for the NN configuration.
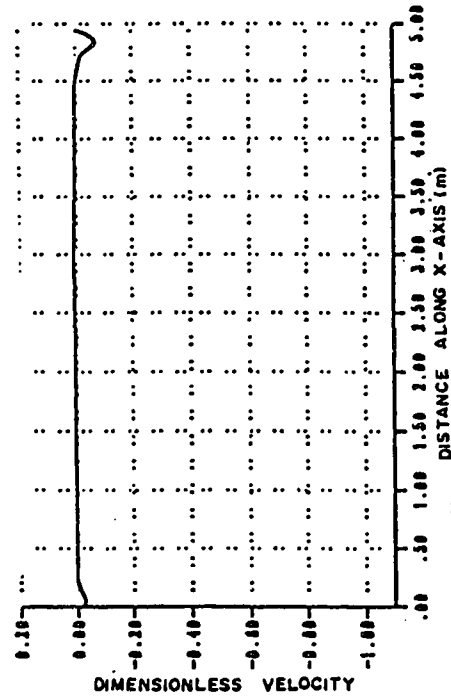
b) Y/H = 0.28 and Z/W = 0.84

d) Y/H = 0.91 and Z/W = 0.84

a) Y/H = 0.051 and Z/W = 0.84
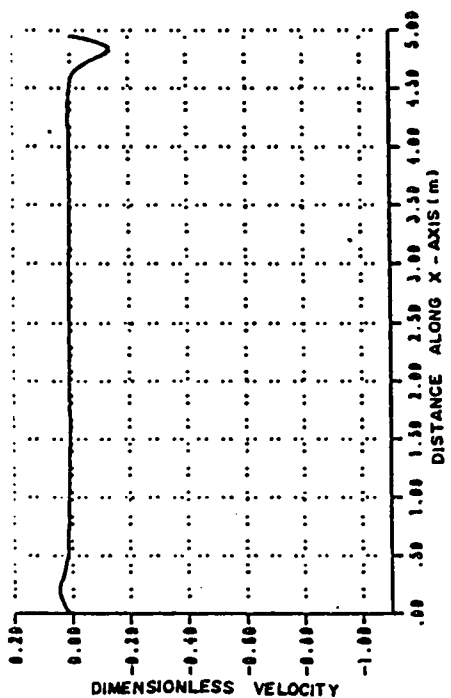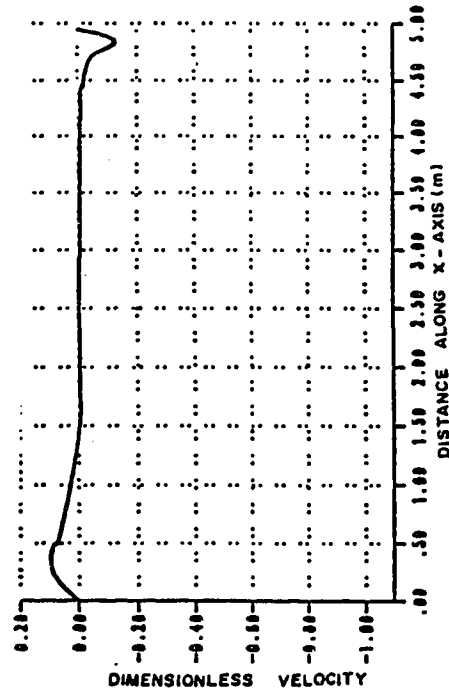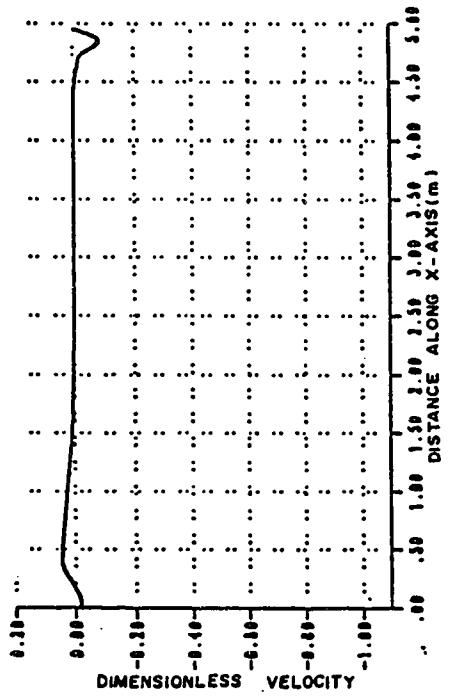
c) Y/H = 0.64 and Z/W = 0.84

Figure 7.77. Dimensionless velocity profiles over length of room near right wall at noon, Tin = 10 °C and Uin = 2.2 m/sec for the NN configuration.

ity profile up to the edges of the outlet, are nearly zero. The velocity profiles in Figs. 7.75 and 7.77 are comparable, and a discussion of the former is given. In Fig. 7.75a, the majority of the dimensionless velocity profile is zero, except at the East and West sides of the room where a negative velocity profile peak appears. In Fig.7.75.b the peak of the negative velocity profile close to the East wall extends lower, while that close to the West wall almost completely disappears, whereas in Fig. 7.77.b the peak close to the West wall is positive. Figs. 7.75.c and 7.75.d are similar except that the peaks of the velocity profiles are relatively smaller in the latter and these peaks appear as a positive velocity profile close to the West wall and a negative velocity profile close to the East wall in both figures.

(iii) Velocity Profiles at 3:00 P.M.

The plots of Figs. 7.78 and 7.80 are both plotted at the symmetry plane of the room having a U_{in} of 1.9 m/sec. in the former figure and 3.5 m/sec. in the latter, while T_{in} in both is the same and equal to 15°C. Figs.7.79 and 7.81 are plotted close to the right wall of the room having U_{in} and T_{in} as given in Figs. 7.78 and 7.80, respectively. In Fig. 7.78.a, the velocity profile is nearly zero except close to the East and West walls, where negative peaks of the velocity profile appear. In Fig. 7.80.a, the depth of penetration of the air jet from the inlet is relatively larger than that of Fig. 7.78.a due to the relatively larger U_{in} in the former figure furthermore, the negative peak close to the East wall of the latter figure is larger. Moving upwards closer to the ceiling, we see that the negative peak of the velocity profile adjacent to the East wall, in both Figs. 7.78.b and 7.80.b have increased and the negative peak of the profile opposite the

287
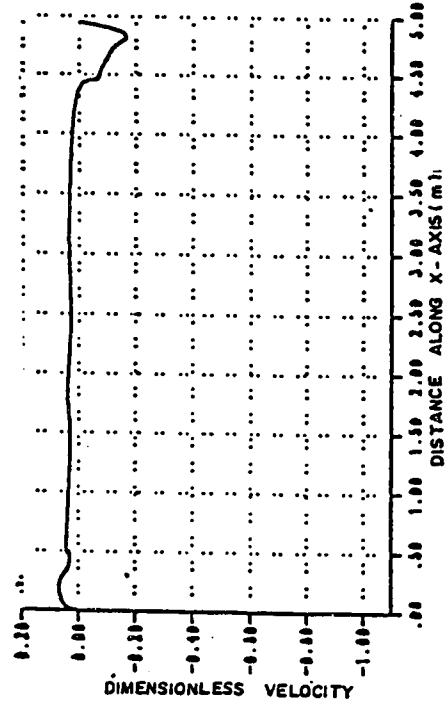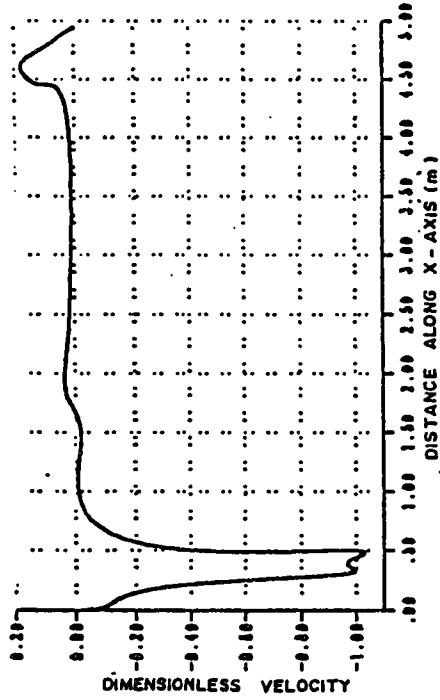
a) Y/H = 0.051 and Z/W = 0.5
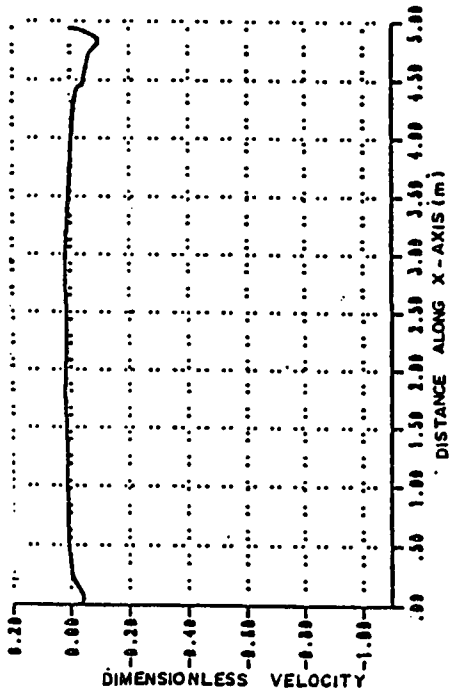
b) Y/H = 0.28 and Z/W = 0.5
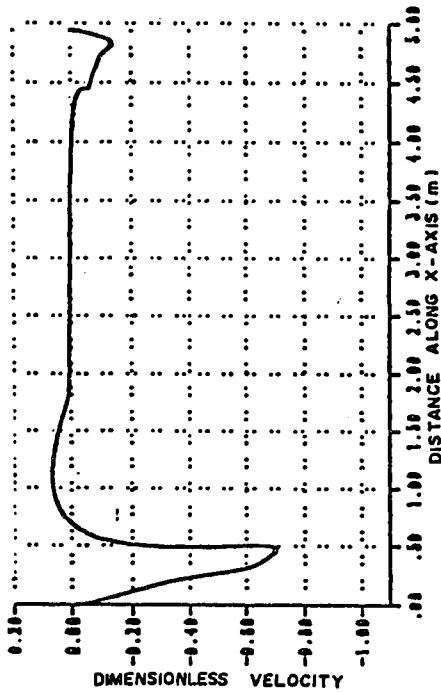
c) Y/H = 0.64 and Z/W = 0.5

d) Y/H = 0.91 and Z/W = 0.5

Figure 7.78. Dimensionless velocity profiles over length of room at mid section at 3 pm, Tin = 15 °C and Uin = 1.9 m/sec for the NN configuration.
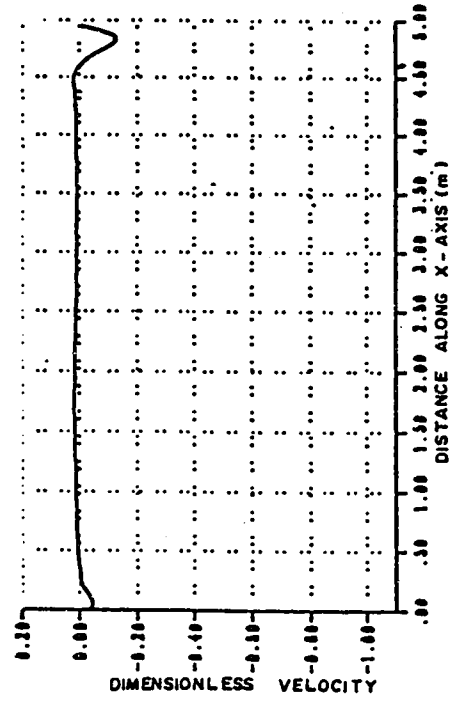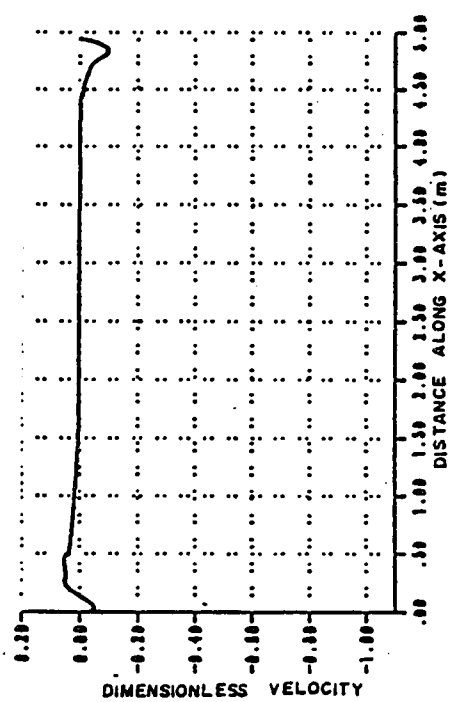
b) Y/H = 0.28 and Z/W = 0.84
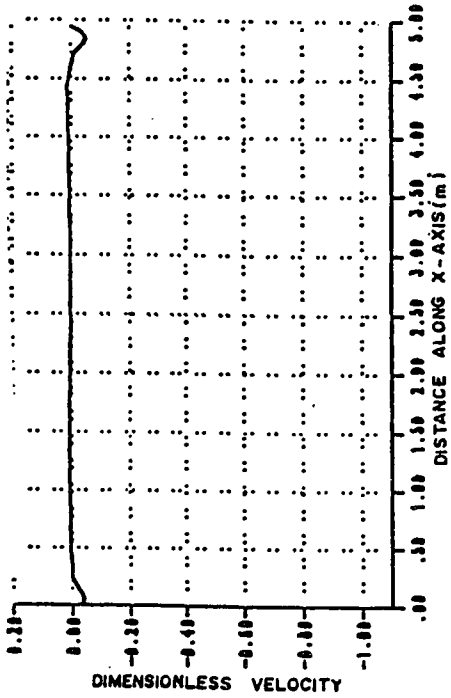
a) Y/H = 0.051 and Z/W = 0.84
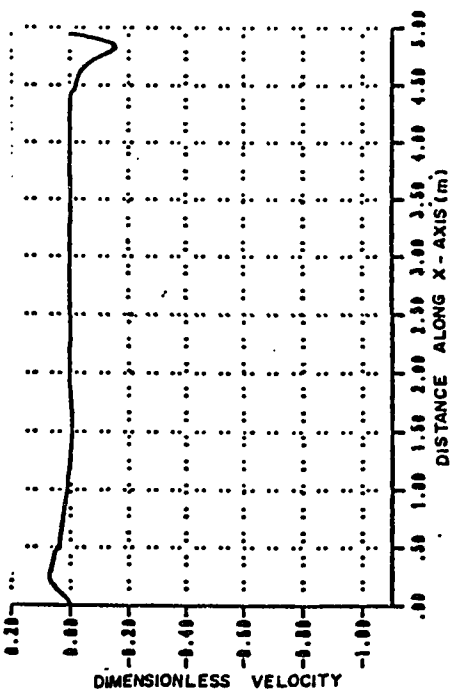
d) Y/H = 0.91 and Z/W = 0.84

c) Y/H = 0.64 and Z/W = 0.84

Figure 7.79. Dimensionless velocity profiles over length of room near right wall at 3 pm, Tin = 15 °C and Uin = 1.9 m/sec for the NN configuration.
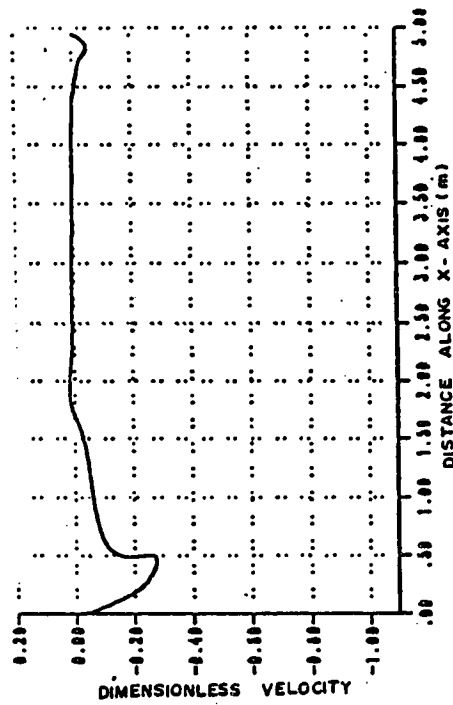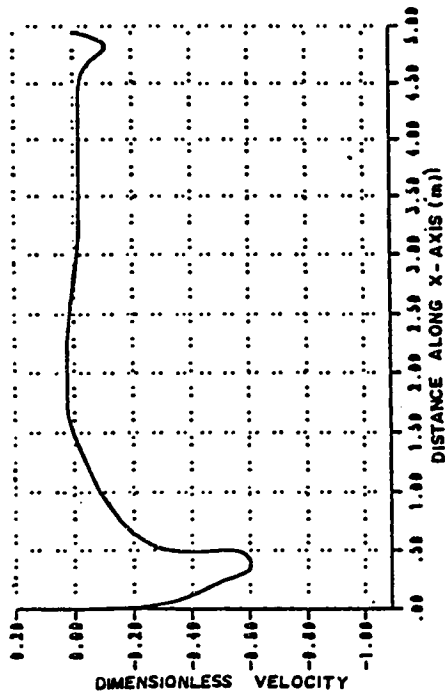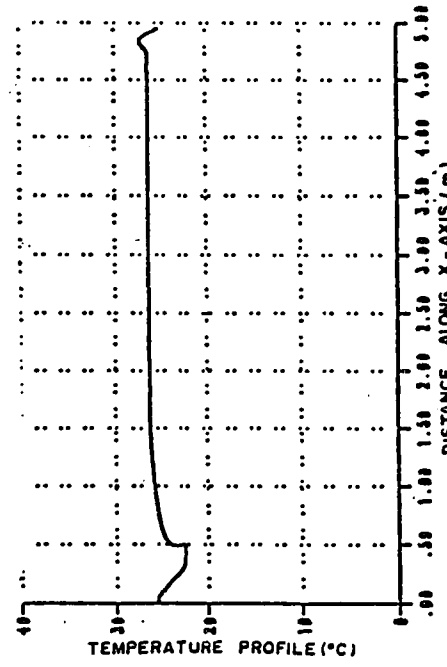
b) Y/H = 0.28 and Z/W = 0.5
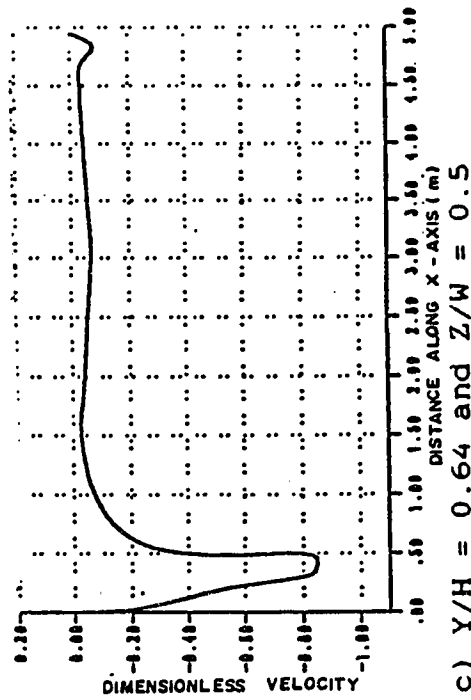
d) Y/H = 0.91 and Z/W = 0.5
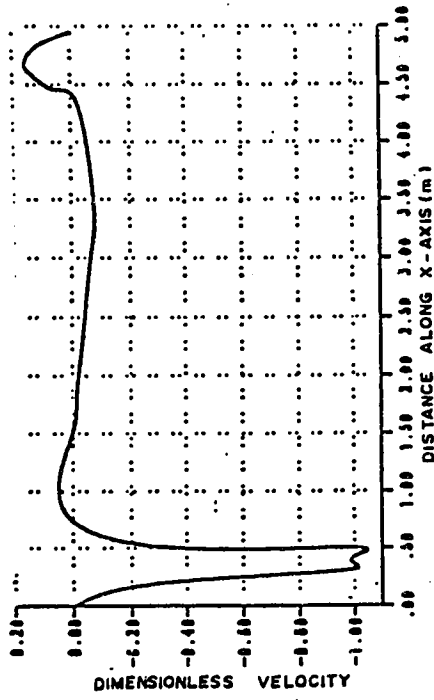
a) Y/H = 0.051 and Z/W = 0.5

c) Y/H = 0.64 and Z/W = 0.5

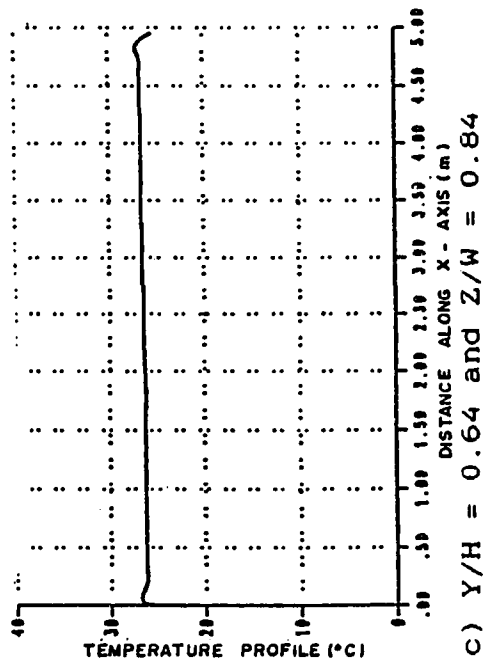Figure 7.80. Dimensionless velocity profiles over length of room at mid section at 3 pm, Tin = 15 °C and Uin = 3.5 m/sec for the NN configuration.
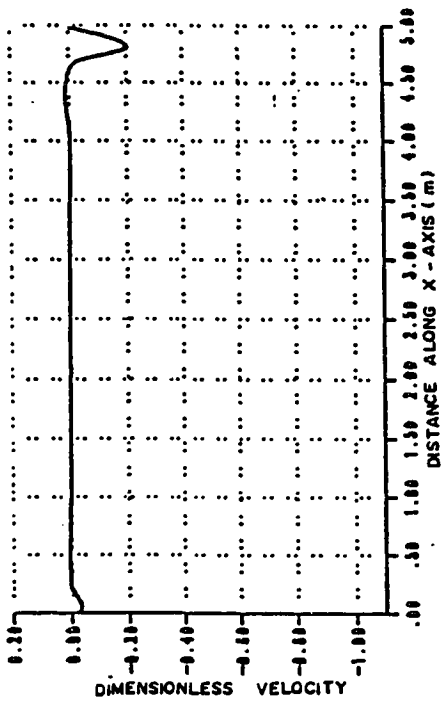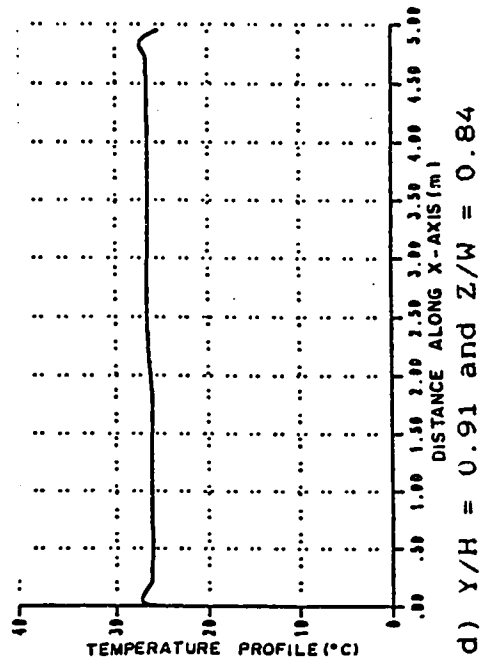
a) Y/H = 0.051 and Z/W = 0.84

b) Y/H = 0.28 and Z/W = 0.84
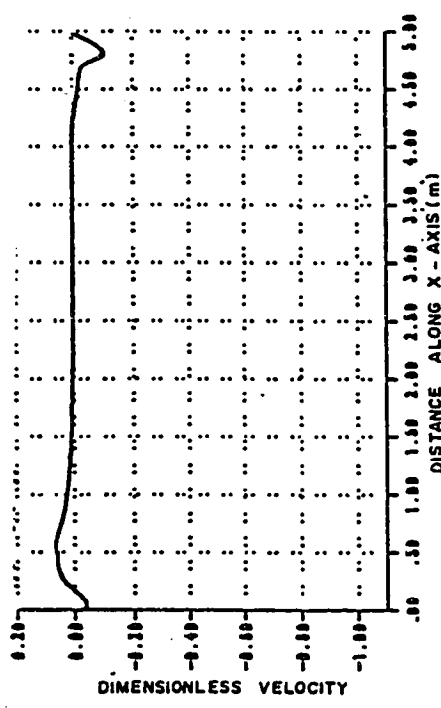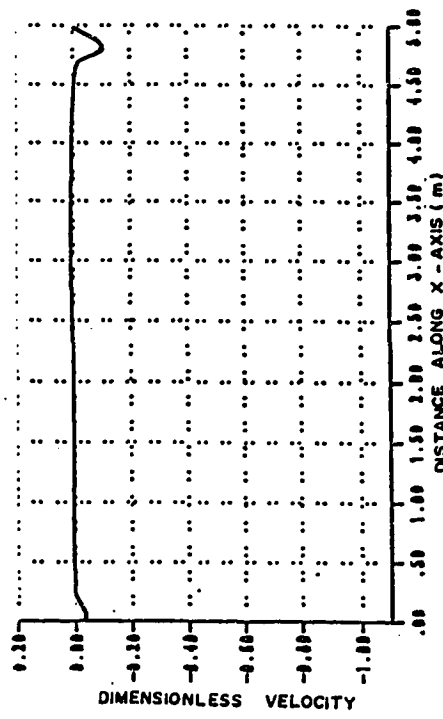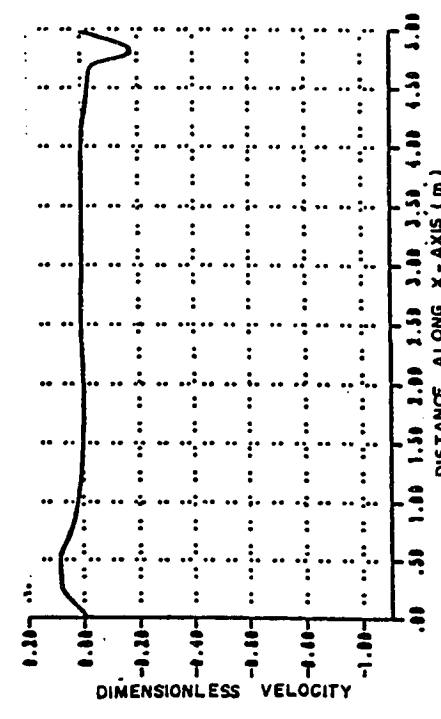
c) Y/H = 0.64 and Z/W = 0.84
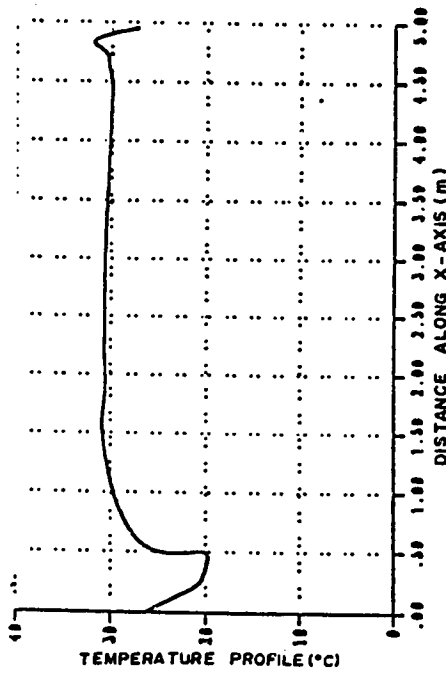
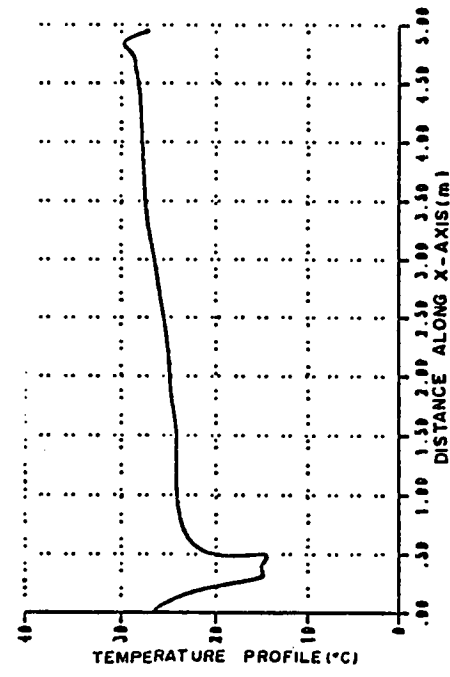d) Y/H = 0.91 and Z/W = 0.84

Figure 7.81. Dimensionless velocity profiles over length of room near right wall at 3 pm, Tin = 15 °C and Uin = 3.5 m/sec for the NN configuration.

inlet opening has increased in the latter figure while that in the former figure is positive, but relatively small, indicating that the affect of the air jet from the inlet has completely been depleted and the buoyancy forces overcomes the inertia forces. In Fig. 7.80.c the velocity profile is completely negative such that the peak of the profile opposite the inlet opening has increased further and the peak opposite the outlet opening has reduced and in Fig. 7.78.c, this peak has also reduced but the peak opposite the inlet opening has now become negative but less than that of Fig.7.80.c. In Figs. 7.78.d and 7.80.d, the profiles are comparable such that the velocity profiles have a negative peak opposite the inlet opening and a positive peak opposite the outlet opening, the remaining profile in the former figure is nearly zero while in the latter, the East part is negative and the West is partly negative and partly positive. The velocity profiles of Figs.7.79 and 7.81 are comparable and a discussion of the former is given. In Fig.7.79.a the velocity profile is nearly all zero except adjacent to the East and West walls where negative peaks appear, and an identical occurrence happens in Fig. 7.79.b, except that the extent of the peak opposite the outlet opening is larger. In Fig. 7.79.c, the negative peak of the velocity profile close to the East wall remains but is larger while that in Fig.7.81.c has reduced in comparison to Fig. 7.81.b. There now also appears a positive peak of the velocity profile adjacent to the West wall in Figs. 7.79.c and 7.81.c. Finally, the profiles of Figs. 7.79.d and 7.81.d resemble those of Figs. 7.79.c and 7.81.c, respectively but less pronounced.

7.2.2.3 Temperature Contours

Temperature contours at planes similar to those described for the WE configuration are given below.

(i) Temperature Contours at 9:00 A.M.

The T_{in} and U_{in} for the temperature contours of Fig.7.82 are 15°C and 1.9 m/sec., respectively, while those of Fig. 7.83 are 22°C and 1.9 m/sec., respectively. Comparing Figs. 7.82.a and 7.83.a, we note that the general appearance for both are the same such that the relatively lowest temperature is close to the West wall and the highest is close to the center of the room. Furthermore, Fig. 7.82.a has relatively less variation of temperature near the center of the room than that of Fig. 7.83.a. In Figs. 7.82.b and 7.83.b the overall level of temperature is less than that of Figs. 7.82.a and 7.83.a, as is the relative variations of temperature .. The contours in Figs. 7.82.c and 7.83.c are similar in the sense that the relatively coolest region is adjacent to the West wall, while the warmest is adjacent to the East wall and the pattern of the contours in the former figure resemble concentric semi-circles with the center adjacent to the West wall, while the pattern of the contours in the latter figure are more or less parallel to the West and East walls.

(ii) Temperature Contours at 12:00 Noon

The T_{in} and U_{in} for the temperature contours of Fig.7.84 are 15°C and 1.9 m/sec., while those of Fig. 7.85 are 10°C and 2.2 m/sec., respectively. In Figs. 7.84.a and 7.85.a, the warmest region is close to the central
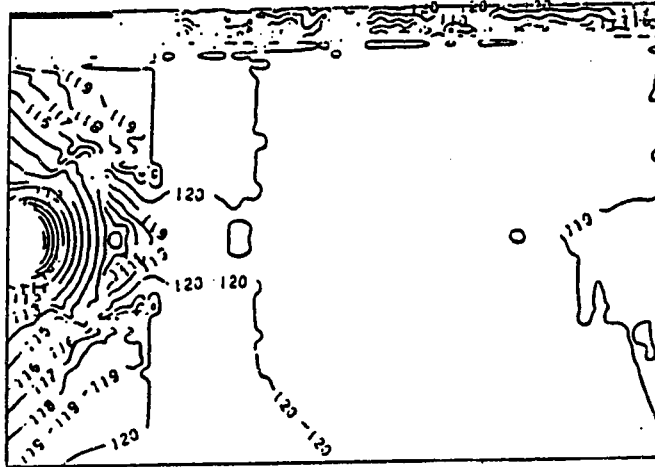
a) Y = 0.76 m,   Fac = 5.0
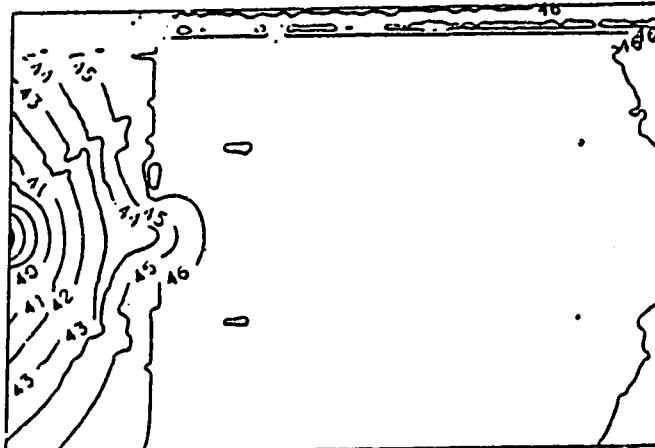
b) Y = 1.76 m,   Fac = 2.0
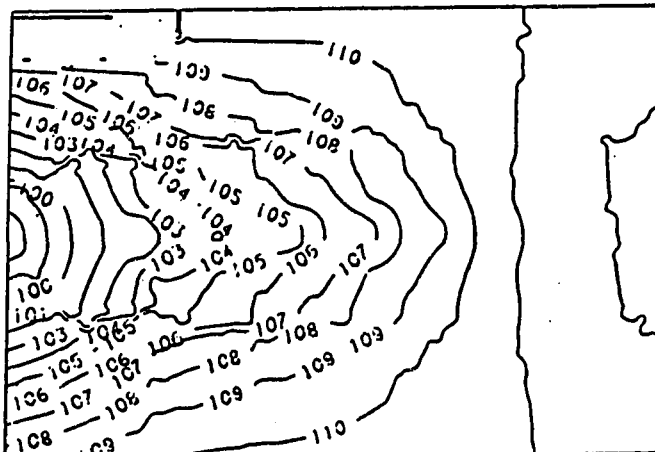
c) Y = 2.51 m,   Fac = 5.0

Figure 7.82. Temperature contours in the X-Z plane at 9 am,
Tin = 15 °C and Uin = 1.9 m/sec for the NN
configuration.
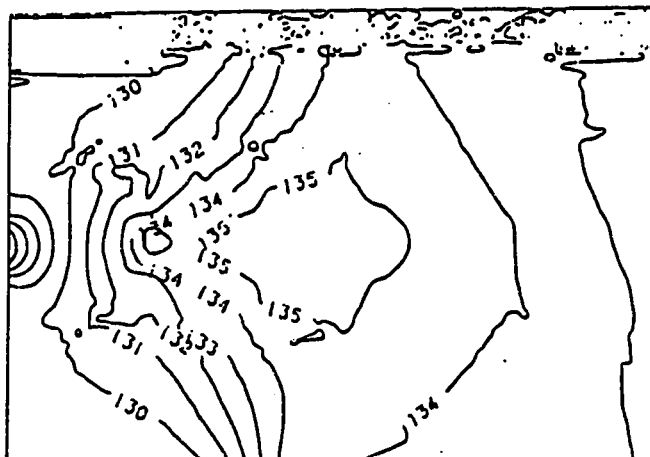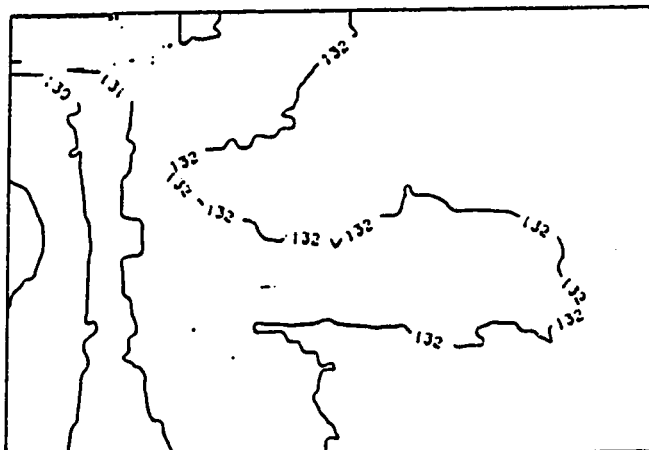
a) Y = 0.76 m,   Fac = 5.0
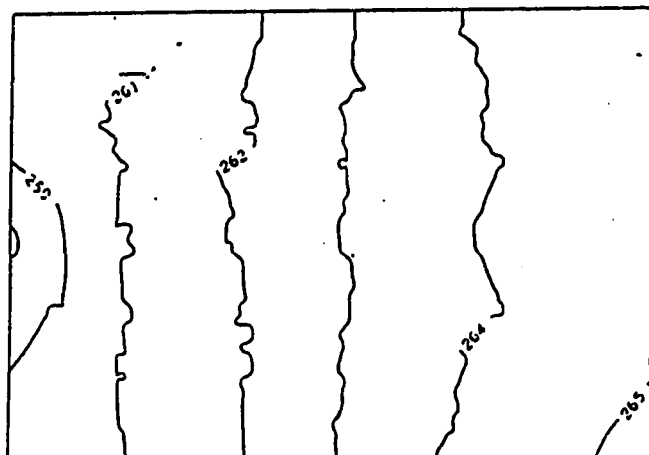
b) Y = 1.76 m,   Fac = 5.0

c) Y = 2.51 m,   Fac = 10.0

Figure 7.83. Temperature contours in the X-Z plane at 9 am,
            Tin = 22 °C and Uin = 1.9 m/sec for the NN
            configuration.
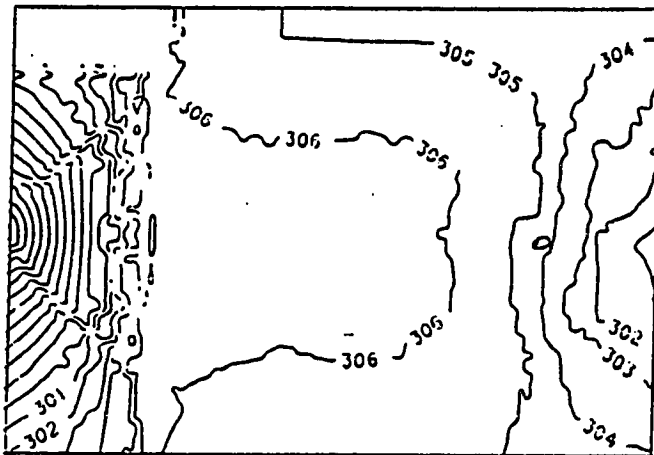
a) Y = 0.76 m,   Fac = 10.0
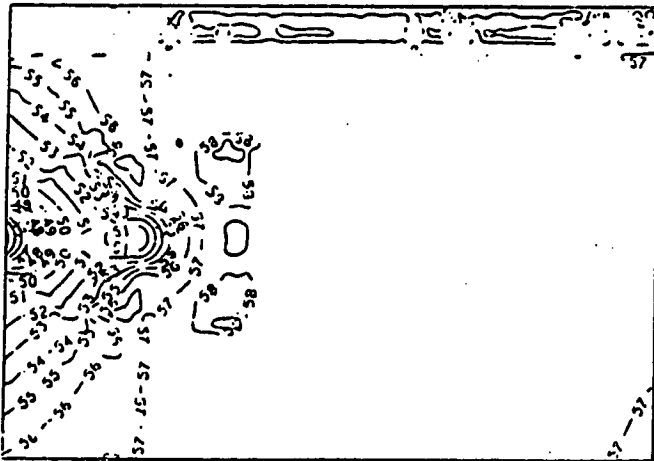
b) Y = 1.76 m,   Fac = 2.0
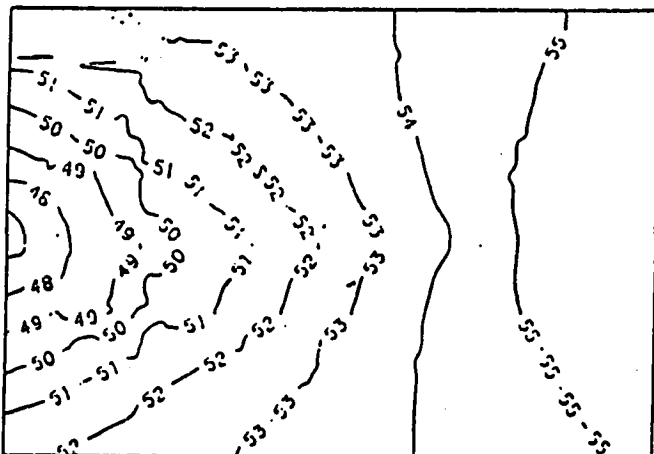
c) Y = 2.51 m,   Fac = 2.0

Figure 7.84. Temperature contours in the X-Z plane at noon,
Tin = 15 °C and Uin = 1.9 m/sec for the NN
configuration.
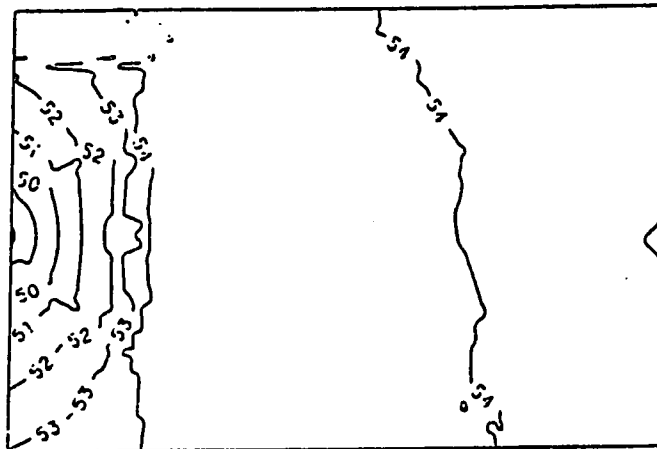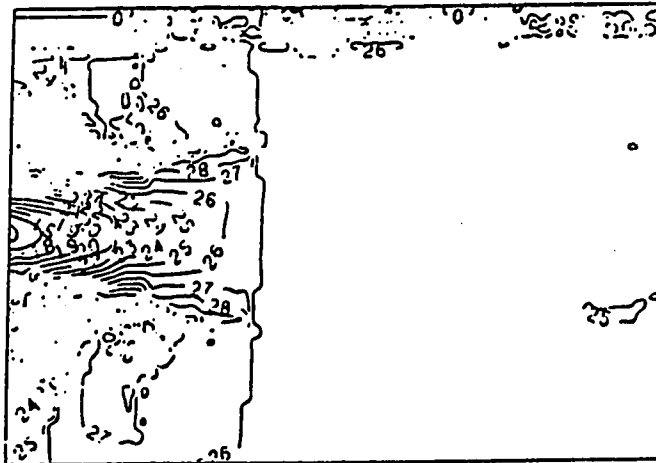
a) Y = 0.76 m,   Fac = 2.0

b) Y = 1.76 m,   Fac = 1.0
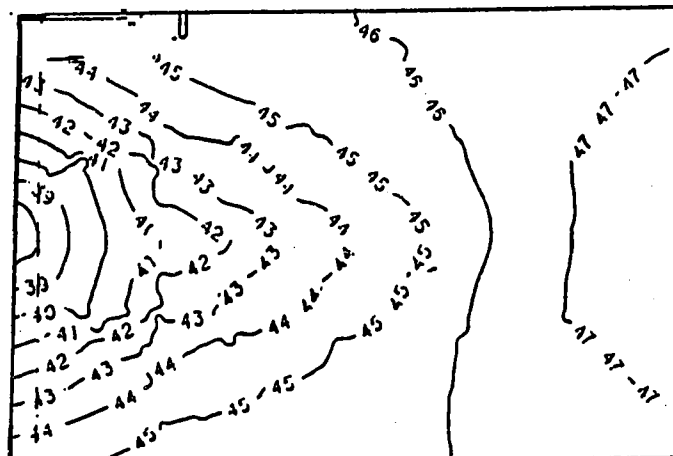
c) Y = 2.51 m,   Fac = 2.0

Figure 7.85. Temperature contours in the X-Z plane at noon,
Tin = 10 °C and Uin = 2.2 m/sec for the NN
configuration.

area of the room and the level of temperature in the former figure is higher than that in the latter. In Figs. 7.84.b and 7.85.b the overall appearance is comparable such that the lowest temperature is adjacent to the West wall while about 1/3rd the distance from the West wall the temperature reaches a maximum, and beyond this region moving towards the East wall, the temperature variation is low. Figs. 7.84.c and 7.85.c, are similar, except that the level of temperature is higher in the former. The relative pattern for both figures is such that the lowest temperature is close to the center of the West side of the occupied zone and increasing from this point in a concentric nature having the relative maximum temperature close to the East side of the occupied zone.

(iii) Temperature Contours at 3:00 P.M.

The T_{in} and U_{in} for the temperature contours of Fig.7.86 are 15°C and 1.9 m/sec., respectively, while those of Fig. 7.87 are 15°C and 3.5 m/sec., respectively. Fig. 7.86.a almost seems symmetrical such that the highest temperature is in the center of the room while the lowest are at the centers of the East and West sides of the occupied zone. In Fig. 7.87.a the relative variation in temperature is high in the region of the West wall and the relatively lowest temperature is at the center of the West side of the occupied zone, while the relatively highest temperature is close to the center of the room. In Fig. 7.86.b the variation in temperature is high close to the West side of the occupied zone and reduces as you progress towards the East side, a similar event occurs in Fig. 7.87.b, although the variations close to the West side of the occupied zone are not as pronounced and the relative highest temperature in this figure is in the Eastern part of the occ-

a) Y = 0.76 m,   Fac = 10.0
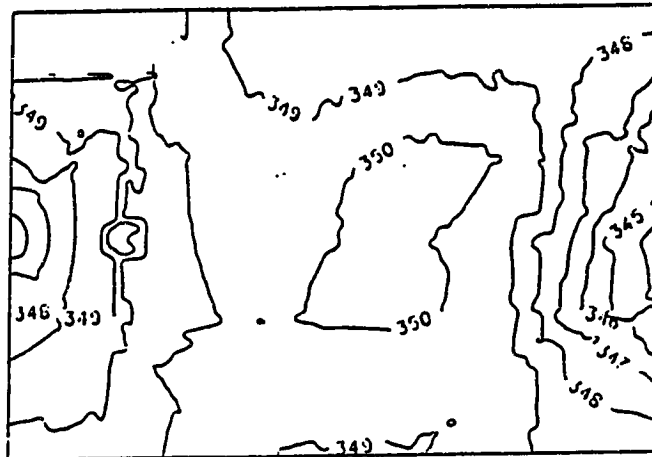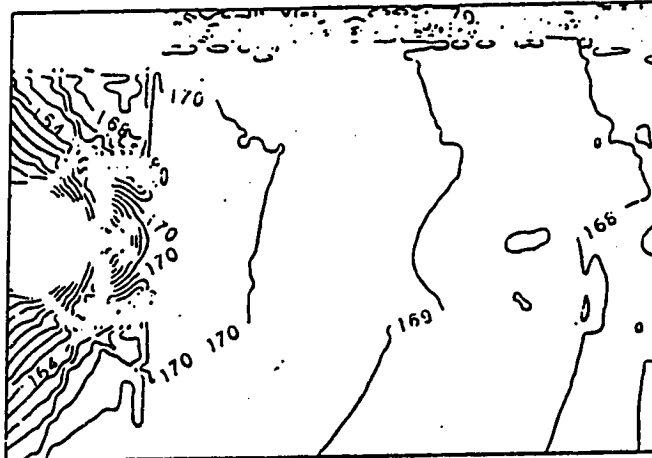
b) Y = 1.76 m,   Fac = 5.0
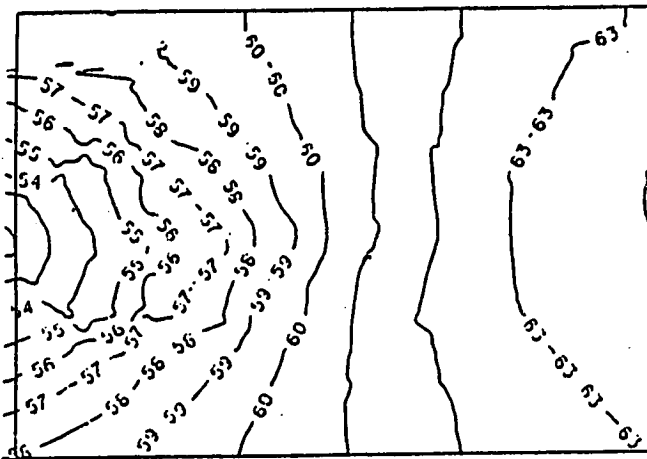
c) Y = 2.51 m,   Fac = 2.0

Figure 7.86. Temperature contours in the X-Z plane at 3 pm,
              Tin = 15 °C and Uin = 1.9 m/sec for the NN
              configuration.
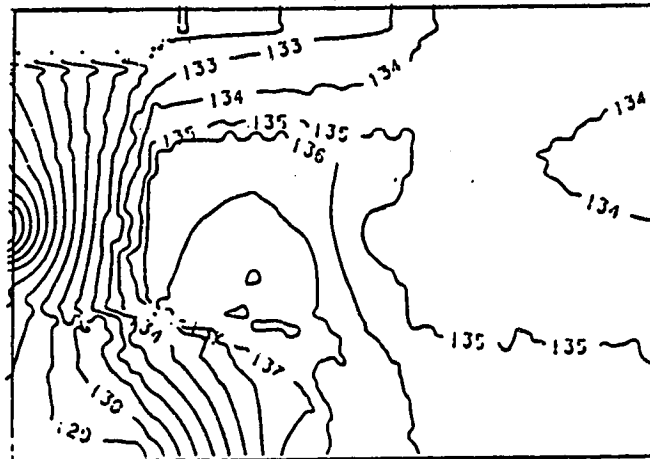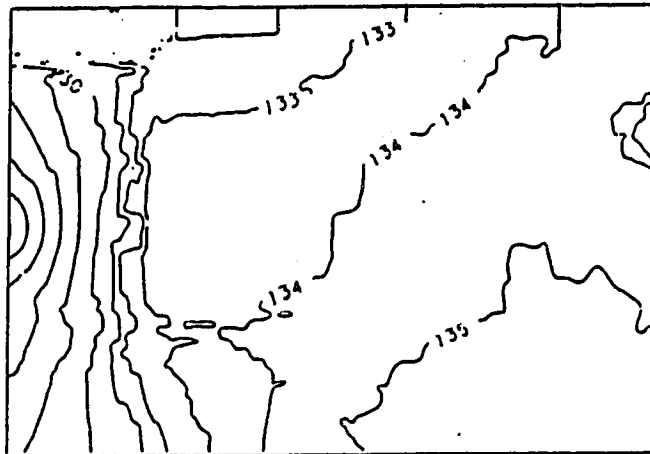
a) Y = 0.76 m,   Fac = 5.0

b) Y = 1.76 m,   Fac = 5.0
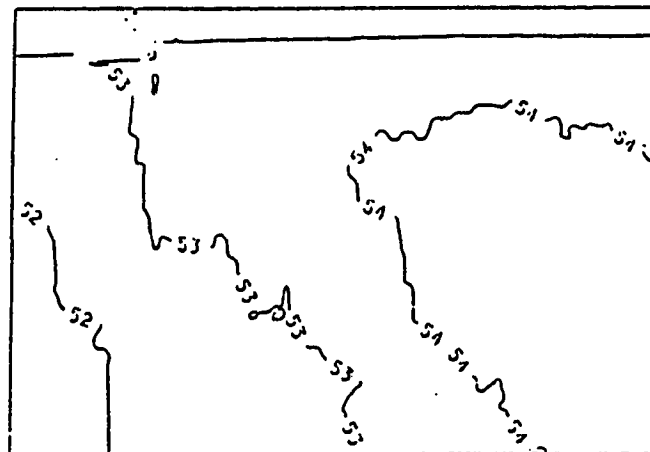
c) Y = 2.51 m,   Fac = 2.0

Figure 7.87. Temperature contours in the X-Z plane at 3 pm,
Tin = 15 °C and Uin = 1.9 m/sec for the NN
configuration.

upied zone, while that of Fig. 7.86.b is at about 1/3rd the distance from the West side of the occupied zone. In Fig. 7.86.c concentric temperature contours , as discussed earlier, appear here such that the lowest temperature is close to the center of the West side of the occupied zone increasing as you move towards the East wall, where the highest occurs in the region adjacent to the East side of the occupied zone. In Fig. 7.87.c, the temperature is nearly uniform with the relative lowest temperature at the West side of the occupied zone and the highest is in the vicinity of the East side.

7.2.2.4 Temperature Profiles

Temperature profiles are plotted at locations similar to that of the velocity profiles reported earlier, and are plotted for all cases considered in the NN configuration . This with some relevant discussions now follow.

(i) Temperature Profile at 9:00 A.M.

Figs. 7.88 and 7.89 are temperature profiles at the symmetry plane of the room and close to the East wall, respectively and at different heights above the floor having a T_{in} = 15°C and U_{in} = 1.9 m/sec. In Fig. 7.88.a a low temperature peak appears opposite to the inlet opening while the highest value of the temperature occurs opposite the outlet opening and the profile inbetween is mostly uniform. Observations similar to this is noted in Fig.7.88.b to Fig.7.88.d with the lowest temperature peak appearing in the plot taken closest to the ceiling. The general features of Fig.7.89 resemble that of Fig. 7.88 and, therefore, the discussion given to the latter group of figures are extended to the former figures, with the exception that the part of the temperature profile opposite the inlet opening in Fig. 7.89.d
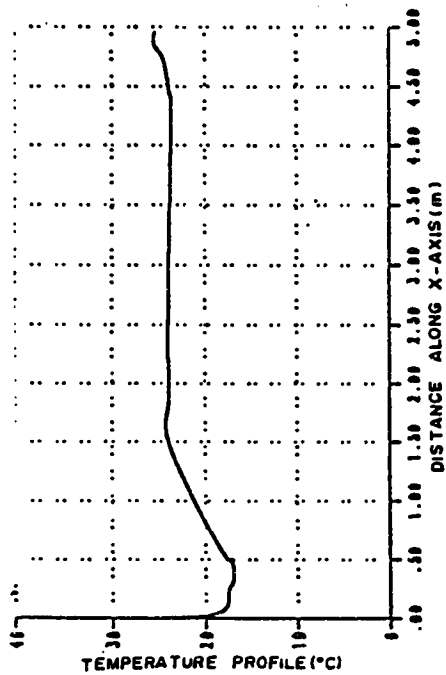
b) Y/H = 0.28 and Z/W = 0.5

d) Y/H = 0.91 and Z/W = 0.5

a) Y/H = 0.051 and Z/W = 0.5
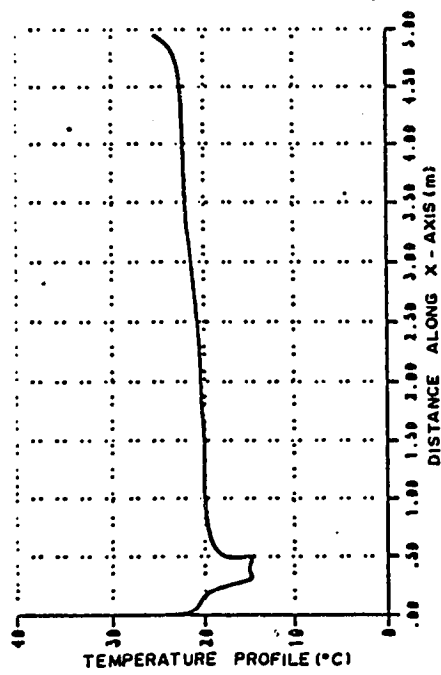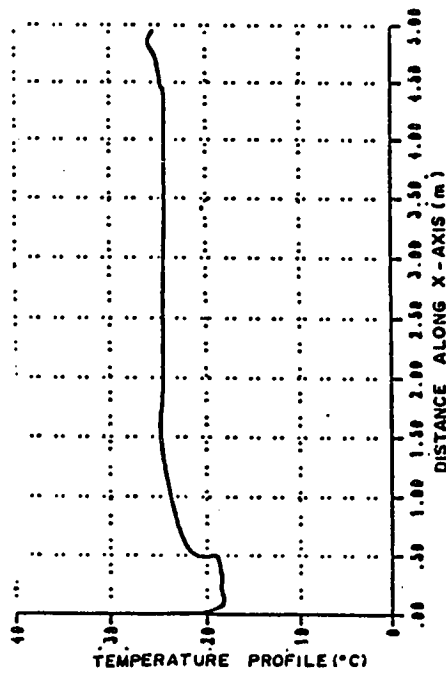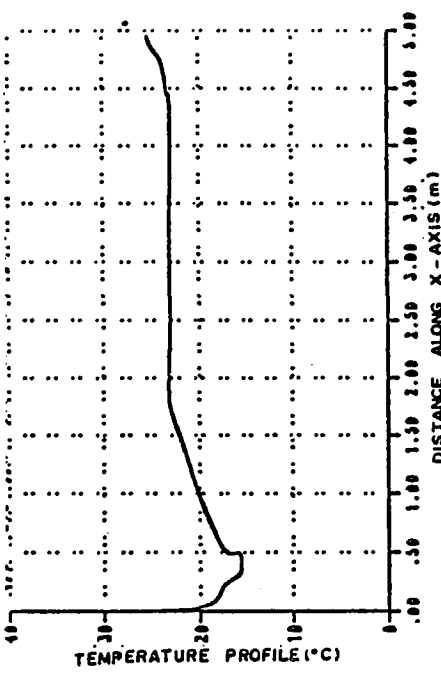
c) Y/H = 0.64 and Z/W = 0.5

Figure 7.88. Temperature profiles over length of room at mid section at 9 am,
Tin = 15 °C and Uin = 1.9 m/sec for the NN configuration.

a) Y/H = 0.051 and Z/W = 0.84

b) Y/H = 0.28 and Z/W = 0.84
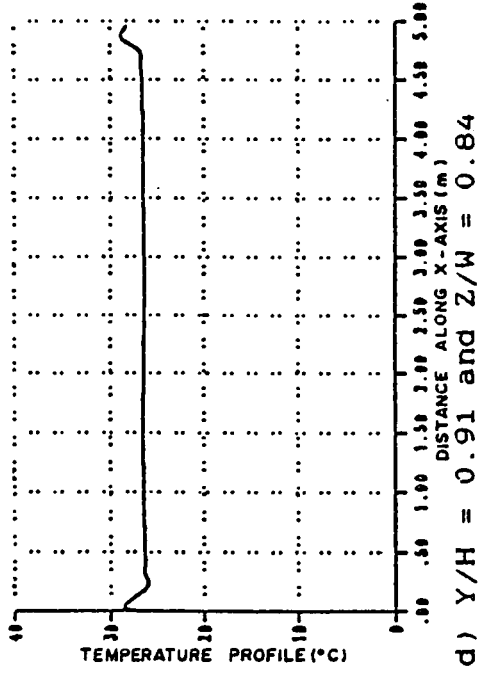
c) Y/H = 0.64 and Z/W = 0.84

d) Y/H = 0.91 and Z/W = 0.84
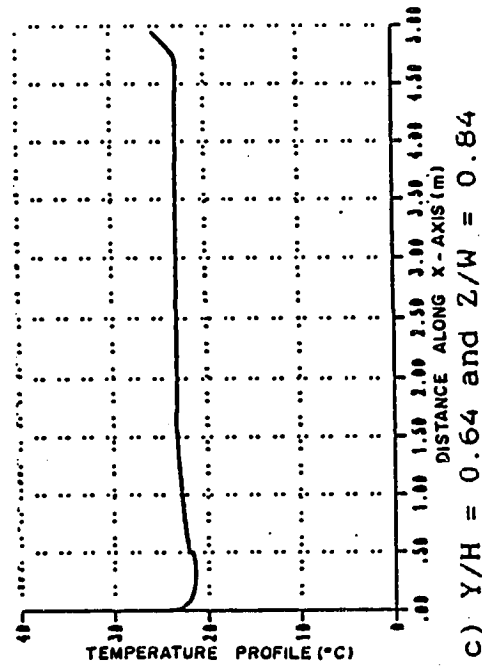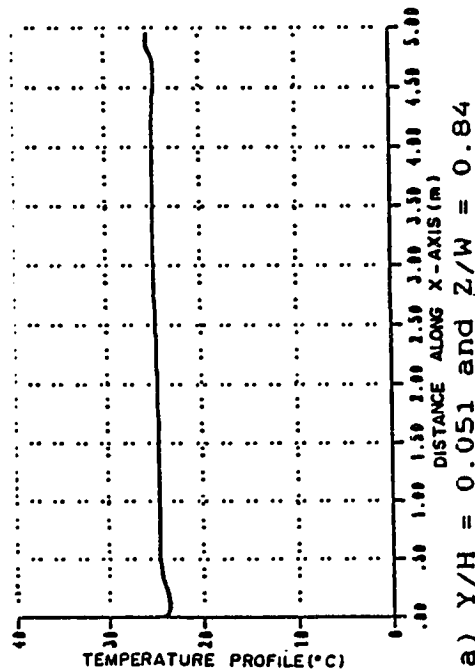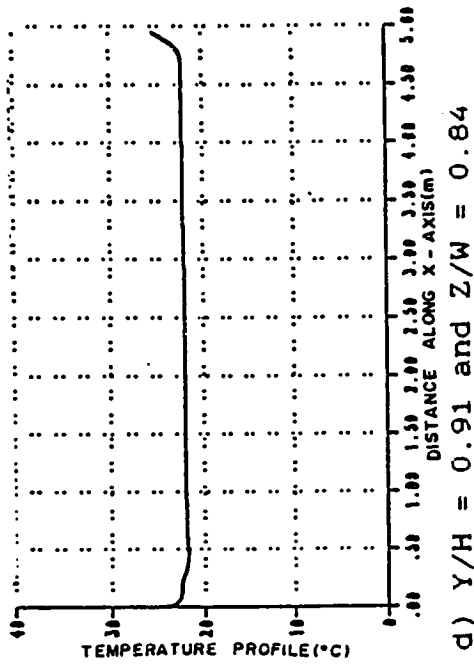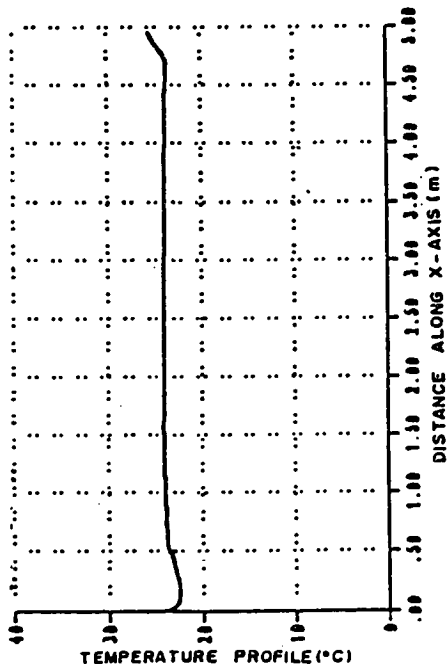
Figure 7.89. Temperature profiles over length of room near right wall at 9 am, Tin = 15 °C and Uin = 1.9 m/sec for the NN configuration.

is not the lowest temperature . General agreement exists between the plots of Fig.7.90, having a T_{in} = 22°C and a U_{in} = 1.9 m/sec., and Fig. 7.88 and consequently the description presented for the latter figures shall follow for the former. The plots of Fig.7.91 are plotted at T_{in} and U_{in} identical to that of Fig. 7.90. In Fig.7.91.a the temperature profile is nearly uniform with a high peak close to the East wall while in the Western half of the room, the profile level seems to drop. Figs. 7.90.b to 7.90.d are comparable such that two temperature profile peaks appear close to the West and East walls, while the profile of the space inbetween is approximately uniform.

(ii) Temperature Profiles at 12:00 Noon

In Figs. 7.92 and 7.93 the temperature profiles at various heights above the floor are plotted for a T_{in} = 15°C and a U_{in} = 1.9 m/sec. In Fig. 7.92.a two distinctive peaks in the temperature profile occur opposite the inlet and outlet openings, while the profile inbetween is nearly uniform. In Figs. 7.92.b to 7.92.d the forms are comparable such that the highest peak occurs opposite the outlet opening while the lowest is opposite the inlet opening and the profile inbetween is almost uniform except in Fig. 7.92.d where this profile is sloping from East to West. The temperature profile in Figs. 7.93.a to 7.93.d are comparable and resembles that of Fig.7.92.a except in the part of the temperature profile opposite the inlet opening in Figs.7.93.c and 7.93.d where there is no more obvious peak. The T_{in} and U_{in} of Fig. 7.94 are 10°C and 2.2 m/sec., respectively and the general features of this group of figures resemble that of Fig. 7.92, described above except that in Fig. 7.94.d there is no obvious temperature
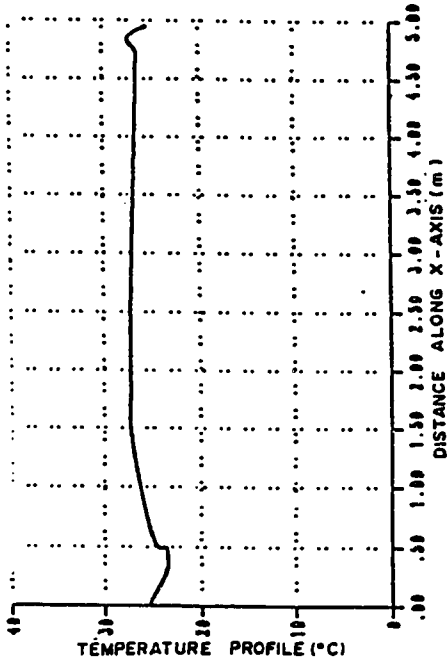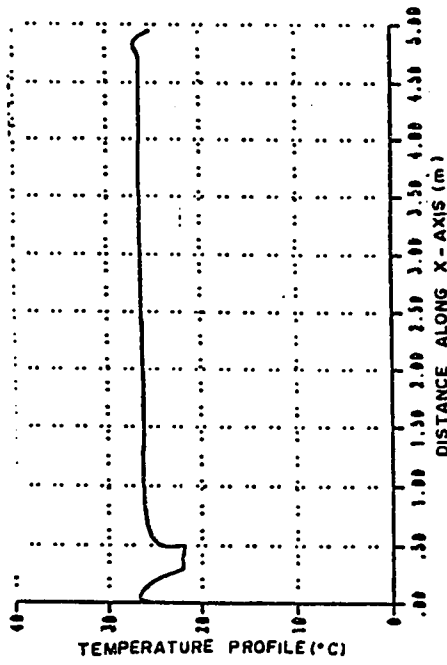
a) Y/H = 0.051 and Z/W = 0.5
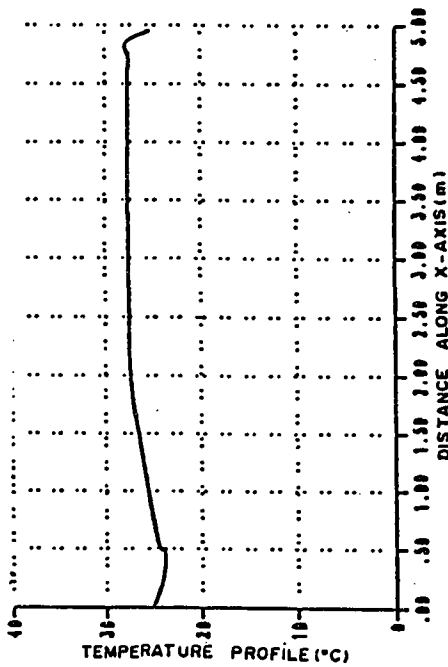
b) Y/H = 0.28 and Z/W = 0.5

c) Y/H = 0.64 and Z/W = 0.5

d) Y/H = 0.91 and Z/W = 0.5

Figure 7.90. Temperature profiles over length of room at mid section at 9 am, Tin = 22 °C and Uin = 1.9 m/sec for the NN configuration.
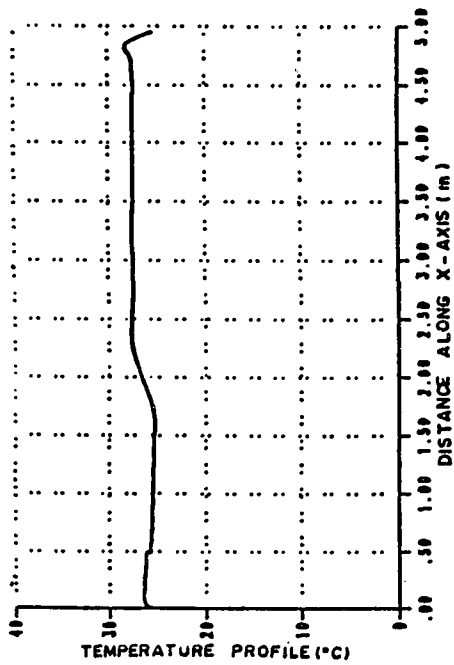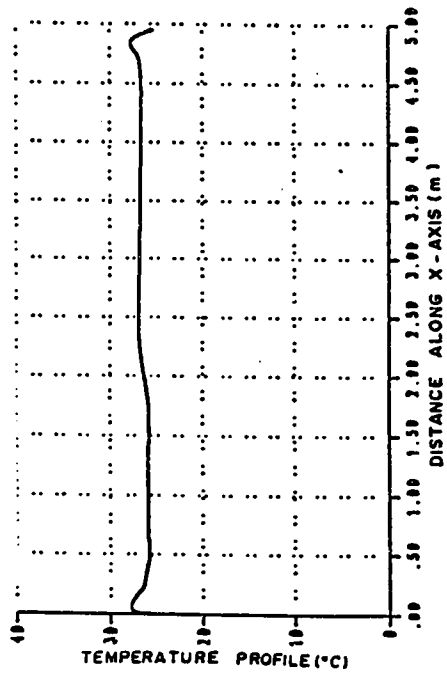
b) Y/H = 0.28 and Z/W = 0.84

d) Y/H = 0.91 and Z/W = 0.84

a) Y/H = 0.051 and Z/W = 0.84

c) Y/H = 0.64 and Z/W = 0.84

Figure 7.91. Temperature profiles over length of room near right wall at 9 am, Tin = 22 °C and Uin = 1.9 m/sec for the NN configuration.
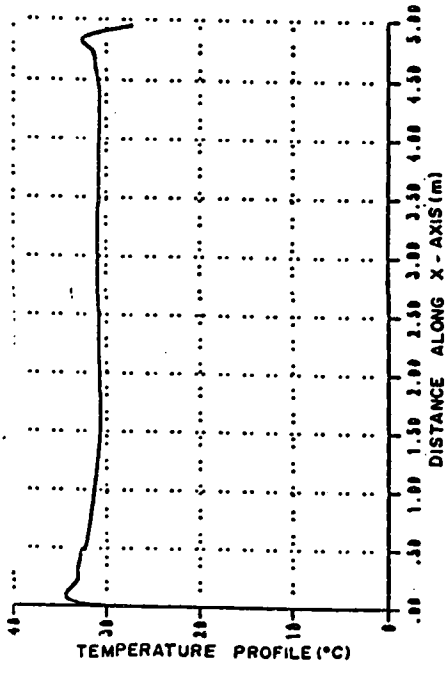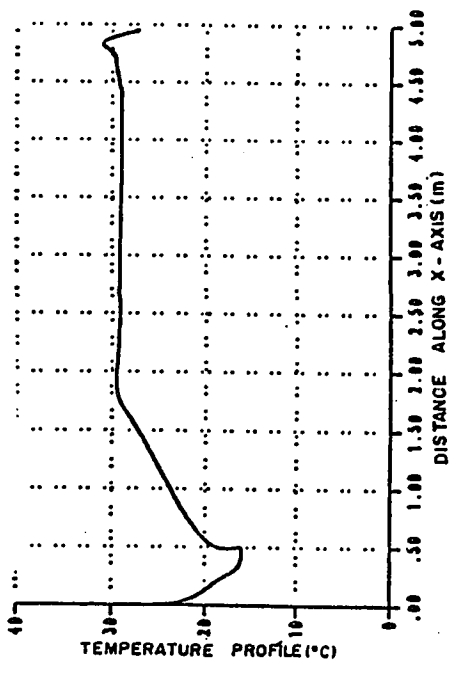
Figure 7.92. Temperature profiles over length of room at mid section at noon, $T_{in} = 15\,°C$ and $U_{in} = 1.9\,m/sec$ for the NN configuration.

307.
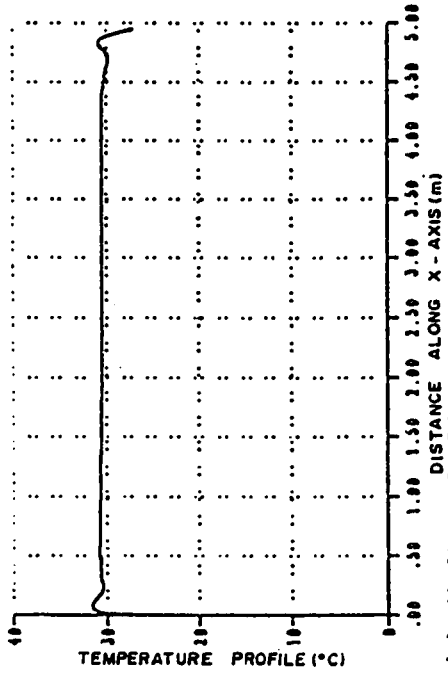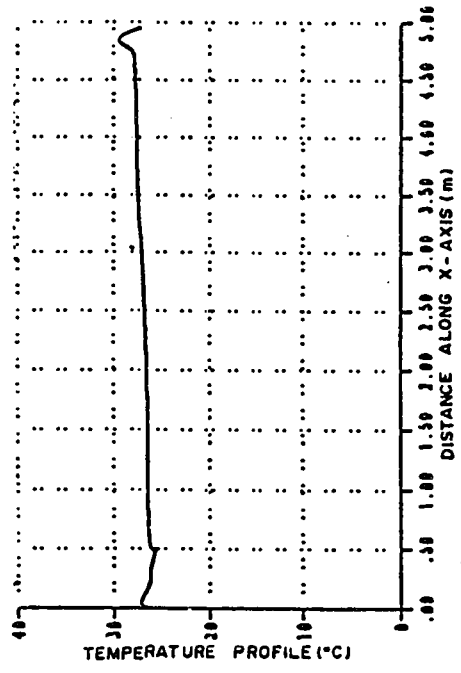
a) Y/H = 0.051 and Z/W = 0.84
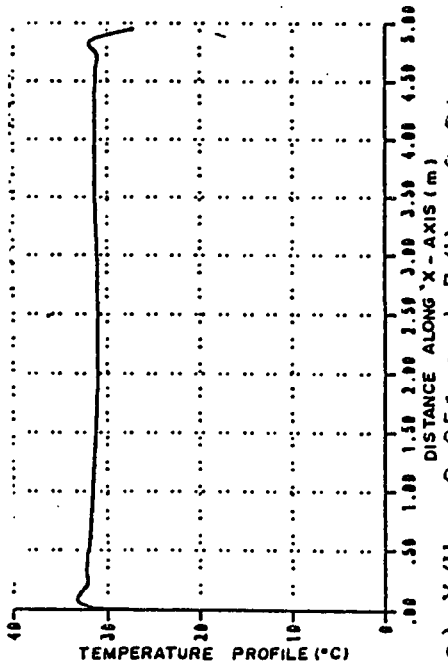
b) Y/H = 0.28 and Z/W = 0.84
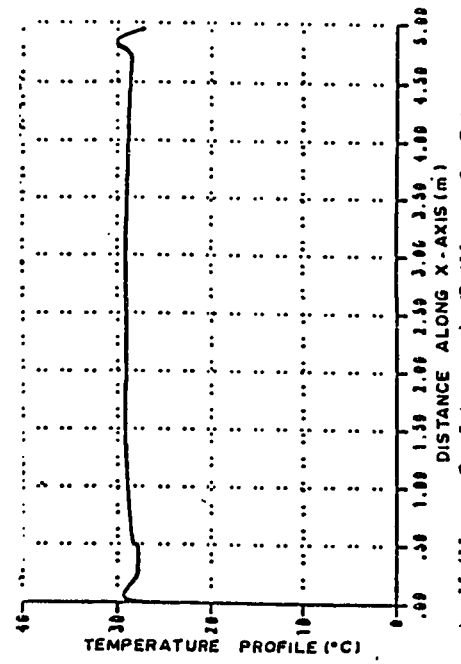
c) Y/H = 0.64 and Z/W = 0.84

d) Y/H = 0.91 and Z/W = 0.84

Figure 7.93. Temperature profiles over length of room near right wall at noon, Tin = 15 °C and Uin = 1.9 m/sec for the NN configuration.
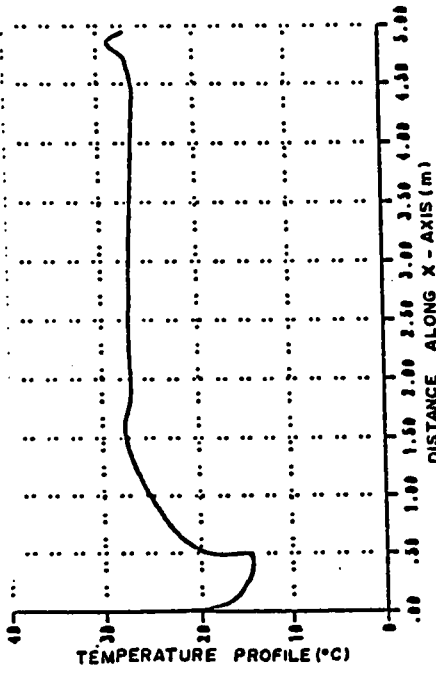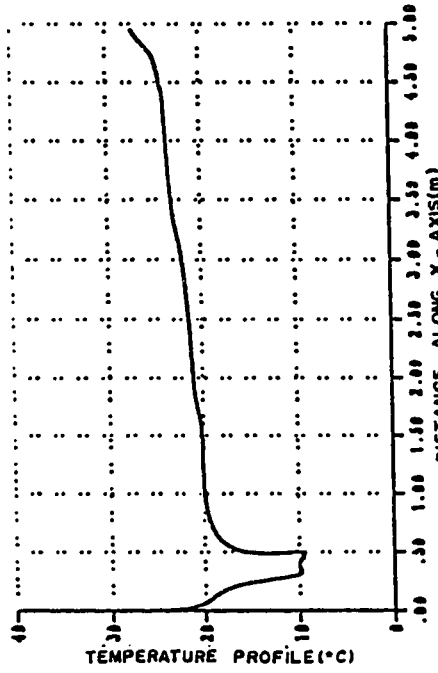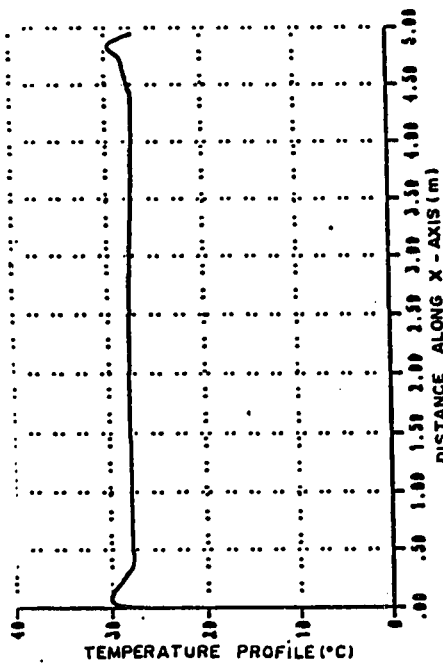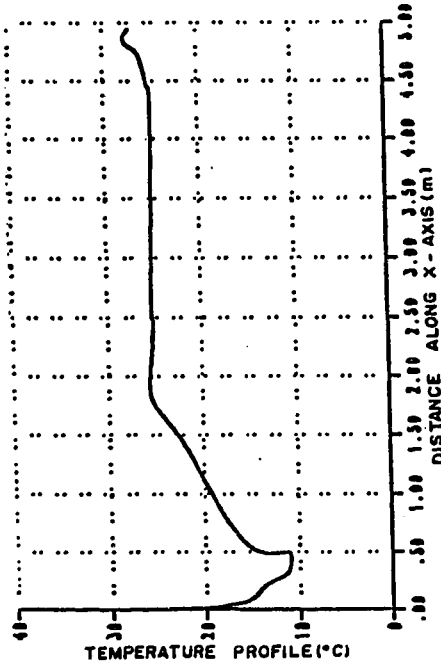
Figure 7.94. Temperature profiles over length of room at mid section at noon, Tin = 10 °C and Uin = 2.2 m/sec for the NN configuration.
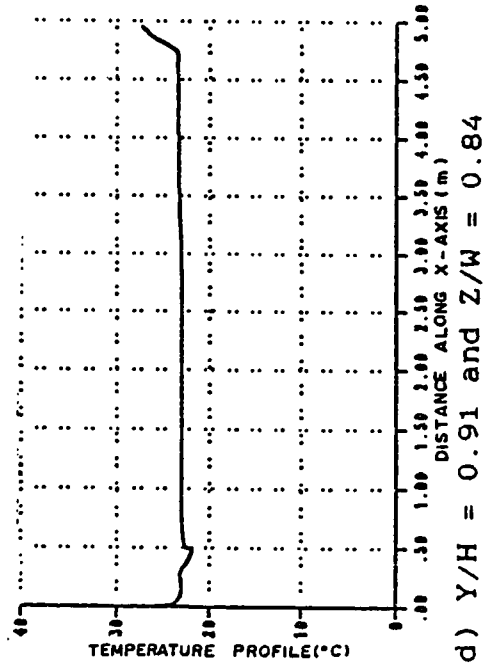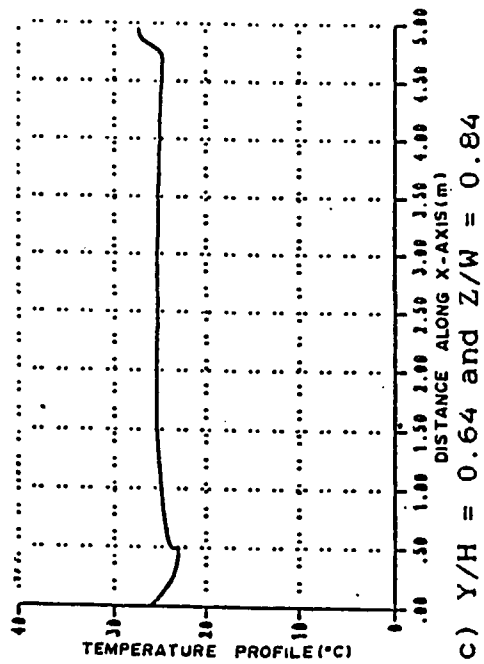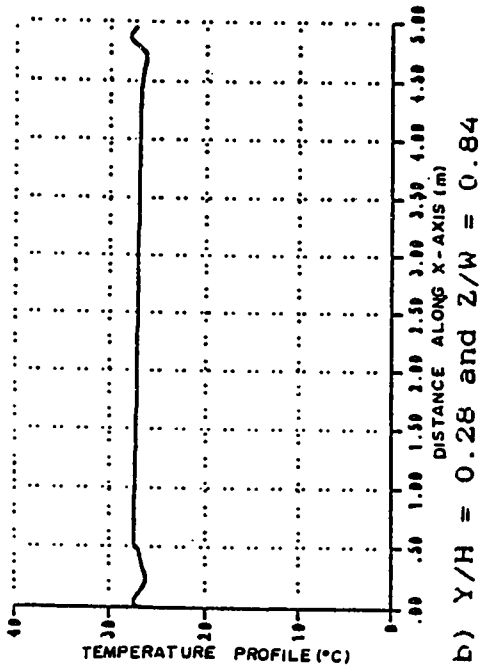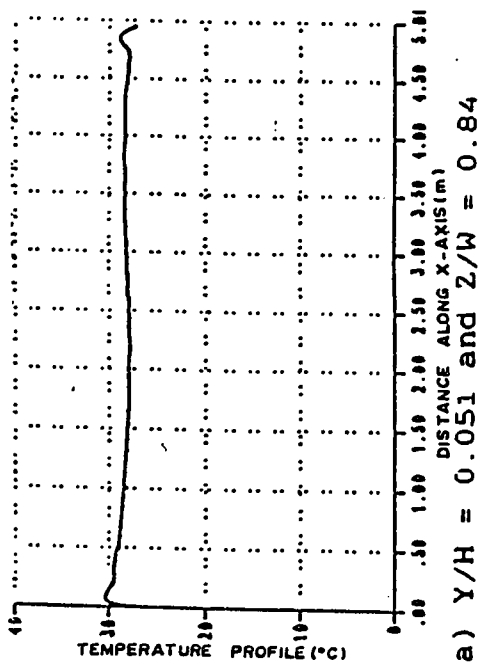
Figure 7.95. Temperature profiles over length of room near right wall at noon, Tin = 10 °C and Uin = 2.2 m/sec for the NN configuration.

peak opposite the outlet opening as in Fig. 7.92.d. In Fig. 7.95 the T_{in} and U_{in} adopted is equivalent to that of Fig. 7.94 and the general shape of the temperature profile in Fig. 7.95.a is comparable to that of Fig.7.93.a. In Figs. 7.95.b to 7.95.d the feature of the temperature profiles are nearly similar such that the relatively largest temperature is opposite the outlet opening while the lowest is opposite the inlet and the remaining profile inbetween is approximately uniform.

(iii) Temperature Profiles at 3:00 P.M.

In Figs. 7.96 and 7.97 the temperature profiles at various heights above the floor are plotted for a T_{in} = 15°C and a U_{in} = 1.9 m/sec. Furthermore, similar profiles are plotted in Figs. 7.98 and 7.99 having T_{in} = 15°C and U_{in} = 3.5 m/sec. In Fig. 7.96.a, the temperature profile has two peaks opposite the inlet and outlet openings, while the profile inbetween is nearly uniform. The temperature profiles of Figs.7.96.b to 7.96.d all have a similar general shape, such that the relatively highest temperature is opposite the outlet opening while the lowest is opposite the inlet opening and the profile inbetween is approximately uniform except in Fig.7.96.d where it slopes gradually from the East to the West side of the room. The temperature profiles of Fig.7.97 are similar in shape to that of Fig.7.96.a. The temperature profiles of Fig.7.98 are comparable and resemble those of Figs. 7.96.c and 7.96.d. In Fig. 7.99.a the peak of the temperature profile is opposite the outlet opening while the remaining part of the room is nearly at a uniform temperature except that the relative level of the temperature changes close to the center of the room. The general appearance of Figs.7.99.b to 7.99.d resembles that of Fig.7.96.a.
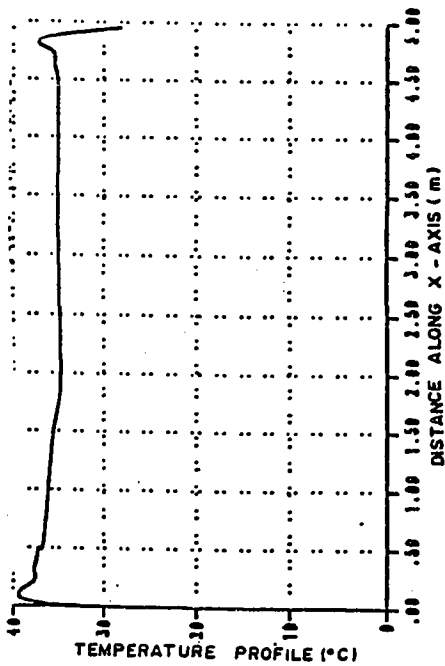
a) Y/H = 0.051 and Z/W = 0.5
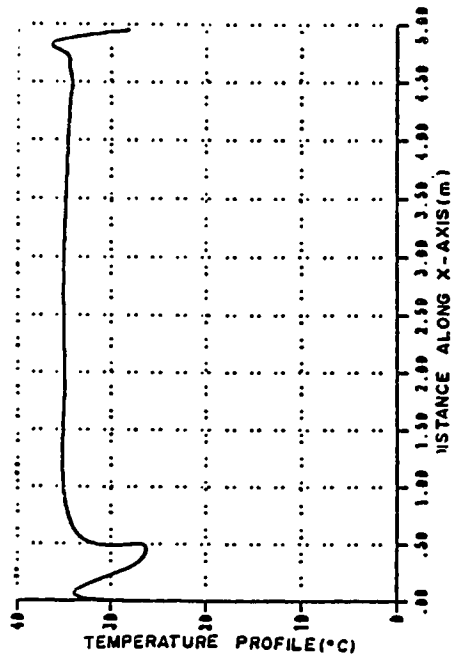
b) Y/H = 0.28 and Z/W = 0.5
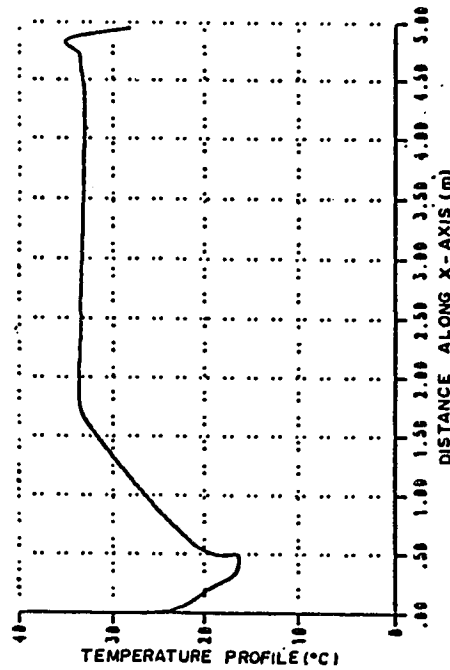
c) Y/H = 0.64 and Z/W = 0.5
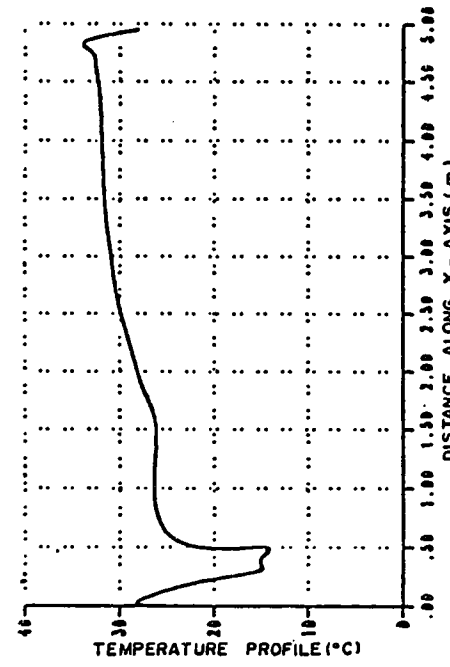
d) Y/H = 0.91 and Z/W = 0.5

Figure 7.96. Temperature profiles over length of room at mid section at 3 pm, Tin. = 15 °C and Uin = 1.9 m/sec for the NN configuration.

312

a) Y/H = 0.051 and Z/W = 0.84

b) Y/H = 0.28 and Z/W = 0.84

c) Y/H = 0.64 and Z/W = 0.84
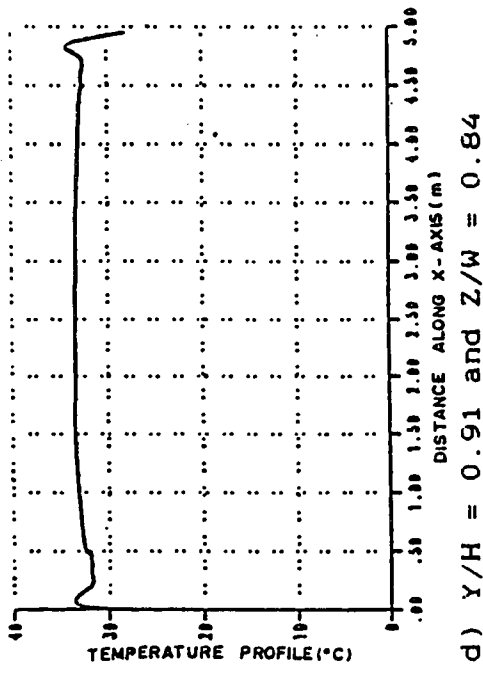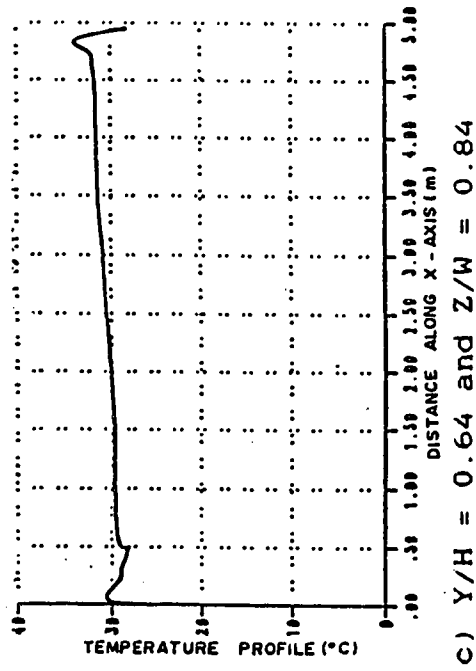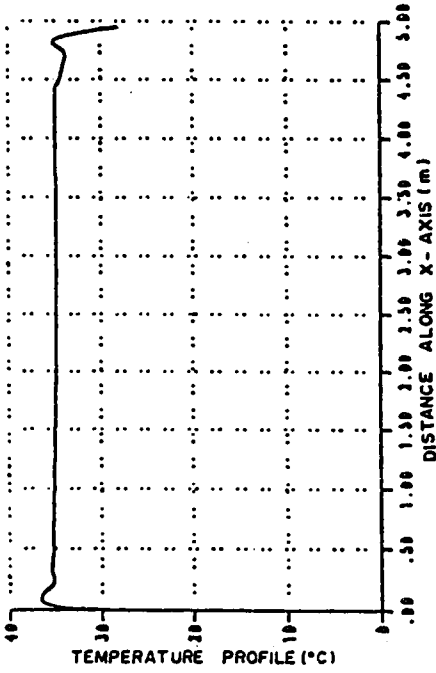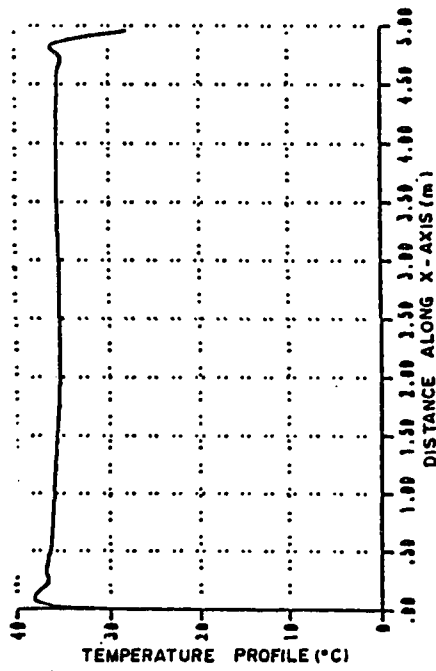
d) Y/H = 0.91 and Z/W = 0.84

Figure 7.97. Temperature profiles over length of room near right wall at 3 pm, Tin = 15 °C and Uin = 1.9 m/sec for the NN configuration.
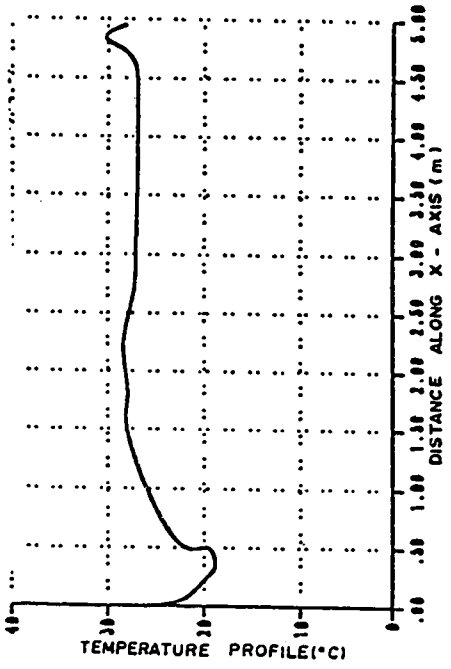
a) Y/H = 0.051 and Z/W = 0.5
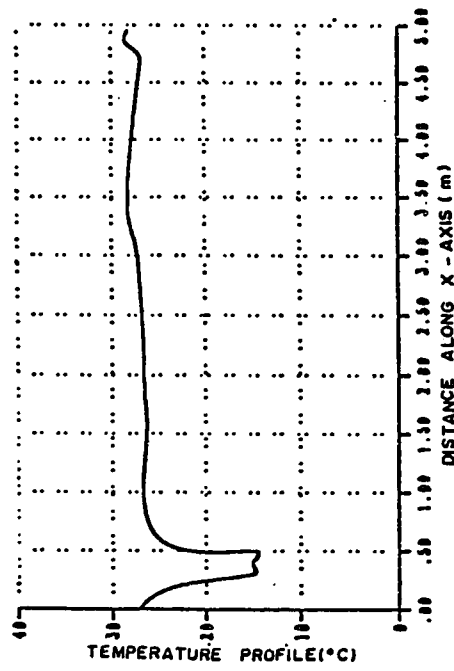
b) Y/H = 0.28 and Z/W = 0.5
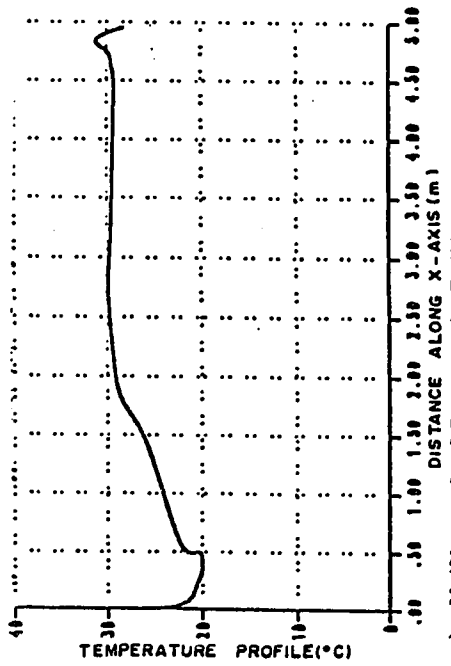
c) Y/H = 0.64 and Z/W = 0.5
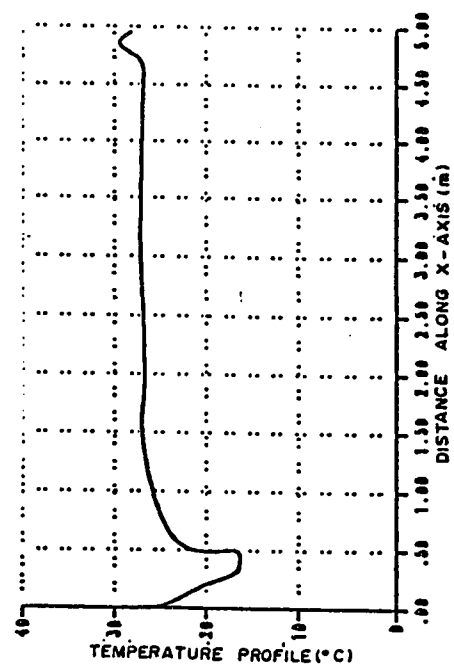
d) Y/H = 0.91 and Z/W = 0.5

Figure 7.98. Temperature profiles over length of room at mid section at 3 pm, Tin = 15 °C and Uin = 3.5 m/sec for the NN configuration.

a) Y/H = 0.051 and Z/W = 0.84

b) Y/H = 0.28 and Z/W = 0.84

c) Y/H = 0.64 and Z/W = 0.84

d) Y/H = 0.91 and Z/W = 0.84
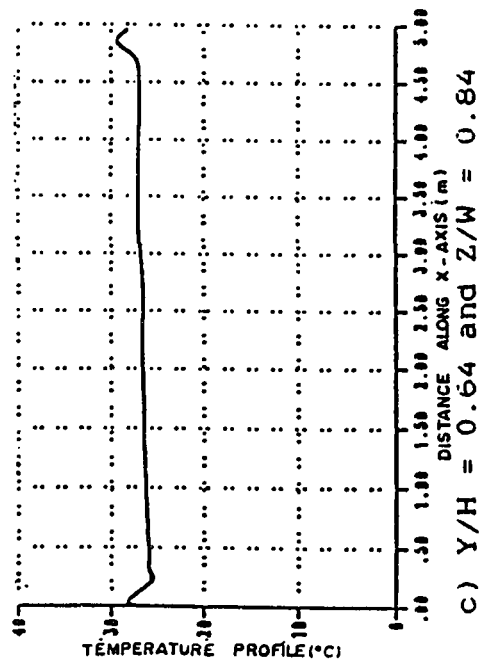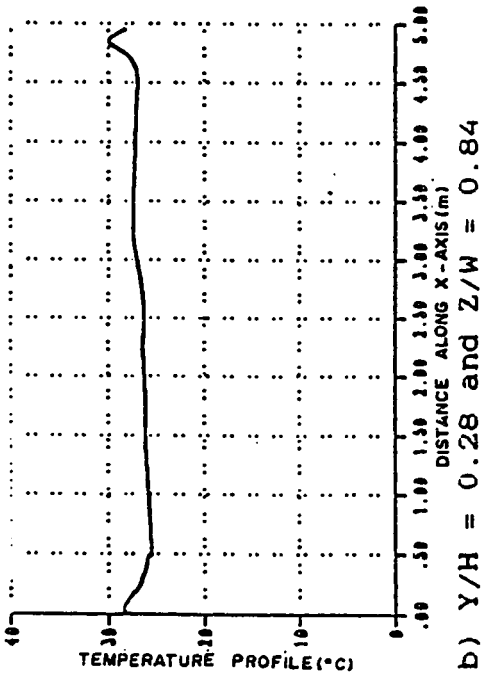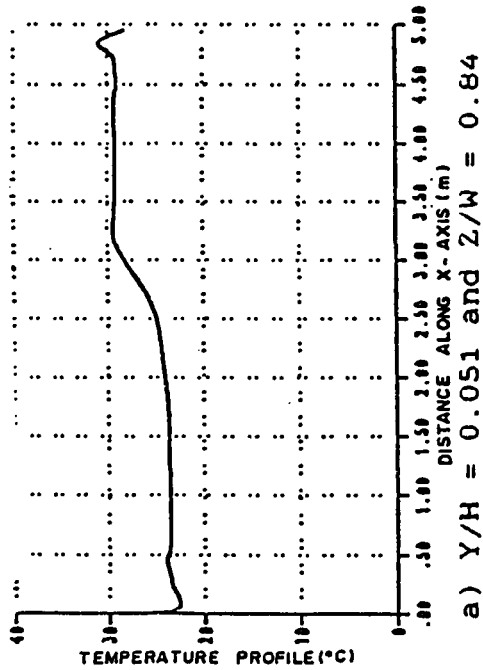
Figure 7.99. Temperature profiles over length of room near right wall at 3 pm, Tin = 15 °C and Uin = 3.5 m/sec for the NN configuration.

7.2.2.5 PMV contours

PMV Contours similar to that described in the WE configuration are plotted here.

(i) *PMV Contours at 9:00 A.M.*

The PMV Contours at 9:00 A.M. for the sitting posture are given in Figs. 7.100 and 7.101, having a T_{in} and U_{in} of 15°C and 1.9 m/sec., in the former figure, respectively and in the latter figure $T_{in} = 22°C$ and $U_{in} = 1.9$ m/sec. . Figs. 7.102 and 7.103 are plotted for the standing postures having a T_{in} and U_{in} as used in Figs. 7.100 and 7.101, respectively. Comparing Figs. 7.100.a and 7.101.a we notice that all PMVs in the former figure is lower than zero while in the latter, it is mostly zero (see Table 7.3). At 0.6 m above the floor the PMV contours are shown in Fig. 7.100.b and Fig.7.101.b where the general shape is comparable having the lowest negative PMV at the West edge of the occupied zone, but the level of the PMV in the latter figure is much closer to thermal neutrality (i.e. PMV = 0) than the former. Similar observations may be made in Figs. 7.100.c and 7.101.c where the PMVs in the former is all negative while in the latter, the PMVs are close to thermal neutrality. Similar observations may be made in Figs. 7.100.e and 7.101.e. The general conclusions and observations regarding the standing posture (Figs. 7.102 and 7.103) are similar to that made for the sitting posture and, therefore, no discussions on this are warranted.
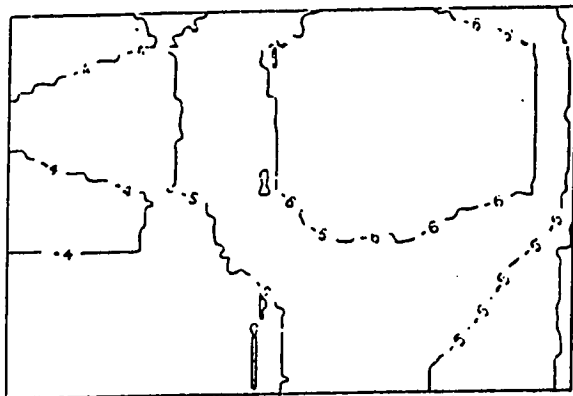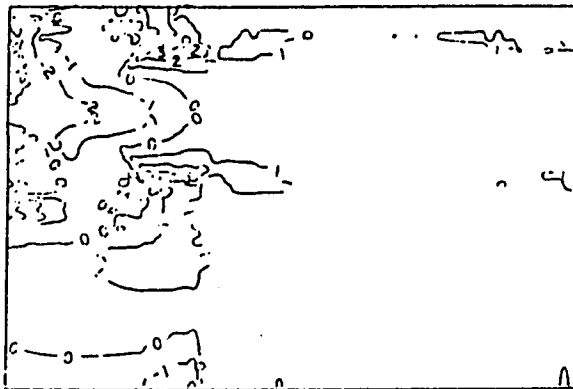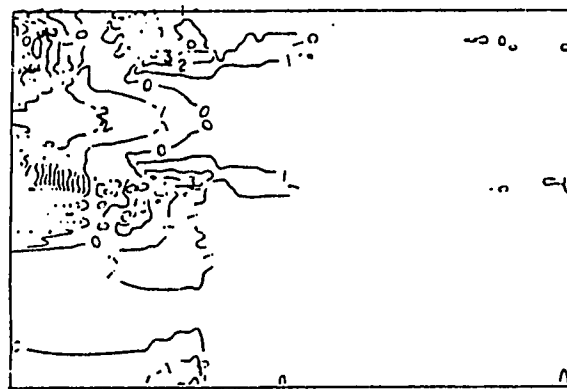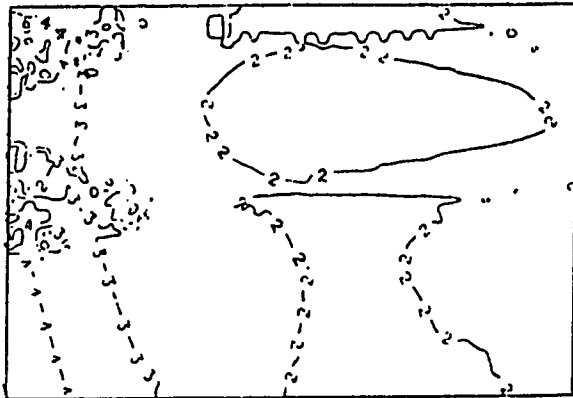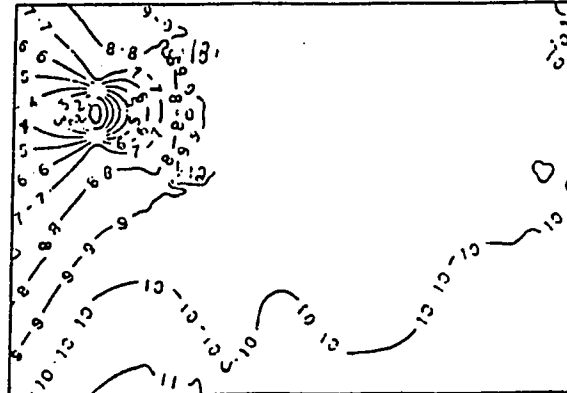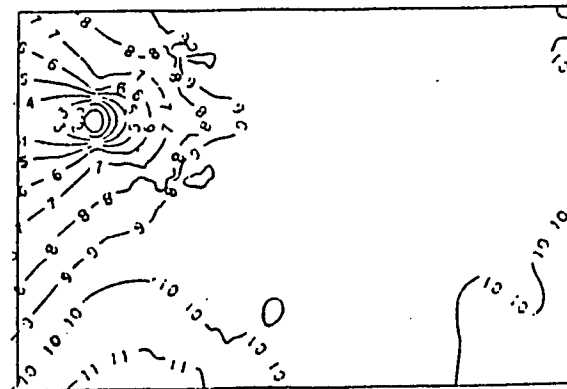
a) Y = 0.24 m, Fac = 10.0
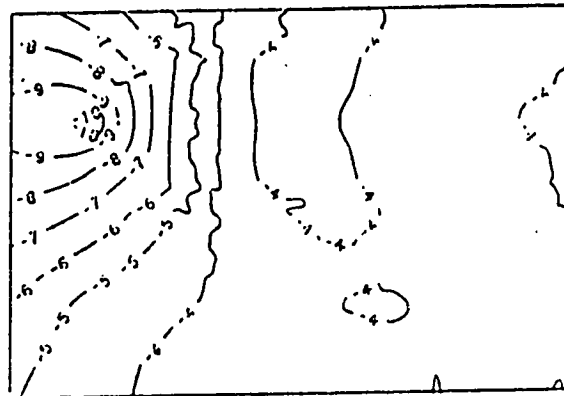
b) Y = 0.60 m, Fac = 10.0
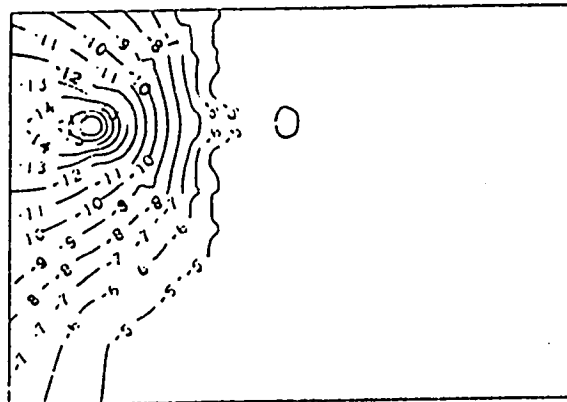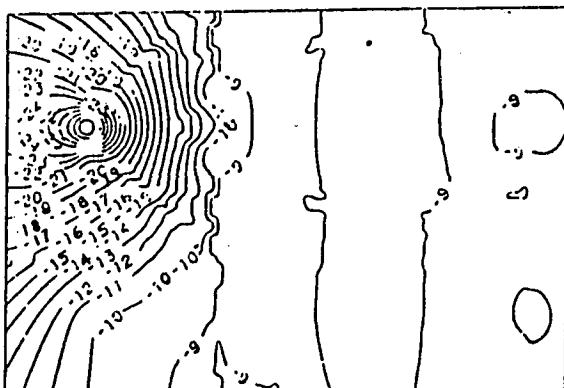
c) Y = 1.00 m, Fac = 10.0

d) CMPMV   Fac = 20.0
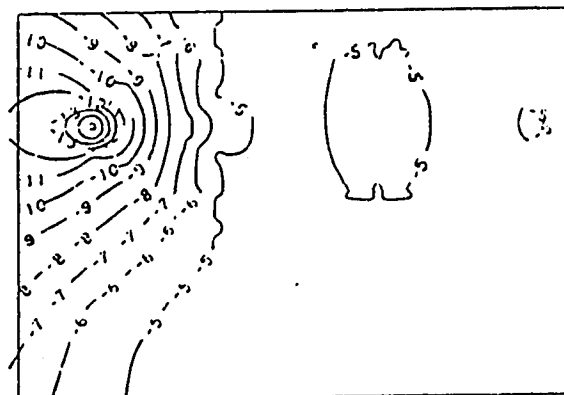
e) SAPMV   Fac = 10.0

Figure 7.100. PMV contours for the sitting posture in
the X-Z plane at 9 am, Tin = 15 °C and
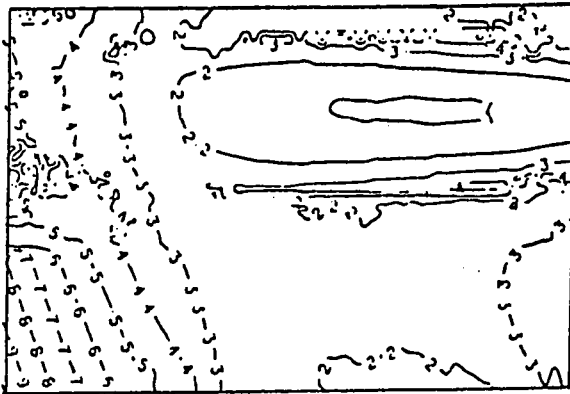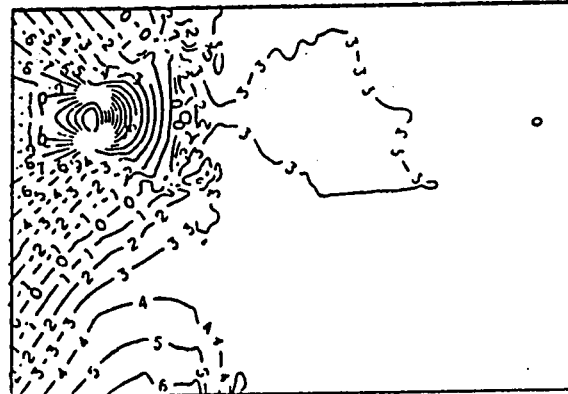Uin = 1.9 m/sec. for the NN configuration.
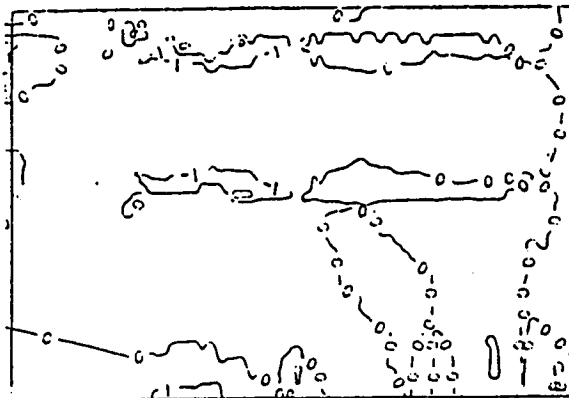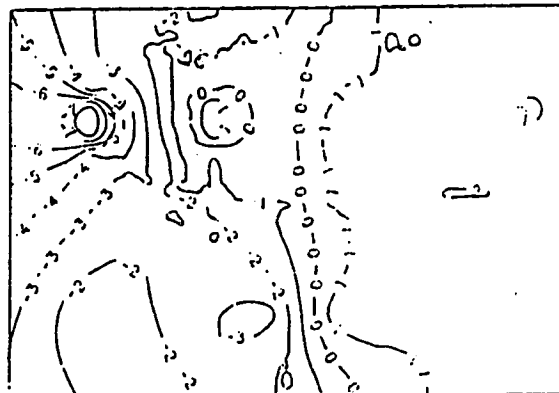
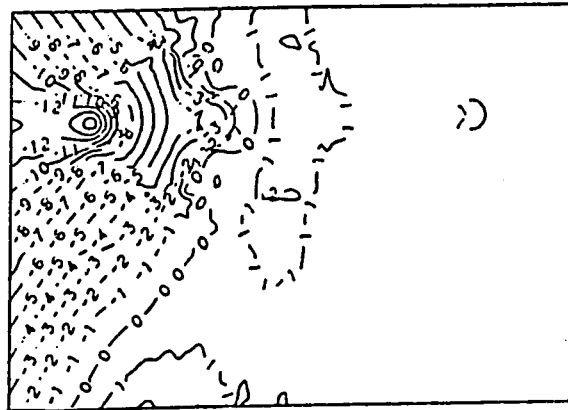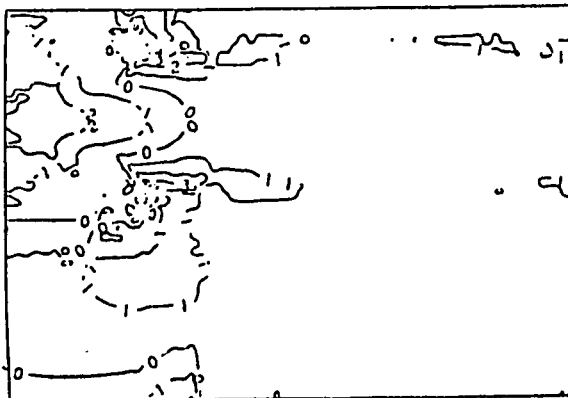a) Y = 0.24 m, Fac = 10.0
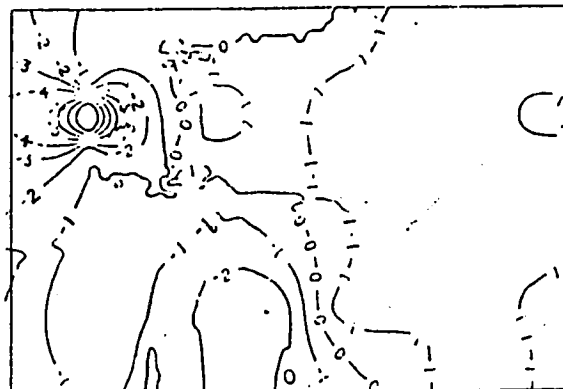
b) Y = 0.60 m, Fac = 10.0
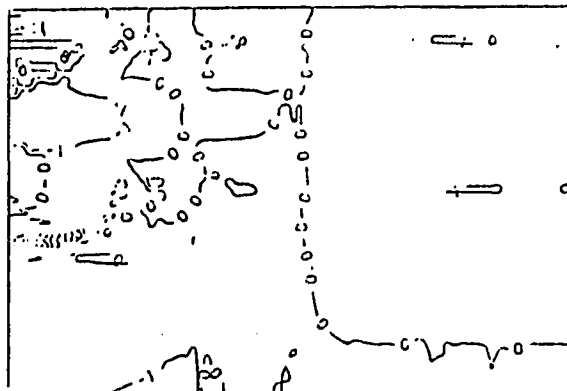
c) Y = 1.00 m, Fac = 10.0
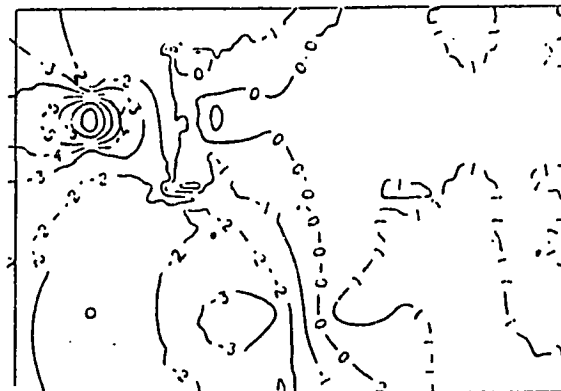
d)   CMPMV   Fac = 2.0

e) SAPMV   Fac = 10.0

Figure 7.101. PMV contours for the sitting posture in
the X-Z plane at 9 am, Tin = 18 °C and
Uin = 1.9 m/sec. for the NN configuration.
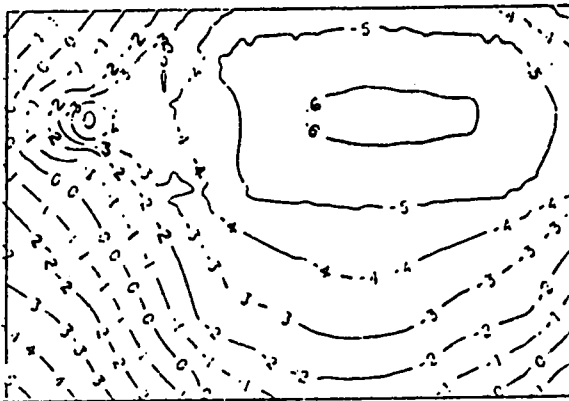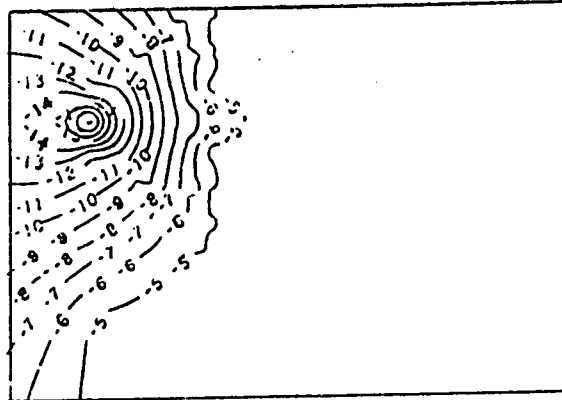
a) Y = 0.24 m, Fac = 10.0
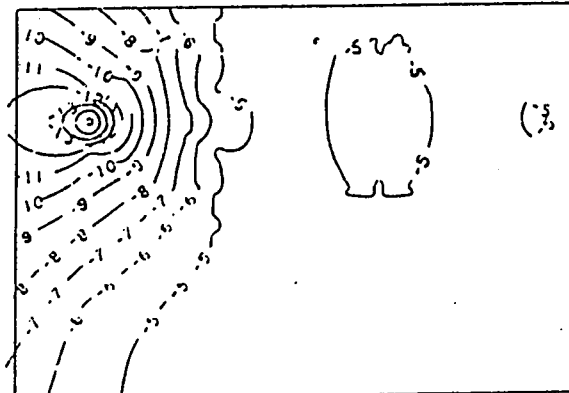
b) Y = 0.60 m, Fac = 10.0
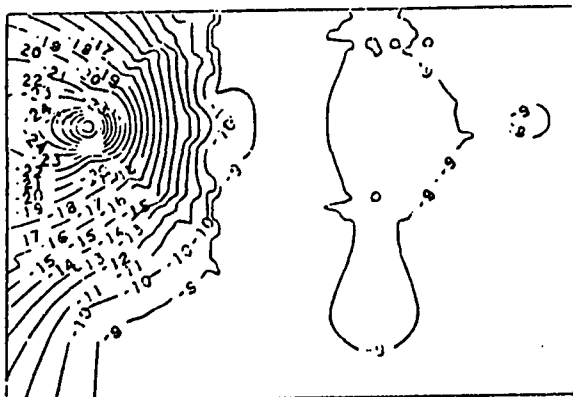
c) Y = 1.00 m, Fac = 10.0
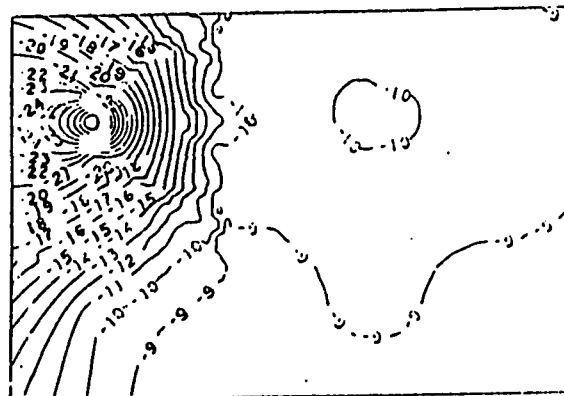
d) CMPMV   Fac = 20.0

e) SAPMV   Fac = 20.0

Figure 7.102. PMV contours for the standing posture in
the X-Z plane at 9 am, Tin = 15 °C and
Uin = 1.9 m/sec. for the NN configuration.
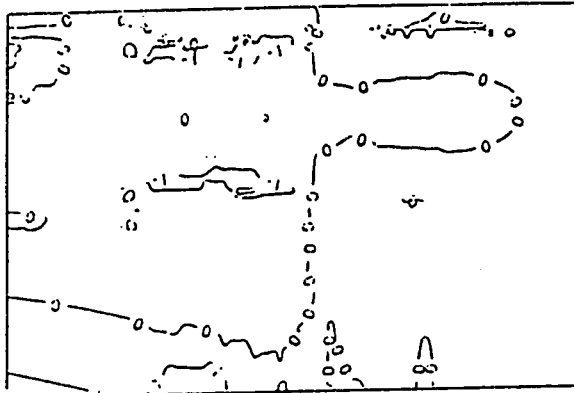
a) Y = 0.24 m, Fac = 1.0
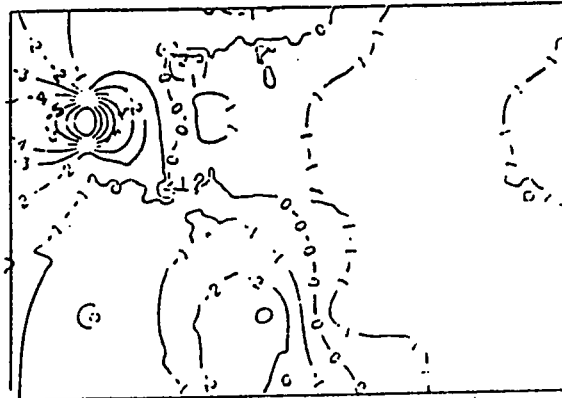
b) Y = 0.60 m, Fac = 10.0
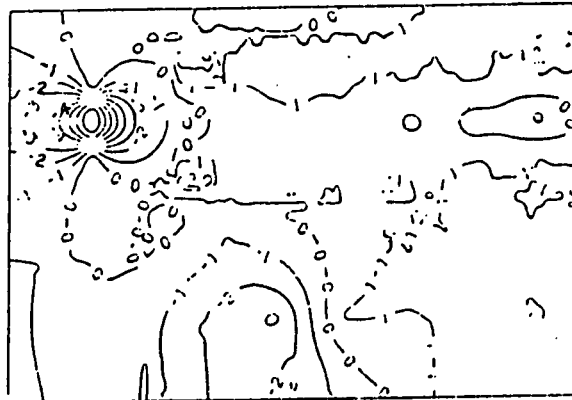
c) Y = 1.00 m, Fac = 10.0
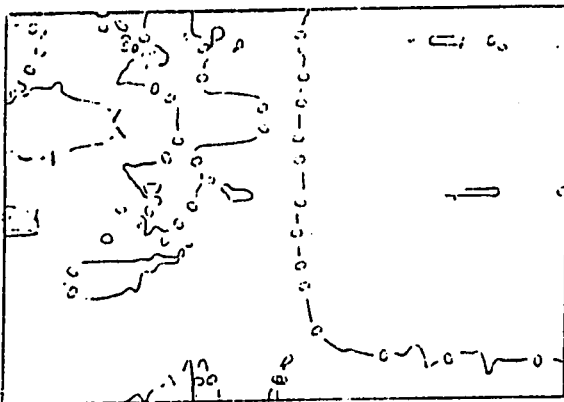
d) CMPMV   Fac = 2.0
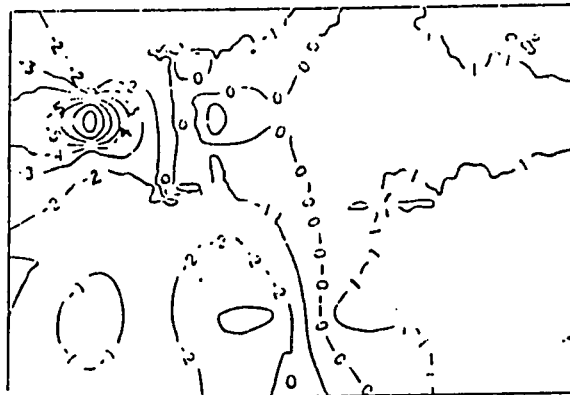
e) SAPMV   Fac = 10.0

Figure 7.103. PMV contours for the standing posture in the X-Z plane at 9 am, Tin = 18 °C and Uin = 1.9 m/sec. for the NN configuration.

(ii) PMV Contours at 12:00 Noon

The PMV contours for the sitting posture at Noon are given in Figs.7.104 and 7.105 where T_{in} and U_{in} are 15°C and 1.9 m/sec. in the former and 10°C and 2.2 m/sec. in the latter, respectively. Figs. 7.106 and 7.107 are plotted for the standing posture, having T_{in} and U_{in} as given in Figs. 7.104 and 7.105, respectively. Figs. 7.104.a and 7.105.a seem comparable having the largest PMV at the West side of the occupied zone and the lowest close to the center of the room, the relative magnitudes of the PMV in the latter figure is closer to thermal neutrality than the former. Figs. 7.104.b and 7.105.b are moderately comparable such that the lowest PMV in both appears in concentric contours close to the West side of the occupied zone although the relative PMVs in the latter is closer to thermal neutrality than the former. Similar observations may be said regarding Figs. 7.104.c and 7.105.c. The CMPMVs given in Figs. 7.104.d and 7.105.d show that the majority of contours lie closer to thermal neutrality in the latter figure relative to the former. Observations similar to these are made for the SAPMVs of Figs. 7.104.e and 7.105.e. The general conclusions and observations made for the sitting posture is similar to that of the standing posture given in Figs. 7.106 and 7.107 and, therefore, no discussions on this are necessary.

(iii) PMV Contours at 3:00 P.M.

The PMV contours for the sitting posture at 3:00 P.M. are given in Figs.7.108 and 7.109 where T_{in} and U_{in} are 15°C and 1.9 m/sec. in the for-

a) Y = 0.24 m, Fac = 5.0
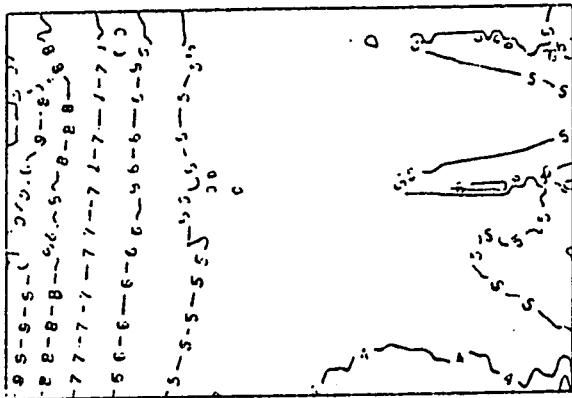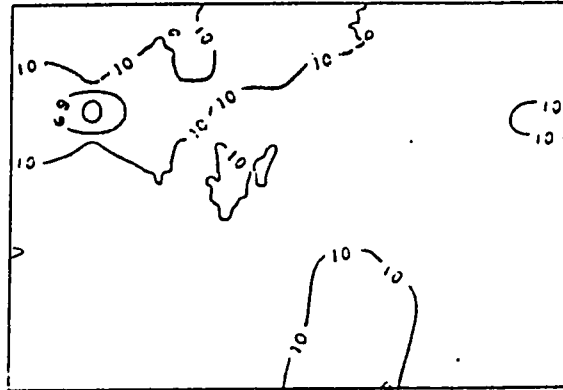
b) Y = 0.60 m, Fac = 10.0
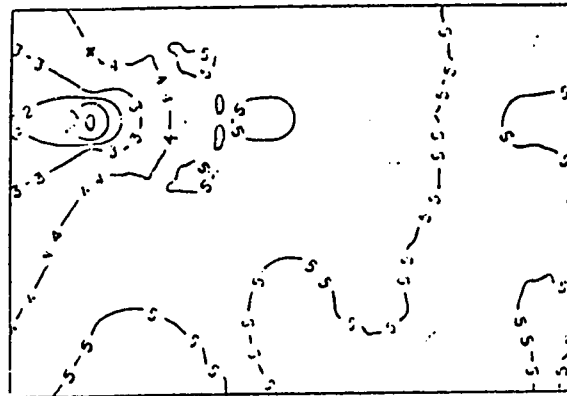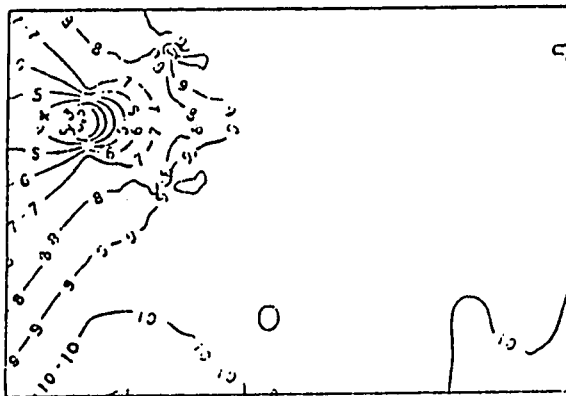
c) Y = 1.00 m, Fac = 5.0
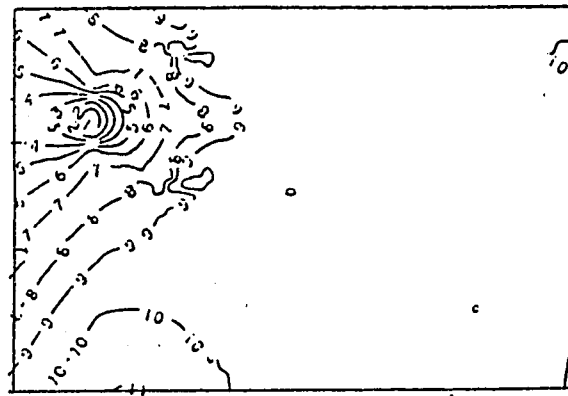
d) CMPMV   Fac = 10.0

e) SAPMV   Fac = 10.0

Figure 7.104. PMV contours for the sitting posture in
the X-Z plane at noon, Tin = 15 °C and
Uin = 1.9 m/sec. for the NN configuration.
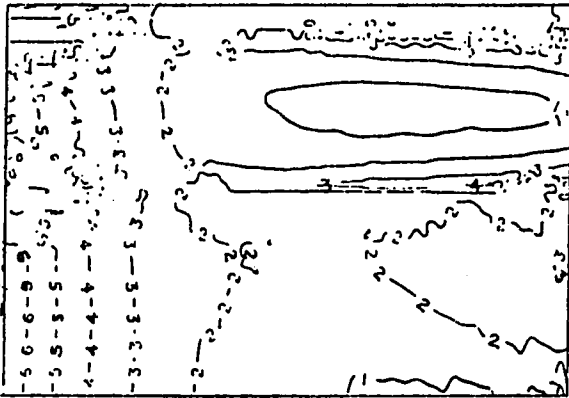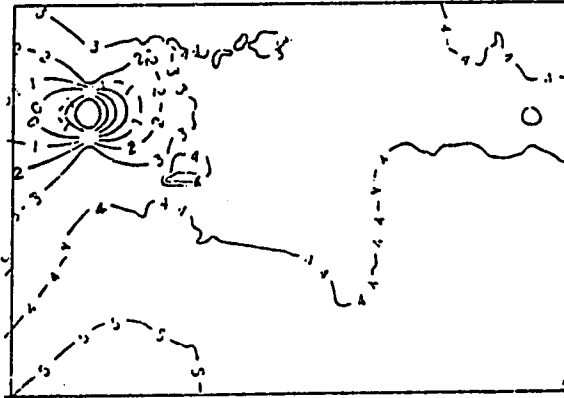
a) Y = 0.24 m, Fac = 5.0
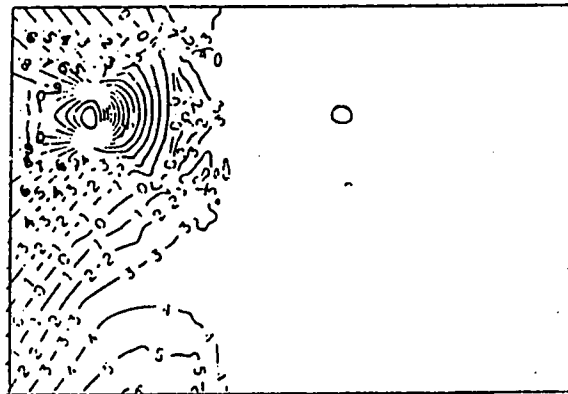
b) Y = 0.60 m, Fac = 10.0

c) Y = 1.00 m, Fac = 10.0

d) CMPMV   Fac = 2.0

e) SAPMV   Fac = 2.0

Figure 7.105. PMV contours for the sitting posture in
the X-Z plane at noon, Tin = 10 °C and
Uin = 2.2 m/sec. for the NN configuration.

a) Y = 0.24 m, Fac = 2.0

b) Y = 0.60 m, Fac = 10.0

c) Y = 1.00 m, Fac = 5.0

d) CMPMV   Fac = 10.0

e) SAPMV   Fac = 10.0

Figure 7.106. PMV contours for the standing posture in
the X-Z plane at noon, Tin = 15 °C and
Uin = 1.9 m/sec. for the NN configuration.

a) Y = 0.24 m, Fac = 5.0

b) Y = 0.60 m, Fac = 10.0

c) Y = 1.00 m, Fac = 5.0
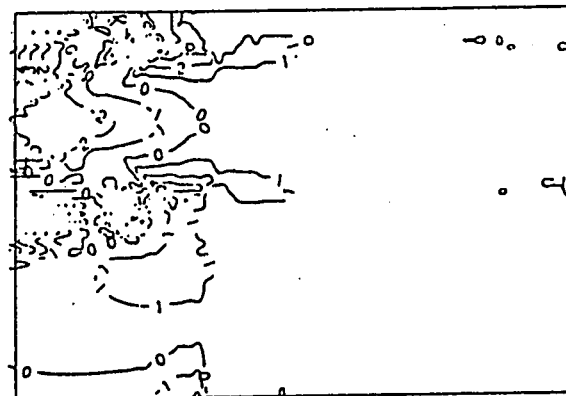
d) CMPMV   Fac = 2.0

e) SAPMV   Fac = 2.0

Figure 7.107. PMV contours for the standing posture in
the X-Z plane at noon, Tin = 10 °C and
Uin = 2.2 m/sec. for the NN configuration.
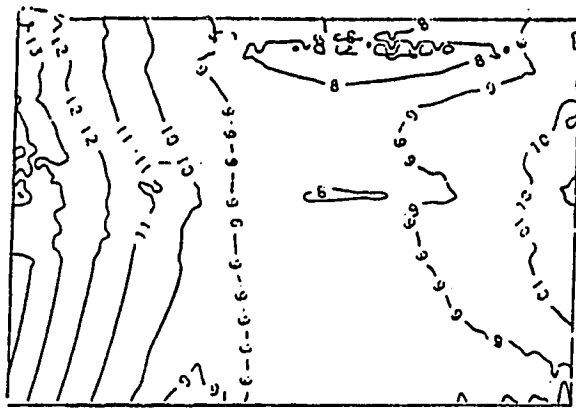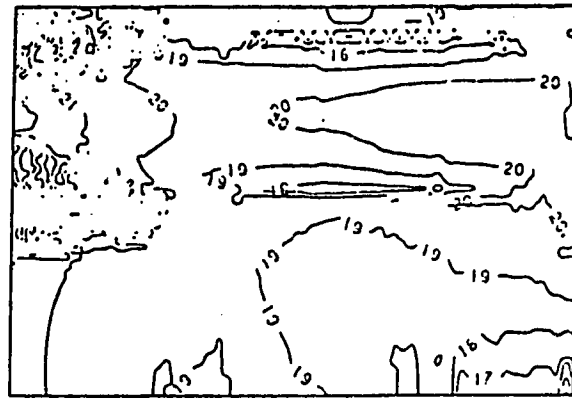
a) Y = 0.24 m, Fac = 5.0   b) Y = 0.60 m, Fac = 10.0
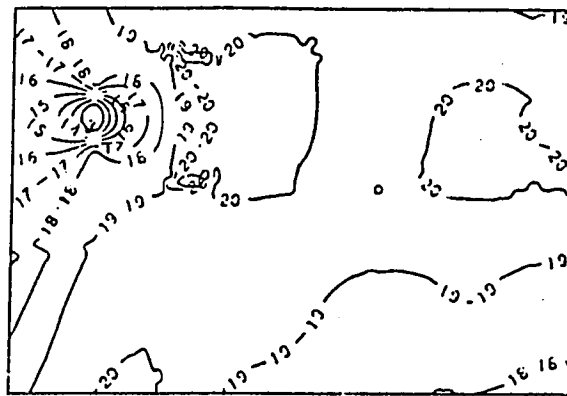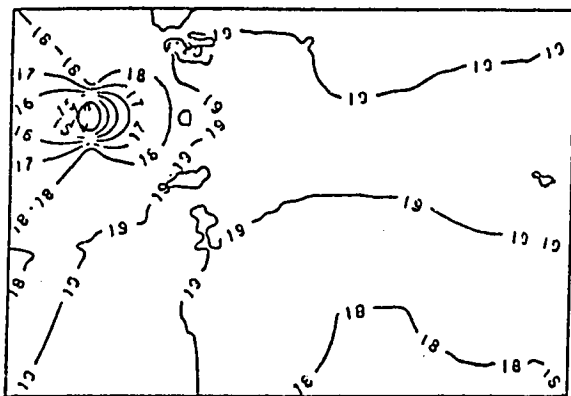
c) Y = 1.00 m, Fac = 10.0
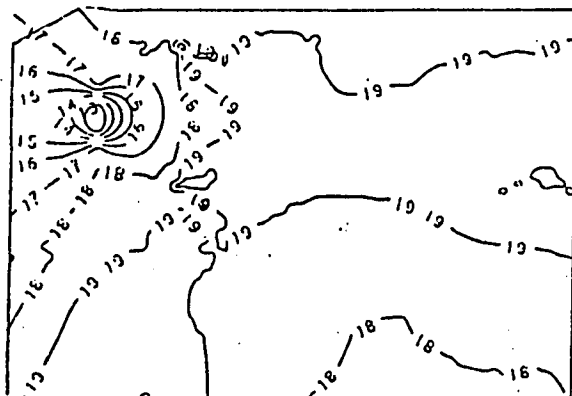
d) CMPMV   Fac = 10.0   e) SAPMV   Fac = 10.0

Figure 7.108. PMV contours for the sitting posture in
            the X-Z plane at 3 pm, Tin = 15 °C and
            Uin = 1.9 m/sec. for the NN configuration.
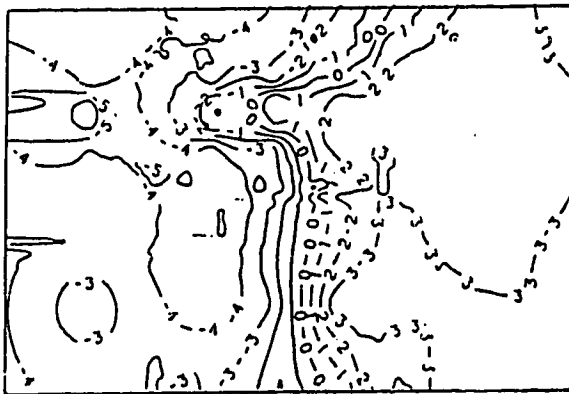
a) Y = 0.24 m, Fac = 5.0
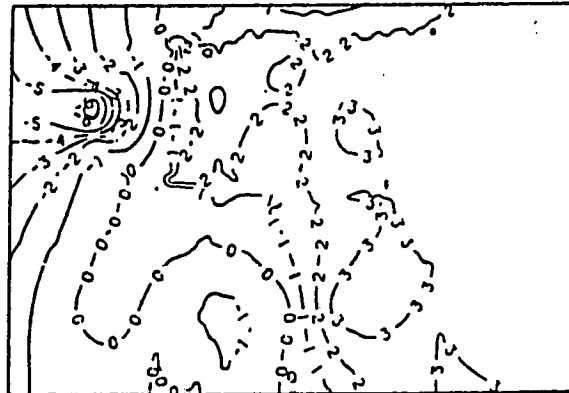
b) Y = 0.60 m, Fac = 5.0
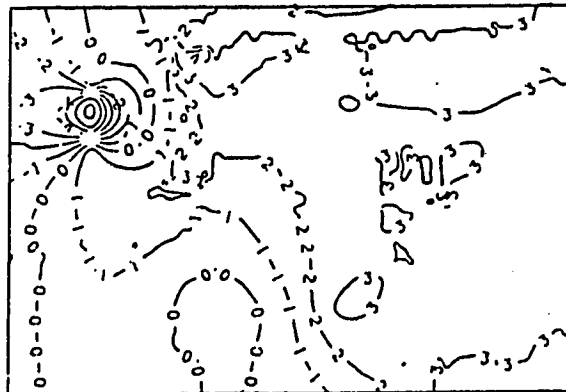
c) Y = 1.00 m, Fac = 5.0
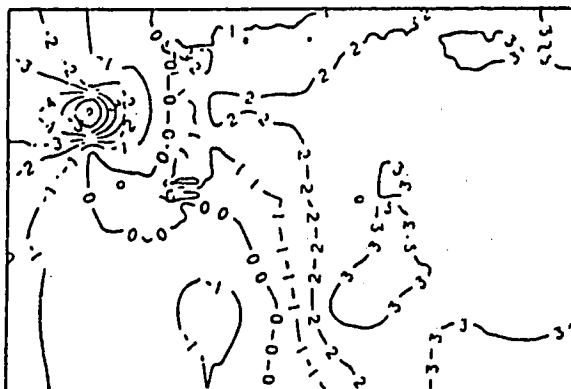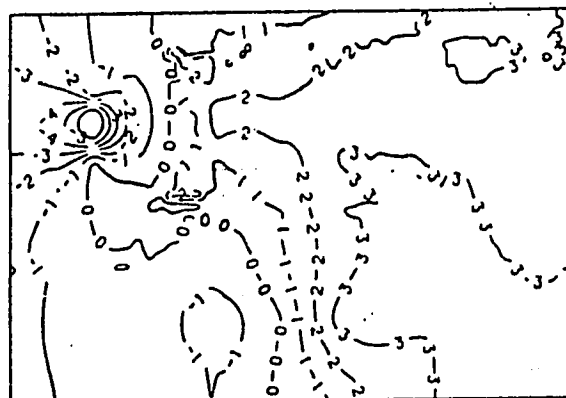
d)   CMPMV   Fac = 5.0

e) SAPMV   Fac = 5.0

Figure 7.109. PMV contours for the sitting posture in
the X-Z plane at 3 pm, Tin = 15 °C and
Uin = 3.5 m/sec. for the NN configuration.

mer and 15°C and 3.5 m/sec. in the latter, respectively. Figs. 7.110 and 7.111 are plotted for the standing posture, with T_{in} and U_{in} as used in Figs. 7.108 and 7.109, respectively. In Fig.7.108.a the central region of the occupied zone has, relatively the lowest value of PMV while the highest is close to the West side of the occupied zone. In Fig. 7.109.a, the relatively lowest PMV values are close to the West of the occupied zone and the highest is in the Eastern part of the occupied zone while in the center of this zone, the PMV is close to thermal neutrality. The general distribution of PMV in Fig. 7.108.b is similar to Fig. 7.108.a except that in the former figure, the variation of PMV is not as high as in the latter figure. Figs. 7.109.b to 7.109.e are comparable in the general distribution of PMV such that the PMVs are in a concentric shape close to the West of the occupied zone where the relative lowest PMVs exist and in Eastern part of the occupied zone the PMVs are largest, furthermore in Fig. 7.109.d it should be noted that the majority of the CMPMVs are close to thermal neutrality. The distribution of PMVs in Figs. 7.108.c to 7.108.e are similar to that of Fig. 7.109.b except that the level of PMVs are higher. In Fig. 7.108.d all of the CMPMVs are higher than one, which is beyond the comfort level (see Table 7.3). The general conclusions and observations made for the PMVs in the sitting posture is similar to that for the standing posture given in Figs. 7.110 and 7.111 and, therefore, no discussions on this are necessary.
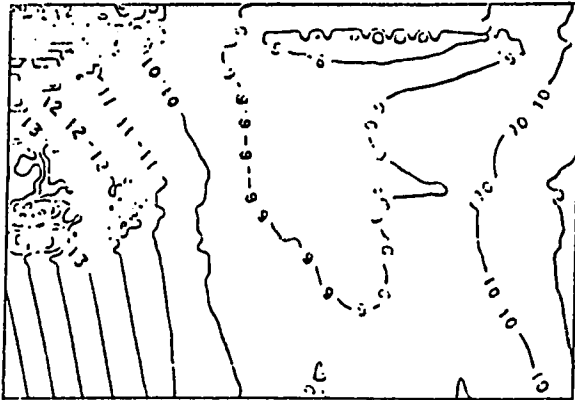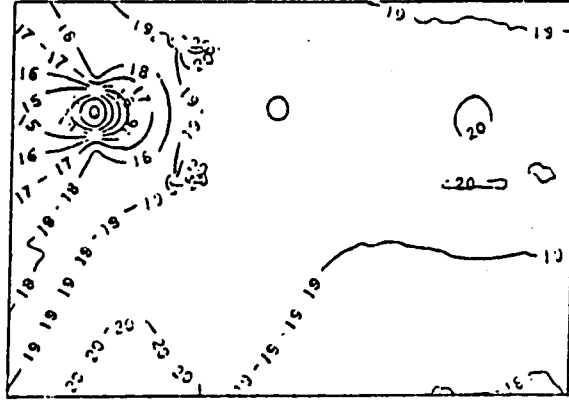
a) Y = 0.24 m, Fac = 5.0

b) Y = 0.60 m, Fac = 10.0

c) Y = 1.00 m, Fac = 2.0
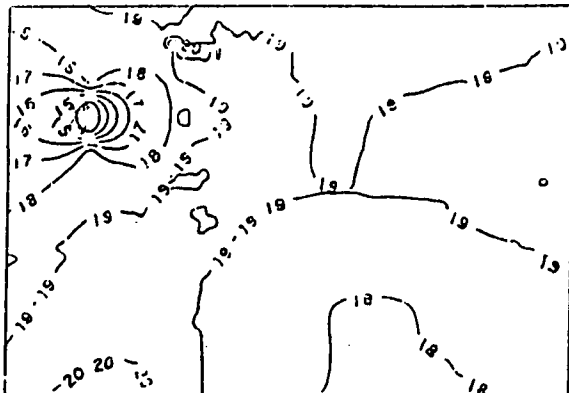
d) CMPMV   Fac = 10.0

e) SAPMV   Fac = 10.0

Figure 7.110. PMV contours for the standing posture in
the X-Z plane at 3 pm, Tin = 15 °C and
Uin = 1.9 m/sec. for the NN configuration.

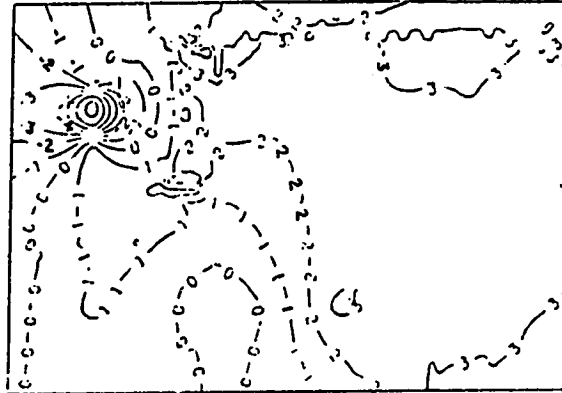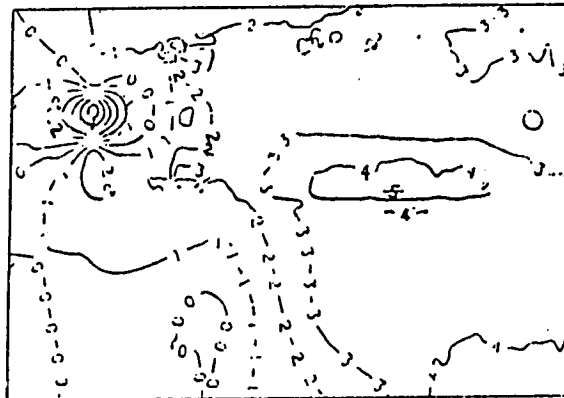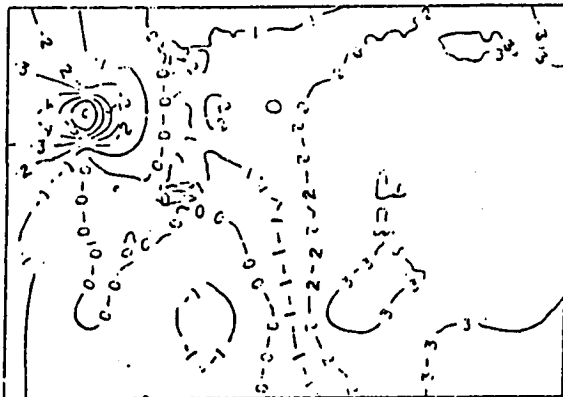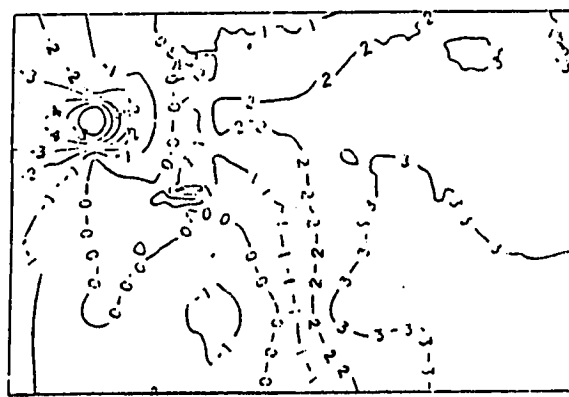a) Y = 0.24 m, Fac = 2.0

b) Y = 0.60 m, Fac = 5.0

c) Y = 1.00 m, Fac = 5.0

d) CMPMV   Fac = 5.0

e) SAPMV   Fac = 5.0

Figure 7.111. PMV contours for the standing posture in
the X-Z plane at 3 pm, Tin = 15 °C and
Uin = 3.5 m/sec. for the NN configuration.

7.2.3 The SN Configuration

In this configuration only the boundary conditions of the Noon time is investigated. The first run was initiated with a T_{in} and a U_{in} of 15°C and 1.9 m/sec., respectively which did not achieve an acceptable level of comfort. Therefore, other values of T_{in} and U_{in} were used and the one producing the 'best' level of comfort is reported which was at a T_{in} and U_{in} of 15°C and 2.8 m/sec., respectively.

7.2.3.1 Velocity vector plots

The velocity vector plots are taken at locations similar to that of the NN configuration described above. The x-y and x-z velocity vector plots for T_{in} = 15°C and U_{in} = 1.9 m/sec. are given in Figs. 7.112 and 7.113, respectively, while those for T_{in} = 15°C and U_{in} = 2.8 m/sec. are given in Figs. 7.114 and 7.115, respectively. The plots in Figs. 7.112.a and 7.114.a are nearly comparable such that relatively high velocities appear close to the ceiling and the East Wall. In Fig.7.112.b a clockwise vortex appears bounded by the East wall up to about 3/4th the length of the room, while in the remaining part of the room, opposite the inlet opening, the velocity vectors are highest and moving from the floor towards the ceiling. In Fig. 7.114.b an observation similar to that in Fig. 7.112.b appears here, except that the velocity vectors in the middle of the room are almost horizontal and moving from East to West. The velocity vector plots close to the right side of the room are plotted in Figs. 7.112.c and 7.114.c, where the general pattern of the velocity vectors here, resemble that of Fig. 7.112.a and
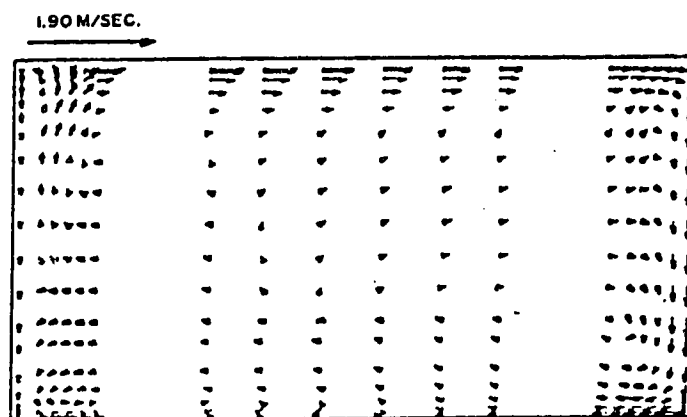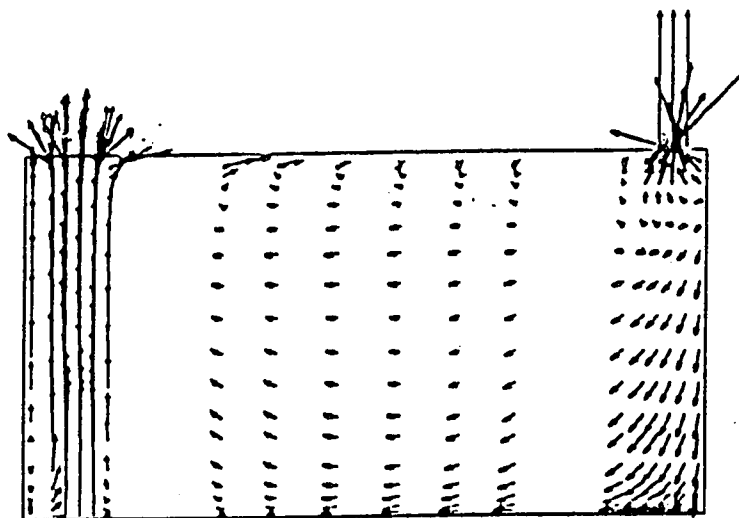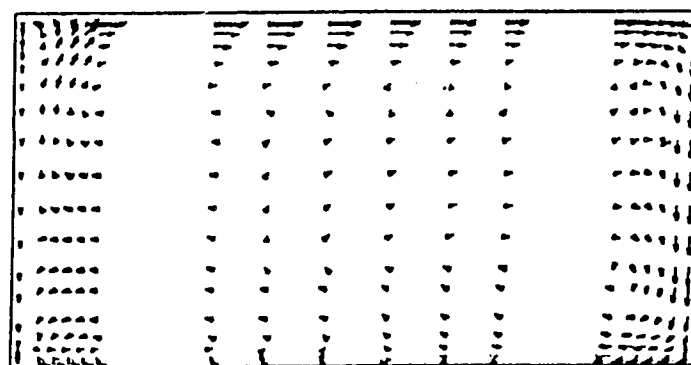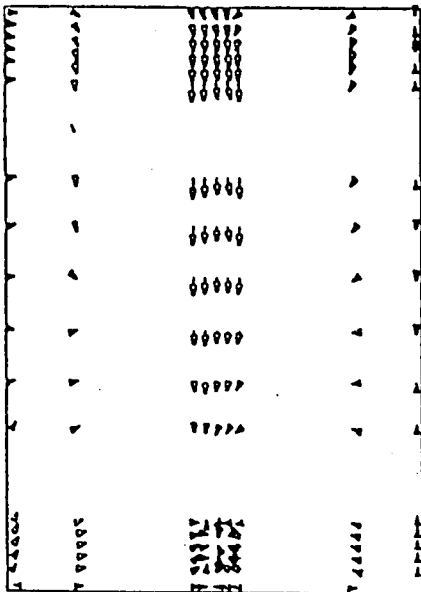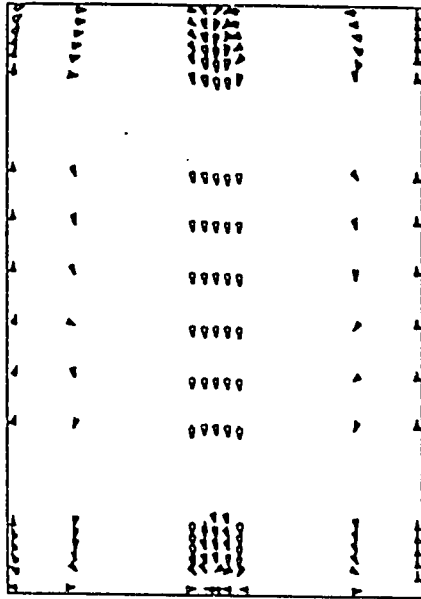
a) X-Y Section at Z = 0.600 m

b) X-Y Section at Z = 1.850 m

c) X-Y Section at Z = 3.100 m

Figure 7.112. Velocity vector plots in the X-Y plane at noon, Tin = 15 °C and Uin = 1.9 m/sec for the SN configuration.
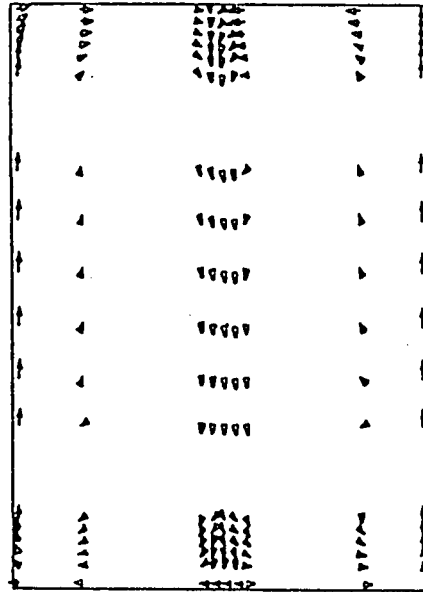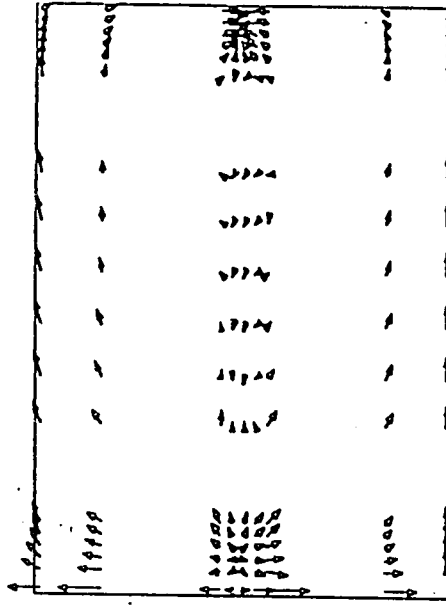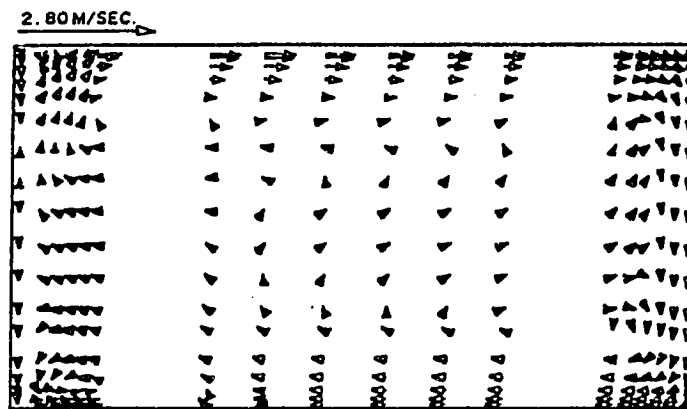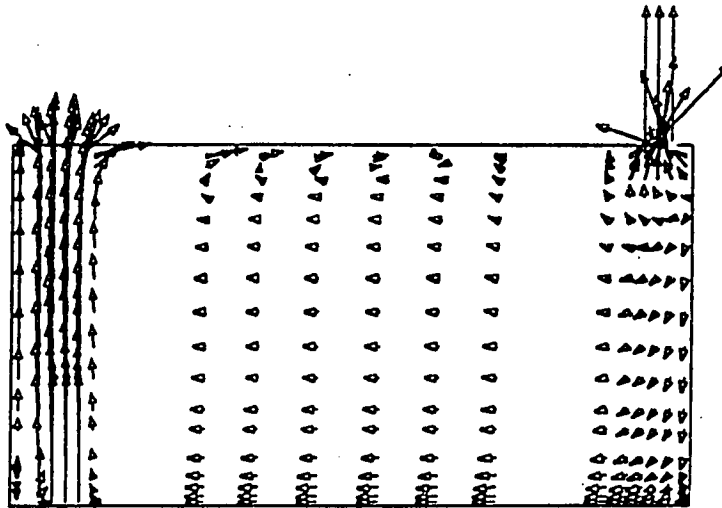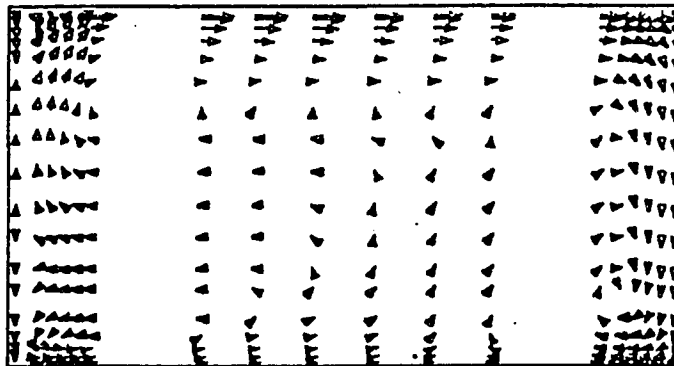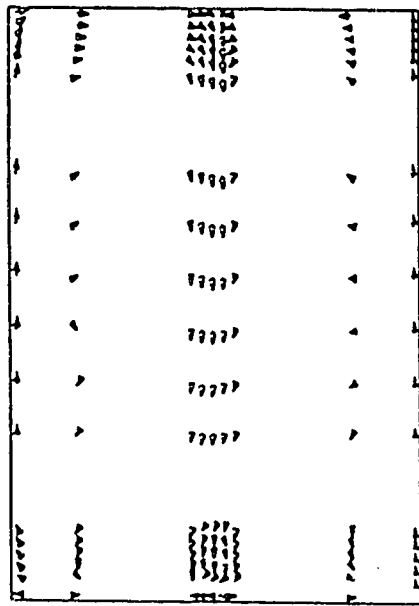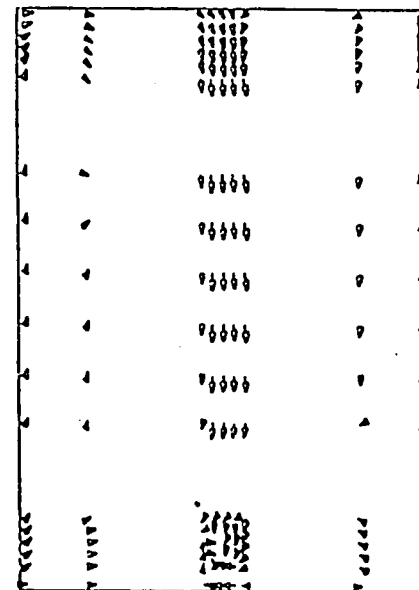
332

b) X-Z Section at Y = 0.756 m

d) X-Z Section at Y = 2.510 m

1.90M/SEC.

a) X-Z Section at Y = 0.141 m

c) X-Z Section at Y = 1.759 m

Figure 7.113. Velocity vector plots in the X-Z plane at noon, Tin = 15 °C and Uin = 1.9 m/sec for the SN configuration.

2.80 M/SEC.

a) X-Y Section at Z = 0.600 m

b) X-Y Section at Z = 1.850 m

c) X-Y Section at Z = 3.100 m
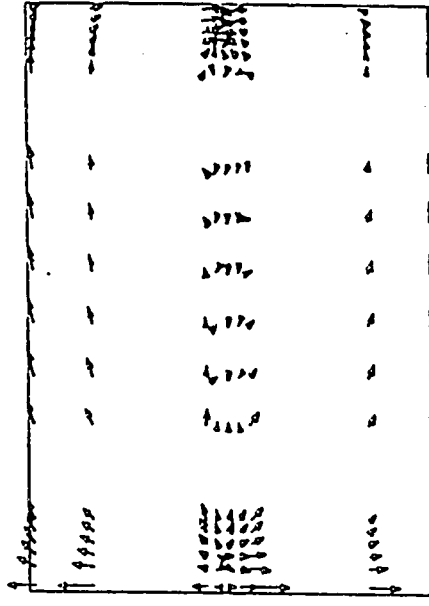
Figure 7.114. Velocity vector plots in the X-Y plane at noon,
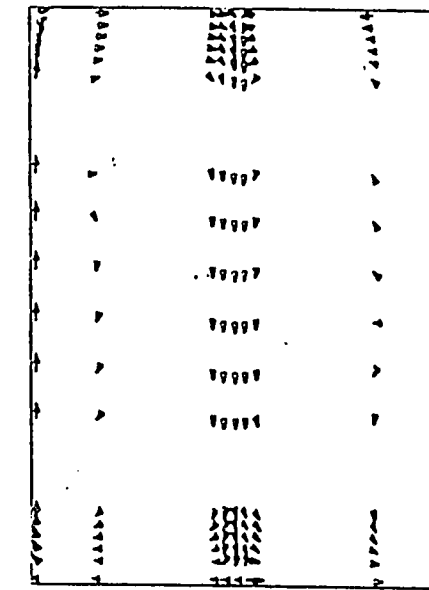Tin = 15 °C and Uin = 2.8 m/sec for the SN
configuration.

b) X-Z Section at Y = 0.756 m

d) X-Z Section at Y = 2.510 m

a) X-Z Section at Y = 0.141 m

c) X-Z Section at Y = 1.759 m

2.80M/SEC.

Figure 7.115. Velocity vector plots in the X-Z plane at noon, Tin = 15 °C and Uin = 2.8 m/sec for the SN configuration.

7.114.a. The x-z velocity vector plots close to the floor are plotted in Figs. 7.113.a and 7.115.a where the vectors at the symmetry plane are moving from the East wall to the West wall of the room and the remaining vectors are as depicted in the figures. At a height of 0.76 m and 1.76 m above the floor the velocity vectors are given in Figs. 7.113.b, 7.115.b and Figs. 7.113.c, 7.115.c, respectively, which have similarities with the velocity vector plot of Fig. 7.113.a, except that the vectors adjacent to the right and left walls are larger in Fig. 7.113.c and 7.115.c and also the velocity vectors at the mid-section of the room in Fig. 7.113.a is larger. Velocity vector plots close to the ceiling are given in Figs. 7.113.d and 7.115.d which are similar such that the general direction of flow is from the West side of the room to the East side except opposite the inlet opening where the velocity vectors move in all directions.
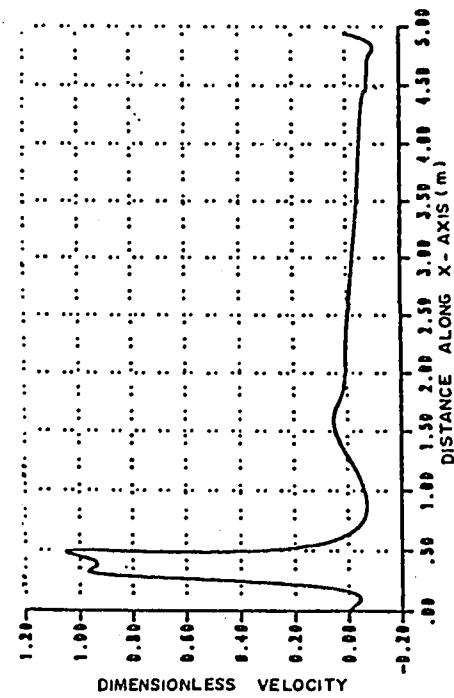
7.2.3.2 Velocity profiles

The velocity profiles are plotted for the Noon time boundary condition at locations identical to that given in the NN configuration . The velocity profiles at the mid-section of the room are given in Figs. 7.116 and 7.118 where T_{in} = 15°C in both and U_{in} = 1.9 m/sec. in the former profile and 2.8 m/sec, in the latter. Velocity profiles away from the mid section and close to the right wall of the room are given in Figs. 7.117 and 7.119, where the T_{in} and U_{in} are in the same order mentioned above for Figs. 7.116 and 7.118, respectively. Comparing Figs. 7.116 and 7.118 we note that they have similar general features therefore, a discussion only on Fig. 7.116 is necessary. The peak of the velocity profile opposite the inlet open-
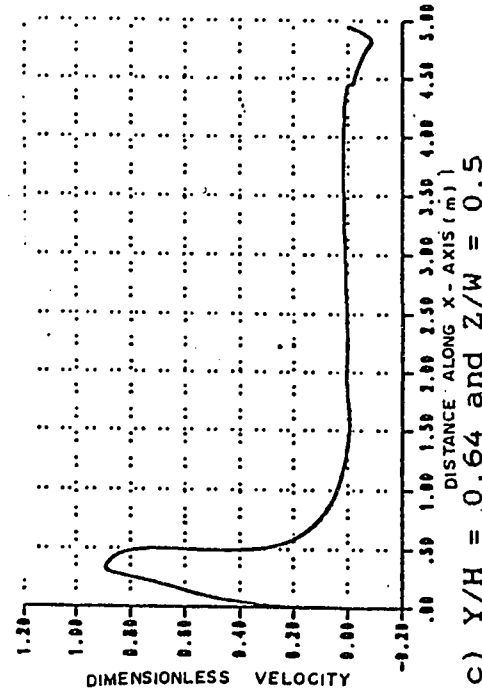
336
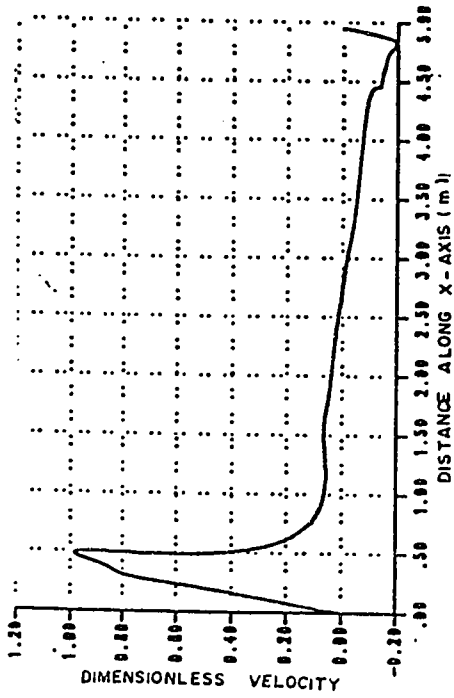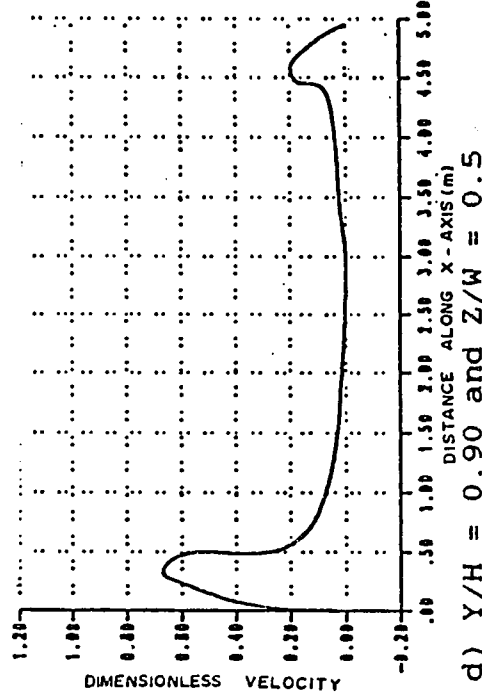
b) Y/H = 0.28 and Z/W = 0.5

a) Y/H = 0.050 and Z/W = 0.5

d) Y/H = 0.90 and Z/W = 0.5

c) Y/H = 0.64 and Z/W = 0.5

Figure 7.116. Dimensionless velocity profiles over length of room at mid section at noon, Tin = 15 °C and Uin = 1.9 m/sec for the SN configuration.

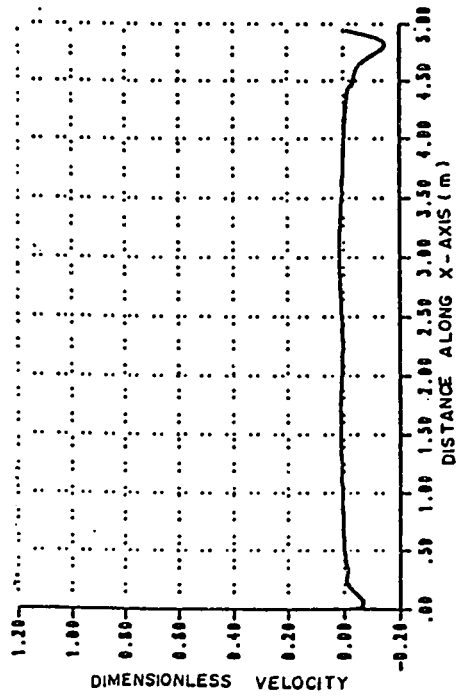a) Y/H = 0.050 and Z/W = 0.8

b) Y/H = 0.28 and Z/W = 0.8

c) Y/H = 0.64 and Z/W = 0.8

d) Y/H = 0.90 and Z/W = 0.8

Figure 7.117. Dimensionless velocity profiles over length of room near right wall at noon, Tin = 15 °C and Uin = 1.9 m/sec for the SN configuration.

338

b) Y/H = 0.28 and Z/W = 0.5

d) Y/H = 0.90 and Z/W = 0.5

a) Y/H = 0.050 and Z/W = 0.5

c) Y/H = 0.64 and Z/W = 0.5

Figure 7.118. Dimensionless velocity profiles over length of room at mid section at noon, Tin = 15 °C and Uin = 2.8 m/sec for the SN configuration.

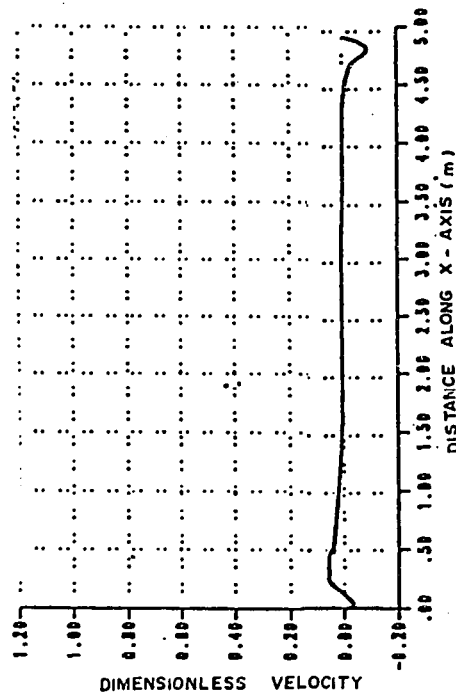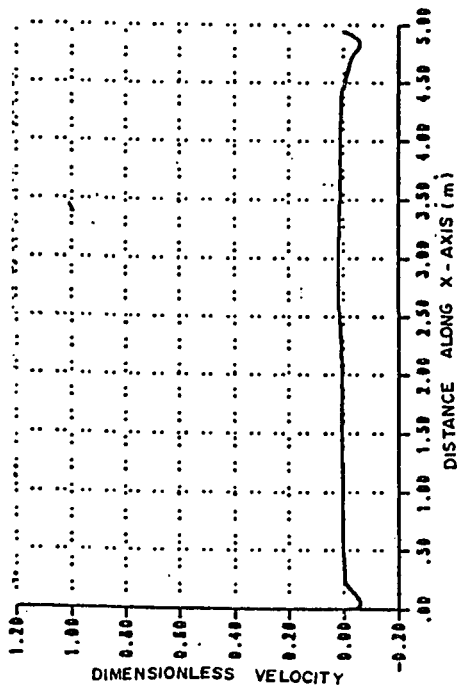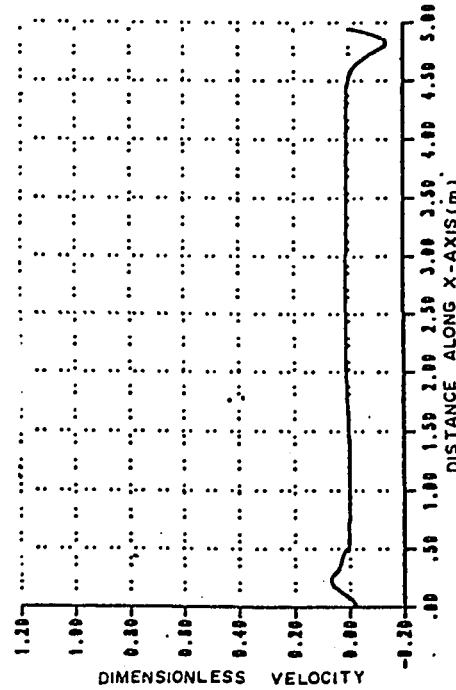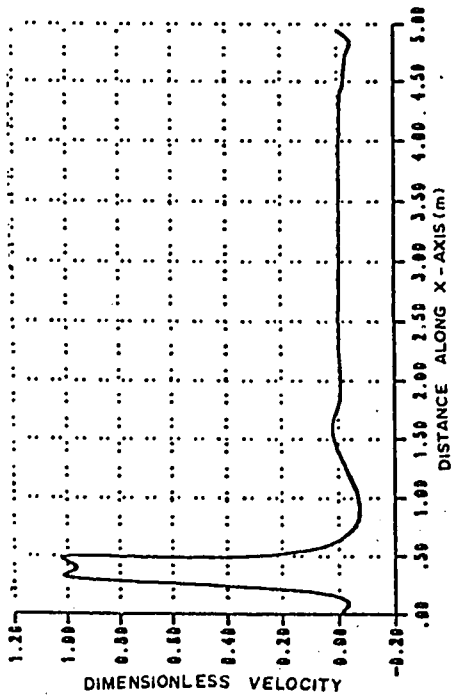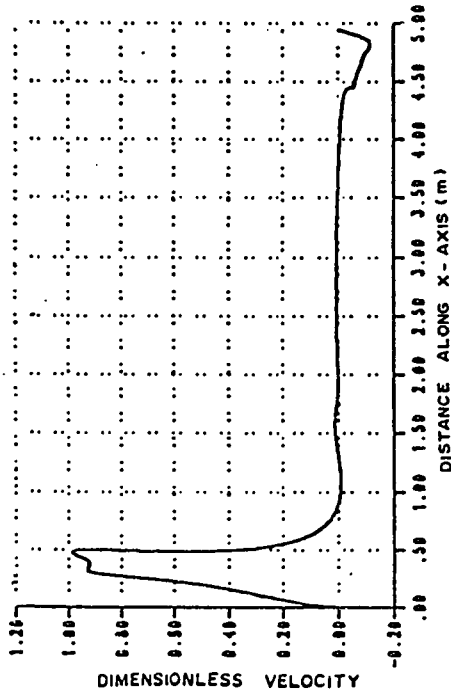a) Y/H = 0.050 and Z/W = 0.8

b) Y/H = 0.28 and Z/W = 0.8

c) Y/H = 0.64 and Z/W = 0.8

d) Y/H = 0.90 and Z/W = 0.8
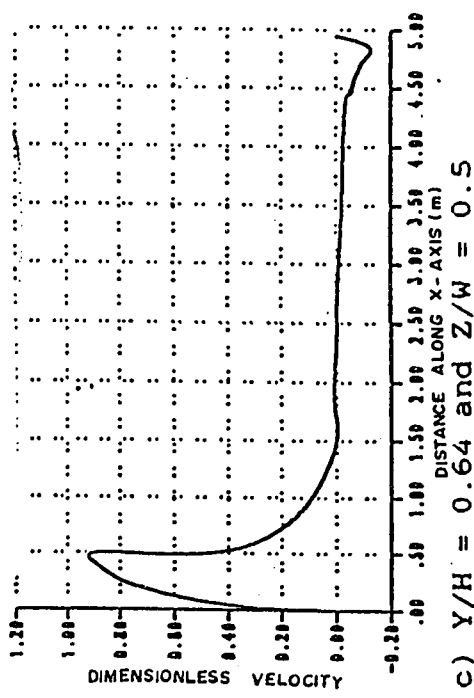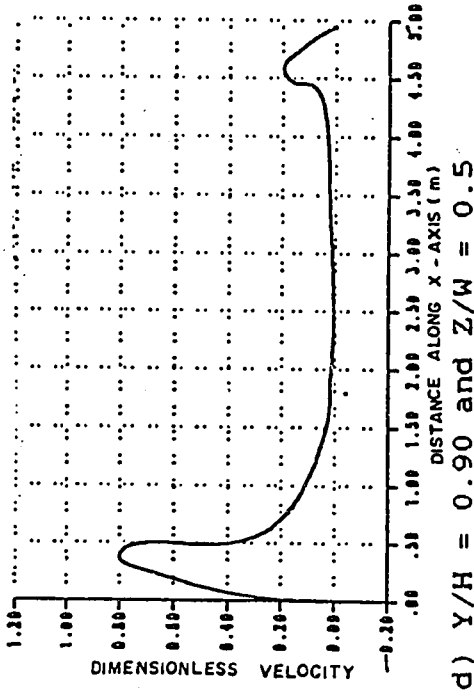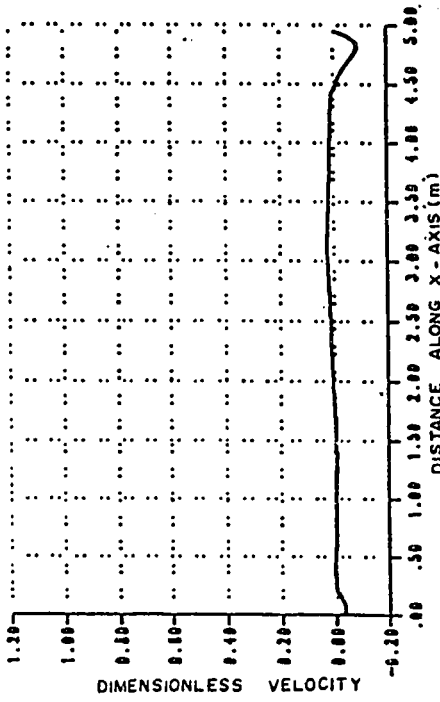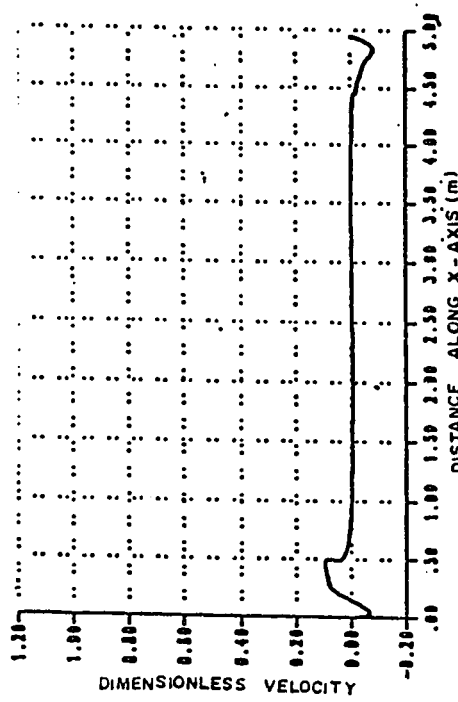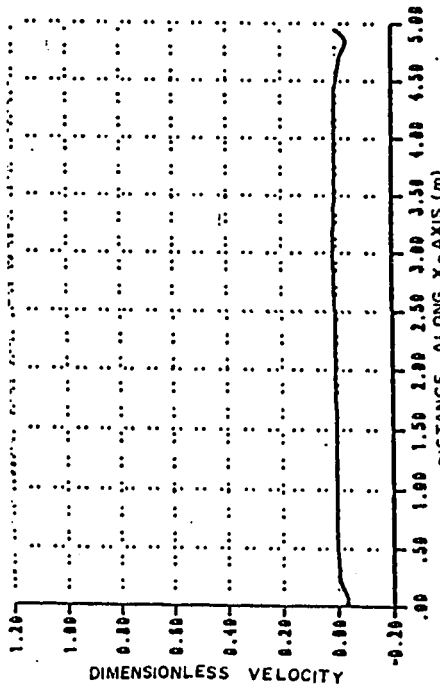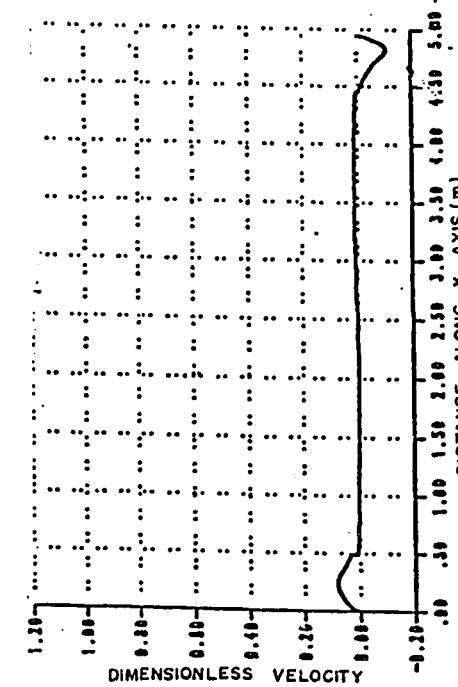
Figure 7.119. Dimensionless velocity profiles over length of room near right wall at noon, Tin = 15 °C and Uin = 2.8 m/sec for the SN configuration.

ing reaches close to one in Fig. 7.116.a while the remaining profile is relatively close to zero except opposite the outlet opening, where a negative peak is observed. The general appearance of the velocity profiles in Figs. 7.116.b and 7.116.c resembles that of Fig. 7.116.a described earlier, except that the negative peak in Fig. 7.116.b is relatively the largest. At the farthest point away from the floor at a height of 2.5 m, the positive peak, opposite the inlet opening, remains but reduces considerably, while the profile opposite the outlet opening now becomes positive. Away from the mid-section of the room and close to the right wall (at $z = 3.1$ m) the general features of the velocity profiles for the two cases reported here, given in Figs. 7.117 and 7.119 are similar and a discussion of the former is given. In Fig. 7.117.a the velocity profile is mostly zero except adjacent to the West and East sides of the room where small negative peaks of the velocity profile appear. This form also appears in Fig. 7.117.b except that the negative peak adjacent to the East wall is relatively larger. Closer to the ceiling at a height of 1.76 m above the floor, the velocity profile is plotted in Fig. 7.117.c which is generally, similar to those given in Figs. 7.117.a and 7.117.b except, that the peak of the velocity profile adjacent to the West wall is now positive. The velocity profile closest to the ceiling is given in Fig. 7.117.d and resembles that of Fig. 7.117.c, with the positive peak, close to the West wall, relatively larger.

7.2.3.3 *Temperature contours*

The temperature contours for the SN configuration are taken at the same planes of the temperature contours of the previously described con-

figurations . The contours for both cases reported here are given in Figs. 7.120 and 7.121 where T_{in} in both is identical and equal to 15°C while U_{in} in the former figure is 1.9 m/sec. and in the latter it is 2.8 m/sec. The temperature contours shown in Figs. 7.120.a and 7.121.a have a comparable distribution such that the highest temperature is in the Western side of the occupied zone, close to the center of the room. Although it is noted here that the variations in temperature and its level close to the center of the room is higher in the latter figure. At a height of 1.76 m above the floor (the upper edge of the occupied zone), the temperature contours are plotted in Figs. 7.120.b and 7.121.b. The two are similar in form such that the highest temperature appears in the central region of the room while the lowest is adjacent to the West edge of the occupied zone and the relative variations in temperature for both are nearly identical. Close to the ceiling of the room at y = 2.5 m, Fig. 7.120.c shows the relative lowest temperature at the West side of the occupied zone and increasing as we move towards the East side and this similarly occurs in Fig. 7.121.c.

7.2.3.4 Temperature profiles

Temperature profiles at locations similar to those of the NN config- uration are plotted here. The temperature profiles at the mid-section of the room are given in Figs. 7.122 and 7.124 where T_{in} = 15°C in both and U_{in} = 1.9 m/sec., in the former profile and 2.8 m/sec., in the latter. Temp- erature profiles away from the mid-section and close to the right wall of the room are plotted in Figs. 7.123 and 7.125, where T_{in} and U_{in} are in the same order given in Figs.7.122 and 7.124, respectively. Comparing Figs.
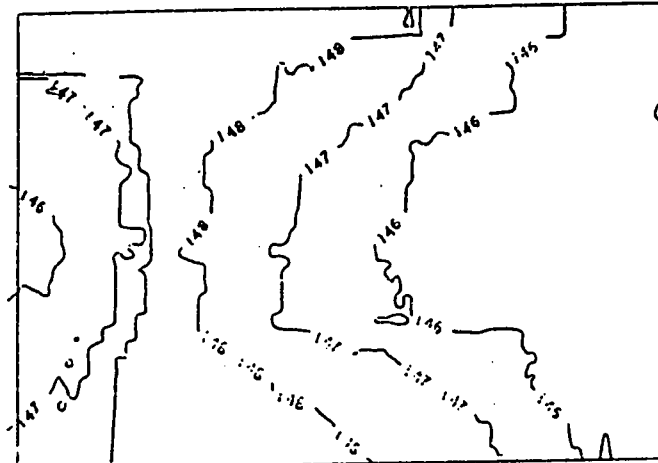
a) Y = 0.76 m, Fac = 5.0
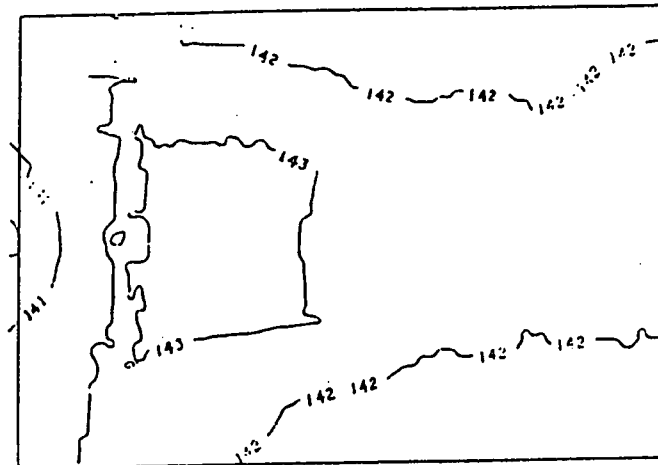
b) Y = 1.76 m, Fac = 5.0
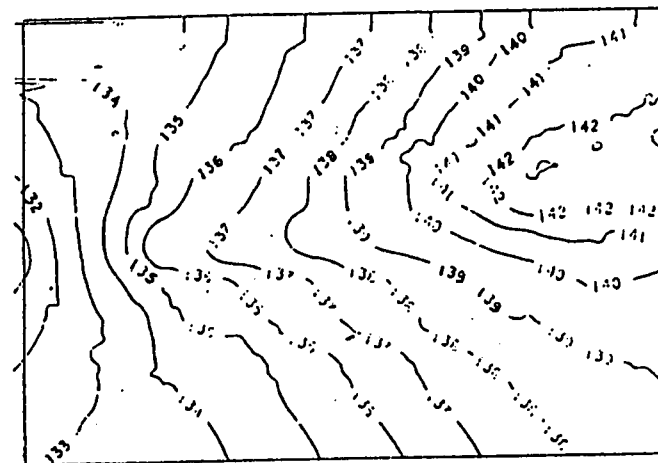
c) Y = 2.51 m, Fac = 5.0

Figure 7.120. Temperature contours in the X-Z plane at noon, Tin = 15 °C and Uin = 1.9 m/sec for the SN configuration.
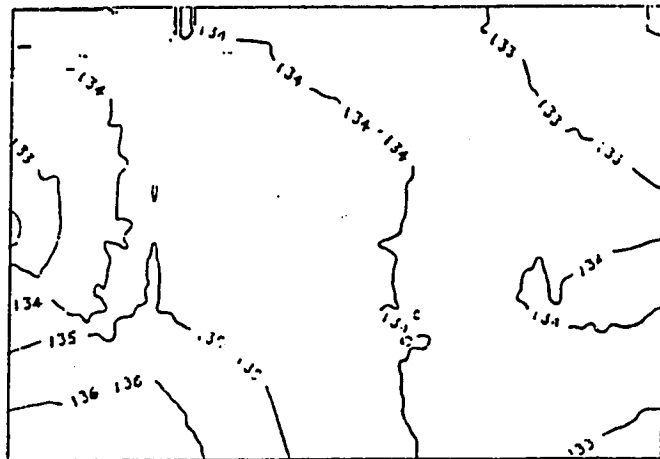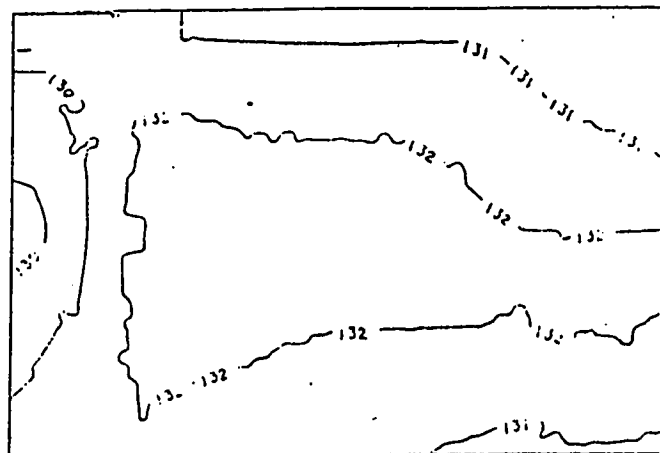
a) Y = 0.76 m, Fac = 5.0

b) Y = 1.76 m, Fac = 5.0
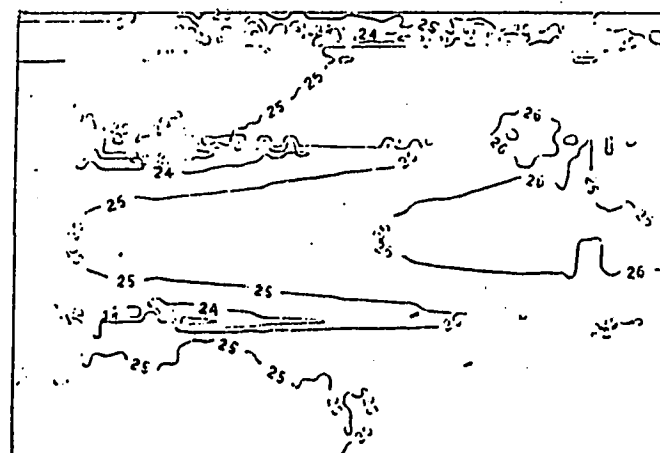
c) Y = 2.51 m, Fac = 1.0

Figure 7.121. Temperature contours in the X-Z plane at noon, Tin = 15 °C and Uin = 2.8 m/sec for the SN configuration.
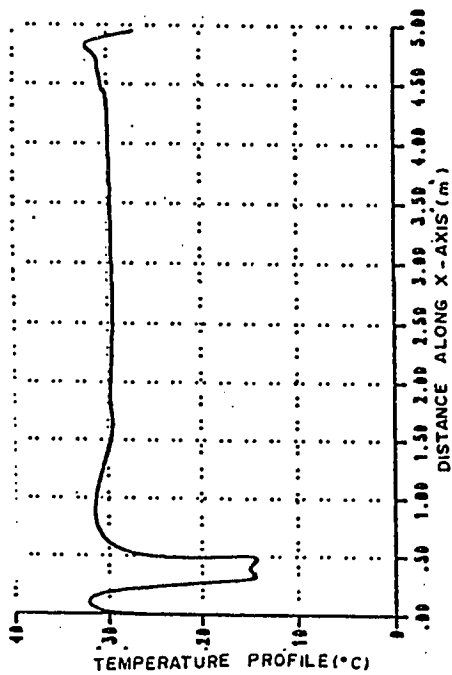
b) Y/H = 0.28 and Z/W = 0.5

a) Y/H = 0.050 and Z/W = 0.5
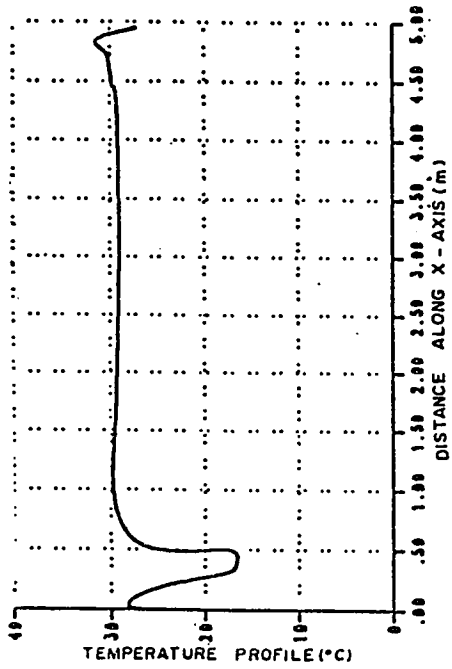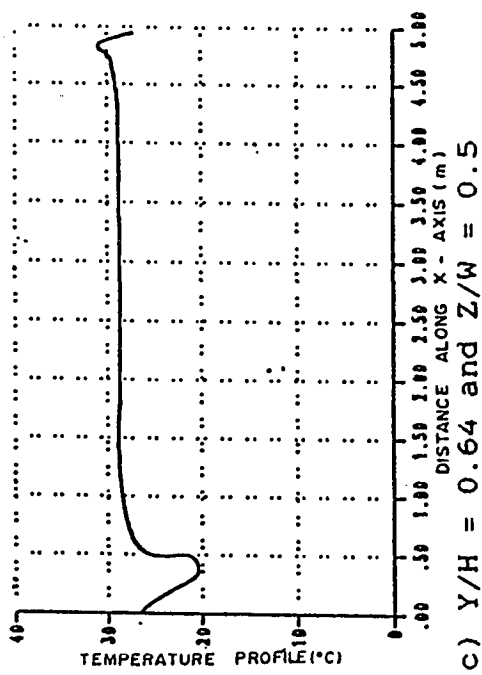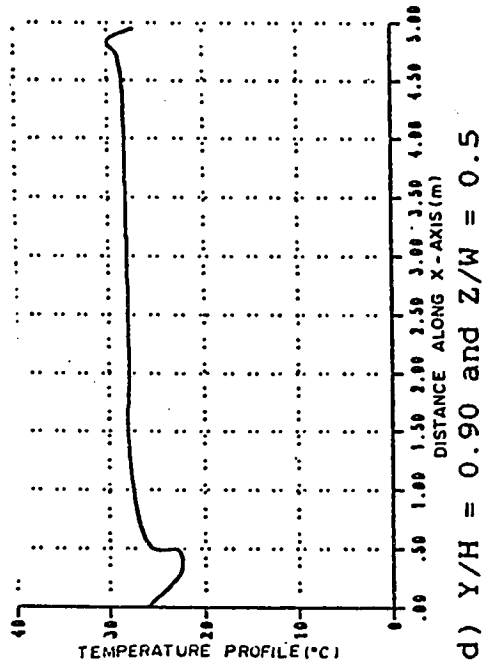
d) Y/H = 0.90 and Z/W = 0.5

c) Y/H = 0.64 and Z/W = 0.5

Figure 7.122. Temperature profiles over length of room at mid section at noon, Tin = 15 °C and Uin = 1.9 m/sec for the SN configuration.

a) Y/H = 0.050 and Z/W = 0.8

b) Y/H = 0.28 and Z/W = 0.8

c) Y/H = 0.64 and Z/W = 0.8

d) Y/H = 0.90 and Z/W = 0.8
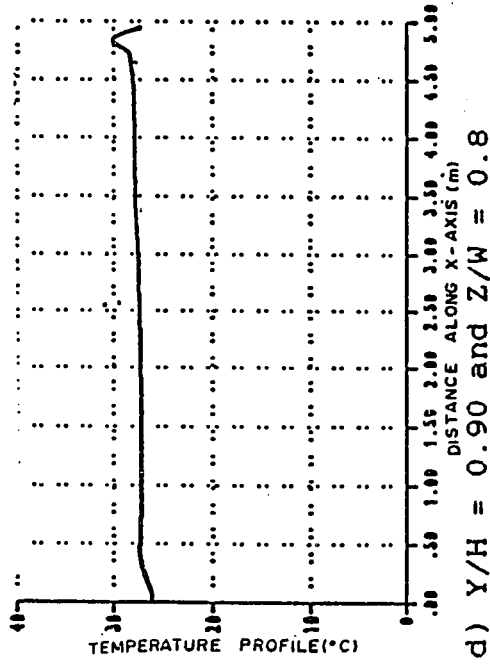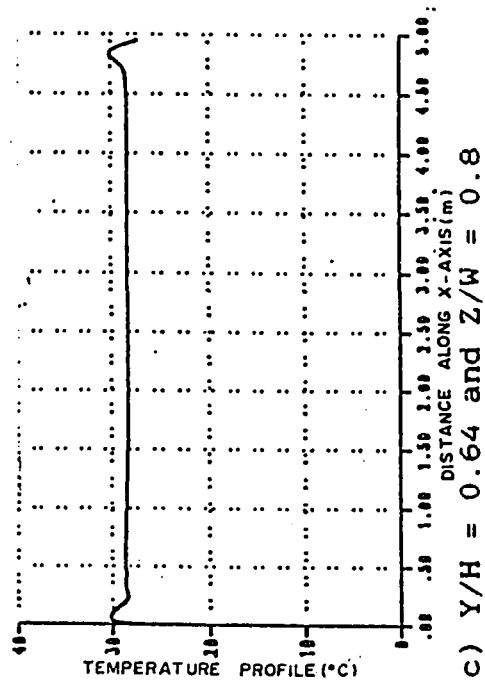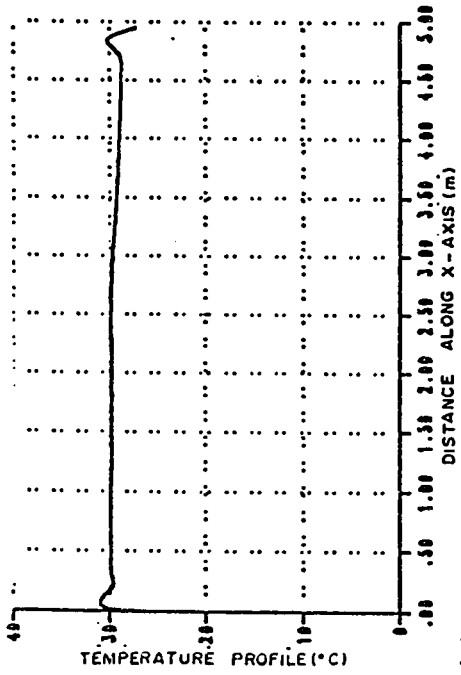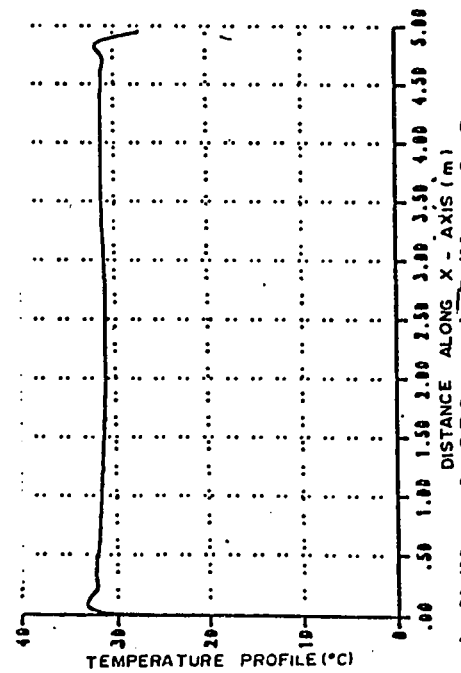
Figure 7.123. Temperature profiles over length of room near right wall at noon, Tin = 15 °C and Uin = 1.9 m/sec for the SN configuration.

346

b) Y/H = 0.28 and Z/W = 0.5

d) Y/H = 0.90 and Z/W = 0.5
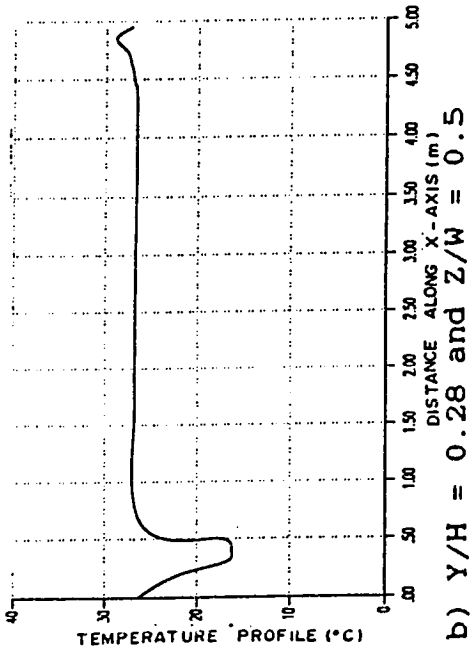
a) Y/H = 0.050 and Z/W = 0.5
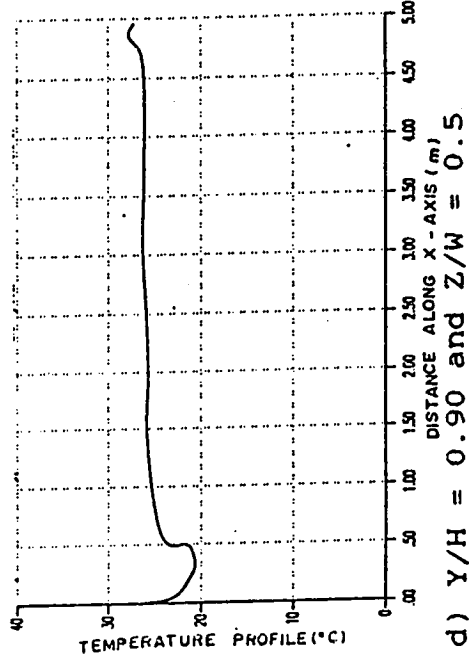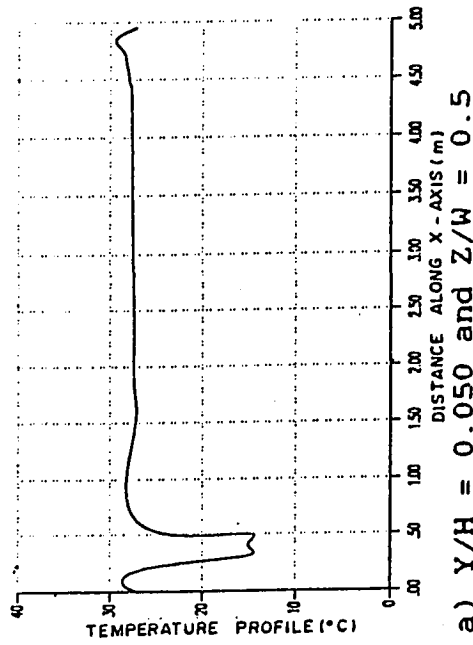
c) Y/H = 0.64 and Z/W = 0.5
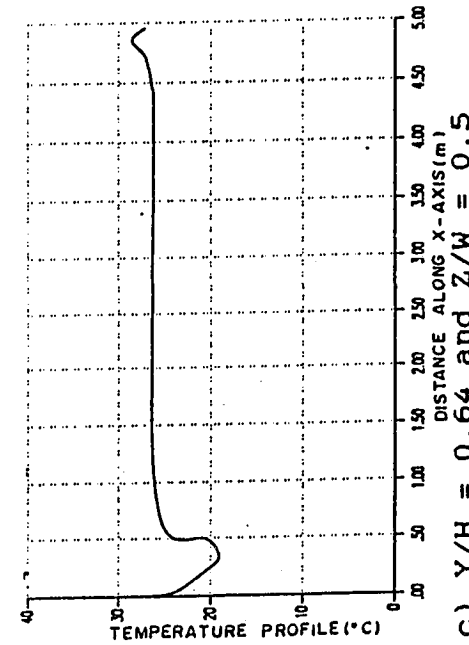
Figure 7.124. Temperature profiles over length of room at mid section at noon. Tin = 15 °C and Uin = 2.8 m/sec for the SN configuration.

347

b) Y/H = 0.28 and Z/W = 0.8

d) Y/H = 0.90 and Z/W = 0.8

a) Y/H = 0.050 and Z/W = 0.8

c) Y/H = 0.64 and Z/W = 0.8
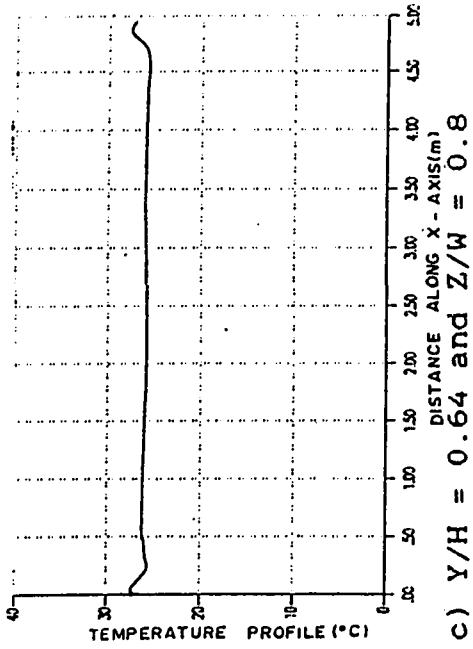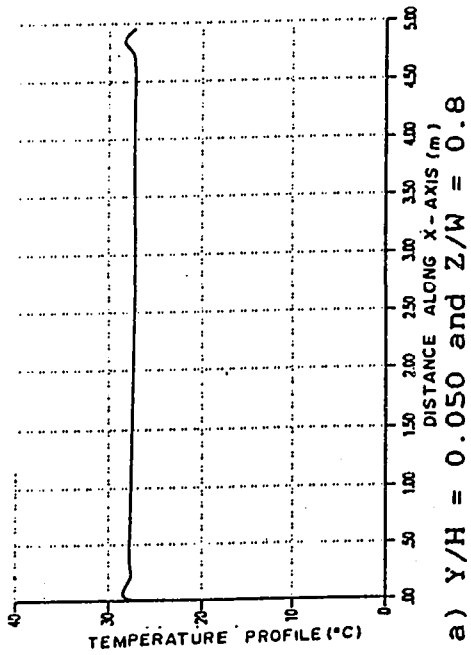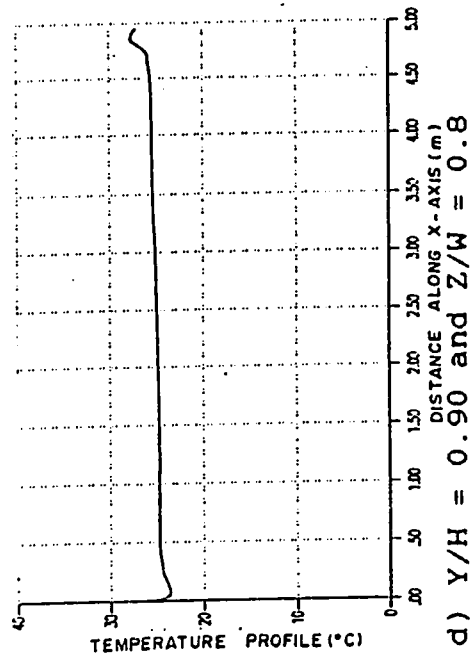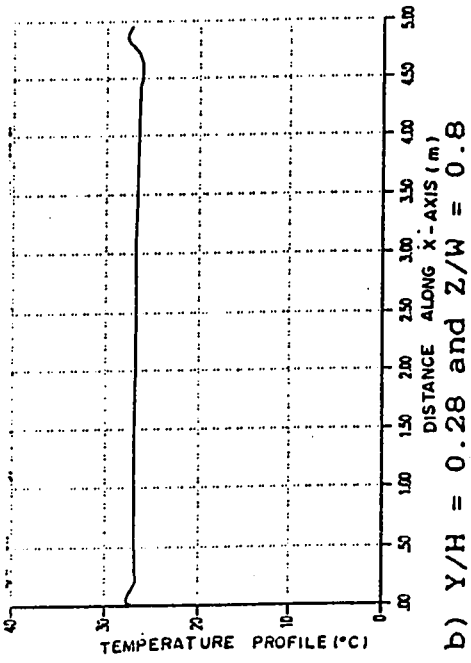
Figure 7.125. Temperature profiles over length of room near right wall at noon, Tin = 15 °C and Uin = 2.8 m/sec for the SN configuration.

7.122 and 7.124, we note that the general features of both are similar and a discussion of the former temperature profiles is given. In Fig. 7.122.a the temperature profiles are mostly uniform over the length of the room except opposite the inlet opening, where a large peak of low temperature appears, and opposite the outlet, a moderate peak of relatively high temperature occur. Moving away from the inlet opening at different heights from the floor (Figs. 7.122.b, 7.122.c and 7.122.d), the general characteristics of the temperature profile resembles that discussed above but the peaks at the West and East sides of the room are decreasing as we move away from the inlet opening. Close to the right wall, the temperature profiles are given in Figs. 7.123 and 7.125 which are similar, and a discussion of the former figure is given. In Fig. 7.123.a the temperature profile is nearly uniform except adjacent to the West and East sides of room where moderate peaks of relatively higher velocities occur. This is repeated in Figs. 7.123.b to 7.123.d except that in the latter figure a peak is evident only adjacent to the East side of the room, while no peak appears opposite the inlet opening.

7.2.3.5 PMV contours

PMV contours for the Noon boundary conditions are plotted at identical planes to the previously discussed configurations. The PMV contours for the sitting posture are given in Figs. 7.126 and 7.128 where the T_{in} in both are identical and equal to 15°C while U_{in} is 1.9 m/sec. in the former and 2.8 m/sec. in the latter. The PMV contours for the standing posture are given in Figs. 7.127 and 7.129 such that the T_{in} and U_{in} are
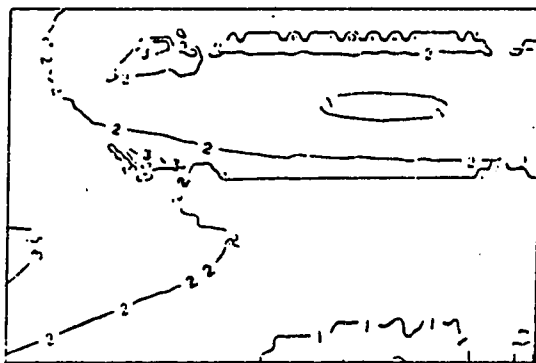
a) Y = 0.24 m, Fac = 2.0
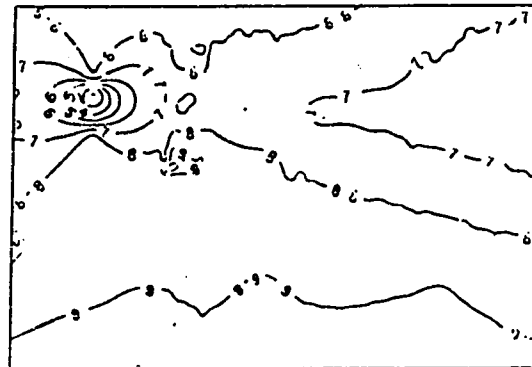
b) Y = 0.60 m, Fac = 10.0
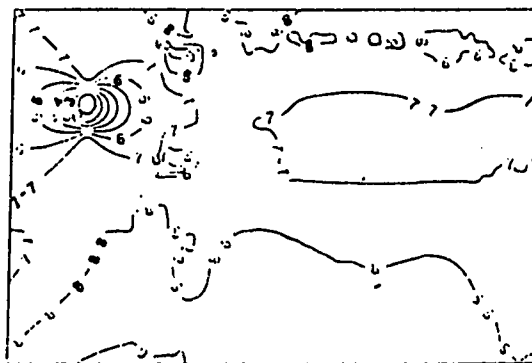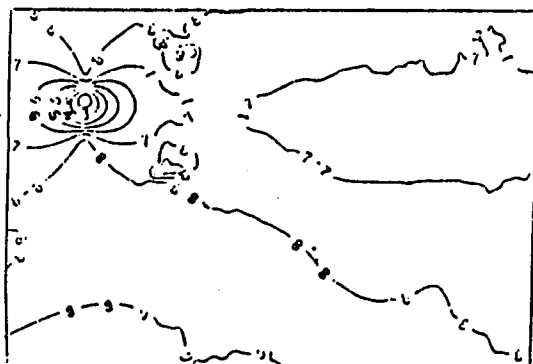
c) Y = 1.00 m, Fac = 10.0
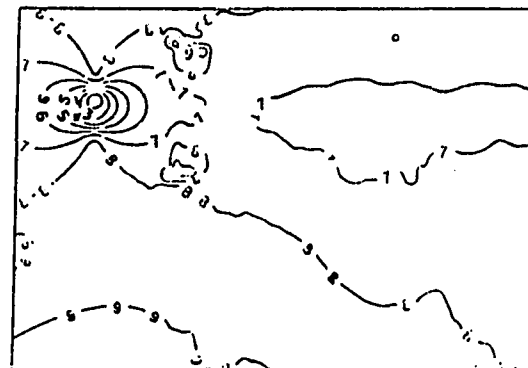
d) CMPMV   Fac = 10.0

e) SAPMV   Fac = 10.0

Figure 7.126. PMV contours for the sitting posture in
the X-Z plane at noon, Tin = 15 °C and
Uin = 1.9 m/sec. for the SN configuration.
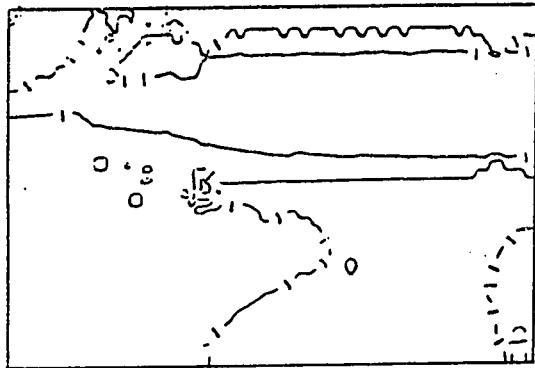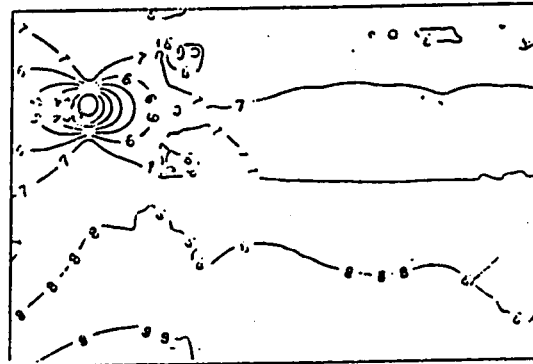
a) Y = 0.24 m, Fac = 1.0
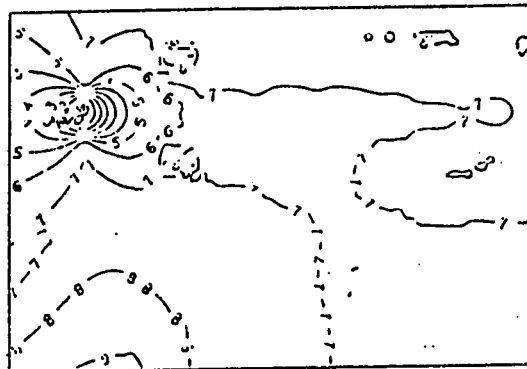
b) Y = 0.60 m, Fac = 10.0
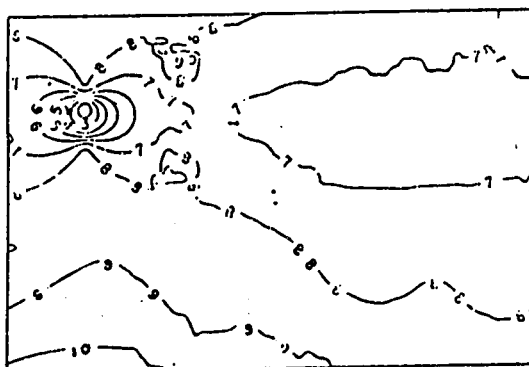
c) Y = 1.00 m, Fac = 10.0
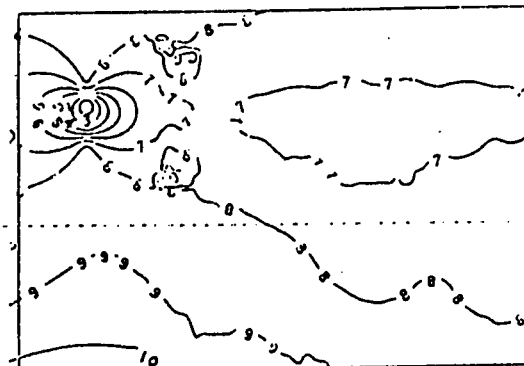
d) CMPMV   Fac = 10.0

e) SAPMV   Fac = 10.0

Figure 7.127. PMV contours for the standing posture in
the X-Z plane at noon, Tin = 15 °C and
Uin = 1.9 m/sec. for the SN configuration.
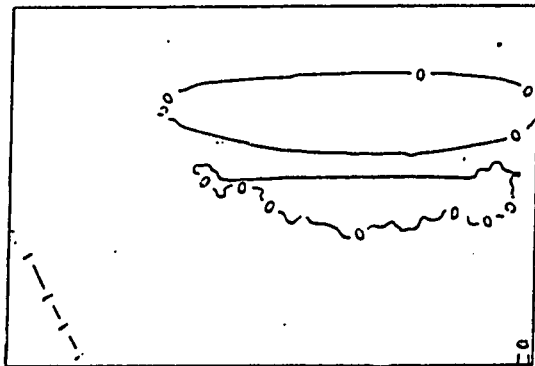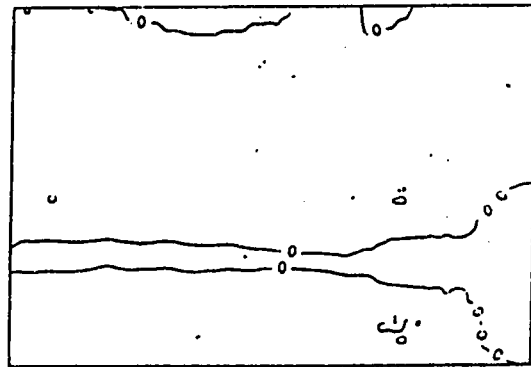
a) Y = 0.24 m, Fac = 1.0
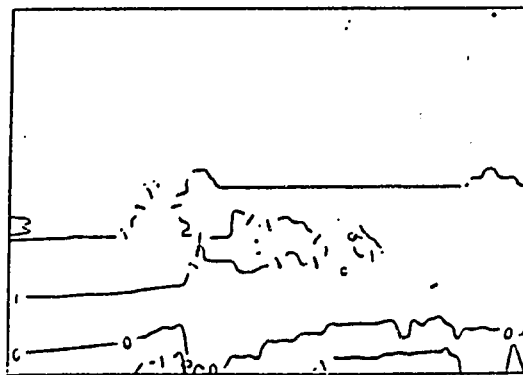
b) Y = 0.60 m, Fac = 1.0

c) Y = 1.00 m, Fac = 2.0
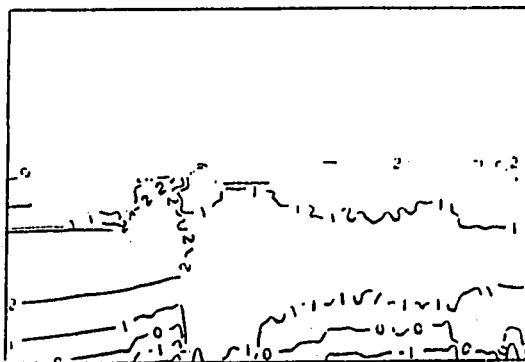
d)   CMPMV   Fac = 5.0
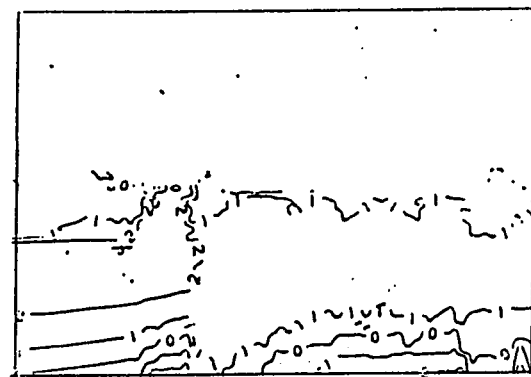
e) SAPMV   Fac = 5.0

Figure 7.128. PMV contours for the sitting posture in
the X-Z plane at noon, Tin = 15 °C and
Uin = 2.8 m/sec. for the SN configuration.
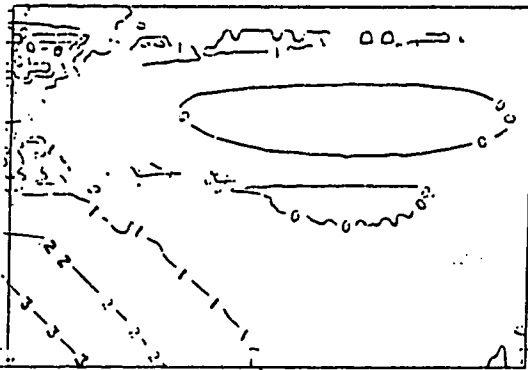
a) Y = 0.24 m, Fac = 2.0
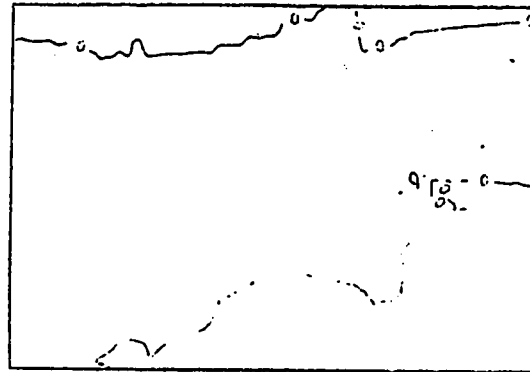
b) Y = 0.60 m, Fac = 1.0
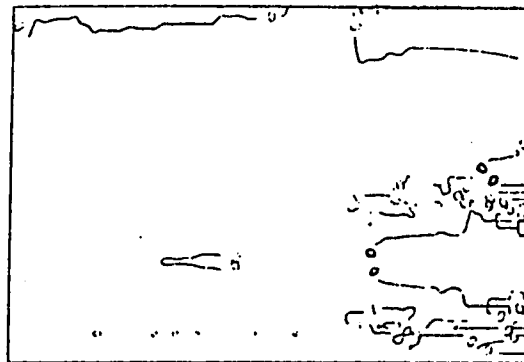
c) Y = 1.00 m, Fac = 1.0
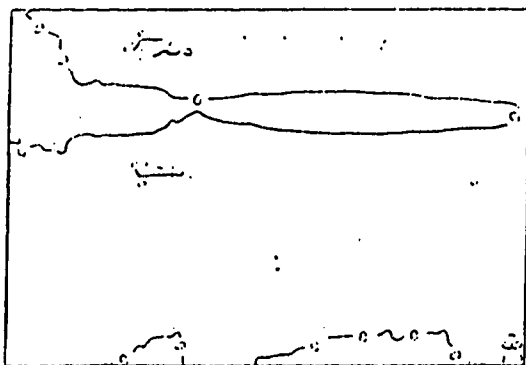
d) CMPMV   Fac = 1.0
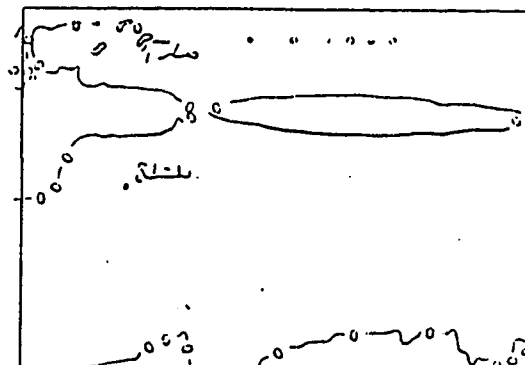
e) SAPMV   Fac = 1.0

Figure 7.129. PMV contours for the standing posture in
the X-Z plane at noon, Tin = 15 °C and
Uin = 2.8 m/sec. for the SN configuration.

assigned the same values used in Figs. 7.126 and 7.128, respectively. Comparing Figs. 7.126.a and 7.128.a we notice that the central region of the occupied zone in the latter is at, or close to thermal neutrality (see Table 7.3), while that in the former figure is beyond the accepted level of comfort, described earlier. Similar observations to those in Figs.7.126.a and 7.128.a are made in Figs. 7.126.b, 7.126.c, 7.128.b and 7.128.c, indicating that the thermal response of the occupants remain almost un-altered and that the conditions applied to the set-up of Fig. 7.128 achieves an acceptable level of comfort. This observation is confirmed by comparing the CMPMVs of Figs. 7.126.d and 7.128.d and similarly the SAPMVs of Figs. 7.126.e and 7.128.e. The general observations and conclusions regarding the standing posture plotted in Figs. 7.127 and 7.129 are similar to that for the sitting posture and consequently no discussions on this are necessary.

7.2.4 The NE Configuration

In this configuration only the boundary conditions resulting from the time of 12:00 Noon are considered and the results of two runs are reported which both have a U_{in} of 1.9 m/sec. and a T_{in} of 15°C and 10°C , respectively. Plots relevant to the study of the level of comfort are given below.

7.2.4.1 Velocity vector plots

Velocity vector plots in the x-y planes are shown in Figs. 7.130 and 7.132 for U_{in} of 1.9 m/sec in both figures, and a T_{in} of 15°C and 10°C, respectively. Horizontal x-z velocity vector plots are plotted in Figs. 7.131

a) X-Y Section at Z = 0.600 m

b) X-Y Section at Z = 1.850 m

c) X-Y Section at Z = 3.100 m
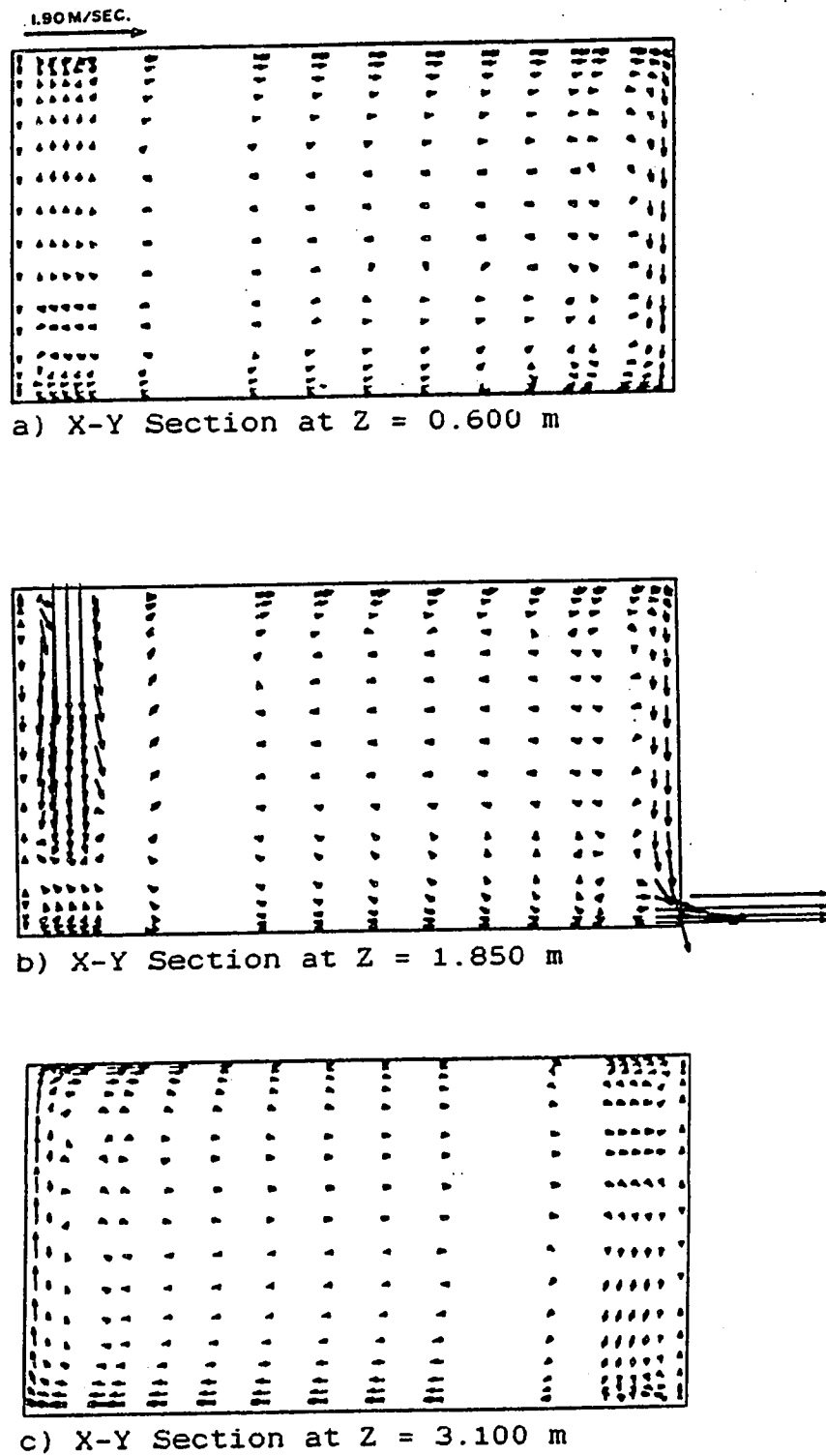
Figure 7.130. Velocity vector plots in the X-Y plane at noon, Tin = 15 °C and Uin = 1.9 m/sec for the NE configuration.

355

b) X-Z Section at Y = 0.756 m

d) X-Z Section at Y = 2.510 m

1.90 M/SEC.

a) X-Z Section at Y = 0.141 m

c) X-Z Section at Y = 1.759 m
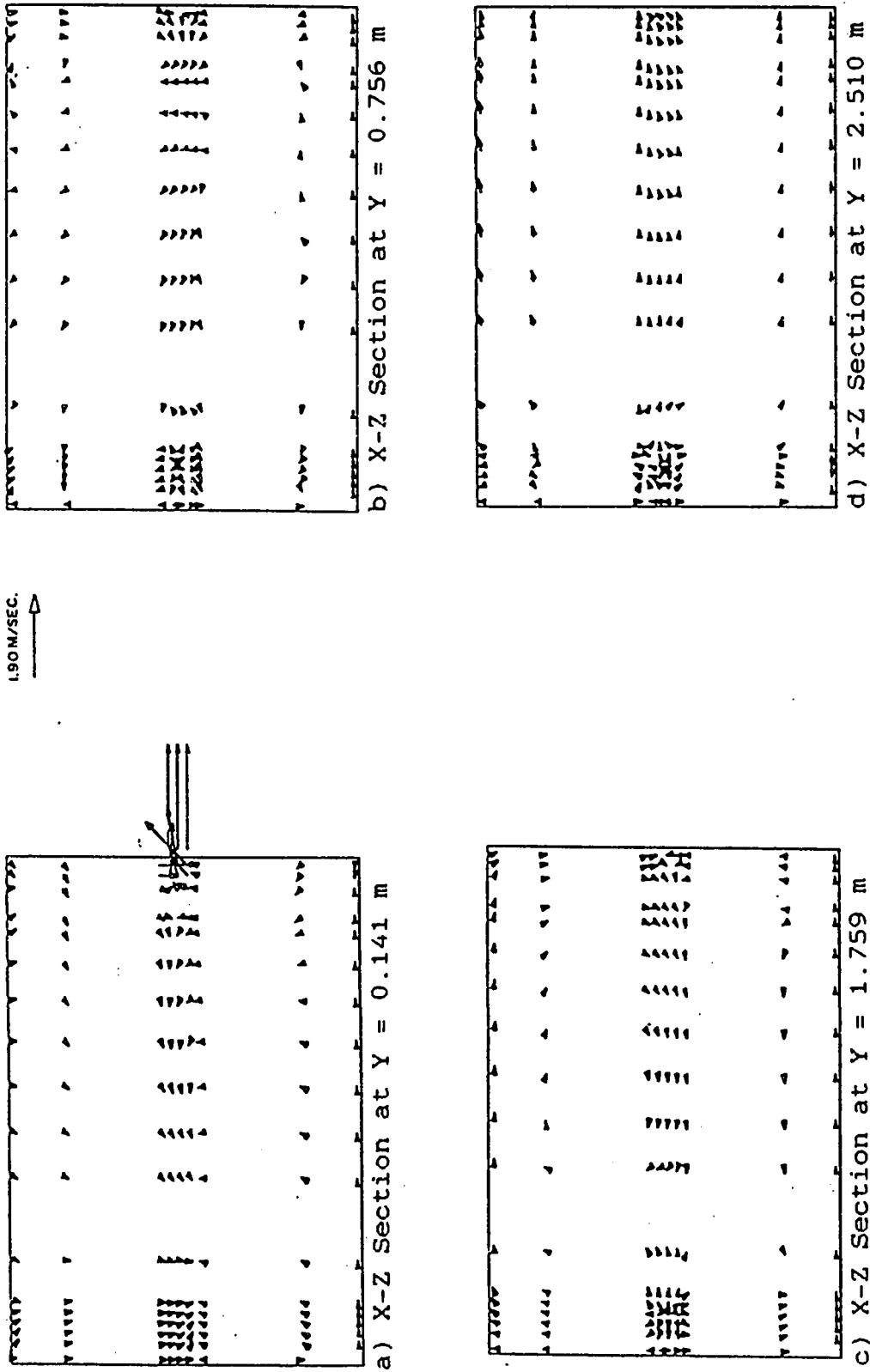
Figure 7.131. Velocity vector plots in the X-Z plane at noon, Tin = 15 °C and Uin = 1.9 m/sec for the NE configuration.
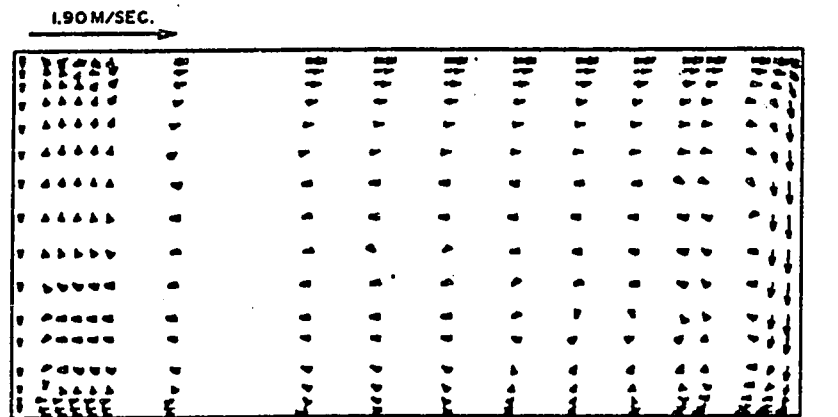
a) X-Y Section at Z = 0.600 m
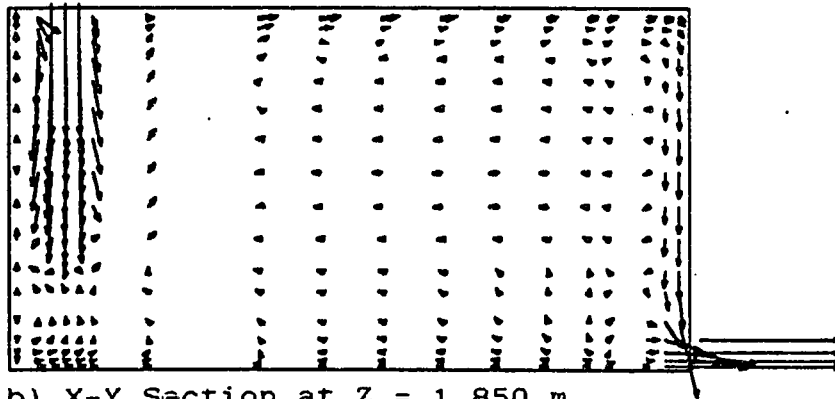
b) X-Y Section at Z = 1.850 m
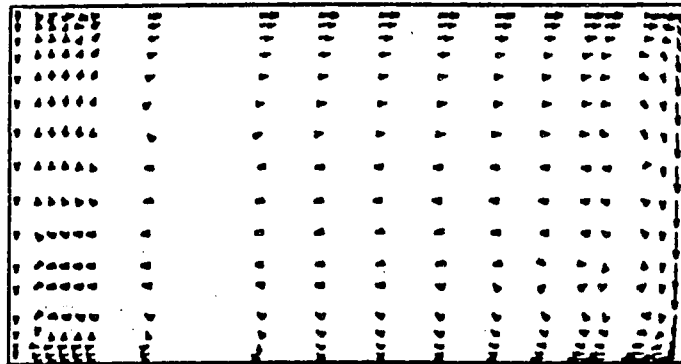
c) X-Y Section at Z = 3.100 m

Figure 7.132. Velocity vector plots in the X-Y plane at noon, Tin = 10 °C and Uin = 1.9 m/sec for the NE configuration.

357

1.90M/SEC.

a) X-Z Section at Y = 0.141 m

b) X-Z Section at Y = 0.756 m

c) X-Z Section at Y = 1.759 m

d) X-Z Section at Y = 2.510 m
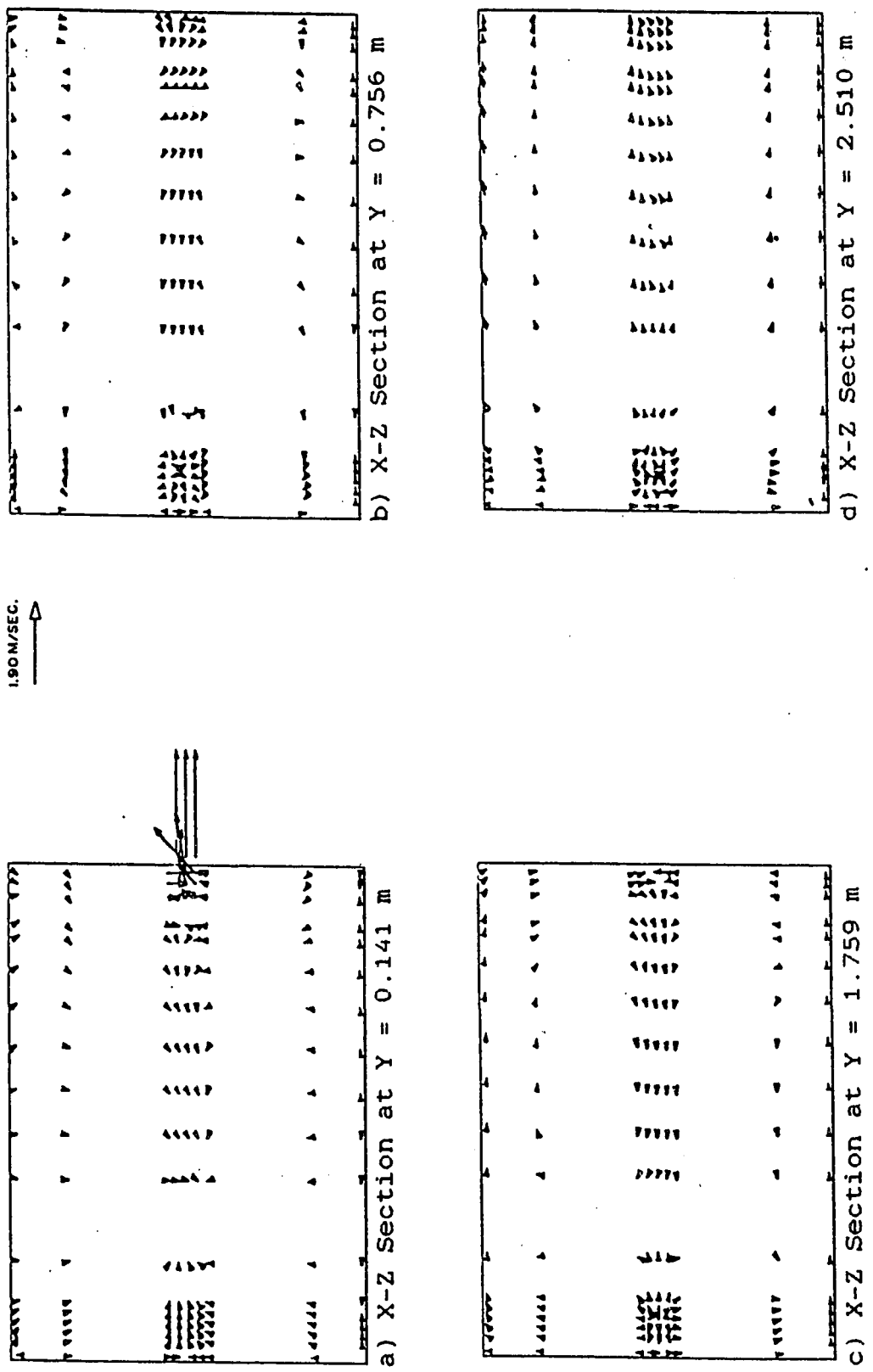
Figure 7.133. Velocity vector plots in the X-Z plane at noon, Tin = 10 °C and Uin = 1.9 m/sec for the NE configuration.

and 7.133 and have T_{in} and U_{in} identical to those of Figs. 7.130 and 7.132, respectively. Comparing Figs. 7.130.a and 7.132.a we see that the velocities adjacent to the ceiling and East wall are relatively higher than those in the remaining parts of the room while opposite the inlet opening there appears a general tendency for the velocity to move upwards. A similarity exists between the velocity vector patterns of Figs. 7.130.a and 7.130.c, therefore what has been said regarding the former figure applies to the latter and the same reasoning follows for Fig. 7.132.a and 7.132.c. At the mid-section of the room in Fig. 7.130.b observations similar to that above is made here except the velocities under the inlet opening are moving downwards. The velocity vector plots in the x-z planes given in Figs. 7.131 and 7.133 are comparable therefore a discussion of the former figure is supplied. In Fig. 7.131.a the velocity vectors are leaving the room through the outlet at the middle of the East wall while at the mid-plane of the room the main direction of the flow is from the East to the West wall and in the remaining part of the room no definite directions are observed. Figs. 7.131.b and 7.131.c resemble that described above except there are no velocity vectors leaving the room on the East wall. In Fig. 7.131.d the velocity vectors have a general tendency to flow from the West to the East walls of the room.

7.2.4.2 Velocity profiles

The velocity profiles here are plotted for the Noon time boundary condition at locations identical to that given in the NN configuration . The velocity profiles at the mid-section of the room are given in Figs.7.134

and 7.136 where T_{in} in the former is 15°C and in the latter it is 10°C while U_{in} in both is identical and equal to 1.9 m/sec. Velocity profiles away from the mid-section of the room and close to the right wall of the room are given in Figs. 7.135 and 7.137, where the T_{in} and U_{in} are equal to that of of Figs. 7.134 and 7.136, respectively. Comparing Figs. 7.134 and 7.135, we note that they have similar general features therefore, a discussion of the former figure is necessary. The velocity profile close to the floor is given in Fig. 7.134.a which has a slope of zero throughout except close to the West and East walls where moderate negative peaks of the velocity profile appears. The velocity profiles of Figs. 7.134.b to 7.134.d are comparable to that of the velocity profile of Fig. 7.134.a except that the peaks on both sides of the room has grown larger and that the peak of the velocity profile opposite the inlet opening is now much larger than that close to the East wall. The general forms of the velocity profiles of Figs. 7.135 and 7.137 are comparable thus a. discussion on the former is warranted. The velocity profiles of Figs. 7.135.a and 7.135.b resemble that of Fig. 7.134.a. The velocity profile of Fig. 7.135.c resembles that of Fig. 7.135.a except that the negative peak close to the East wall is now a positive peak and similarly the same is observed in the velocity profile of Fig.7.135.d.

7.2.4.3 Temperature contours

The temperature contours , here are plotted at locations identical to that of the previous configurations and for the Noon boundary conditions. These are shown in Figs. 7.138 and 7.139 where T_{in} in the former is 15°C and in the latter, it is 10°C while U_{in} in both is identical and equal to

a) Y/H = 0.050 and Z/W = 0.5

b) Y/H = 0.28 and Z/W = 0.5

c) Y/H = 0.64 and Z/W = 0.5
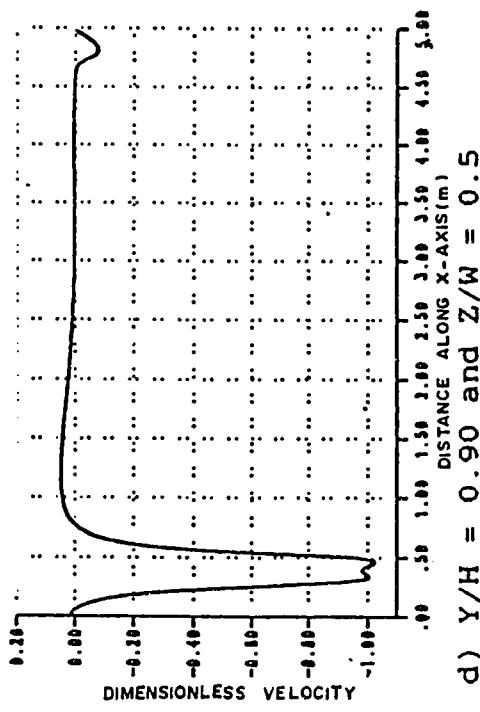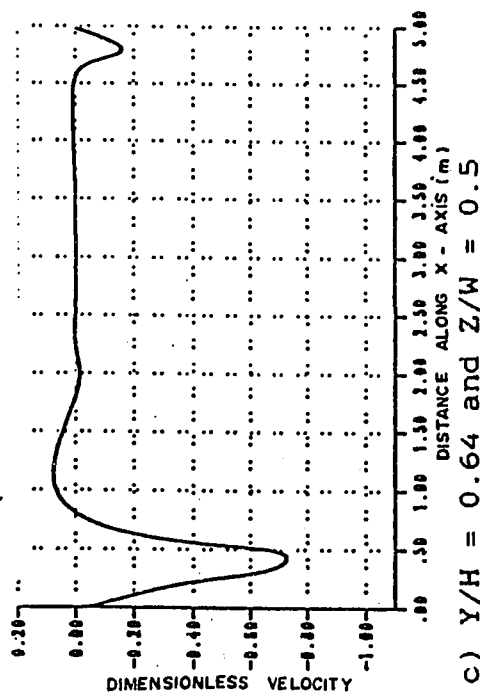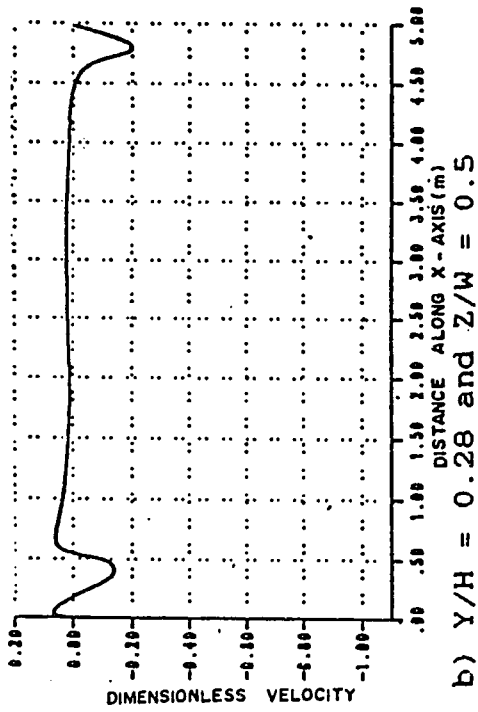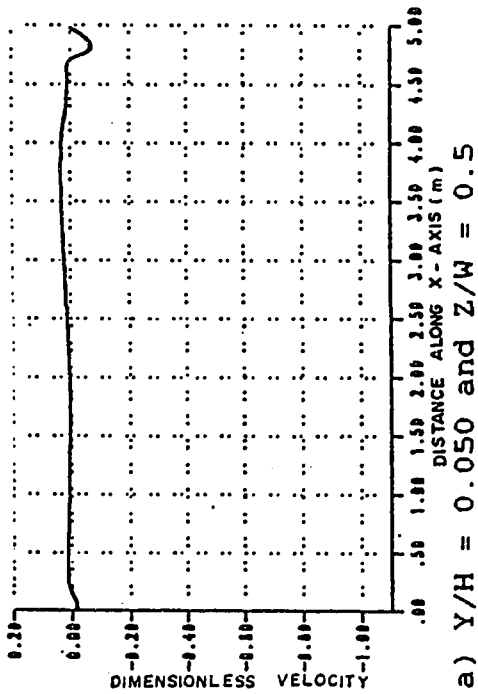
d) Y/H = 0.90 and Z/W = 0.5

Figure 7.134. Dimensionless velocity profiles over length of room at mid section at noon, Tin = 15 °C and Uin = 1.9 m/sec for the NE configuration.
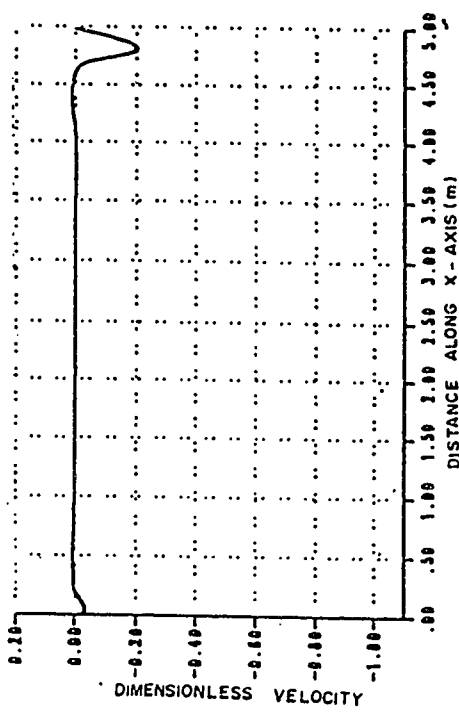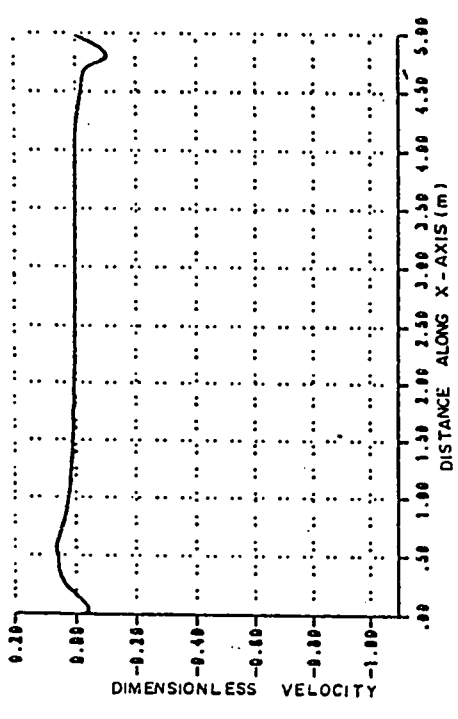
b) Y/H = 0.28 and Z/W = 0.8
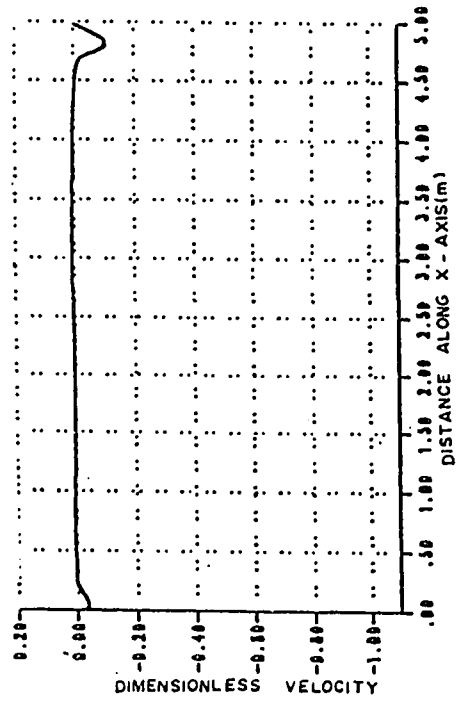
a) Y/H = 0.050 and Z/W = 0.8
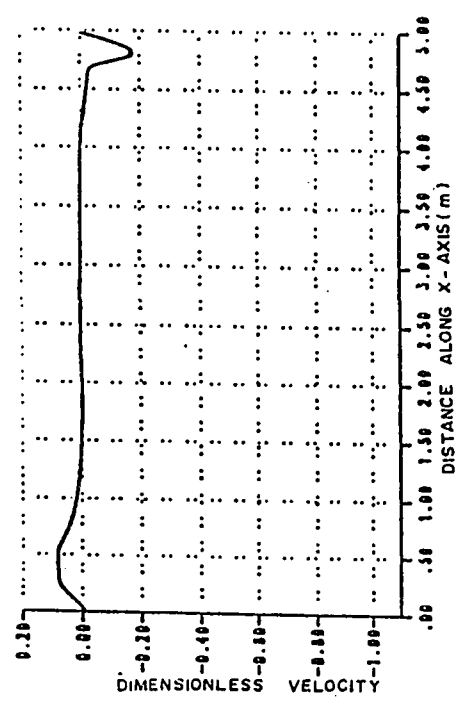
d) Y/H = 0.90 and Z/W = 0.8

c) Y/H = 0.64 and Z/W = 0.8

Figure 7.135. Dimensionless velocity profiles over length of room near right wall at noon, Tin = 15 °C and Uin = 1.9 m/sec for the NE configuration.
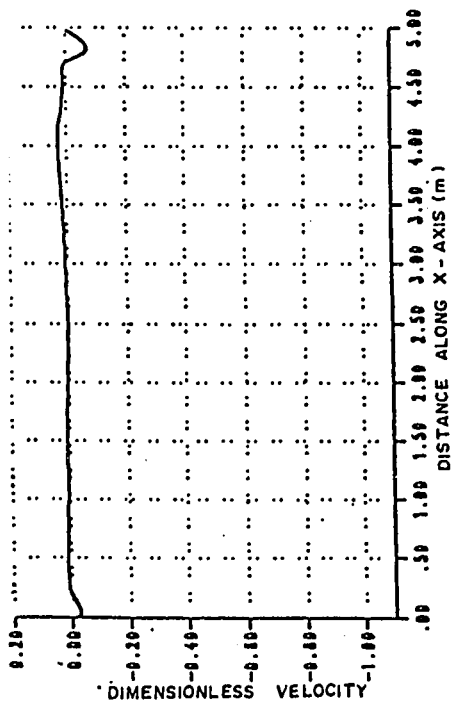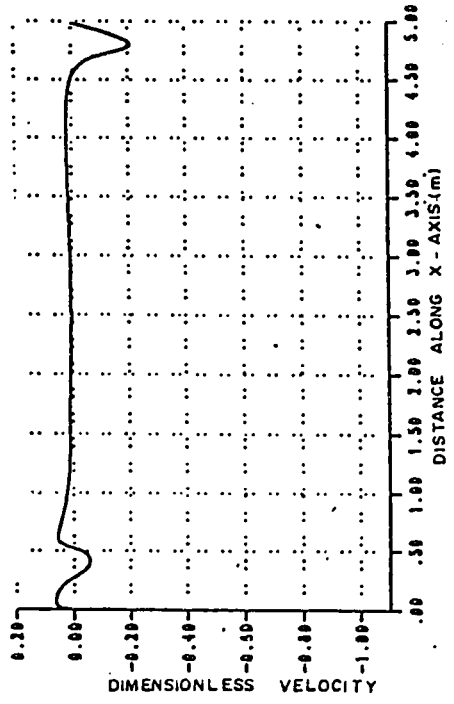
a) Y/H = 0.050 and Z/W = 0.5
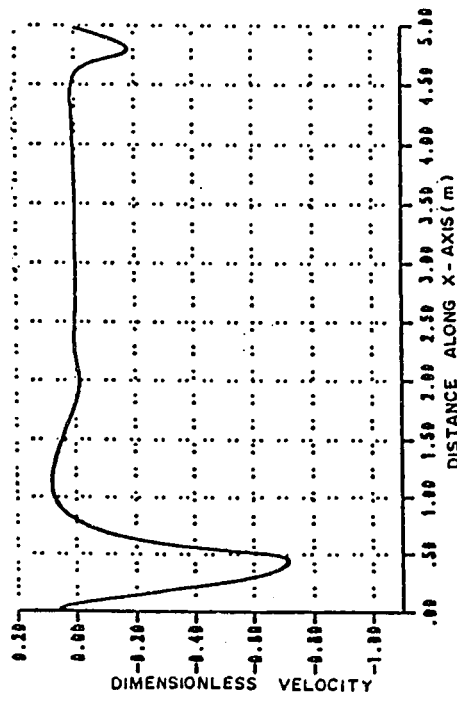
b) Y/H = 0.28 and Z/W = 0.5
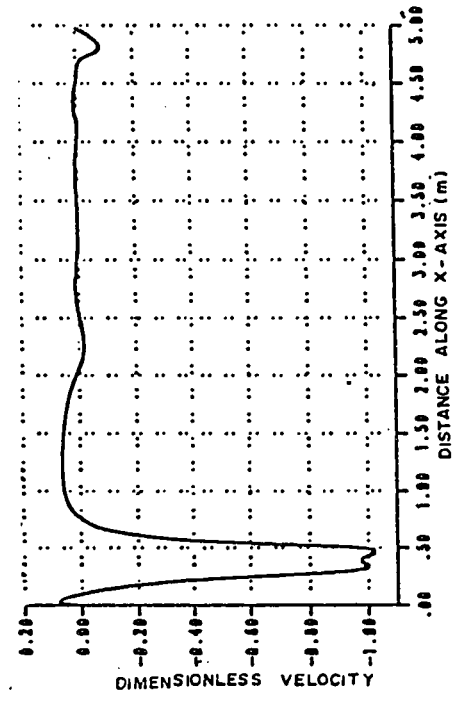
c) Y/H = 0.64 and Z/W = 0.5

d) Y/H = 0.90 and Z/W = 0.5

Figure 7.136. Dimensionless velocity profiles over length of room at mid section at noon, Tin = 10 °C and Uin = 1.9 m/sec for the NE configuration.
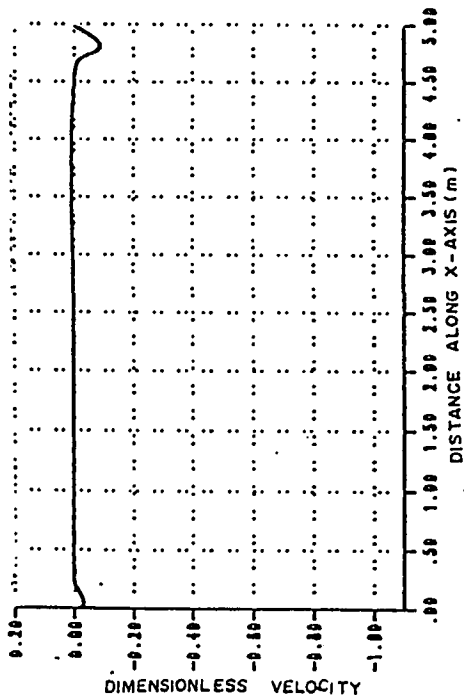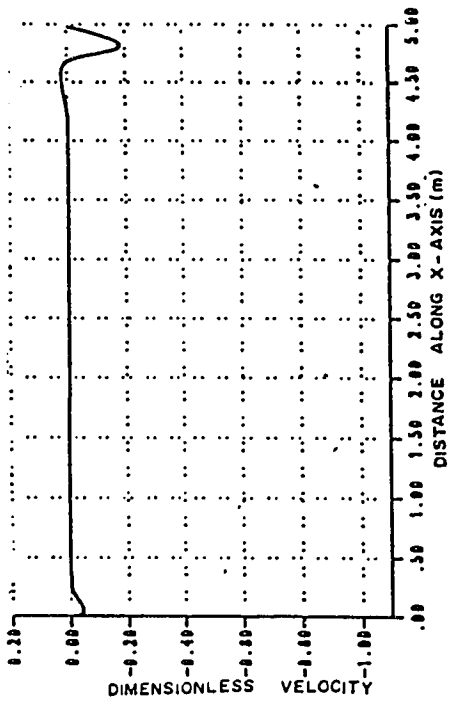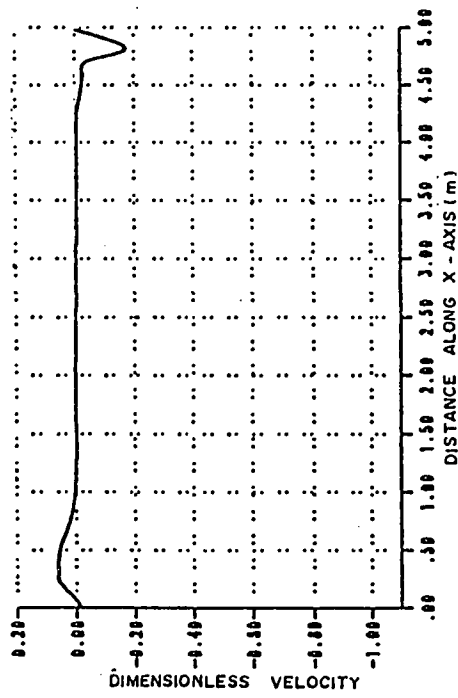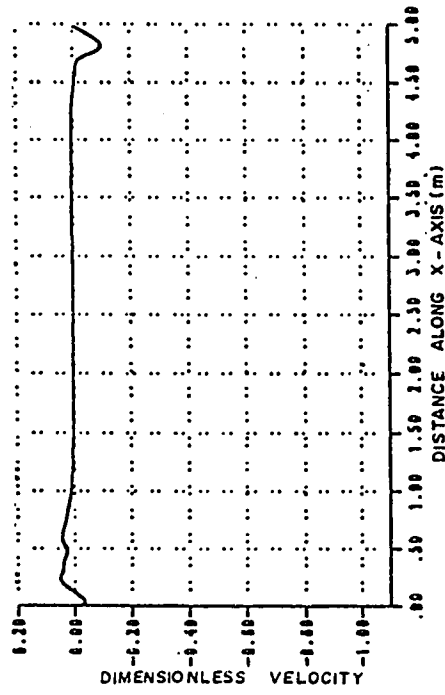
Figure 7.137. Dimensionless velocity profiles over length of room near right wall at noon, Tin = 10 °C and Uin = 1.9 m/sec for the NE configuration.

a) Y/H = 0.050 and Z/W = 0.8

b) Y/H = 0.28 and Z/W = 0.8

c) Y/H = 0.64 and Z/W = 0.8

d) Y/H = 0.90 and Z/W = 0.8
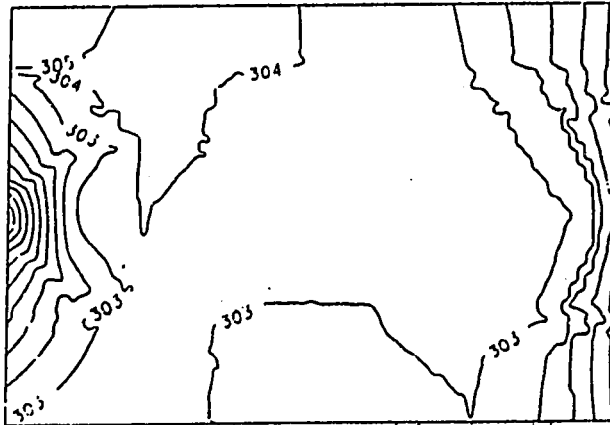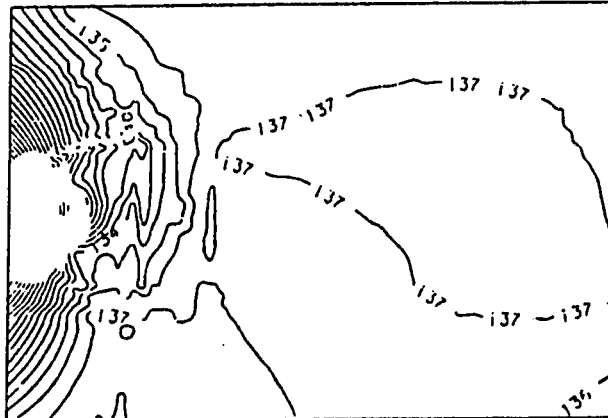
a) Y = 0.76 m,   Fac = 10.0
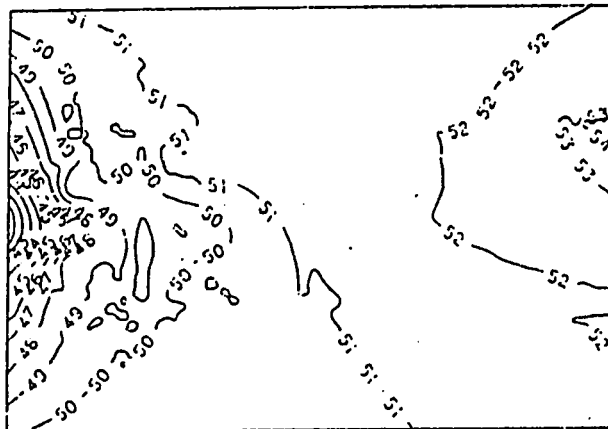
b) Y = 1.76 m,   Fac = 5.0

c) Y = 2.51 m,   Fac = 2.0

Figure 7.138. Temperature contours in the X-Z plane at noon, Tin = 15 °C and Uin = 1.9 m/sec for the NE configuration.

a) Y = 0.76 m,   Fac = 5.0
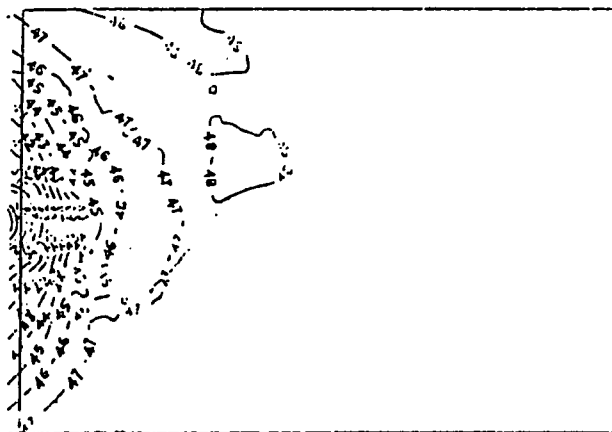
b) Y = 1.76 m,   Fac = 2.0
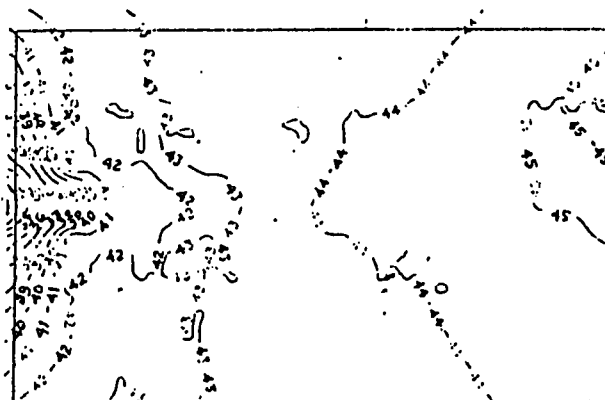
c) Y = 2.51 m,   Fac = 2.0

Figure 7.139. Temperature contours in the X-Z plane at noon,
Tin = 10 °C and Uin = 1.9 m/sec for the NE
configuration.

1.9 m/sec. Comparing Figs. 7.138.a and 7.139.a, we observe a similar general distribution such that the level of temperatures on the West and East sides of the occupied zone are lowest while the variation of temperature in the center of the room is relatively low. Moving upwards to a height of 1.76 m above the floor the temperature contours are plotted in Figs. 7.138.b and 7.139.b in which the general patterns of both plots are similar, with the coolest region being the West side of the occupied zone, while in the remaining part of the room the temperature is nearly uniform. The temperature contours plotted in Figs. 7.138.c and 7.139.c are similar such that the lowest temperature appears close to the West side of occupied zone in the form of concentric semicircles, while the relatively highest temperature is close to the middle of the East side of the occupied zone, and the temperature inbetween progressively increases as you move from the West to the East side of the occupied zone.

7.2.4.4 Temperature profiles

Temperature profiles at locations similar to those of the NN configuration are plotted here. The temperature profiles at the mid-section of the room are given in Figs. 7.140 and 7.142 where U_{in} in both is 1.9 m/sec, while T_{in} in the former is 15°C and in the latter it is 10°C. Temperature profiles away from the mid-section and close to the right wall of the room are plotted in Figs. 7.141 and 7.143, where T_{in} and U_{in} are as given in Fig. 7.140 and 7.142, respectively. Comparing the temperature profiles at the mid-section of the room given in Figs. 7.140 and 7.142 we observe that the two figures are similar and a discussion of the former figure is satisfactory.
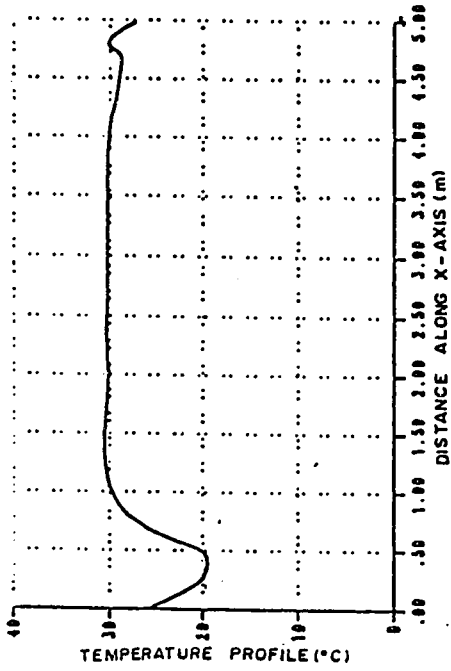
b) Y/H = 0.28 and Z/W = 0.5
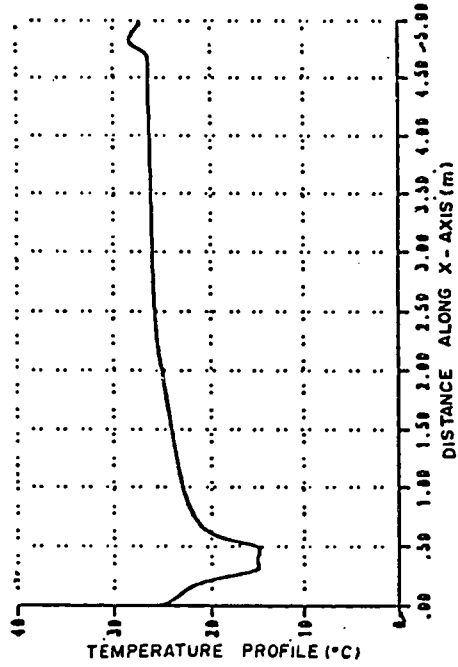
d) Y/H = 0.90 and Z/W = 0.5
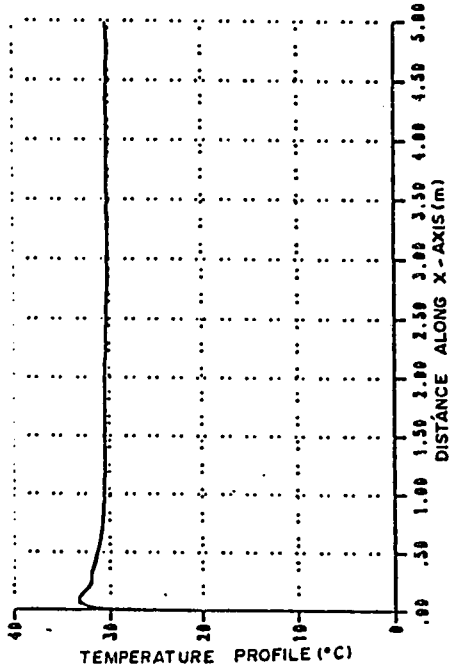
a) Y/H = 0.050 and Z/W = 0.5
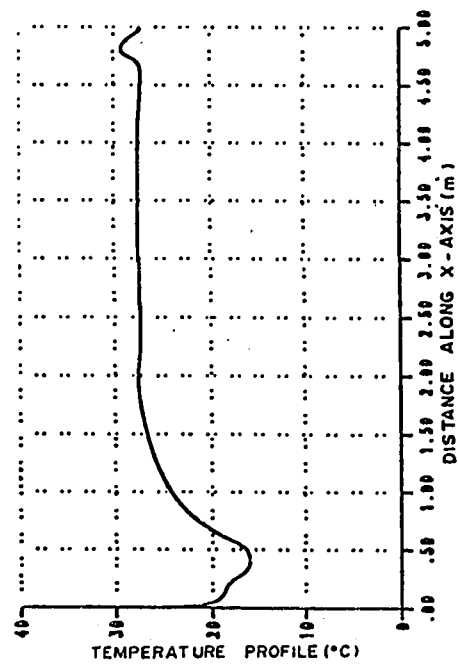
c) Y/H = 0.64 and Z/W = 0.5

Figure 7.140. Temperature profiles over length of room at mid section at noon, Tin = 15 °C and Uin = 1.9 m/sec for the NE configuration.

368

a) Y/H = 0.050 and Z/W = 0.8

b) Y/H = 0.28 and Z/W = 0.8

c) Y/H = 0.64 and Z/W = 0.8
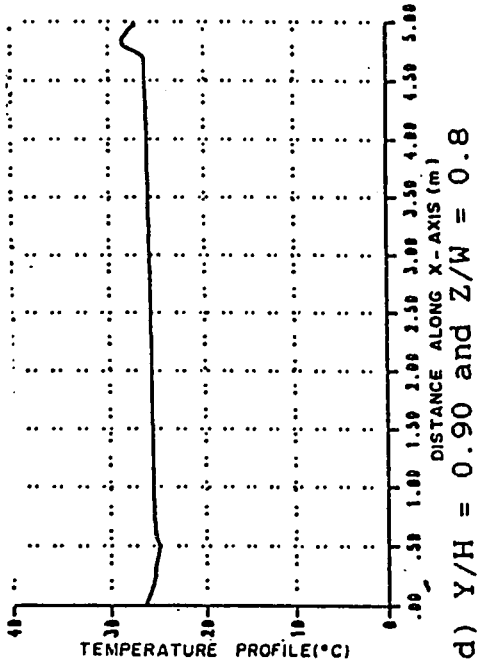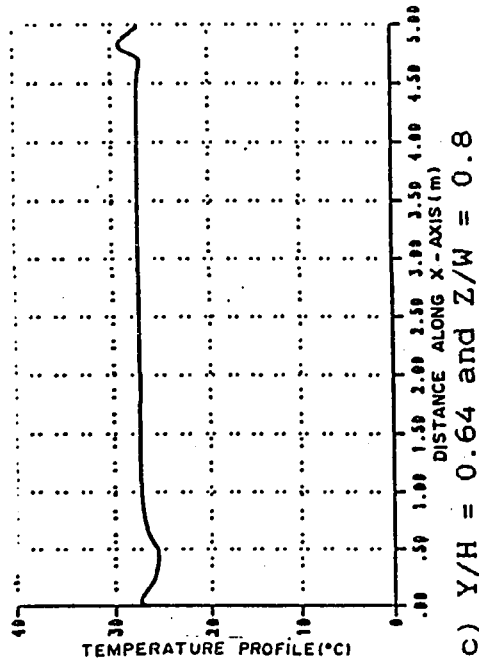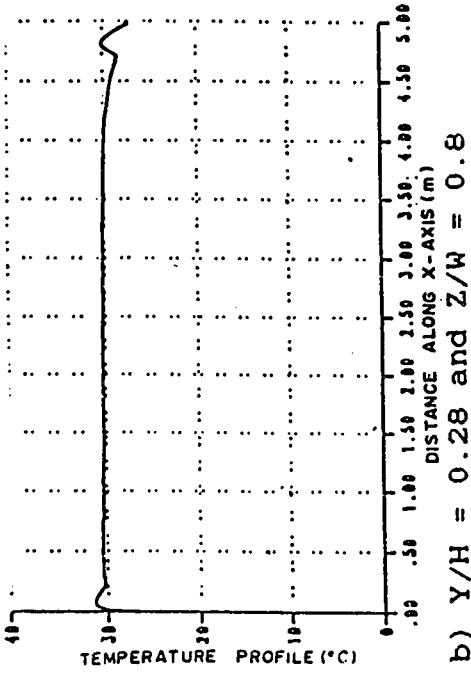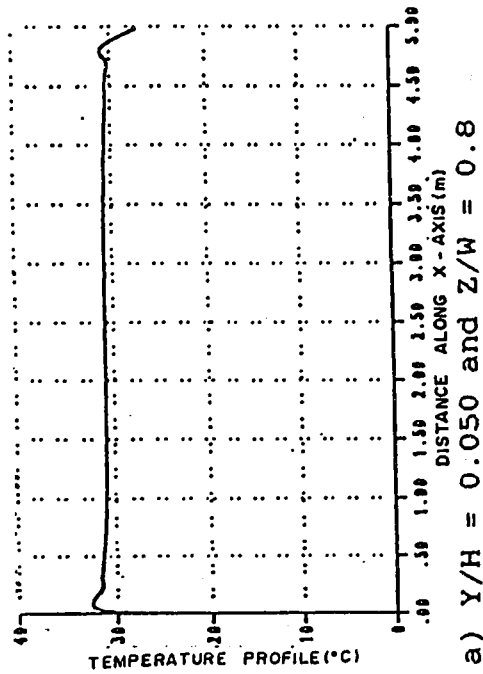
d) Y/H = 0.90 and Z/W = 0.8

Figure 7.141. Temperature profiles over length of room near right wall at noon, Tin = 15 °C and Uin = 1.9 m/sec for the NE configuration.
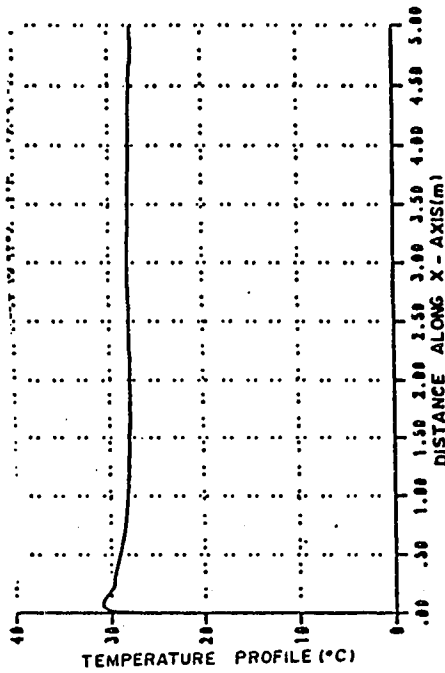
a) Y/H = 0.050 and Z/W = 0.5
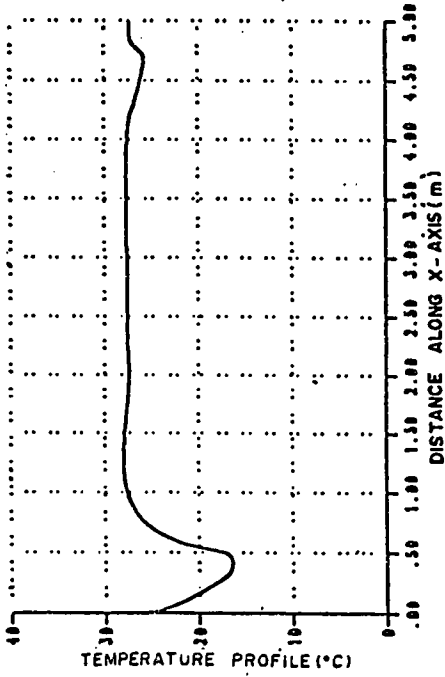
b) Y/H = 0.28 and Z/W = 0.5
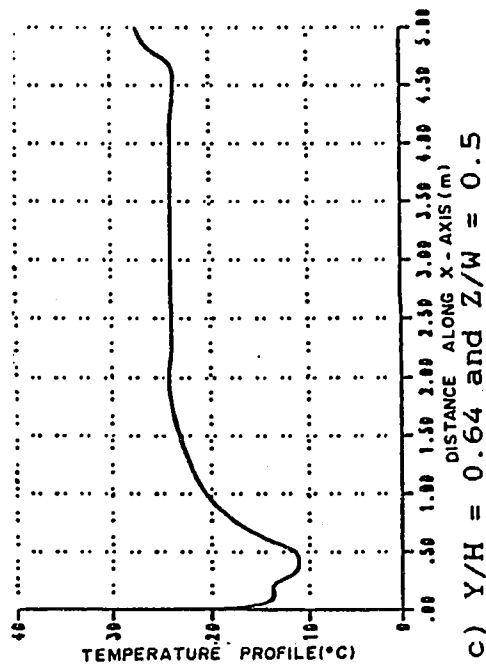
c) Y/H = 0.64 and Z/W = 0.5
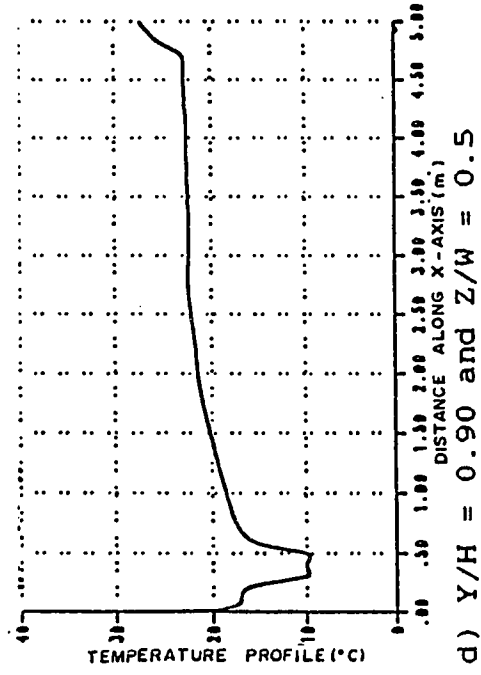
d) Y/H = 0.90 and Z/W = 0.5

Figure 7.142. Temperature profiles over length of room at mid section at noon, Tin = 10 °C and Uin = 1.9 m/sec for the NE configuration.

b) Y/H = 0.28 and Z/W = 0.8

d) Y/H = 0.90 and Z/W = 0.8

a) Y/H = 0.050 and Z/W = 0.8

c) Y/H = 0.64 and Z/W = 0.8
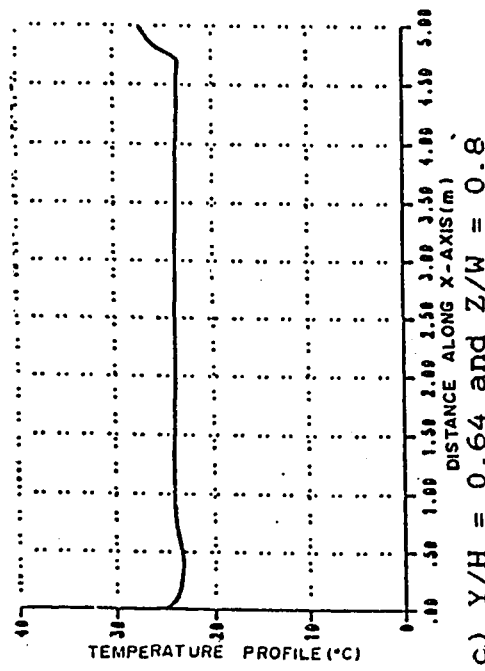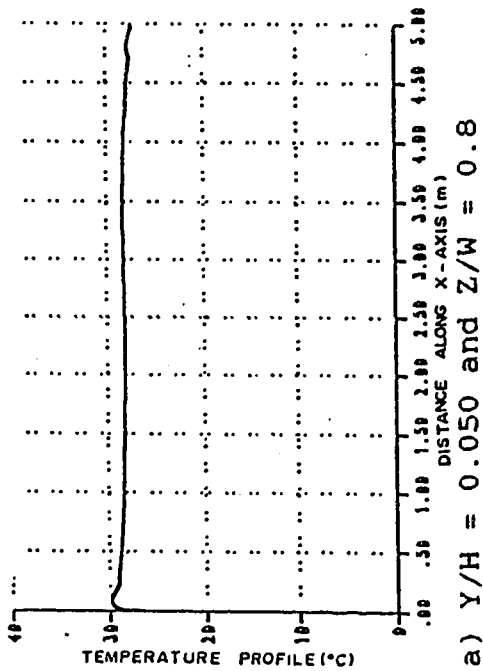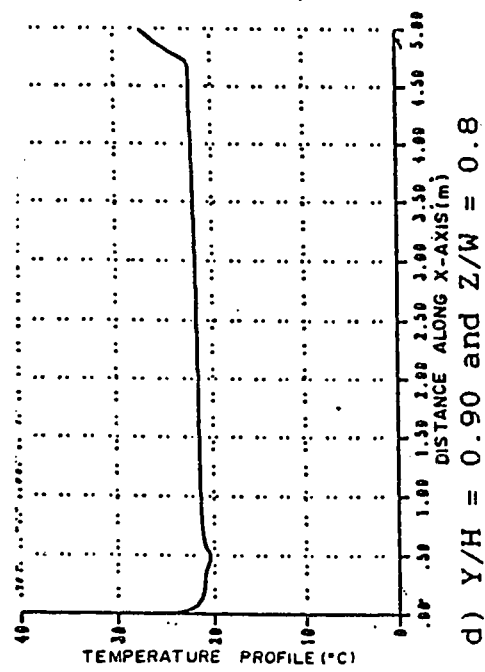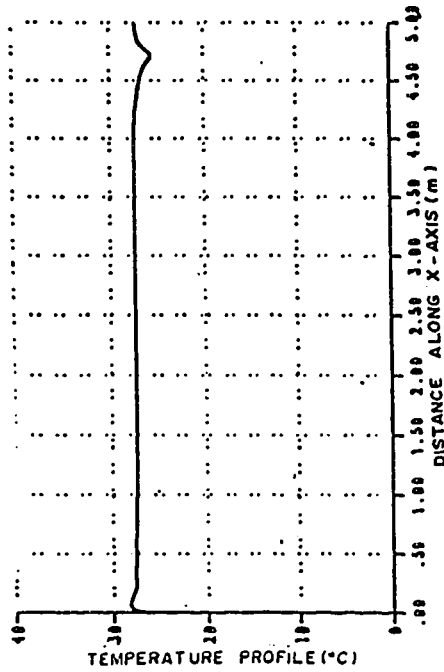
Figure 7.143. Temperature profiles over length of room near right wall at noon,
Tin = 10 °C and Uin = 1.9 m/sec for the NE configuration.

In Fig. 7.140.a the temperature is nearly uniform except close to the West wall where a relative high peak occurs. In Fig. 7.140.b we observe that most of the temperature profile within the room is uniform except opposite the inlet opening where a low temperature peak appears and adjacent to the East wall where a moderately higher peak is evident. Observations similar to this is noticed as we ascend closer to the ceiling in Figs. 7.140.c and 7.140.d. Close to the right wall of the room the temperature profiles , plotted in Figs. 7.141 and 7.143, have a general similar pattern, thus a discussion of only Fig. 7.141 is given. The temperature profile close to the floor in Fig. 7.141.a, is nearly uniform except for moderate peaks of relatively higher temperature appear adjacent to the West and East walls. This observation is evident in Fig. 7.141.b and Fig. 7.143.b except that the peak adjacent to the East wall in Fig. 7.143.b is inverted. In Fig. 7.141.c the general shape of the temperature profile resembles that of Fig. 7.141.a except that the peak of the temperature profile close to the West wall is inverted, while in Fig. 7.143.c, close to the East wall, there is no peak evident except that the relatively highest temperature appears adjacent to the East wall while the remaining part of the room is at a uniform temperature . The temperature profile in Fig. 7.141.d resemble that of Fig. 7.141.c except that the level of temperature is reduced and the same follows for Fig. 7.143.d, relative to Fig.7.134.c.

7.2.4.5 PMV contours

PMV contours at the Noon boundary conditions are plotted at identical planes to the previously discussed configurations . The PMV contours for the sitting posture are given in Figs. 7.144 and 7.146 where the

U_{in} in both are identical and equal to 1.9 m/sec, while the T_{in} is 15°C in the former and 10°C in the latter. The PMV contours for the standing posture are given in Figs. 7.145 and 7.147 such that the T_{in} and U_{in} are assigned the same values as that in Figs. 7.144 and 7.146, respectively. Comparing Figs. 7.144.a and 7.146.a, we notice that the highest PMV appears adjacent to the West side of the occupied zone while the relative lowest is close to the center of the room and the PMV contours in the latter figure is relatively closer to thermal neutrality than in the former. Moving upwards to a height of 0.6 m above the floor the PMV contours are plotted in Figs. 7.144.b and 7.146.b where it is observed that the PMV contours in the latter figure is almost uniform while in the former, concentric contours of PMV appear adjacent to the West side of the occupied zone whereas the remaining part of the room is nearly uniform. At a height of 1.0 m above the floor the PMV contours are plotted in Figs.7.144.c and 7.146.c where the variations in the PMV on the West side of the occupied zone is relatively high whereas no such variations appear in the latter figure and the level of PMVs in Fig. 7.146.c are at or close to thermal neutrality. By observing the CMPMVs of Figs. 7.144.d and 7.146.d we have a general impression on the sensation response of the occupants such that in the latter figure, the CMPMVs are close to thermal neutrality while in the former figure, the CMPMVs are not as close. Similar observations may be noticed for the SAPMVs of Figs. 7.144.e and 7.146.e. The general observation and conclusions regarding the PMV contours for the standing posture are given in Figs. 7.145 and 7.147 which are similar to that observed in the sitting posture and consequently no discussions on this are necessary.
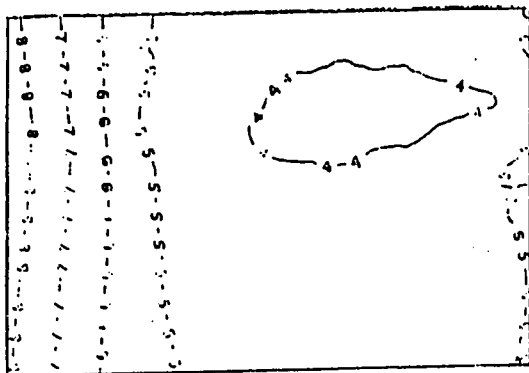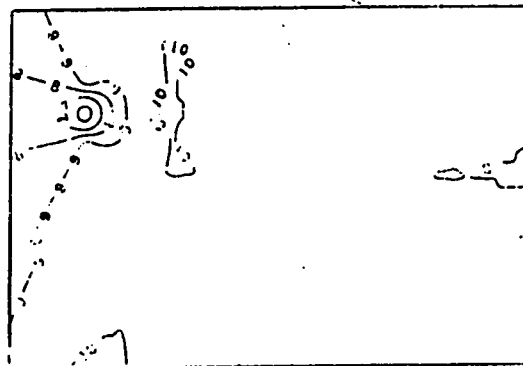
a) Y = 0.24 m, Fac = 5.0

b) Y = 0.60 m, Fac = 10.0
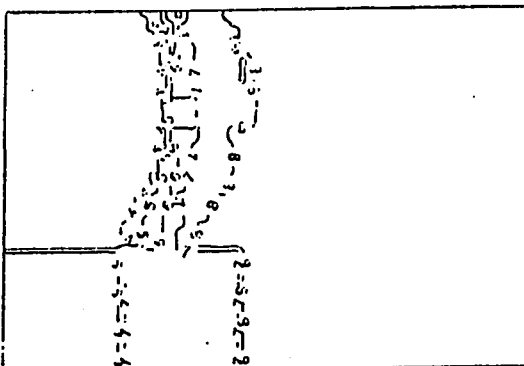
c) Y = 1.00 m, Fac = 5.0
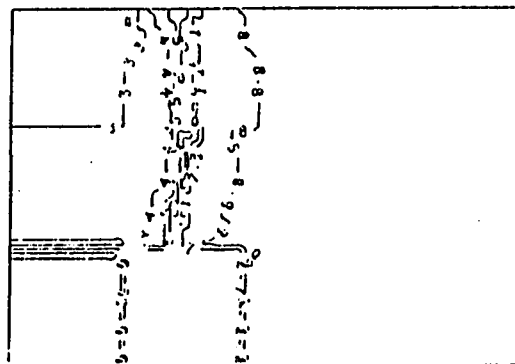
d) CMPMV Fac = 10.0

e) SAPMV Fac = 10.0

Figure 7.144. PMV contours for the sitting posture in the X-Z plane at noon, Tin = 15 °C and Uin = 1.9 m/sec. for the NE configuration.
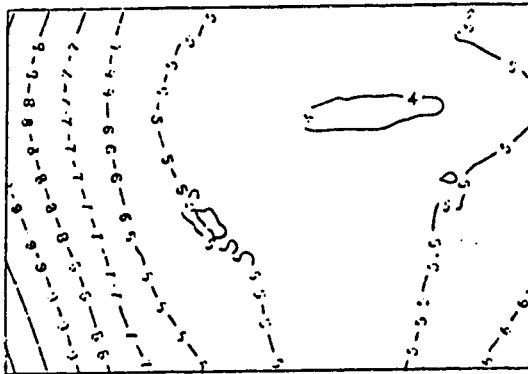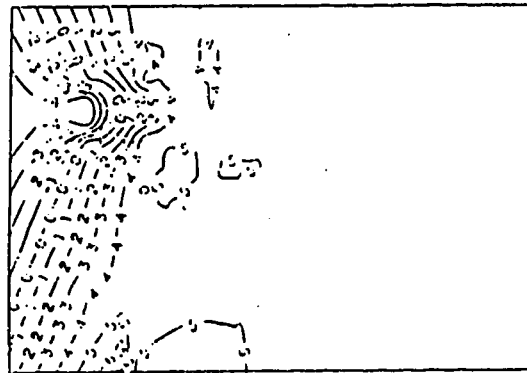
a) Y = 0.24 m, Fac = 5.0
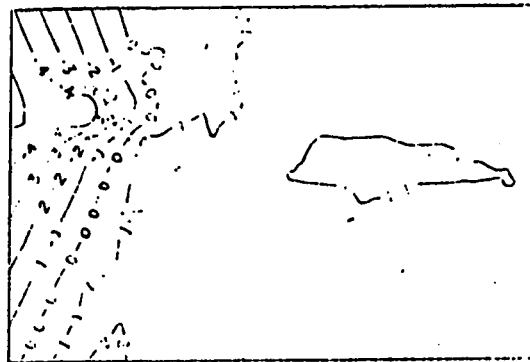
b) Y = 0.60 m, Fac = 5.0

c) Y = 1.00 m, Fac = 2.0
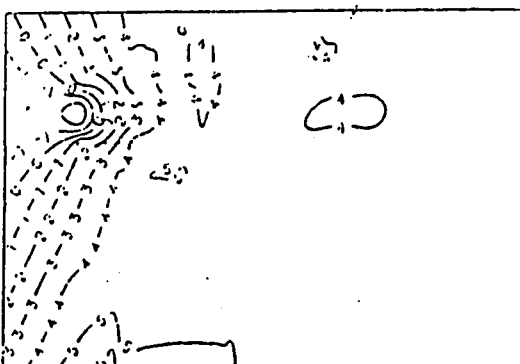
d) CMPMV   Fac = 5.0

e) SAPMV   Fac = 5.0

Figure 7.145. PMV contours for the standing posture in
the X-Z plane at noon, Tin = 15 °C and
Uin = 1.9 m/sec. for the NE configuration.
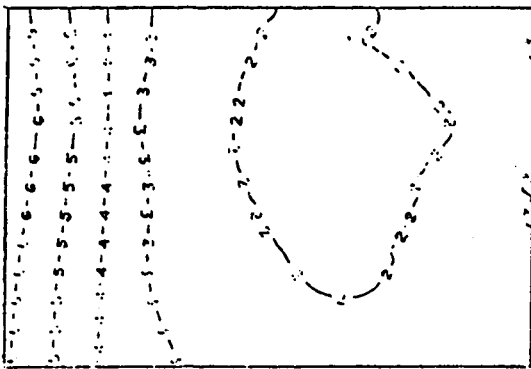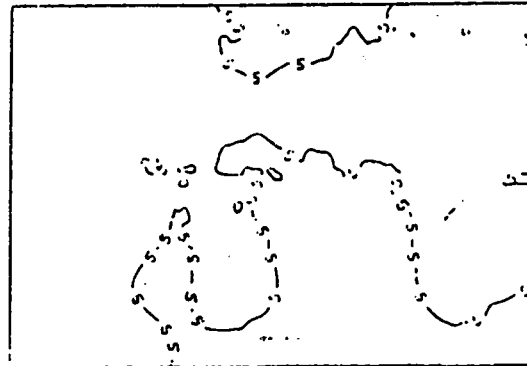
a) Y = 0.24 m, Fac = 5.0
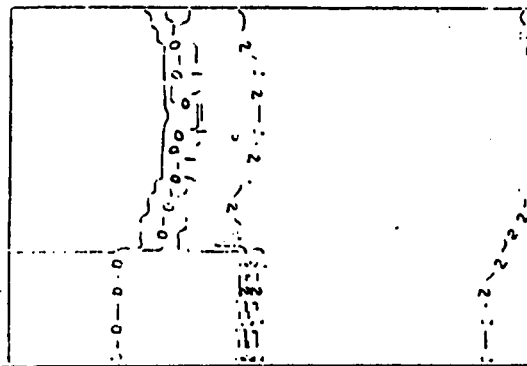
b) Y = 0.60 m, Fac = 10.0
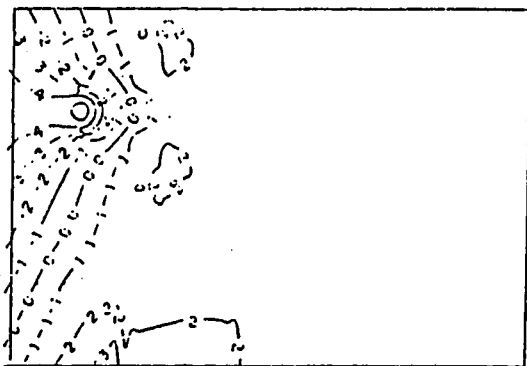
c) Y = 1.00 m, Fac = 10.0
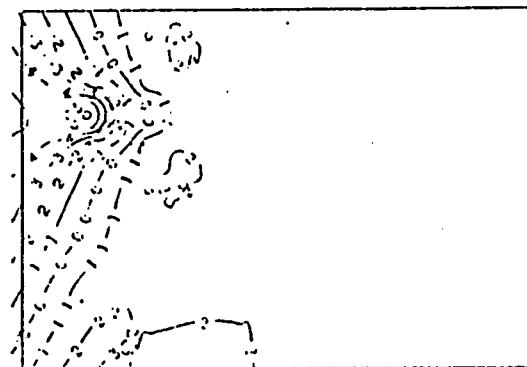
d)   CMPMV   Fac = 5.0

e) SAPMV   Fac = 5.0

Figure 7.146. PMV contours for the sitting posture in the X-Z plane at noon, Tin = 10 °C and Uin = 1.9 m/sec. for the NE configuration.
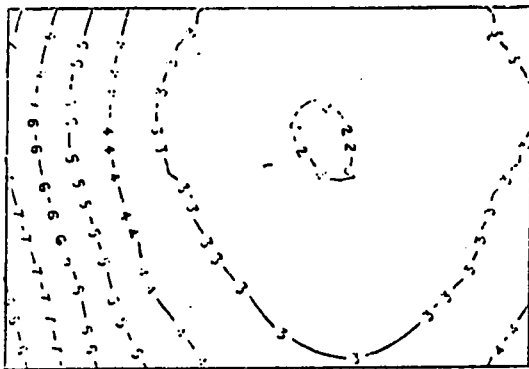
a) Y = 0.24 m, Fac = 10.0
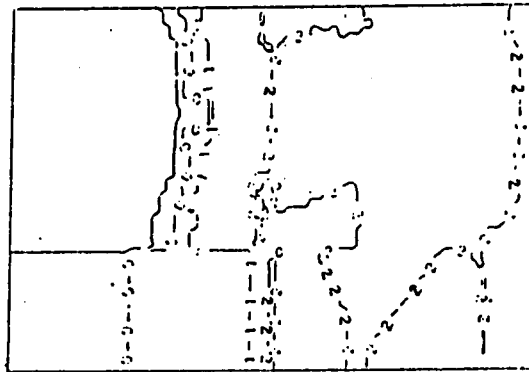
b) Y = 0.60 m, Fac = 5.0
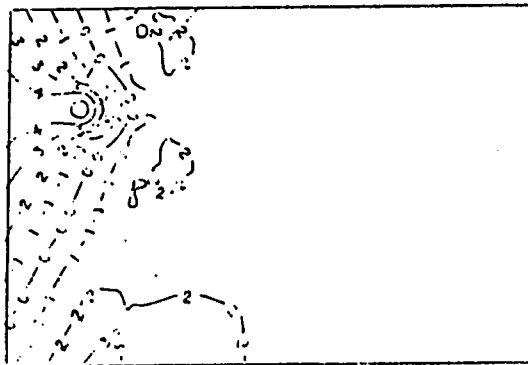
c) Y = 1.00 m, Fac = 10.0
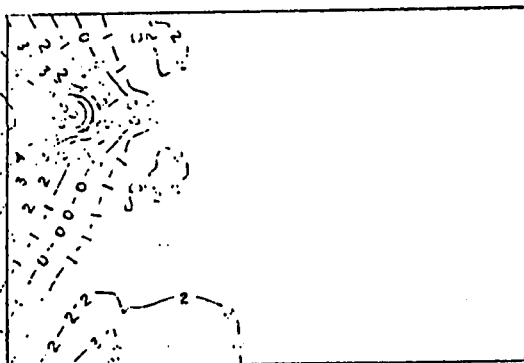
d) CMPMV   Fac = 10.0
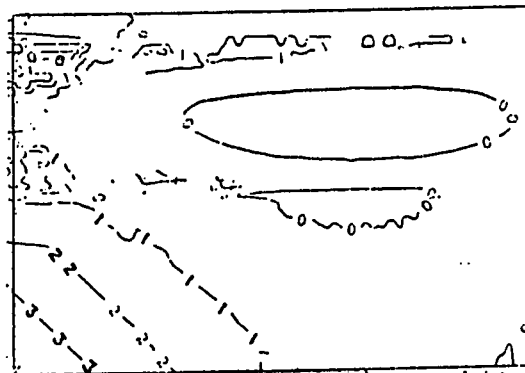
e) SAPMV   Fac = 2.0

Figure 7.147. PMV contours for the standing posture in
the X-Z plane at noon, Tin = 10 °C and
Uin = 1.9 m/sec. for the NE configuration.

7.3 The Percentage of Comfort Attained by the Various Configurations

In the previous subsections a detailed account of the variables describing the flow field has been given, together with distributions of the PMV indices within the occupied zone of the room. But to make a definite and decisive judgement on how much a particular room configuration and boundary condition satisfy comfort, a check is made on the value of the PMV at each node within the occupied space of the room and if at least 80% of the occupants are comfortable, corresponding to a |PMV| of 0.8, or at most 20% of the Percentage of People Dissatisfied (PPD), see Fig. 5.12, then the room for the prevailing conditions are claimed to be comfortable [7 , 51]. A table of this for the various configurations and boundary conditions listed above is given below in Table 7.5, such that the first run attempted and the run attaining the 'best' comfort are reported. It should be noted that for most of the different configurations and boundary conditions listed, the achievement of 100% comfortability (i.e., 20% PPD) was not possible, although numerous attempts have been made.

The computer facilities employed to execute the runs listed in Table 7.5 is an IBM-3090 mainframe computer.

It should be noted that the absolute residual source sum attained for the SN configuration remains larger than in the other configurations investigated which may be on account of the fact that the air jet leaving the inlet is acting against the force of gravity and thus the resultant air jet will tend to flow at an angle as the flow progresses upwards, and probably what is known as *false diffusion* , described in detail by Patankar [43], might have a serious affect on convergence.

Table 7.5: The various configurations and resulting occupancy comfort

Configu-ration	Time of Day	T_{in} (°C)	U_{in} (m/sec.)	CPU (min.)	No. of itera-tions	Absolute Residual Source Sum	Code Number	Percentage of People Achieving PMV=|0.8|	
								Sitting Posture	Standing Posture
WE	9 A.M.	15.0	1.9	13.0	752	0.05	WE01	97.6	97.5
WE	9 A.M.	18.0	1.9	13.35	773	0.05	WE02	100.0	100.0
WE	12 Noon	15.0	1.9	12.3	717	0.05	WE03	27.2	28.6
WE	12 Noon	12.0	3.0	22.5	1357	0.05	WE04	100.0	99.5
WE	3 P.M.	15.0	1.9	12.1	699	0.05	WE05	0.0	0.0
WE	3 P.M.	10.0	4.0	28.8	1748	0.05	WE06	98.5	98.0
NN	9 A.M.	15.0	1.9	13.0	702	0.05	NN01	93.3	93.9
NN	9 A.M.	22.0	1.9	19.0	1146	0.05	NN02	99.4	99.0
NN	12 Noon	15.0	1.9	13.4	799	0.05	NN03	23.0	22.2
NN	12 Noon	10.0	2.2	19.5	1166	0.05	NN04	96.6	95.6
NN	3 P.M.	15.0	1.9	16.3	975	0.05	NN05	2.0	2.2
NN	3 P.M.	15.0	3.5	29.4	1832	0.067	NN06	93.5	94.6
SN	12 Noon	15.0	1.9	37.8	2340	0.093	SN01	95.1	92.6
SN	12 Noon	15.0	2.8	49.3	2700	0.1	SN02	100.0	99.6
NE	12 Noon	15.0	1.9	28.9	1628	0.95	NE01	60.0	52.5
NE	12 Noon	10.0	1.9	24.9	1531	0.062	NE02	95.2	94.5

By simple comparisons of Table 7.5 we note the following :

i. The WE configuration required relatively more energy to be expended than the NN configuration (see Table 7.5), such that at 9 A.M., the T_{in} (at WE02) is much lower in the WE than in the NN (at NN02) for identical U_{in} to achieve an acceptable level of comfort. At 12 Noon, although the T_{in} (at WE04) for the comfortable situation is slightly higher than the T_{in} (at NN04), but the U_{in} in the former is larger than that in the latter. At 3 P.M., the T_{in} (at WE06) is much lower than the T_{in} (at NN06) and the U_{in} is larger in the former than in the latter.

ii. As the location of the inlet opening for the NN configuration is such that if the U_{in} is large enough than the air jet will directly pour into the occupied zone and thus relatively moderate changes in the magnitude of U_{in} for the NN configuration is directly felt within the occupied zone of the room, in comparison to the WE configuration where the bulk of the air jet passes along the upper edge of the occupied zone. This effect is obvious when comparing WE06 and NN06 where in the former a few runs were required to achieve the comfort listed in Table 7.5, but in the latter, the author, after conducting numerous runs, was not able to achieve a level of comfort comparable to that of the WE06. This is also obvious when comparing the NN and WE for the other times.

iii.   In practical engineering situations, the variations in the U_{in} and T_{in} for the corresponding changes of the time of day, necessary to achieve comfort, is difficult attain exactly, furthermore as NN is relatively more sensitive to changes at the inlet conditions; therefore, uncomfortable responses would be anticipated from the NN configuration more frequently than from the WE configuration .

iv.   The SN configuration required, relatively moderate effort in attaining a T_{in} and U_{in} that achieve an acceptable level of comfort. The U_{in} at SN02 is relatively higher than that in NN04 so that most of the air will probably flow to a height above the occupied zone and consequently the majority of the air movement in the occupied zone is not directly from the air jet.

v.   The comfort level attained in the NE configuration at Noon (NE02) is, relatively the lowest, the reason for this is most probably due to the fact that the affect of the air jet from the inlet opening is similar to that by NN, described above, causing the bulk of the air jet directly from the inlet to penetrate into the occupied zone. Furthermore, the outlet is now at the bottom of the East wall so that this will inspire the air jet to be drawn even further into the occupied zone and thus the sensitivity to the conditions at the inlet opening is more pronounced here.

7.4 Grid Study

The grid size used in all runs up to this point is a 20x20x11 grid in the x, y and z directions, respectively. There have been attempts to use larger and smaller grid sizes and observing the resulting effect this will have on the resulting occupancy comfort. This is given in Table 7.6. It should be mentioned here that in view of the different grid sizes employed, the corresponding Absolute Residual Source Sum (ARSS) used will vary according to the number of grid points for the particular grid studied so that the 13x13x11 grid has 1859 grid points while the 20x20x11 grid has 4400 grid points and the ARSS employed in the latter grid size was 0.05, thus assuming a linear relationship between the two grid sizes listed, we would require the ARSS for the former grid to be approximately 0.02 and similar reasoning follows for the other grid sizes listed in Table 7.6. Comparing the percentage of people having | PMV | ≤ 0.8 we may notice the results for all grids considered are nearly similar that in the sitting posture for the 13x13x11 grid size but for the remaining grids listed in Table 7.6, the results are fairly close. It should be noted that no effort has been expended on varying the Under Relaxation Factor (URF), described earlier, for the various grid sizes employed, except in the 20x20x11 grid, such that the values of the URFs depends on many parameters, one of which is the grid size of the flow field. Therefore, the CPU time and number of iterations listed in Table 7.6 for the various grid sizes may be reduced by obtaining a 'best' group of URFs. It should be mentioned here that investigations were made using the same grid size (i.e. : 20x20x11) but changing the value of the ARSS.

TABLE 7.6 : The different grid sizes investigated

Configu-ration	Time of Day	T_{in} (°C)	U_{in} (m/sec.)	CPU (min.)	No. of Itera-tions	ARSS	Grid Size	Percentage of people Achieving PMV=$[0.8]$	
								Sitting Posture	Standing Posture
WE	9 A.M.	15.0	1.9	14.5	2370	0.01	13X13X11	92.3	96.1
WE	9 A.M.	15.0	1.9	18.3	1760	0.01	15x15x11	97.1	96.8
WE	9 A.M.	15.0	1.9	13.0	752	0.05	20x20x11	97.6	97.5
WE	9 A.M.	15.0	1.9	24.8	630	0.08	20x20x19	97.5	97.5
WE	9 A.M.	15.0	1.9	48.0	450	0.13	25x25x19	97.5	97.3

7.5   Results of the Investigations of a Different Scheme and Algorithm

The algorithm employed in the source code is the SIMPLE algorithm, described earlier, and an attempt to introduce the SIMPLER algorithm [46]. was not successful as the author made numerous runs but the results were unstable and prone to divergence thus it was concluded that the SIMPLER algorithm proved inappropriate to investigations similar to the ones conducted in this research.

The power-law finite difference scheme recommended by Patankar [43]. has been tested in this source code instead of the hybrid scheme, described earlier, but the CPU time needed to achieve identical ARSS was relatively higher in the power-law scheme than that in the hybrid scheme, which may probably be due to the extra effort required by the computer to process the terms containing the exponent and, therefore, the hybrid scheme was kept.

CHAPTER VIII

CONCLUSIONS AND RECOMMENDATIONS

In view of what has been investigated in this research the following conclusions are made :

1. The TEACH-3D source code, employed in this research, is a relatively powerful program; yet, the fashion in which it was written is easy to comprehend and thus making any adjustments or modifications possible.

2. Results of an experimental set-up, done by others, was simulated by the code and compared favourablly to the empirical measurements .

3. The NN configuration at all times considered (i.e., NE02,NE04 and NE06) performed relatively better than the corresponding WE configuration (i.e.: WE02, WE04,WE06) from a stand point of energy efficiency (i.e.: lower values of T_{in} and U_{in} were required to achieve comfort.) .

4. The occupancy comfort response, in terms of PMV indexes, is more favourable in the WE configuration than in the NN configuration .

5. The occupancy response in the NN and NE configurations are very sensitive to relatively minor changes to the T_{in} and U_{in}.

6. The SN configuration performed 'best' regarding the occupancy comfort response .

7. The occupancy comfort response to the NE configuration (NE02) was, relatively the worst .

8. For the NN and NE configurations it was not possible to achieve a better occupancy comfort response than those listed in Table 7.5.

9. The SIMPLER algorithm and power-law scheme are not suitable for room ventilation investigations similar to those conducted here.

10. At various sizes of the grid the occupancy response was similar, except for the 13X13X11 grid size, whereas the CPU time expended was always greater than that of the original 20X20X11 grid size.

11. Increasing the Absolute Residual Source Sum(ARSS) by 20 % reduced the CPU time required to converge by about 10 % , with no serious difference in the resulting occupancy response.

RECOMMENDATIONS :

For the specific investigations conducted here, some recommendations are as follows :

1. It is recommended not to employ the SIMPLER algorithm and/or the power-law scheme.

2. The SN or WE configurations are recommended over the others to attain an acceptable level of comfort.

3. Saving of CPU time may be made by using a moderately larger ARSS at the cost of minor changes on the results of the computed occupancy comfort .

4. Relatively large values of U_{in} in the NN and NE configurations are discouraged.

5. Relatively low values of U_{in} in the SN configuration is also discouraged.

6. Inlet openings in the SN, NE and NN configurations should be kept flush with the side walls.

7. The inlet opening in the WE configuration should be kept close to the ceiling and higher than the upper edge of the occupied zone.

NOMENCLATURE

A   Control volume surface area.

A_{Du} Du Bois area : surface area of the human body.

A_{eff} Effective radiation area of the human body.

AMAX1(,)   Maximum value of the parameters within brackets.

A_o Surface area of the inlet opening.

A_p Projected surface area of the human body.

Ar   Archimedes number.

a   Coefficient of the discretization equation.

b   Constant term in the discretization equation.

C_1 , C_2 , C_D
and C_μ Constants used in the k- ϵ turbulence model.

C_p Specific heat of air at constant pressure.

c′   Term used in the Line-By-Line(LBL) method.

D   Diffusion conductance across the face of a control volume.

d	Coefficient of the pressure correction equation.
d_i	Second derivative of $S_i(x)$ in the cubic-spline method.
E	Friction coefficient used in the log-law, and equals 9.793.

EXPX, EXPY and EXPZ   Grid expansion coefficient in the x, y and z directions, respectively.

E_d	Heat loss by water vapor diffusion through skin.
E_{sw}	Heat loss by evaporation of sweat from skin.
E_{re}	Latent respiration heat loss.
e	Emitance of the outer surface of the clothed body.
F	Angle factor. Mass flow rate across the face of a control volume.
f_{cl}	Ratio of the surface area of the clothed body to the nude body.
f_{eff}	Ratio of the effective radiation area of the clothed body to the total surface area of the body.
f_p	Projected area factor of the human body.

g	Gravitational acceleration.
g_i	Gravitational acceleration in the x_i direction.
H	Internal heat production of the human body.
H_ε	Height of the room or square root of the cross-sectional area of the room, normal to the inlet opening.
h	Height of the human body.
h_c	Convective heat transfer coefficient.
h_i	Term used in the cubic-spline method, and equals the spacing between two adjacent grid nodes.
I	Inertia relaxation factor.
I_{cl}	Intrinsic insulation and represents the thermal resistance from the skin to the outer surface of the clothed body.
I_u	Turbulence intensity used in the k-ε turbulence model.
J_x, J_y and J_z	Total(convection + diffusion) fluxes acting on the x, y and z control volume surfaces, respectively.
K	Dry heat transfer from the skin to the outer surface of the clothed body.

k	Turbulent kinetic energy.
L	Dry respiration heat loss from the human body. Turbulent length scale.
L_o	Human body thermal load.
M	Metabolic rate of human body.
m	Permeance coefficient of the skin.
NI, NJ and NK	Number of grid nodes in the x, y and z directions, respectively.
Pe	Peclet number.
p	Pressure.
p'	Pressure correction.
p_a	Partial pressure of water vapor in ambient air.
p_s	Saturated vapor pressure at skin temperature.
Q_c	Heat loss by convection from the outer surface of the clothed body.
Q_r	Heat loss by radiation from the outer surface of the clothed body.

q_w Heat flux at the wall surface.

R Residual source sum of the discretized equation.

Re Reynolds number.

r_m Distance from center of person to wall, used in angle factor calculations.

S_i Cubic spline polynomial.

Momentum source term in the x_i direction.

S_l Constant used in Sutherlands theory of viscosity, equal to 110 °K for air.

S_T Heat generation source term due to viscous dissipation.

S_Φ Source term in the general differential equation.

$S_{\Phi,c}$ Constant part of S_Φ.

$S_{\Phi,p}$ Coefficient of Φ.

T Temperature.

T_a Temperature of air.

T_{cl} Mean temperature of outer surface of clothed body.

T_{mrt} Mean radiant temperature.

T_s	Mean skin temperature.
T_w	Temperature at wall surface.
T^+	Dimensionless Temperature.
t	Time.
t_i	Distance between the center of a human body and a wall, used in the cubic-spline method.
Δt	Time increment.
U	Time mean velocity component in the x direction.
U_i	Instantaneous velocity component in the x direction.
U_τ	Friction velocity.
U^+	Dimensionless velocity.
U'	Velocity correction in the x direction.
u_i	Fluctuating velocity component in the x direction.
V	Time mean velocity component in the y direction.
$\vec{V}$	Resultant velocity vector parallel to wall.
V'	Velocity correction in the y direction.

W   Time mean velocity component in the z direction.

     External mechanical work of human body.

W' Velocity correction in the z direction.

w   Human body mass.

x, y, z   Coordinate directions.

x_i Coordinate direction in tensor notation.

Δx , Δy

and Δz Widths of the control volume in the x, y and z directions, respectively.

δx , δy

and δz Distances between two adjacent grid points in the x, y and z directions, respectively.

y_i Term used in the cubic-spline polynomial, to represent the angle factor.

y^+ Local Reynolds number.

Greek symbols

α — Constant used to evaluate the inertia relaxation factor, and equal to 0.2.

β — Volumetric expansion coefficient.

Γ — Laminar diffusivity of heat.

Γ_k — Diffusion coefficient in turbulent kinetic energy.

Γ_t — Turbulent diffusivity of heat.

Γ_ε — Diffusion coefficient in the dissipation of turbulent kinetic energy.

Γ_Φ — Diffusion coefficient for Φ.

$\delta_{i,j}$ — Kronecker delta(0 if $i \neq j$ and 1 if $i = j$).

δ_{tol} — Tolerance used in estimating T_{cl}.

ε — Dissipation of turbulent kinetic energy.

η — External mechanical efficiency of human body.

κ — Von Karmans constant, equal to 0.4187.

λ — Thermal diffusivity.

λ_d Heat of vaporization of water.

λ_ε Turbulence constant equal to 0.005.

μ Dynamic laminar or molecular viscosity.

μ_t Turbulent or Eddy viscosity.

v Kinematic molecular viscosity.

ρ Density of air.

σ Stefan-Boltzmans constant and equal to

$4.96 \cdot 10^{-8}$ kcal/ $m^{2} \cdot K^{4}$.

Viscous laminar number used in the log-law of the wall

and is represented by $C_p \cdot \mu / \lambda$.

σ_k Empirical constant used in the k- ε turbulence model.

σ_t Empirical constant used in the k- ε turbulence model.

Turbulent Prandtl number.

σ_ε Empirical constant used in the k- ε turbulence model.

τ_w Wall shear stress.

Φ General dependent variable.

Subscripts

B   Buoyancy.

E   Adjacent grid node neighbour in the positive x direction, on the East side of the grid point under study.

e   Exit port.
East surface of control volume cell between grid points P and E.

i, j, k   Summation indicies.

i   Inlet port.

L   Adjacent grid node neighbour in the negative z direction, on the Left side of the grid point under study.

l   Left surface of control volume cell between grid points P and L.

N   Adjacent grid node neighbour in the positive y direction, on the North side of the grid point under study.

n   North surface of control volume cell between grid points P and N.

o   Outlet port.

P   Central grid node of control volume under study.

R   Adjacent grid node neighbour in the positive z direction, on the Right side of the grid point under study.

r   Right surface of control volume cell between grid points P and R.

S   Adjacent grid node neighbour in the negative y direction, on the South side of the grid point under study.

s   South surface of control volume cell between grid points P and S.

T   Temperature.

t   Turbulent.

W   Adjacent grid node neighbour in the negative x direction, on the West side of the grid point under study.

w   West surface of control volume cell between grid points P and W.

Superscripts

‾ Time mean value.

* Previous iteration or guessed value of a variable.

ʹ Fluctuation of a variable.

Correction of a variable.

REFERENCES

1. Hinze, J.O., *Turbulence*, 2nd Edition, McGraw-Hill Book Company, New York, 1975.

2. Schlichting, H. *Boundary Layer Theory*, 7th Edition, McGraw-Hill Book Company, New York, 1979.

3. Rodi, W., *Turbulence Models and Their Application in Hydraulics*, 2nd Edition, International Association of Hydraulic Research, Monograph, Delft, The Netherlands, 1984.

4. Murakami, S., S. Kato and Y. Suyama, *Three-Dimensional Numerical Simulation of Turbulent Airflow in a Ventilated Room by Means of a Two-Equation Modsel*, ASHRAE Transactions, Volume 93, Part 2, 1987.

5. Davidson, Lars, *Numerical Simulation of Turbulent Flow in Ventilated Rooms*, Ph.D. Thesis, Chalmers University of Technology, Goteborg, Sweden, 1989.

6. Restivo, A.M., *Turbulent Flow in Ventilated Rooms*, Ph.D. Thesis, Imperial College of London, 1979.

7. Fanger, P.O., *Thermal Comfort*, Robert E. Krieger Publishing Co., Malbar, Florida, 1982.

8.   Fanger, P.O., *Calculation of Thermal Comfort : Introduction of a Basic Comfort Equation*, ASHRAE Transactions, Volume 73, Part 2, 1967.

9.   Gagge, A.P., J.A.J. Stolwijk and Y. Nishi, *An Effective Temperature Scale Based on a Simple Model of Human Physiological Regulatory Response*, ASHRAE Transactions, Volume 70, Part 1, 1970.

10.   Berglund, Larry, *Mathematical Models for Predicting the Thermal Comfort Response of Building Occupants*, ASHRAE Transactions, Volume 84, Part 1, pp.735-749, 1978.

11.   Rolloos, M., *Possibilities and Limitations for the Prediction of Air Flow Patterns, Temperatures and Velocities in Large Halls Using Scale Models.* Proceedings of the Meeting of Commission E1 of the International Institute of Refrigeration, pp.245-256, Belgrade, 1977.

12.   Neilson, P.V., *Flow in Airconditioned Rooms*, Ph.D. Thesis, Technical University of Denmark, Copenhagen, 1974.

13.   Holmberg R., Larsson, M. and Sundqust, S.G., *Calculation of Velocity Distribution in a Ventilated Room*, V.V.S., Stockholm, No. 10, 1975.

14.   Gosman, A.D., W.K. Pun, A.K. Runchal, D.B. Spalding and M. Wolfshtein, *Heat and Mass Transfer in Recirculating Flows*, Academic Press, London and New York, 1969.

15. Launder, B.E. and D.B. Spalding, *The Numerical Computation of Turbulent Flows*, Journal of Computer Methods in Applied Mechanics and Engineering, Volume 3, pp.269-289, 1974.

16. Hjertager, B.H. and B.F. Magnussen, *Numerical Prediction of Three-Dimensional Turbulent Buoyant Flow in Ventilated Rooms*, in Heat Transfer and Turbulent Buoyant Convection, edited by : Spalding, D.B. and N.H. Afgan, Hemisphere Publishing Corporation, pp.429-441, 1977.

17. Neilson, P.V., A. Restivo and N.H. Whitelaw, *The Velocity Characteristics of Ventilated Rooms*, Transactions of the ASME Journal of Fluids Engineering, Volume 100, pp.291-298, September, 1978.

18. Larsson, M., and R. Holmberg, *Calculations of Thermally-influenced Movements of Air in a Ventilated Room*, V.V.S. Stockholm, Vol.48, pp.115-117, 1977.

19. Neilson, P.V., A.M. Restivo and J.H. Whitelaw, *Buoyancy Affected Flows in Ventilated Rooms*, Numerical Heat Transfer, Volume 2, pp.115-127, 1979.

20. Gosman, A.D., P.V. Neilson, A.M. Restivo and J.H. Whitelaw, *The Flow Properties of Rooms with Small Ventilation Openings*, Transactions of the ASME Journal of Fluids Engineering, Volume 112, pp.316-323, 1980.

21. Sakamoto, Y. and Y. Matsuo, *Numerical Predictions of Three-Dimensional Flow in a Ventilated Room Using Turbulence Models.* Applied Mathematical Modelling, Volume 4, February, pp.67-72, 1980.

22. Harlow, F.H. and J.E. Welsh, *Numerical Calculations of Time-Dependent Viscous Incompressible Flow of Fluid With Free Surface,* The Physics of Fluids, Vol.8, pp.2182-2189, 1965.

23. Lilly, D.K. *The Representation of Small Scale Turbulence in Numerical Simulation Experiments,* Proc. IBM Sci. Comp. Symp. on Env. Sci., IBM-FORM No. 320-1951, pp.195-210, 1967.

24. Deardorff, J.W. *A Numerical Study of Three-Dimensional Turbulent Channel Flow at Large Reynolds Number,* J. Fluid Mech., Vol.41, pp.452-480, 1970.

25. Hjertager, B.H., and B.F. Magnussen, *A Numerical Study of Three-Dimensional Jet Induced Flow in Rectangular Enclosures,* Computers and Fluids, Volume 9, No.4, pp.395-407, 1981.

26. Markatos, N.C. *Computer Analysis of Building-Ventilation and Heating Problems.* CHAM Internal Report No.TR/92, May 1983.

27. Spalding, D.B. *A General Purpose Computer Program for Multi-dimensional one- and two- phase flow.* Mathematics and Computers in Simulation, XXIII, pp. 267-276, 1981.

28. Kato, S. and S. Murakami, *Three Dimensional Numerical Simulation of Turbulent Air Flow in Ventilated Room, By Means of 2-Equation Model*, Int. Symp. on Computational Fluid Dynamics, Tokyo, pp.560-571, 1985.

29. Whittle, G.E., *Computation of Air Movement and Convective Heat Transfer Within Buildings*, Int. J. of Ambient Energy, Vol.7, No.3, pp.151-164, July, 1986.

30. Alamdari, F., G.P. Hammond and W.S. Mohammad, *Computation of Air Flow and Convective Heat Transfer Within Space-Conditioned, Rectangular Enclosures*, Proceedings of the 5th International Symposium on the Use of Computers for Environmental Engineering Related to Buildings, Bath, pp.191-205, 1986.

31. Gosman, A.D., and W.M. Pun, *Calculation of Recirculating Flows*, Mech. Engg. Dept., Report HTS/75/2, 2nd edition, Imperial College of Science and Technology, London, 1974.

32. Gosman, A.D., and F.J.K. Ideriah, *TEACH-T : A General Computer Program for Two-Dimensional, Turbulent, Recirculating Flows*, Dept. of Mech. Engg., Imperial College of Science and Technology, London, 1976.

33. CIBSE Guide A5 : *Thermal Response of Buildings*, CIBSE, London, England, 1979.

34. Qingyan, C. and J. Vander Kooi, *Measurements and Computations of Air Movement and Temperature Distribution in a Climate Room*, 17th Int. Congress on the Developments in Refrigeration, pp.23-28, 1987.

35. Pun, W.M. and D.B. Spalding, *A General Computer Program for Two-Dimensional Elliptic Flows*, HTS/76/2 Imperial College of Science and Technology, London, 1976.

36. Kurabuchi, T. and T. Kusuda, *Numerical Prediction for Indoor Air Movement*, ASHRAE Journal, pp.26-30, December 1987.

37. Davidson, Lars and E. Olsson, *Calculation of Some Parabolic and Elliptic Flows Using a New One-Equation Turbulence Model*, Proc. of the 5th Int. Conf. on Numerical Methods in Laminar and Turbulent Flow, Montreal, Vol. 1, pp.411-422, 1987.

38. Galpin, P.F. and G.D. Raithby, *Numerical Solution of Problems in Incompressible Fluid Flow : Treatment of the Temperature-Velocity Coupling*, Numerical Heat Transfer, Vol.10, p.,105, 1986.

39. Van Doormaal, J.P. and G.D. Raithby, *Enhancements of the SIMPLE Method for Predicting Incompressible Fluid Flow*, Numerical Heat Transfer, Vol.7, pp. 147-163, 1984.

40. Awbi, H.B., *Application of Computational Fluid Dynamics in Room Ventilation*, Building and Environment, Vol.24, No.1, pp. 73-84, 1989.

41. Davidson, Lars, and E. Olsson, *Calculation of Age and Local Purging Flow Rate in Rooms* Building and Environment, Vol.22, No.2, pp.111-127, 1987.

42. Larsson, M., *Predictions of Buoyancy Influenced Flow in Ventilated Industrial Halls*, Proc. of Heat Transfer in Buildings, Durbrovnik, 1977.

43. Patankar, S.V., *Numerical Heat Transfer and Fluid Flow*, McGraw-Hill Book Co., New York, 1980.

44. Patankar, S.V., and D.B. Spalding, *A Calculation Procedure for Heat, Mass and Momentum Transfer in Three-Dimensional Parabolic Flows*, Int. Journal of Heat and Mass Transfer, Vol.15, pp.1787-1806, 1972.

45. ROOMVENT, Air Distribution in Ventilated Spaces, Stockholm, Sweden, June, 1987.

46. Patankar, S.V. *A Calculation Procedure for Two-Dimensional Elliptic Situations*, Numerical Heat Transfer, Vol.4, pp.409-425, 1981.

47. Patankar, S.V. and D.B. Spalding *Heat and Mass Transfer in Boundary Layers*, 2nd edition, Intertext, London, 1970.

48. Hammond, G.P., *Turbulent Prandtl Number Distribution Within the Constant Stress/Heat-Flux Region of a Near Wall Flow*, SME Report No.8401, School of Mec. Engg., Cranfield Institute of Technology, Bedford, U.K., January, 1984.

49. Hammond, G.P., *Turbulent Prandtl Number Within Near-Wall Flow*, AIAA Journal, Vol.23, No.11, pp.1668-1669, Nov. 1985.

50. Nishi, Y., *Field Assessment of Thermal Characteristics of Man and His Environment by Using a Programmable Pocket Calculator*, ASHRAE Transactions, Vol.83, pt.1, pp.103-124, 1977.

51. ASHRAE Standard, *Thermal Environmental Conditions for Human Occupancy*, ANSI/ASHRAE 55-1981.

52. Davidson, Lars and P. Hedberg, *A General Computer Program for Transient, Three-Dimensional, Turbulent, Recirculating Flows*, Report No. 86/13, Department of Applied Thermodynamics and Fluid Mechanics, Chalmers University of Technology, Goteborg, Sweden, December 1986.

53. Kays, W.M. and M.E. Crawford, *Convective Heat and Mass Transfer*, Second edition, McGraw-Hill Book Co., 1980.

54. Hossain, M.S. and W. Rodi, *Equations for Turbulent Buoyant Flows and Their Modelling*, Report SFB 80/T/46, December 1974, Karlsruhe University.

55. Launder, B.E. and D.B. Spalding, *Lectures in Mathematical Models of Turbulence*, Academic Press, 1972.

56. Turbulence, Editor P. Bradshaw, *Topics in Applied Physics*, Volume 12, Published by Springer-Verlag, 1976.

57. Hjertager, B.H., *Three-Dimensional Modelling of Flow, Heat Transfer, and Combustion*, in Handbook of Heat and Mass Transfer, Gulf Publishing Co., 1986.

58. Patel, M.K., Markatos, N.C. and Cross, M., *A Critical Evaluation of Seven Discretization Schemes for Convection-Diffusion Equations*, Int. J. for Numerical Methods in Fluids, Vol. 5, pp. 225-244, 1985.

59. Patel, M.K. and Markatos, N.C., *An Evaluation of Eight Discretization Schemes for Two-Dimensional Convection-Diffusion Equations*, Int. J. for Numerical Methods in Fluids, Vol. 6, pp. 129-154, 1986.

60. Connell, S.D. and P. Stow,

   The Pressure Correction Methods, J. of Computers and Fluids, Vol. 14, No. 1, pp. 1-10, 1986.

61. Jang, D.S., R. Jetli and S. Acharya, *Comparison of the PISO, SIMPLER and SIMPLEC Algorthims for the treatment of the Pressure-Velocity Coupling in Steady Flow Problems*, J. of Numerical Heat Transfer, Vol. 10, pp. 209-228, 1986.

62. Raithby, G.D. and G.E. Schneider, *Numerical Solution of Problems in Incompressible Fluid Flow: Treatment of the Velocity - Pressure Coupling*, J. of Numerical Heat Transfer, Vol. 2, No. 2, pp. 417-440, 1979.

63. Pachner, Jaroslav, *Handbook of Numerical Analysis Applications with Programs for Engineers and Scientists*, McGraw-Hill Book Co., New York, 1984.

64. Cheny, Ward and David Kincaid, *Numerical Mathematics and Computing,* Books/Cole Publishing Co., 1980.

65. ASHRAE Handbook of Fundamentals, *Physiological Principles for Comfort and Health,* pp. 8.1 - 8.32, Chapter 8, 1985.

66. Azer, Naim Z., Sungnan Hsu, *The Prediction of Thermal Sensation from a Simple Model of Human Physiological Regulatory Response,* ASHRAE Transactions, Vol. 80, Part 1, pp. 88-102, 1977.

67. Incropera, Frank P. and David P. DeWitt, *Fundamentals of Heat Transfer,* John Wiley and Sons, New York, 1981.

68. Thomas, Lindon C. *Fundamentals of Heat Transfer,* Prentice-Hall Inc., 1980.

69. Syed, Saadat A. and Chiappetta, Louis M. *Finite Difference Methods for Reducing Numerical Diffusion in TEACH-Type Calculations,* Paper No. AIAA-85-0057, AIAA 23rd Aerospace Sciences Meeting, Reno, Nevada, 1985.

70. Ideriah, F.J.K., *Prediction of Turbulent Cavity Flow Driven by Buoyancy and Shear,* J. of Mechanical Engineering Science, Vol. 22, pp. 287-295, 1980.

VITA

ADEL SULAIMAN HAMAD AL-HAMED

Candidate for the Degree of

Master of Science in Mechanical Engineering

Thesis : *DETERMINING VELOCITY, TEMPERATURE AND OCCUPANCY COMFORT WITHIN A 3-D. ROOM.*

Biographical :

Personal Data : Born in Khobar, Saudi Arabia, June 12, 1961.

Education : Graduated from Dammam High School in 1979; received the Bachelor of Science degree from King Fahd University of Petroleum and Minerals, with a major of Civil Engineering in 1983.

Professional Experience : Assistant Engineer in S.H. Consulting Firm, 1983-1984; graduate assistant, King Fahd University of Petroleum and Minerals, 1984-1990.